

UNIVERSITÉ DU QUÉBEC
INSTITUT NATIONAL DE LA RECHERCHE SCIENTIFIQUE
CENTRE EAU TERRE ENVIRONNEMENT

**AMPHIBOLITE FACIES GOLD MINERALIZATION: AN EXAMPLE FROM
THE ROBERTO DEPOSIT, ELEONORE PROPERTY, JAMES BAY,
QUEBEC**

Par

Jean-François RAVENELLE

Thèse présentée pour l'obtention du grade de *Philosophiæ Doctor*, Ph.D.
en sciences de la Terre

Jury d'évaluation

Examineurs externes

Dr. Michel Gauthier
Université du Québec à Montréal

Dr. Robert Moritz
Université de Genève

Examineurs internes

Dr. Patrick Mercier-Langevin
Commission géologique du Canada

Dr. Léopold Nadeau
Commission géologique du Canada

Directeur de recherche

Dr. Benoit Dubé
Commission géologique du Canada

Codirecteur de recherche

Dr. Michel Malo
INRS Eau Terre Environnement

© droits réservés de Jean-François RAVENELLE, 2013



ACKNOWLEDGMENTS

This study would not be completed without the guidance of my supervisor Benoit Dubé. Thank you Benoit for all the time and effort invested in this project, for the numerous weeks spent with me in the field, for your constant encouragements, and for the valuable scientific and personal mentorship provided during the past years. Special thanks to my supervisor Michel Malo as well as Léopold Nadeau for your constant academic and personal support throughout this study.

Thank you to the entire staff at Opinaca Mines for your constant logistical support and camaraderie, especially to Jacques Simoneau, Nathalie Prud'homme, Jorge Ortega, Julie Doyon, and Peter Lauder. Thank you to Hervé Thiboutot for your scientific interest and for your plan to strip the very large outcrop. This study would not have been possible without André Gaumond and Paul Archer at Virginia Mines who gave us the opportunity to undertake the study. Thank you to Virginia Mines' geology team for your constructive input. Thank you to Vicki McNicoll from the Geological Survey of Canada for your significant contribution and excellent work on the geochronology. Thank you to Michel Gauthier from the Université du Québec à Montréal for your constructive input and for sharing your knowledge of the James Bay region. Thank you to Daniel Bandyayera and your team from the Ministère des Ressources Naturelles et de la Faune du Québec for giving us the opportunity to be involved in your study.

I am grateful to all organizations who financially supported this study, including the Natural Sciences and Engineering Research Council (NSERC), Goldcorp Inc./Opinaca Mines Ltd., Virginia Mines Inc., the Geological Survey of Canada (GSC), the Institut National de la Recherche Scientifique (INRS), the Prospectors and Developers Association of Canada (PDAC), the Geological Association of Canada (GAC), and the Consorem.

Thank you to my family for your constant support and encouragements, for your patience, and for always believing that all sacrifices were worth doing. Special thanks to my wife Christine for supporting me at all times, for your positive attitude, and for foreseeing the value in all tough situations. Thanks to my kids Maya and Maxim for inspiring and motivating me to complete this work.



ABSTRACT

The Roberto gold deposit represents one of the most significant gold discoveries of the past 10 years in Canada. The latest resource estimation (publicly released in February 2010) indicated a total of more than 9 million ounces (280 t) of inferred (6.25 Moz, 194 t) and indicated resources (3.15 Moz, 98 t). The geology of the Roberto deposit differs from most Archean gold deposits of the Superior Province. After initial inspection of the deposit prior to this study, it was recognized that it could not clearly be identified as a typical quartz-carbonate gold deposit or as a gold deposit that formed at shallower depth. It was also recognized that the geological context of the deposit is complex, being characterized by stockwork and replacement-style mineralization hosted within highly deformed and metamorphosed turbiditic metagreywacke and paragneiss. The Roberto deposit is a landmark for future gold exploration within the under-explored northern part of the Superior Province. However, being an atypical gold deposit, the key geological parameters involved in its genesis need to be identified in order to understand its formation and define exploration criteria that will help discover similar gold deposits in the James Bay territory and elsewhere in amphibolite-grade terranes of the Superior Province.

The purpose of this thesis is to present a geological description of the Roberto gold deposit and provide insights on geological features that played a role in its formation. Using regional and local geological mapping, structural analysis, 3D modelling, core logging, petrography, and geochronology, efforts are focused on acquiring an understanding of the regional geology, the relative ages of the main lithological units, the geochemical characteristics of the deposit, and the relative timing between gold mineralization, deformational events, and magmatic phases.

The Roberto deposit is located on the Éléonore property which straddles the contact between the Archean metasedimentary Opinaca Subprovince and the volcano-plutonic La Grande Subprovince. The main deformation responsible for regional metamorphism and the predominant east-west structural fabric is attributed to D_2 within both subprovinces. The Opinaca Subprovince is a migmatite terrane with metamorphic grade reaching the granulite facies. The metamorphic grade in the La Grande Subprovince ranges from greenschist to amphibolite facies. The presence of widespread conglomeratic sequences within the La Grande indicates that an important uplift (potentially associated with D_1) occurred in the area. Such conglomeratic sequences may mask important deformation zones that may have played a role in the metallogenic history of the region. Further work is required in to determine whether such deformation zones juxtaposed the two terranes or whether the current terrane distribution reflects the original setting of the area.

The bulk of the auriferous system primarily occurs in a series of sub-parallel decameter-scale auriferous zones globally confined to a km-scale steeply-plunging polyfolded geometry that has been traced to more than 1500 meters below surface. Two principal auriferous zones, referred to as Roberto and East-Roberto, can be distinguished from one another based on their structural style, mineralogy, gold content, and stratigraphic position. The Roberto auriferous zone (typically averaging 12 g/t Au over 10 meters) represents the main phase of gold mineralization and consists of stockworks of K-bearing veins and veinlets and Ca-bearing quartz veins contained within K-altered thinly-bedded greywacke. The K-bearing veinlets are typically composed of quartz, microcline, dravite (Mg-rich tourmaline), biotite, arsenopyrite/löllingite, and pyrrhotite. Ca-bearing quartz veins of the Roberto zone are typically composed of quartz, amphibole, diopside, titanite, carbonate, pyrrhotite, arsenopyrite/löllingite, and locally visible gold. The East-Roberto auriferous zone (up to 8 g/t Au over 6 m) is composed of several

mineralogical assemblages that have different textural characteristics including hydrothermal breccias, veins, and zones of silica replacement. In terms of mineralogy, the Ca-bearing alteration of the Roberto and East-Roberto zones in association with microcline, tourmaline, arsenopyrite, and pyrrhotite shares analogies with the mineralogical assemblage that characterizes the gold-skarn hydrothermal signature of amphibolite-facies gold deposits such as those found in hypozonal orogenic settings.

Geochronological work indicates that a wide span of maximum ages occurs within Roberto's sedimentary sequence suggesting the presence of two sedimentary sequences. The greywacke host rock of the Roberto zone, dated at <2675 Ma (Geochron-ELE-05-08), is significantly younger than the phase of the Ell Lake diorite dated at ca. 2705 Ma (David, 2005), which rules out the hypothesis that Roberto is genetically related to the dated phase of the Ell Lake intrusion.

The Roberto deposit is affected by polyphase folding but is not hosted within a shear zone. Field observations indicate that the main part of the gold mineralization has been overprinted by D_2 and D_3 . Only in one specific location has our structural analysis enabled us to generate arguments supporting syn- D_2 ore deposition. The argument consists in the presence of a meter-scale F_2 Z-fold where Roberto's auriferous stockwork is preferentially developed in the short limb of the fold and is primarily composed of axial-planar and bedding-parallel auriferous veins and veinlets, suggesting that its formation was controlled by folding. However, since field observations commonly suggest that auriferous bodies have been overprinted by D_2 rather than being generated during active F_2 folding, it can only be concluded that the main auriferous event either occurred before or very early during D_2 . At deposit-scale, auriferous zones are confined to the F_2/F_3 refolded geometry which suggests that auriferous zones were preserved in fold hinges as opposed to being destroyed and remobilized on highly stretched limbs. F_2 and F_3 folds control the finite deposit-scale geometry of the main auriferous zones and the attitudes of ore shoots within those zones.

The mineralogy and the metamorphic textures of auriferous material suggest that the veins and disseminated ore have been generated before or during the peak of metamorphism, which agrees with the pre- to early- D_2 timing established from the structural analysis. A study of sulphide minerals with a scanning electron microscope (SEM) confirms that gold mineralization either occurred before the peak of metamorphism in association with pre-peak arsenopyrite, or precipitated with löllingite at near peak conditions.

Geochronology constrains the absolute age of the main stage of gold mineralization to occur between ca. 2675 Ma and 2603 Ma, the maximum age of Roberto's host rock and the age of a pegmatite dyke that crosscuts the main auriferous zones, respectively. Some of the pegmatite dykes that crosscut the mineralized zones are auriferous, which is interpreted to result from a contamination process caused by emplacement of dykes through mineralized material. Other pegmatite dykes are in petrogenetic continuity with auriferous quartz-feldspar veins, and crosscutting relationships between two aplite dykes and an auriferous quartz vein indicate that such dykes were broadly coeval with a part of the gold mineralization which occurred between ca. 2615 Ma and 2607 Ma. Pegmatite magmatism was therefore contemporaneous with a part of the gold mineralization and/or represents a second stage of gold mineralization.

Even though geochronological data from the Ell Lake diorite and Roberto's host rocks rules out the hypothesis that Roberto's hydrothermal system is genetically related to the Ell Lake intrusion, the potential input from magmatic fluids in generating the main part of the gold mineralization should not be discarded, as indicated by the presence of feldspar porphyry dykes dated at ca. <2680 Ma in the vicinity of the deposit.

The contrasts between the various styles of gold mineralization, from early stockwork to late pegmatitic veins, indicate that Roberto was affected by a long-lasting tectono-metamorphic event during which gold mineralization was generated, deformed, metamorphosed, and remobilized. The tectonic setting of the area represents an important clue in understanding the genesis of the Roberto deposit, and even though the origin of the low-P high-T metamorphism is unknown, a "deep-earlier" type model explains the early timing of gold mineralization relative to deformation and metamorphism. Accordingly, the potential input of metamorphic fluids should not be ruled out on the basis that gold mineralization was introduced early relative to tectono-metamorphic events. This could further suggest that Ca-bearing veins and replacement represent metamorphosed equivalents of quartz-carbonate veins and carbonate alteration typical of orogenic deposits, respectively. Targeting regions affected by large-scale folds, especially near the contact between the Opinaca and La Grande Subprovinces, might prove to be a valuable prospecting criterion.

SOMMAIRE RÉCAPITULATIF

Le gisement d'or Roberto représente l'une des découvertes les plus significatives des 10 dernières années au Canada. L'estimation de ressources la plus récente (rendue publique en février 2010) indique un total de plus de 9 millions d'onces (280 t), incluant 6,25 Moz (194 t) de ressources inférées et 3,15 Moz (98 t) de ressources indiquées (Goldcorp Inc., 2010). La géologie du gisement Roberto diffère de la plupart des gisements aurifères archéens de la Province du lac Supérieur. Suite à une analyse initiale du gisement, il a été reconnu que le gisement ne pouvait pas être clairement identifié comme un gisement orogénique typique ou comme un gisement qui s'est formé à faible profondeur comme par exemple un gisement épithermal. Il a également été reconnu que le contexte géologique du gisement est complexe, étant caractérisé par des stockwerks encaissés dans des métawackes et des paragneiss très déformés et métamorphisés. Le gisement Roberto est un point de repère pour l'exploration aurifère dans le nord de la Province du lac Supérieur. Cependant, étant un gisement aurifère atypique, les principaux paramètres géologiques impliqués dans sa genèse doivent être identifiés afin de comprendre sa formation et de pouvoir définir des critères d'exploration qui aideront à découvrir d'autres gisements similaires sur le territoire de la Baie James et ailleurs dans la Province du lac Supérieur.

Le but de cette thèse est de présenter une description géologique du gisement Roberto et de caractériser les éléments géologiques qui ont joué un rôle dans sa formation. Par l'entremise de la cartographie géologique régionale et locale, l'analyse structurale, la modélisation 3D, l'analyse de carottes de forage, et la pétrographie, les efforts sont axés sur l'acquisition d'une compréhension de la géologie régionale, des caractéristiques géochimiques du gisement, et de la chronologie relative entre la minéralisation aurifère, les épisodes de déformation, et les phases magmatiques. De plus, des travaux de géochronologie connexes sont utilisés pour déterminer les âges relatifs des principales unités lithologiques.

Géologie régionale et locale

Le gisement Roberto est situé sur la propriété Éléonore, qui chevauche le contact entre la Sous-province métasédimentaire archéenne d'Opinaca et la Sous-province volcano-plutonique de La Grande (Figure 2.1.1). La déformation principale responsable du métamorphisme régional et de la fabrique structurale prédominante orientée est-ouest est attribuée à D_2 . Les plis (P_2) sont modérément à fortement plongeants et sont serrés à isoclinaux. Des domaines d'étirement intense représentés par la présence de L-tectonites sont fréquents et indiquent que D_2 a localement causé une déformation en constriction importante. Plusieurs zones de déformation intense orientées nord-est et nord-ouest ont été cartographiées dans la Sous-province de La Grande. Ces zones de déformation montrent généralement un aplatissement intense localement associé à une linéation d'étirement bien développée en aval-pendage. Aucune évidence macroscopique ou microscopique de D_1 n'a été trouvée sur les affleurements de la région environnante du gisement. Cependant, la répétition d'unités observée sur la carte géologique de surface pourrait suggérer que D_1 a produit des plis isoclinaux à grande échelle. Une troisième génération de structure a généré des plis P_3 associés avec une fabrique de plan axial orientée est-nord-est et ouest-nord-ouest. Les plis P_3 sont couramment observés en affleurements et se distinguent par leur style plus ouvert et par le fait qu'ils plissent la foliation S_2 . Des plis P_4 sont localement documentés et sont associés à une fabrique pénétrative ou une crénulation orientée nord-ouest.

Les deux sous-provinces d'Opinaca et La Grande sont caractérisées par différents degrés de métamorphisme et un comportement rhéologique différent tel que représenté par un style de déformation plus ductile dans les roches de l'Opinaca. Il n'est pas clair, cependant, si les deux terranes sont dans leur environnement tectonique initial ou s'ils ont été juxtaposés au cours de l'évolution tectonique de la région. Aucune structure juxtaposant des roches de différents grades métamorphiques n'a clairement été reconnue près de la frontière entre les deux sous-provinces jusqu'à présent. Gauthier et Larocque (1998) décrivent le contact entre les deux sous-provinces comme étant un isograde métamorphique qui coïncide avec l'apparition d'unités paragneissiques à proximité des séquences de wacke. Cette interprétation est conforme à celle de Franconi (1978). Une interprétation alternative a été proposée par Bandyayera et al. (comm. pers., 2008) qui ont reconnu une structure linéaire dans le grain magnétique d'un récent levé magnétique aéroporté à l'échelle régionale. Cette structure linéaire pourrait indiquer la présence d'une faille entre les deux sous-provinces. Ceci est d'une importance majeure car cette structure pourrait avoir joué un rôle clé dans le développement de la minéralisation aurifère sur la propriété Éléonore qui se trouve à proximité de cette frontière.

Géologie du gisement Roberto

La majeure partie du système aurifère est confinée à une série de zones subparallèles d'échelle décamétrique qui sont contenues dans la charnière d'un pli fortement plongeant d'échelle kilométrique et qui a été tracée à plus de 1500 mètres sous la surface. Deux zones aurifères principales, appelés Roberto et Roberto-Est, se distinguent par leur style structural, leur minéralogie, et leurs teneurs en or. La géométrie du pli d'échelle kilométrique est complexe et est interprétée comme résultant de l'interférence entre des plis P_3 , P_2 , et potentiellement P_1 (Figure 3.3.29). Plusieurs zones de déformation intense de moins d'un mètre d'épaisseur et plusieurs failles cassantes recoupent le gisement et compliquent sa géométrie. Les unités lithologiques présentes à proximité du gisement Roberto comprennent des wackes, un conglomérat localement interlité avec des arénites, des roches pélitiques contenant des aluminosilicates, des schistes à biotite (localement aurifères), des formations de fer rubanées, et des paragneiss. Plusieurs âges géochronologiques ont été produits récemment au sein de la séquence sédimentaire encaissant le gisement. Ces âges varient de $<2675 \pm 6$ Ma pour la roche hôte du gisement à $<2714 \pm 2$ Ma pour le wacke massif situé à l'est de la zone Roberto-Est, suggérant la présence de deux séquences sédimentaires. Des études lithogéochimiques indiquent que les métawackes des deux séquences ont des compositions similaires. Des travaux de géochronologie indiquent également que l'âge maximal des paragneiss (ca. 2680 Ma) est dans la limite d'âge de la plus jeune séquence de wacke. Les paragneiss et les séquences de métawackes ne peuvent donc pas être distingués en fonction de leurs âges maximaux. Leur minéralogie est également semblable. Les paragneiss n'appartiennent donc probablement pas à une séquence sédimentaire différente qui a été juxtaposée aux roches sédimentaires de plus bas grade métamorphique. Les paragneiss sont plutôt interprétés comme représentant des métawackes équivalents aux wackes environnants mais de plus haut grade métamorphique.

Le gisement et les unités lithologiques environnantes sont recoupés par un important essaim de dykes de pegmatite (Figure 3.2.14). Les dykes de pegmatite sont localement aurifères et contiennent des proportions variables de tourmaline, d'arsénoopyrite, et de pyrrhotite. Ces essaims de dykes de pegmatite peuvent provenir d'une intrusion distale située relativement loin de la zone du gisement, ou peuvent encore représenter des produits distaux de la migmatisation associée à la Sous-province d'Opinaca. Des travaux de géochronologie indiquent

que le magmatisme pegmatitique a été actif pendant une période d'environ 13 millions d'années (ca. 2616 Ma à ca. 2603 Ma). Selon leur chronologie relative avec la déformation D_2 , il semble y avoir au moins deux générations de dykes de pegmatite. Les dykes de la première génération sont localement boudinés et/ou plissés par des plis P_2 , tandis que ceux de la seconde génération ne sont pas affectés par les structures D_2 . Une petite intrusion à porphyres de feldspaths est située dans la partie nord du gisement, et des dykes de même type sont localement observés.

Zone Roberto

La zone Roberto (typiquement 12 g/t Au sur 10 mètres) représente le noyau du système hydrothermal aurifère et la plus importante zone du gisement. La géométrie globale de la zone Roberto correspond à un synforme fortement-plongeant (Figure 3.2.7). Lorsqu'exposée à la surface, la zone Roberto est confinée à un wacke finement-lité délimité par des unités de wacke massif. Sa géométrie est localement plus complexe, lorsqu'elle est anastomosée et transposée par la déformation.

La zone Roberto consiste en un stockwerk de veines et de veinules de quartz riches en potassium et calcium contenues dans des wackes riches en microcline. Les veinules contenant du potassium sont généralement composées de quartz, de microcline, de dravite (tourmaline riche en Mg), de biotite, d'arsénopyrite/löllingite, et de pyrrhotite (Figure 3.5.59). Les veines de quartz contenant du calcium sont généralement composées de quartz, d'amphibole, de diopside, de titanite, de carbonate, de pyrrhotite, d'arsénopyrite/löllingite, et localement d'or visible. L'une des veines de quartz contenant du calcium est de 30 à 50 cm d'épaisseur et délimite le bord ouest de la zone Roberto sur plusieurs dizaines de mètres (Figure 3.5.61). Les régions du stockwerk de Roberto qui contiennent de hautes teneurs en or (> 20 g/t Au) sont associés à de fortes proportions de microcline fine, de dravite et d'arsénopyrite/löllingite ce qui donne une couleur brun-rosée à la roche. En carotte de forage, la minéralisation en stockwerk coïncide généralement avec une stratification bien définie caractérisée par des veinules de quartz-tourmaline et de microcline transposées en bande. Une des caractéristiques importantes du stockwerk de Roberto est que, bien que les veines et les veinules soient orientées dans plusieurs directions, elles sont couramment orientées parallèles au litage et à la foliation S_2 (Figure 3.5.62). Lorsqu'elles sont parallèles aux plans de foliation S_2 , les veinules sont assimilables à un clivage, et lorsqu'elles sont localisées le long des plans de litage, elles sont couramment crénelées par S_2 . Les veines de quartz contenant des silicates de calcium sont d'autre part généralement parallèles au litage. Ces veines sont couramment boudinées et plissées par des plis P_2 (Figure 3.5.63). Le stockwerk aurifère est localement développé préférentiellement dans le flanc court de plis P_2 (Figures 3.5.55 et 3.5.64), ce qui suggère que les mécanismes de plissement ont joué un rôle dans la formation du stockwerk. Le stockwerk aurifère est toutefois localement très déformé par D_2 (Figure 3.5.65).

Zone Roberto-Est

À l'échelle du gisement, la Zone Roberto-Est (jusqu'à 8 g/t Au sur 6 m) est en contact avec une unité de wacke massif située à l'ouest de la séquence à porphyroblastes d'aluminosilicates. Bien que la répartition globale de la zone Roberto-Est soit globalement relativement simple, sa géométrie interne est complexe. La zone Roberto-Est est composée de

plusieurs assemblages minéralogiques qui montrent différentes caractéristiques texturales (Figure 3.5.58). L'enveloppe ouest de la zone Roberto-Est comprend des brèches hydrothermales caractérisées par des fragments millimétriques de métawacke angulaires de couleur brun-rosée composés de diverses proportions de microcline, de biotite et de feldspath saussuritisés qui sont recoupés par des veinules de quartz contenant des silicates de calcium. Ces brèches hydrothermales contiennent des teneurs en or anormales (<1 g/t Au). Le noyau de la zone Roberto-Est se caractérise par un rubanement bien défini composé de filons leucocrates à calc-silicates injectés dans des wackes fortement altérés en tourmaline. Ces veines contenant des calc-silicates sont caractérisées par la présence de diopside, de tourmaline, et localement de microcline. Des plis P_2 isoclinaux sont couramment développés dans le matériel rubané, ce qui indique qu'au moins une partie de l'altération hydrothermale et de la minéralisation a été affectée par D_2 . L'intensité de l'altération augmente en s'approchant d'une faille cassante post-minéralisation orientée vers le nord qui délimite le côté est de la zone Roberto-Est, où les différents assemblages minéralogiques sont progressivement remplacés par du quartz, formant une zone de remplacement en silice de près d'un mètre de largeur. Ces zones de remplacement en silice sont associées à des valeurs aurifères significatives (≥ 5 g/t Au) et contiennent des proportions variables de quartz, de microcline, de tourmaline, d'actinolite, de diopside, de feldspath saussuritisés, de clinozoisite, et d'arsénopyrite.

Autres zones aurifères

À l'échelle du gisement, les caractéristiques minéralogiques et texturales qui définissent les zones Roberto et Roberto-Est se retrouvent dans d'autres zones aurifères, où elles sont distribuées de façon sporadique. Par conséquent, bien que Roberto et Roberto-Est représentent des zones aurifères distinctes, elles représentent aussi des types d'assemblages de minéralisation et d'altération qui forment les principaux constituants d'autres zones aurifères. En général, ces zones aurifères sont composées de diverses proportions de minéraux calco-silicatés, de microcline, de tourmaline, d'arsénopyrite, et de pyrrhotite, mais elles ne possèdent pas le stockwerk aurifère de Roberto ou le rubanement intense de la zone Roberto-Est. Une de ces zones aurifères est la zone Mid-Roberto, qui se ramifie à partir de la zone Roberto et rejoint la zone Roberto-Est. Certaines zones aurifères sont contenues dans d'autres unités lithologiques, comprenant des unités de conglomérat, des schistes à biotite, et des unités de paragneiss. Dans le flanc nord du pli à l'échelle du gisement, les zones aurifères sont localement associées avec des veines de quartz-arsénopyrite qui contiennent localement de l'or visible. Les zones aurifères contenues dans des paragneiss intersectées en forage possèdent des attributs différents et semblent avoir été soumises à un degré de métamorphisme plus élevé. Par exemple, une zone minéralisée à très forte teneur en or (60 g/t Au sur 30 mètres) intersectée en profondeur ($\sim 1,2$ km sous la surface) est associée à des veines de quartz-feldspath-arsénopyrite-pyrrhotite qui contiennent de l'or visible, mais où les assemblages calco-silicatés ou riches en microcline sont absents (Figure 3.5.69). Il est important de noter que ces veines de quartz-feldspath-arsénopyrite-pyrrhotite se transforment localement et progressivement en matériel pegmatitique, ce qui suggère qu'elles sont génétiquement liées à un épisode de magmatisme pegmatitique (3.5.69c). D'autres zones aurifères dans des paragneiss sont caractérisées par des veines de quartz-arsénopyrite-pyrrhotite où le quartz est saccharoïdal et contenues dans des assemblages de feldspaths-biotite-pyrrhotite-arsénopyrite (Figure 3.5.69d). D'autres zones aurifères sont connues, telles que la zone Puncho ($\sim 1-2$ g/t Au), qui est contenue dans des formations de fer rubanées, et la zone Mayappo (1-2 g/t Au), qui est caractérisée par une altération riche en calcium.

Altération hydrothermale

Les zones aurifères sont globalement associées à un vaste système hydrothermal qui crée des altérations riches en silice, calcium, potassium, et bore. Ce système hydrothermal affecte toutes les unités lithologiques sauf les dykes de pegmatite. En dehors des zones aurifères, les roches affectées par cette altération contiennent souvent des teneurs anormales en or (<100 et > 500 ppb Au) et localement des teneurs plus élevées (> 1 g/t Au). Les caractéristiques texturales de l'altération varient en fonction de la roche hôte. Dans les roches contenant des aluminosilicates, l'altération se présente sous forme de bandes de remplacement concordantes et discordantes au litage (Figure 3.5.8a et 3.5.8b). Dans les wackes lités et massifs, la distribution de l'altération est contrôlée par des fractures et forme des bandes de remplacement de 1 à 5 cm de largeur, certaines sont associées à des veines de quartz-feldspath. Dans le wacke massif, l'altération se présente localement sous forme de stockwerks (Figure 3.5.8e).

Des veines de quartz, feldspath potassique, tourmaline et arsénopyrite sont plus jeunes que les veines qui contiennent des calc-silicates et les bandes de remplacement (Figure 3.5.70). Ces veines contiennent généralement des valeurs anormales en or (<1 g/t Au) et sont localement en-échelon ce qui suggère que leur distribution est contrôlée par la déformation. Ces veines de quartz-feldspath sont à leur tour recoupées par les dykes de pegmatite.

Chronologie relative entre la minéralisation aurifère, la déformation et le métamorphisme

D'un point de vue macroscopique, il est clair que toutes les veines qui contiennent des calc-silicates et les bandes de remplacement à l'intérieur et en dehors des zones aurifères ont été affectées par D_2 . Par exemple, les relations de terrain montrent que les veines qui contiennent des calc-silicates et les bandes de remplacement ont été plissées, transposées, et boudinées par D_2 (Figure 3.5.34). Aucune veine calco-silicatée ou bande de remplacement postérieures à D_2 n'a été documentée.

Les évidences microscopiques que la déformation D_2 a affecté les veines qui contiennent des calc-silicates comprennent: l'omniprésence de l'extinction ondulante dans les grains de quartz, les lamelles de déformation dans le quartz et le plagioclase, et les macles de déformation au sein du plagioclase et des grains de calcite. D'autres porphyroblastes présents dans les veines qui contiennent des calc-silicates ou dans les bandes de remplacement, y compris la biotite et les amphiboles, sont localement orientés par S_2 ou de façon aléatoire. Le fait que certains des porphyroblastes orientés de façon aléatoire sont localement automorphes et semblent post-tectoniques suggère que les conditions appropriées à leur croissance ont continué après D_2 et D_3 , peut-être dû à un épisode de recristallisation statique tardi-à post-tectonique (Ravenelle et al., 2010). Le fait que les porphyroblastes de diopside dans les veines qui contiennent des calc-silicates ne soient pas orientés par S_2 et qu'ils coexistent avec les porphyroblastes d'amphiboles qui sont eux-mêmes affectés par S_2 , suggère que les porphyroblastes de diopside ont également été affectés par D_2 . Les cristaux de tourmaline situés à l'intérieur ou dans les lisières des veines qui contiennent des calc-silicates sont communément orientés par S_2 , spécifiquement dans les plans verticaux (Figure 3.5.40). Ceci suggère que les cristaux de tourmaline ont été affectés par D_2 , et que leur axe long est

subparallèle à la linéation L_2 qui est quasi verticale. Les cristaux de tourmaline ont donc été générés avant ou pendant D_2 .

Dans les veines qui contiennent des calc-silicates, les minéraux interprétés comme appartenant à un stade de métamorphisme prograde comprennent: la biotite, le diopside, la microcline, le plagioclase, et la tourmaline. Dans les bandes de remplacement, les minéraux progrades comprennent la biotite, le grenat, et le plagioclase. Les assemblages de minéraux rétrogrades sont difficiles à déterminer car toutes les phases hydratées ne sont pas nécessairement rétrogrades: certaines peuvent résulter de l'altération hydrothermale (Meinert, 1992). Les minéraux hydratés comprennent: la clinozoïsite/épidote, la chlorite, la prehnite, la muscovite, et la saussurite/séricite qui remplacent le plagioclase. Le remplacement de l'amphibole et des sulfures par la clinozoïsite et l'épidote se produit aussi dans d'autres gisements aurifères métamorphisés au faciès des amphibolites, où il est attribué métamorphisme rétrograde (Neumayr et al., 1993). Dans les environnements de skarn, la présence de la prehnite et de l'épidote est communément attribuée à l'altération hydrothermale (Pan, Fleet et Stone, 1991). Bien que la calcite remplace localement le plagioclase, qui pourrait suggérer un processus rétrograde, certains porphyroblastes de calcite peuvent être progrades. Des études détaillées de conditions de pression et de température sont nécessaires afin de déterminer les conditions de formation des phases hydratées qui remplacent les minéraux progrades et déterminer si elles résultent de métamorphisme rétrograde ou bien de l'altération hydrothermale.

La chronologie relative des veines qui contiennent du microcline et/ou de la biotite par rapport à l'événement de déformation D_2 peut être déterminée à partir de relations de terrain. Les caractéristiques structurales de ces veines sont particulièrement bien définies dans le stockwerk de la zone Roberto où il peut être vu même si la plupart des veinules ont été plissées, crénulées et transposées par D_2 (Figure 3.5.52), quelques-unes définissent un clivage orienté parallèle au plan axial des plis P_2 (3.5.53a). L'inspection pétrographique indique que les veinules plissées et celles de plan axial aux plis sont en continuité pétrogénétique (c'est-à-dire que les grains de minéraux à l'intérieur des veines chevauchent les limites des veines) (Figure 3.5.53), ce qui pourrait suggérer que leur mise en place était synchrone. Toutefois, puisque les veines sont recristallisées (indiqué par la présence de grains de quartz polygonaux), les relations de recoupement initiales ont pu être effacées. Le fait que certaines des veinules ont été mises en place lors de la formation du clivage S_2 indique que leur mise en place est synchrone avec D_2 . Cette interprétation est également en accord avec l'observation que le stockwerk aurifère est localement développé préférentiellement sur le flanc court d'un pli P_2 ce qui suggère que les mécanismes de plissement ont localement contrôlé la formation du stockwerk (Ravenelle et al., 2010). Cependant, puisque les veinules du stockwerk sont aussi intensément déformées par D_2 , elles doivent avoir été mises en place au début de la déformation D_2 . Cette interprétation exige que D_2 soit un événement progressif qui s'est étendue sur une longue période de temps. L'étirement prononcé observé sur les sections verticales du stockwerk indique que l'axe X de l'ellipse de déformation est fortement plongeant dans le stockwerk, ce qui corrobore le style de la déformation D_2 observé ailleurs sur la propriété Éléonore.

Un microscope électronique à balayage (MEB) a été utilisé pour étudier les relations texturales des minéraux sulfurés qui sont autrement difficiles à documenter avec un microscope pétrographique. L'étude a été réalisée sur des échantillons du stockwerk Roberto, de la zone Roberto-Est, d'une veine de quartz aurifère contenant du diopside, d'un paragneiss aurifère, d'une zone de sulfures massifs contenue dans un dyke de pegmatite, de dykes de pegmatite, et d'un dyke d'aplite. Les résultats indiquent que tous les échantillons qui contiennent de l'arsénopyrite contiennent aussi de la löllingite, et que les cristaux de löllingite sont séparés de la

pyrrhotite par l'arsénopyrite et ne touchent pas la pyrrhotite (Figure 3.5.75). Cette texture suggère que la löllingite fut rétrogradée en pyrrhotite et arsénopyrite. La löllingite et l'arsénopyrite sont présentes au sein d'un porphyroblaste de diopside (3.5.75b), ce qui suggère que les sulfures ont subi l'épisode de métamorphisme prograde qui a conduit à la formation du porphyroblaste de diopside. Ces observations suggèrent que les cristaux d'arsénopyrite se sont formés avant ou près du pic métamorphique. Dans certains échantillons, de l'or visible est présent aux joints de grains löllingite-arsénopyrite et/ou sous forme d'inclusions visibles dans l'arsénopyrite (Figure 3.5.76). Ces relations texturales indiquent que l'or fut initialement contenu à l'intérieur des cristaux de löllingite et que la minéralisation aurifère est par conséquent antérieure à la phase de métamorphisme rétrograde. Nous ne pouvons toutefois pas déterminer si la minéralisation aurifère s'est mise en place avant le pic métamorphique en association avec l'arsénopyrite, ou si elle a été introduite près du pic métamorphique durant le métamorphisme prograde de l'arsénopyrite en löllingite.

Géochronologie

Des travaux de géochronologie ont été menés dans les laboratoires de la Commission géologique du Canada (CGC) afin de définir la chronologie relative entre les wackes turbiditiques hôtes de la zone Roberto, les séquences de conglomérats régionaux, la phase minéralisée de la diorite du lac Ell, et le magmatisme pegmatitique. Les âges maximaux des roches d'origine sédimentaire ont été obtenus en utilisant la géochronologie U-Pb de haute précision par la spectrométrie de masse d'ions secondaires (SHRIMP) et la spectrométrie de masse à ionisation thermique (TIMS). Les éléments suivants peuvent être déduits à partir des travaux de géochronologie:

- Le wacke hôte de la zone Roberto, daté à <2675 Ma (Geochron-ELE-05-08), est nettement plus jeune que la phase de la diorite du Lac Ell datée à ca. 2705 Ma (David, 2005), ce qui exclut l'hypothèse que le gisement Roberto est génétiquement lié à la phase datée de l'intrusion du Lac Ell.
- Les relations de recoupement entre les deux dykes d'aplite (Geochron-ELE-08-19 et Geochron-ELE-08-20) et une veine de quartz aurifère (Figure 3.5.71) indiquent qu'une partie de la minéralisation aurifère s'est mise en place entre 2615 et 2607 Ma.
- La phase de minéralisation aurifère principale doit avoir eu lieu avant ca. 2603 Ma, l'âge d'un dyke de pegmatite qui recoupe la zone Roberto. Ce dyke de pegmatite recoupe aussi la faille fragile de Roberto-Est ce qui indique que le mouvement le long de la faille doit aussi avoir eu lieu avant ca. 2603 Ma.
- La zone Roberto-Est, ou la faille cassante située le long de sa limite à l'est, marque potentiellement le contact entre les deux séquences de wacke, comme illustré par les âges maximaux de wackes massifs (ca. 2714 Ma, Geochron-ELE-09-21) et d'aluminosilicates (ca. 2697 Ma, Geochron-ELE-05-02) comparés à l'âge maximal du wacke hôte à la zone Roberto (ca. 2675 Ma, Geochron-ELE-05-08) (Figure 3.2.3).
- Les âges maximaux des paragneiss (ca. 2685 Ma, Geochron-ELE-05-07 et ca. 2675 Ma, Geochron-ELE-06-11) sont dans les limites d'âges de la plus jeune séquence de wacke. Les paragneiss et les séquences de métawacke adjacentes ne peuvent donc pas être distingués en fonction de leurs âges maximaux.
- La présence d'un dyke d'aplite plissé par des plis P_2 (Geochron-ELE-08-19) et d'une pegmatite boudinée par D_2 (Geochron-ELE-07-17) datés à ca. 2615 Ma et 2616 Ma, respectivement, indique que D_2 était encore actif autour de 2615 Ma, et représente donc

un événement tectonique et métamorphique plus jeune que les événements préalablement décrits dans la Province du lac Supérieur.

Discussion: Cadre tectonique

La localisation du gisement Roberto à proximité de la frontière de deux sous-provinces de grades métamorphiques différents est un élément clé pour comprendre le contexte tectonique du gisement. Deux scénarios peuvent expliquer la présence de deux terranes adjacents ayant un grade métamorphique différent: 1. la distribution actuelle est primaire et reflète le contexte tectonique original de la région; 2. les deux terranes ont été juxtaposés pendant ou après avoir été métamorphisés. Le second scénario nécessite la présence d'une zone de déformation importante à proximité du contact entre les deux sous-provinces. Une telle zone de déformation n'a toutefois pas été observée dans la région étudiée. On pourrait quand même s'attendre à ce qu'une telle zone soit masquée par les intrusions distribuées le long du contact entre les deux sous-provinces.

On peut conclure que la région fut affectée par une longue période de métamorphisme et de déformation. Les roches volcaniques mafiques de la propriété Éléonore sont recouvertes en discordance par des séquences de conglomérats datées à $<2702 \pm 3$ Ma, ce qui peut impliquer qu'un soulèvement tectonique a eu lieu à environ 2702 Ma. Ces séquences conglomératiques peuvent masquer des zones de déformation importantes qui peuvent avoir joué un rôle dans l'histoire métallogénique de la région. Le fait que D_2 a déformé un dyke de pegmatite daté à ca. 2616 Ma et un dyke d'aplite daté à ca. 2615 Ma indique que D_2 était toujours actif à ce moment.

Discussion: Chronologie relative entre la minéralisation aurifère à la déformation

La chronologie relative entre la minéralisation aurifère et les événements de déformation est un élément clé pour comprendre la genèse du gisement. Les relations de terrain documentées indiquent que toutes les veines des zones aurifères principales ont été déformées par D_2 , et que toutes les veines qui contiennent des calc-silicates, les veines de quartz-feldspath, et les dykes de pegmatite ont été déformés par D_3 . Ce n'est que dans un endroit précis, que l'analyse structurale a permis de générer des arguments en faveur de la déposition d'or syn- D_2 . L'argument consiste en la présence d'un pli P_2 en Z, où le stockwerk de la zone Roberto est préférentiellement développé dans le flanc court du pli et se compose principalement de veines et veinules aurifères de plan axial au pli et parallèles au litage, ce qui suggère que sa formation fut contrôlée par les mécanismes de plissement. Les veinules de plan axial définissent un clivage de pression-dissolution et les veines parallèles au litage sont crénulées par S_2 indiquant qu'elles ont été progressivement déformées après avoir été mises en place.

Les observations de terrain suggèrent plus communément que les structures aurifères ont été déformées par D_2 au lieu d'avoir été générées durant du plissement actif associé à D_2 . À ce stade, cependant, il ne peut être conclu que l'événement aurifère principal soit survenu avant au lieu de très tôt au cours de D_2 . Des travaux de géochronologie détaillés devront être menés afin de déterminer l'âge absolu de la minéralisation aurifère et de la déformation D_2 afin de déterminer lequel des deux scénarios est le plus plausible.

Discussion: Chronologie relative entre la minéralisation aurifère et le métamorphisme

La minéralogie et les textures du matériel aurifère suggèrent que les veines et la minéralisation disséminée ont été générées avant ou pendant le pic du métamorphisme. Les assemblages minéralogiques au sein des roches altérées en K et Ca sont dominées par des minéraux généralement considérés progrades (par exemple la biotite, la microcline, le diopside, et le grenat), et un métamorphisme prograde est nécessaire pour expliquer la texture recristallisée, équigranulaire, et polygonale des grains de microcline dans les roches altérées en K et la taille relativement grande (3-10 mm) des porphyroblastes de diopside dans les veines de quartz-tourmaline-arsénopyrite. De plus, la texture saccharoïdale des veines de quartz-feldspath-biotite-arsénopyrite-pyrrhotite aurifères dans les paragneiss suggère fortement que la texture de recristallisation métamorphique est superposée sur la minéralisation préexistante.

La chronologie relative entre la minéralisation aurifère et le pic du métamorphisme est plus précisément déterminée par l'étude au MEB réalisée sur les minéraux sulfurés. L'étude suggère que les minéraux sulfurés ont une histoire métamorphique complexe impliquant des réactions progrades et rétrogrades, et que les grains d'arsénopyrite se sont formés avant le pic du métamorphisme. Le fait que les bandes de remplacement métagénétiques contenues dans la séquence à aluminosilicates soient délimitées par des halos où les porphyroblastes d'aluminosilicates ne se sont pas développés (Figure 3.5.44) suggère également qu'une partie du système hydrothermal a eu lieu avant la formation des minéraux du pic métamorphique. Puisque le pic métamorphique s'est produit lors de D_2 , la chronologie de développement entre l'événement aurifère principal et le pic métamorphique est en accord avec la formation pré- à tôt- D_2 établie à partir des caractéristiques structurales de la minéralisation aurifère.

Discussion: Chronologie relative entre la minéralisation aurifère et le magmatisme

Les données géochronologiques provenant de la diorite du Lac Ell et des roches hôtes de Roberto réfutent l'hypothèse que le système hydrothermal de Roberto est génétiquement lié à l'intrusion du Lac Ell. Il existe des preuves que certains dykes de pegmatite aurifères recoupent clairement les zones aurifères et sont postérieurs à D_2 , ce qui suggère que la présence d'or dans certains dykes de pegmatite est en partie liée à un processus de contamination qui résulte de la mise en place de dykes à travers du matériel minéralisé. D'autre part, la présence de dykes de pegmatite qui semblent localement être contemporains aux zones minéralisées et la continuité pétrogénétique des dykes de pegmatite avec certaines veines de quartz-feldspath aurifères suggère qu'un épisode de pegmatite (et d'aplite) daté entre 2615 Ma et 2607 Ma était contemporain à une partie de la minéralisation aurifère. Cet épisode de minéralisation aurifère liée à certaines pegmatites peut potentiellement représenter un deuxième stade minéralisation aurifère.

Discussion: Contrôles structuraux sur la minéralisation aurifère

À l'échelle du gisement, la répartition globale des zones aurifères principales indique que le gisement a été plissé par des plis P_2 et P_3 . Indépendamment du fait que le rôle actif des plis P_2 dans la genèse du gisement est ambigu, il existe des preuves que les plis P_2 et P_3 contrôlent la géométrie des zones aurifères principales et l'attitude des *ore shoots* au sein de ces zones. Les zones aurifères sont globalement contenues dans une géométrie qui résulte de l'interférence entre les plis P_2 et P_3 , ce qui suggère que les zones aurifères ont été préservées dans les charnières de plis au lieu d'être détruites et remobilisées sur les flancs des plis. Comme l'ont démontré d'autres chercheurs, le plissement peut jouer un rôle actif dans la remobilisation et la transposition de minéralisation le long d'axes privilégiés, généralement l'axe des plis (Marshall et Gilligan, 1993). D'autres exemples où la minéralisation aurifère est spatialement associée à des plis P_2 et/ou P_3 existent ailleurs dans la région (ex. propriété Auclair de Mines Virginia (Chapdelaine et Huot, 1997) et propriété Clearwater d'Eastmain Resources (Cadieux, 2000; Tremblay, 2006). Cibler les régions affectées par des plis à grande échelle, en particulier près du contact entre les sous-provinces d'Opinaca et de La Grande, pourrait s'avérer un précieux critère de prospection.

Discussion: Provenance du système hydrothermal

En termes de minéralogie, l'altération riche en calcium caractérisée par la présence de diopside, d'actinolite, et de clinozoïsite, en association avec la microcline, la tourmaline, l'arsénopyrite, et la pyrrhotite partage des caractéristiques avec l'assemblage minéralogique qui caractérise la signature hydrothermale des gisements d'or de type skarn au faciès des amphibolites (Mueller et Groves, 1991) tels que ceux trouvés dans les contextes orogéniques hypozonaux.

À ce stade, il est toutefois difficile de déterminer si le système minéralisé s'est mis en place en relation avec: 1. un système hydrothermal aurifère qui fut par la suite déformé et métamorphisé; 2. un système orogénique hydrothermal contrôlé par des réactions métamorphiques progrades associées à la migmatitisation d'Opinaca; ou 3. une combinaison des deux.

La précocité de la minéralisation aurifère par rapport à la déformation et au métamorphisme n'exclut pas l'apport potentiel de fluides hydrothermaux mésothermaux provenant de la destruction de minéraux hydratés au cours de réactions métamorphiques progrades. Certains chercheurs ont en effet démontré que différents niveaux de la croûte peuvent subir des épisodes métamorphiques à des moments différents (Stüwe, Will et Zhou, 1993). Stüwe (1998) introduit le concept de "profond-tard" et "profond-tôt" pour caractériser des relations temporelles métamorphiques et différents scénarios où les fluides libérés à certains niveaux de la croûte peuvent se mettre en place dans des roches qui sont sur des trajectoires rétrogrades ou progrades ailleurs dans l'empilement métamorphique. Dans le scénario "profond-tard", le pic du métamorphisme se produit à des niveaux profonds plus tard qu'aux niveaux peu profonds. La dévolatilisation prograde peut ainsi être active en profondeur alors que les roches à des niveaux moins profonds sont sur la voie rétrograde (Stüwe, 1998). Ce scénario est pertinent pour de nombreux gisements orogéniques où la mise en place de veines de quartz aurifères est postérieure au pic métamorphique des roches encaissantes, mais est lié au même événement métamorphique (Stüwe, 1998). Dans le scénario "profond-tôt", le pic du métamorphisme se produit à des niveaux peu profonds plus tard qu'aux niveaux profonds, de sorte que les fluides métamorphiques progrades libérés au cours de la dévolatilisation en profondeur s'infiltrent dans les niveaux moins profonds qui eux sont sur leur chemin prograde (Stüwe, 1998). La prévalence

d'un scénario plutôt qu'un autre est en partie liée au mécanisme de chaleur. La provenance de chaleur découlant d'un épaissement de la croûte et de l'enfouissement de roches à des niveaux crustaux profonds mènera à une chronologie du métamorphisme "profond-tard", tandis que la provenance de chaleur liée à une accumulation magmatique venant du bas ou à une intrusion magmatique localisée dans le milieu de la croûte mènera au scénario "profond-tôt" (Stüwe, 1998). Bien que le mécanisme de chaleur n'est pas contraint dans la région environnante du gisement Roberto, un scénario "profond-tôt" pourrait expliquer la précocité de la minéralisation aurifère par rapport à la déformation et au métamorphisme, et le fait qu'une partie de la minéralisation aurifère datée entre 2615 et 2607 Ma est nettement plus jeune que l'âge des deux épisodes de migmatisation documentés dans l'Opinaca qui sont datés à ca. 2671 Ma et ca. 2647 Ma. Par conséquent, l'apport potentiel de fluides métamorphiques ne devrait pas être exclue sur la base que la minéralisation aurifère a été introduite tôt par rapport aux événements tectono-métamorphiques régionaux. Cela pourrait d'autant plus suggérer que les veines qui contiennent des calc-silicates et les bandes de remplacement riches en calcium représentent des équivalents métamorphiques de veines de quartz-carbonate et d'altération en carbonate qui sont typiques des gisements orogéniques.

L'apport potentiel de fluides magmatiques ne devrait également pas être ignoré. Bien que les travaux de datation de la diorite du Lac Eil et des roches hôtes de Roberto réfutent l'hypothèse que le système hydrothermal de Roberto est génétiquement liée à la phase datée de l'intrusion, et même si la plupart des dykes de pegmatite sont clairement postérieure aux principales zones aurifères, la présence d'intrusions à porphyres de feldspath à proximité du gisement et la présence de dykes de pegmatite qui semblent localement être contemporains avec une partie de la minéralisation aurifère indique que certaines phases magmatiques puissent avoir été contemporaines avec une partie de la minéralisation aurifère. L'évidence de la contemporanéité de certaines pegmatites avec la minéralisation aurifère réside dans le fait que des relations de recoupement contradictoires ont été observées en affleurement. Plus précisément, une veine de quartz contenant de l'or visible et de l'arsénopyrite recoupe un dyke de pegmatite avec un cœur aplitique et un autre dyke similaire recoupe la veine de quartz aurifère. Ces relations impliquent que des veines de quartz aurifères ont été générés lors de la mise en place de dykes de pegmatite, mais ne requiert pas nécessairement que la veine et les dykes soient génétiquement reliés. Toutefois, certains dykes de pegmatite semblent bien être cogénétiques avec une partie de la minéralisation, notamment les dykes de pegmatite présents dans la zone à forte teneur en or intersectée en profondeur et qui sont en continuité pétrogénétique avec des veines de quartz-feldspath aurifères. Le contraste entre les différents styles de minéralisation aurifère, des stockwerks minéralisés aux veines pegmatitiques, peuvent indiquer que le gisement Roberto a été affecté par un long événement tectono-métamorphique au cours duquel la minéralisation aurifère s'est mise en place, fut déformée, métamorphosée, et remobilisée dans un scénario tectono-métamorphique de type "profond-tôt".

Discussion: Comparaison avec d'autres gisements aurifères

Le gisement Roberto partage des analogies avec plusieurs types de gisements d'or, mais possède aussi des caractéristiques qui lui sont uniques. Par exemple, en termes d'assemblages d'altération et de la minéralogie des sulfures, Roberto est similaire aux gisements de type orogénique métamorphisés au faciès des amphibolites. Des veines laminées et des veines d'extension tel que retrouvées dans les gisements orogéniques sont localement présentes à Roberto. Toutefois, dans les gisements orogéniques, ces veines sont contenues dans des zones de cisaillement, ce qui n'est pas le cas à Roberto. L'altération potassique et

alumineuse caractéristique des gisements épithermaux est présente à Roberto, mais la minéralogie des sulfures, les textures minérales (veines colloformes et crustiformes), et le style de minéralisation caractéristique des gisements épithermaux ne sont pas présents à Roberto. Le gisement Roberto ne possède pas de lentilles de sulfures massifs qui caractérisent les gisements de type SMV aurifères, et bien que sa minéralogie d'altération présente des similitudes avec des gisements liés aux intrusions, Roberto est pauvre en cuivre et ne démontre pas de relation claire avec les phases intrusives documentées.

Même si le gisement Roberto ne peut pas facilement être considéré comme un type de gisement bien précis, il partage plusieurs attributs avec les gisements d'or métamorphisés au faciès des amphibolites. Ces attributs incluent histoire géologique qui s'étend sur plusieurs millions d'années, deux stades de minéralisation aurifère, des caractéristiques structurales complexes, une chronologie relative ambiguë entre la minéralisation aurifère et les épisodes de déformation, et des assemblages d'altération de type skarn.

Conclusions

- Le gisement Roberto est un gisement d'or épigénétique contenu au sein d'une séquence turbiditique métamorphisée au faciès amphibolite. La phase principale de la minéralisation aurifère est associée à des stockwerks de veines de biotite-tourmaline-microcline-arsénopyrite-pyrrhotite et des veines de quartz qui contiennent des calc-silicates, de l'arsénopyrite, et de la pyrrhotite contenus dans des roches sédimentaires altérées en microcline-tourmaline-arsénopyrite-pyrrhotite. En termes de minéralogie, l'altération riche en calcium caractérisée par la présence de diopside, d'actinolite, et de clinozôisite, en association avec le microcline, la tourmaline, l'arsénopyrite, et la pyrrhotite partage des analogies avec l'assemblage minéralogique qui caractérise la signature hydrothermale des skarns aurifères aux faciès des amphibolites tels que retrouvés dans les contextes orogéniques hypozonaux.
- Le gisement Roberto est affecté par de multiples épisodes de plissement, mais n'est pas contenu dans une zone de cisaillement. Les observations de terrain indiquent que la partie principale de la minéralisation aurifère a été affectée par D_2 avant d'être déformée par D_3 . Il y a seulement un endroit où l'analyse structurale a permis d'émettre des arguments qui supportent une mise en place de la minéralisation aurifère syn- D_2 .
- La minéralogie et les textures du matériel aurifère suggèrent que les veines et la minéralisation disséminée ont été générées avant ou pendant le pic du métamorphisme. De plus, l'étude des minéraux sulfurés avec le MEB indique que le gisement Roberto fut affecté par un métamorphisme complexe impliquant des réactions progrades et rétrogrades.
- Puisque plusieurs évidences pointent vers une mise en place précoce de la majeure partie de la minéralisation aurifère par rapport à la déformation et au métamorphisme, le contexte tectonique de la zone représente un indice important dans la compréhension de la genèse du gisement Roberto. Même si l'origine du contexte de pression-température métamorphique est inconnue, un scénario "profond-tôt" pourrait expliquer la précocité de la minéralisation aurifère par rapport à la déformation et au métamorphisme. En conséquence, l'apport potentiel des fluides métamorphiques ne devrait pas être exclue sur la base que la minéralisation aurifère ait été introduite tôt par rapport aux événements tectono-métamorphiques. Cela pourrait en outre suggérer que les veines de quartz qui contiennent des calc-silicates et le remplacement riche en calcium représentent des équivalents

métamorphisés des veines de quartz-carbonate et de l'altération en carbonate qui sont typiques des gisements de type orogénique.

- Les travaux de géochronologie déterminent l'âge absolu du stade principal de la minéralisation aurifère entre ca. 2675 Ma et 2603 Ma, l'âge maximal de la roche hôte du gisement Roberto et l'âge d'un dyke de pegmatite qui recoupe les zones aurifères principales, respectivement.
- Le fait que certains dykes de pegmatite qui recoupent les zones minéralisées soient aurifères est interprété comme résultant d'un processus de contamination causé par la mise en place de dykes à travers du matériel minéralisé. D'autre part, certains dykes de pegmatite sont en continuité pétrogénétique avec des veines de quartz-feldspath aurifères, et des relations de recoupement entre deux dykes d'aplite et une veine de quartz aurifère indiquent que ces dykes sont contemporains avec une partie de la minéralisation aurifère qui s'est mise en place entre 2615 Ma et 2607 Ma. On peut donc conclure que le magmatisme pegmatitique était contemporain avec au moins une partie de la minéralisation aurifère et/ou représente un second stade de minéralisation aurifère.
- Même si les données géochronologiques de la diorite du Lac Ell et des roches hôtes du gisement Roberto réfutent l'hypothèse que le système hydrothermal de Roberto est génétiquement lié à la phase datée de l'intrusion du Lac Ell, le rôle de fluides magmatiques dans la genèse du gisement ne devrait pas être ignoré, puisque des intrusions de porphyres à feldspath sont présentes près du gisement.
- Les contrôles structuraux du gisement Roberto sont difficiles à déterminer puisque les relations structurales de base sont obscurcies par le niveau de déformation élevé. Il y a plusieurs évidences que du glissement post-minéralisation lié aux mécanismes de plissement s'est produit le long des plans de litage de la zone Roberto, mais le rôle de ce glissement dans la mise en place de fluides hydrothermaux riches en or reste spéculatif. La zone Roberto-Est a la particularité d'être distribuée le long d'une faille cassante, et bien que cette faille ait accommodé du mouvement post-minéralisation, elle pourrait préalablement avoir servi de voie pour canaliser les fluides hydrothermaux avant d'être réactivée.
- À l'échelle du gisement Roberto, il existe des évidences que les plis P_2 et P_3 contrôlent la géométrie des zones aurifères principales. Les zones aurifères sont globalement confinées à une structure de plis P_2 et P_3 qui suggère que les zones aurifères ont été préservées dans les charnières de plis au lieu d'être détruites et remobilisées sur les flancs des plis. D'autres exemples où la minéralisation en or est spatialement associée à des plis P_2 et/ou P_3 sont présents ailleurs dans la région de la Baie James (ex. propriété Auclair de Mines Virginia (Chapdelaine et Huot, 1997) et propriété Clearwater d'Eastmain Resources (Cadieux, 2000; Tremblay, 2006).
- Cibler les régions affectées par du plissement, en particulier près du contact entre les sous-provinces d'Opinaca et de La Grande, pourrait se révéler un précieux critère de prospection.

TABLE OF CONTENTS

ACKNOWLEDGMENTS	iii
ABSTRACT	iv
SOMMAIRE RÉCAPITULATIF	viii
TABLE OF CONTENTS	xxii
LIST OF TABLES	xxvi
LIST OF FIGURES	xxviii
1 INTRODUCTION	1
1.1 Purpose of Study	1
1.2 Objectives	3
1.1 Methodology	4
1.1.1 Methodology for Determining the Geological Setting of the Deposit	4
1.1.2 Methodology for Determining the Morphological, Geochemical, Metallogenic, and Metamorphic Characteristics of Gold Mineralization and Associated Hydrothermal Alteration 4	4
1.1.3 Methodology for Determining the Timing between Gold mineralization, Deformational/Metamorphic Events, and other Geological Features	5
2 REGIONAL GEOLOGY	7
2.1 Eastmain River Domain of the La Grande Subprovince	8
2.1.1 Lithology	9
2.1.2 Structural Geology and Metamorphism	11
2.2 Opinaca Subprovince.....	12
2.2.1 Lithology	12
2.2.2 Structural Geology and Metamorphism	12
2.3 Nature of the Boundary between the La Grande and Opinaca Subprovinces	13
2.4 Distribution of Gold Deposits within the Region	14
2.5 Geology of the Éléonore Property.....	17
2.5.1 Lithology	18
2.5.2 Lithogeochemistry.....	22
2.5.3 Structural Geology of the Éléonore Property	27
2.5.4 Alteration and Mineralization	48
3 GEOLOGY OF THE ROBERTO DEPOSIT	51
3.1 Geology of the Roberto Deposit: Introduction.....	51
3.2 Lithology.....	52

3.2.1	Supracrustal Units	52
3.2.2	Intrusive Phases	71
3.3	Structural Geology of the Roberto Deposit	76
3.3.1	Planar and Linear Fabrics.....	76
3.3.2	Folds and Fold Interference at Surface	80
3.3.3	High Strain Zones.....	84
3.3.4	Faults and Slip Surfaces.....	93
3.3.5	Late Brittle Faults and Breccia.....	99
3.3.6	Geometrical and Structural Characteristics of the Deposit	101
3.4	Metamorphism	116
3.4.1	Metamorphic Assemblages	116
3.4.2	Timing with Deformational Events	122
3.5	Alteration and Mineralization.....	123
3.5.1	Introduction.....	124
3.5.2	Least Altered Samples.....	126
3.5.3	Aluminous Assemblages	131
3.5.4	Ca-bearing Alteration.....	133
3.5.5	Potassic Alteration.....	183
3.5.6	East-Roberto Auriferous Zone	203
3.5.7	Roberto Auriferous Zone	206
3.5.8	Other Auriferous Zones	214
3.5.9	Quartz-Feldspar Veins.....	217
3.5.10	Mineralized Pegmatites	218
3.5.11	Occurrence of Sulphide Minerals Relative to Peak of Metamorphism.....	219
4	Geochronology	227
4.1	Samples Location	227
4.2	Interpretation of Result.....	231
5	Discussion	233
5.1	Tectonic Setting	233
5.2	Relative Timing of Gold Mineralization with Deformation, Metamorphism, and Magmatic Phases	235
5.3	Structural Controls on Gold Mineralization	240
5.4	Nature of the Hydrothermal System.....	241
5.5	Comparison with other Canadian Gold Deposits.....	242

5.6	Comparison with other Amphibolite-Facies Gold deposits	246
5.7	Speculative Genetic Model	248
6	Conclusions	251
7	References	255
8	Annex 1: Mapping Techniques and Use of Three-Dimensional software.....	265
8.1	Detailed Mapping of the Large Stripped Outcrop.....	265
8.2	Construction of 3D Representations	269
8.2.2	Visualization of Structural Data Measured on Oriented Core	274
8.3	Integration of Data to Perform Analysis and Queries.....	278
8.3.1	2D- ArcGIS	278
8.3.2	3D-Gocad	281
9	Annex 2: Detailed Map of the Large Stripped Outcrop.....	283

LIST OF TABLES

Table 2.4.1: General characteristics of selected gold deposits of the James Bay area.....	16
Table 2.5.1: Major element averages of Éléonore's turbidite sequence and selected Archean sequences.....	22
Table 2.5.2: Minor element averages of Éléonore's turbidite sequence and selected Archean sequences.....	23
Table 3.2.1: Major element averages of selected lithological units and/or sedimentary sequences present near the Roberto deposit.....	60
Table 3.2.2: Selected minor element averages of selected lithological units and/or sedimentary sequences present near the Roberto deposit.....	60
Table 3.2.3: Major element averages of aluminosilicate-free and aluminosilicate-bearing metasedimentary rocks in Roberto's aluminosilicate-bearing sequence compared with a reference average composition of high grade pelitic schists from (Shaw, 1956).....	67
Table 3.2.4: Selected minor element averages of aluminosilicate-free and aluminosilicate-bearing metasedimentary rocks in Roberto's aluminosilicate-bearing sequence.....	67
Table 3.5.1: Mineralogy and average gold content of Ca-bearing replacement and of host rocks within aluminosilicate-bearing sequence.....	138
Table 3.5.2: Symbols of minerals used in this study.....	139
Table 3.5.3: Mineralogy and average gold content of Ca-bearing replacement in massive greywacke and of massive greywacke host rocks.....	141
Table 3.5.4: Mineralogy and average gold content of calc-silicate-bearing veins in greywacke and of greywacke host rocks.....	144
Table 3.5.5: Mineralogy and average gold content of calc-silicate-bearing veins and host rocks in East-Roberto zone.....	147
Table 3.5.6: Mineralogy and average gold content of calc-silicate-bearing veins and host rocks in Roberto zone.....	149
Table 3.5.7: Mineralogy and average gold content of Ca-bearing replacement and host rocks in Roberto zone.....	151
Table 3.5.8: List of minerals replacing prograde minerals within Ca-altered rocks.....	178
Table 3.5.9: Mineralogy of K-altered rocks.....	185
Table 3.5.10: Major element averages of K-altered and least-altered equivalents.....	192
Table 3.5.11: Selected minor element averages of K-altered and least-altered equivalents.....	192
Table 4.1.1 Characteristics of geochronological samples analyzed on the Eleonore property.....	227
Table 5.5.1: General characteristics of various types Canadian gold deposits.....	244
Table 5.5.2: General characteristics of selected amphibolite-facies gold deposits.....	244

LIST OF FIGURES

Figure 1.1.1: Schematic diagram showing the distribution of different types of gold deposits in function of crustal levels	2
Figure 2.1.1: Regional geological map showing the location of the Éléonore property.....	8
Figure 2.1.2: a) Simplified regional geological setting of the Roberto gold deposit. Selected lineation measurements are represented on the map. b) and c) Equal area nets (lower hemisphere) showing the distribution of lineation and pole to S_2 foliation for the Opinaca and La Grande subprovinces, respectively.....	10
Figure 2.4.1: Regional geological map showing the location of the Éléonore property and significant gold prospects and deposits.....	14
Figure 2.5.1: Map showing location of outcrops within Éléonore property and associated joint ventures.....	17
Figure 2.5.2: Simplified geological map of the Éléonore property.....	19
Figure 2.5.3: Photographs of mafic rocks concordant to bedding planes within conglomeratic units.....	20
Figure 2.5.4: Chronostratigraphic column illustrating the relative chronology of supracrustal and intrusive phases of the Éléonore property.....	22
Figure 2.5.5: Chondrite-normalized (Sun and McDonough, 1989) spider diagram of Éléonore's turbidite sequence and other turbiditic sequences of the Superior Province.....	24
Figure 2.5.6: Box diagrams showing range of Éléonore's property unaltered turbidites major and selected minor element concentrations.....	25
Figure 2.5.7: Photographs showing: a) intense flattening strain associated with S_2 in conglomerate. b) well-developed mineral lineation on S_2 plane in greywacke. c) and d): deformed conglomerate in plan (YZ plan of strain ellipsoid) (c), and cross section view (XZ plan of strain ellipsoid) (d). e) S_3 crenulation cleavage affecting S_2 foliation. f) well-developed mineral lineation (parallel to green pen) in S_3 defined by deformed aluminosilicate porphyroblasts.	28
Figure 2.5.8: Geological map of the region around the Éléonore property showing the distribution of lithological units, main tectonic fabric (S_2), and fold axial traces.....	31
Figure 2.5.9: Geological map of the Éléonore property with the location of the Roberto Deposit.....	32
Figure 2.5.10: Photographs showing: a) F_1 fold refolded by F_2 fold in mafic sedimentary rocks. b) F_1 fold refolded by F_2 fold in paragneiss c) and d) tight F_2 folds in S_0 within greywacke. e) F_3 fold in S_0 - S_2 within greywacke. f) F_3 fold in pegmatite dykes emplaced parallel to S_0 within paragneiss where S_3 completely overprinted S_2	34
Figure 2.5.11: Geological map of an area located 15 km to the west of the Éléonore property (see location on Figure 2.5.8) showing and F_2/F_3 interference pattern.....	36
Figure 2.5.12: Geological map of an area located 20 km to the north of the Éléonore property (see Figure 2.5.8) showing and F_2/F_3 interference pattern.....	37
Figure 2.5.13: Geological map of an area located 20 km to the NW of the Éléonore property (see Figure 2.5.8) showing and F_3 fold refolded by a large-scale F_4 fold.....	38

Figure 2.5.14: Schematic representations constructed using Mathematica© illustrating the effect of changes in the dip of F_2 axial planes prior to F_3 folding on the finite geometry.....	39
Figure 2.5.15: Interpreted structural geology of the Roberto area.....	41
Figure 2.5.16: Schematic diagrams constructed in Mathematica© illustrating one of three possible scenarios to explain the co-linearity between measurements of mineral lineations and F_3 fold axes.....	43
Figure 2.5.17: Photographs in conglomerate sequences showing: a) shear zone dragging S_2 fabric with an apparent sinistral motion in plan view. b) several meters wide high strain zone. The green rock is a mafic dyke crosscutting conglomerate and deformed by the high strain zone. c) section view of high strain zone shown in (b) where conglomerate fragments are highly stretched, d) well-developed lineation in high strain zone.....	45
Figure 2.5.18: Interpreted structural geology of the western region of the property.....	46
Figure 2.5.19: Airborne magnetic map of the region displayed on Figure 2.5.18.....	47
Figure 2.5.20: Geological map of the Éléonore property showing the distribution of samples affected by potassic alteration and samples interpreted to be the least altered.....	48
Figure 3.2.1: Geological map of the Roberto deposit showing distribution of lithological units and location of natural and stripped outcrops.....	53
Figure 3.2.2: Photographs showing examples of sedimentary features present in Roberto's turbiditic sequence.....	54
Figure 3.2.3: Geological map of the large stripped outcrop showing the distribution of principal lithological units.....	55
Figure 3.2.4: Geological map of the Roberto area showing the distribution of samples analyzed to compare the geochemistry of the two inferred sedimentary sequences.....	57
Figure 3.2.5: Box diagrams comparing major and selected minor element concentrations of the least altered samples within the two inferred sedimentary sequences.....	58
Figure 3.2.6: Chondrite-normalized (Sun and McDonough, 1989) spider diagram comparing trace element signature of the two inferred sedimentary sequences.....	60
Figure 3.2.7: Gocad snapshots showing three different views of the deposit's geometry.....	61
Figure 3.2.8: Photographs of drillcore showing: a) spatial association between arenite, thinly-bedded arenite, and conglomerate (drill hole ELE-07-395 between 615 and 633 meters). b) arenite brecciated by tourmaline veins (drill hole ELE-07-388 between 541 and 548 meters).....	63
Figure 3.2.9: Photograph showing aluminosilicate-bearing rock in drillcore (drill hole ELE-07-399 between 62 and 79 meters).....	64
Figure 3.2.10: Photograph showing folded aluminosilicate-rich and aluminosilicate-poor layers within an aluminosilicate-bearing sequence.....	65
Figure 3.2.11: Microphotograph (polarized light) showing fibrolite porphyroblast retrograded to muscovite.....	66
Figure 3.2.12: Photographs showing: a) quartz-rich and pyrite-rich layers in banded iron formation (BIF) located in the northern part of the deposit. b) quartz-rich and pyrite-rich layers in BIF in drillcore.....	68

Figure 3.2.13: Photographs of paragneiss showing: a) granoblastic texture. b) coarse granoblastic texture. c) ductily deformed pegmatite dykes. d) aluminosilicate-bearing paragneiss (white mineral is sillimanite).	70
Figure 3.2.14: Lithological map of the Roberto deposit showing the distribution of pegmatite dyke swarms and diabase dykes.	72
Figure 3.2.15: Gocad snapshot showing distribution of pegmatite dyke swarms (purple) and diabase dykes (green) in 3D.	73
Figure 3.2.16: Photographs of pegmatites showing: a) spodumene (Li-pyroxene)-bearing pegmatite in drillcore of hole ELE-07-494W01. b) photomicrograph of sample shown in (a) showing spodumene replacing albite. c) aluminosilicate (fibrolite)-bearing pegmatite in paragneiss located on trench DEC-08-06. d) photomicrograph of sample shown in (c) showing texture of fibrolite crystal. e) layered aplitic pegmatite on trench DEC-08-10. f) coarse-grained pegmatite west of the Roberto Zone on the large stripped-outcrop.	74
Figure 3.3.1: Geological map of the Roberto deposit area showing the distribution of structural fabrics.	78
Figure 3.3.2: Field photographs and photomicrographs showing: a) sawed sample from the eastern part of the large stripped outcrop showing F_2 fold devoid of axial planar foliation and transected by S_3 . b) photomicrograph (natural light) of a region of sample shown in (a) (white square) showing a planar fabric attributed to S_3 . c) photomicrograph from a sample in the eastern part of the large stripped outcrop (cross-polarized light) showing biotite crystals oriented by S_3 (green lines) and relict S_2 fabric (yellow lines) in microcline poikiloblasts (white contours) where biotite crystals remained oriented parallel to S_2 . d) photomicrograph showing close-up of (c). e) stretching lineation developed on S_2 planes within the East-Roberto Zone. f) mineral lineation defined by biotite crystals in S_3 on paragneiss outcrop located west of the large stripped outcrop.	79
Figure 3.3.3: Map showing the distribution of structural measurements in the vicinity of the Roberto deposit.	80
Figure 3.3.4: Photographs showing: a) isoclinal F_2 Z-fold with axial planar foliation (S_2). b) F_2 sheath folds in high strain zone. c) F_2 sheath fold located outside high strain zone (50 meters from it). d) F_3 folds in S_0/S_2 .	81
Figure 3.3.5: Geometry of sheath folds interpreted from photographs of slices through a hand sample located in a high strain zone of the large stripped outcrop (same location as folds on Figure 3.3.4b).	82
Figure 3.3.6: Photographs showing: a) $F_1(?)$ - F_2 interference pattern. b) and c) F_2 - F_3 coaxial fold interference patterns in mineralized material.	83
Figure 3.3.7: Geological map and interpreted structural geology of stripped outcrop DEC-08-06b showing a F_2/F_3 coaxial interference pattern.	84
Figure 3.3.8: Geological map of the Roberto deposit showing location of documented high strain zones (circled numbers).	85
Figure 3.3.9: Photographs showing: a) highly strained conglomerate. b) high strain zone affecting quartz-tourmaline veins and microcline-rich rock. Note the very fine grain size of the microcline-rich rock. c) highly strained quartz-feldspar veinlets in high strain zone. d) highly strained paragneiss (plan view). e) highly strained paragneiss and pegmatite (section view). f) highly strained auriferous veins and veinlets in drillcore.	86

Figure 3.3.10: a) Photograph showing plan view of oriented sample in high strain zone. b) photograph of sample shown in (a) showing location of thin sections in plan (YZ plane of the strain ellipsoid) and section (XZ plane of the strain ellipsoid) view. c) and d) photomicrographs in natural light showing highly strained minerals (white = quartz, grey = sericitized feldspar, green = amphibole) in plan (c) and section view (d).....	87
Figure 3.3.11: Interpreted photographs showing: a) F_2 fold in calc-silicate-bearing veins with cm-scale high strain zones that caused transposition parallel to the fold's axial plane. b) centimeter-scale high strain zones that completely transposed the limbs of an F_2 fold, of which only the hinge was preserved.....	88
Figure 3.3.12: Photographs showing: a) rotated clast in highly strained conglomerate (located at circled number 4 on Figure 3.3.8) indicative of dextral strike-slip motion (rolling structures of (Van Den Driessche and Brun, 1987)). b) high strain parallel to S_2 in metasomatized rocks of the large stripped outcrop (vertical section looking towards the east).....	89
Figure 3.3.13: Geological map of the eastern portion of the large stripped outcrop showing the distribution of high strain zones.....	90
Figure 3.3.14: Line drawings showing: a) interpreted kinematics of conjugate shear zones present on the large stripped outcrop based on the distribution of shear zones (thick lines) and S_2 fabric (thin lines). b) distribution of conjugate shear zones (thick lines) and regional foliation (thin lines) of the Proterozoic St-Cast granites (France) (modified from Gapais et al., 1987).....	90
Figure 3.3.15: Geological map of a portion of the large stripped outcrop showing the distribution of quartz veins along one shear zone.....	92
Figure 3.3.16: Schematic diagrams showing 3D patterns of conjugate shear zones that affected the External Crystalline Massifs of the Central Alps (modified from Gapais et al., 1987): a) 3 stages of increasing bulk strain interpreted for the Aar granites, which is interpreted to result from coaxial deformation. b) 3D shear zone pattern of the Gotthard granites, which is interpreted to result from non-coaxial deformation.....	93
Figure 3.3.17: Photographs showing: a) offsets along S_2 planes. b) shear plane sub-parallel to S_2 in Roberto's auriferous stockwork. c) dragging of S_2 and isoclinally-folded material of the East-Roberto zone along a slip plane.....	94
Figure 3.3.18: Photographs showing: a) auriferous stockwork of the Roberto zone showing slip movement along bedding and S_2 planes. b) slip planes oriented parallel and at some angle to bedding which dragged veins emplaced parallel to S_2 . c) interpreted drawing of photograph shown in (a) showing details of multiple slip surfaces (thin lines = veins emplaced parallel to S_2 and/or S_2 , black regions = beds, dashed lines = slip planes, all other lines = veins).....	96
Figure 3.3.19: Map of the large stripped outcrop showing the interpreted trace of S_2	97
Figure 3.3.20: Close-ups of various parts of the large stripped outcrop. a) extensional quartz veins distributed along the East-Roberto zone whose distribution is consistent with the dextral drag observed in S_2 (see Figure 3.3.19). b) and c) photographs showing details of inserts (b) and (c) shown on (a). d) sets of extensional quartz veins located west of the Roberto zone whose distributions appear to be controlled by bedding-parallel slip. e) pegmatite dykes distributed nearby the Mid-Roberto zone whose distribution is consistent with the observed sinistral drag in S_2 (see Figure 3.3.19).....	98

Figure 3.3.21: Photographs of the pegmatite dyke dated at ca. 2603 Ma showing: a) pegmatite dyke cross-cutting the slip plane that affects the East-Roberto zone. b) F_3 folds in the pegmatite dyke shown in (a).	99
Figure 3.3.22: Photographs showing: a) late brittle fault (center of photograph) from trench DEC-08-06. b) brecciated region associated with late fault on the large stripped outcrop. c) epidote-rich brecciated fault zone on trench DEC-08-06.	100
Figure 3.3.23: Maps showing: a) location of the large fault structure located to the east of the deposit. This structure offset diabase dykes. b) fault structure seen on airborne magnetic map. c) fault structure as shown on aerial photograph.	101
Figure 3.3.24: Gocad snapshots showing the deposit's geometry and two E-W sections (looking north) showing variations in the dip of lithological units and auriferous zones.	103
Figure 3.3.25: Simplified map showing the distribution of the S_2 and S_3 fabric, the asymmetry of outcrop-scale F_3 folds, and the axial traces of F_3 folds.	104
Figure 3.3.26: Simplified map showing the distribution of the S_2 and S_3 fabric, the interpreted trace of bedding, the asymmetry of outcrop-scale F_2 folds, and the interpreted axial traces of F_1 , F_2 , and F_3 folds.	105
Figure 3.3.27: Map of the large stripped outcrop showing the distribution of linear features (fold axes and lineations), high strain zones, and interpreted trace of bedding and S_2 fabric.	107
Figure 3.3.28 Gocad snapshots showing: a) distribution of lithological units and auriferous zones. b) N-S section (looking east) showing an interpreted trace of the distribution of aluminosilicate-bearing rocks (white line) underneath the large stripped outcrop (horizontal green line).	109
Figure 3.3.29: Geological maps of the Roberto deposit area showing: a) distribution of lithological units constructed from projection of 3D reconstruction. b) stylized distribution of lithological units assuming that the observed discontinuities of map shown in (a) correspond to highly transposed F_2 fold limbs.	111
Figure 3.3.30: Photographs showing: a) F_2 folding associated with intense transposition in incompetent bed located in the eastern part of the large stripped outcrop. b) F_3 fold in S_0/S_2 with two faults parallel to S_3 on the short limb of the fold on an outcrop located ~500m east of the large stripped outcrop. c) rotated blocks along lithological units in a shear zone located in the southern part of the Éléonore property.	112
Figure 3.3.31: a) to c) 3D Gocad reconstructions for the first 400 meters of the Roberto deposit showing the distribution of auriferous zones (transparent blue), high grade auriferous zones (red), and aluminosilicate-bearing rocks (pale yellow). b) Distribution of selected auriferous zones and associated median planes used to calculate a fold axis for the "outcrop area". c) Distribution of selected auriferous zones and associated median planes used to calculate a fold axis for the "lake area". d) to i) Equal area nets (lower hemisphere) showing the distribution of structural measurements extracted from Gocad and/or structural measurements collected on the stripped outcrop.	115
Figure 3.4.1: Simplified geological map of the Roberto area showing the lower grade window of metagreywacke and the surrounding paragneiss, migmatites, and intrusive rocks.	116
Figure 3.4.2: Natural light (left) and cross-polarized (right) photomicrographs of sillimanite. a) and b) fibrolite porphyroblasts locally replaced by muscovite. c) and d) sillimanite needles coexisting with biotite.	117

Figure 3.4.3: Cross-polarized photomicrograph showing examples of a microcline poikiloblast (a) and plagioclase porphyroblasts (b).	118
Figure 3.4.4: Cross-polarized photomicrograph showing examples of sillimanite coexisting with microcline (a) and plagioclase (b).	118
Figure 3.4.5: Petrogenetic grid for pelitic metasedimentary rocks from (Yardley, 1989)	119
Figure 3.4.7: Natural light (left) and cross-polarized (right) photomicrographs showing the progressive retrogradation of sillimanite and microcline to muscovite and quartz. a) and b) muscovite replacing the extremities of sillimanite porphyroblast. c) and d) muscovite porphyroblasts with preserved relics of sillimanite.	121
Figure 3.4.8: a) to d) Natural light (left) and cross-polarized (right) photomicrographs of crenulated S ₂ foliation defined by biotite crystals. e) photograph of S ₃ crenulation from which photomicrographs a) to d) were taken. f) close-up on e).	123
Figure 3.5.1: Gocad snapshot showing the distribution of auriferous zones.	125
Figure 3.5.2: Geological map showing the location of the two principal (Roberto and East-Roberto) and one subsidiary (Mid-Roberto) auriferous zones present on the large stripped outcrop.	126
Figure 3.5.3: A-CN-K ternary plot of "unaltered" metasedimentary rocks from the Quetico Subprovince.	128
Figure 3.5.4: A-CN-K ternary plots of selected lithological units within Éléonore's turbidite sequence. a) and b): greywacke. c) and d): massive greywacke. e) and f): aluminosilicate-bearing sequence. g) paragneiss.	129
Figure 3.5.5: Diagrams comparing the element and oxide concentrations in aluminosilicate-bearing rocks with concentrations in "old greywacke" (a) and in "massive greywacke" (b).	133
Figure 3.5.6: Geological map of the Roberto deposit area showing regions and hand samples affected by Ca-bearing alteration.	134
Figure 3.5.7: Gocad snapshot showing the distribution of Ca-bearing alteration from which the map of Figure 3.5.6 was constructed.	135
Figure 3.5.8: Photographs showing: a) Ca-bearing replacement concordant to bedding in aluminosilicate-bearing rocks. b) Ca-bearing replacement discordant to bedding in aluminosilicate-bearing rocks. c) Ca-bearing replacement in massive greywacke. Note the local presence of quartz-feldspar veins. d) pervasive Ca-bearing replacement in massive greywacke. e) fracture-controlled Ca-bearing stockwork in greywacke. f) Ca-bearing replacement in auriferous stockwork of Roberto.	136
Figure 3.5.9: Geological map of the large stripped outcrop showing the distribution of Ca-bearing alteration.	137
Figure 3.5.10: Photographs showing: a) Ca-bearing replacement in aluminosilicate-bearing rocks on outcrop. b) details of Ca-bearing replacement on sawed section of sample shown in (a). c) close-up of section shown in (b).	138
Figure 3.5.11: Natural light (left) and cross-polarized (right) photomicrographs of Ca-bearing replacement and host rocks in aluminosilicate-bearing sequence. a) and b) aluminosilicate-free host rock in contact with Ca-replacement. c) and d) outer part of Ca-bearing replacement. e) and f) central part of Ca-replacement.	140

Figure 3.5.12: Photographs showing: a) Ca-bearing replacement within massive greywacke on outcrops. b) details of Ca-bearing replacement on sawed section of sample shown in (a)..	141
Figure 3.5.13: Natural light (left) and cross-polarized (right) photomicrographs of Ca-bearing replacement in massive greywacke and of massive greywacke host rocks. a) and b) least-altered massive greywacke located far from any significant Ca-bearing alteration. c) and d) massive greywacke host near Ca-bearing replacement. e) and f) massive greywacke host in contact with Ca-bearing replacement.....	142
Figure 3.5.14: Photographs showing: a) calc-silicate-bearing vein in greywacke on outcrops. b) details of calc-silicate-bearing vein on sawed section of sample shown in (a).....	144
Figure 3.5.15: Natural light (left) and cross-polarized (right) photomicrographs of calc-silicate-bearing vein in greywacke and of greywacke host rocks. a) and b) least-altered greywacke located far from any significant Ca-bearing alteration. c) and d) greywacke host near calc-silicate-bearing vein. e) and f) greywacke host in contact with calc-silicate-bearing vein.....	145
Figure 3.5.16: Photographs showing: a) calc-silicate-bearing vein in East-Roberto zone on outcrops. b) details of calc-silicate-bearing vein on sawed section of sample shown in (a).....	147
Figure 3.5.17: Natural light (left) and cross-polarized (right) photomicrographs of calc-silicate-bearing vein in East-Roberto zone and of East-Roberto host rocks. a) and b) East-Roberto host near calc-silicate-bearing vein. c) and d) East-Roberto host in contact with calc-silicate-bearing vein. e) and f) calc-silicate-bearing vein in East-Roberto zone.....	148
Figure 3.5.18: Photographs showing: a) calc-silicate-bearing vein and Ca-bearing replacement in Roberto zone on outcrops. b) details of calc-silicate-bearing vein and Ca-bearing replacement on sawed section of sample shown in (a).	149
Figure 3.5.19: Natural light (left) and cross-polarized (right) photomicrographs of calc-silicate-bearing vein and Ca-bearing replacement in Roberto zone. a) and b) Ca-bearing replacement near calc-silicate-bearing vein. c) and d) calc-silicate-bearing vein in Roberto.....	150
Figure 3.5.20: Photographs showing: a) Ca-bearing replacement in Roberto zone on outcrops. b) details of sample shown in (a).....	151
Figure 3.5.21: Natural light (left) and cross-polarized (right) photomicrographs of Ca-bearing replacement (near calc-silicate-free vein) and host rocks in Roberto zone. a) and b) host rock in contact with Ca-bearing replacement. c) and d) Ca-bearing replacement near calc-silicate-free vein in Roberto. e) and f) calc-silicate-free vein in Roberto zone.....	152
Figure 3.5.22: Photographs showing: a) thick diopside-bearing vein located in between East-Roberto and Roberto auriferous zones. b) microcline- and tourmaline-rich selvages associated with a diopside-bearing vein.....	153
Figure 3.5.23: Photograph showing sample (TR-3) used to create isocons for Ca-replacement in aluminosilicate-bearing sequence.	154
Figure 3.5.24: Isocon diagrams and corresponding mass balance histograms for Ca-bearing replacement in aluminosilicate-bearing sequence. a) isocon diagram and mass balance histogram for the aluminosilicate-free part (TR-3b). b) isocon diagram and mass balance histogram for the outer part of the Ca-bearing replacement (TR-3c).	155
Figure 3.5.25: Box diagrams showing the range of oxide concentrations of Ca-bearing alteration and host rocks within aluminosilicate-bearing sequence..	157

Figure 3.5.26: Photograph showing sample (JFR-07-328) used to create isocons for Ca-replacement in greywacke host rocks.....	159
Figure 3.5.27: Isocon diagrams and corresponding mass balance histograms for a greywacke hosting a calc- silicate-bearing vein (JFR-07-328, Figure 3.5.26). a) isocon diagram and mass balance histogram for the greywacke host located near the calc-silicate-bearing vein. b) isocon diagram and mass balance histogram for the greywacke in contact with the calc-silicate-bearing vein (see Figure 3.5.26).	160
Figure 3.5.28: Box diagrams showing the range of oxide concentrations of calc-silicate-bearing veins and greywacke host rocks.	161
Figure 3.5.29: Photograph showing sample (JFR-08-392) used to create isocons for Ca-bearing replacement near calc-silicate-free quartz-biotite veins in Roberto.....	163
Figure 3.5.30: Isocon diagrams and corresponding mass balance histograms for Ca-bearing replacement (near calc-silicate-free quartz-biotite vein) and Roberto host rocks (from sample JFR-08-392). a) Roberto host located near Ca-bearing replacement. b) Roberto host rock in contact with Ca-bearing replacement. c) Ca-bearing replacement near calc-silicate-free quartz-biotite vein in Roberto.....	164
Figure 3.5.31: Isocon diagram and corresponding mass balance histogram for Ca-bearing replacement (near calc-silicate-free vein) assuming that the protolith is the "host rock in contact with Ca-bearing replacement" part of sample JFR-08-392 (Figure 3.5.29).....	165
Figure 3.5.32: Photograph showing how Ca-bearing replacement locally appears to be superimposed on pre-existing minerals of Roberto's auriferous stockwork..	166
Figure 3.5.33: Box diagrams showing the range of oxide concentrations of calc-silicate-bearing veins and Ca-bearing replacement in function of their location.....	168
Figure 3.5.34: Photographs showing various calc-silicate-bearing veins or Ca-bearing replacement bands folded by F_2 folds. a) folded calc-silicate-bearing veins transposed by high strain zones. b) F_2 fold in Ca-bearing replacement band with highly transposed limbs. c) isoclinally folded calc-silicate-bearing vein within East-Roberto zone. d) and e) folded Ca-bearing replacement bands in aluminosilicate-bearing sequence.....	171
Figure 3.5.35: Photographs of calc-silicate-bearing veins or Ca-bearing replacement bands transposed by S_2 and/or L_2 . a) and b) calc-silicate-bearing veins transposed by high strain zones. c) vertical section showing highly transposed Ca-bearing replacement bands. d) lineated calc-silicate-bearing veins on vertical section of East-Roberto zone. e) highly transposed calc-silicate-bearing veins, quartz veins, and tourmaline-rich host rock in drillcore of East-Roberto zone.....	172
Figure 3.5.36: Photographs showing boudinaged calc-silicate-bearing veins or Ca-bearing replacement bands. a) boudinaged replacement bands within aluminosilicate-bearing rock. b) boudinaged calc-silicate-bearing veins in paragneissic rock. c) boudinaged diopside-bearing vein in drillcore. d) sawed sample face showing boudinaged diopside-bearing vein.	173
Figure 3.5.37: Photomicrographs in cross-polarized light of deformed crystals within calc-silicate-bearing veins. a) subgrain boundaries (sub-vertical) within quartz grain. b) deformation lamellae (top-left to lower-right) within quartz grain. c) subgrains (right-hand side of crystal) and deformation twins in plagioclase crystals. d) two sets of deformation twins in calcite grain.....	174
Figure 3.5.38: Natural light (left) and cross-polarized (right) photomicrographs showing preferentially-oriented or randomly-oriented biotite porphyroblasts within calc-silicate-bearing	

veins or Ca-bearing replacement. a) and b) preferentially oriented biotite with Ca-bearing replacement. c) and d) coarser-grained randomly-oriented biotite porphyroblasts within Ca-bearing replacement. e) and f) coarse-grained randomly-oriented biotite porphyroblasts within calc-silicate-bearing vein.	175
Figure 3.5.39: Natural light (left) and cross-polarized (right) photomicrographs showing preferentially-oriented or randomly-oriented amphibole porphyroblast within calc-silicate-bearing veins or Ca-bearing replacement. a) and b) amphibole porphyroblasts oriented by S_2 in Ca-bearing replacement. c) and d) large amphibole porphyroblasts randomly oriented within Ca-bearing replacement. Note the presence of oriented biotite porphyroblasts. e) and f) diopside porphyroblasts coexisting with deformed amphibole porphyroblasts.	176
Figure 3.5.40: Natural light photomicrographs of tourmaline crystals within a calc-silicate-bearing vein shown in plan (a) and vertical (b) views.	177
Figure 3.5.41: Natural light (left) and cross-polarized (right) photomicrographs of biotite porphyroblasts retrograded to various minerals within Ca-altered rocks. a) and b) biotite retrograded to chlorite. c) and d) biotite retrograded to chlorite, prehnite, and muscovite. e) and f) randomly-oriented biotite porphyroblasts replaced by prehnite.	179
Figure 3.5.42: Natural light (left) and cross-polarized (right) photomicrographs of amphibole porphyroblasts and sulphides retrograded and/or altered to various minerals within Ca-altered rocks. a) and b) pyrrhotite inclusion within amphibole porphyroblast replaced by epidote. c) and d) pyrrhotite replaced by clinozoisite and amphibole replaced by prehnite. e) and f) retrograde prehnite rim between randomly-oriented amphibole porphyroblasts and pyrrhotite.	180
Figure 3.5.43 Cross-polarized photomicrographs of plagioclase altered to various minerals within Ca-altered rocks. a) plagioclase altered to sericite and saussurite. b) plagioclase altered to sericite and carbonate.	181
Figure 3.5.44: Photograph showing aluminosilicate-free halos around Ca-bearing bands hosted by the aluminosilicate-bearing sequence.	182
Figure 3.5.45: Geological map of the Roberto deposit showing the distribution of samples affected by potassic alteration and samples considered to be the least altered.	184
Figure 3.5.46: Natural light (left) and cross-polarized (right) photomicrographs of K-altered greywacke located outside (a, b) and within (c, d) auriferous zones.	186
Figure 3.5.47: Natural light (left) and cross-polarized (right) photomicrographs of K-altered greywacke in massive greywacke (a, b) and aluminosilicate-bearing rocks (c, d).	187
Figure 3.5.48: Natural light (left) and cross-polarized (right) photomicrographs of microcline and/or biotite bearing veins and veinlets within Roberto zone. a) and b) microcline-tourmaline-arsenopyrite-pyrrhotite-bearing quartz veinlets. c) and d) biotite (locally replaced by chlorite)-arsenopyrite-pyrrhotite-bearing quartz vein in Roberto zone.	188
Figure 3.5.49: Box diagrams comparing the range of oxide concentrations of K-altered and least-altered equivalents for greywacke, massive greywacke, and aluminosilicate-bearing rocks.	190
Figure 3.5.50: Isocon diagrams and corresponding mass balance histograms for K-altered rock types and least-altered equivalents constructed from the average compositions listed in tables 3.5.1 and 3.5.2. a) isocon diagram and mass balance histogram for least-altered greywacke and K-altered greywacke located outside mineralized zones. b) isocon diagram and mass balance histogram for least-altered greywacke and K-altered greywacke located within mineralized zones.	193

Figure 3.5.51: Chondrite-normalized (Sun and McDonough, 1989) spider diagram comparing trace element signatures of K-altered rocks and least-altered equivalents.....	196
Figure 3.5.52: Photographs and photomicrographs showing folded and transposed microcline and/or biotite bearing quartz veins and veinlets within the auriferous stockwork of the Roberto zone. a) isoclinally folded quartz vein in "PQ" size drillcore with axial-plane oriented sup-parallel to core axis. b) transposed and tightly folded veinlets on a polished vertical section of an hand sample. c) folded and transposed vein in drillcore. d) and e) natural light (d) and cross-polarized (e) photomicrographs of a isoclinally folded and boudinaged veinlet hosted within a microcline and arsenopyrite rich matrix.....	198
Figure 3.5.53: Photographs and photomicrographs which show textural characteristics of crenulated quartz veinlets and axial-planar quartz veinlets within the auriferous stockwork of the Roberto zone. a) and b) field examples of crenulated veinlets and axial-planar veinlets. c) and d) natural light (c) and cross-polarized (d) photomicrographs showing textures of a crenulated veinlet and an axial-planar veinlet. e) and f) close-up of (c) and (d)..	199
Figure 3.5.54: Photograph of Roberto's auriferous stockwork showing microcline and/or biotite bearing quartz veinlets emplaced along S_2 planes through the generation of a cleavage oriented at high angle to bedding planes.....	200
Figure 3.5.55: a) Photograph showing a part of Roberto's auriferous stockwork where the stockwork is preferentially developed on the short limb of a meter-scale F_2 Z-fold. b) interpreted drawing of the photograph in (a) showing the details of the auriferous stockwork.....	201
Figure 3.5.56: Photomicrographs showing biotite defining S_2 (a: natural, b: cross-polarized) and recrystallized polygonal microcline and quartz (b to d). In (c), tourmaline crystals are defining S_2	202
Figure 3.5.57: Geological map of the large stripped outcrop showing the distribution of the principal auriferous zones and different generations of veins.....	203
Figure 3.5.58: Photographs of various alteration facies present in the East-Roberto auriferous zone. a) and b) hydrothermal breccia. c) and d) highly strained calc-silicate-bearing veins interlayered with tourmaline-rich rock. e) and f) silica-flooding bounded by East-Roberto slip plane.....	205
Figure 3.5.59: Photographs and photomicrographs showing different characteristics of the Roberto zone. a) preserved bedding in sedimentary unit that hosts the Roberto zone. b) K-altered rocks associated with microcline and/or biotite bearing veinlets. c) high grade material (> 20 g/t Au). d) Roberto stockwork in drillcore. e) microphotograph showing gold hosted by arsenopyrite crystal. f) microphotograph showing arsenopyrite crystals hosted by a quartz veinlet of the auriferous stockwork with abundant tourmaline in the selvages.....	208
Figure 3.5.60: Photographs of Ca-bearing replacement within Roberto's auriferous stockwork. a) bleached-regions correspond to metasomatic replacement of plagioclase to saussurite and sulphides by clinozoisite. b) Ca-replacement superimposed on quartz-tourmaline veinlets. c) metasomatic replacement of plagioclase to saussurite in the selvages of a vein containing abundant chlorite and prehnite replacing biotite. d) close-up of (c).....	209
Figure 3.5.61: a) Geological map of a part of the large stripped outcrop showing the distribution of the vein (yellow lines) that bounds the western contact of the Roberto zone. b) photograph showing the mineralogy of the vein shown in (a). c) photograph showing F_3 folds and D_2 boudins in the quartz-actinolite-arsenopyrite-pyrrhotite vein shown in (a) and (b).	210

Figure 3.5.62: Photographs showing randomly-oriented veins (a) and veins with attitudes controlled by bedding and foliation planes (b) within Roberto's auriferous stockwork.	211
Figure 3.5.63: Photographs showing calc-silicate-bearing quartz-biotite veins emplaced parallel to bedding planes in Roberto's auriferous stockwork.	212
Figure 3.5.64: Photographs showing auriferous stockwork preferentially developed on the short limbs of F_2 folds.	212
Figure 3.5.65: Photographs showing highly transposed parts of the Roberto zone. a) layering defined by multiple quartz veins transposed along the S_2 foliation. b) Boudinaged calc-silicate-bearing vein oriented parallel to S_2	212
Figure 3.5.66: Photographs showing a) fault planes within Roberto's auriferous stockwork, and (b), a fault bounding the stockwork.	213
Figure 3.5.67: Photographs showing stockworks locally developing in association with quartz veins and/or veinlets filling fractures outside Roberto's principal stockwork.	213
Figure 3.5.68: Mosaic photograph showing an auriferous stockwork developing in association with a calc-silicate-bearing quartz vein located a few meters from Roberto's main stockwork.	214
Figure 3.5.69: Photographs of drillcore showing high grade mineralization associated with quartz-feldspar veins (a and b) that locally become pegmatitic (c), and gold mineralization hosted by paragneissic rocks (d).	216
Figure 3.5.70: Photographs of quartz-feldspar veins.	217
Figure 3.5.71: Geological map of trench 08-10 showing cross-cutting relationships between aplitic pegmatite dykes and an auriferous quartz vein associated with a mineralized zone.	219
Figure 3.5.72: Sulphidation curves in the system Fe-As-S in the stability range of arsenopyrite (shaded).	221
Figure 3.5.73: Sketches from Tomkins and Mavrogenes (2001) showing examples of possible textural relations arising from prograde and retrograde metamorphic reactions discussed in the text. a) Incomplete prograde metamorphism of arsenopyrite to löllingite and pyrrhotite. b) Complete prograde metamorphism of arsenopyrite to löllingite and pyrrhotite. c) Complete prograde metamorphism of arsenopyrite to löllingite and pyrrhotite with subsequent retrograde metamorphism back to arsenopyrite.	221
Figure 3.5.74: Theoretical sketches from Tomkins and Mavrogenes (2001) showing progressive stages of destruction of gold-bearing löllingite during stages of retrograde metamorphism (reaction 2). a) Initially, no gold is visible and a thin band of new gold-free arsenopyrite separates pyrrhotite from gold-bearing löllingite. b) With further consumption of löllingite and pyrrhotite, native gold appears at the löllingite-arsenopyrite interface c) As retrograde metamorphism continues, native gold starts to form within the löllingite crystal. d) Eventually, all of the löllingite is consumed and only arsenopyrite and pyrrhotite remain.	222
Figure 3.5.75: SEM photomicrographs showing: a) löllingite grain rimmed by arsenopyrite and pyrrhotite. b) arsenopyrite-löllingite composite grain hosted by a diopside porphyroblast. c) blocky arsenopyrite replacing löllingite. d) complex recrystallization texture in pyrrhotite grain (all different colored phases are pyrrhotite).	224
Figure 3.5.76: SEM photomicrographs showing: a) löllingite grain rimmed by arsenopyrite. b) close-up on (a) showing gold grains distributed along löllingite-arsenopyrite boundaries. c) löllingite grain rimmed by arsenopyrite and pyrrhotite showing large gold grains distributed along	

löllingite-arsenopyrite boundaries and numerous gold inclusions within arsenopyrite. d) close-up on (c) showing numerous gold inclusions within arsenopyrite.	225
Figure 4.1.1: Map showing the location of analyzed geochronological samples in the vicinity of the Roberto deposit.	228
Figure 4.1.2: Photographs of selected geochronological samples in outcrops. a) Geochron-ELE-05-01: Roberto host rock (adjacent to Roberto zone). b) Geochron-ELE-05-02: Al-bearing metasedimentary rock (contains Ca-bearing replacement band). c) Geochron-ELE-05-03: conglomerate. d) Geochron-ELE-05-06: Al-bearing metasedimentary rock. e) Geochron-ELE-05-08: Roberto host rock (in Roberto zone). f) Geochron-ELE-06-12: feldspar-porphyry dyke (contains various rock fragments).	229
Figure 5.2.1: Schematic representation of the timing of selected geologic events relative to gold mineralization.	239
Figure 8.1.1: Map showing available outcrop exposures and localization of Roberto's auriferous zones.	265
Figure 8.1.2: Bird's eye view of the large stripped outcrop that exhibits the core of Roberto's auriferous system.	267
Figure 8.1.3: Detailed map of the large stripped outcrop created using RTK GPS and ArcGIS..	268
Figure 8.2.1: Gocad snapshot showing a surface with sharp dip changes and "bull's eye" regions.	271
Figure 8.2.2: Gocad snapshots showing how surfaces are constructed. a) Well markers added on selected drill hole traces. b) Surface created from well markers displayed in (a).	271
Figure 8.2.3: Gocad snapshots showing various steps of method used to generate surfaces. a) Surfaces respecting initial rules/assumptions, created from well markers. b) Sets of digitized parallel curves filling gaps between surfaces shown in (a). c) Surfaces created through interpolation of curves shown in (b).	272
Figure 8.2.4: Final aspect of lithological surfaces created through the method elaborated in this study.	273
Figure 8.2.5: Gocad snapshots showing: a) Sets of horizontal parallel curves delimitating the distribution of dyke swarms (in this case pegmatite dykes). b) Surfaces created by interpolating through sets of parallel curves shown in (a).	274
Figure 8.2.6: Photographs of : a) Reflex ACT© core orientating device. b) Oriented core onto which core's low side can be marked.	275
Figure 8.2.7: Gocad Snapshot showing visual aspects of structural data (e.g. foliation measurements) displayed on a drill hole trace.	276
Figure 8.2.8: Figure comparing surface and subsurface structural measurements of main foliation over a selected area of the Roberto deposit. a) Gocad snapshot showing 3D structural tablets of foliation measurements measured at surface (red/orange) and foliation measurements measured on oriented drillcore (yellow/green). b) Equal area net (lower hemisphere) showing the attitude of poles to foliation displayed in (a).	277
Figure 8.3.1: Views of stripped outcrop in ArcGIS showing: a) Query results (green circle) for surface hand samples that are sedimentary rocks with less than 1000 ppb of gold in which	

microcline has been petrographically observed. b) Query results of (a) color-coded according to their arsenic content.	279
Figure 8.3.2: View of stripped outcrop in ArcGIS showing channel samples color-coded according to their gold content.	280
Figure 8.3.3: Gocad snapshot of the Roberto deposit showing multi-sourced data imported into Gocad's 3D environment.	281
Figure 8.3.4: Example of a drill hole log created in Gocad showing variations of selected major elements with depth.	282
Figure 9.1.1: Detailed map of the large stripped outcrop showing distribution of lithological units, veins, and structural features. Coordinates are in UTM Nad83.	283

1 INTRODUCTION

The Roberto gold deposit represents one of the most significant gold discoveries of the past 10 years in Canada. The multi-million ounces gold deposit was discovered by Virginia Gold Mines (now Virginia Mines) in 2004 on their Éléonore property located in the James Bay territory, Quebec. The region then rapidly became a key target for gold exploration because of its potential to host a new gold district. In May 2006, Goldcorp Inc. acquired 100% of the property with the intention of developing the deposit through their Opinaca Mines Ltd. wholly-owned subsidiary. Since then, Opinaca Mines Ltd. conducted an intensive drilling program in order to better define the extent of mineralized zones. The latest resource estimation (publicly released in February 2010) indicated a total of more than 9 million ounces (280 t) of inferred (6.25 Moz, 194 t) and indicated resources (3.15 Moz, 98 t) (Goldcorp, 2010).

The geology of the Roberto deposit differs from most Archean gold deposits of the Superior Province in that it is characterized by stockwork and replacement-style mineralization hosted within amphibolite facies turbiditic metagreywacke and paragneiss. Contrary to the well-studied and well-explored Abitibi greenstone belt of the Superior Province, gold exploration in the James Bay territory is more recent and the geoscience knowledge base is more limited. The Roberto deposit is a landmark for future gold exploration within the under-explored northern part of the Superior Province. However, being an atypical gold deposit, the key geological parameters involved in its genesis need to be identified in order to understand its formation and define exploration criteria that will help discover similar gold deposits in the James Bay territory and elsewhere in the Superior Province.

1.1 Purpose of Study

The study of gold deposits hosted in metamorphic terranes is generally complex and often controversial (e.g. Groves et al., 2003). This complexity is in part related to the protracted and complex deformational, metamorphic, and magmatic history of the geological settings and the difficulty to determine the timing of gold relative to these events. Gold deposits can form during orogenesis, in association with metamorphic fluids (e.g. Dubé and Gosselin, 2007), or in shallower environments (e.g. Figure 1.1.1) and be buried, deformed, and metamorphosed during subsequent orogenic events. Although deformation and metamorphism may obscure primary

genetic relationships, thorough analysis and recognition of key geological features can commonly be used to unravel the genetic history of a given gold deposit.

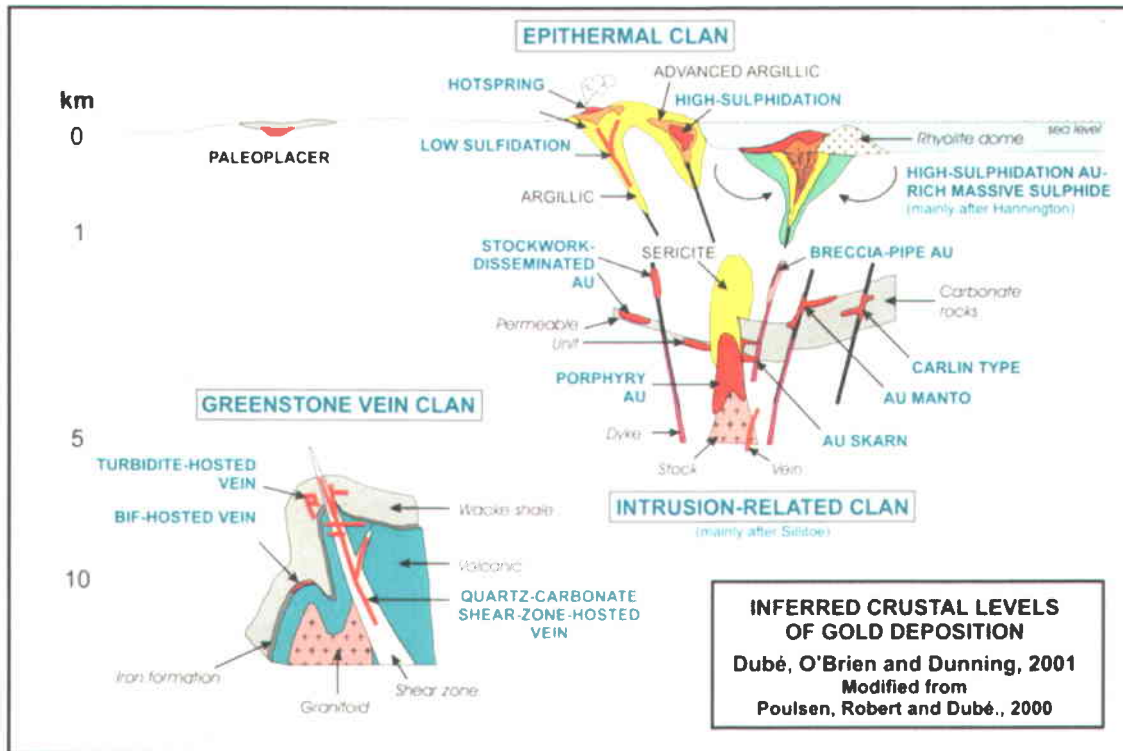


Figure 1.1.1: Schematic diagram showing the distribution of different types of gold deposits in function of crustal levels. (From Dubé and Gosselin, 2007)

Gold deposits that form during orogenesis in association with metamorphic fluids are commonly referred to, among other names, as greenstone-hosted deposits, mesothermal gold deposits, orogenic deposits, and lode-gold deposits (Dubé and Gosselin, 2007 (and references therein)). Such deposits are widespread in Archean terranes of the world, and represent one of the most important type of gold deposits in Canada including the renowned greenstone-hosted quartz-carbonate gold deposits of the Abitibi Subprovince. Gold mineralization within those deposits is typically associated with structurally-controlled quartz-carbonate fault-filled veins hosted within brittle-ductile shear zones that affect greenschist to amphibolite facies mafic volcanic rocks (Robert and Brown, 1986; Robert et al., 2005; Dubé and Gosselin, 2007).

After initial inspection of the Roberto deposit prior to this study, it was recognized that the deposit couldn't clearly be identified as a typical quartz-carbonate gold deposit or as a gold deposit that formed at shallower depth. It was also recognized that the geological context of the deposit is complex, being hosted by highly deformed and metamorphosed rocks. The high

metamorphic grade resulted in the occurrence of mineral assemblages that are not typical of gold deposits of the Abitibi Subprovince, and in that context, Roberto is different. In addition, the deposit is located in the hinge of a km-scale fold which could indicate that deformational events played a role in preserving and/or controlling sites of gold mineralization. Another important aspect of the geological setting of Roberto is the presence of a nearby dioritic stock (Ell Lake intrusion) (Savard and Ouelette, 2005) that locally hosts gold-copper mineralization and that locally contains alteration zones that share some analogies in terms of style and composition to the alteration zones of Roberto. This spatial association could suggest that Roberto is an intrusion-related deposit, perhaps a porphyry-style type, and hence genetically related to the Ell Lake intrusion. These contrasting genetic models illustrate the main objective of this study, that is to document and weight key geological characteristics of the deposit allowing to circumscribe the genetic model and its potential impact for exploration. Each of these unconstrained genetic models has specific consequences on the exploration parameters to be used to discover similar deposits in the area. This illustrates the importance of establishing the relative timing between gold mineralization, unconformities, pluton emplacement, metamorphism, and deformational events in order to generate a well-defined genetic and exploration model(s). Detailed and comprehensive documentation of geological relationships is therefore needed to define and test genetic models for the Roberto deposit.

1.2 Objectives

Based on regional and local geological mapping, structural analysis, core logging, petrography, and geochronology, the objectives of this study are to:

- Acquire an understanding of the regional and local geology.
- Determine the geological parameters involved in the formation and distribution of gold mineralization of the Roberto deposit.
- Determine the relative chronology between gold mineralization, tectono-metamorphic events, and magmatic phases.
- Determine the relative ages of the main lithological units by incorporating geochronology work done at the Geological Survey of Canada by V. McNicoll and B. Dubé.
- Define the geochemical characteristics of the deposit and its hydrothermal footprint.
- Define exploration criteria that may be used to discover similar deposits elsewhere in the James Bay area and in the Superior Province.

1.1 Methodology

This section presents and describes the methodology used to fulfill the principal objectives mentioned above which include: determining the geological setting of the deposit, defining the morphological, geochemical, metallogenic, and metamorphic characteristics of gold mineralization and associated hydrothermal alteration, and establishing the timing between gold mineralization, deformational/metamorphic events, and other geological features.

1.1.1 Methodology for Determining the Geological Setting of the Deposit

A good knowledge of the geological setting of the deposit is required in order to properly locate the deposit within the adequate tectonic setting. Chapter 2 presents the regional and local geology of the Roberto deposit based on previous studies and literature. The geological setting of the deposit was studied in greater details during the course of this study through geological mapping at various scales (deposit- to regional-scale (1:50,000)). In 2006, a part of the geological mapping was conducted in partnership with the Ministère des Ressources Naturelles et de la Faune du Québec (MRNF). Structural geology was combined with geochronology of metasedimentary, metavolcanic, and intrusive rocks in order to define the chronostratigraphy and adequately locate the host rocks of the deposit within the established chronostratigraphic framework. The study also focused on determining the structural characteristics of deformational and metamorphic events that affected the Éléonore property and surrounding areas.

1.1.2 Methodology for Determining the Morphological, Geochemical, Metallogenic, and Metamorphic Characteristics of Gold Mineralization and Associated Hydrothermal Alteration

The main characteristics of mineralized zones and associated hydrothermal alteration are presented in Chapter 3. The morphological characteristics and the geometry of auriferous zones are determined through geological mapping, drillcore analysis, petrography, and 3D modeling. The mineralogical and petrographic characteristics of mineralization and alteration facies that form the principal constituents of auriferous zones are also defined. The geochemical characteristics of such constituents are determined using box diagrams and isocon diagrams. Petrography is used to document important textural characteristics that can be used to establish timing relationships between mineralization/alteration and deformational/metamorphic events. A

section is devoted to the mineralogy and the textures of sulphide minerals in order to determine their occurrences relative to the peak of metamorphism. Another section presents geochemical profiles and characterizes the hydrothermal footprint of the deposit.

1.1.3 Methodology for Determining the Timing between Gold mineralization, Deformational/Metamorphic Events, and other Geological Features

A good understanding of the relative timing between gold mineralization, deformational/metamorphic events, and other geological features (intrusive phases, unconformities, etc.) is required to determine whether the deposit formed in association with geological features proper to its geological setting prior to being deformed and metamorphosed, or directly formed during and in association with deformational/metamorphic events.

Chapter 3 focuses on characterizing important aspects of the geology of the Roberto deposit and establishing key relationships that can be used to determine the relative timing between gold mineralization and other geological features. Important morphological characteristics of lithological units are determined through geological mapping and drillcore analysis. Such characteristics are combined with geochemistry, petrography, and geochronology in order to better characterize individual lithological units and determine their relative chronology, define the stratigraphy, and investigate the presence of unconformities. A large portion of Chapter 3 is devoted to the structural geology of the deposit. Through geological mapping of outcrops, drillcore analysis, and petrography, morphological characteristics of fabrics, folds, high strain zones, and faults associated with deformational events are presented. The chronology and interference between structural features related to various deformational events are also presented. Surface and subsurface data are integrated within a common 3D environment (using Gocad), which enables to better characterize and model the geometry of auriferous zones and the distribution of associated hydrothermal alteration, lithological units, and structural features. The last part of Chapter 3 describes the relative chronology between auriferous and deformational structures based on key structural observations and cross-cutting relationships documented between various geological features. Structural analysis is also used to investigate potential structural controls on gold mineralization.

Metamorphic mineral assemblages of mineralized and non-mineralized rocks were petrographically determined and are used to approximate the pressure and temperature conditions of metamorphism. The relative timing between main metamorphic events and gold

mineralization is investigated through macroscopic and microscopic textural relationships within mineral assemblages of auriferous rocks.

Chapter 4 lists all geochronological data cited in the thesis. Chapter 5 discusses the tectonic setting of the Roberto deposit, the timing of the gold mineralization relative to deformation and metamorphism, the structural controls on gold mineralization, and the nature of the auriferous hydrothermal system. The last part of Chapter 5 compares key elements of the Roberto deposit to other Canadian and amphibolite facies gold deposits.

2 REGIONAL GEOLOGY

The Éléonore property straddles the boundary between the Opinaca Subprovince, dominated by amphibolite to granulite facies metasedimentary rocks, and the Eastmain domain of the La Grande Subprovince, comprising lower grade greenschist to amphibolite facies volcano-plutonic assemblages (Figure 2.1.1). The La Grande Subprovince is crescent-shaped wrapping the south, west, and north flanks of the Opinaca Subprovince (Figure 2.1.1). At regional-scale, it is subdivided into a northern and a southern part referred to as the La Grande River and Eastmain River domains, respectively (Gauthier and Larocque, 1998) (Figure 2.1.1). Since it hosts the Roberto deposit, this section focuses on the geological characteristics of the Eastmain River domain, specifically in the vicinity of the Éléonore property.

2.1 Eastmain River Domain of the La Grande Subprovince

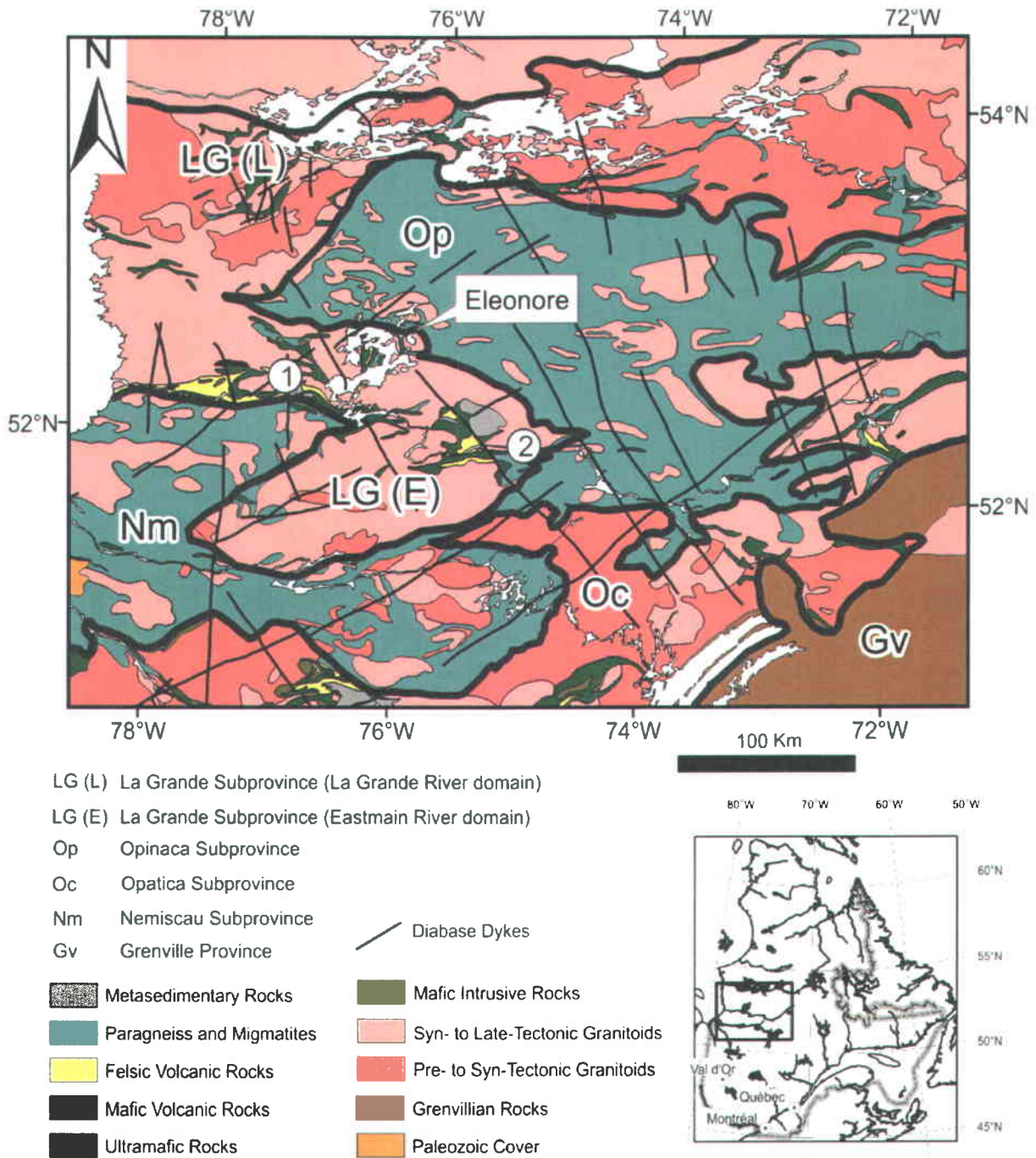


Figure 2.1.1: Regional geological map showing the location of the Éléonore property. Circled numbers 1 and 2 indicate the location of the Lac Duxbury area and the Secteur Village area respectively (see text for details). Modified from Thériault and Bilodeau, 2001.

2.1.1 Lithology

The Eastmain River domain of the La Grande Subprovince consists of greenschist to amphibolite facies volcanic and metasedimentary rocks (Moukhsil et al., 2003). The volcanic sequence is composed of four cycles of tholeiitic rocks dated between 2752 and 2703 Ma that generated komatiitic to rhyolitic lavas and/or tuffs with local calc-alkaline affinities (Kauputauch, Natel, Anatacau-Pivert, and Komo-Kasak formations) (Moukhsil et al., 2003). Older komatiites, related sills (2.82 Ga), and Mesoarchean basement (3.33 - 2.79 Ga) are present in the western part of the La Grande Subprovince (Percival, 2007). The volcanic sequence is overlain by conglomerates and turbiditic greywacke locally containing volcanoclastic/tuffaceous sequences and minor iron formations (Clarkie and Anaconda formations) (Moukhsil et al., 2003). Franconi's (1978) vintage study of the region suggests that conglomerate sequences were unconformably deposited on the volcanic pile and represent the base of the sedimentary sequence. Felsic volcanic and volcanoclastic rocks associated with quartz-feldspar porphyries (Wabamisk Formation) dated at 2703 ± 8 Ma and 2705 ± 3 Ma (Gauthier and Larocque, 1998) are locally present between the mafic volcanic rocks and the sedimentary sequence (Franconi, 1978; Gauthier and Larocque, 1998).

Greenschist to amphibolite facies volcanic and metasedimentary rocks of the Eastmain River domain are intruded by syn-volcanic/ syn-tectonic tonalite, granodiorite and diorite intrusions dated between 2747 and 2710 Ma (Moukhsil et al., 2003). In the vicinity of the Éléonore Property, the supracrustal sequence is cut by the large syn-volcanic tonalitic to dioritic Kasipasikatch intrusion (renamed Opinaca pluton by Bandyayera and Fliszár (2007)) and the tonalitic to dioritic Ell Lake intrusion (Figure 2.1.2). The Ell Lake intrusion located only 3 km southwest of the Roberto deposit is of particular importance since it contains Cu-Ag-Au-Mo mineralization. Late syn- to post-tectonic granodiorite and pegmatite intrusions associated with migmatization of the Opinaca metasedimentary rocks also intrude Eastmain River domain rocks and the La Grande Subprovince at large locally forming km-scale intrusions (Figure 2.1.2) (Bandyayera and Fliszár, 2007).

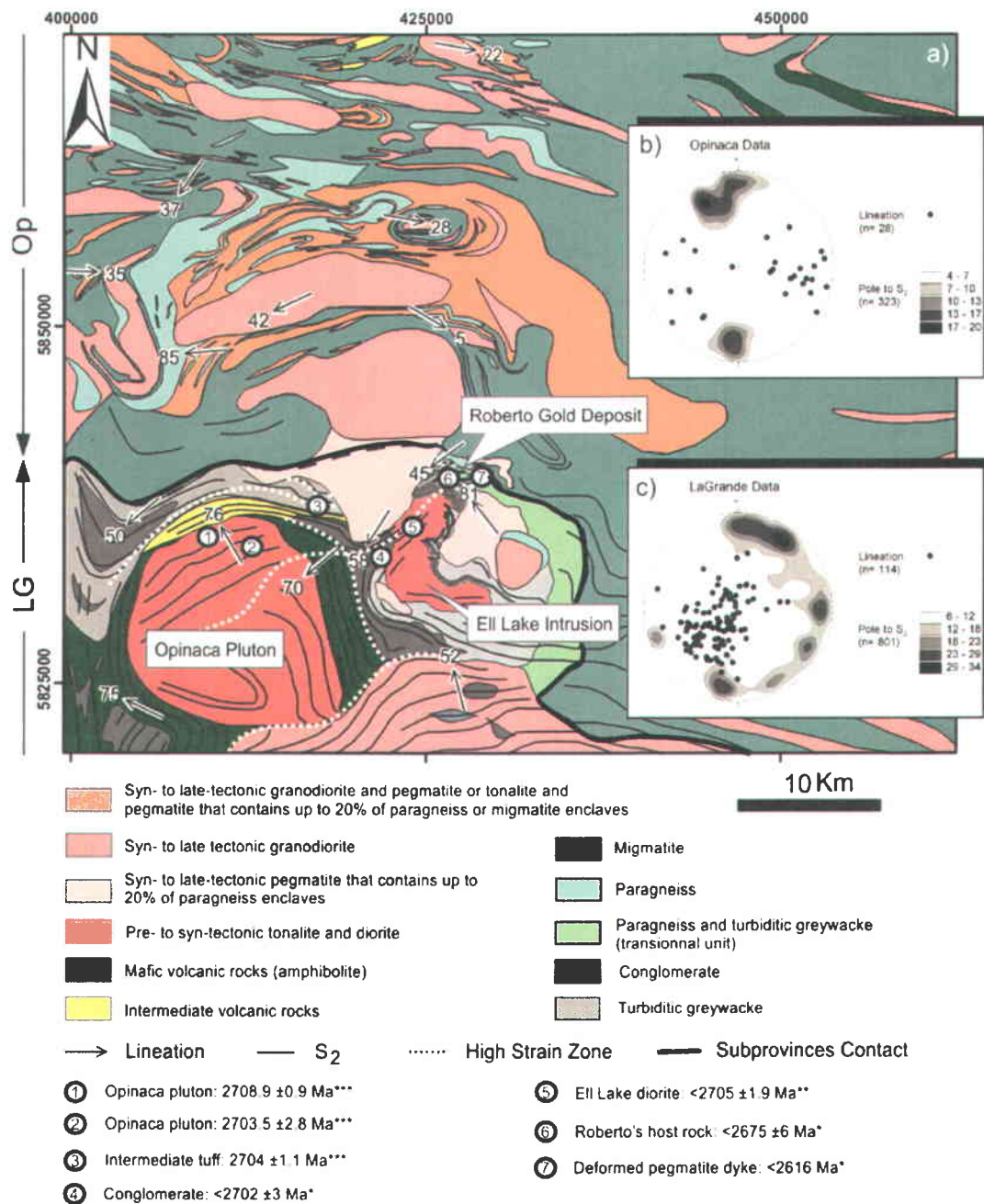


Figure 2.1.2: a) Simplified regional geological setting of the Roberto gold deposit. Selected lineation measurements are represented on the map. b) and c) Equal area nets (lower hemisphere) showing the distribution of lineation and pole to S₂ foliation for the Opinaca and La Grande subprovinces, respectively. Note the shallower plunges of lineations within the Opinaca Subprovince. Structural data selected from Bandyayera and Fliszár (2007) and this study. Circled numbers show location of geochronological sampling sites (*Ravenelle et al. (2010), **David (2005), *** Bandyayera and Fliszár (2007)). Coordinates are in UTM Nad83. Figure from Ravenelle et al., 2010; modified from maps RP 2007-05-C001 and RP 2007-05-C002 of Bandyayera and Fliszár, 2007.

2.1.2 Structural Geology and Metamorphism

Evidence for three generations of deformational structures is found in the Eastmain River domain (Moukhsil et al., 2003; Bandyayera and Fliszár, 2007). The first deformational event (D_1) is best documented in the Secteur Village (SNRC 33B/03) and Lac Duxbury area (SNRC 33C/05) (Figure 2.1.1) (Moukhsil et al., 2003). Structures attributed to D_1 are cryptic in our study area and reside in the presence of local intrafolial folds (Bandyayera and Fliszár, 2007) and F_1 folds seen refolded by F_2 folds (see section 2.5.3.2 *Folds, Fold Interference, and Finite Geometry*). Previous studies hence labeled the main deformational event as D_1 instead of D_2 (e.g. Franconi, 1978; Moukhsil, 2000). The main regional deformation responsible for the predominant ~E-W structural fabric that affects prograde metamorphic minerals is attributed to D_2 (Bandyayera and Fliszár, 2007). The S_2 fabric is penetrative and is generally oriented parallel to primary layering of volcanic and sedimentary sequences. In the study area, the attitude of S_2 is greatly influenced by competent intrusive bodies, as can be seen around the Opinaca pluton, where the fabric both overprints the igneous texture and molds the outline of the intrusion (Figure 2.1.2). The complex pattern of the S_2 foliation within the Opinaca pluton is in part attributed to dragging caused by nearby high strain zones. Areas of intense stretching evidenced by the presence of L-tectonites are common and indicate that D_2 locally caused significant constrictional strain. F_2 folds are moderately- to steeply-plunging, tight to isoclinal, and are commonly associated with well-developed stretching and mineral lineation oriented subparallel to their fold axis. The third deformational event (D_3) generated folds with ENE- to WNW-striking axial planes that are steeply-plunging and nearly coaxial with F_2 folds. S_3 is generally penetrative and locally realigned metamorphic minerals initially developed during D_2 . A fourth deformational event with a deformation style similar to D_3 was also documented near the Éléonore property (see section 2.5.3 *Structural Geology of the Éléonore Property*).

Metamorphic grade increases up-stratigraphy (Gauthier and Larocque, 1998) as illustrated by greywacke units that gradually develop paragneissic fabrics towards the contact with the Opinaca Subprovince. The distribution of high grade rocks along the La Grande Subprovince's boundary is perceived as a thermal aureole developed around the migmatized Opinaca Subprovince.

2.2 Opinaca Subprovince

2.2.1 Lithology

The migmatized metasedimentary rocks of the Opinaca Subprovince are intruded by syn- to post-tectonic granodiorite and granitic pegmatite (Figures 2.1.1 and 2.1.2) that have a peraluminous signature indicative of S-type magmatism (Moukhsil et al., 2003). The youngest ages reported for such intrusions include the ca. 2618 +18/-13 Ma obtained from the Du Vieux Comptoir granite, located ~85 km west of the Roberto deposit, and the ca. 2618 ±2 Ma for a pegmatitic tonalite in the Lac Sakami region, located ~75 km NW of the Roberto deposit (David and Parent, 1997). Small ultramafic intrusions and thin volcanic units were locally mapped (Franconi, 1983; Simard and Gosselin, 1999). Metamorphic grade systematically increases from amphibolite to granulite facies from the margins to the center of the Opinaca basin (Moukhsil et al., 2003).

2.2.2 Structural Geology and Metamorphism

Evidence for only two deformational events, hereafter referred to as D_2 and D_3 are found in the Opinaca Subprovince. The S_2 fabric can be traced across the metamorphic isograd that separates the La Grande and the Opinaca subprovinces, where it gradually develops from a penetrative fabric into a paragneissic fabric and migmatitic layering. In the Opinaca, D_3 did not produce a penetrative fabric. Crenulation cleavages attributed to D_3 occur locally.

Primary layering and the S_2 fabric are locally refolded by tight doubly-plunging folds rotating L_2 lineations to shallower plunges (Figures 2.1.2b and 2.1.2c) and resulting in the formation of domes and basins (Remick, 1977) (Figure 2.1.2a). These later folds are attributed to D_3 , although local doming following the diapiric emplacement of syn- to late-tectonic intrusions might also be responsible for the finite geometry in the Opinaca Subprovince (Bandyayera and Fliszár, 2007). No high strain zones were so far recognized within the Opinaca. It should be noted, however, that evidence of high strain zones might have been obliterated by high grade metamorphism.

The fact that the S_2 fabric gradually develops into a paragneissic and/or migmatitic layering suggests that high grade metamorphism was synchronous with D_2 (Simard and

Gosselin, 1999). The presence of late anatexic injections locally discordant to the main fabric indicates that migmatization outlasted D₂ culmination (Simard and Gosselin, 1999).

Two episodes of prograde metamorphism are documented in the Opinaca (Bandyayera et al., 2010). Bandyayera et al. (2010) attribute the metamorphic peak to the first episode, which is interpreted to be coeval with the migmatization of the Opinaca basin and is dated at 2671.6 ± 1.8 Ma (Bandyayera et al., 2010). The second episode is interpreted to be post-peak and is dated at ca. 2647 Ma (Wodicka, Lamothe and Leclair, 2009; Bandyayera et al., 2010). This second episode is attributed to a second stage of migmatization.

2.3 Nature of the Boundary between the La Grande and Opinaca Subprovinces

The two subprovinces have distinct metamorphic grades and different rheological behavior as portrayed by the more ductile deformational style of the Opinaca. It is not clear, however, whether the two contrasting terranes are in their original setting or if they were juxtaposed during the tectonic evolution of the area. No tectonic structure juxtaposing rocks of different metamorphic grades has so far been recognized in the field at the boundary between the Eastmain River domain of the La Grande and the Opinaca Subprovince. The latter was described by Gauthier and Larocque (1998) as a metamorphic isograd marking the appearance of paragneissic units from the underlying greywacke sequences, an interpretation consistent with that of Franconi (1978), who initially suggested that La Grande stratigraphy gives way to higher grade sedimentary rocks of the Opinaca as part of a continuous conformable sequence. The recognition on a recent regional-scale airborne magnetic survey of a discontinuity in the magnetic grain which could locally mark a tectonic boundary between the two domains (Bandyayera et al., pers. comm., 2008) offer an alternative interpretation awaiting confirmation. In view of the above, it appears that this boundary may not conform to a single geological feature but records a complex and variably preserved overprinting history. This is of chief importance since it may have played a key role for the development of mineralization on the Éléonore property which happens to straddle this boundary.

2.4 Distribution of Gold Deposits within the Region

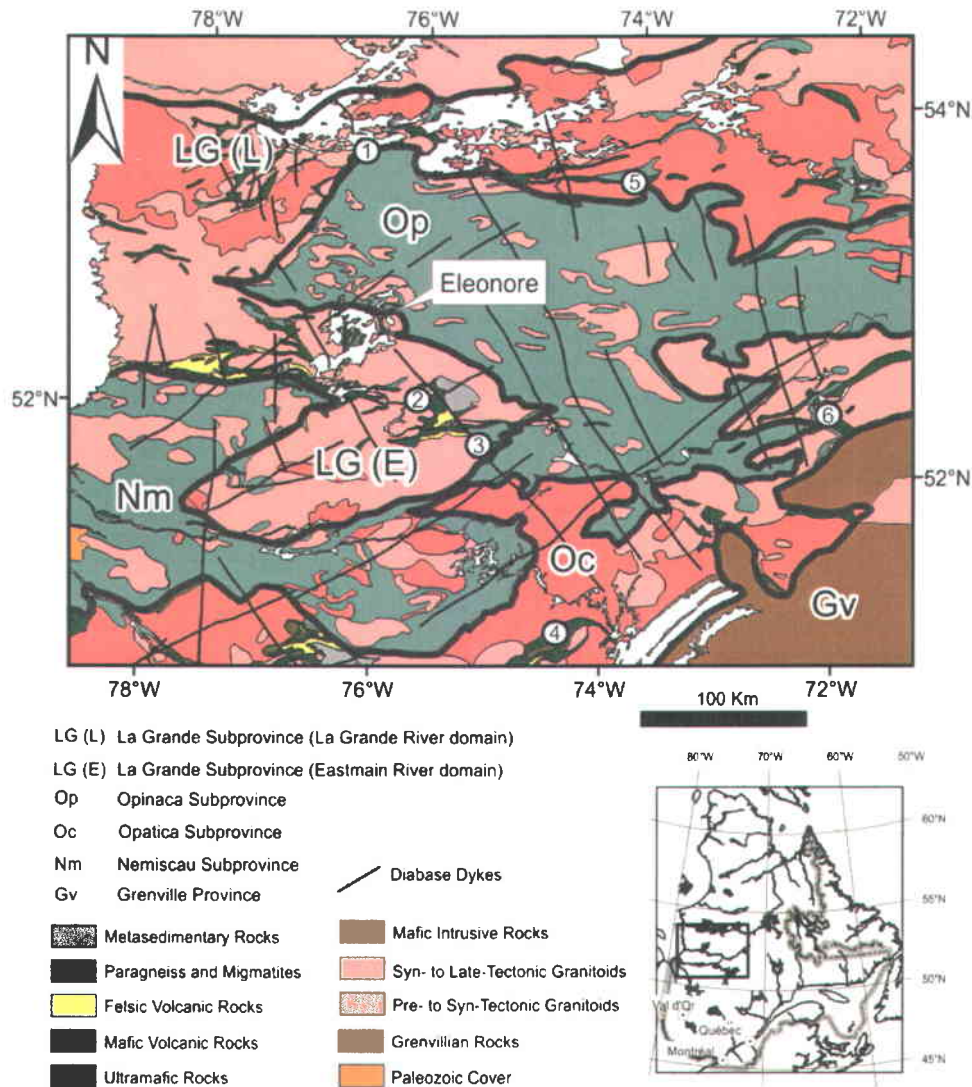


Figure 2.4.1: Regional geological map showing the location of the Éléonore property and significant gold prospects and deposits. Circled numbers: 1. La-Grande-Sud; 2. Clearwater; 3. Auclair; 4. Troilus mine; 5. Corvet Est; 6. Eastmain mine. (Figure from Ravenelle et al., 2010; modified from Thériault and Bilodeau, 2001)

The locations of the principal gold occurrences in the James Bay area are displayed on Figure 2.4.1. The main occurrences include the Clearwater, the Auclair, the Eastmain, the Corvet-Est, and the La-Grande-Sud deposits. A large portion of those occurrences are located near the margins of Opinaca paragneiss and migmatites. The general characteristics of these deposits in terms of age, host rocks, alteration assemblages, sulphide mineralogy, mineralization

style, and structural setting are summarized in Table 2.4.1. In terms of gold content, the Clearwater, La Grande Sud, and Eastmain deposits are the most significant with non-official inferred and indicated gold resources totalizing ~1 Moz Au (Eastmain_Resources_Inc., 2011), 350,000 oz. Au (Virginia_Mines_Inc., 2010), and 255,000 oz. Au (Eastmain_Resources_Inc., 2011), respectively.

The Clearwater deposit is located the closest to Roberto (Figure 2.4.1). It is principally characterized by decimeter- to metre-scale gold-bearing quartz-tourmaline±calcite veins emplaced along the axial plane of F_2 folds (Tremblay, 2006). The F_2 folds fold an earlier well-defined penetrative fabric which itself affects swarms of quartz-feldspar porphyry dykes (Tremblay, 2006). According to the description of Cadieux (2000) and Tremblay (2006), the S_1 fabric at Clearwater corresponds to the principal regional fabric, which is referred to as S_2 in this study. In our terminology, the veins would then be axial-planar to F_3 folds. At Auclair, gold mineralization occurs as replacement ore confined to banded iron formations located in the hinge of F_2 folds (Chapdelaine and Huot, 1997). Again, we suspect that such folds, which fold the main tectonic grain, correspond to F_3 folds in our terminology. At the Eastmain deposit, gold mineralization occurs in association with stratabound silicification hosted within a shear zone developed along the contact between mafic and ultramafic rocks (Couture and Guha, 1990). At Corvet-Est, gold mineralization primarily occurs in association with disseminated sulphides hosted within highly-strained dacitic rocks (Aucoin, 2008). Based on Re/Os geochronology on arsenopyrite, Aucoin (2008) determined that the age of gold mineralization is ca. 2663 Ma, and that the dominant alteration assemblage results from an episode of retrograde metamorphism superimposed on pre-existing ore. At the La Grande Sud deposit, gold mineralization occurs as veins and disseminated ore in sheared tonalite and mafic dykes (Mercier-Langevin, 2000; Virginia_Mines_Inc., 2011).

Table 2.4.1: General characteristics of selected gold deposits of the James Bay area. ¹(Cadieux, 2000; Tremblay, 2006), ² (Chapdelaine and Huot, 1997), ³(Eastmain Resources_Inc., 2011), ⁴(Aucoin, 2008), ⁵ (Mercier-Langevin et al., 2012; Virginia Mines Inc., 2010).

Gold Deposit	Age	Host Rocks	Alteration Assemblage	Sulphide Minerals	Mineralization Style	Structural Setting	Operator
Clearwater ¹	Archean	mafic volcanic and volcanoclastic rocks	Qtz, Ti, Cc, Ac, Bo	Cpy, Po, Py	laminated and extensional veins	fold hinges	Eastmain Resources
Auclair ²	Archean	iron formation	Ca-Mg-Fe-rich silicates	Po, Py, Asp	metasomatic replacement	fold hinges	Virginia Mines
Eastmain Mine ³	Archean	ultramafic rocks	Qtz	Po, Py, Cpy	stratabound silicification	NA	Eastmain Resources
Corvet-Est ⁴	~2663 Ma	dacite	Ti, Al, Sr, Chl	Py, Asp, Po, Cpy	disseminated	high strain zones	Virginia Mines
La-Grande-Sud ⁵	2732-2721 Ma	tonalite and mafic dykes	Sr, Chl, Bo, Cb	Cpy, Py, Asp	veins and disseminated	shear zones	Virginia Mines

2.5 Geology of the Éléonore Property

This section presents the geology of the Éléonore property. Emphasis is put on the lithological and geochemical characterization of the main rock units, and on their structural and metamorphic overprint. Although presented in detail in chapter 4, geochronological results are incrementally presented to complement important aspects documented in this section.

The Éléonore property and related joint ventures cover an area of approximately 250 km² (Figure 2.5.1). Although water bodies cover approximately one third (80 km²) of the property, a considerable amount of outcrops are available and permit detailed geological observation and mapping (Figure 2.5.1).

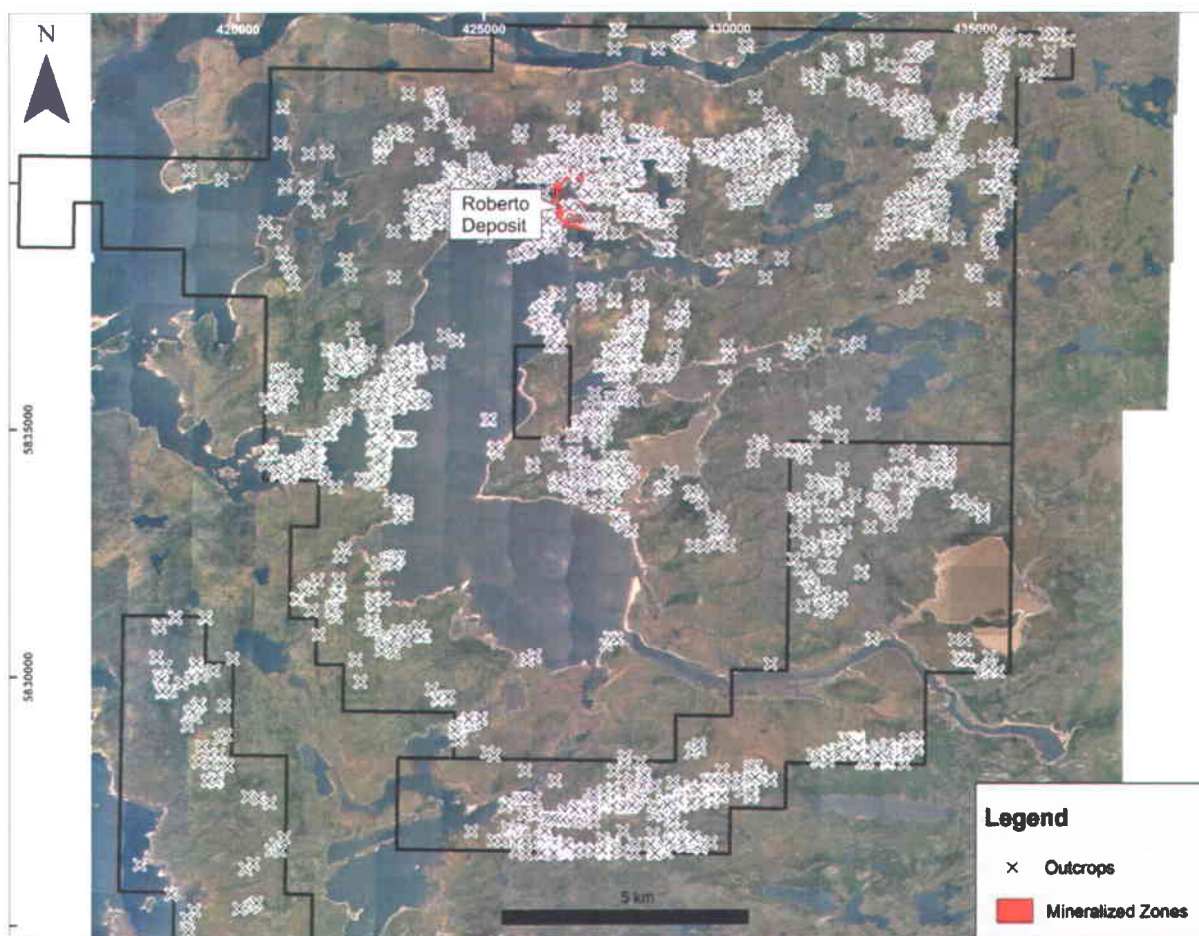


Figure 2.5.1: Map showing location of outcrops within Éléonore property and associated joint ventures. Air photograph courtesy of Opinaca Mines Ltd.

2.5.1 Lithology

In the vicinity of the Éléonore property, La Grande supracrustal rocks consist of locally-pillowed basalts and minor intermediate to felsic lapilli tuffs of the Kasak Formation (dated at 2704 ± 1 Ma (Bandyayera and Fliszár, 2007)), which are unconformably overlain by a clastic sequence comprising several conglomerate units (dominated by rounded cm- to dm-scale diorite blocks) intercalated with turbiditic greywacke units (Figure 2.5.2). This clastic sequence is referred to as the Low Formation, and could correspond to Labbé and Grant's (1998) Clarkie Formation (Bandyayera and Fliszár, 2007). The maximum age for the conglomerate deposition of a sample taken on the Éléonore property is 2702 ± 3 Ma (Ravenelle et al., 2010). The fact that the detrital zircon population shows a peak at 2707 Ma, corresponding within errors to the age of the nearby Ell Lake intrusion (see below), may at first suggest deposition stratigraphically immediately above the Ell Lake intrusion. However, it was locally observed that the Ell Lake intrusion cut through the conglomerate sequences and is hence younger. The apparent conflicting relationship has potentially been resolved by recent geochronological work which indicates that the maximum age of the sedimentary sequence cut by the intrusion is ca. 2714 Ma (Dubé, pers. comm., 2009). This suggests that sedimentation occurred discontinuously over a protracted time. This interpretation is further discussed in section 3.2 *Lithology*.

The local presence of andalusite-cordierite-garnet assemblages within the Low Formation (Bandyayera and Fliszár, 2007) potentially reflects the local pelitic character of this formation and independently signals major changes in sedimentary regime. Banded iron formations have also been locally mapped within the Low Formation.

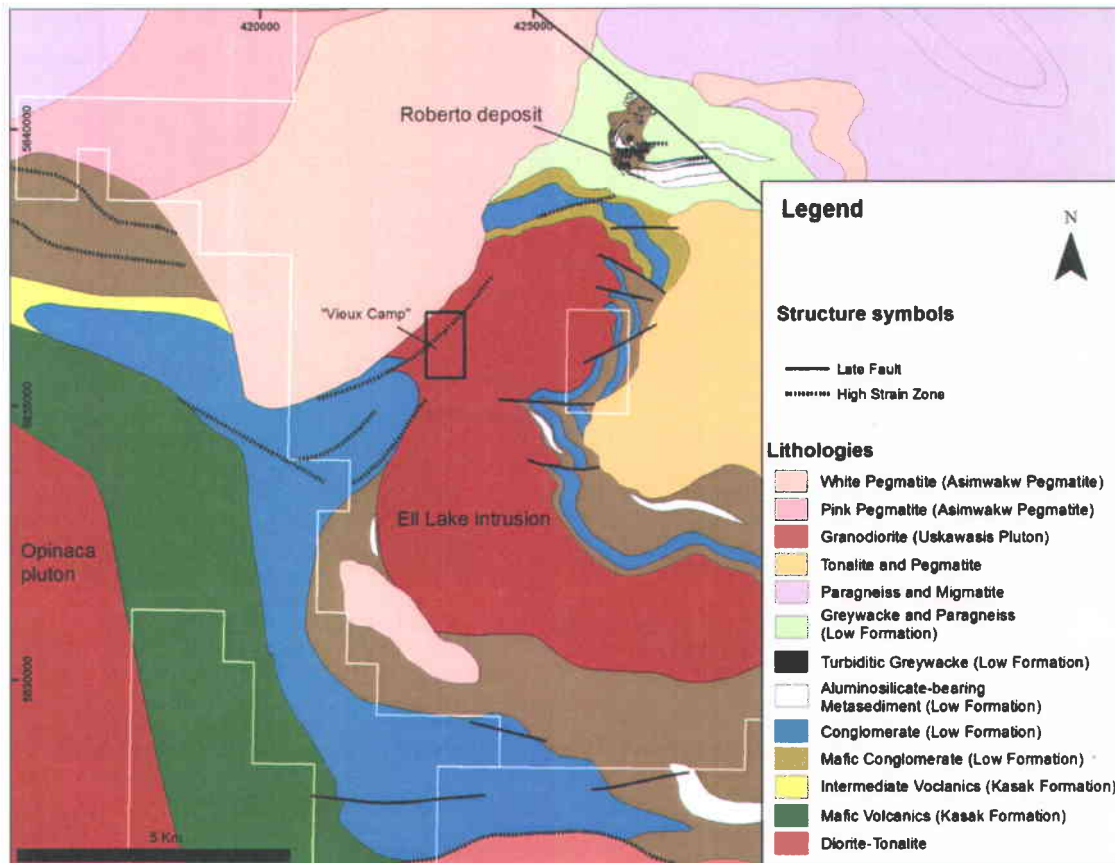


Figure 2.5.2: Simplified geological map of the Éléonore property. (modified from Bandyayera and Fliszár, 2007)

The most significant intrusion on the Éléonore Property is the Eil Lake intrusion, which was the subject of a study by the research network DIVEX (Diversification de l'exploration minérale au Québec). The Eil Lake intrusion is the host of several Cu-Ag-Au±Mo showings that are located 7 km southwest of the Roberto deposit. The mineralized part of the Eil Lake intrusion is referred to as the "Vieux Camp" (Figure 2.5.2). The intrusion comprises several dioritic and tonalitic phases locally cut by feldspar-porphyry dykes (Bécu et al., 2007). The auriferous zones are generally associated with semi-massive to massive chalcopyrite-pyrrhotite impregnations, disseminations, and replacement with traces of molybdenite (Bécu et al., 2007). Prominent tourmaline alteration zones that resemble Roberto's tourmaline-rich stockwork (see below) are present in the vicinity of the auriferous zones, hence suggesting that mineralization at Roberto and Eil Lake could be related. The study of Bécu et al. (2007) focused on the characterization of the mineralized zones hosted by the Eil Lake diorite in order to better define their relative timing within the magmatic history and overprinting deformational events. During the course of this

study, the potential genetic relationship between the Ell Lake diorite and the Roberto deposit is investigated through geochronology.

Large pegmatite intrusions are present on the Éléonore property. These pegmatite intrusions include several compositional facies ranging from tonalitic to granitic. The pegmatite intrusion located west of the Roberto deposit (Figure 2.5.2) is referred to as the Asimwakw pegmatite (Bandyayera and Fliszár, 2007). The Asimwakw pegmatites are only located near the contact between the Opinaca and La Grande Subprovinces (Bandyayera and Fliszár, 2007). They are typically white pegmatite containing between of 2 and 20% tourmaline and 5 to 20% enclaves of metasedimentary rocks (Bandyayera and Fliszár, 2007).

A set of NE-trending diabase dykes crosscuts the Éléonore property. These dykes are attributed to the Senneterre swarm, estimated to have been emplaced at ca. 2216 \pm 8/-4 Ma (Buchan, Mortensen and Card, 1993; Bandyayera and Fliszár, 2007). These Proterozoic dykes record no evidence for metamorphism and regional deformation (Bandyayera and Fliszár, 2007). Mafic rocks that are concordant and interbedded with bedding planes are locally observed in conglomeratic sequences of the Éléonore property (e.g. Figure 2.5.3). Such mafic rocks locally contain layers of mm- to cm-scale amygdular nodules (Figure 2.5.3). These mafic rocks record the main S₂ fabric confirming their Archean age.

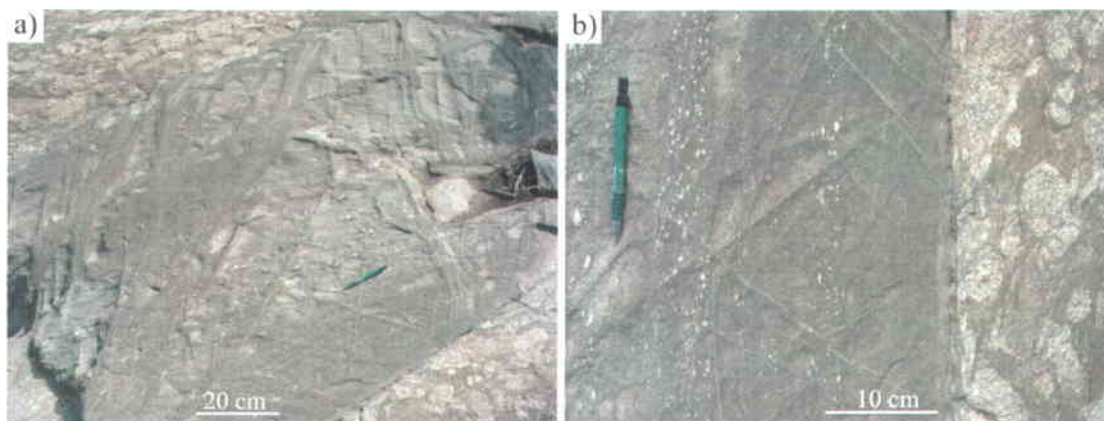
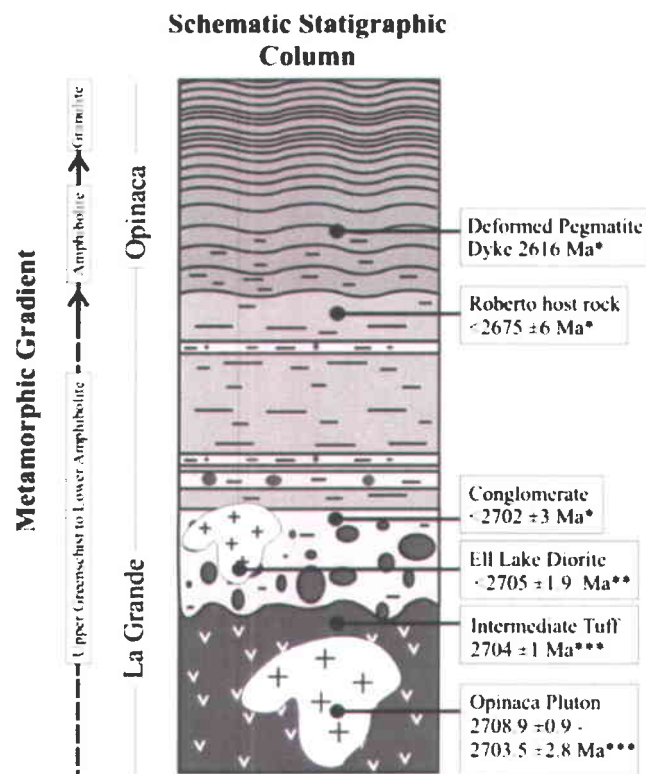


Figure 2.5.3: Photographs of mafic rocks concordant to bedding planes within conglomeratic units. Note the presence of amygdular nodules that define layers in (b).

A schematic chronostratigraphic column with age constraints for the Éléonore property is presented on Figure 2.5.4. The oldest lithological units are represented by mafic volcanic rocks

that are intruded by dioritic to tonalitic phases of the Opinaca pluton dated between 2708.9 ± 0.9 and 2703.5 ± 2.8 (Bandyayera and Fliszár, 2007). The mafic volcanic rocks are conformably overlain by intermediate tuff units, and unconformably overlain by conglomerate sequences. The metamorphic grade systematically increases approaching the Opinaca Subprovince, where paragneiss units gradually overcome metagreywacke. The fact that D_2 affected a pegmatite dyke dated at 2616 Ma within paragneiss units of the Opinaca (Figure 2.5.4) (see upcoming sections for details) indicates that D_2 was still active at ca. 2616 Ma, and therefore represents a much younger tectonic and metamorphic event than other events recorded elsewhere in the Superior Province (e.g. Percival, 2007).



Legend

 Migmatite	 Conglomerate
 Paragneiss	 Mafic and Intermediate Volcanics
 Turbitic Metagreywacke	 Felsic and or intermediate intrusives

Figure 2.5.4: Chronostratigraphic column illustrating the relative chronology of supracrustal and intrusive phases of the Éléonore property. (*Ravenelle et al. (2010), **David (2005), ***Bandyayera and Fliszár (2007)). Figure from Ravenelle et al. (2010).

2.5.2 Lithochemochemistry

This section presents the major, minor and trace elements geochemistry of the principal lithological units present on the Éléonore property. Hand samples were analyzed by X-Ray fluorescence (XRF) or inductively coupled plasma (ICP) spectrometry by SGS Minerals Canada for major element geochemistry. Minor and trace elements including As, B, Au, S, and CO₂ were analyzed through various methods (see Appendix A for listing of methods used on individual samples). Averages are calculated and are compared with regional and/or reference compositions.

2.5.2.1 Turbiditic Greywacke Sequence

A total of 60 unaltered samples of turbiditic greywacke from the Éléonore property were analyzed. The methodology used to select samples that are the least altered is described in section 3.5.2 *Least-altered Samples*. Of the 60 samples, 45 were analyzed in the course of this study. These were collected within 1 kilometer of the Roberto deposit. The remaining 15 analyses are reported from (Bandyayera et al., 2010). Averaged major and trace elements concentrations are reported in Tables 2.5.1 and 2.5.2 along with compositional data from other turbiditic sequences of the Superior Province. This data is also presented as a chondrite-normalized spider diagram (Figure 2.5.5) and box diagrams (Figure 2.5.6) to facilitate empirical comparison. Except for Au, As and B contents of the Éléonore samples which are significantly enriched compared to those of other Superior Province average turbidites, the Éléonore samples are undistinguishable from the latter in their major and trace element contents.

Table 2.5.1: Major element averages of Éléonore's turbidite sequence and selected Archean sequences. (NA= Not available)

ANALYTE	SiO ₂	Al ₂ O ₃	CaO	MgO	Na ₂ O	K ₂ O	Fe ₂ O ₃	MnO	TiO ₂	P ₂ O ₅	Cr ₂ O ₃	LOI	Sum	CO ₂	S
DETECTION (Highest)	0.01	0.01	0.01	0.03	0.02	0.01	0.01	0.01	0.01	0.01	0.01	0.01	0.01	0.01	0.01
UNITS	wt. %	wt. %	wt. %	wt. %	wt. %	wt. %	wt. %	wt. %	wt. %	wt. %	wt. %	wt. %	wt. %	wt. %	wt. %
Eleonore (this study n = 45; Rheume et al., 2009 n = 15) (Standard Deviation)	62.4 4.5	15.5 14	3.6 14	3.8 1.7	3.4 0.9	2.6 0.6	5.9 1.6	0.1 0.0	0.5 0.1	0.2 0.1	0.03 0.02	1.3 10	99.3 11	0.2 0.6	0.2 0.2
La Grande (Rheume et al. 2009 n = 49) (Standard Deviation)	63.1 5.6	16.3 2.0	3.8 1.7	2.7 1.7	3.8 1.1	2.1 0.9	5.9 3.5	0.1 0.1	0.5 0.3	0.2 0.2	0.02 0.02	1.3 0.8	99.8 0.1	NA	0.2 0.7
Opinaca (Rheume et al., 2009 n = 39; Doyon, 2004 n = 14) (Standard Deviation)	63.0 4.4	15.7 2.4	3.4 0.9	3.5 1.8	3.6 0.9	2.4 1.0	6.4 2.8	0.1 0.1	0.5 0.1	0.2 0.2	0.03 0.01	1.4 0.7	100.2 0.8	NA	NA
Nemiscau (Doyon, 2004 and references therein n = 31) (Standard Deviation)	65.4 4.1	15.7 1.6	2.9 1.1	3.0 1.1	3.2 0.6	2.4 0.8	6.6 1.7	0.1 0.0	0.6 0.2	0.1 0.1	NA	1.2 0.8	100.3 0.6	NA	NA
Pontiac (Doyon, 2004 and references therein n = 68) (Standard Deviation)	64.1 3.4	16.9 1.8	2.3 0.8	3.5 0.9	3.5 0.8	2.7 1.0	6.1 1.1	0.1 0.0	0.6 0.1	0.2 0.0	NA	1.5 0.8	101.5 0.8	NA	NA
Quetico (Doyon, 2004 and references therein n = 40) (Standard Deviation)	64.2 3.6	16.0 1.4	2.6 1.1	3.0 0.7	3.1 1.0	2.6 0.9	7.4 3.2	0.1 0.0	0.6 0.1	0.2 0.1	NA	1.6 0.6	101.0 0.9	NA	NA

Table 2.5.2: Minor element averages of Éléonore's turbidite sequence and selected Archean sequences. Number of data: Éléonore (P₂O₅ = 60, Cr₂O₃ = 48, Ba = 60, LOI = 60, CO₂ = 45, S = 58, Au = 58, As = 60, B = 58); La Grande (P₂O₅ = 49, Cr₂O₃ = 49, Ba = 49, LOI = 49, CO₂ = 0, S = 49, Au = 49, As = 49, B = 2); Nemiscau (P₂O₅ = 31, Cr₂O₃ = 0, Ba = 12, LOI = 8, CO₂ = 0, S = 0, Au = 0, As = 0, B = 0); Opinaca (P₂O₅ = 53, Cr₂O₃ = 39, Ba = 52, LOI = 53, CO₂ = 0, S = 39, Au = 39, As = 39, B = 0); Pontiac (P₂O₅ = 68, Cr₂O₃ = 0, Ba = 67, LOI = 68, CO₂ = 0, S = 2, Au = 0, As = 0, B = 0); Quetico (P₂O₅ = 40, Cr₂O₃ = 0, Ba = 40, LOI = 25, CO₂ = 14, S = 11, Au = 0, As = 0, B = 0). (NA= Not available)

ANALYTE	Au	As	B	Sb	Ag	Cu	Zn	Pb	Y	Zr	Ba	Li	Rb	Sr
DETECTION (Highest)	5	3	10	5	2	0.5	0.5	2	0.5	0.5	3	1	2	2
UNITS	PPB	PPM	PPM	PPM	PPM	PPM	PPM	PPM	PPM	PPM	PPM	PPM	PPM	PPM
Eleonore (this study n = 45; Rheume et al., 2009 n = 15) (Standard Deviation)	48 104	84 161	73 167	5 6	<2 0	40 25	69 18	23 24	11 5	115 24	788 404	69 28	109 49	623 297
La Grande (Rheume et al. 2009 n = 49) (Standard Deviation)	3 16	129 798	2 9	0 0	<2 0	38 67	51 22	5 6	11 5	135 145	592 386	NA 70	95 311	545 311
Opinaca (Rheume et al., 2009 n = 39) (Standard Deviation)	1 0	2 5	0 0	0 0	<2 0	31 24	57 15	5 4	13 6	130 27	621 305	NA 103	116 207	517 207
Nemiscau (Doyon, 2004 and references therein n = 31) (Standard Deviation)	NA 4	NA 31	NA 218	NA 4	NA 31	NA 218	NA 102	NA 130	14 4	137 31	620 218	NA 102	115 130	374 130
Pontiac (Doyon, 2004 and references therein n = 67) (Standard Deviation)	NA 8	6 8	NA NA	0 0	NA 18	42 20	112 20	NA NA	14 3	139 111	835 295	NA 29	83 211	437 211
Quetico (Doyon, 2004 and references therein n = 40) (Standard Deviation)	NA 4	NA 31	NA 274	NA 4	NA 31	39 19	92 31	NA NA	16 4	130 31	614 274	NA 837	352 124	352 124

The range of major and minor elements concentrations of the Éléonore property are presented on box diagrams (Figure 2.5.6). Other turbiditic sequences of the Superior Province are also presented for comparison. The box plots were created using the sample populations that were used to calculate averages of Tables 2.5.1 and 2.5.2. The results show that the range of Éléonore's major element concentrations does not differ significantly from the ranges observed in other turbiditic sequences. On the other hand, the box plots clearly show that the Au, As, and B contents of the Éléonore samples are significantly higher than the other sequences. This might indicate that samples considered to be the least-altered were in fact altered to some degree. However, it is difficult to determine whether this enrichment in Au, As, and B results from a certain degree of hydrothermal alteration or simply reflects the primary composition of the sedimentary sequence. In light of recent studies which demonstrated the importance of gold-bearing diagenetic arsenopyrite in the genesis of orogenic and Carlin-type deposits (Large et al., 2007; Large et al., 2009), the nature of this geochemical enrichment is relevant. This surpasses the scope of this study but should be investigated by future studies.

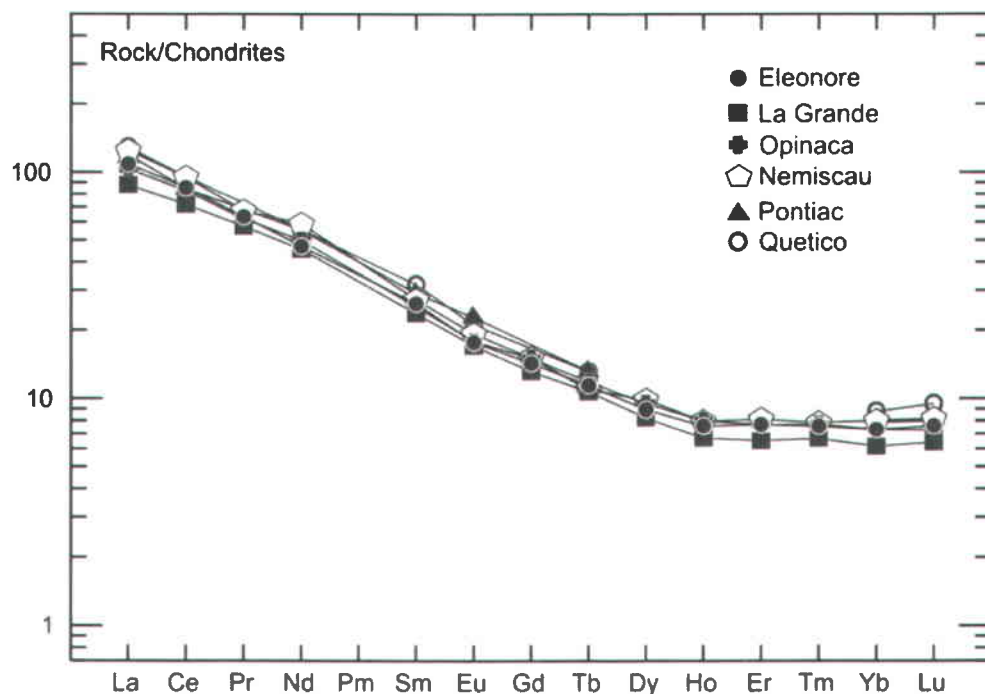


Figure 2.5.5: Chondrite-normalized (Sun and McDonough, 1989) spider diagram of Éléonore's turbidite sequence and other turbiditic sequences of the Superior Province. Trace element concentrations displayed on the diagram represent averages of trace elements within each suite (Éléonore: average of 29 samples; La Grande: average of 49 samples; Opinaca: average of 52 samples; Nemiscau: average of 11 samples; Pontiac: average of 51 samples; Quetico: average of 24 samples).

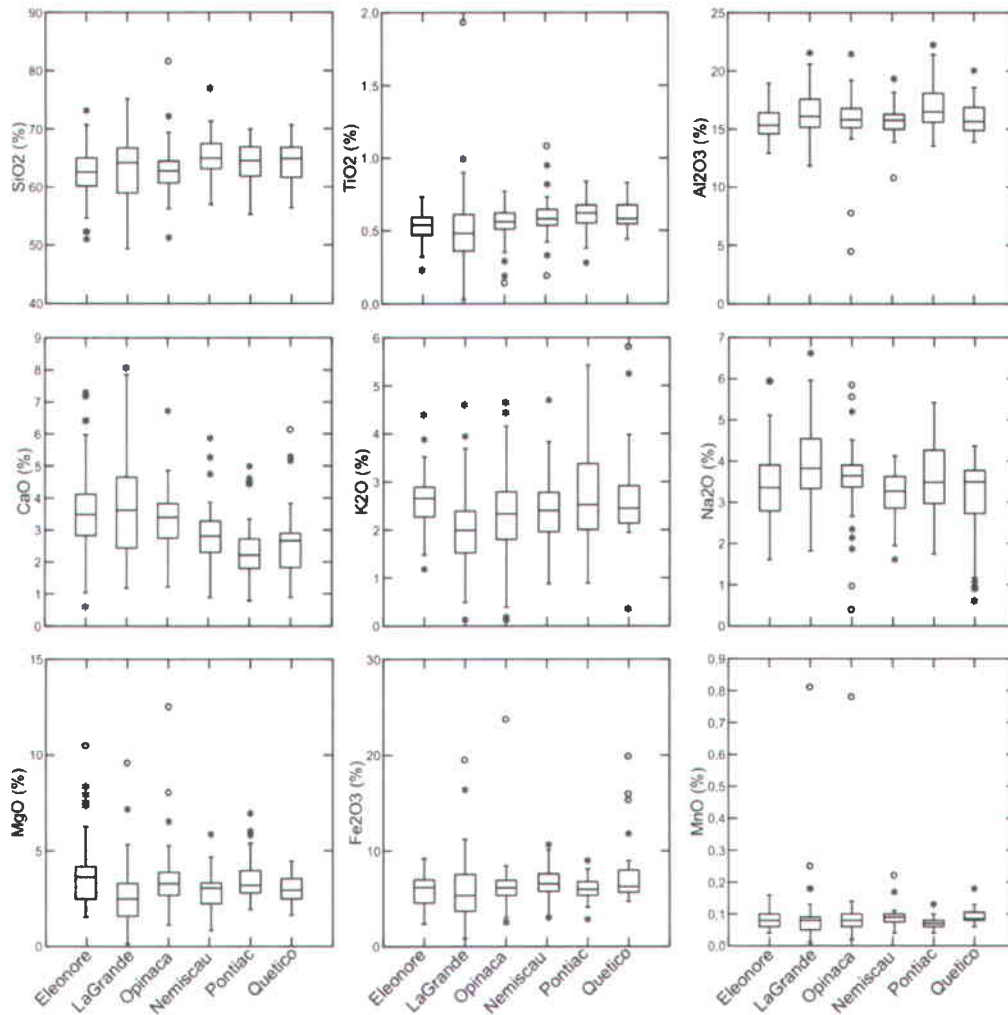


Figure 2.5.6: Box diagrams showing range of Éléonore's property unaltered turbidites major and selected minor element concentrations. Other turbiditic sequences of the Superior Province are displayed for comparison. The central horizontal line marks the median of the population. The length of each box shows the range within which the central 50% of the values plot, with the box edges at the first and third quartiles. The whiskers show the range of observed values that plot within the inner fences, defined as 1.5 and -1.5 times the absolute value of the box. Values between inner and outer fences (3 and -3 times the absolute value of the box) are marked with asterisks. Values beyond the outer fences are marked with empty circles. Data reported from Tables 2.5.1 and 2.5.2.

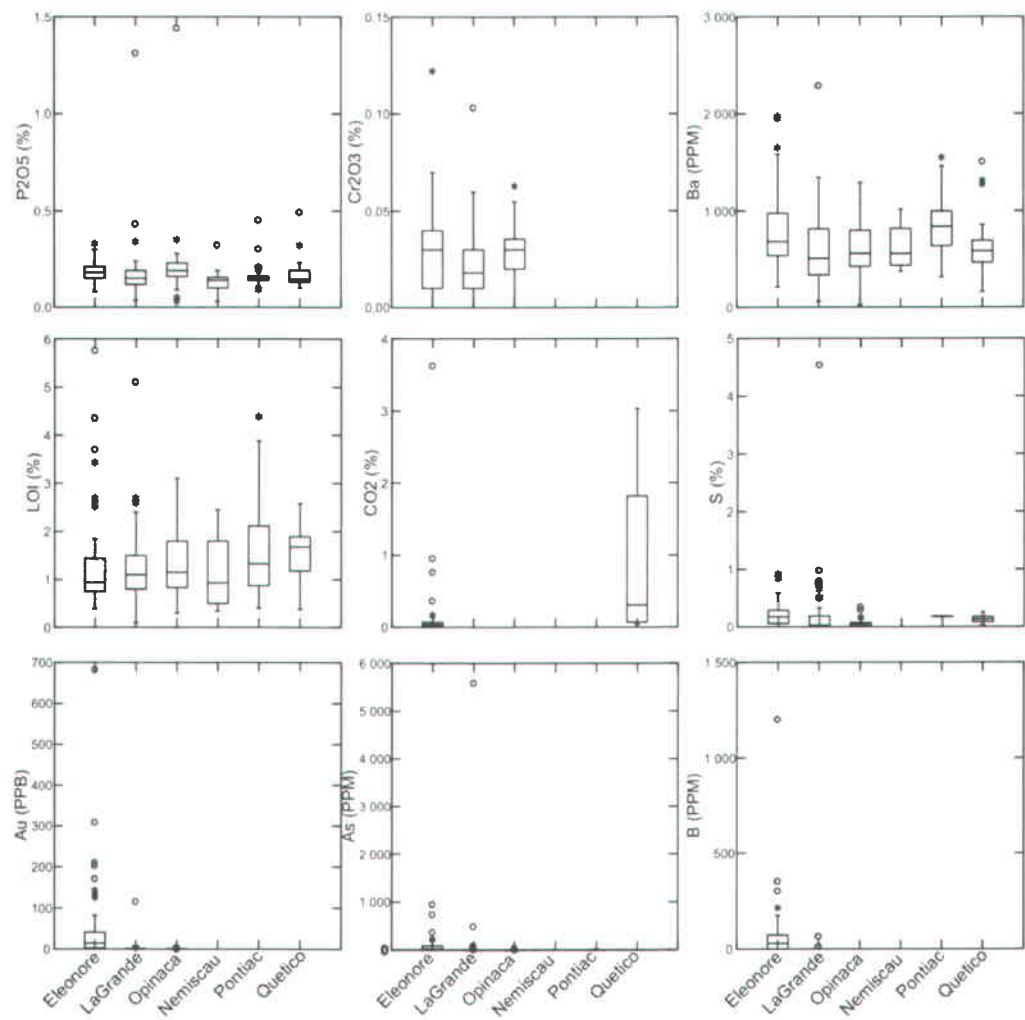


Figure 2.5.6: (continued).

2.5.3 Structural Geology of the Éléonore Property

This section presents the structural geology of the Éléonore Property. In order to better understand the polydeformed nature of the area and place the structural attributes of the property into regional context, structural relationships established within selected regions located outside the property are integrated in the description.

2.5.3.1 *Planar and Linear Fabrics*

In agreement with the previous description of regional deformational events, the principal tectonic fabric in the study area is interpreted to be S_2 . The S_2 fabric is penetrative and is defined by prograde metamorphic minerals (typically biotite and aluminosilicates) in upper greenschist rocks where it is generally oriented parallel to relict bedding of metavolcanic and metasedimentary rocks. In higher grade rocks, the S_2 fabric corresponds to migmatitic and/or gneissic layering. Pegmatitic/partial melt material also commonly lays parallel to S_2 planes. S_2 locally records significant strain as evidenced in rocks containing mesoscopic strain markers (e.g. conglomerate, breccia, etc.) (Figure 2.5.7a). A well-defined mineral lineation is typically developed on S_2 planes (Figure 2.5.7b), and L-tectonites signal significant constrictional strain (Figures 2.5.7c and 2.5.7d). The maximum stretch of such L-tectonites is generally better observed on vertical sections which indicates that the long axis (X axis) of the strain ellipsoid is steeply-plunging. The attitude of S_2 is greatly influenced by competent intrusive bodies, as recorded in the envelope of the Opinaca pluton, where the S_2 fabric overprints the magmatic texture and molds the outline of the intrusion (Figure 2.5.8). The S_3 fabric is penetrative in lower-grade rocks and occurs as a crenulation cleavage in well-foliated higher-grade paragneiss (Figure 2.5.7e). Its orientation varies from NE-SW to ESE-WNW (Figure 2.5.9). Where penetrative, S_3 commonly completely obliterates S_2 by reorienting the metamorphic minerals that previously defined S_2 . In these instances the S_3 fabric can usually be distinguished from S_2 based on the style of associated folds (see section 2.5.3.2 *Folds, Fold Interference, and Finite Geometry*).



Figure 2.5.7: Photographs showing: a) intense flattening strain associated with S_2 in conglomerate. b) well-developed mineral lineation on S_2 plane in greywacke. c) and d): deformed conglomerate in plan (YZ plan of strain ellipsoid) (c), and cross section view (XZ plan of strain ellipsoid) (d). The intense rod-like stretching of fragments in section view indicates that the rock has been subjected to constrictional strain and formed L-tectonites. e) S_3 crenulation cleavage affecting S_2 foliation. f) well-developed mineral lineation (parallel to green pen) in S_3 defined by deformed aluminosilicate porphyroblasts.

The overprinting of S_3 adds a significant complexity to the structural analysis of the region. A well-defined lineation is commonly visible on S_3 foliation planes (Figure 2.5.7f). However, it is not clear whether this lineation resulted from a new mineral growth during D_3 or

from the transposition of L_2 within S_3 during D_3 (see section 2.5.3.2 *Folds, Fold Interference, and Finite Geometry*).

A later fabric, S_4 , shares similarities with S_3 as it occurs as a penetrative fabric or a crenulation cleavage. It is distinguished from S_3 based on its orientation (NW-SE) (Figure 2.5.9) and by the fact that it has no associated mineral lineation.

Figure 2.5.8: Geological map of the region around the Éléonore property showing the distribution of lithological units, main tectonic fabric (S₂), and fold axial traces (modified from maps RP 2007-05-C001 and RP 2007-05-C002 of Bandyayera and Fliszár, 2007). The distribution fold axial traces (this study) is discussed in section 2.5.3.2 *Folds, Fold Interference, and Finite Geometry*. Dip label of structural measurements are not displayed to simplify the map. Coordinates are in UTM Nad83.

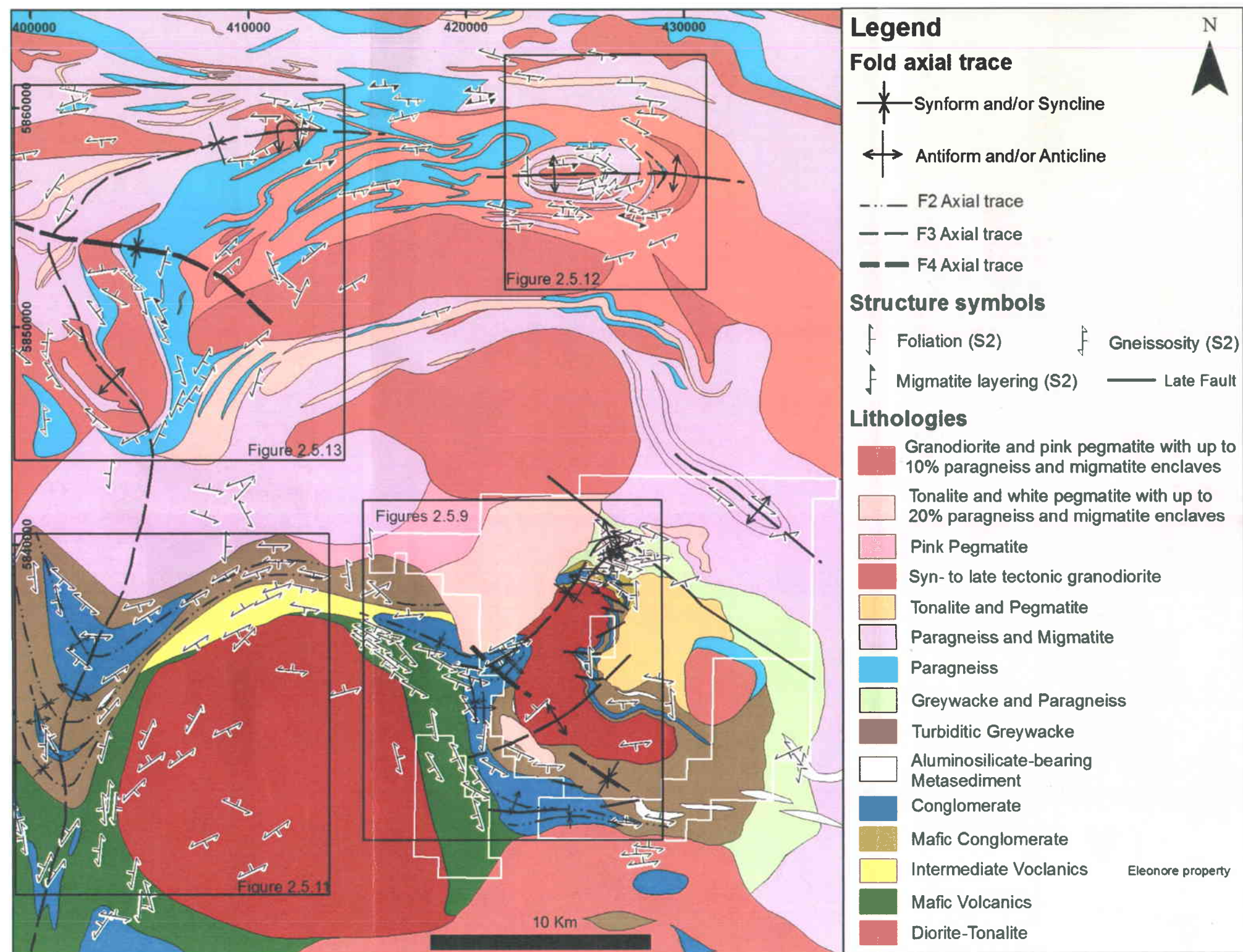
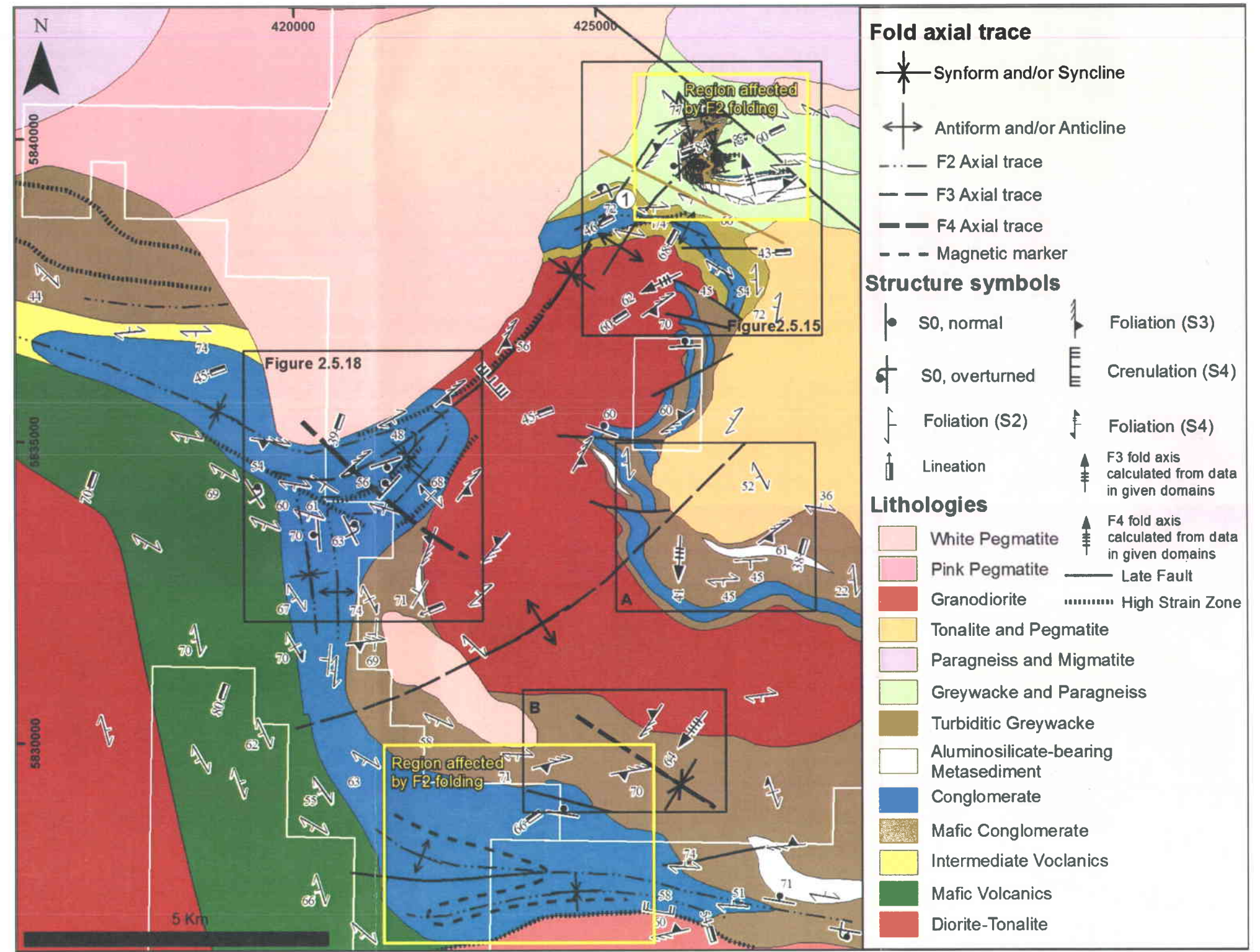


Figure 2.5.9: Geological map of the Éléonore property with the location of the Roberto Deposit. Data outside the Éléonore property are from Bandyayera and Fliszár (2007). Coordinates are in UTM Nad83.



2.5.3.2 Folds, Fold Interference, and Finite Geometry

Outcrop-scale F_1 folds are uncommon, and mapped at only one location on the Éléonore property (Figure 2.5.10a, Figure 2.5.9 circled number 1) and at one location in the Opinaca Subprovince (Figure 2.5.10b). Their attitudes and contribution to the map pattern remains undetermined. Nonetheless, F_1 folds are considered responsible for some of the bedding polarity reversals locally documented in areas free of F_2 and younger folds.

Outcrop-scale F_2 folds are also uncommon on the Éléonore property being confined to specific domains as for example the Roberto deposit area and the southern area of the property (Figure 2.5.9). In those domains, F_2 folds occur at both outcrop- and map-scale, and are typically asymmetrical (commonly Z-folds) tight-to-isoclinal (Figures 2.5.10c and 2.5.10d). In the Roberto deposit area, F_2 folds are steeply plunging with fold axes sub-parallel to the mineral lineation (see section 3.3 *Structural Geology of the Roberto deposit*). Outside the Roberto deposit area, the attitudes of F_2 folds are difficult to determine since they are not commonly observed on outcrops and their isoclinal style limits the use and accuracy of π plots to calculate fold axes. Nonetheless, their attitude can globally be deduced from the fold interference map patterns that resulted from their interference with other fold phases (see below). In certain areas, km-scale F_2 folding causes bedding polarity reversals in sedimentary sequences (Figure 2.5.9). The axial trace of F_2 folds can therefore be deduced from the distribution of facing reversals and attitudes of S_2 (Figure 2.5.9). In the southern part of the property, a Z-shaped F_2 fold is interpreted based on the distribution of a magnetic marker within conglomerate units (Figure 2.5.9).



Figure 2.5.10: Photographs showing: a) F_1 fold refolded by F_2 fold in mafic sedimentary rocks. b) F_1 fold refolded by F_2 fold in paragneiss c) and d) tight F_2 folds in S_0 within greywacke. e) F_3 fold in S_0 - S_2 within greywacke. f) F_3 fold in pegmatite dykes emplaced parallel to S_0 within paragneiss where S_3 completely overprints S_2 . All photographs were taken in greywacke of the Éléonore property, except for (b) which was taken about 30 km to the north in the Opinaca Subprovince.

Map-scale F_3 folds dictate the map pattern. They are defined by the pattern of the main foliation (S_2) and lithological contacts (Figure 2.5.9). F_3 folds are invariably open (Figures 2.5.10e and

2.5.10f) with or without an axial planar foliation or crenulation. In the La Grande Subprovince, S_3 locally obliterates S_2 in regions affected by significant F_3 folding (e.g. Figure 2.5.10f). In the Opinaca Subprovince, F_3 folds generally show no axial planar fabrics. At map-scale F_3 folds are directly related to the attitude of lithological units controlled by F_2 folding prior to D_3 , and can easily be calculated from π plots of S_0 and S_2 (see below). The axial trace of F_3 folds can be deduced based on the folded pattern in S_0 and S_2 and the attitudes of S_3 (Figure 2.5.9).

The effect of F_4 folds on the map pattern is evidenced by changes in the orientation of F_3 axial traces (Figure 2.5.9). F_4 folds are not common on outcrops, but where present in the study area, they are open and steeply-plunging. The attitudes of F_4 folds are directly controlled by the geometry of previous folding events.

The map pattern of the Éléonore property is in part controlled by the Ell Lake diorite and pegmatites which occupies a large portion of the area (Figure 2.5.9). Axial traces were interpreted (Figure 2.5.9), but the finite geometry of the property remains ambiguous since the attitudes of F_2 folds are cryptic. Nonetheless, the geometrical relationships between the various fold phases can easily be defined in regions outside the property. For example, an F_2/F_3 mushroom type interference patterns (type 2 (Ramsay and Huber, 1987)) with ~E-W striking F_2 folds refolded by a NNE-SSW striking upright antiformal F_3 fold is present in the La Grande Subprovince about 15 km west of the study area (Figure 2.5.11). Similar patterns also occur in the Opinaca Subprovince, about 20 km to the north (Figure 2.5.12) and 20 km to the NW of the Éléonore Property (Figure 2.5.13). There, the presence of doubly-plunging F_3 folds (Figures 2.5.12 domains A and B and Figure 2.5.13 domains A and A') suggests that the type of fold interference is transitional between mushroom and dome-and-basin geometry. The doming might result either from the diapiric emplacement of syn- to late-tectonic intrusions (Bandyayera and Fliszár, 2007; Ravenelle et al., 2010) or simply reflect dip variations of F_2 axial planes prior to F_3 folding (Figure 2.5.14). The mushroom and dome-and-basin interference patterns indicate that: 1) the axial planes and fold axes of the two fold phases were oriented at high angles to each other, and 2) the attitude of F_2 fold axes must have been shallowly plunging prior to D_3 . The axial trace of the F_3 fold interpreted on Figure 2.5.11 can be traced through the Opinaca Subprovince to the north where it is refolded by a large-scale shallowly-plunging F_4 fold (Figure 2.5.8). The latter resulted in the rotation of F_3 fold axis from moderately-plunging towards the south in the southern portion of the map, to shallowly-plunging towards the WNW in the north (Figure 2.5.13).

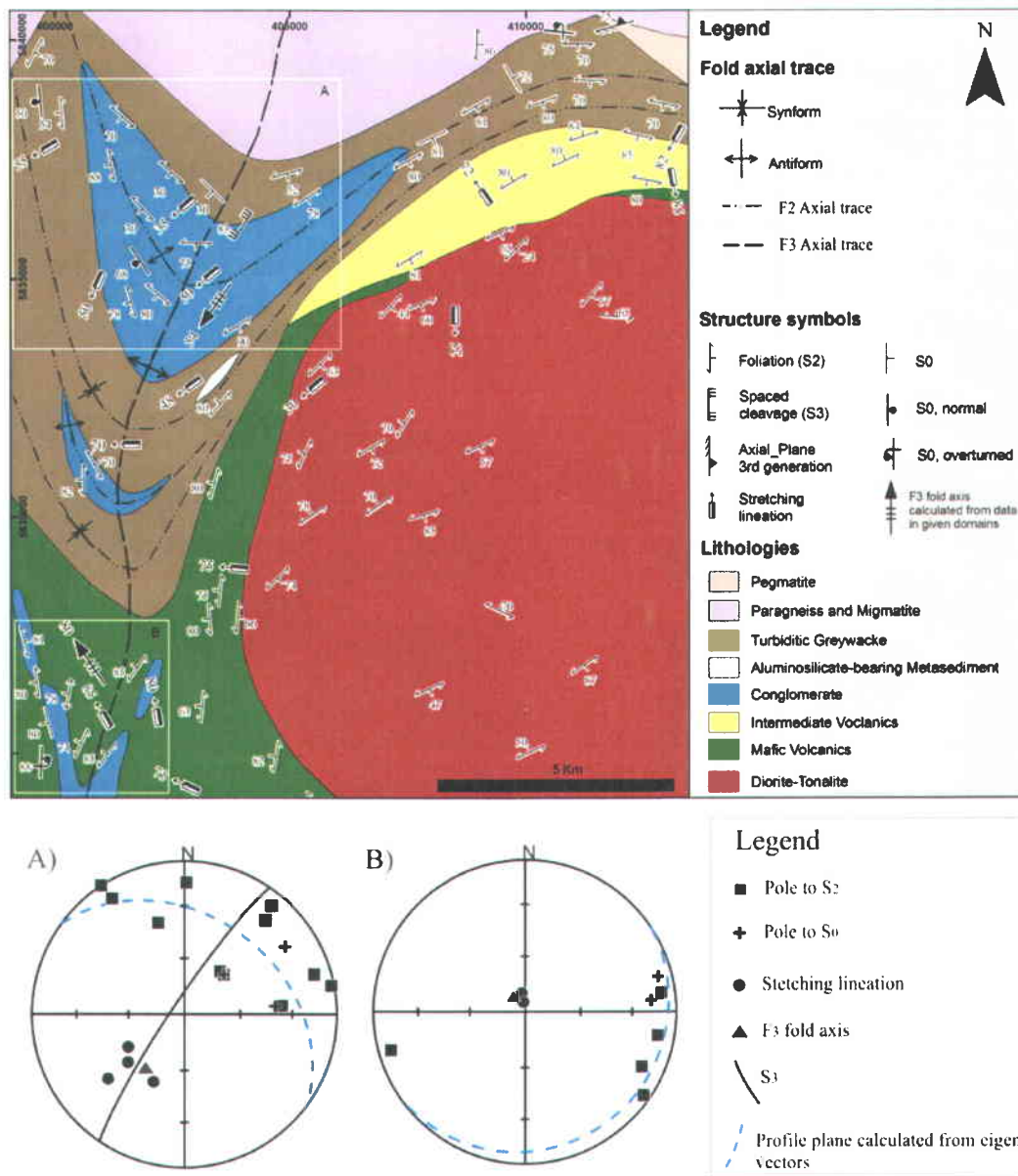


Figure 2.5.11: Geological map of an area located 15 km to the west of the *Éléonore* property (see location on Figure 2.5.8) showing and F_2/F_3 interference pattern. F_2 folds are interpreted based on the map pattern and the distribution of stratigraphic facings (younging directions). Data from domains A and B are plotted on stereonets A and B, respectively. Note how calculated F_3 fold axes in S_0/S_2 are sub-parallel to mineral lineations in respective domains. Map modified from Bandyayera and Fliszár (2007). Coordinates are in UTM Nad83.

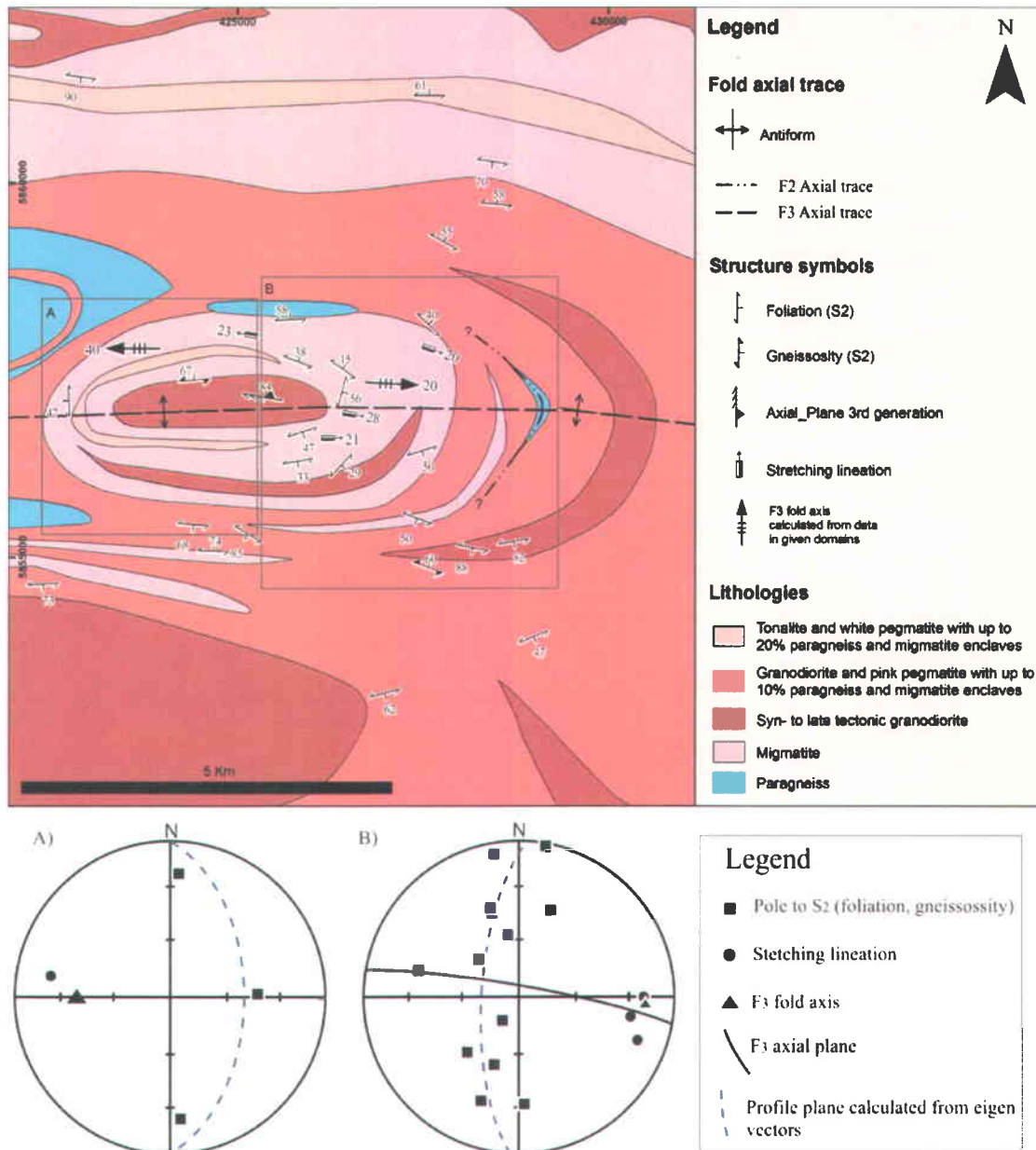


Figure 2.5.12: Geological map of an area located 20 km to the north of the Éléonore property (see Figure 2.5.8) showing an F_2/F_3 interference pattern. F_2 folds are interpreted based on the map pattern. Note the change in plunge of the F_3 fold from domain A to domain B. Data from domains A and B are plotted on stereonet A and B, respectively. The presence of a granodiorite intrusion in the core of the dome structure might indicate that doming is in part related to its diapiric emplacement. Note how calculated F_3 fold axes in S_0/S_2 are sub-parallel to mineral lineations in respective domains. Map modified from Bandyayera and Fliszár (2007). Coordinates are in UTM Nad83.

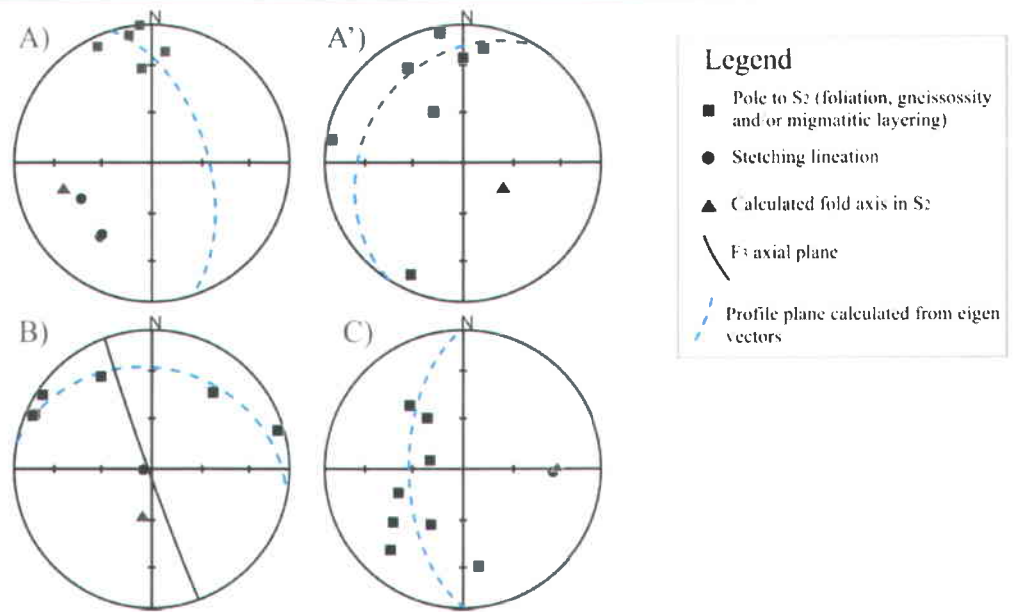
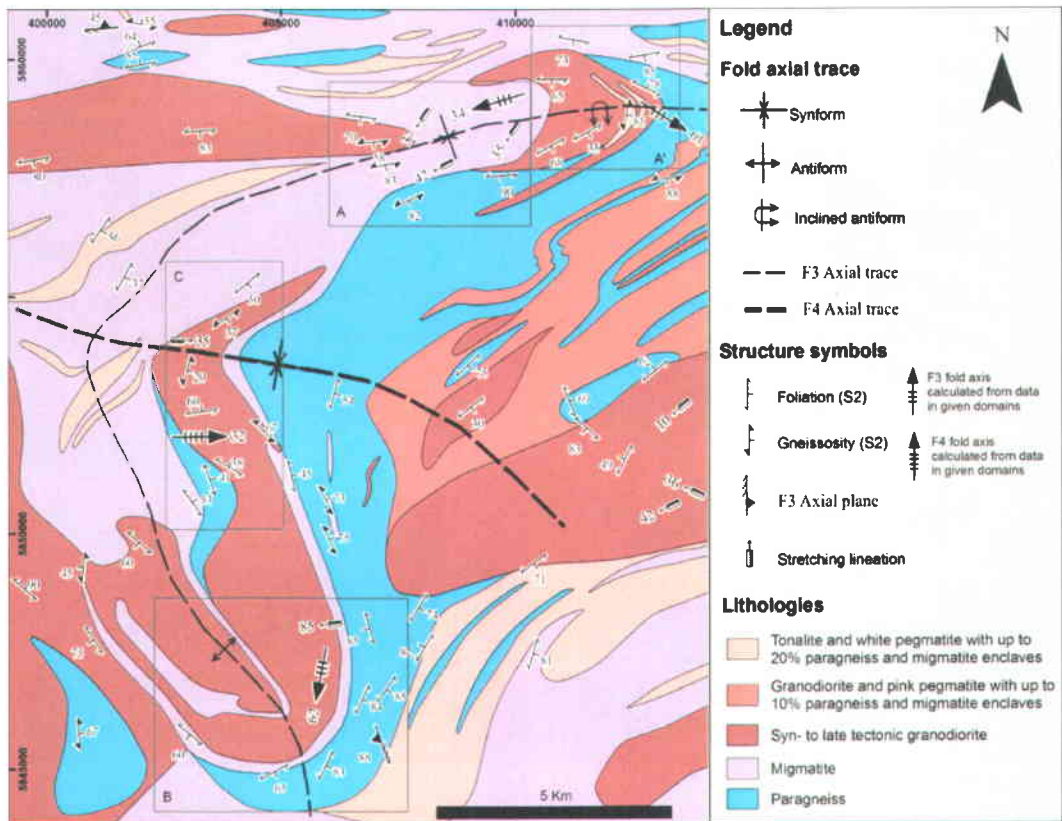


Figure 2.5.13: Geological map of an area located 20 km to the NW of the Éléonore property (see Figure 2.5.8) showing an F_3 fold refolded by a large-scale F_4 fold. Note the change in plunge of the F_3 fold from domain A to domain A'. Data from domains A, A', B, and C are plotted on stereonets A, A', B, and C, respectively. Note how calculated F_3 (and F_4 ; stereonet C) fold axes in S_0/S_2 are sub-parallel to mineral lineations in respective domains. Map modified from Bandyayera and Fliszár (2007). Coordinates are in UTM Nad83.

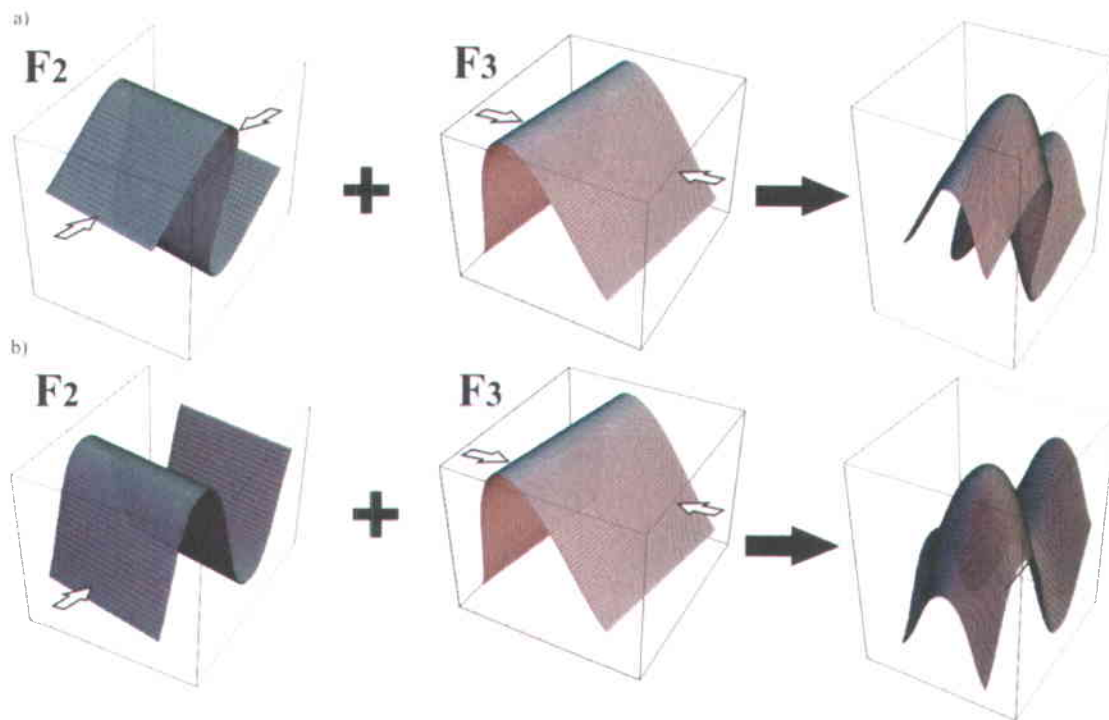


Figure 2.5.14: Schematic representations constructed using Mathematica© illustrating the effect of changes in the dip of F_2 axial planes prior to F_3 folding on the finite geometry. Moderately-dipping F_2 axial plane in (a) results in a transitional between a mushroom and a dome-and-basin geometry after F_3 folding, whereas steeply-dipping F_2 axial plane in (b) results in a dome-and-basin geometry after F_3 folding.

The interpreted distribution of F_2 , F_3 , and F_4 axial traces on the Éléonore property (Figure 2.5.9) is similar to the one interpreted at a larger scale (Figure 2.5.8), suggesting that the Éléonore property has a similar finite geometry. The distribution of the thick conglomerate unit (Figure 2.5.9) hence probably results from mushroom-like F_2/F_3 interference. In the central portion of the map, the F_2/F_3 interference is itself distorted by F_4 folds (Figure 2.5.9).

Although calculated F_3 fold axes in the composite S_0/S_2 fabric are generally moderately-plunging to the SW on the property (Figure 2.5.9), a significant change in the plunge of calculated F_3 fold axes is observed in the Roberto area, where it is steeply-plunging towards the north (Figures 2.5.9 and 2.5.15). Three scenarios might result in such a change: 1) the F_3 geometry is folded by a shallowly-plunging F_4 synform, 2) the change in the attitudes of F_3 folds is controlled by the initial geometry of S_0 and S_2 prior to D_3 , which might have been influenced by the presence of the Eil Lake intrusion, and 3) the large-scale NW-striking fault which truncates the north-eastern part of the deposit dragged the F_3 geometry upward (Figure 2.5.15). The first scenario is not favored because S_4 foliation and F_4 folds have not been recognized in the area. The third scenario appears more plausible because the fault offsets Proterozoic diabase dykes

and therefore postdates D_3 . However, the net slip along this fault is not determined so the inferred vertical displacement along the fault remains speculative. The preferred scenario is therefore that the variations in the attitude of F_3 folds are caused by the initial geometry of the region prior to D_3 . The changes in lineation orientations, which are typically parallel to F_3 fold axes (see section 2.5.3.3 *Parallelism of Lineations and Fold Axes*), are documented in the southern part of the property adjacent to large intrusive bodies (Figure 2.5.9).

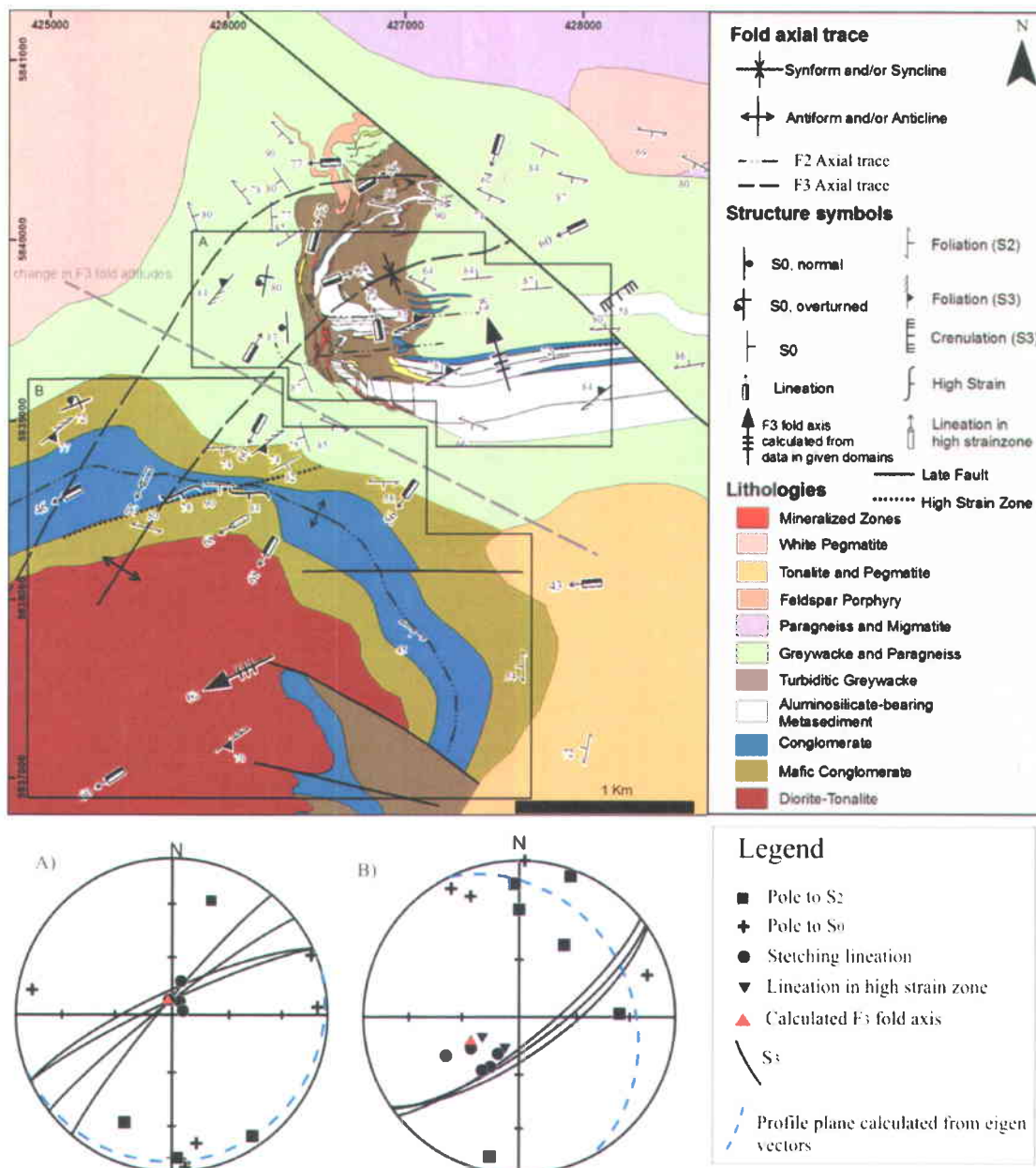


Figure 2.5.15: Interpreted structural geology of the Roberto area. Note the change in attitude of calculated F₃ folds from domain A to domain B (separated by grey dashed-line). Data from domains A and B are plotted on stereonets A and B, respectively. Note how calculated F₃ fold axes in S₀/S₂ are sub-parallel to mineral lineations in respective domains. Coordinates are in UTM Nad83.

2.5.3.3 *Parallelism of Lineations and Fold Axes*

The co-linearity between mineral lineations and F_3 fold axes is striking on the study area (stereonet of Figures 2.5.11 to 2.5.13, and Figure 2.5.15). This could be achieved in three different ways. The mineral lineation may have been generated: 1) synchronously and sub-parallel to F_3 fold axes, 2) during D_2 and subsequently rotated parallel to F_3 fold axes, or 3) during D_2 sub-perpendicular to F_2 fold axes, its co-linearity with F_3 fold axes resulting from the fact that the sub-perpendicular orientations of the folds, as schematically illustrated on Figure 2.5.16. Given that lineations are typically formed along with the foliation plane on which they occur (Duebendorfer, 2003), and since lineations are measured in S_2 and S_3 is not well developed in those areas, the first scenario is unlikely. The third scenario is also not favored because where observed on outcrops, the lineation is parallel to F_2 fold axes, not orthogonal. However, a potential caveat to the latter statement is that local parallelism between F_2 fold axes and mineral lineations might result from progressive rotation of fold axes towards the stretching direction during folding, as described by (Williams, 1978; Skjerna, 1980). Such a process requires high strain and could lead to the formation of sheath folds (Cobbold and Quinquis, 1980). F_2 sheath folds are indeed locally present in the Roberto area (see *section 3.3 Structural Geology of the Roberto Deposit*), but non-sheath F_2 folds with fold axes oriented sub-parallel to mineral lineation are also documented. There is therefore an ambiguity concerning the true geometrical relationships between F_2 fold axes and the mineral lineation. Nonetheless, the second scenario is the simplest and agrees with the fact that the lineation is defined by the same metamorphic minerals as S_2 and is contained within S_2 . In order to realign the lineation parallel to F_3 fold axes during folding, however, significant homogeneous strain is required. The fact that the calculated F_4 fold of Figure 2.5.13 is also parallel to the lineation (stereonet "C") suggests that such a process might be common, specifically in higher grade rocks where folding likely results from an important component of homogeneous flattening.

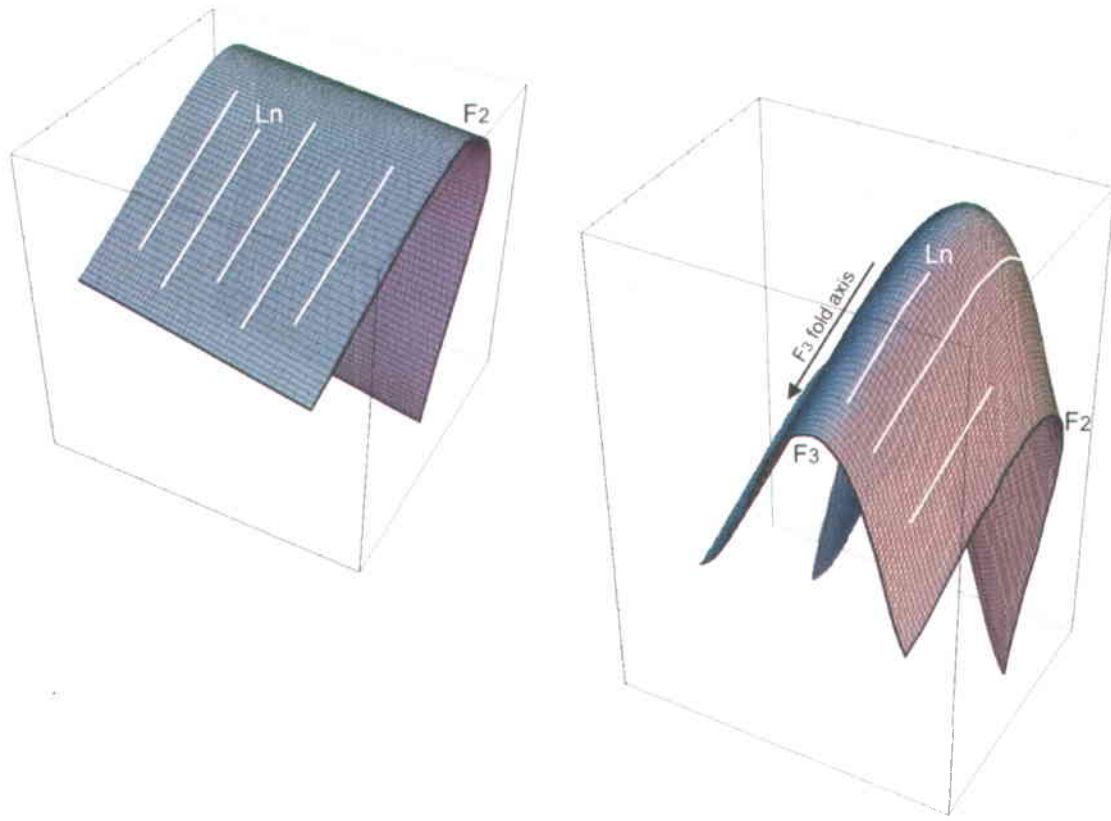


Figure 2.5.16: Schematic diagrams constructed in Mathematica® illustrating one of three possible scenarios to explain the co-linearity between measurements of mineral lineations and F_3 fold axes. Since the two fold phases are nearly orthogonal to each other, mineral lineations (L_n) generated sub-perpendicular to F_2 fold axes (left diagram) will be sub-parallel to F_3 fold axes once refolded by F_3 folds (right diagram). Although the lineation is drawn on S_0 instead of S_2 , the geometrical relationship is the same since F_2 folds are near isoclinal.

2.5.3.4 High Strain Zones

Kilometer-scale high strain zones transect the Éléonore property at two localities, one in the western part of the property and the other near the Roberto deposit (Figure 2.5.9). High strain zones of the western part of the property occur at outcrop scale where they are less than 1 meter wide (Figure 2.5.17a), and are inferred to occur at map scale from discontinuities in airborne magnetic surveys (Figures 2.5.18 and 2.5.19). Since evidence of movement is documented on outcrops (dragging of S_2 along the high strain zones, Figure 2.5.17a) and interpreted at map-scale (Figures 2.5.18 and 2.5.19), the high strain zones of the western domain can be referred to as shear zones. The shear zones are associated with a well-developed lineation whose orientation suggests that movement along the shear zones was oblique (Figure 2.5.18). Although they have different orientations, the attitudes of lineations in

NW- and NE-trending shear zones are the same (Figures 2.5.18 and 2.5.19) which may suggest that they are part of a conjugate pair. The fact that the shear zones drag S_2 and that the attitudes of S_2 are distributed around a small circle whose cone axis has an attitude similar to the attitudes of lineations measured in shear zones (Figure 2.5.18) suggests that the shear zones locally controlled the attitude of S_2 . The fact that the attitudes of the NE-trending shear zones, lineations, and S_3 fabric are distributed along a small circle whose cone axis has an attitude similar to calculate F_4 fold axes (Figure 2.5.18) suggests that F_4 folds controlled the attitude of those structural features in that region. The attitude of the NW-trending shear zone, which is subparallel to the axial trace of the F_4 fold, might explain why the latter shear zone does not appear to be affected by the F_4 fold.

In the Roberto area, high strain zones are wider (Figures 2.5.17b and 2.5.17c), but lack evidence for apparent lateral displacement. Such high strain zones are also associated with well-developed lineations (Figure 2.5.17d). In that region, however, lineations measured in high strain zones have attitudes subparallel to the regional lineation (L_2) (Figure 2.5.15) which suggests that the high strain zones are in part compatible with D_2 and could therefore be syn- D_2 . It is not clear whether or not the high strain zones controlled the distribution of S_2 in that region, which might alternatively be controlled by F_3 folds (Figure 2.5.15).

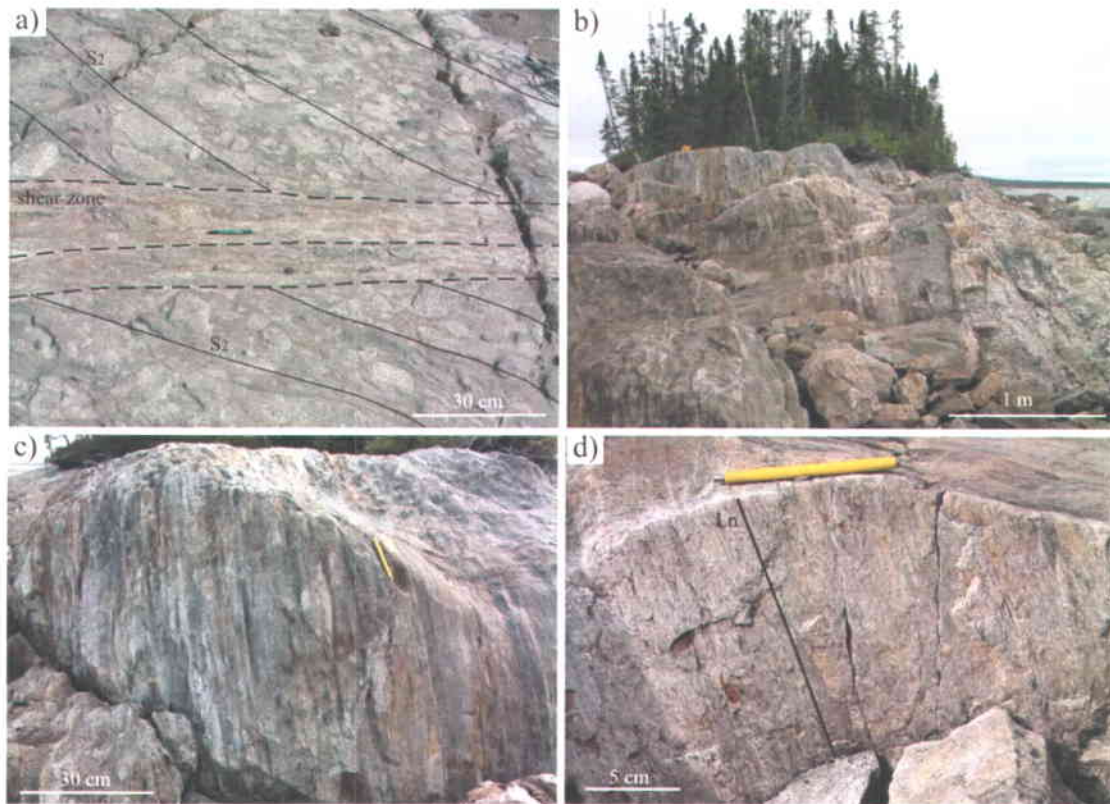


Figure 2.5.17: Photographs in conglomerate sequences showing: a) shear zone dragging S_2 fabric with an apparent sinistral motion in plan view. b) several meters wide high strain zone. The green rock is a mafic dyke crosscutting conglomerate and deformed by the high strain zone. c) section view of high strain zone shown in (b) where conglomerate fragments are highly stretched, d) well-developed lineation in high strain zone. Photographs (c) and (d) courtesy of Benoît Dubé. Photograph (a) from region shown on Figure 2.5.18. Photograph (b), (c), and (d) from region shown in Figure 2.5.15.

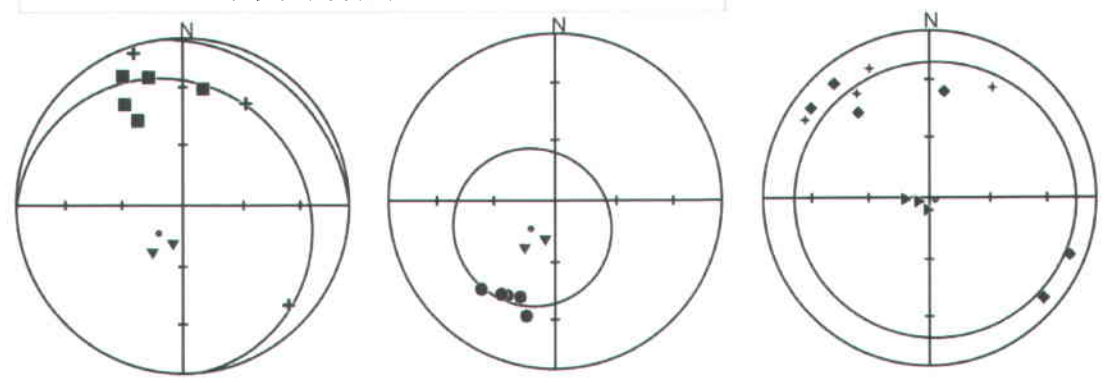
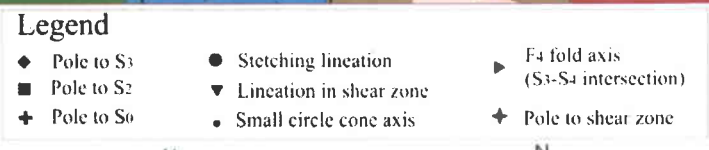
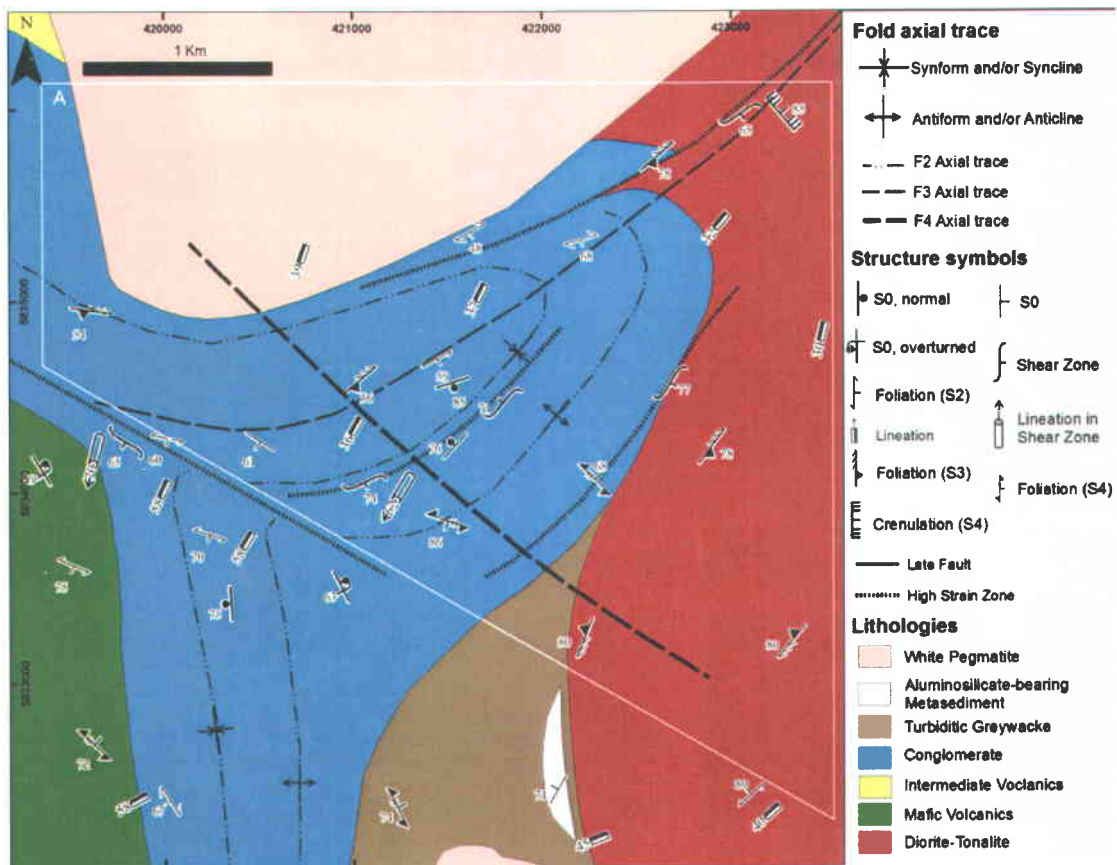


Figure 2.5.18: Interpreted structural geology of the western region of the property. The presence of shear zones and F₄ folds add to the complexity of the area. Stereonets (lower hemisphere) include data from domain "A". Lineations measured in shear zones have attitudes similar to cone axes of small circles which approximate the distribution of poles to S₂ and S₀ and lineation measurements (first two stereonets). F₄ fold axes have attitudes similar to the cone axis of a small circle which approximates the distribution of NE-trending shear zones (stereonet on the right). Coordinates are in UTM Nad83.

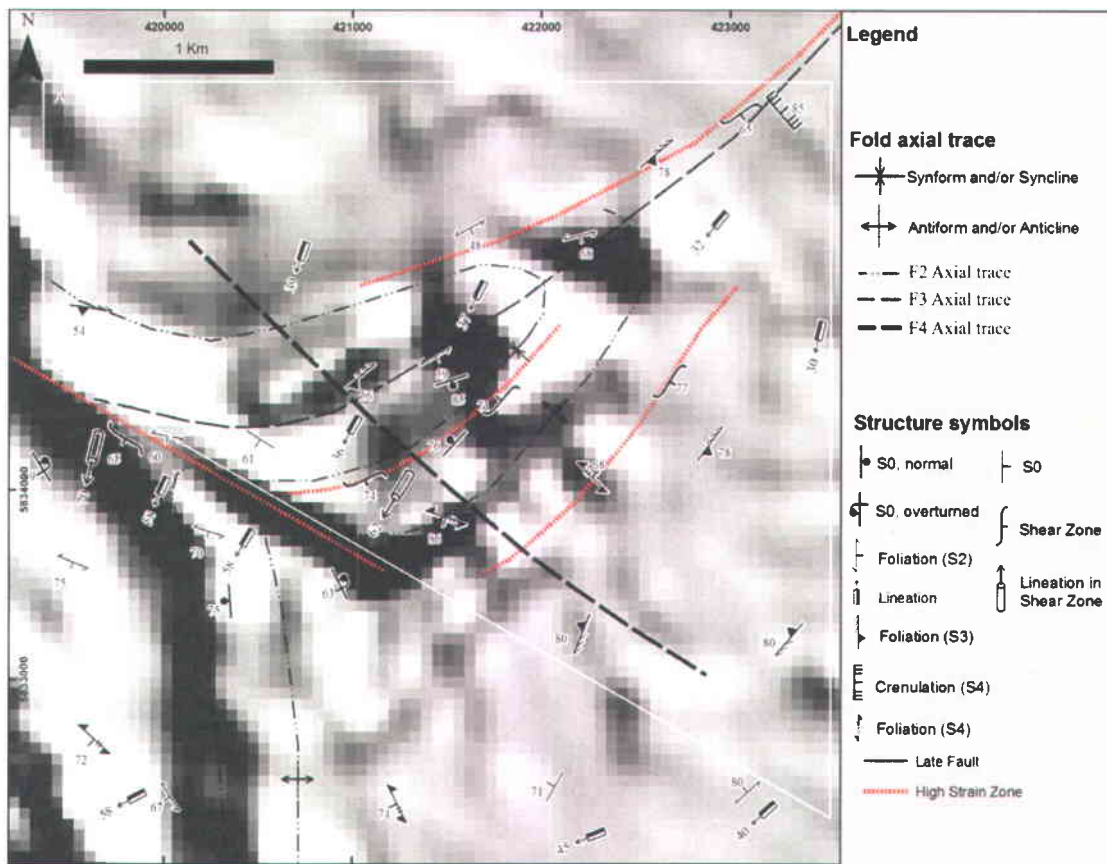


Figure 2.5.19: Airborne magnetic map of the region displayed on Figure 2.5.18. Note the presence of discontinuities, specifically the one corresponding with the NW-trending shear zone. Magnetic map modified from (Goldack-Airborne-Surveys, 2008). Coordinates are in UTM Nad83.

2.5.4 Alteration and Mineralization

Several gold occurrences are found on the Éléonore property. Figure 2.5.20 shows the distribution of potassic alteration within analyzed rock samples following the analysis performed in section 3.5.2 *Least Altered Samples*.

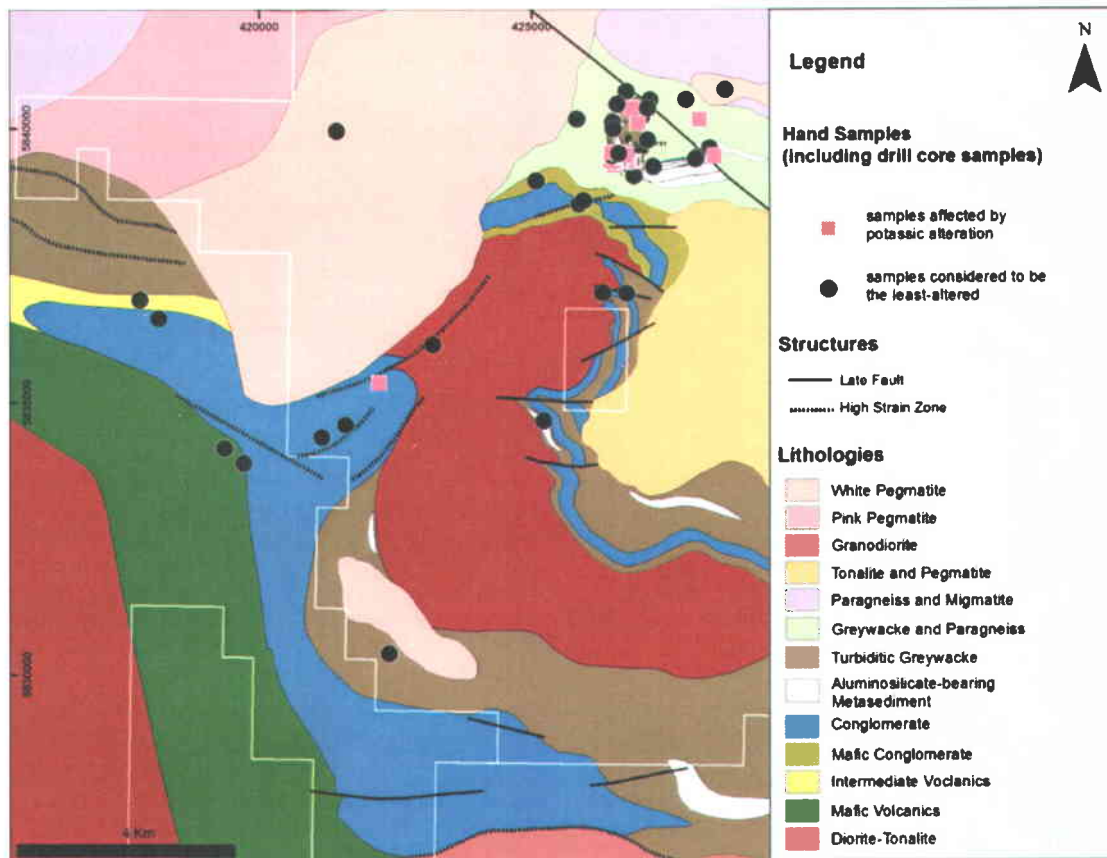


Figure 2.5.20: Geological map of the Éléonore property showing the distribution of samples affected by potassic alteration and samples interpreted to be the least altered. Some samples of the Roberto deposit area represent drillcore samples vertically projected on the surface map. Coordinated are in UTM Nad83.

Although not displayed on Figure 2.5.20, potassic alteration has also been recognized within an area of the Ell Lake diorite referred to as the “Vieux Camp” (Bécu et al., 2007). Potassic alteration is also proximal to auriferous zones (Bécu et al., 2007).

The most significant showings are hosted by the Ell Lake intrusion (2705 ± 1.9 Ma; David, 2005) and consist of Cu-Au-Ag mineralization located 7 km southwest of the Roberto deposit (Figure 2.5.2). The characteristics and the relative timing of these intrusion-hosted mineralizations were studied by (Bécu et al., 2007). The intrusion consists of dioritic and tonalitic

phases locally cut by feldspar-porphyry dykes. The auriferous zones are generally associated with semi-massive to massive chalcopyrite \pm pyrrhotite impregnations, disseminations, and replacement with rare traces of molybdenite. Prominent tourmaline alteration zones that resemble Roberto's tourmaline-rich stockwork (see below) are present in the vicinity of the auriferous zones, which may suggest that mineralization at Roberto and at the Ell Lake diorite share some common attributes and could be related. Several sub-metric high strain zones and well-developed down-dip lineation (L_2) on foliation planes have been mapped in the area. During the course of this study, the potential genetic relationship between the Ell Lake diorite and the Roberto deposit was investigated through geochronology.

3 GEOLOGY OF THE ROBERTO DEPOSIT

This chapter presents a comprehensive description of the geology of the Roberto deposit. The mineralogical, geochemical, and textural characteristics of auriferous zones, associated hydrothermal alteration, and host lithological units are presented. A particular emphasis is put on the structural geology of the area and on the timing between deformational events and gold mineralization. The magmatic and metamorphic history of the deposit area is documented, and key observations are presented in order to provide insights on the relative chronology between gold mineralization, magmatic phases, and deformational/metamorphic events. Although treated in details in Chapter 4, geochronological data is incrementally integrated in this chapter to complement various aspects of the description.

A multidisciplinary approach, new mapping techniques, and state of the art three-dimensional software (Gocad) are combined to provide a modern take on the study of the Roberto deposit. The methodology and the details of the techniques used are described in *Annex 1*. Surface data extracted from natural outcrops, local stripped outcrops, and a very large stripped outcrop (100m x 400m) is combined with subsurface data extracted from hundreds of drill holes in order to determine the structural and general geological characteristics of auriferous zones, alteration facies, and lithological units. Petrography and/or geochemistry of surface and subsurface samples are utilized to: 1) characterize the metallogenic and metamorphic attributes of gold mineralization and associated alteration; 2) define the lithogeochemistry and metamorphic assemblages of lithological units; and 3) describe the mineralogical and textural characteristics of structural fabrics.

3.1 Geology of the Roberto Deposit: Introduction

The Roberto deposit occurs within a km-scale steeply-plunging fold that affects upper-greenschist to lower-amphibolite sequences of the La Grande Subprovince's Low Formation. In the vicinity of the deposit, the Low Formation is composed of turbiditic greywacke, conglomerate units locally interbedded with arenite, thinly bedded arenites, aluminosilicate-porphyroblasts-bearing units, biotite schists, and minor banded cherty iron formations. Gold mineralization is principally hosted within quartz \pm microcline \pm actinolite \pm diopside \pm biotite-arsenopyrite-pyrrhotite-löllingite veins hosted within turbiditic greywacke, but is locally found as disseminated-

ore in greywacke and arenites and hosted by quartz-arsenopyrite-pyrrhotite-löllingite ± feldspar veins in paragneiss and biotite schists. Gold mineralization is associated with a protracted hydrothermal system characterized by distal calcium-bearing assemblages, where pyrrhotite and pyrite are dominant sulphide minerals, and auriferous potassium- and boron-rich assemblages where arsenopyrite and pyrite are dominant sulphide phases.

The rocks are cut by a swarm of locally-auriferous pegmatite dykes, which are on average less than one meter wide and up to hundreds of meters in length. A 0.05 km² feldspar porphyry intrusion is located in the northern part of the deposit, and minor (less than 5 metre thick) feldspar porphyry dykes are locally documented. Approaching the migmatized Opinaca Subprovince to the east, paragneiss units become more abundant, as regional metamorphic grade gradually increases.

3.2 Lithology

This section presents the characteristics of the principal lithological units present in the vicinity of the Roberto deposit. The distribution of lithological units is presented using 3D representations constructed in Gocad, and 2D surface maps created in ArcGIS. Macroscopic characteristics are presented through photographs of surface outcrops, hand samples, and drillcore. Mineralogical and textural characteristics determined through petrographic work are also presented. Moreover, geochemical attributes of selected lithological units are presented. All geochemical analyses presented were performed on rock samples taken during the course of this study. Only samples located within a 1.5 km radius of the core of the deposit were selected. Even though all rocks are metamorphosed, the term “meta” is not always included in rock type nomenclature for simplicity.

3.2.1 Supracrustal Units

3.2.1.1 *Turbiditic Greywacke*

Turbiditic greywacke is the most common rock type in the vicinity of the Roberto deposit and represents the principal host rock of auriferous zones. The distribution of greywacke units is

represented on Figure 3.2.1.¹ Even though they have been metamorphosed and deformed, sedimentary attributes including cross-beds, storm beds, graded beds, and channels have been very well preserved, and can locally be used to establish younging direction of sedimentary sequences (Figure 3.2.2). Bedding can be recognized based on compositional criteria, differences in color, and presence or absence of sedimentary features. Within turbiditic sequences, massive greywacke devoid of sedimentary structures locally form thick (meter-scale) beds that alternate with bedded and laminated units. One particular massive greywacke is found on the large stripped outcrop between the aluminosilicate porphyroblast-bearing unit and East-Roberto auriferous zone (Figure 3.2.3).

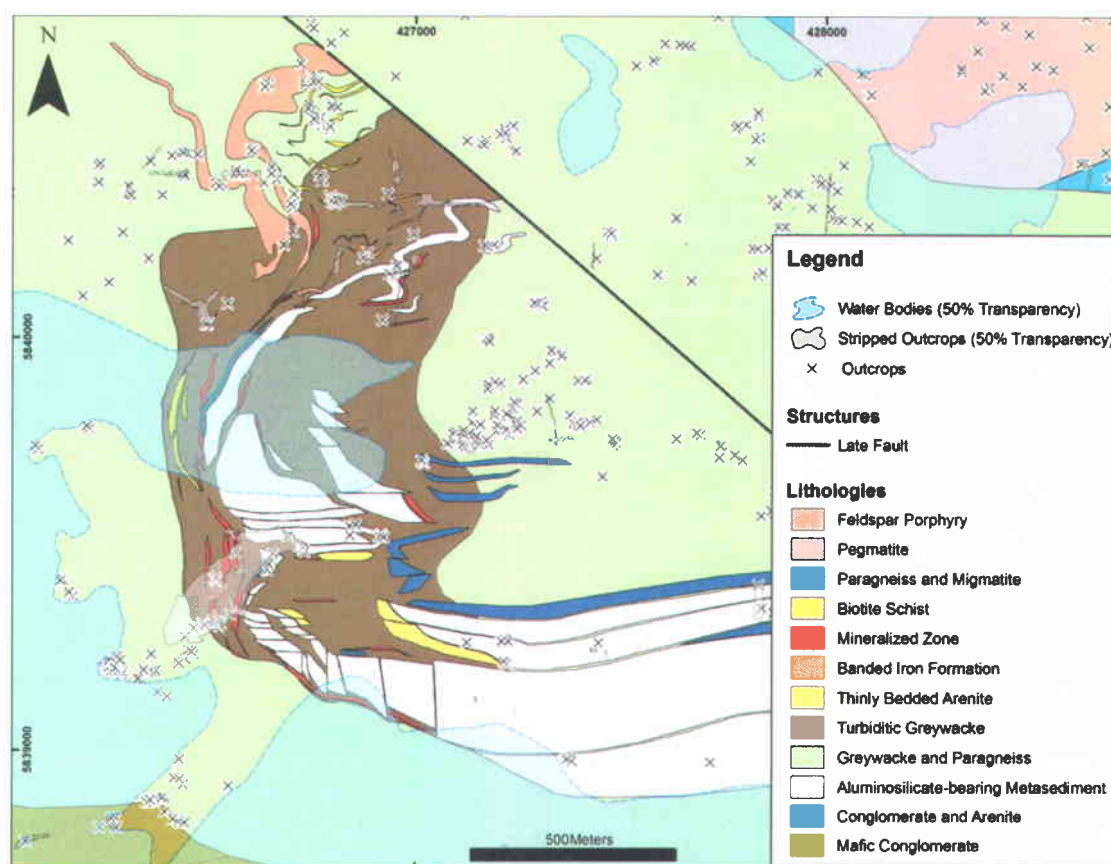


Figure 3.2.1: Geological map of the Roberto deposit showing distribution of lithological units and location of natural and stripped outcrops. A large proportion of the deposit is either not exposed at surface or submerged under water. This geological map was primarily constructed from vertical projection of 3D

¹ The structural style, with many faults/discontinuities, partly results from the assumptions from which the 3D model was constructed (see section 3.1.2 *Construction of 3D representations*). Geological interpretations of the discontinuities are presented in section 3.3.6.2 *Nature of Discontinuities Observed in 3D Representations*.

representations built from drillcore data. Many discontinuities observed in the map pattern results from assumptions utilized to construct the 3D model (see *Annex 1*). Pegmatite dyke swarms and diabase dykes that intrude the deposit area are not displayed to simplify the view. Coordinates are in UTM Nad83.

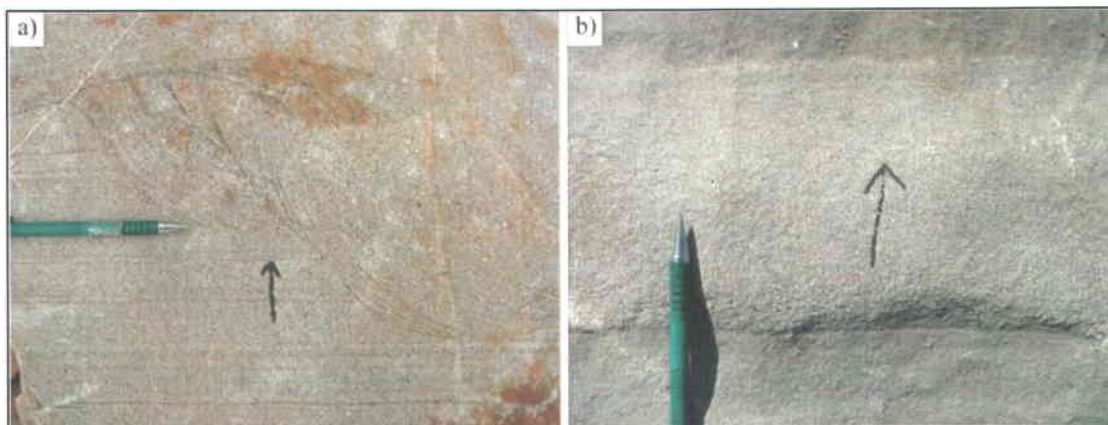


Figure 3.2.2: Photographs showing examples of sedimentary features present in Roberto's turbiditic sequence. Such features can be utilized to determine younging direction of sedimentary sequences (represented by arrows). a) Channel. b) Graded bed.

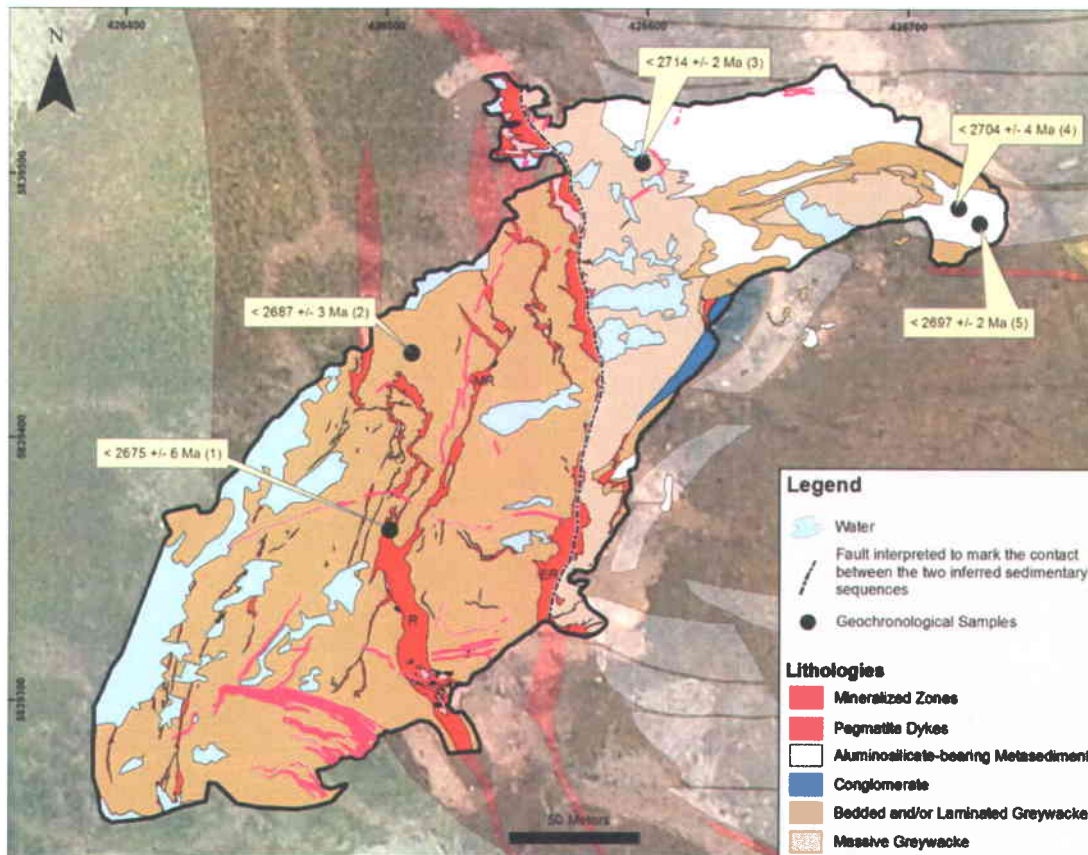


Figure 3.2.3: Geological map of the large stripped outcrop showing the distribution of principal lithological units. Geological map of the deposit area shown on Figure 3.2.1 is displayed in the background using 70% transparency over aerial photograph. Location and maximum ages of geochronological samples are indicated: (1) Geochron-ELE-05-08, (2) Geochron-ELE-05-01, (3) Geochron-ELE-09-21, (4) Geochron-ELE-05-06, (5) Geochron-ELE-05-02. R = Roberto, ER = East-Roberto, MR = Mid-Roberto. All geochronological data from Dubé pers. comm. (2010), except for Geochron-ELE-05-08 which is from Ravenelle et al., 2010. Coordinates are in UTM Nad83.

In terms of mineralogy, the turbiditic greywacke units are composed of varying proportions of quartz, feldspars (plagioclase and microcline), biotite, and amphiboles (typically actinolite). Massive greywacke units are composed of the same phases, but generally have greater proportions of amphiboles.

A total of 5 geochronological samples of metasedimentary rocks were sampled to investigate the age relationships between the principal sedimentary lithological units present near the Roberto deposit. All samples were analyzed by Vicki McNicoll at the Geological Survey of Canada (GSC) laboratory in Ottawa (see Chapter 4 *Geochronology* for diagrams and detailed description of geochronological techniques utilized). Location and maximum age obtained for each sample are indicated on Figure 3.2.3. The ages presented here are from (Dubé et al., 2011) and Dubé pers. comm. 2010. The wide span of maximum ages potentially indicates that

the contact between the two sedimentary sequences inferred from the geology of the Éléonore property might be present on the stripped outcrop. Considering the difference of maximum ages between the sample in Roberto (<2675 +/- 6 Ma (1)) and the sample in the massive greywacke (<2714 +/- 2 Ma (3)), the East-Roberto zone or the brittle fault located along its eastern limit could potentially mark the contact between the two sequences (Figure 3.2.3).

Box and spider diagrams of major and selected minor elements were constructed in order to investigate whether the two inferred sedimentary sequences have distinct geochemical characteristics. Greywacke samples located west of the East-Roberto zone are considered to belong to the “younger” greywacke sequence (Figure 3.2.4). Results of greywacke samples of the “older” sequence were separated into greywacke and massive greywacke subgroups and compared with results of the “younger” greywacke sequence (Figure 3.2.5 and 3.2.6). All samples are considered to be the least altered samples of the Roberto area (following section 3.5.2 *Least Altered Samples*) and represent subsets of the sample population used to calculate averages for the Éléonore property listed in Table 2.5.1 and 2.5.2. Results for samples of the whole Éléonore property are also displayed on the diagrams for comparison. Samples located farther from the inferred contact between the two sequences and that did not clearly belong to either one of the two sequences were left in the Éléonore property subset. Averages of major and selected minor elements of the two sequences are listed in Tables 3.2.1 and 3.2.2.

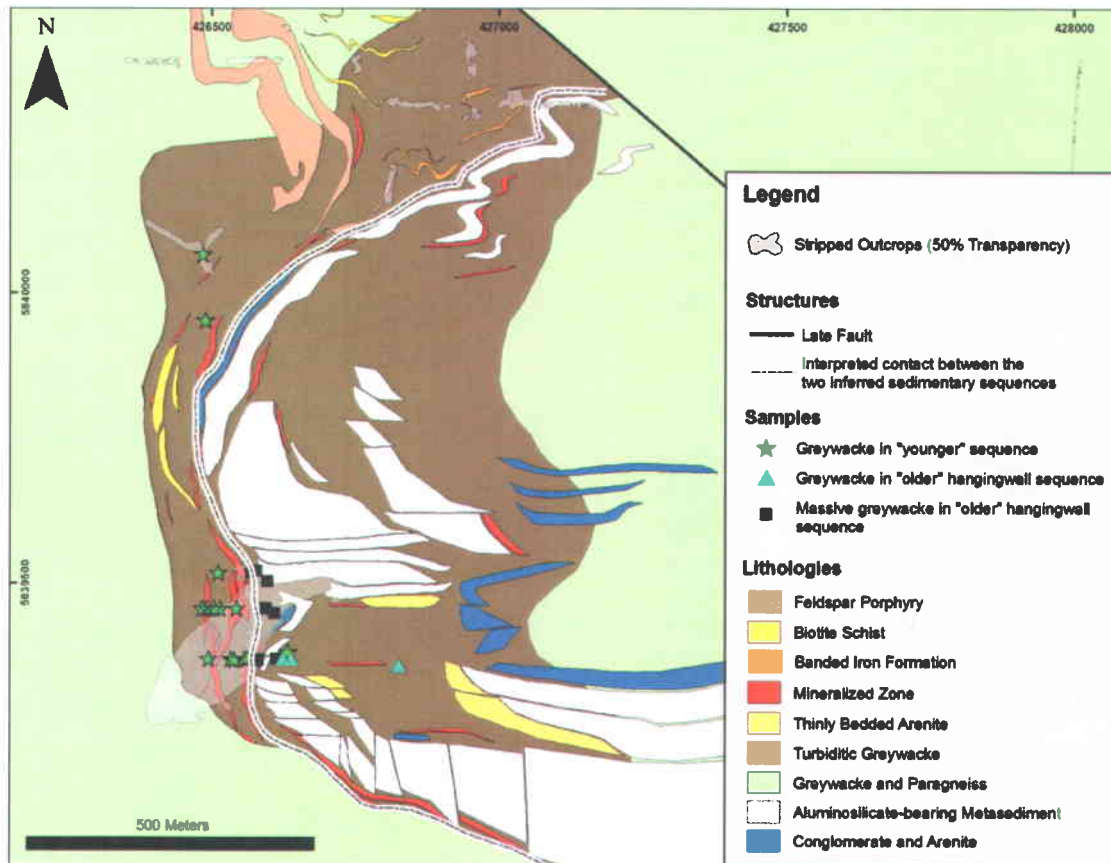


Figure 3.2.4: Geological map of the Roberto area showing the distribution of samples analyzed to compare the geochemistry of the two inferred sedimentary sequences. An interpretative contact between the two sequences is drawn on the map. Some samples are drillcore samples and their location corresponds to a vertical projection of their subsurface location (hence explaining why one of the "younger" samples plots to the right of the interpreted contact). Geochemical results are presented on Figures 3.2.5 and 3.2.6.

Results indicate that although the "younger" greywacke sequence shows more variations in terms of CaO and Na₂O content, and that the "older" massive greywacke sequence shows more variations in terms of K₂O contents, the major element geochemistry of the two sequences is very similar (Figure 3.2.5). This similarity is also illustrated by average compositions, which are indistinguishable when standard deviations are taken into account (Table 3.2.1). The higher gold and arsenic content of the "younger" greywacke sequence (Figure 3.2.5 and Table 3.2.2) might result from its proximity to the ore zone and is most probably not a primary feature. In terms of trace elements, the two sequences are also indistinguishable (Figure 3.2.6).

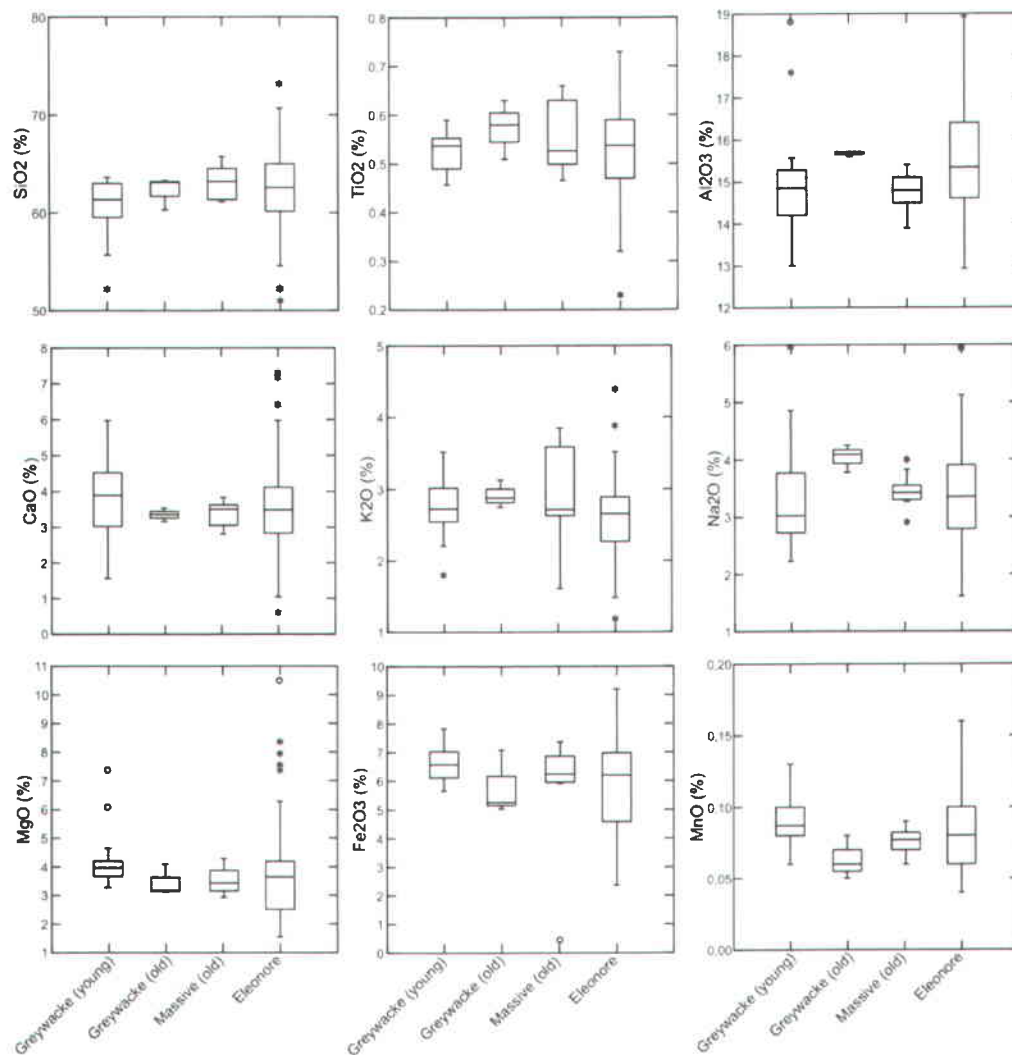


Figure 3.2.5: Box diagrams comparing major and selected minor element concentrations of the least altered samples within the two inferred sedimentary sequences. Results for the whole Éléonore property are also displayed for comparison. The center horizontal line marks the median of a given suite. The length of each box shows the range within which the central 50% of the values fall, with the box edges at the first and third quartiles. The whiskers show the range of observed values that fall within the inner fences, defined as 1.5 and -1.5 times the absolute value of the box. Values between inner and outer fences (3 and -3 times the absolute value of the box) are plotted with asterisks. Values beyond the outer fences are plotted with empty circles. All samples from this study except for 15 samples in Éléonore data which are from Bandyayera et al., 2010. Number of samples: greywacke (young) = 14; greywacke (old) = 3; massive greywacke (old) = 10; Éléonore = 60. Location of samples is indicated on Figure 3.2.4.

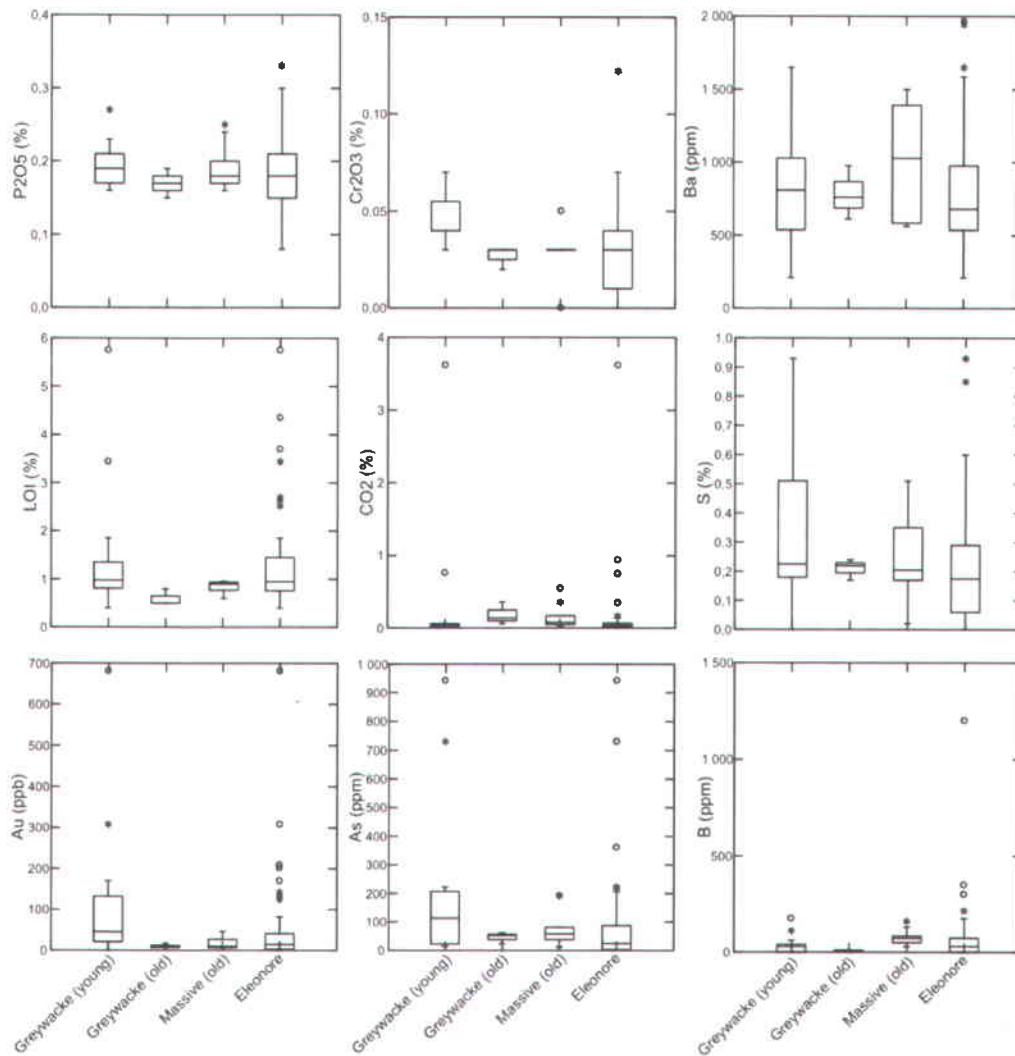


Figure 3.2.5: (continued). Number of samples: greywacke (young) = 14; greywacke (old) = 3; massive greywacke (old) = 10; Éléonore = 60 (except for Cr₂O₃ (48), CO₂ (45), S (58), Au (58), As (60), and B (58)). Location of samples is indicated on Figure 3.2.4.

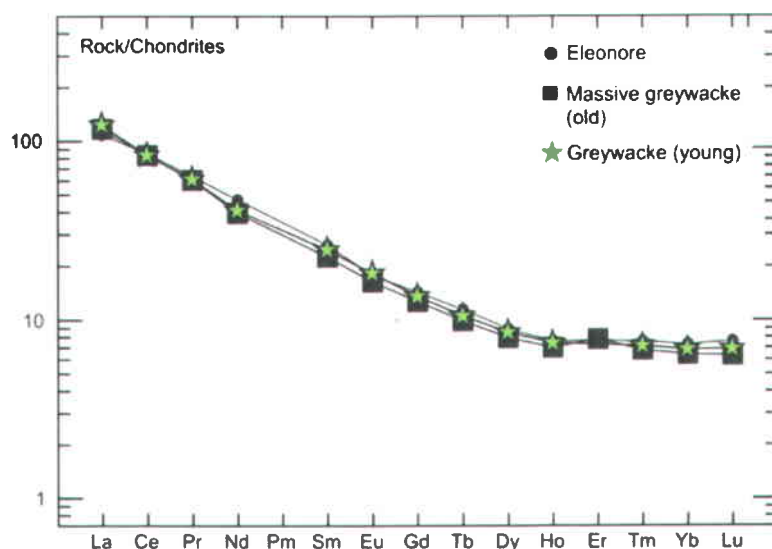


Figure 3.2.6: Chondrite-normalized (Sun and McDonough, 1989) spider diagram comparing trace element signature of the two inferred sedimentary sequences. Results for the whole Éléonore property are also displayed for comparison. Samples from the “older” greywacke sequence were not analyzed for trace elements. Trace element concentrations displayed on the diagram represent averages of least altered samples analyzed for trace elements within each suite (Éléonore: average of 29 samples; Massive greywacke (old): average of 5 samples; Greywacke (young): average of 7 samples).

Table 3.2.1: Major element averages of selected lithological units and/or sedimentary sequences present near the Roberto deposit.

ANALYTE	SiO ₂	Al ₂ O ₃	CaO	MgO	Na ₂ O	K ₂ O	Fe ₂ O ₃	MnO	TiO ₂	P ₂ O ₅	Cr ₂ O ₃	LOI	Sum	CO ₂	S
DETECTION	0.01	0.01	0.01	0.03	0.02	0.01	0.01	0.01	0.01	0.01	0.01	0.01	0.01	0.01	0.01
UNITS	%	%	%	%	%	%	%	%	%	%	%	%	%	%	%
Greywacke (young) (n = 14)	60.6	15.0	3.9	4.3	3.3	2.7	6.6	0.1	0.5	0.2	0.0	1.5	98.8	0.3	0.3
(Standard Deviation)	3.3	1.6	1.2	1.1	1.1	0.4	0.6	0.0	0.0	0.0	0.0	1.4	0.8	1.0	0.3
Greywacke (old) (n = 3)	62.2	15.7	3.3	3.5	4.0	2.9	5.8	0.1	0.6	0.2	0.0	0.6	99.1	0.2	0.2
(Standard Deviation)	1.7	0.1	0.2	0.6	0.2	0.2	1.1	0.0	0.1	0.0	0.0	0.2	0.2	0.2	0.0
Massive greywacke (old) (n = 14)	63.2	14.7	3.4	3.5	3.5	2.9	5.9	0.1	0.5	0.2	0.0	0.9	99.3	0.2	0.2
(Standard Deviation)	1.8	0.5	0.4	0.5	0.3	0.7	2.0	0.0	0.1	0.0	0.0	0.1	1.5	0.2	0.1
Eleonore (this study n = 45; Bandyayera et al., 2010 n = 15)	62.4	15.5	3.6	3.8	3.4	2.6	5.9	0.1	0.5	0.2	0.03	1.3	99.3	0.2	0.2
(Standard Deviation)	4.5	1.4	1.4	1.7	0.9	0.6	1.6	0.0	0.1	0.1	0.02	1.0	1.1	0.6	0.2

Table 3.2.2: Selected minor element averages of selected lithological units and/or sedimentary sequences present near the Roberto deposit.

ANALYTE	Au	As	B	Sb	Ag	Cu	Zn	Pb	Y	Zr	Ba	Li	Rb	Sr
DETECTION	5	3	10	5	2	0.5	0.5	2	0.5	0.5	3	1	2	2
UNITS	ppb	ppm												
Greywacke (young) (n = 14)	120	204	39	7	<2	45	75	27	12	112	844	77	119	637
(Standard Deviation)	182	279	49	8		21	6	24	2	19	453	33	36	220
Greywacke (old) (n = 3)	10	46	7	13	<2	51	72	58	10	130	783	74	95	622
(Standard Deviation)	5	19	6	2		15	2	37	1	15	182	13	13	55
Massive greywacke (old) (n = 14)	16	76	79	5	<2	45	73	23	11	126	997	60	99	632
(Standard Deviation)	14	65	40	4		20	6	23	1	30	379	21	29	75
Eleonore (this study n = 45; Bandyayera et al., 2010 n = 15)	48	84	73	5	<2	40	69	23	11	115	788	69	109	623
(Standard Deviation)	104	161	167	6		25	18	24	5	24	404	28	49	297

3.2.1.2 Conglomerate Units Locally Interbedded with Arenite

Polymictic conglomerates are present as lens-shaped units. Their distribution is shown on Figures 3.2.1, 3.2.3, and 3.2.7. The conglomerates generally contain blocks of felsic rocks and sedimentary rocks. The dm-scale diorite blocks contained within the conglomerate present in the southern part of the Éléonore Property are not present in these units. In terms of mineralogy, the matrix of the conglomerate units is similar to turbiditic greywacke.

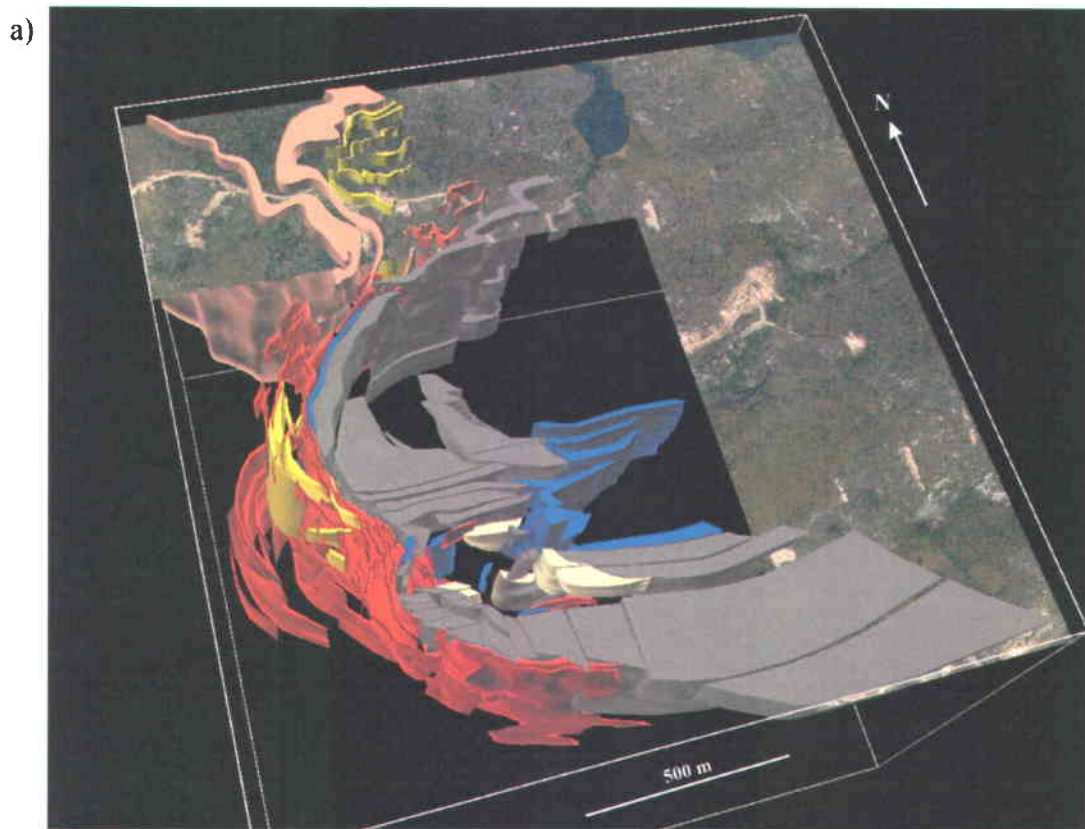


Figure 3.2.7: Gocad snapshots showing three different views of the deposit's geometry. Lithological units are color-coded following the legend of Figure 3.2.1 (red: auriferous zones, grey: aluminosilicate-bearing metasedimentary rocks, blue: conglomerate and arenite, yellow: biotite schist, orange: banded iron formation (Puncho zone), pale yellow: thinly bedded arenite, pink: feldspar porphyry). Turbiditic greywacke and paragneiss are the dominant rock types present in empty regions of the 3D space. Pegmatite dyke swarms and diabase dykes are not displayed to simplify visualization. Photograph of surface is lowered from its initial elevation to allow better visualization of the geometry. The methodology used to construct such representations is described in *Annex 1*. a) Photograph is cropped out to enable visualization of the subsurface. b) and c) The southern upper part of the deposit was removed at various depths to allow better visualization of the geometry.

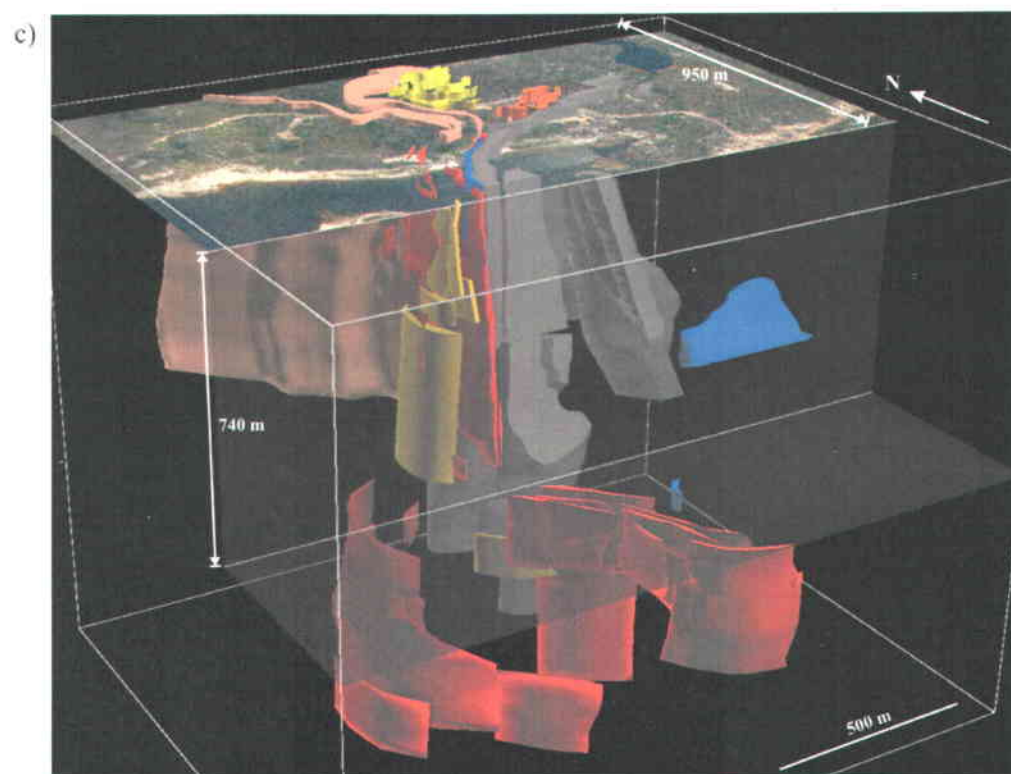
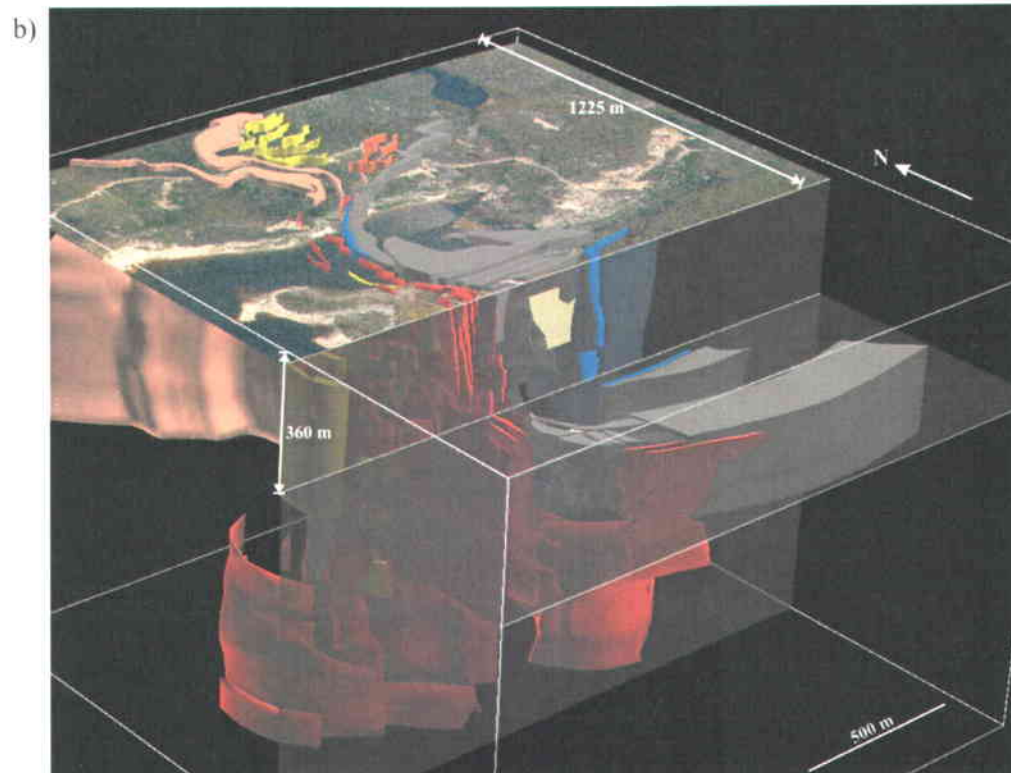


Figure 3.2.7 Continued.

The conglomerate units are locally in contact or interbedded with white arenitic beds and thinly-bedded arenites (Figure 3.2.8a). Such spatial relationship between conglomerates and arenitic rocks has been documented elsewhere in other Archean turbiditic sequences (Condie, 1981). In the study area, those units form a mappable formation which is locally dominated by one or more rock types. The arenitic beds locally host auriferous zones and are locally brecciated by tourmaline-rich veins (Figure 3.2.8b). Locally, thinly-bedded arenites are not spatially associated with conglomerates or white arenites. Such arenitic units were mapped and modeled separately (Figure 3.2.1, 3.2.7).



Figure 3.2.8: Photographs of drillcore showing: a) spatial association between arenite, thinly-bedded arenite, and conglomerate (drill hole ELE-07-395 between 615 and 633 meters). b) arenite brecciated by tourmaline veins (drill hole ELE-07-388 between 541 and 548 meters). Photographs courtesy of Opinaca Mines Ltd.

3.2.1.3 *Aluminosilicate-Bearing Greywacke Units*

The distribution of aluminous metasedimentary rocks, primarily characterized by the presence of mm- to cm-scale aluminosilicate porphyroblasts, is represented on Figures 3.2.1, 3.2.3, and 3.2.7. Such units are easily recognizable in drillcore (Figure 3.2.9) and represent the best marker to map the subsurface. It is still uncertain whether the presence of aluminosilicate porphyroblasts is related to acid-leached sedimentary rocks that generated aluminosilicate porphyroblasts during metamorphism, or simply reflects the metamorphosed primary pelitic character of the rocks. However, since aluminosilicate-bearing metapelites are common in the region (Bandyayera and Fliszár, 2007), and since their distribution near the Roberto deposit locally follows the distribution of conglomerate and/or arenite (Figures 3.2.1, 3.2.7), the aluminous units are here interpreted to represent pelite-rich lithological units which are prone to develop aluminosilicate porphyroblasts. Thus porphyroblasts-rich and porphyroblasts-poor layers are thought to reflect primary compositional layering (Figure 3.2.10). Geochronological samples analyzed to obtain the maximum age of the aluminosilicate-bearing rocks ($< 2704 \pm 4$ Ma and $< 2697 \pm 2$ Ma (Dubé pers. comm. 2010) suggests that it belongs to the “older” sedimentary sequence (Figure 3.2.3).



Figure 3.2.9: Photograph showing aluminosilicate-bearing rock in drillcore (drill hole ELE-07-399 between 62 and 79 meters). White porphyroblasts are aluminosilicates. Photograph courtesy of Opinaca Mines Ltd.

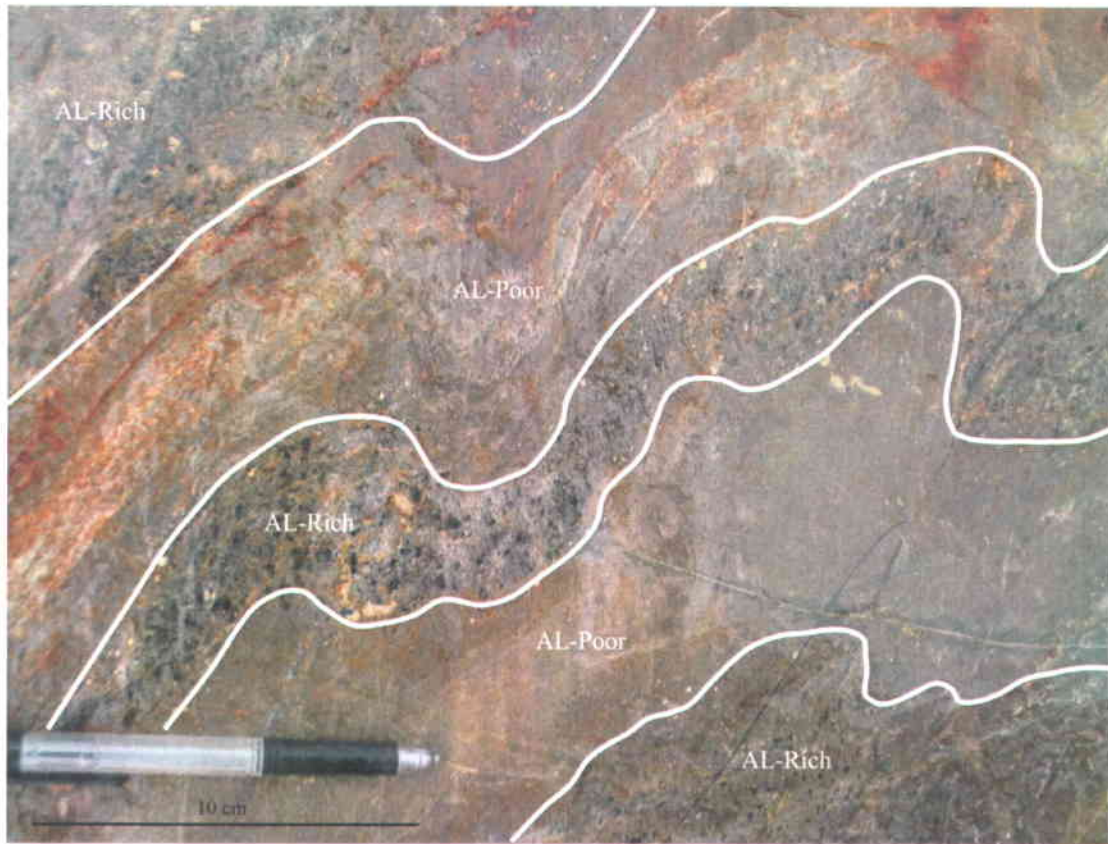


Figure 3.2.10: Photograph showing folded aluminosilicate-rich and aluminosilicate-poor layers within an aluminosilicate-bearing sequence. Dark mineral in aluminosilicate-rich layers is chlorite replacing aluminosilicate.

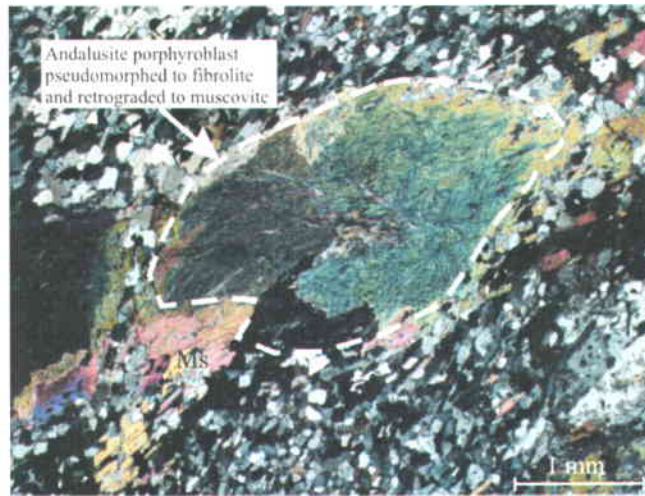


Figure 3.2.11: Microphotograph (polarized light) showing fibrolite porphyroblast retrograded to muscovite. From (Ravenelle et al., 2010).

In terms of mineralogy, the aluminous rocks are dominated by andalusite porphyroblasts (usually totally retrograded), fine-grained microcline, biotite, and quartz. Muscovite poikiloblasts and amphibole and sillimanite porphyroblasts are also locally present. The andalusite porphyroblasts are commonly entirely pseudomorphosed to fibrolite and retrograded to chlorite-sericite-muscovite (Figure 3.2.11), and locally pseudomorphosed to margarite (Ravenelle et al., 2010).

Major and selected minor element geochemistry of the aluminosilicate-bearing sequence is presented in Tables 3.2.3 and 3.2.4. Rocks within the aluminosilicate-bearing sequence were divided into aluminosilicate-free and aluminosilicate-bearing subgroups (individual beds like the ones of Figure 3.2.10 were analyzed separately). All samples are considered to be least altered samples of aluminosilicate-bearing sequences present in the Roberto area and represent subsets of the sample population used to calculate the average composition of Éléonore's turbidite sequence. A reference composition of high grade pelitic schists is included in Table 3.2.3 for comparison. Results show that if standard deviations are considered, the major element composition of the aluminous sequence near Roberto is similar to reference compositions of high grade pelitic schists (Table 3.2.3).

Table 3.2.3: Major element averages of aluminosilicate-free and aluminosilicate-bearing metasedimentary rocks in Roberto's aluminosilicate-bearing sequence compared with a reference average composition of high grade pelitic schists from Shaw (1956).

ANALYTE	SiO ₂	Al ₂ O ₃	CaO	MgO	Na ₂ O	K ₂ O	Fe ₂ O ₃	MnO	TiO ₂	P ₂ O ₅	Cr ₂ O ₃	LOI	Sum	CO ₂	S
DETECTION (Highest)	0.01	0.01	0.01	0.03	0.02	0.01	0.01	0.01	0.01	0.01	0.01	0.01	0.01	0.01	0.01
UNITS	%	%	%	%	%	%	%	%	%	%	%	%	%	%	%
AL-free beds in AL-sequence (n = 4) (Standard Deviation)	68.0 1.9	16.2 0.7	3.6 0.4	2.0 0.5	3.1 0.3	2.2 0.3	3.7 0.8	0.1 0.0	0.4 0.1	0.1 0.0	0.0 0.0	1.0 0.4	100.4 0.8	0.1 0.1	0.1 0.1
AL-bearing beds in AL-sequence (n = 5) (Standard Deviation)	67.1 2.8	16.7 0.9	2.1 0.5	2.5 0.3	2.5 0.5	3.1 0.4	4.4 0.9	0.1 0.0	0.5 0.1	0.1 0.0	0.0 0.0	1.4 0.3	100.6 0.3	0.0 0.1	0.2 0.1
High Grade Pelitic Schists (Shaw, 1956) (Standard Deviation)	63.5 8.9	17.4 5.1	1.2 0.9	2.3 1.8	2.0 1.1	3.4 1.3	2.0 1.7		0.8 0.7			2.4 1.5		0.2 0.2	

Table 3.2.4: Selected minor element averages of aluminosilicate-free and aluminosilicate-bearing metasedimentary rocks in Roberto's aluminosilicate-bearing sequence.

ANALYTE	Au	As	B	Sb	Ag	Cu	Zn	Pb	Y	Zr	Ba	Li	Rb	Sr
DETECTION (Highest)	5	3	10	5	2	0.5	0.5	2	0.5	0.5	3	1	2	2
UNITS	ppb	ppm	ppm	ppm	ppm	ppm	ppm	ppm	ppm	ppm	ppm	ppm	ppm	ppm
AL-free beds in AL-sequence (n = 4) (Standard Deviation)	22 2.9	21 11	78 22	4 5	<2 5	27 16	67 17	15 6	5 1	110 18	479 179	51 7		1154 768
AL-bearing beds in AL-sequence (n = 5) (Standard Deviation)	16 17	32 15	104 24	5 8	<2 8	37 12	67 17	24 19	5 1	109 26	719 194	70 31	104 23	501 231

3.2.1.4 Banded Cherty Iron Formations

Banded cherty iron formations are locally present in the northern part of the Roberto deposit (Figures 3.2.1, 3.2.7). These iron formations are composed of alternating quartz-rich and pyrite-rich layers (Figure 3.2.12), and are locally associated with mudstones. The pyrite-rich layers generally contain about 25% pyrite, with traces of arsenopyrite, pyrrhotite, and chalcopyrite. The iron formations locally host gold mineralization (generally < 2 g/t Au) and are the principal constituent of the Puncho Zone. The location of the Puncho Zone is indicated on Figure 3.2.7.

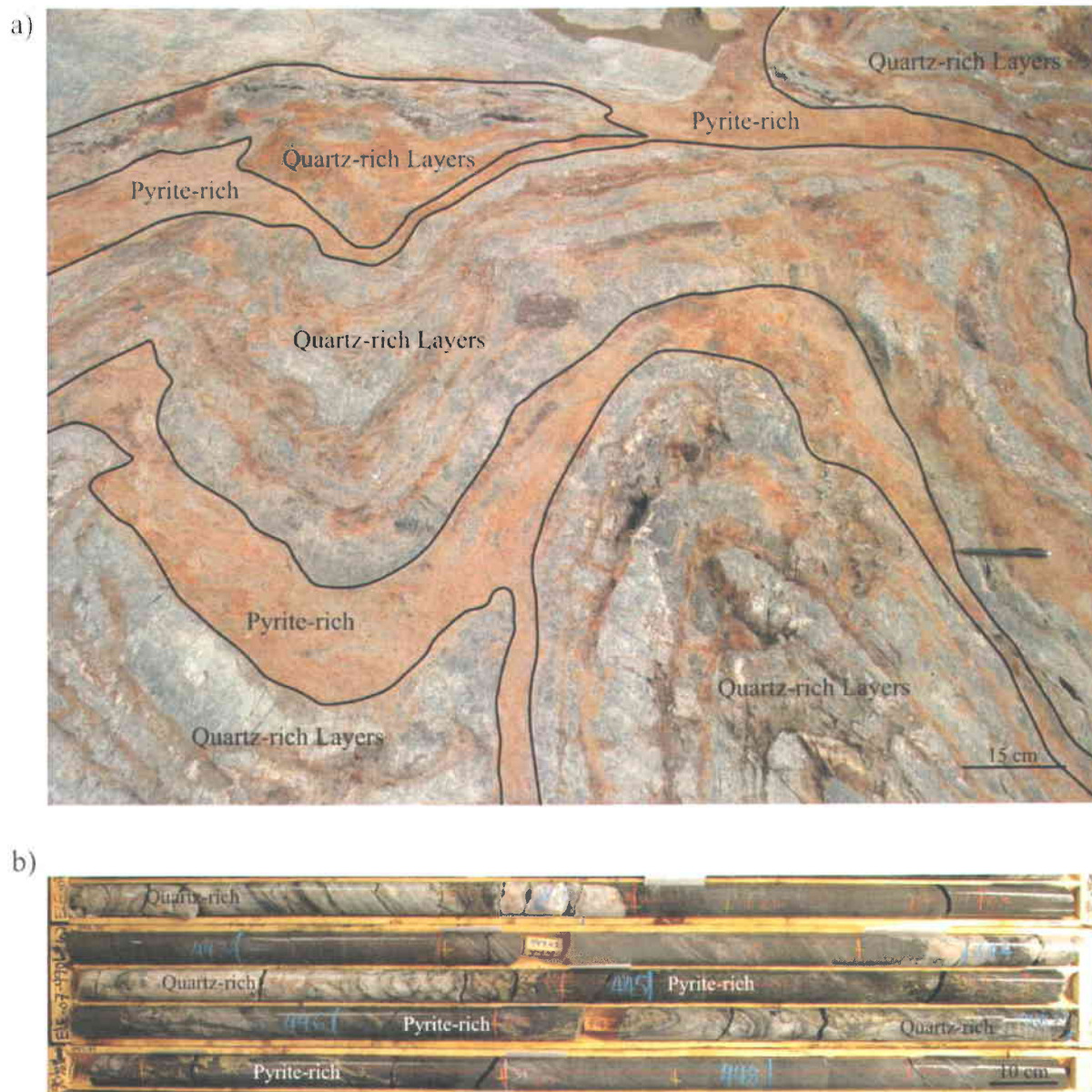


Figure 3.2.12: Photographs showing: a) quartz-rich and pyrite-rich layers in banded iron formation (BIF) located in the northern part of the deposit. b) quartz-rich and pyrite-rich layers in BIF in drillcore. Yellow mineral is pyrite. Photo courtesy of Opinaca Mines Ltd.

3.2.1.5 Biotite Schists

Several lenses of biotite schist that locally host gold mineralization were intersected in drillcore near the principal auriferous zones and in the northern part of the deposit (Figures 3.2.1, 3.2.7). They are interpreted to either represent highly-strained lithological units (e.g.

metamorphosed mudstone), and/or altered units (potassic alteration). The schists typically fine-grained, lepidoblastic, and contain more than 40% biotite and 40% quartz. The schists locally contain 20% quartz-actinolite-rich bands.

3.2.1.6 *Paragneiss*

Paragneiss units are widely distributed around the Roberto deposit and locally host gold mineralization. Paragneiss units are primarily characterized by granoblastic and/or saccharoidal textures (Figures 3.2.13a and 3.2.13b), and commonly host ductily deformed cm-scale pegmatite dykes (Figure 3.2.13c). In the vicinity of the Roberto deposit, paragneiss transition into greywacke and vice-versa (even at the outcrop scale), which makes it difficult to delineate their distribution. Although paragneiss units are interpreted to be higher grade metamorphic equivalents of surrounding metagreywacke, their mineralogy is generally similar. For example, aluminosilicate-bearing rocks gradually develops a granoblastic texture as metamorphic grade increases (Figure 3.2.13d), but preserves the same mineralogy. The proportions of minerals vary, however, and paragneiss units generally contain higher percentages of biotite.

At deposit-scale, regions that contain paragneiss and greywacke were delineated from regions that only contain greywacke (Figure 3.2.1). Regions containing paragneiss and greywacke also contain transitional units characterized by intermediate grain sizes. Spatial association between swarms of pegmatite dykes and paragneiss units locally occurs, especially on drill sections. Such spatial relationships suggest that some of the paragneiss were generated in association with pegmatite dyke emplacement.

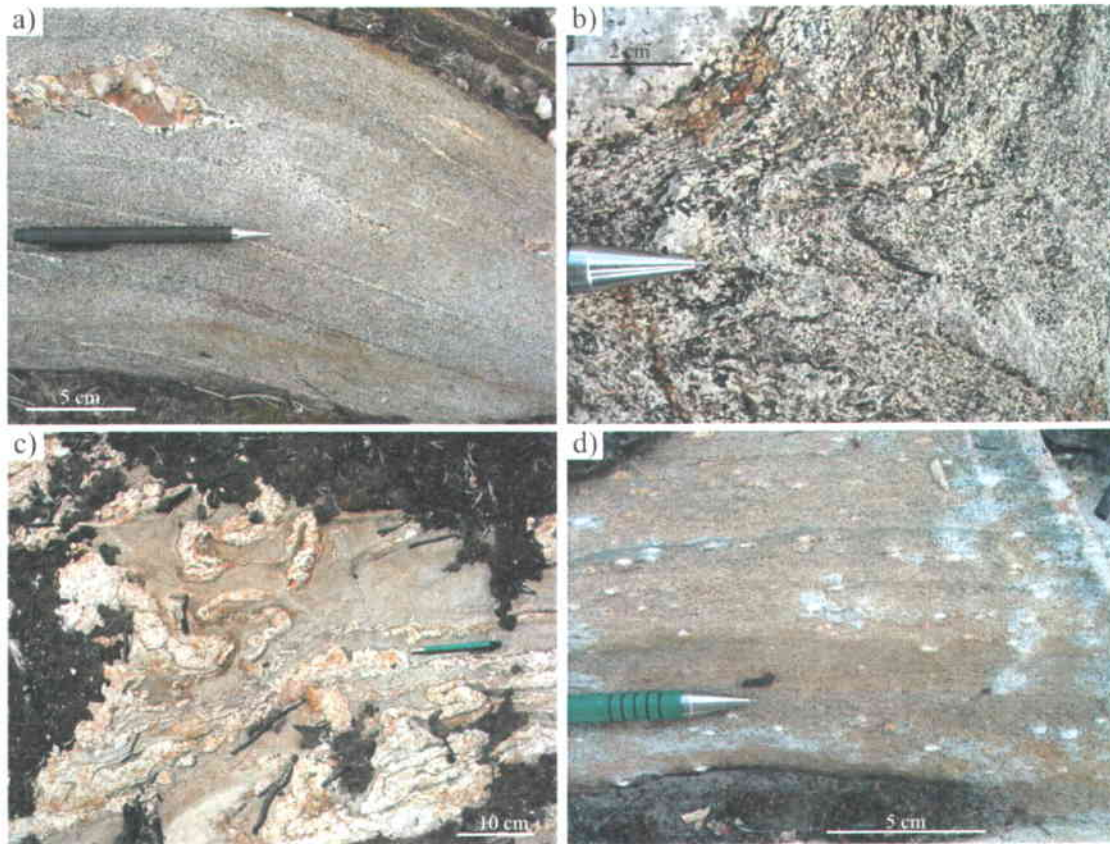


Figure 3.2.13: Photographs of paragneiss showing: a) granoblastic texture. b) coarse granoblastic texture. c) ductily deformed pegmatite dykes. d) aluminosilicate-bearing paragneiss (white mineral is sillimanite).

In order to determine the age relationships between lower-grade and higher-grade rocks, two paragneiss samples were subjected to geochronological analysis to obtain their maximum ages of deposition (Figure 3.2.14). The results indicate that maximum ages of paragneiss units are within limits of the “younger” greywacke sequence at ca. 2680 Ma (Dubé pers. comm. 2010) (see Chapter 4 *Geochronology*). Paragneiss and lower-grade metagreywacke sequences therefore cannot be distinguished in terms of their maximum ages of deposition. Similar paragneiss and metagreywacke ages suggest that high-grade rocks do not belong to a different sedimentary sequence tectonically juxtaposed to lower-grade rocks. As presented in section 2.5.2 *Lithogeochemistry of the Éléonore Property*, paragneiss and metagreywacke also have similar bulk compositions.

3.2.2 Intrusive Phases

3.2.2.1 *Pegmatite Dykes*

The deposit and surrounding rocks are cut by an important swarm of pegmatite dykes. The thickness of individual dykes ranges from few centimeters to few meters, and their length commonly surpasses a hundred meters. The swarms are widely distributed over the deposit area, but are generally not present within aluminosilicate-bearing rocks (Figures 3.2.14 and 3.2.15). In drillcore, pegmatite dykes do cut through the diorite intrusion located in the northern part of the deposit area.

The mineralogy of pegmatite dykes is typically composed of quartz, perthitic microcline, plagioclase, and tourmaline, with traces of garnet, muscovite, sulphides (mainly arsenopyrite and pyrrhotite), and rare apatite and spodumene (Figures 3.2.16a and 3.2.16b). Aluminosilicate (fibrolite) occurs at one locality, within a pegmatite hosted by aluminosilicate-bearing rocks (Figures 3.2.16c and 3.2.16d). Crystal sizes vary significantly from dyke to dyke, from fine-grained layered aplite (Figure 3.2.16e) to very coarse-grained pegmatite (Figure 3.2.16f).

The presence of muscovite, garnet, and tourmaline are indicative of the peraluminous nature that characterizes the lithium-cesium-tantalum (LCT) pegmatite family (London, 2008). The pegmatite dykes locally host gold mineralization, and are sometimes surrounded by tourmaline-arsenopyrite-rich selvages in the country rocks. The mineralized characteristics of pegmatite dykes are described in details in section 3.5 (*Alteration and mineralization*).

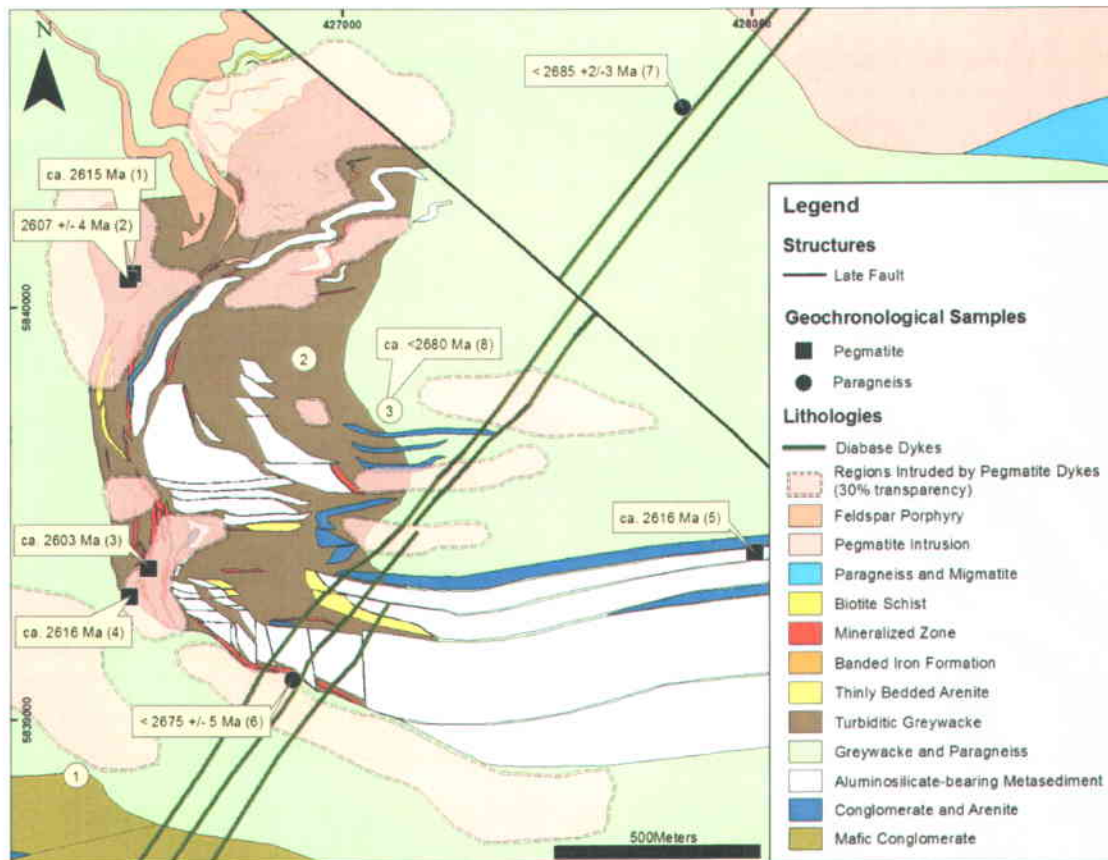


Figure 3.2.14: Lithological map of the Roberto deposit showing the distribution of pegmatite dyke swarms and diabase dykes. Regions identified as “pegmatite dyke swarms” correspond to regions within which high percentages (10-30%) of discrete pegmatite dykes are present. Location and maximum ages of pegmatite and paragneiss geochronological samples are indicated: pegmatites: (1) Geochron-ELE-08-19, (2) Geochron-ELE-08-20, (3) Geochron-ELE-07-15, (4) Geochron-ELE-07-16, (5) Geochron-ELE-07-17; paragneiss: Geochron-ELE-06-11 (6), Geochron-ELE-05-07 (7). All geochronological data from Dubé et al. pers. comm., (2010, 2009). Circled numbers 1, 2, and 3 indicate location of ultramafic sills, feldspar porphyry dyke, and a dated feldspar porphyry dyke (Geochron-ELE-06-12 (8)), respectively. Coordinates are in UTM Nad83.

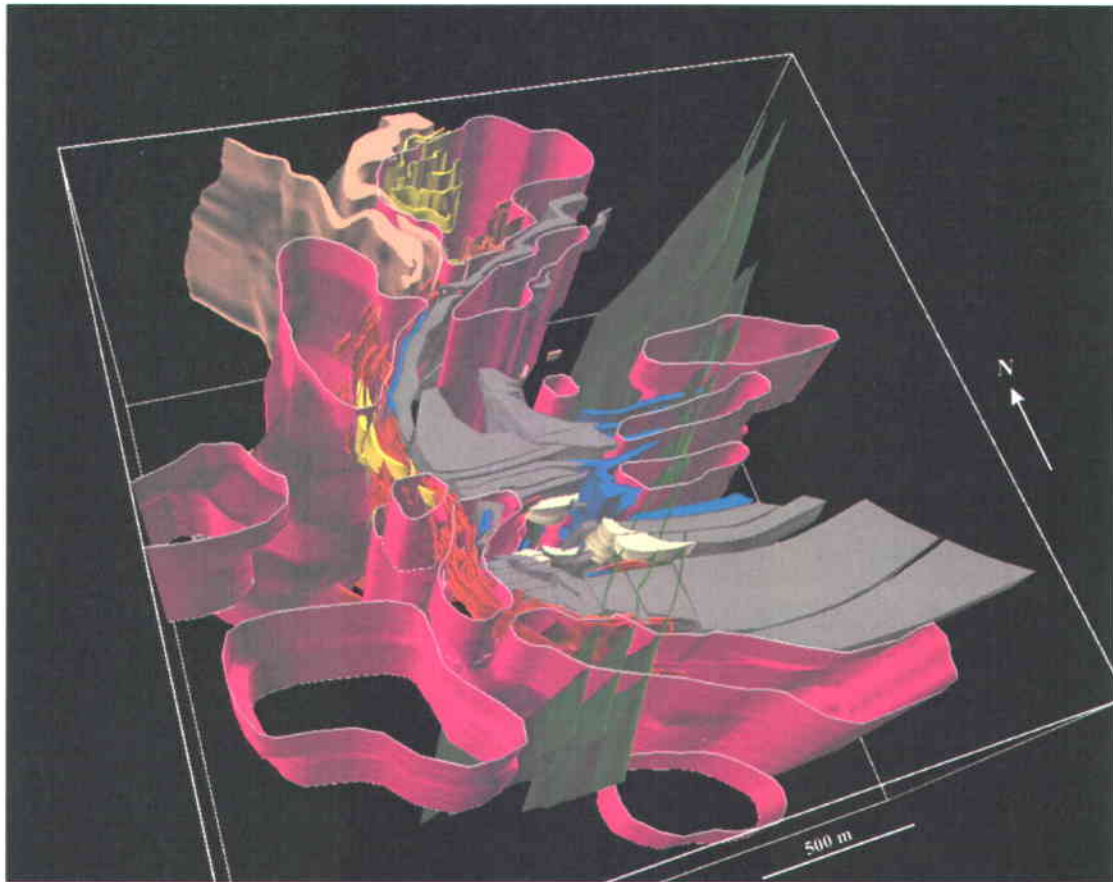


Figure 3.2.15: Gocad snapshot showing distribution of pegmatite dyke swarms (purple) and diabase dykes (green) in 3D. Regions identified as “pegmatite dyke swarms” correspond to regions within which high percentages (10-30%) of discrete pegmatite dykes are present. Other lithological units are color-coded following the legend of Figure 3.2.1 (red: auriferous zones, grey: aluminosilicate-bearing metasedimentary rock, blue: conglomerate and arenite, yellow: biotite schist, orange: banded iron formation, pale yellow: thinly bedded arenite, pink: feldspar porphyry). Turbiditic greywacke and paragneiss are the dominant rock types present in empty regions of the 3D space. Refer to Figure 3.1.8 to see how surface envelopes showing the distribution of pegmatite dyke swarms were constructed.

The origin of the pegmatite dyke swarm present in the vicinity of the Roberto deposit is not known. It is believed, however, that the pegmatites have an allogenic origin, since their host rocks lack textural evidence of partial melting. The source pluton from which such a swarm could originate has however not been identified. London (2008) stated that pegmatite dykes can migrate kilometers from their source pluton if an effective flux (e.g. Boron, Phosphorous, Fluorine, and H₂O) is present in the pegmatite-forming melt, and/or if an enhanced thermal aureole associated with a large pluton caused the host rocks to reach temperatures above the normal geothermal gradient. In this instance, since

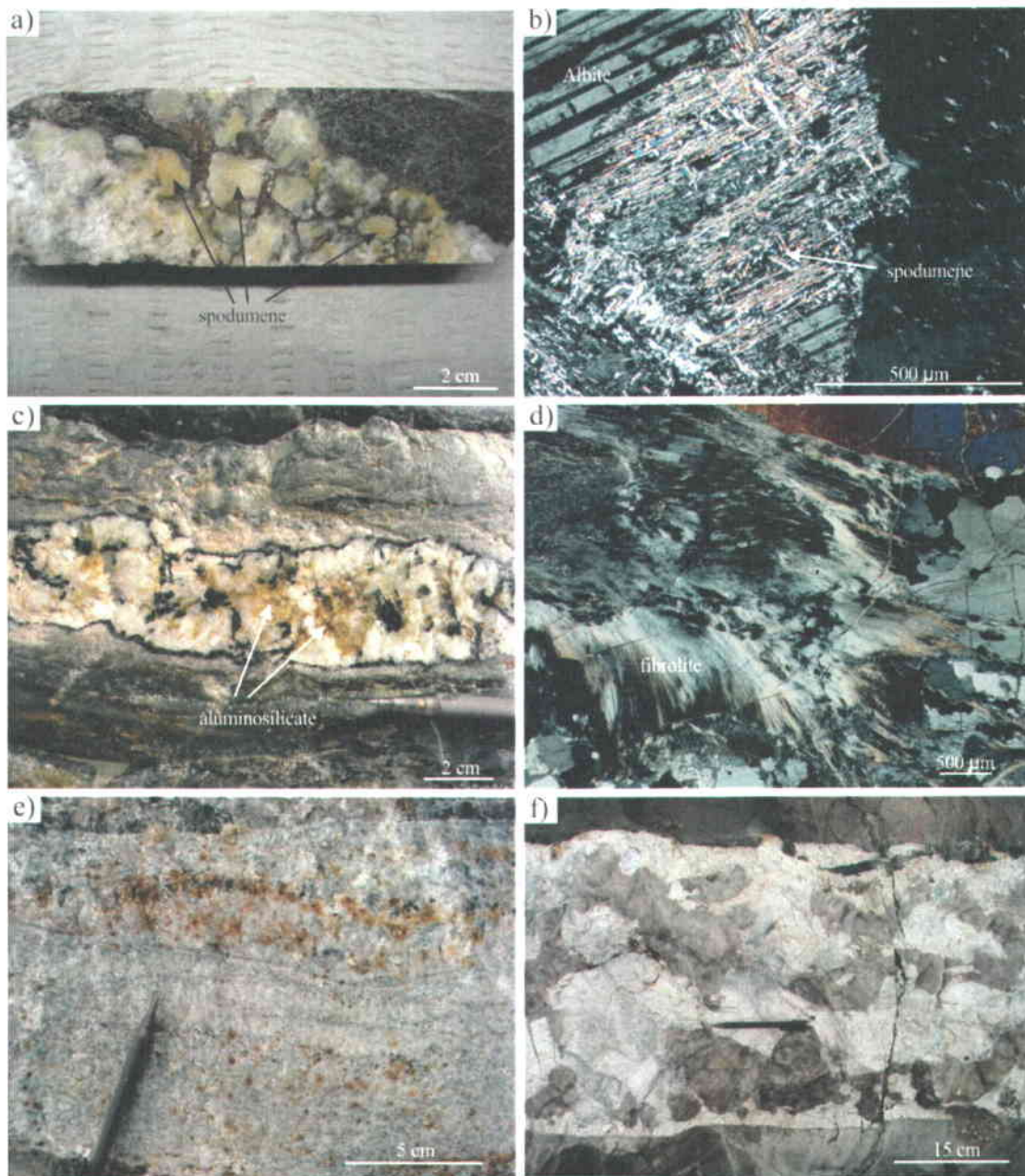


Figure 3.2.16: Photographs of pegmatites showing: a) spodumene (Li-pyroxene)-bearing pegmatite in drillcore of hole ELE-07-494W01. Pinkish brown mineral is pyrrhotite. b) photomicrograph of sample shown in (a) showing spodumene replacing albite. Scale bar is 500 μm . c) aluminosilicate (fibrolite)-bearing pegmatite in paragneiss located on trench DEC-08-06. d) photomicrograph of sample shown in (c) showing texture of fibrolite crystal. Scale bar is 500 μm . e) layered aplitic pegmatite on trench DEC-08-10. Rusty spots are arsenopyrite crystals. f) coarse-grained pegmatite west of the Roberto Zone on the large stripped-outcrop.

tourmaline (boron-rich) is an important phase of pegmatites found near the Roberto deposit, and since the Roberto area is surrounded by high-temperature paragneissic rocks (Figure 3.2.14, see section 3.4 *Metamorphism* for temperature estimates), the pegmatite dyke swarm may

originate from an intrusion located relatively far from the deposit area. Alternatively, the pegmatites may represent distal products of the migmatized Opinaca Subprovince that do not originate from a unique source pluton. According to London (2008), a study of gradients in metamorphic grade and trends of chemical fractionation within the pegmatite group could provide a way to prospect for the source pluton. Such a study was however not undertaken in the course of this project.

A total of three pegmatite dykes and two aplite dykes were dated by U/Pb geochronology (see Chapter 4 *Geochronology*). The results show that pegmatitic magmatism was active over a period of ~13 Ma in the vicinity of the Roberto deposit (ca. 2616 Ma to ca. 2603 Ma) (Figure 3.2.14). Crosscutting relationships and relative chronology of various geological features related to individual dated pegmatite dykes will be treated in upcoming sections.

3.2.2.2 *Feldspar Porphyry*

A small feldspar porphyry intrusion (~50,000 m²) is located in the northern part of the deposit (Figures 3.2.14 and 3.2.15). The intrusion is principally composed of two lenticular bodies discordant to stratigraphic layering (Figures 3.2.14 and 3.2.15). The intrusive bodies are typically characterized by the presence of xenoliths of various origins, including sedimentary and intermediate to mafic rock fragments. The mineralogy of such intrusions is dominated by quartz and porphyritic microcline with biotite and pyrite. Smaller feldspar porphyry dykes of similar mineralogy (few meters in thickness) and which contain xenoliths have also been documented, specifically in the structural hanging wall of the deposit (Figure 3.2.14: circled numbers 2, and Figure 3.2.15). Such feldspar porphyry dykes locally host anomalous gold values. The feldspar porphyries are affected by the S₂ foliation indicating that they were emplaced before or early during D₂.

Geochronology was used to investigate whether feldspar porphyries near Roberto bear genetic relationships with the Ell Lake intrusion (2705 Ma) and Opinaca Pluton (2707 Ma). The age obtained for a feldspar porphyry dyke located in the structural hanging wall of the deposit is < 2680 Ma (Dubé pers. comm. 2009), which suggests that no genetic relationship exists between the dated phases of the Ell Lake intrusion and the dated feldspar porphyry dyke.

3.2.2.3 Diabase Dykes and Ultramafic Sills

A set of NE-trending diabase dykes crosscuts the deposit (Figures 3.2.14 and 3.2.15). These dykes are interpreted to belong to the Senneterre dyke swarm, which are estimated to have been emplaced at ca. 2216 \pm 8/-4 Ma (Buchan, Mortensen and Card, 1993; Bandyayera and Fliszár, 2007), and represent one of the only lithological units which have not been affected by regional deformation (Bandyayera and Fliszár, 2007). Mafic to ultramafic volcanic rocks, similar to those observed elsewhere on the Éléonore property, are present in the south-western region of the deposit area (Figure 3.2.14: circled number 1). Unlike the diabase dykes, these rocks have recorded significant strain related to regional deformation.

3.3 Structural Geology of the Roberto Deposit

This section presents the structural geology of the Roberto deposit. Structural analysis was performed through detailed mapping of natural and stripped outcrops, drillcore analysis, and constructions of 3D Gocad representations that integrate surface and subsurface data. Details of the methods used are presented in *Annex 1*.

3.3.1 Planar and Linear Fabrics

The principal tectonic fabric in the Roberto deposit area is interpreted to be S_2 , except for a NE-trending corridor across the deposit where S_3 locally completely overprinted S_2 (Figure 3.3.1). In that corridor, S_3 formed through rotation of metamorphic minerals that previously defined S_2 (e.g. biotite in Figures 3.3.2a and 3.3.2b; and aluminosilicates). Based on petrographic work, no new metamorphic mineral developed during D_3 . Since S_2 and S_3 are defined by the same metamorphic minerals (mainly biotite and aluminosilicate porphyroblasts), distinction between the two fabrics in the absence of folds can only be inferred based on orientation (Ravenelle et al., 2010). Overprinting relationships between S_2 and S_3 are well illustrated within aluminosilicate-bearing rocks, where on a given outcrop aluminosilicate porphyroblasts affected by S_2 are crenulated by S_3 in one location, but are reoriented parallel to the axial plane of F_3 folds in another. In certain samples within which S_3 overprinted S_2 , S_2 relicts were preserved in microcline poikiloblasts (e.g. Figures 3.3.2c and 3.3.2d). No S_2 relicts were however preserved in aluminosilicate porphyroblasts. A steeply-plunging well-developed

stretching and/or mineral lineation is commonly developed on S_2 foliation planes (Figure 3.3.2e) or S_3 foliation planes in regions where S_3 overprinted S_2 (Figure 3.3.2f).

The distribution of S_2 and S_3 fabrics in the deposit area is represented on Figure 3.3.1. Structural measurements extracted from drillcore data using the Reflex ACT© core orientating device (see *Annex 1*) are also displayed to complement surface data. In drillcore, S_3 is only recognizable where it occurs with S_2 . Where only one fabric is observed, it is interpreted to correspond to S_2 . Significant changes in the attitudes of S_2 are interpreted to result from post- D_2 folding as well as slip along bedding and/or fault surfaces which occurred during late D_2 or early D_3 (see sections 3.3.4 *Faults and Slip Surfaces* and 3.3.6.1 *Global Geometry* for details). The attitudes of the S_3 fabric vary from NNE to ENE (Figure 3.3.1).

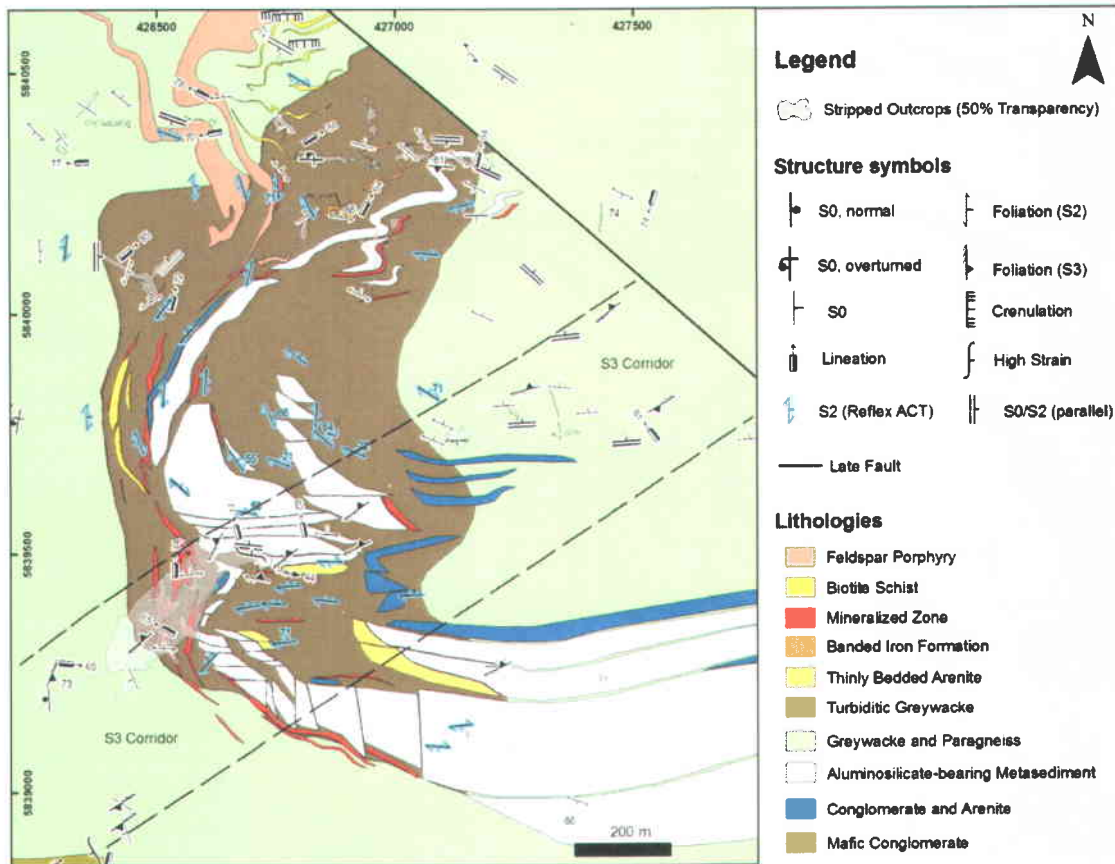


Figure 3.3.1: Geological map of the Roberto deposit area showing the distribution of structural fabrics. Note the presence of a corridor (bounded by dashed lines) where S_3 is particularly well developed. Reflex ACT data (blue symbols) are displayed to complement surface data and represent selected measurements present within 60 meters depth from surface. Dip label of planar structural measurements with dip value greater than 75 degrees are not displayed to simplify the map. The distribution of lithological units is primarily based on an interpretation of the subsurface. Many discontinuities observed in the map pattern results from assumptions utilized to construct the 3D model (see Annex 1). The nature of such discontinuities is discussed in section 3.3.6.2 *Nature of Discontinuities observed in 3D*. Coordinates are in UTM Nad83.

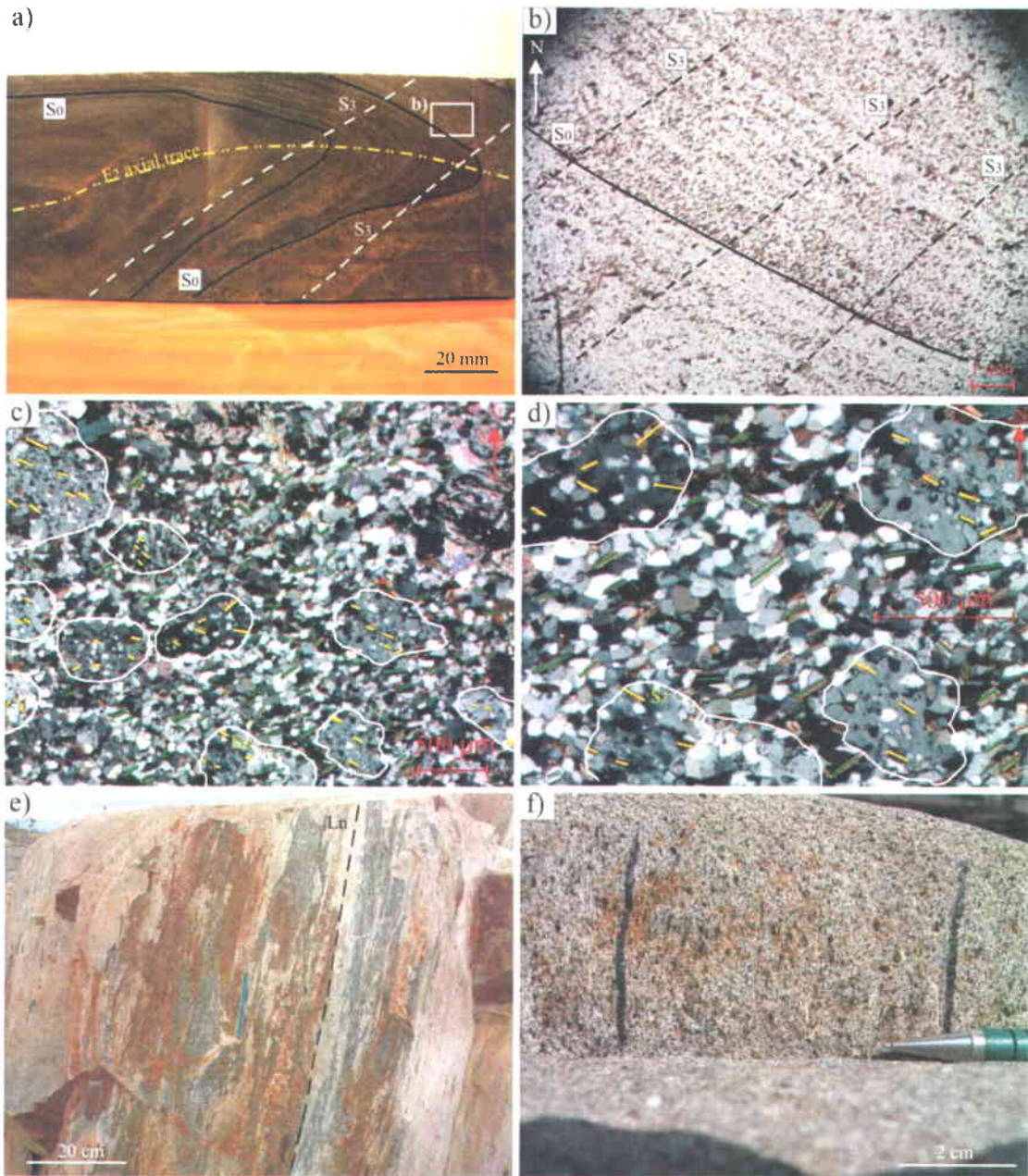


Figure 3.3.2: Field photographs and photomicrographs showing: a) sawed sample from the eastern part of the large stripped outcrop showing F_2 fold devoid of axial planar foliation and transected by S_3 . b) photomicrograph (natural light) of a region of sample shown in (a) (white square) showing a planar fabric attributed to S_3 . c) photomicrograph from a sample in the eastern part of the large stripped outcrop (cross-polarized light) showing biotite crystals oriented by S_3 (green lines) and relict S_2 fabric (yellow lines) in microcline poikiloblasts (white contours) where biotite crystals remained oriented parallel to S_2 . Even though rotation of poikiloblasts could result in a similar scenario, the fact that the relict fabric is similarly oriented in all poikiloblasts suggests that the poikiloblasts did not rotate significantly. d) photomicrograph showing close-up of (c). e) stretching lineation developed on S_2 planes within the East-Roberto Zone. f) mineral lineation defined by biotite crystals in S_3 on paragneiss outcrop located west of the large stripped outcrop.

3.3.2 Folds and Fold Interference at Surface

No clear macroscopic nor microscopic evidence of D_1 was found on outcrops near the Roberto deposit. However, the repetition of units observed on the map pattern could suggest that D_1 affected the rock units and produced tight large-scale folds (1st generation axial trace on Figure 3.3.3). This scenario and alternate explanations for the repetition of units are discussed in greater details in section 3.3.6 *Geometrical and Structural Characteristics of the Deposit*.

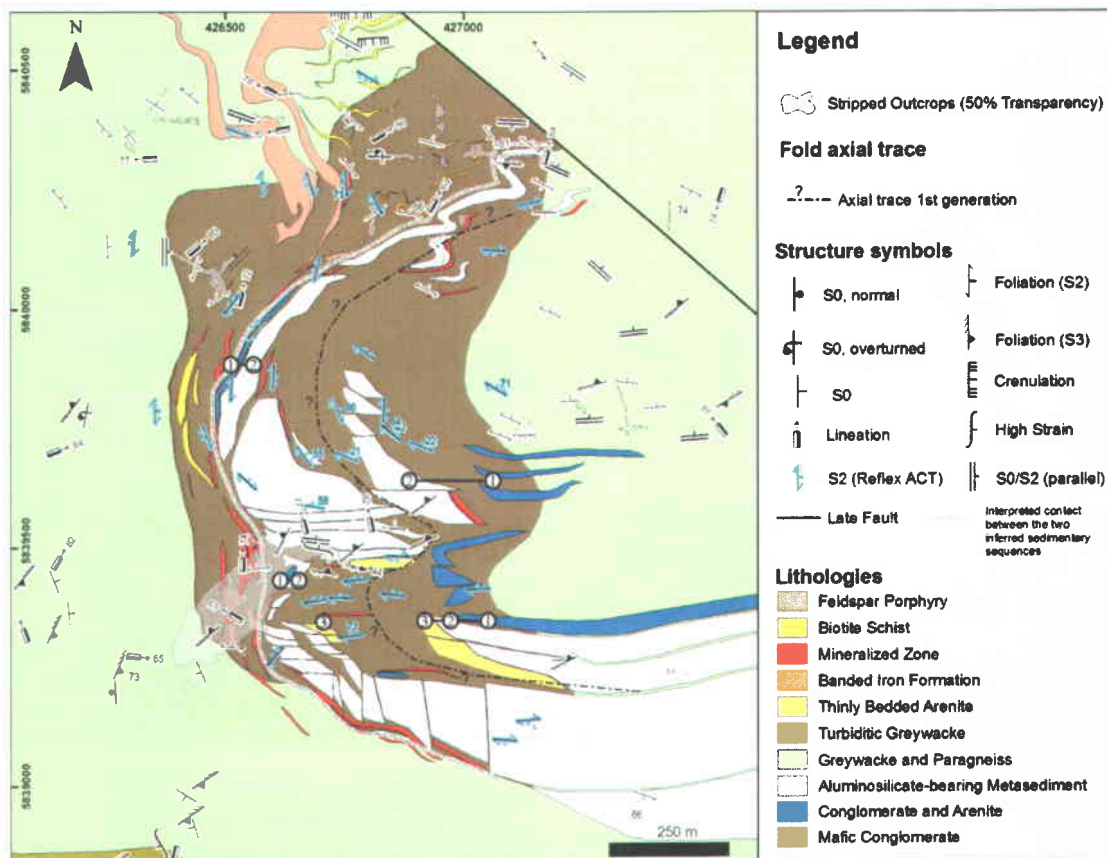


Figure 3.3.3: Map showing the distribution of structural measurements in the vicinity of the Roberto deposit. The axial trace of a large scale F_1 fold can be interpreted from the repetition of lithological units (conglomerate-aluminous rocks-arenite) identified by circled numbers (1-2-3, respectively). Dip label of planar structural measurements with dip value greater than 75 degrees are not displayed to simplify the map. Map modified from Ravenelle et al, 2010). Coordinates are in UTM Nad83.

F_2 folds are documented on outcrops where they are characterized by their tight to isoclinal style of folding and their axial planar S_2 fabric (Figure 3.3.4a). As previously mentioned, F_2 folds are however not always associated with an axial planar cleavage (e.g. Figures 3.3.2a and 3.3.2b). Importantly, F_2 sheath folds are locally documented on the large stripped outcrop,

within (Figure 3.3.4b) (Ravenelle et al., 2010) and at proximity to high strain zones (Figure 3.3.4c). Where observed, the cone axis of such sheath folds is sub-vertical (Figure 3.3.5) (Ravenelle et al., 2010). Regular F_2 folds are commonly steeply plunging in the Roberto area, but in one area of the stripped outcrop, they are moderately plunging to the east. F_3 folds are commonly observed on outcrops and can be recognized by their more open style of folding and by the fact that they fold the S_2 fabric (Figure 3.3.4d).

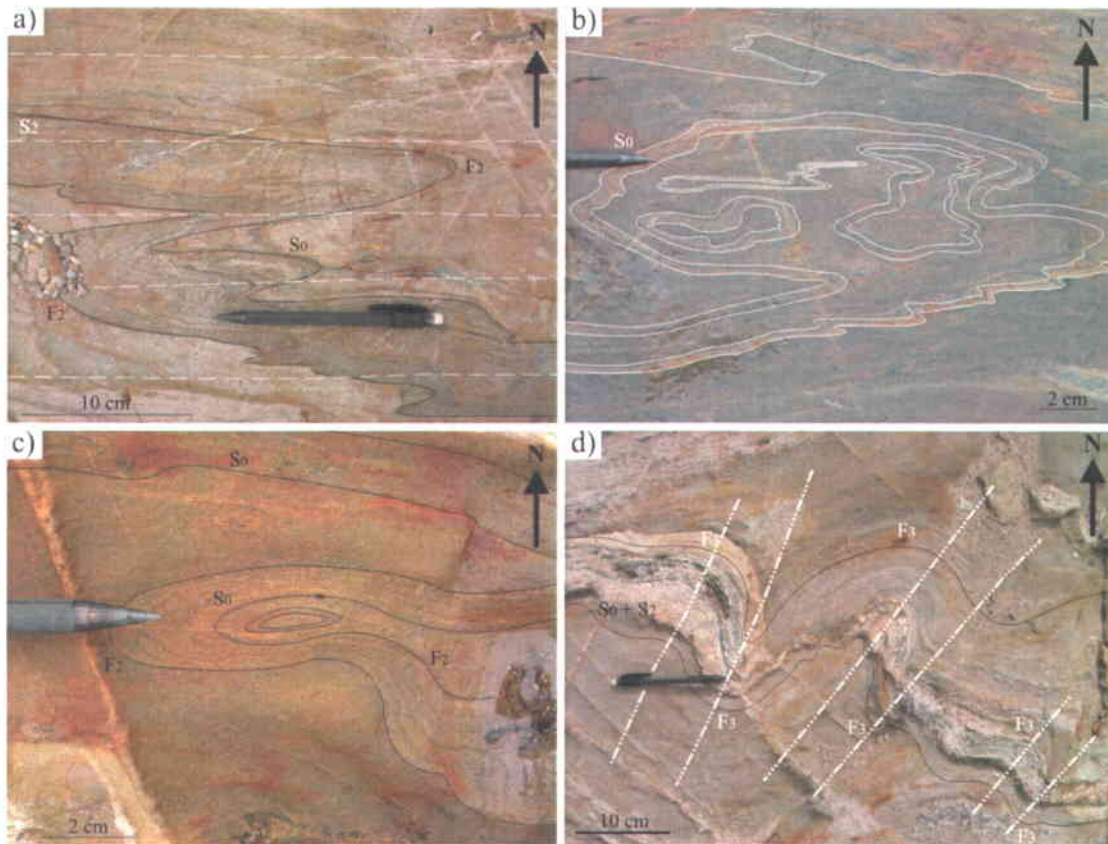


Figure 3.3.4: Photographs showing: a) isoclinal F_2 Z-fold with axial planar foliation (S_2). b) F_2 sheath folds in high strain zone. c) F_2 sheath fold located outside high strain zone (50 meters from it). d) F_3 folds in S_0/S_2 . A metasomatic band is also folded.

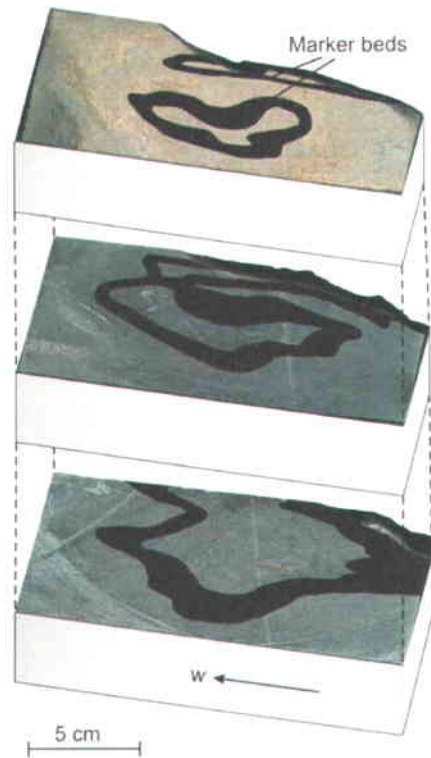


Figure 3.3.5: Geometry of sheath folds interpreted from photographs of slices through a hand sample located in a high strain zone of the large stripped outcrop (same location as folds on Figure 3.3.4b). The cone axis of the sheath folds is sub-vertical. Figure from Ravenelle et al. (2010).

Although evidence of structures associated with D_1 is cryptic in the deposit area, one interference pattern representing a hybrid between a dome-and-basin and mushroom pattern could indicate that F_1 folds indeed affected rock units of the deposit area (Figure 3.3.6a). However, since this pattern has only been documented in one location and since it is located at proximity to well-developed sheath folds, its true significance is debatable. If such pattern truly results from F_1/F_2 interference, then the F_1 folds must have been shallowly-plunging and oriented at high angle to F_2 folds prior to refolding. Where mapped on outcrops of the Roberto area, F_2/F_3 interference patterns are coaxial (type 3 of (Ramsay and Huber, 1987)) (Figures 3.3.6b and 3.3.6c). A similar interference pattern is also present on stripped outcrop DEC-08-06b (Figure 3.3.7).

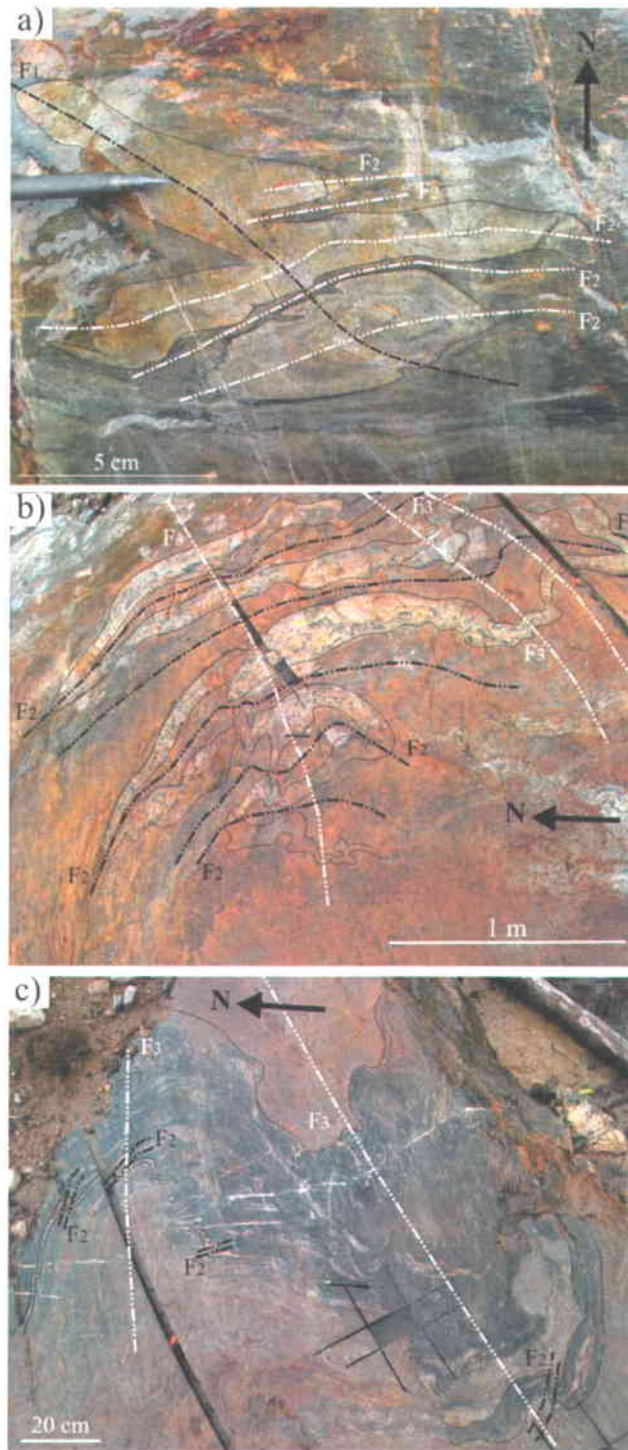


Figure 3.3.6: Photographs showing: a) $F_1(?)$ - F_2 interference pattern. The pattern is intermediate between a dome-and-basin and a mushroom interference pattern. b) and c) F_2 - F_3 coaxial fold interference patterns in mineralized material. Note the folded axial trace of F_2 folds. A similar pattern is observed in lithological units of DEC-08-06b (Figure 3.3.7).

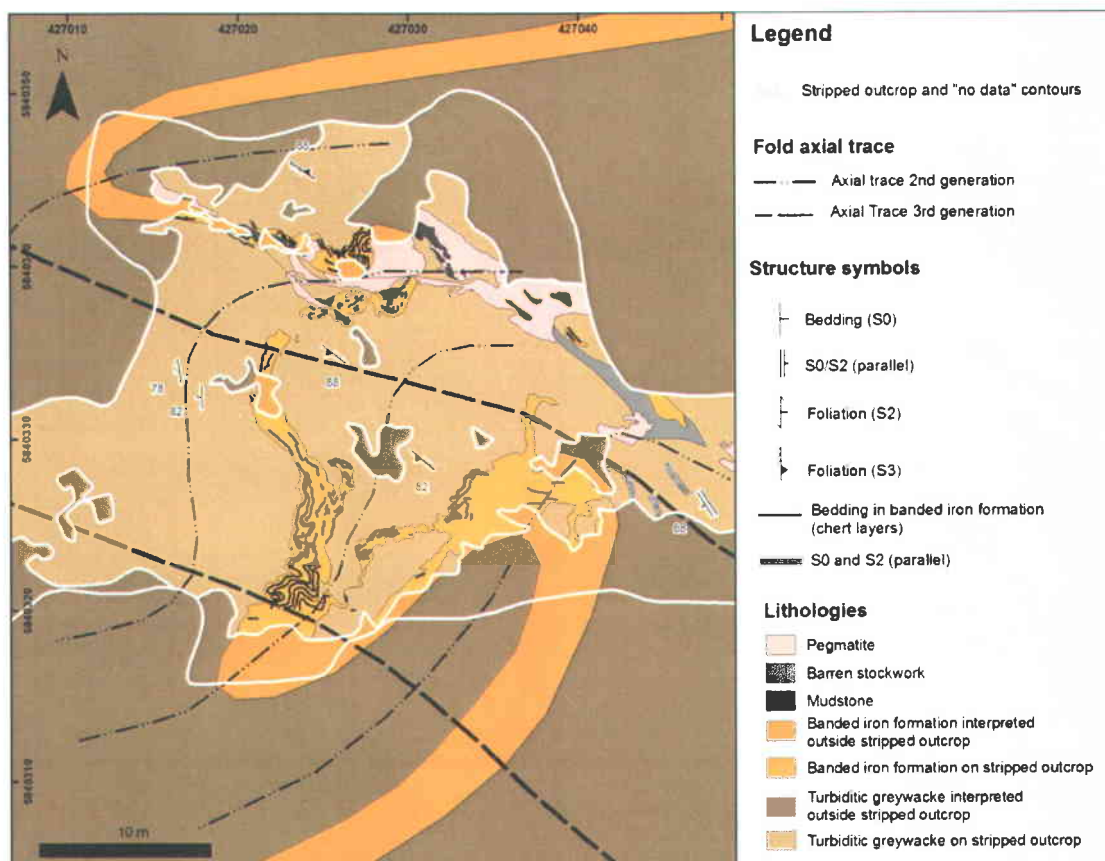


Figure 3.3.7: Geological map and interpreted structural geology of stripped outcrop DEC-08-06b showing a F_2/F_3 coaxial interference pattern. Such a fold interference pattern resembles other patterns mapped on the large stripped outcrop (Figures 3.3.6b and 3.3.6c). S_3 is oriented to the NW in this region (see text for details). Coordinates are in UTM Nad83.

3.3.3 High Strain Zones

3.3.3.1 Description of High Strain Zones

In the deposit area, high strain zones were documented on the large stripped outcrop (Figure 3.3.8, circled number 1), on stripped outcrop "DEC-08-08" (Figure 3.3.8, circled number 2), and on natural outcrops south-west (Figure 3.3.8, circled number 3) and east of the deposit (Figure 3.3.8, circled number 4). All high strain zones are steeply-dipping and are less than 1 meter-wide, except for the high strain zone located to the east of the deposit which is at least 2 meter-wide (Figure 3.3.9a). The high strain zones are characterized by significant flattening and/or constrictional strain (Figures 3.3.9a), small grain size (3.3.9b), and locally by highly strained veinlets injected parallel to the flattening plane (Figure 3.3.9c). The high strain zone

present to the southwest of the deposit affected paragneiss units and pegmatite dykes (Figures 3.3.9d and 3.3.9e).

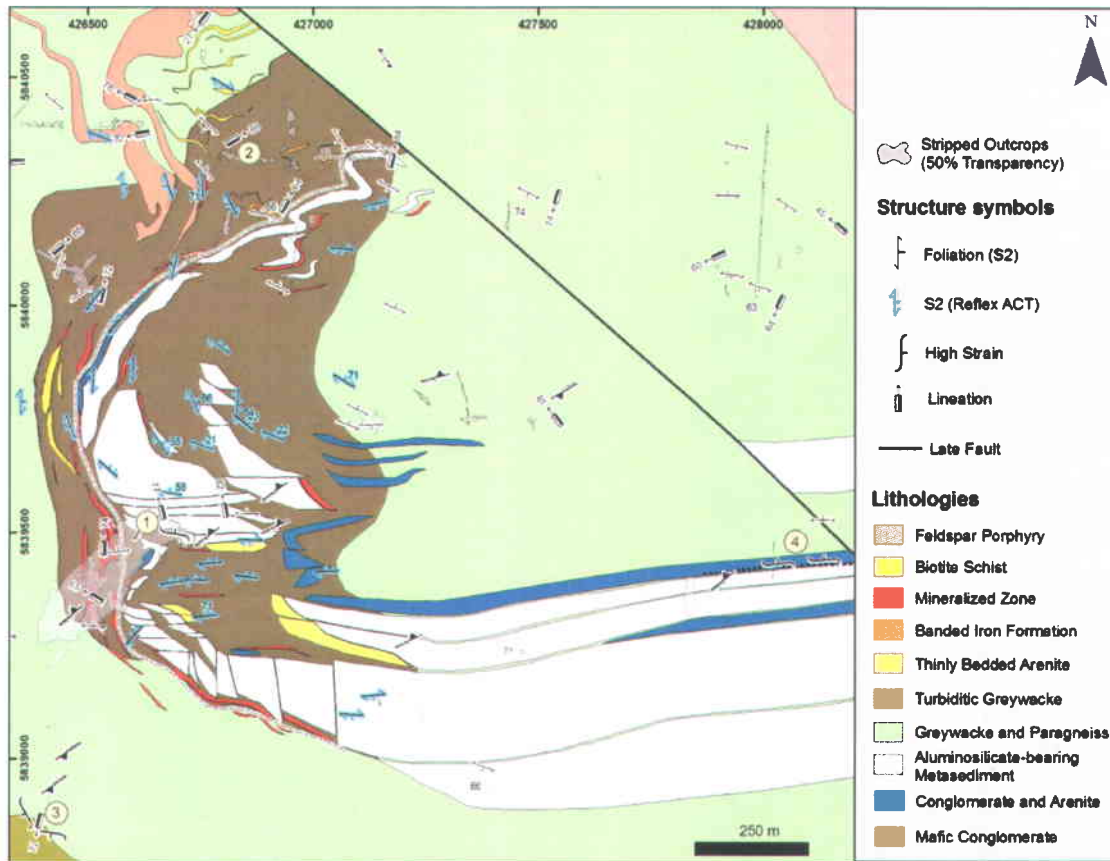


Figure 3.3.8: Geological map of the Roberto deposit showing location of documented high strain zones (circled numbers). Dip label of planar structural measurements with dip value greater than 75 degrees are not displayed to simplify the map. Coordinates are in UTM Nad83.

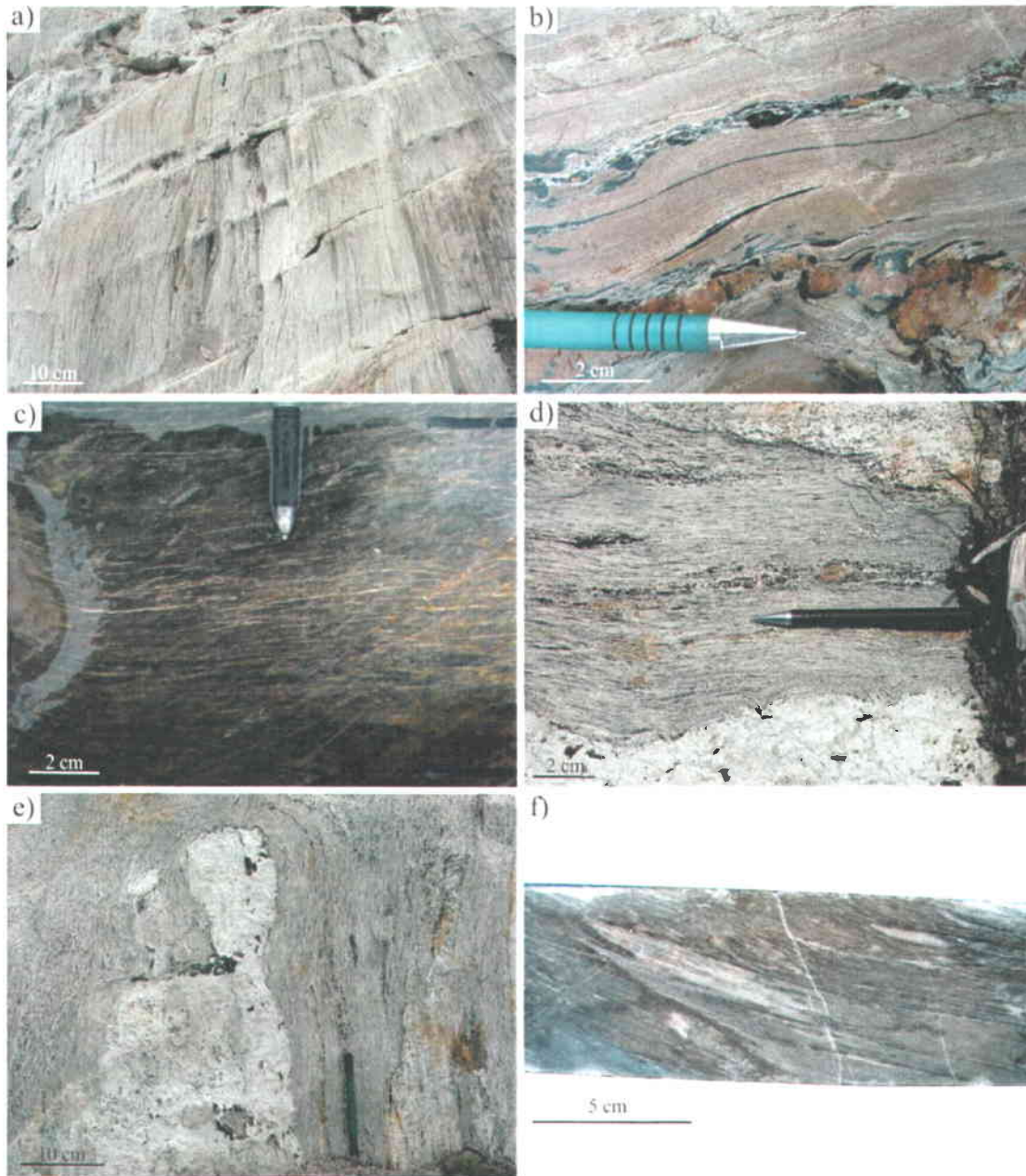


Figure 3.3.9: Photographs showing: a) highly strained conglomerate. Note the highly flattened fragments in the center and in the lower right hand corner of the photograph. b) high strain zone affecting quartz-tourmaline veins and microcline-rich rock. Note the very fine grain size of the microcline-rich rock. c) highly strained quartz-feldspar veinlets in high strain zone. d) highly strained paragneiss (plan view). e) highly strained paragneiss and pegmatite (section view). f) highly strained auriferous veins and veinlets in drillcore.

The mineralogy of the high strain zones is the same as the host rocks. They locally contain retrograde minerals but the retrogradation is not restricted to highly strained rocks (see section 3.4 *Metamorphism*). High strain zones are difficult to recognize in drillcore, unless

strain markers are present (e.g. veins (Figure 3.3.9f) or conglomerate fragments). Besides few exceptions (see section 3.3.3.2 *Interpreted Geometry and Kinematics of High Strain Zones*), individual high strain zones do not generally show evidence of movement, which is why the general term “high strain zone” is preferred over the more specific term “shear zone”. In all high strain zones, quartz grains are significantly more stretched in vertical sections compared to horizontal sections. Such apparent macroscopic differences are also portrayed in thin sections (Figure 3.3.10).

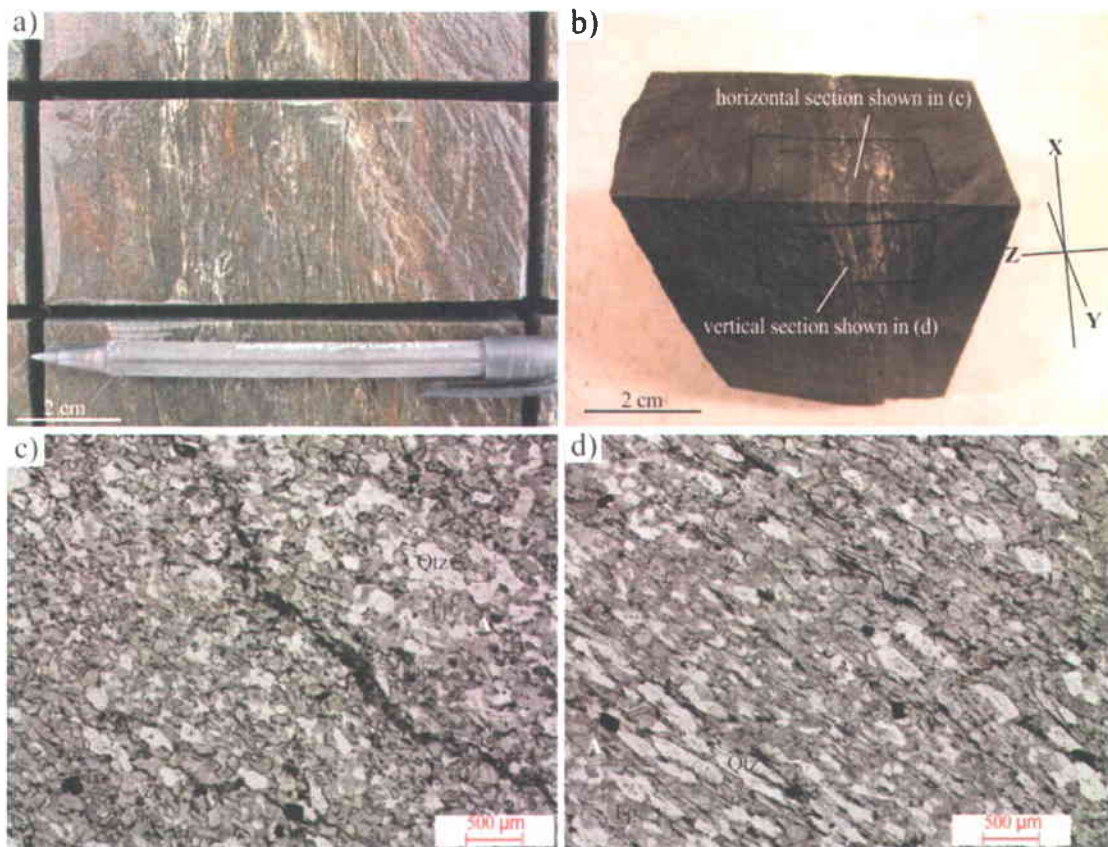


Figure 3.3.10: a) Photograph showing plan view of oriented sample in high strain zone. b) photograph of sample shown in (a) showing location of thin sections in plan (YZ plane of the strain ellipsoid) and section (XZ plane of the strain ellipsoid) view. c) and d) photomicrographs in natural light showing highly strained minerals (white = quartz, grey = sericitized feldspar, green = amphibole) in plan (c) and section view (d). Note the stretching of quartz grains in (d) compared to (c).

High strain zones locally bear spatial and geometric relationships with F_2 folds. For example, sets of high strain zones locally transposed folded material parallel to fold axial planes (e.g. Figure 3.3.11a) and/or completely transposed their limbs (e.g. Figure 3.3.11b) (Ravenelle et al., 2010).

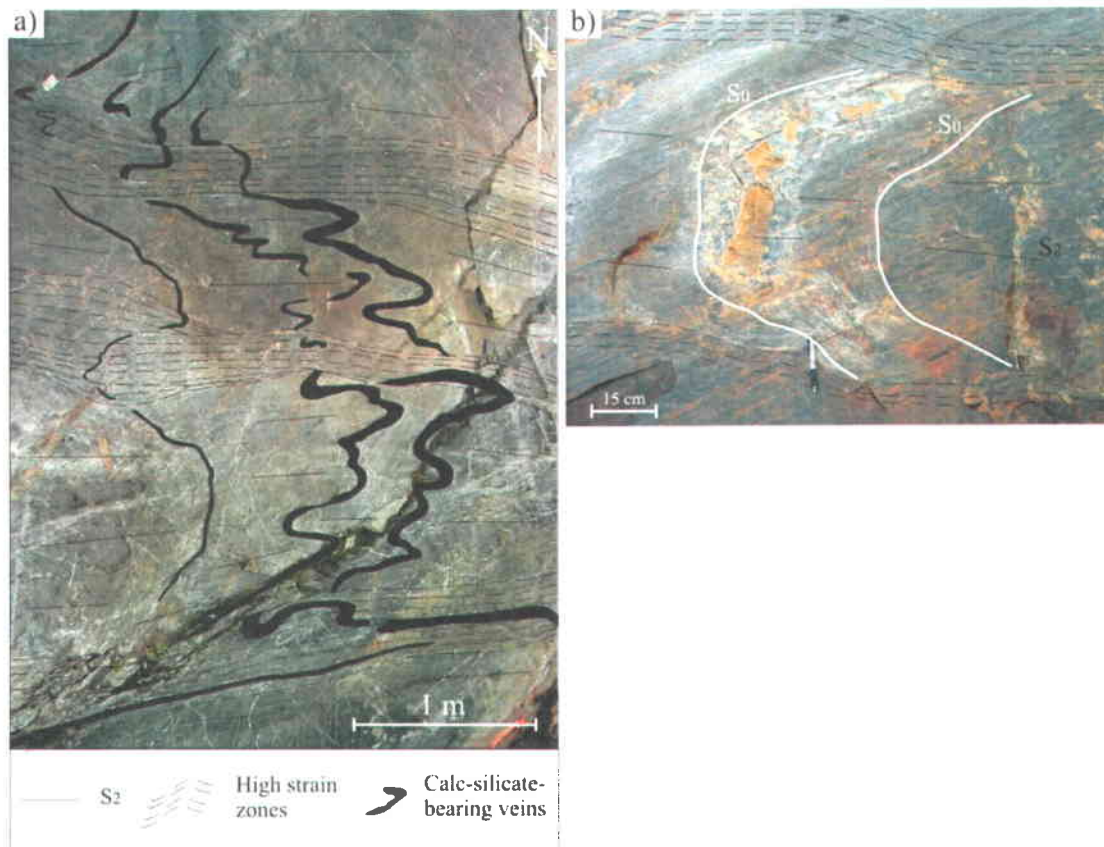


Figure 3.3.11: Interpreted photographs showing: a) F_2 fold in calc-silicate-bearing veins with cm-scale high strain zones that caused transposition parallel to the fold's axial plane. b) centimeter-scale high strain zones that completely transposed the limbs of an F_2 fold, of which only the hinge was preserved. Both photographs from Ravenelle et al. (2010).

3.3.3.2 Interpreted Geometry and kinematics of High Strain Zones

Like previously mentioned, kinematic indicators are not commonly present within high strain zones of the Roberto deposit area. Only the 2 meter-wide high strain zone located to the east of the deposit (circled number 4 of Figure 3.3.8), which affected conglomerate beds, contains a kinematic indicator, which consists in a rotated clast indicative of apparent dextral strike-slip movement (Figure 3.3.12a).

The map pattern of high strain zones present on the large stripped outcrop is illustrated on Figure 3.3.13. There, two sets composed of relatively narrow sub-vertical high strain zones (generally ~20 cm wide, except for two that are between 0.5 and 1 meter wide (Figure 3.3.13) with different orientations are present: one set is oriented sub-parallel to S_2 (E-W) and the other

is oriented to the NW (Figure 3.3.13). Both sets gradually evolve into one another. The angle between the two sets is approximately 130 degrees (Figures 3.3.13 and 3.3.14a), which is consistent with the angle usually observed between conjugate sets of shear zones (Ramsay, 1980). Conjugate sets of shear zones with one set developed along the principal regional foliation have been documented in other regions (e.g. Gapais et al., 1987). Although less strained, lenses of rocks in between shear zones still have accommodated significant amount of strain and transposition, which is specifically noticeable on vertical sections (Figure 3.3.12b).

Even though individual high strain zones of the large stripped outcrop do not contain classical kinematic indicators, the distribution of S_2 and high strain zones shown on Figure 3.3.13 resembles documented patterns of conjugate shear zones (e.g. Figure 3.3.14) and could suggest that movement did occur along those high strain zones (or shear zones in this case). The interpreted kinematics based on such a pattern is shown on Figure 3.3.14a and suggests a strike-slip system.

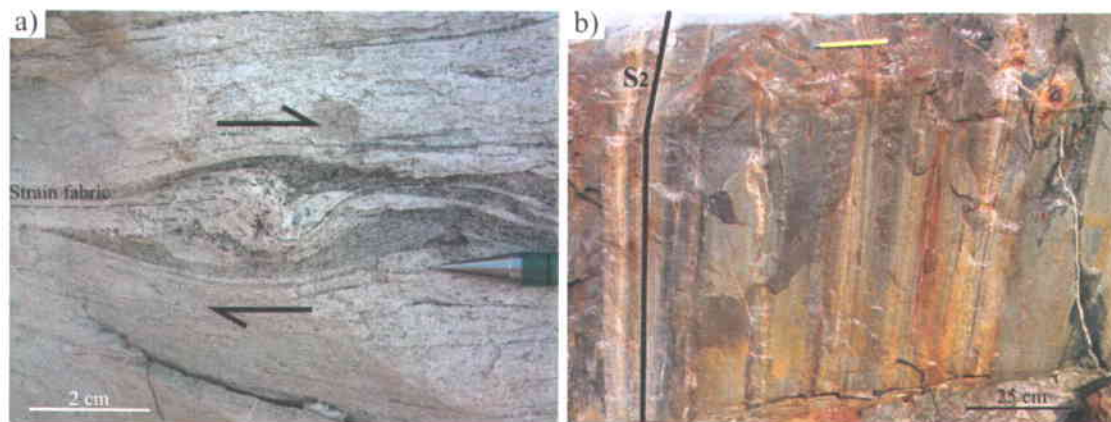


Figure 3.3.12: Photographs showing: a) rotated clast in highly strained conglomerate (located at circled number 4 on Figure 3.3.8) indicative of dextral strike-slip motion (rolling structures of (Van Den Driessche and Brun, 1987)). b) high strain parallel to S_2 in metasomatized rocks of the large stripped outcrop (vertical section looking towards the east). Photograph in (b) courtesy of Benoît Dubé.

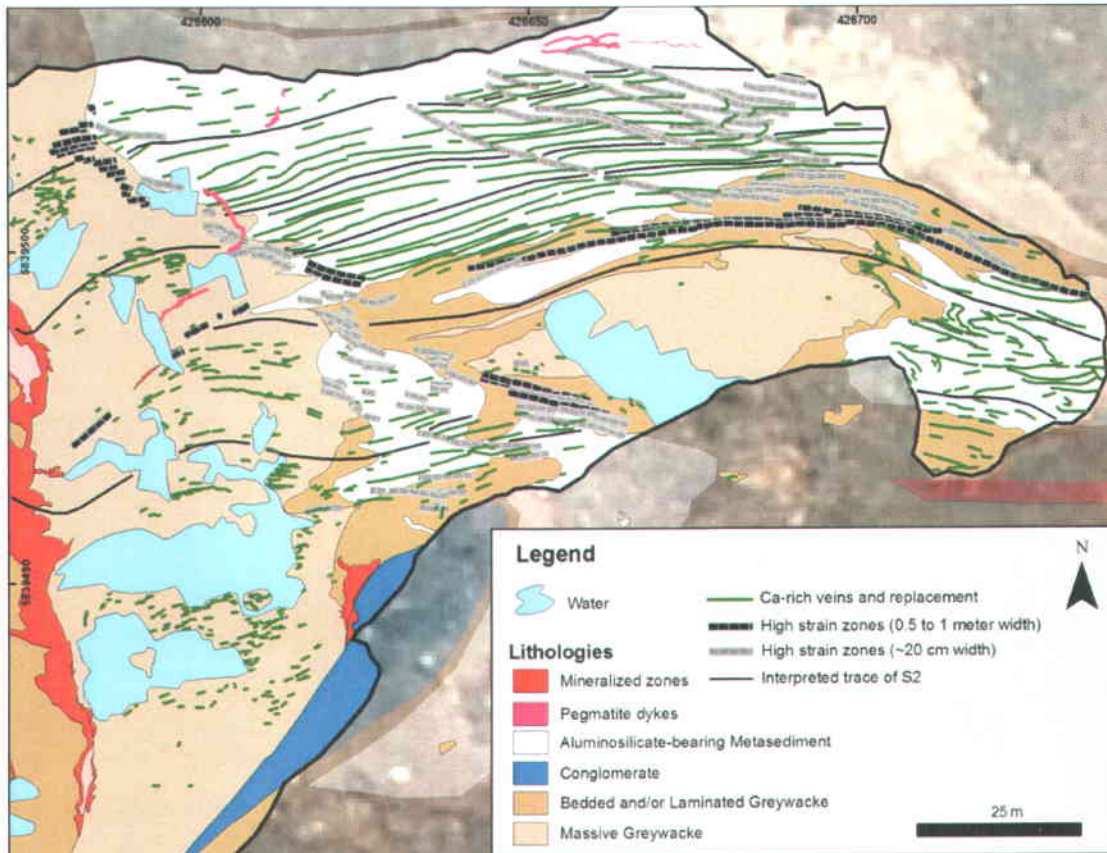


Figure 3.3.13: Geological map of the eastern portion of the large stripped outcrop showing the distribution of high strain zones. Note the presence of two sets, with one being oriented sub-parallel to S_2 , that are separated by an angle of ~ 140 degrees. The distribution of S_2 and calcium-rich veins and replacement transposed parallel to S_2 are affected by the high strain zones.

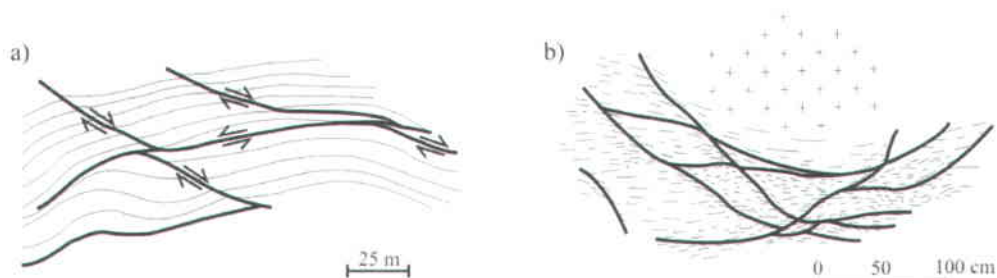


Figure 3.3.14: Line drawings showing: a) interpreted kinematics of conjugate shear zones present on the large stripped outcrop based on the distribution of shear zones (thick lines) and S_2 fabric (thin lines). b) distribution of conjugate shear zones (thick lines) and regional foliation (thin lines) of the Proterozoic St-Cast granites (France) (modified from Gapais et al., 1987). Note the similarity between the two patterns, with one set of shear zones sub-parallel to the main foliation.

Although a strike-slip system is consistent with the distribution of sheeted en-echelon quartz veins present along some of the high strain zones (Figure 3.3.15), the sub-vertical cone

axes of sheath folds (Figure 3.3.5) (Ravenelle et al., 2010), coupled with the sub-vertical attitude of lineations and strain observed on vertical sections (Figure 3.3.10) indicate that the long axis of the strain ellipsoid (X axis) and the transport direction along the inferred shear zones was sub-vertical. The sheeted veins are boudinaged with shallowly-plunging boudins axes, which suggests that they have themselves been affected by the episode of sub-vertical stretching.

The shear zone pattern and the progressive strain history described above, with evidence for horizontal and vertical movement, closely resembles the progressive strain history of shear zones that affected granites of the External Crystalline Massifs of the Central Alps (Gapais et al., 1987). There, Gapais et al. (1987) describe two shear zone systems, one interpreted to result from coaxial deformation and the other from non-coaxial deformation, that lead to conjugate sets of shear zones with sub-vertical lineations and apparent movement on horizontal and vertical surfaces (Figure 3.3.16.). The 3D geometry and kinematics of conjugate sets of shear zones observed there indicate that the shear zone map pattern of the large stripped outcrop is not necessarily inconsistent with the sub-vertical lineation and the inferred sub-vertical movement. It is important to note, however, that since the 3D geometry and kinematics of the high strain zones present on the large stripped outcrop is not documented, the analogy with the shear zone systems described by Gapais et al. (1987) remains purely geometric.

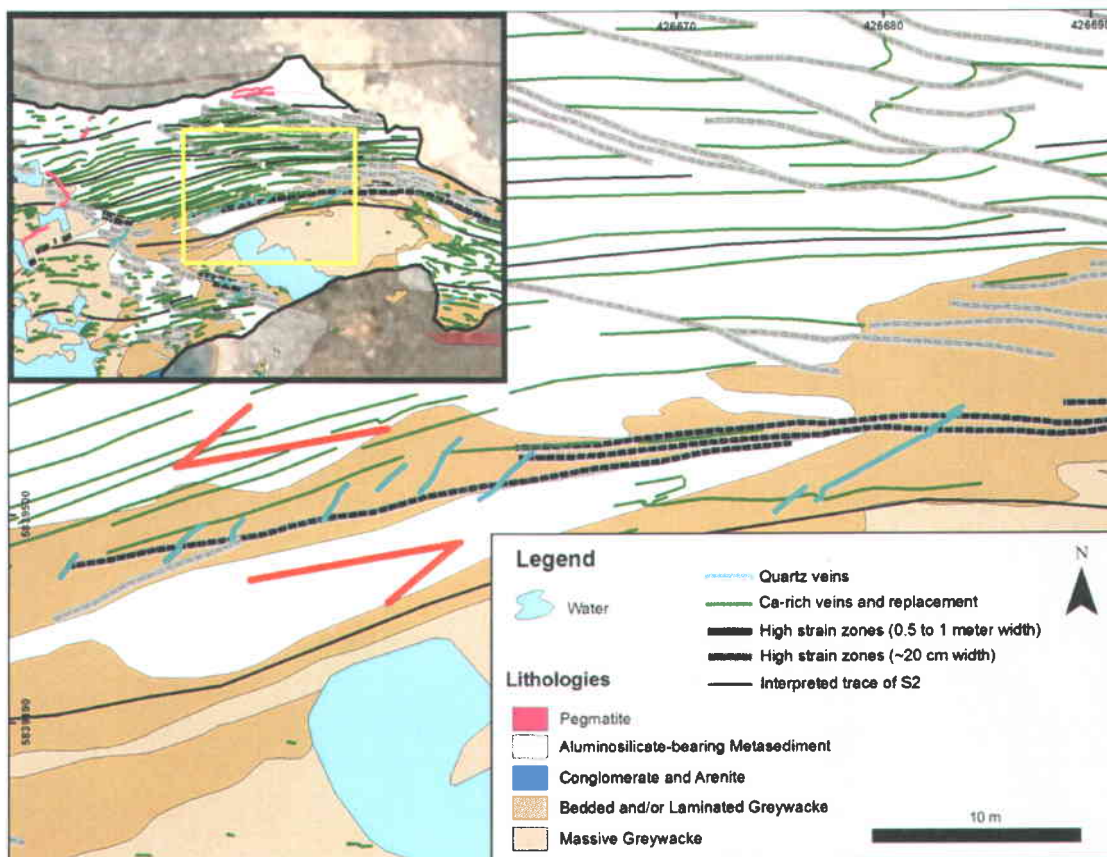


Figure 3.3.15: Geological map of a portion of the large stripped outcrop showing the distribution of quartz veins along one shear zone. The red arrows indicate the interpreted kinematics deduced from the distribution of quartz veins. The inferred movement is the same as the one previously interpreted based on the distribution of the S_2 fabric and Ca-bearing replacement bands (Figure 3.3.14). The map extent, with respect to Figure 3.3.13, is represented by the yellow rectangle in top left corner inset. Coordinates are in UTM Nad83.

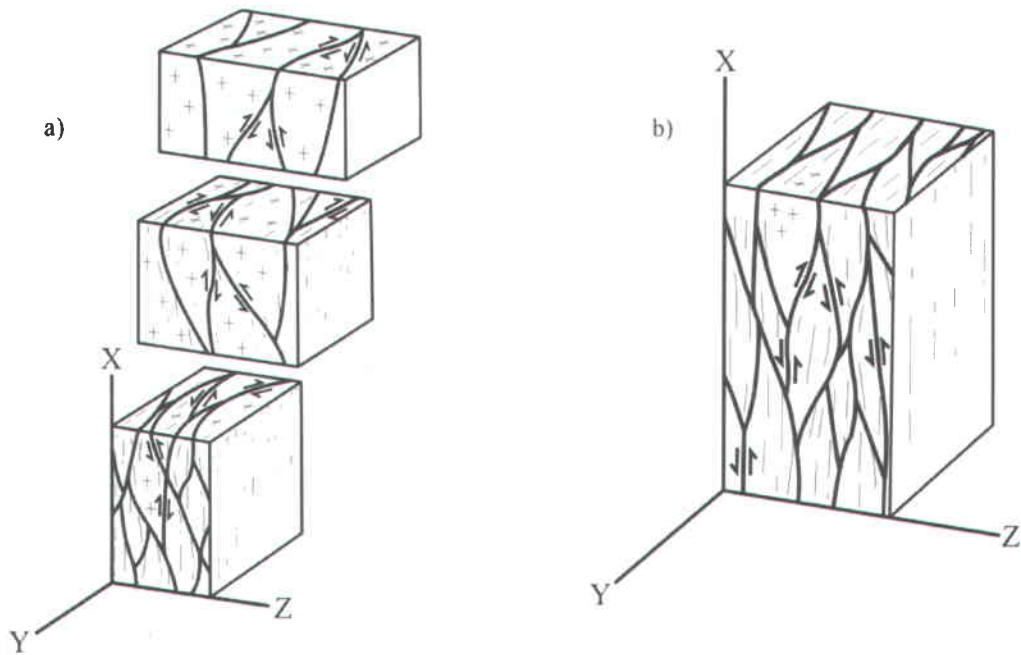


Figure 3.3.16: Schematic diagrams showing 3D patterns of conjugate shear zones that affected the External Crystalline Massifs of the Central Alps (modified from Gapais et al., 1987): a) 3 stages of increasing bulk strain interpreted for the Aar granites, which is interpreted to result from coaxial deformation. b) 3D shear zone pattern of the Gotthard granites, which is interpreted to result from non-coaxial deformation. Both the Aar and the Gotthard shear zone systems are associated with sub-vertical lineations. The X, Y, and Z axes represent the axes of the strain ellipsoid (long, intermediate, and short, respectively).

3.3.4 Faults and Slip Surfaces

3.3.4.1 Description of Faults and Slip Surfaces

Faults and slip surfaces are primarily mapped on the large stripped outcrop and commonly occur along bedding and foliation planes (typically S_2). Such faults and slip surfaces caused offsets (Figure 3.3.17a) and shearing (Figures 3.3.17b and 3.3.17c) which may or may not be associated with folds.

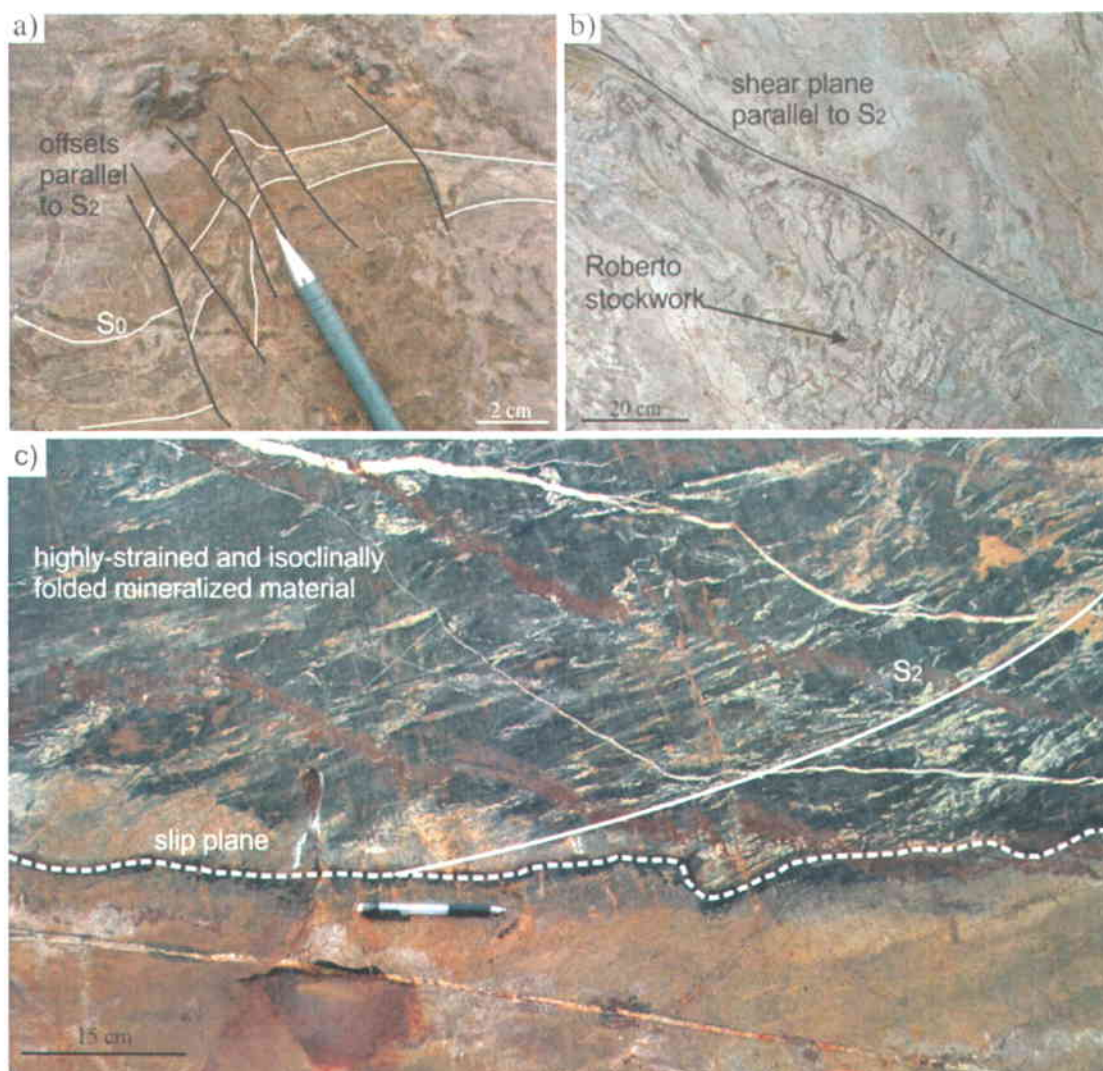


Figure 3.3.17: Photographs showing: a) offsets along S_2 planes. b) shear plane sub-parallel to S_2 in Roberto's auriferous stockwork. c) dragging of S_2 and isoclinally-folded material of the East-Roberto zone along a slip plane (modified from Ravenelle et al., 2010).

The auriferous stockwork of the Roberto Zone was particularly affected by such structures (Figures 3.3.18a and 3.3.18c), as well as by other slip planes which are not oriented parallel to S_0 or S_2 (Figure 3.3.18b). The most significant structures along which movement has occurred are the apparent dextral slip which bounds the East-Roberto zone (Figure 3.3.17c) and the apparent sinistral slip on the Mid-Roberto zone, which both greatly affected the distribution of S_2 on the large stripped outcrop (Figure 3.3.19). The fault structure along the East-Roberto zone is interpreted to mark the contact between two sedimentary sequences of different age (see section 3.2.1.1 *Turbiditic Greywacke* for details). However, the structure is discordant to bedding on either side which suggests that it represents a faulted contact as opposed to an unconformity

(Figure 3.3.19) (see section 3.3.6.1 *Global Geometry* for details). Sheeted quartz veins present along the East-Roberto structure, and whose distribution is consistent with apparent dextral movement (Figure 3.3.20a) might have been generated during this episode of faulting or during its reactivation. Similar sets of sheeted quartz veins are widely distributed over the large stripped outcrop and over the deposit area, and their emplacement may locally be interpreted to result from bedding-parallel slip (Figure 3.3.20d). On the Mid-Roberto zone, the distribution of sheeted pegmatite dykes that crosscut the zone is consistent with the observed sinistral drag in S_2 (Figure 3.3.20e) which could suggest that those pegmatite dykes were generated during post-ore movement along the zone.

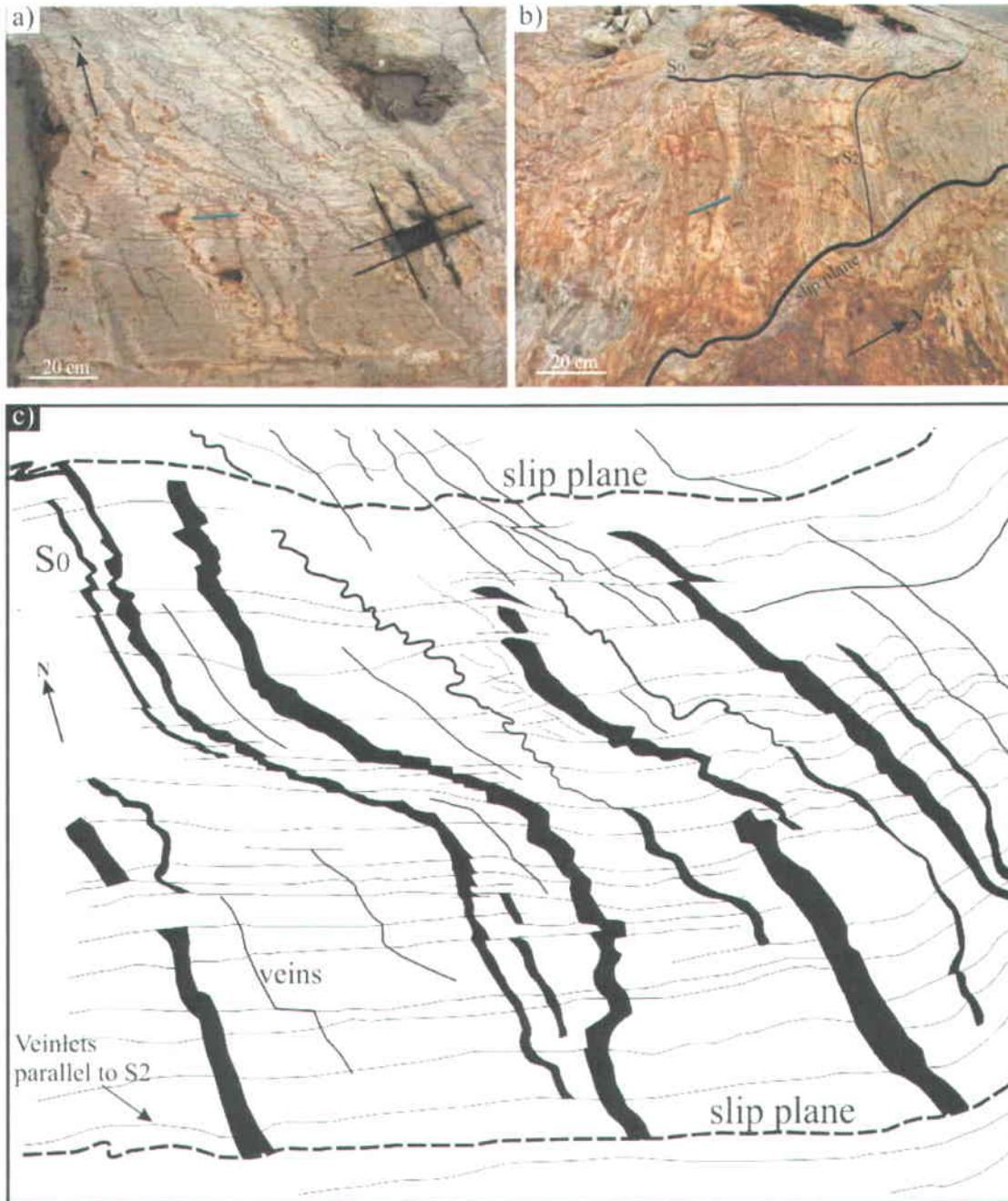


Figure 3.3.18: Photographs showing: a) auriferous stockwork of the Roberto zone showing slip movement along bedding and S_2 planes. Note also the presence of two more significant slip planes at the top and bottom of the photograph. b) slip planes oriented parallel and at some angle to bedding which dragged veins emplaced parallel to S_2 . c) interpreted drawing of photograph shown in (a) showing details of multiple slip surfaces (thin lines = veins emplaced parallel to S_2 and/or S_2 , black regions = beds, dashed lines = slip planes, all other lines = veins). Note the movement along S_2 planes which offset bedding planes in the center of the photograph, and movement along bedding planes in the right hand side which dragged S_2 planes.

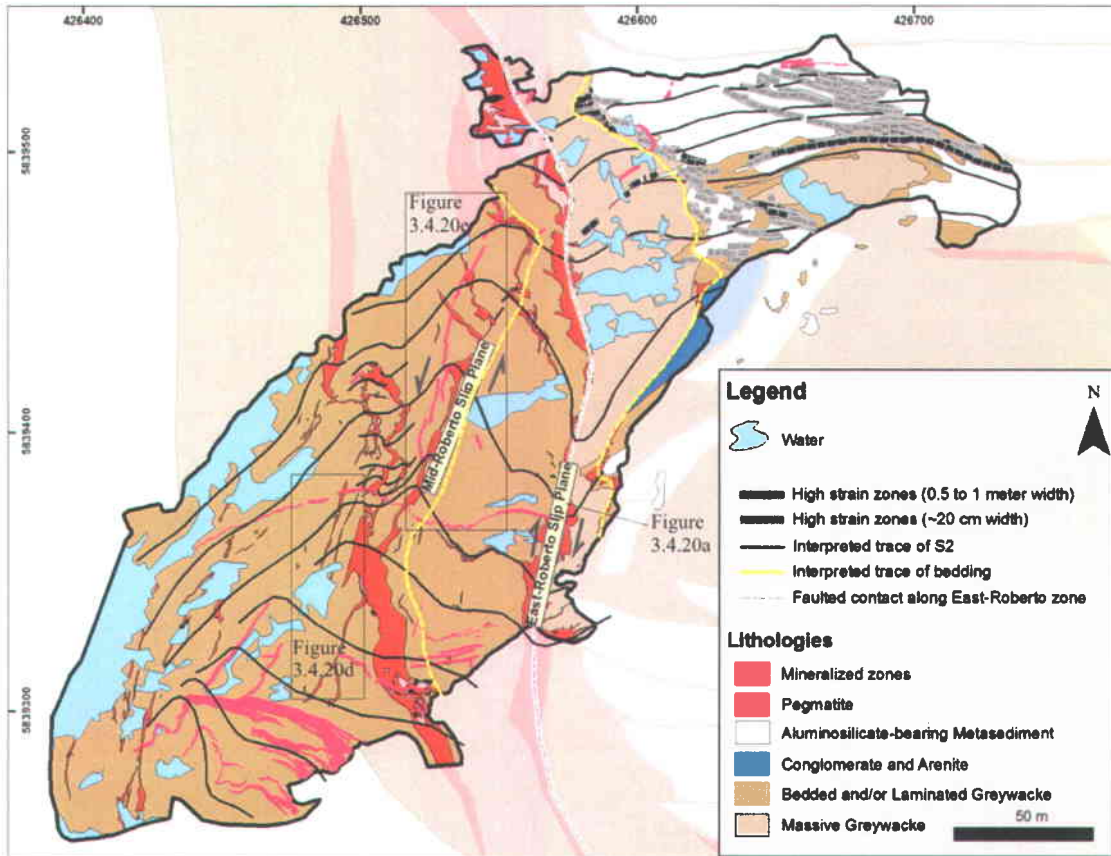


Figure 3.3.19: Map of the large stripped outcrop showing the interpreted trace of S₂. In regions where S₃ overprinted S₂, the attitude of S₂ was estimated from the attitude of F₂ axial planes. Note the significant changes in the attitude of S₂ near the Mid-Roberto and East-Roberto zones. Rectangles indicate locations of inserts of Figure 3.3.20. Grey arrows represent interpreted kinematics based on the distribution of the S₂ fabric. Coordinates are in UTM Nad83.

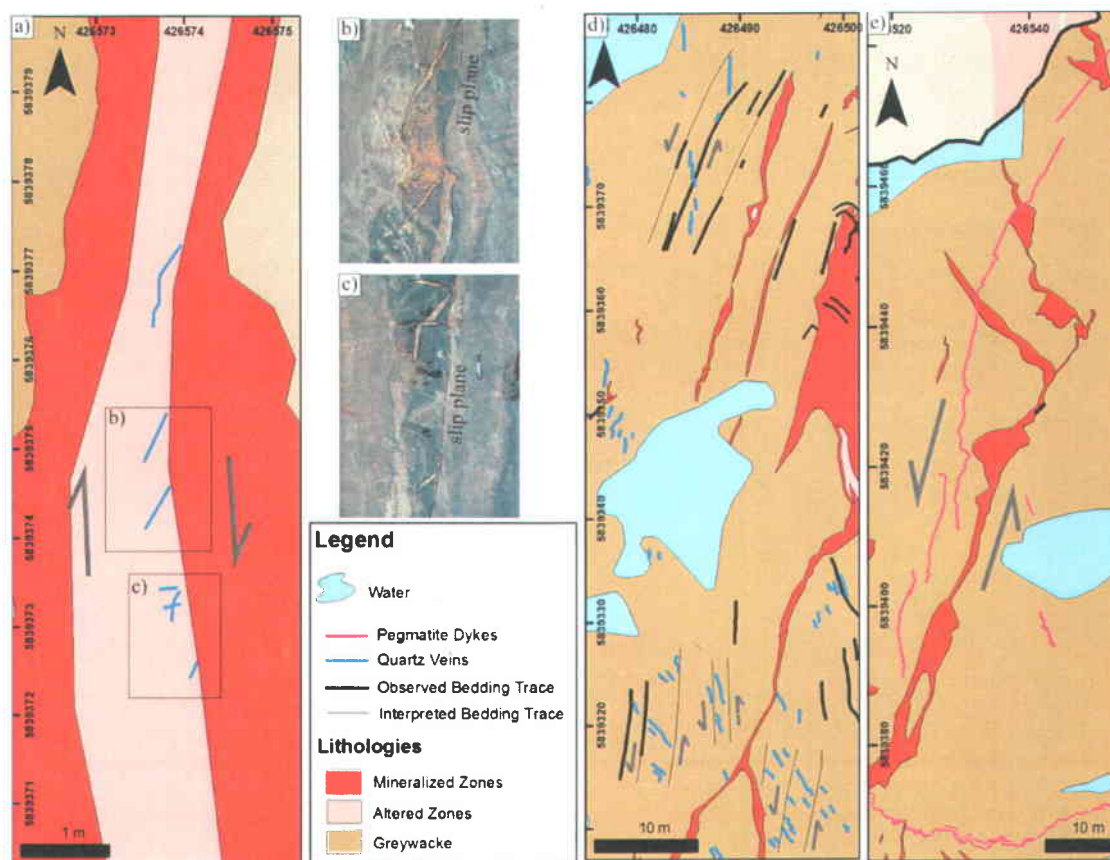


Figure 3.3.20: Close-ups of various parts of the large stripped outcrop. a) extensional quartz veins distributed along the East-Roberto zone whose distribution is consistent with the dextral drag observed in S_2 (see Figure 3.3.19). b) and c) photographs showing details of inserts (b) and (c) shown on (a). d) sets of extensional quartz veins located west of the Roberto zone whose distributions appear to be controlled by bedding-parallel slip. e) pegmatite dykes distributed nearby the Mid-Roberto zone whose distribution is consistent with the observed sinistral drag in S_2 (see Figure 3.3.19). Grey arrows represent interpreted kinematics based on veins or dykes distribution. Coordinates are in UTM Nad83.

3.3.4.2 Timing of Movement along Bedding and Foliation Surfaces with Respect to D_2 and D_3

Dragging and reorientation of S_2 caused by local slip along lithological or fault contacts controlled at least in part the complex distribution of the S_2 fabric on the large stripped outcrop (Figure 3.3.19). The fact that the slip plane of the East-Roberto zone drags the S_2 foliation and F_2 axial planes (Figures 3.3.17c and 3.3.19) strongly suggests that movement along the slip plane occurred after D_2 or very late in D_2 . This agrees with the presence of sheeted extensional quartz veins along the East-Roberto zone whose distribution is consistent with apparent dextral movement along the zone and crosscut the S_2 fabric (Figure 3.3.20a). On the other hand, the fact that a pegmatite dyke cross-cuts the slip plane near the East-Roberto zone (Figure 3.3.21a) but is itself folded by F_3 folds (Figures 3.3.19 and 3.3.21b) indicates that movement along that

slip plane occurred before folding of the pegmatite dyke (i.e. before D_3 or early in D_3). The combination of these observations indicates that movement along the slip plane occurred either late during D_2 or early during D_3 . Since the pegmatite dyke that crosscuts the slip plane is dated at ca. 2603 Ma (Figure 3.3.21), movement along the slip plane must have occurred before ca. 2603 Ma.

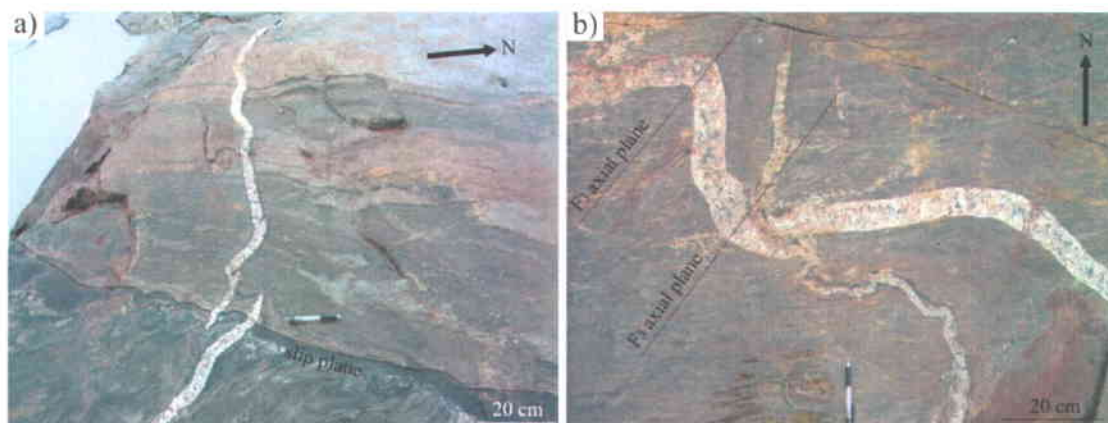


Figure 3.3.21: Photographs of the pegmatite dyke dated at ca. 2603 Ma showing: a) pegmatite dyke cross-cutting the slip plane that affects the East-Roberto zone. b) F_3 folds in the pegmatite dyke shown in (a).

3.3.5 Late Brittle Faults and Breccia

Sets of NW- and NE-striking moderately- to steeply-dipping brittle faults (Figure 3.3.22a) are present over the deposit area and over the whole Éléonore property. These brittle faults are on average less than 5 cm wide, but wider faults (up to 30 cm on the large stripped outcrop and up to several meters wide elsewhere on the Éléonore property) locally occur. The faults commonly contain brecciated pods characterized by fragments of the host rock in a quartz-rich matrix (Figure 3.3.22b). Epidote veins and epidote-rich stockworks are commonly associated with these faults (Figure 3.3.22c).

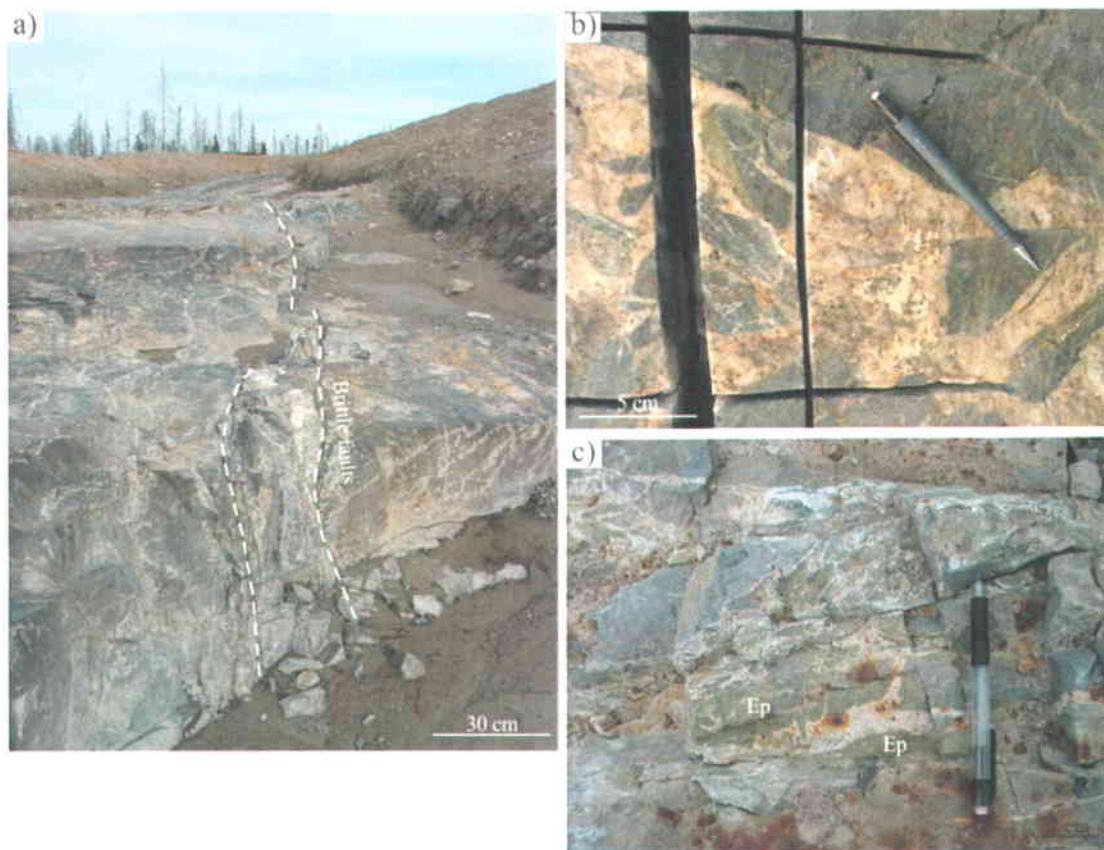


Figure 3.3.22: Photographs showing: a) late brittle fault (center of photograph) from trench DEC-08-06. b) brecciated region associated with late fault on the large stripped outcrop. The breccia is composed of host rock fragments within a quartz-rich matrix. c) epidote-rich brecciated fault zone on trench DEC-08-06.

The local presence of slickenlines indicates that the latest movement along these structures was sub-horizontal. The apparent horizontal displacement along such faults is typically less than 0.5 meters, except for a particularly large structure present to the east of the deposit along which significant movement appears to have taken place (Figure 3.3.23a). This large structure, which can be seen on airborne magnetic surveys (Figure 3.3.23b) and on aerial photographs (Figure 3.3.23c), is locally associated with intense silicification and/or epidote-rich stockworks. The timing of these brittle faults is interpreted to be quite late in the history of the region, since they crosscut all other structures and veins, and also appear to displace young diabase dykes (Figure 3.3.23).

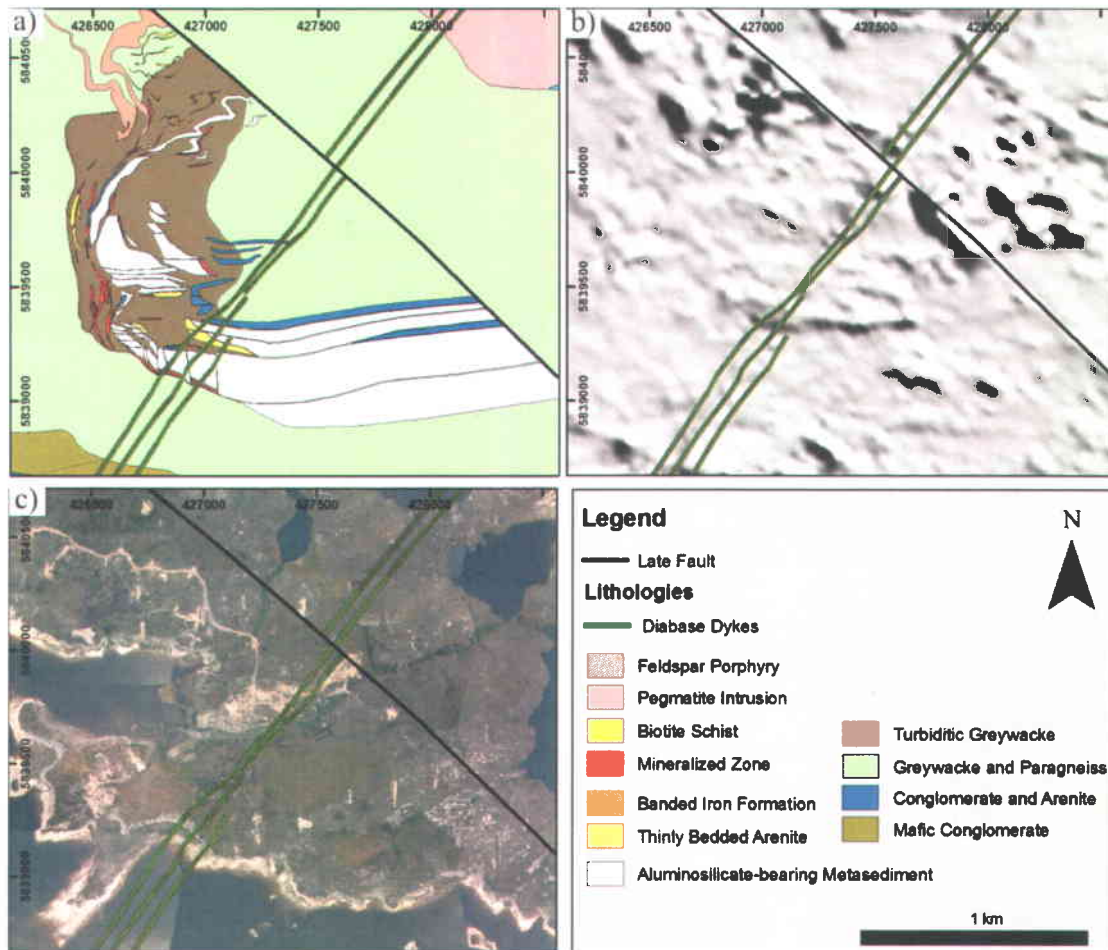


Figure 3.3.23: Maps showing: a) location of the large fault structure located to the east of the deposit. This structure offset diabase dykes. b) fault structure seen on airborne magnetic map. c) fault structure as shown on aerial photograph. Magnetic map and aerial photograph courtesy of Opinaca Mines Ltd.

3.3.6 Geometrical and Structural Characteristics of the Deposit

In the Roberto area, structural analysis can be further constrained by incorporating subsurface data extracted from drillcore and create 3D representations of lithological units and auriferous zones (see *Annex 1* for details regarding the creation of 3D representations). This section utilizes such representations, along with surface maps, to describe the folded geometry and pinpoint important geometrical and structural characteristics of the deposit area.

3.3.6.1 *Global Geometry*

The Roberto deposit is globally confined to a km-scale sub-vertically-plunging polyfolded geometry which has been traced to more than 1500 meters below surface (Figure 3.3.24). The plunging direction of its fold axis and the dip of planar features vary in different parts of the deposit and at depth (Figure 3.3.24). The geometry of the km-scale folded structure is interpreted to result from interference between F_3 , F_2 , and potentially F_1 folds. The largest fold structure is a km-scale F_3 Z-fold in S_0 and S_2 . The simplified map of Figure 3.3.25 clearly illustrates how the F_3 Z-fold controlled the distribution of S_2 . In the northern domain of the fold (domain A of Figure 3.3.25), the fold axis of the F_3 fold calculated from a π plot of S_2 attitudes is sub-vertical and sub-parallel to the stretching lineation (stereonet A of Figure 3.3.25). The attitude of its axial plane is ~ E-W striking and steeply-dipping based on the attitude of S_3 (locally present as a crenulation cleavage) in that domain, although approaching the late fault to the east, the attitude of S_3 rotates to the north-west (Figures 3.3.25 and 3.3.7), perhaps because it was dragged along the fault. In the southern domain (domain B of Figure 3.3.25), the fold axis of the F_3 fold is steeply-plunging to the north-east and the attitude of its axial plane is ~SW striking and steeply-dipping based on the attitude of S_3 in that domain (stereonet B of Figure 3.3.25). The attitude of the calculated fold axis slightly deviates from the attitudes of stretching lineations in that domain (stereonet B of Figure 3.3.25). Z-, S-, and M-folds occur near the inferred F_3 fold hinge (domain B of Figure 3.3.25).

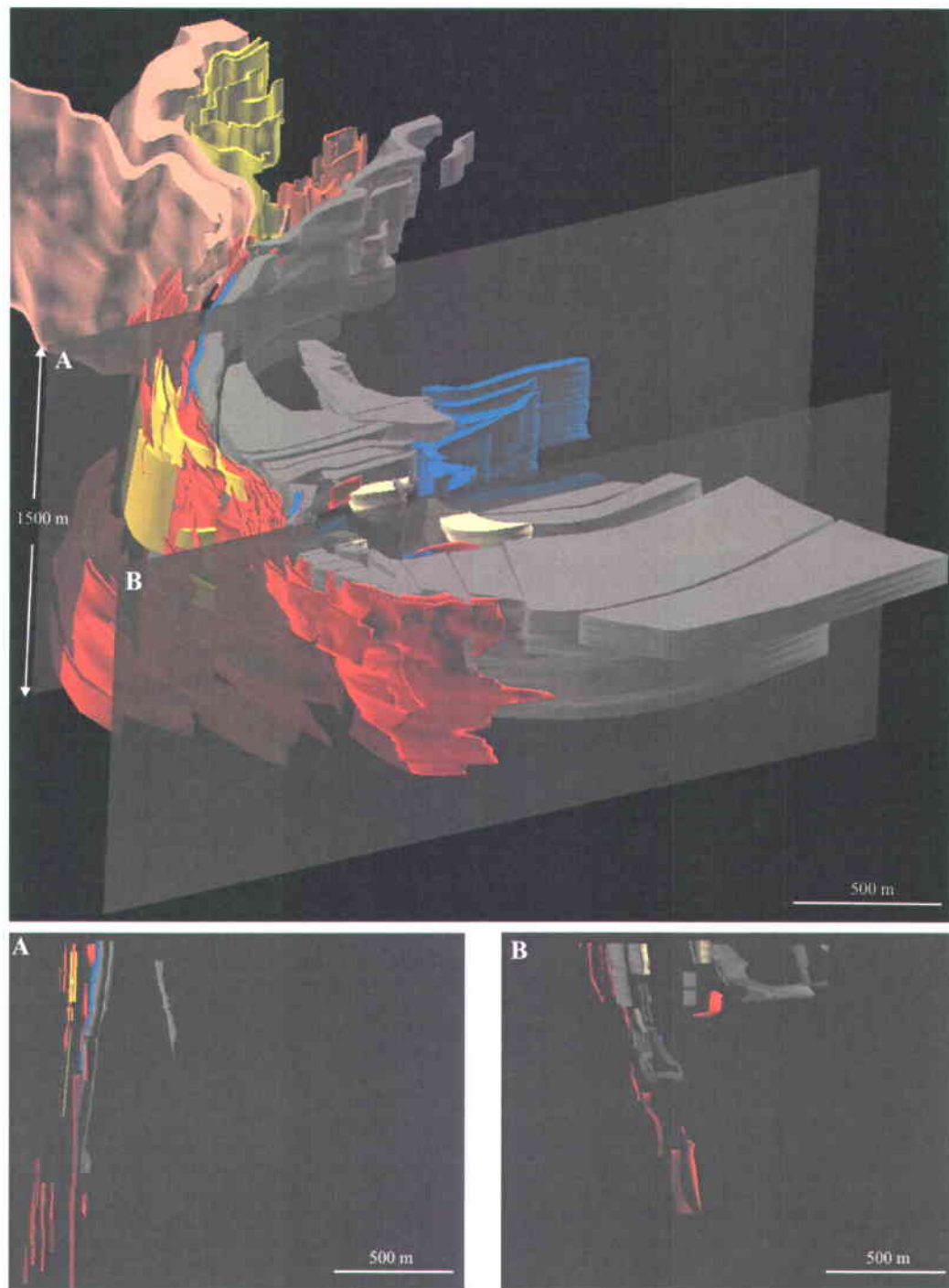


Figure 3.3.24: Gocad snapshots showing the deposit's geometry and two E-W sections (looking north) showing variations in the dip of lithological units and auriferous zones. Lithological units are color-coded (red: auriferous zones, grey: aluminosilicate-bearing metasedimentary rocks, blue: conglomerate and arenite, yellow: biotite schist, orange: banded iron formation (Puncho zone), pale yellow: thinly bedded arenite, pink: feldspar porphyry). Turbiditic greywacke and paragneiss are the dominant rock types present in empty regions of the 3D space. Pegmatite dyke swarms and diabase dykes are not displayed to simplify visualization.

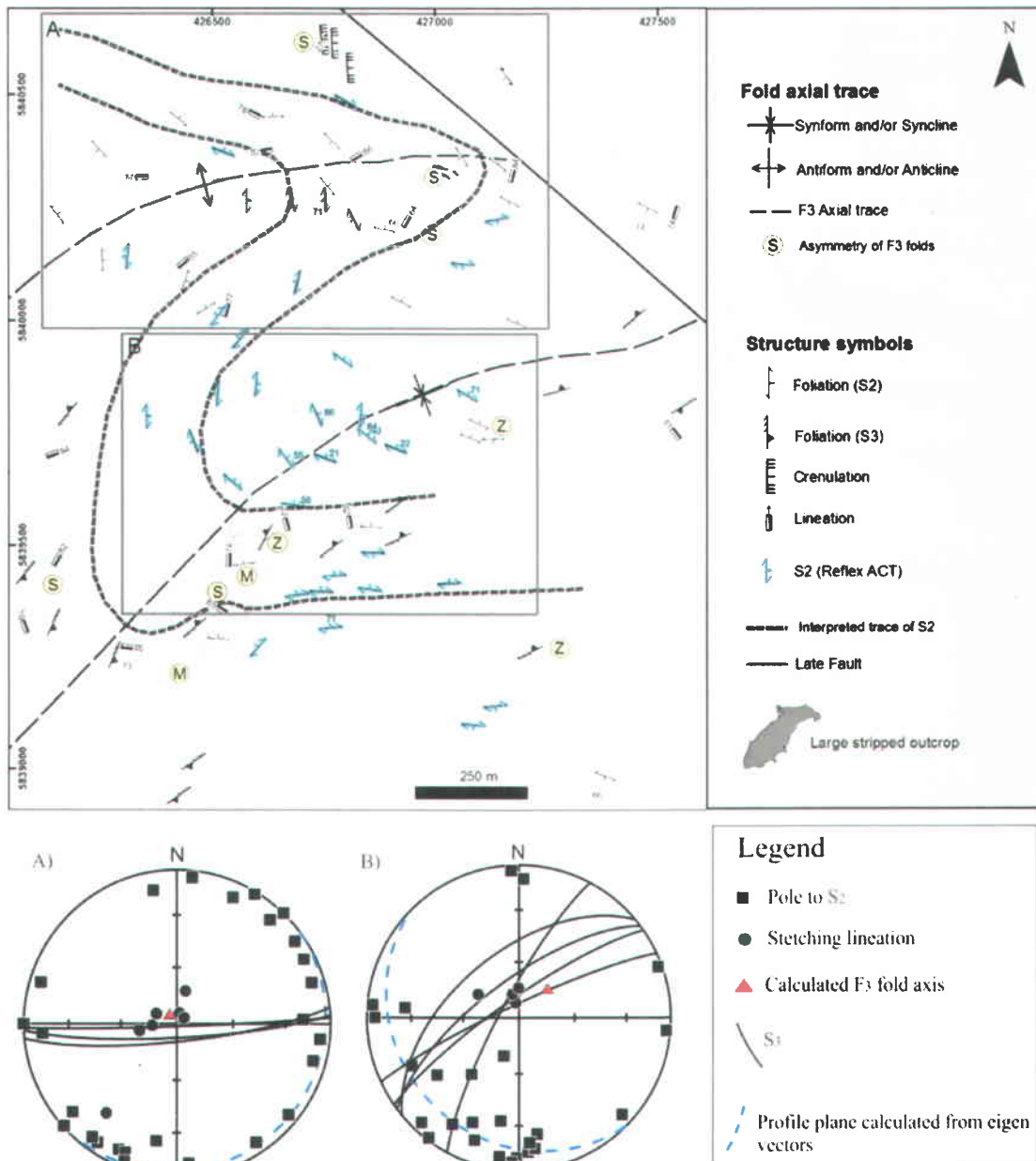


Figure 3.3.25: Simplified map showing the distribution of the S_2 and S_3 fabric, the asymmetry of outcrop-scale F_3 folds, and the axial traces of F_3 folds. Data from domains A and B are plotted on stereonets A and B, respectively. Calculated F_3 fold axes in S_0/S_2 are sub-parallel to mineral lineations in domain A, but slightly deviates from mineral lineations in domain B. Dip label of planar structural measurements with dip value greater than 75 degrees are not displayed to simplify the map. S_2 measurements from drillcore (Reflex ACT) are vertically projected from their location in the subsurface. Coordinates are in UTM Nad83.

The lithological map pattern is more complex than the pattern of the S_2 distribution (Figure 3.3.26). The axial traces of an F_2 Z-fold in S_0 can be interpreted based on the map pattern, the distribution of axial planar S_2 fabric, and the asymmetry of parasitic folds (domain A of Figure 3.3.26).

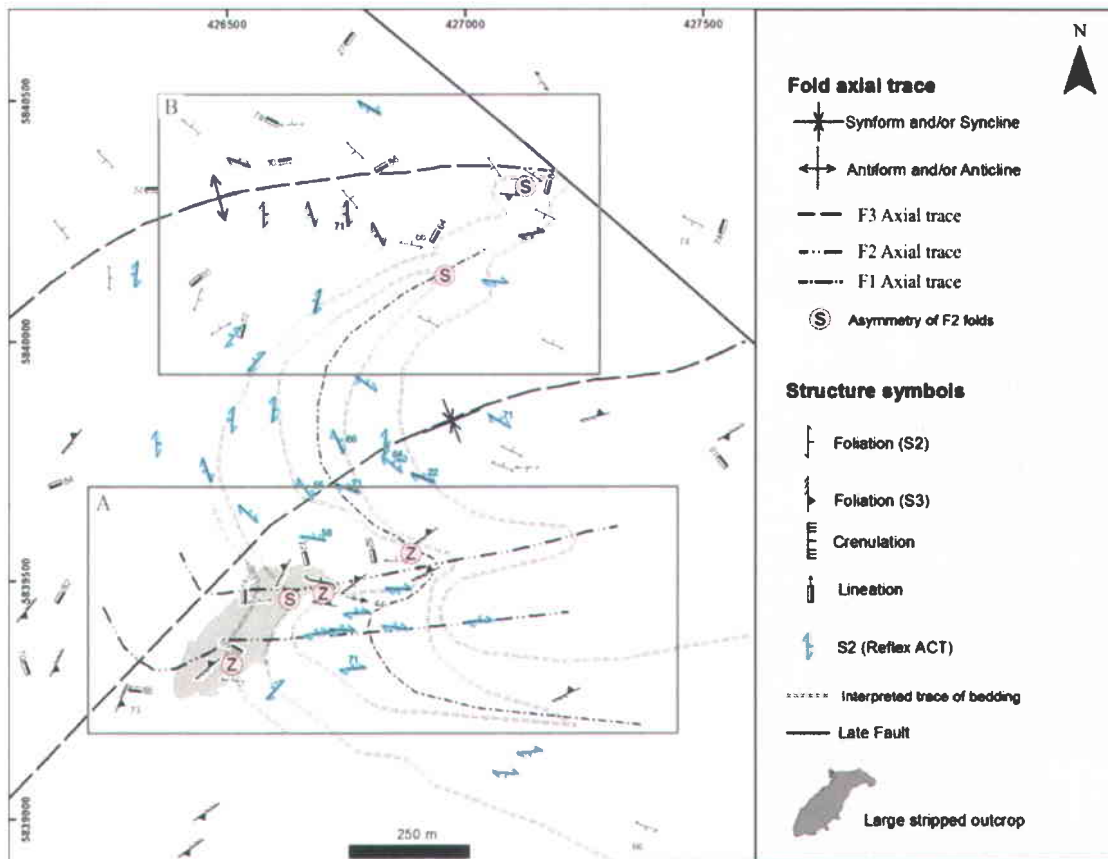


Figure 3.3.26: Simplified map showing the distribution of the S_2 and S_3 fabric, the interpreted trace of bedding, the asymmetry of outcrop-scale F_2 folds, and the interpreted axial traces of F_1 , F_2 , and F_3 folds. Note the interference between the fold phases in domain A. Note also the presence of S-folds on the short limb of the F_2 Z-fold. Dip label of planar structural measurements with dip value greater than 75 degrees are not displayed to simplify the map. S_2 measurements from drillcore (Reflex ACT) are vertically projected from their location in the subsurface. Coordinates are in UTM Nad83.

Fortunately, the large stripped outcrop is located in the hinge of the F_2 Z-fold and permits a more detailed structural analysis of that area. Based on structural analysis performed on the large stripped outcrop, parasitic F_2 folds are steeply-plunging in the western part of the outcrop but moderately- to shallowly-plunging to the ESE in the eastern part (Figure 3.3.27). The shallower plunge of the F_2 folds in the eastern part of the outcrop agrees with the distribution of the aluminosilicate-bearing sequence in 3D which appears to be globally shallowly-dipping below that part of the outcrop (Figure 3.3.28). The attitudes of F_2 folds are generally steep and

sub-parallel to lineation measurements (stereonet A of Figure 3.3.27), except in the eastern part of the outcrop where they are moderately- to shallowly-plunging (stereonet B of Figure 3.3.27). These relationships, coupled with the presence of sheath folds and the almost circular map pattern of nearby lithological units (Figures 3.3.26 to 3.3.28) could indicate the presence of a sheath fold culmination in that area. Alternatively, the variations in the attitude of F_2 folds may be attributed to refolding during D_3 . Other important structural characteristics exposed on the large stripped outcrop (Figure 3.3.27) include: 1. high angles between bedding and S_2 planes, which is consistent with cleavage-bedding relationships typically observed in fold hinges. 2. complex distribution of the S_2 fabric due to slip along bedding and fault planes 3. high strain zones, intense vertical transposition, and sheath folds with sub-vertical cone axis in the eastern part of the outcrop. 4. steeply-plunging lineations. 5. parasitic F_2 S-folds in the short limb of the F_2 Z-fold (Figure 3.3.26).

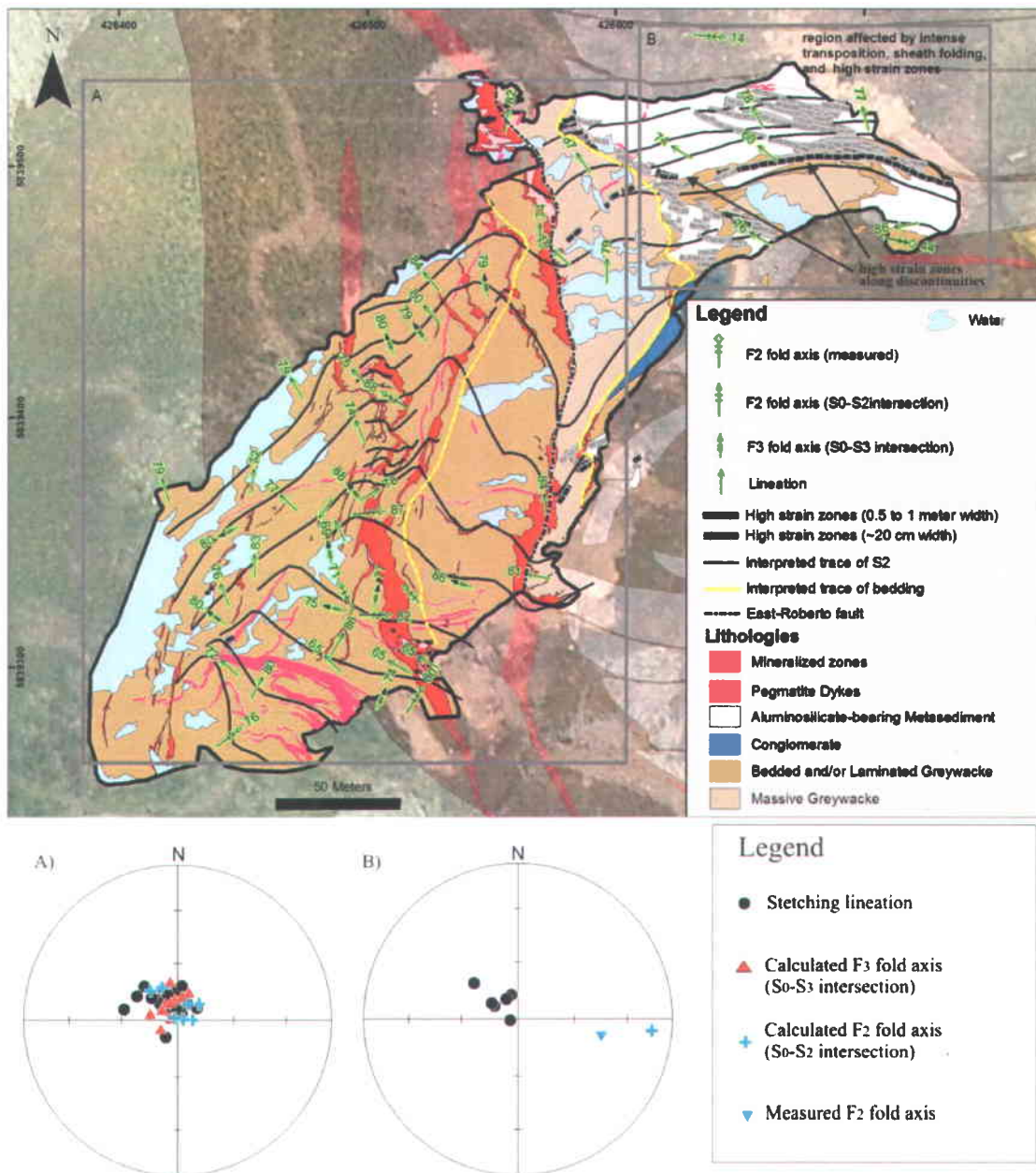


Figure 3.3.27: Map of the large stripped outcrop showing the distribution of linear features (fold axes and lineations), high strain zones, and interpreted trace of bedding and S_2 fabric. Data from domains A and B are plotted on stereonets A and B, respectively. Note how calculated F_2 and F_3 fold axes are sub-parallel to mineral lineations in domain A, and how the attitudes of F_2 folds in domain B differ from the attitudes of mineral lineations in that domain. Note also the presence of meter-scale high strain zones along major discontinuities within the aluminosilicate-bearing sequence. Coordinates are in UTM Nad83.

The map pattern of the deposit area shows a relatively complex deposit-scale symmetrical repetition of lithological units (conglomerate-aluminous rocks-arenitic wacke) (Figure 3.3.3, circled numbers 1-2-3). Although such a repetition might simply illustrate primary

depositional repetitions and hence be purely circumstantial, such a repetition might on the other hand indicate that these lithological units were isoclinally folded prior to the formation of the F_2 Z-fold (Ravenelle et al., 2010). Although evidence for D_1 structures is cryptic in the area, F_1 - F_2 fold interference patterns were locally observed on the Éléonore property (e.g. Figure 2.5.7a), including one pattern located on the large stripped outcrop (Figure 3.3.6a).

The northern limb of the F_2 Z-fold and the S_2 fabric are clearly folded by the larger-scale F_3 fold previously described (Figure 3.3.26). Parasitic F_2 folds are not common in the northern area, but where documented, are steeply-plunging and have an S-asymmetry (domain B of Figure 3.3.26). The global interference pattern between F_2 and F_3 folds resembles other interference patterns observed on outcrops (e.g. Figures 3.3.6b and 3.3.6c). The interference pattern present on trench DEC-08-06b is also similar, although there, the attitude of S_3 has rotated towards the north-west (Figure 3.3.7).

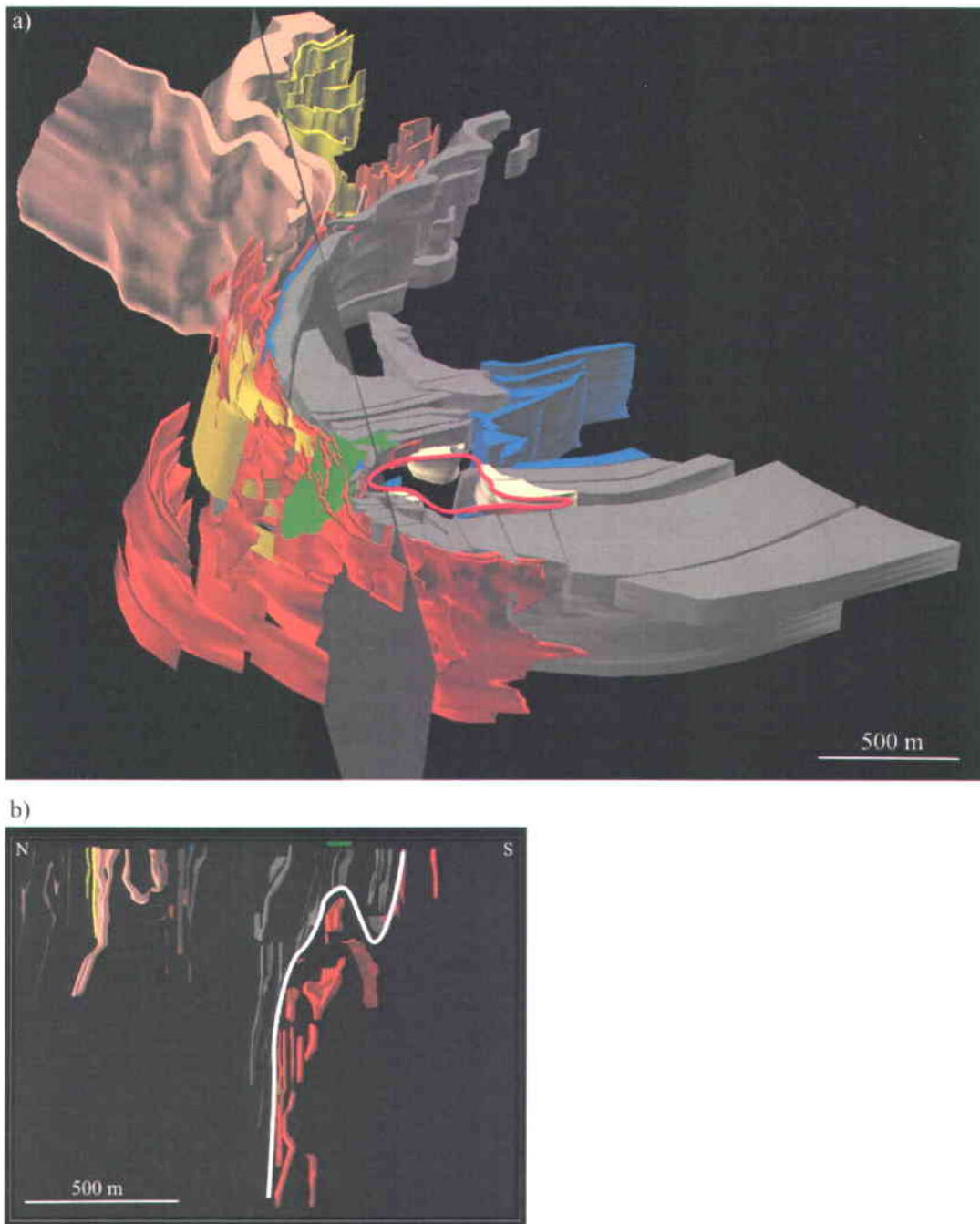


Figure 3.3.28 Gocad snapshots showing: a) distribution of lithological units and auriferous zones. Note the near-circular distribution of thinly-bedded arenites (traced by the pink line) to the east of the large stripped outcrop (green surface). The grey plane marks the location of the section shown in (b). b) N-S section (looking east) showing an interpreted trace of the distribution of aluminosilicate-bearing rocks (white line) underneath the large stripped outcrop (horizontal green line). Lithological units are color-coded (red: auriferous zones, grey: aluminosilicate-bearing metasedimentary rocks, blue: conglomerate and arenite, yellow: biotite schist, orange: banded iron formation, pale yellow: thinly bedded arenite, pink: feldspar porphyry). Turbiditic greywacke and paragneiss are the dominant rock types present in empty regions of the 3D space. Pegmatite dyke swarms and diabase dykes are not displayed to simplify visualization.

3.3.6.2 Nature of Discontinuities Observed in 3D Representations

The numerous and widespread discontinuities/faults observed in 3D reconstructions (e.g. Figure 3.3.28), and consequently on the map pattern from which it is derived (Figure 3.3.29a), directly result from the assumptions used to create the 3D representations (see *Annex 1*). Although such discontinuities may indeed correspond to fault structures, they might alternatively locally correspond to parasitic and/or transposed folds. This scenario specifically appears to apply to discontinuities of the eastern part of the large stripped outcrop. There, the presence of high strain zones near the inferred discontinuities (Figure 3.3.27), along with the presence of preserved F_2 fold hinges with highly transposed limbs (Figure 3.3.11b), suggests that the discontinuities resulted from a combination of folding and intense transposition. Figure 3.3.29b captures a stylized version of the lithological map pattern based on the highly strained style of the D_2 deformation observed on outcrops (e.g. Figure 3.3.30a). Less ductile faults also occur on outcrops (e.g. Figures 3.3.30b and 3.3.17a) and may also explain some of the discontinuities mapped. The large ~N-S striking discontinuities in the southern part of the deposit are difficult to explain. They may delineate blocks that rotated during significant slip along bedding-parallel shear planes like commonly observed in shear zones (e.g. Figure 3.3.30c). Since this interpretation is purely speculative, it was not included in the stylized map version of Figure 3.3.29b.

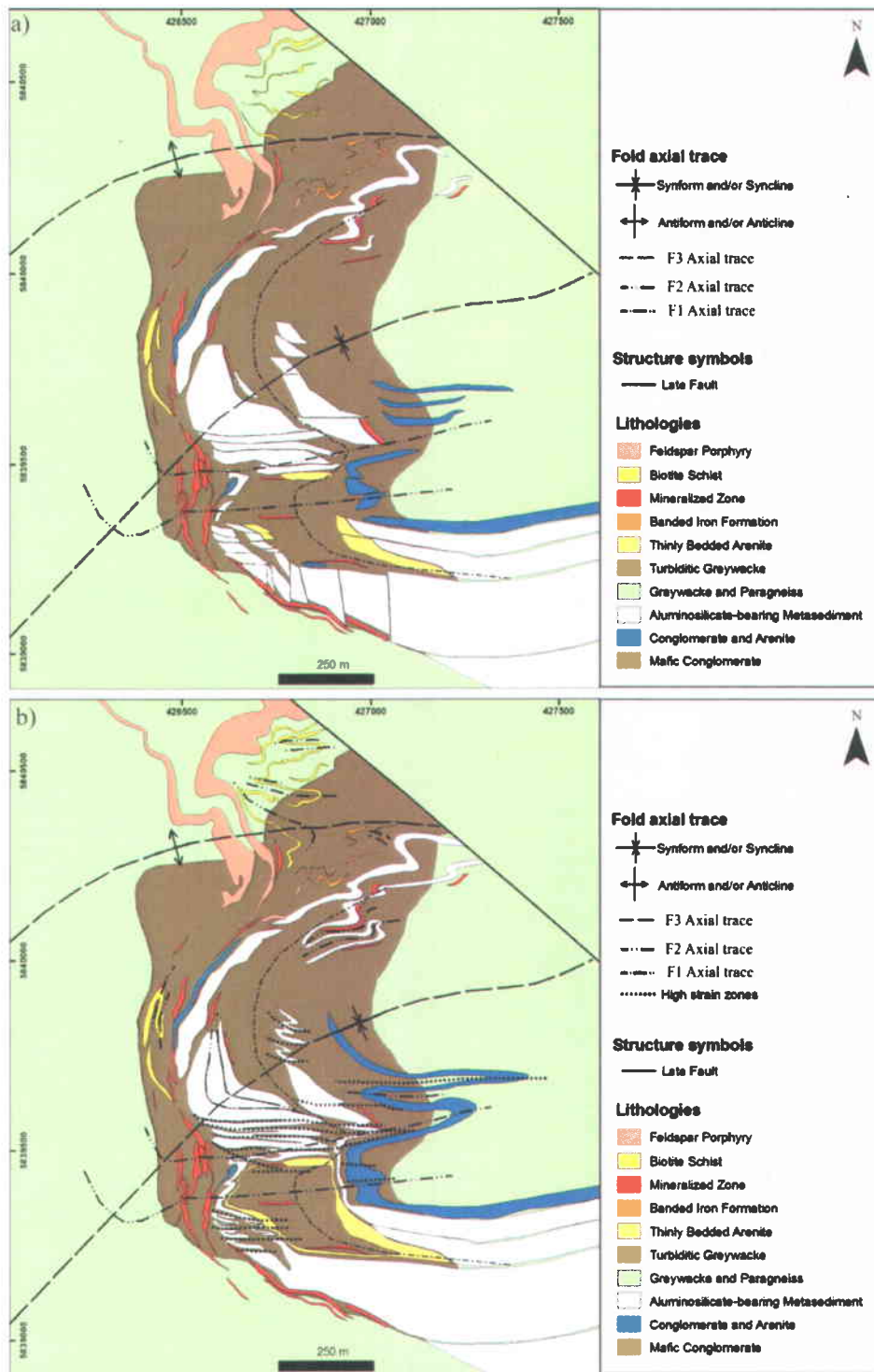


Figure 3.3.29: Geological maps of the Roberto deposit area showing: a) distribution of lithological units constructed from projection of 3D reconstruction. b) stylized distribution of lithological units assuming that the observed discontinuities of map shown in (a) correspond to highly transposed F_2 fold limbs. Axial traces of the three generations of folds are also shown on both maps. Coordinates are in UTM Nad83.

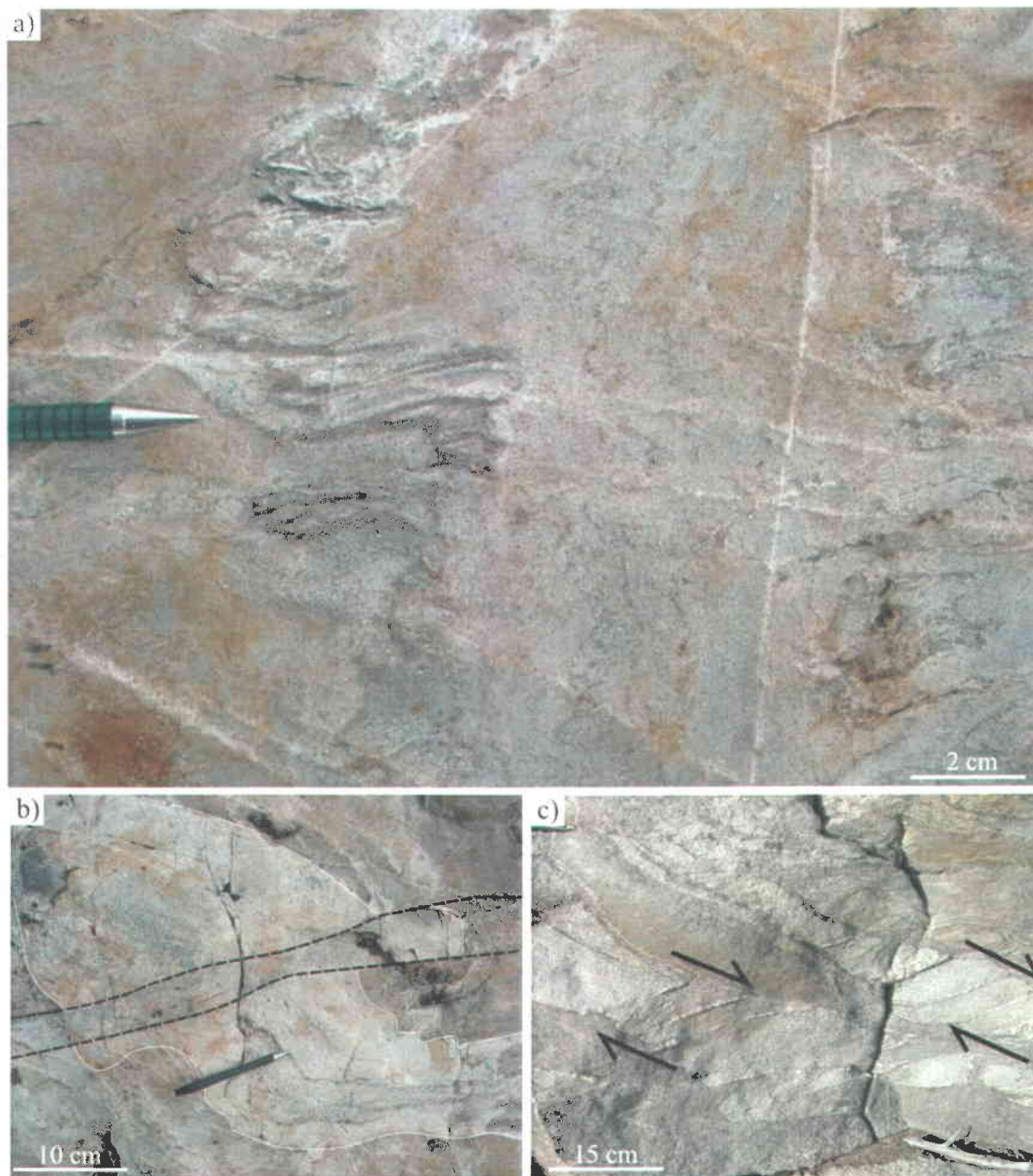


Figure 3.3.30: Photographs showing: a) F_2 folding associated with intense transposition in incompetent bed located in the eastern part of the large stripped outcrop. This deformation style was applied to the map of Figure 3.3.29b to explain some of the discontinuities observed in lithological units. b) F_3 fold in S_0/S_2 with two faults parallel to S_3 on the short limb of the fold on an outcrop located ~500m east of the large stripped outcrop. Such faults could also explain some of the discontinuities observed on the map pattern. c) rotated blocks along lithological units in a shear zone located in the southern part of the Éléonore property. Such a process could possibly explain the N-S discontinuities present in the lower portion of the deposit.

3.3.6.3 *Horizontal and Vertical Thickness Changes*

The thickness of lithological units, especially the aluminosilicate-bearing units, the biotite schist, and the conglomerate and arenitic units, vary significantly within the deposit area (Figures 3.3.28 and 3.3.29). As mentioned previously, the presence of high strain zones and preserved F_2 fold hinges in the thickest part of aluminosilicate-bearing units suggests that the units were intensely transposed and folded, which may explain the increase in thickness. In the case of aluminosilicate units and biotite schist, such thickness changes may alternatively be attributed to local variations in the intensity of the hydrothermal alteration which could have locally precluded the formation of aluminosilicate (Ravenelle et al., 2010) (see *Relative Timing between Calc-silicate Alteration and Metamorphic Peak*). These two explanations are not exclusive of one another and a combination of both factors might explain the observed change in thickness. In the case of the biotite schist and conglomerate and arenitic units, their discontinuous distribution might relate to the fact that they had a primary lenticular distribution, or that they have been significantly boudinaged during deformation. The intense transposition observed on vertical sections (e.g. Figure 3.3.28b) is likely to be associated with intense vertical stretching and boudinaging leading to significant vertical thickness changes. Such a scenario is supported by the presence of macroscopic boudins with sub-horizontal axis on outcrops.

3.3.6.4 *Oreshoots*

Ravenelle et al. (2010) performed a structural analysis on the first 400 meters of the subsurface geology of the Roberto deposit in order to study structural controls on ore shoots. Note that Ravenelle et al. (2010) performed that analysis on a previous 3D model of the deposit area. Figure 3.3.31 shows the presence of two structural domains referred to as “outcrop area” and “lake area”. The two domains were treated separately in the structural analysis of the subsurface.

The distribution of high grade ore shoots, defined by much larger vertical than horizontal extension (Figure 3.3.31a), were modeled by Opinaca Mines Ltd. In order to test the hypothesis that the attitude of ore shoots is controlled by the fold axis of the deposit-scale fold, fold axes controlling the global geometry of auriferous zones in the “outcrop” and “lake” area were calculated (Figures 3.3.31d and 3.3.31e) and compared with the attitude of ore shoots measured for the “outcrop” and “lake” area respectively (Figures 3.3.31f and 3.3.31g). The attitudes of ore

shoots were estimated from Gocad "curves" digitized on the ore shoots. The attitude of the fold axis affecting the auriferous zones of each domain was calculated from the distribution of poles to median planes created for selected sub-planar auriferous zones (Figures 3.3.31d and 3.3.31e) illustrated on Figure 3.3.31b and Figure 3.3.31c for the "outcrop" and "lake" area respectively. The results for the "lake" area indicate that the ore shoots are oriented sub-parallel to the fold axis affecting the auriferous zones (Figure 3.3.31g). The results for the "outcrop" area are not as conclusive, but still suggest a geometrical relationship between some of the ore shoots and the fold axis affecting the auriferous zones (Figure 3.3.31f). The attitudes of ore shoots and fold axes calculated from Gocad fall within the stereonet domain defined by attitudes of lineations and fold axes collected on the stripped outcrop (Figures 3.3.31h and 3.3.31i).

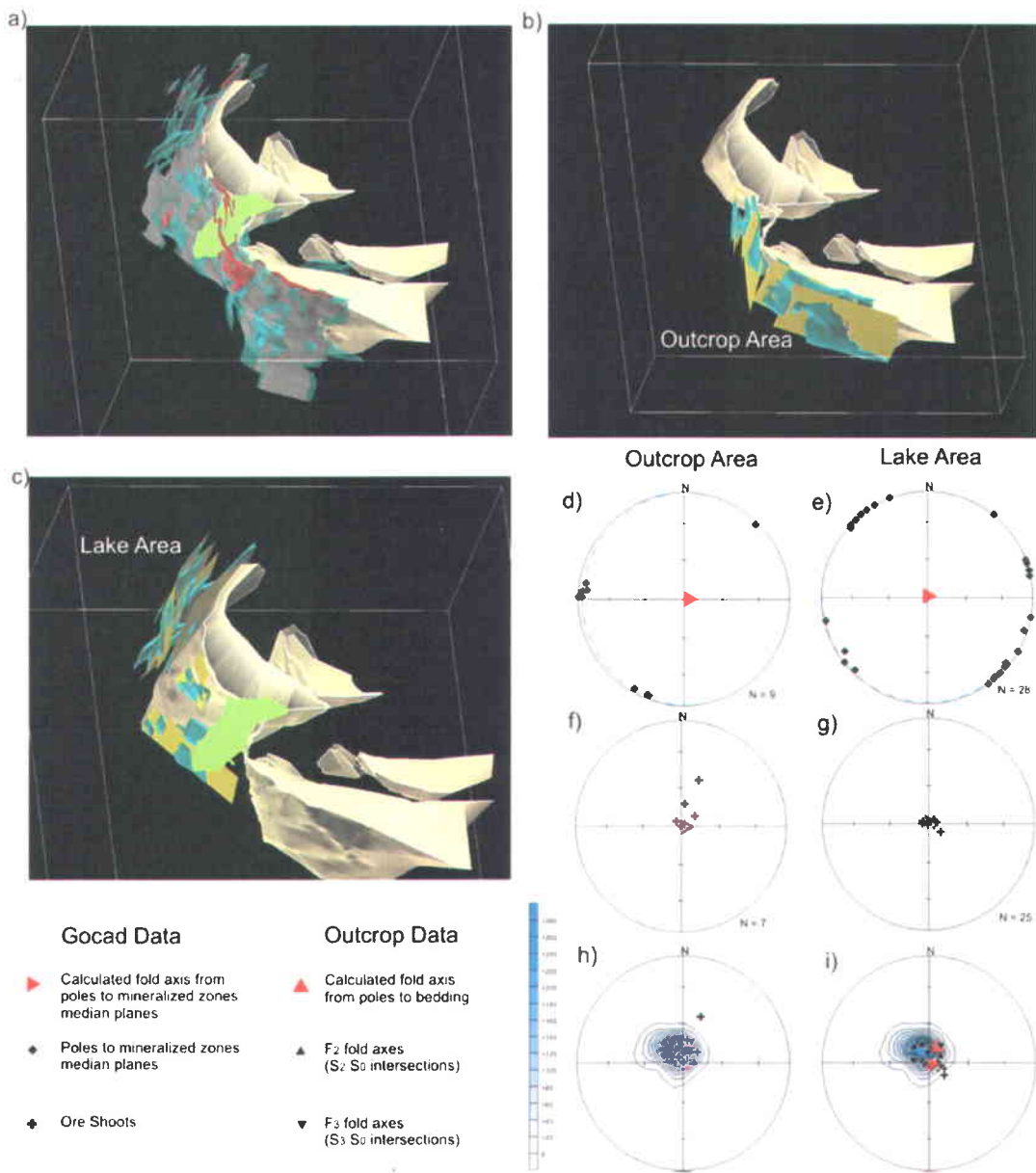


Figure 3.3.31: a) to c) 3D Gocad reconstructions for the first 400 meters of the Roberto deposit showing the distribution of auriferous zones (transparent blue), high grade auriferous zones (red), and aluminosilicate-bearing rocks (pale yellow). Median planes passing through auriferous zones (yellow) and colored outline of the stripped outcrop (green) are also represented. a) General view. b) Distribution of selected auriferous zones and associated median planes used to calculate a fold axis for the "outcrop area". c) Distribution of selected auriferous zones and associated median planes used to calculate a fold axis for the "lake area". d) to i) Equal area nets (lower hemisphere) showing the distribution of structural measurements extracted from Gocad and/or structural measurements collected on the stripped outcrop. d) e) Distribution of poles to auriferous zones median planes and calculated fold axis for the "lake" (88@ 017) and "outcrop" (85@ 091) areas respectively. f) g) Distribution of ore shoots attitudes extracted from Gocad for the "lake" and "outcrop" areas respectively. Fold axes calculated in d) and f) are also represented for comparison. h) i) Synoptic nets showing geometrical relationships between ore shoots, fold axes in auriferous zones calculated from Gocad, fold axis in bedding calculated from outcrop data, and linear measurements (F_2 - F_3 fold axes, lineations (colored contours)) collected on the stripped outcrop.

3.4 Metamorphism

This section presents the metamorphic characteristics of non-mineralized rocks located in the vicinity of the Roberto deposit. The metamorphic characteristics of altered and mineralized rocks are integrated in upcoming sections. The Roberto deposit is located in a window of lower-grade metagreywacke surrounded by higher grade paragneiss and migmatites (Figure 3.4.1). This section primarily focuses on the metamorphic attributes of metagreywacke.

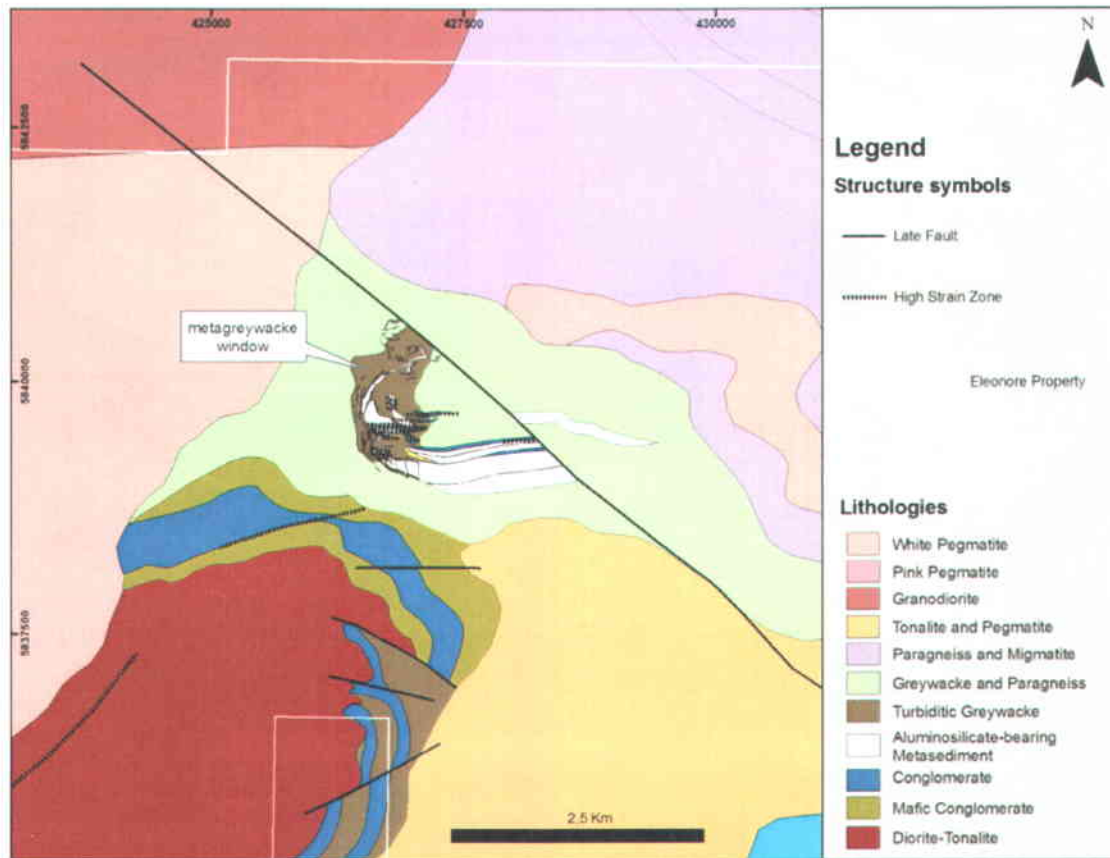


Figure 3.4.1: Simplified geological map of the Roberto area showing the lower grade window of metagreywacke and the surrounding paragneiss, migmatites, and intrusive rocks. Coordinates are in UTM Nad83.

3.4.1 Metamorphic Assemblages

The mineral assemblages of aluminosilicate-bearing rocks are particularly useful to investigate the metamorphic history of rocks because metamorphic reactions involving

aluminosilicates are well documented in the literature. In the vicinity of the Roberto deposit, aluminosilicate-bearing rocks are typically composed of quartz, sillimanite, muscovite, microcline, plagioclase, biotite and minor amounts of tourmaline and sulphides. Sillimanite is usually present as fibrolite (e.g. Figures 3.4.2a and 3.4.2b), although sillimanite needles are also documented (e.g. Figures 3.4.2 c and 3.4.2d).

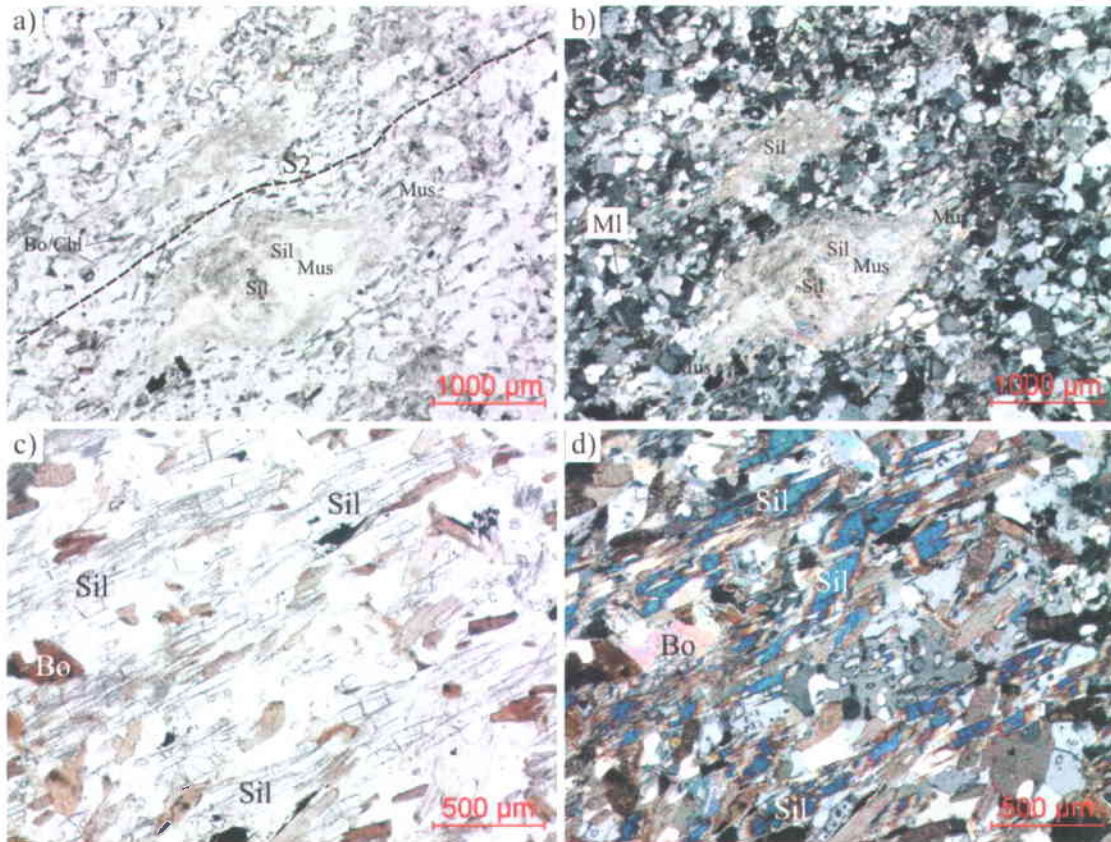


Figure 3.4.2: Natural light (left) and cross-polarized (right) photomicrographs of sillimanite. a) and b) fibrolite porphyroblasts locally replaced by muscovite. The shape of the porphyroblasts suggests that fibrolite represents a pseudomorph of a pre-existing phase which was affected by S_2 . c) and d) sillimanite needles coexisting with biotite.

Microcline porphyroblasts are commonly present as poikiloblasts (e.g. Figure 3.4.3a) and plagioclase as porphyroblasts (e.g. Figure 3.4.3b). Both microcline and plagioclase locally coexist with sillimanite (e.g. Figure 3.4.4). The coexistence of microcline and sillimanite are of importance, since they are the characteristic minerals of the upper sillimanite zone (Yardley, 1989) and might accordingly have been generated through the prograde reaction:



whose distribution in P-T space is well documented for metamorphosed pelitic schists (Figure 3.4.5).

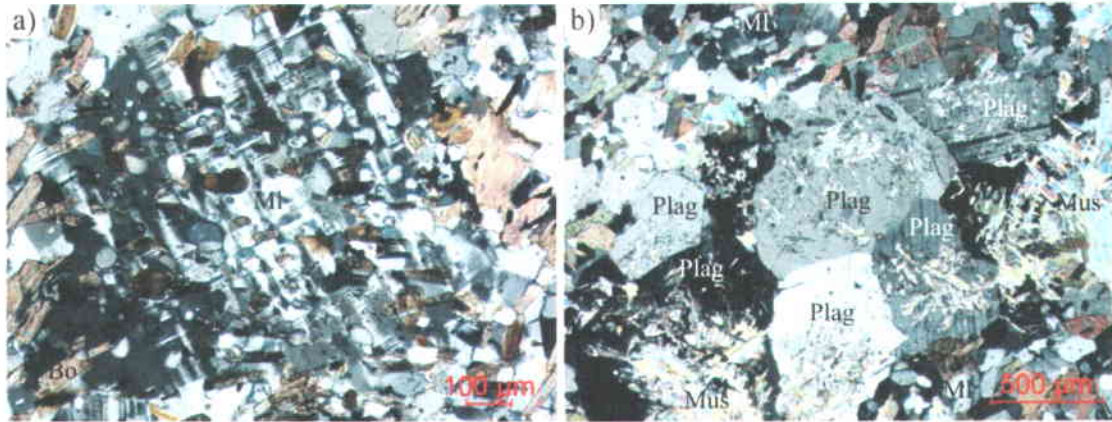


Figure 3.4.3: Cross-polarized photomicrograph showing examples of a microcline poikiloblast (a) and plagioclase porphyroblasts (b).

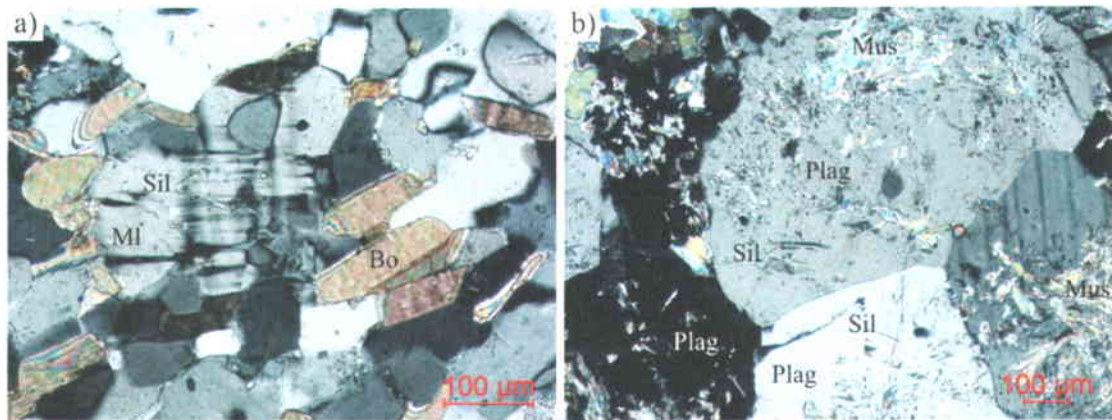


Figure 3.4.4: Cross-polarized photomicrograph showing examples of sillimanite coexisting with microcline (a) and plagioclase (b).

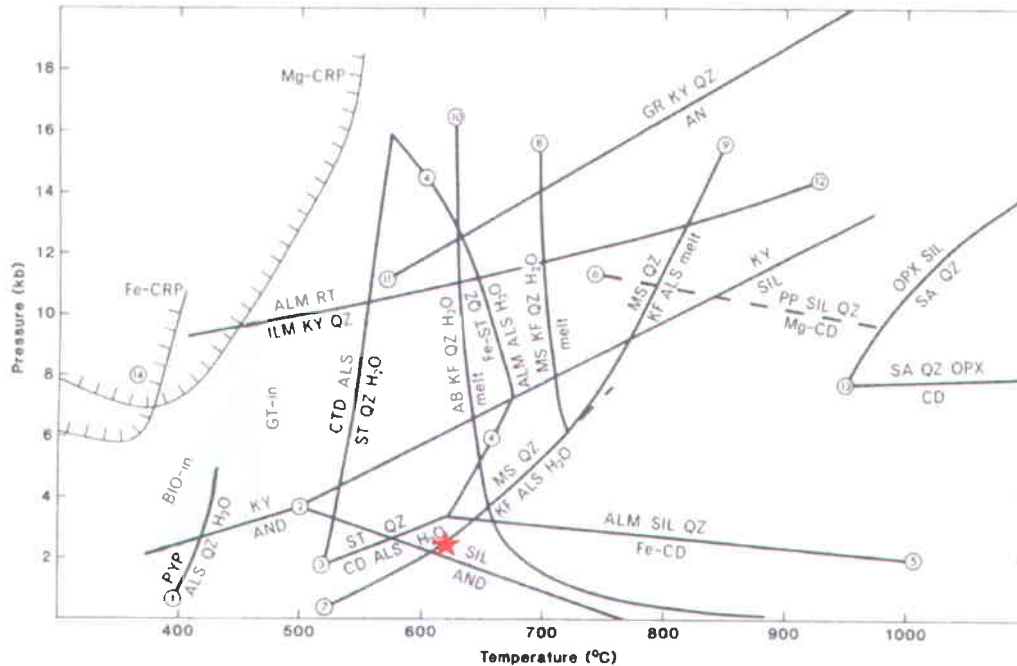
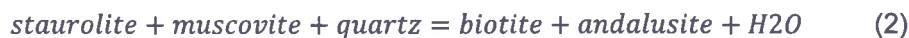


Figure 3.4.5: Petrogenetic grid for pelitic metasedimentary rocks from (Yardley, 1989). The red star indicates the minimum P-T conditions required for the formation of sillimanite through the breakdown of muscovite. The use of the pelitic grid is appropriate in this context since the average composition of aluminosilicate-bearing rocks resembles average compositions of metamorphosed pelitic schists (Table 3.2.3).

For reaction (1) to occur in the sillimanite stability field, pressure must be greater than 2 kb and temperature must be greater than 600°C (Figure 3.4.5). Moreover, since no evidence of melting was found in all inspected thin sections, reaction (1) must have occurred at pressures below 6 kb (Figure 3.4.5). Note also that the shape of the fibrolite porphyroblasts suggests that fibrolite is pseudomorphic. Since sillimanite is known to replace andalusite and that the shape of the porphyroblasts is consistent with the shape of andalusite, we can speculate that andalusite first formed and was later replaced by sillimanite. Such a sequence of events has been documented in other metamorphic terranes, for example in the Connemara (Ireland) (Barber and Yardley, 1985). There, the formation of andalusite occurred through the reaction:



Since no relic staurolite was observed in aluminosilicate-bearing rocks present around the Roberto deposit, the occurrence of reaction (2) remains purely speculative. The inferred minimum P-T peak conditions for the aluminosilicate-bearing rock of the Roberto area indicate that the rocks have at least reached the hornblende hornfels facies and most probably the lower pressure part of the amphibolite facies (Figure 3.4.6).

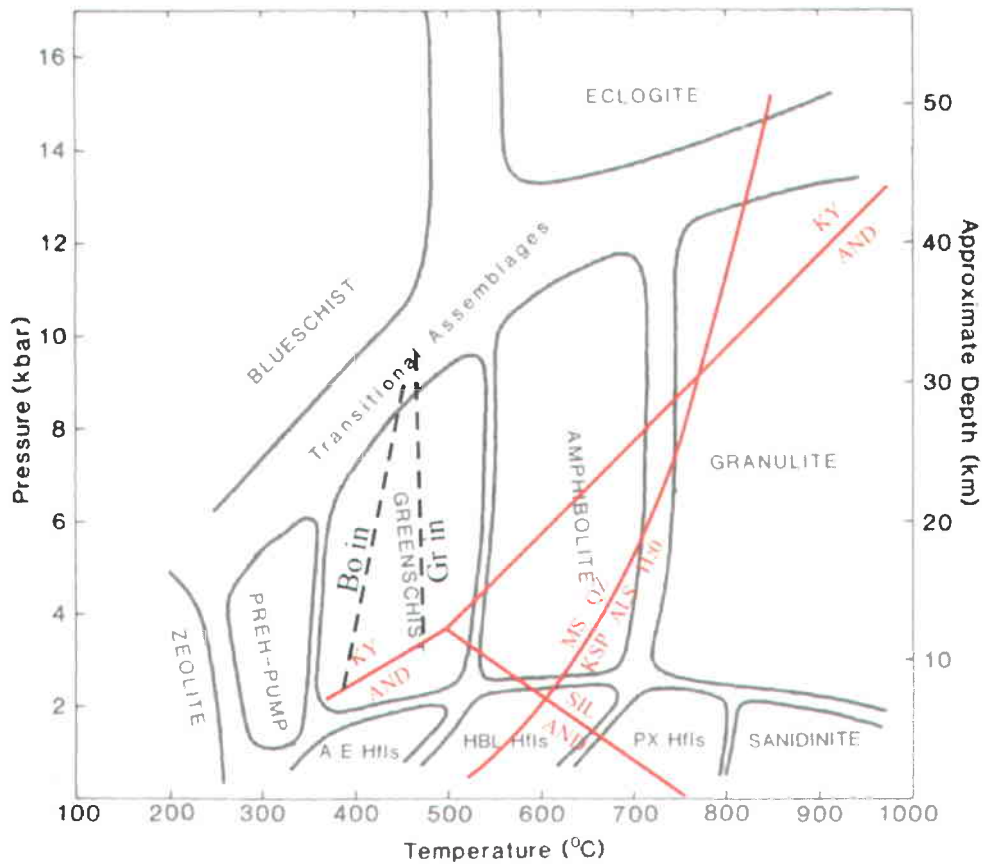


Figure 3.4.6: Metamorphic facies diagram with important reaction curves drawn from Figure 3.4.5. Modified from Yardley, 1989).

Sillimanite porphyroblasts are commonly retrograded to muscovite and quartz, which indicate that the reactants and products of reaction (1) were inverted after peak conditions. Photomicrographs of Figure 3.4.7 show the various stages of muscovite and quartz being formed at the expense of sillimanite and microcline during a retrograde stage of metamorphism. In Figures 3.4.7a and 3.4.7b, it can be seen that muscovite replaced the extremities of the sillimanite porphyroblast, but that the sillimanite core is preserved. Note also that on those Figures, the four phases are in contact with each other. In Figures 3.4.7c and 3.4.7d, only small relics of sillimanite are present within the muscovite porphyroblast. The muscovite crystal in the upper left corner is not oriented by the S_2 fabric which is defined alignment of small biotite porphyroblasts. Figures 3.4.7d and 3.4.7e show another example where only small relics of sillimanite remain in a larger muscovite crystal.

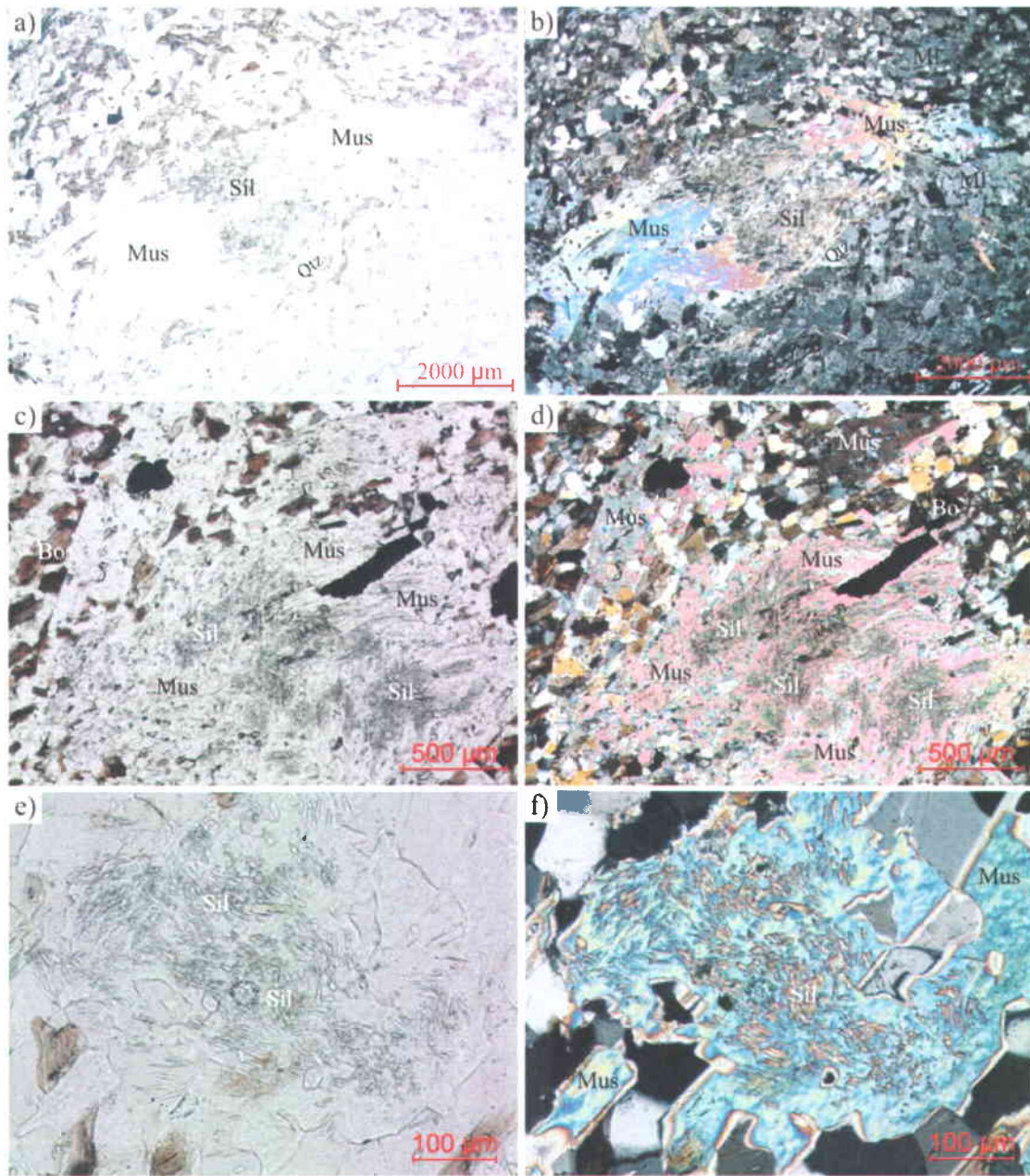


Figure 3.4.7: Natural light (left) and cross-polarized (right) photomicrographs showing the progressive retrogradation of sillimanite and microcline to muscovite and quartz. a) and b) muscovite replacing the extremities of sillimanite porphyroblast. c) and d) muscovite porphyroblasts with preserved relics of sillimanite. Note the post-tectonic texture of the porphyroblast in the upper left corner. e) and f) relic sillimanite within muscovite porphyroblast.

3.4.2 Timing with Deformational Events

The shape of aluminosilicate porphyroblasts indicates that they were affected by S_2 (e.g. Figure 3.4.2a), which suggests that D_2 outlasted their formation. Since the shape of the porphyroblasts is likely inherited from andalusite, the above statement does not necessarily apply to sillimanite. It is clear, however, that since muscovite porphyroblasts are not affected by S_2 or S_3 , their growth has outlasted D_2 and D_3 , (e.g. Figures 3.4.7c, 3.4.7d, 3.4.8a, and 3.4.8b) and hence that the episode of retrograde metamorphism also post-dates D_2 and D_3 . Since the effect of D_3 is typically to fold or crenulate already formed minerals without the generation of new minerals (e.g. Figure 3.4.8), metamorphic conditions during D_2 and D_3 were probably similar.

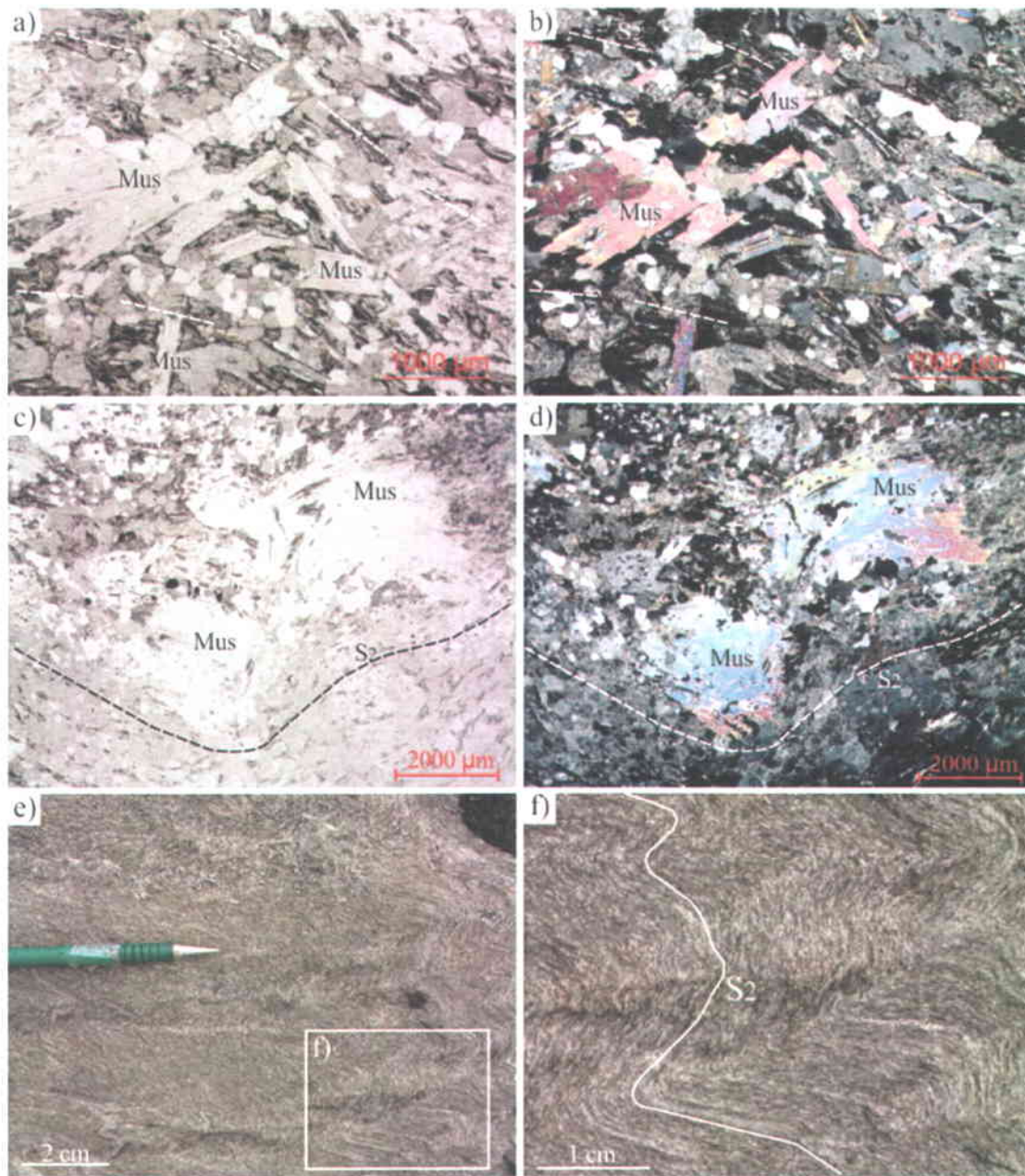


Figure 3.4.8: a) to d) Natural light (left) and cross-polarized (right) photomicrographs of crenulated S₂ foliation defined by biotite crystals. Muscovite porphyroblasts are not affected by S₂ or by the crenulation. e) photograph of S₃ crenulation from which photomicrographs a) to d) were taken. f) close-up on e).

3.5 Alteration and Mineralization

This section summarizes the main characteristics of auriferous zones and alteration assemblages present in the vicinity of the Roberto deposit. A method developed to identify least-

altered samples is first presented. Then, for each alteration and/or mineralization facies, general characteristics are presented, followed by a description of geochemical attributes, and finally by important mineralogical and textural characteristics that can be used to establish timing relationships with deformational and metamorphic events. A section is devoted to the mineralogy and the texture of sulphide minerals which can be used to determine their occurrence relative to the peak of metamorphism.

3.5.1 Introduction

The bulk of the auriferous system occurs in a series of sub-parallel decameter-scale auriferous zones located west of aluminosilicate-bearing rocks (Figure 3.5.1). On the large stripped outcrop, two principal auriferous zones, referred to as Roberto and East-Roberto, can be distinguished from one another based on their structural style, mineralogy, gold content, and stratigraphic position (Figures 3.5.1 and 3.5.2). At deposit-scale, the mineralogical and textural characteristics that define the Roberto and East-Roberto zones are found in other auriferous zones, within which they are sporadically distributed (Figure 3.5.1). Therefore, although Roberto and East-Roberto refer to specific auriferous zones, they also represent types of mineralization and alteration assemblages that form the main constituents of other auriferous zones (Figure 3.5.1). This is also the case for the mineralization known as the Lake Zone and the Mayappo Zone, although Mayappo-type mineralization does not form a continuous auriferous zone (Figure 3.5.1). Other auriferous zones possess unique characteristics, which are generally related to specific host rocks (e.g. biotite schist, paragneiss, iron formation (Puncho zone)) (Figure 3.5.1). Gold mineralization is also hosted by pegmatite dykes but such auriferous zones are sporadic and do not typically form continuous auriferous zones.

Significant gold values are widely distributed over the area and are not restricted to the series of auriferous zones located west of aluminosilicate-bearing rocks. Gold mineralization is associated with a large-scale protracted hydrothermal system composed of Ca-bearing and/or potassic and/or boron-rich assemblages. Another potential alteration facies is represented by aluminous zones which are primarily characterized by the presence of aluminosilicate porphyroblasts. Like previously mentioned, such aluminous zones either represents metapelitic units or acid-leached alteration products that were subsequently metamorphosed.

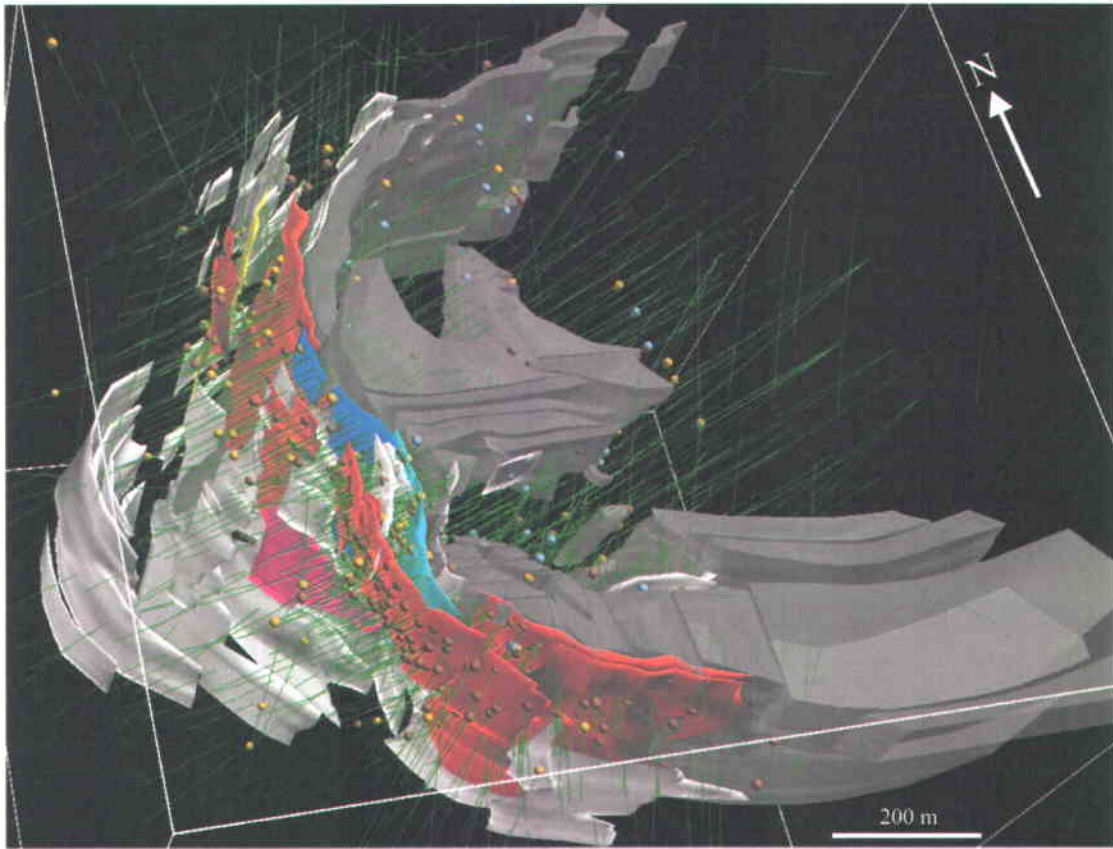


Figure 3.5.1: Gocad snapshot showing the distribution of auriferous zones (red: Roberto zone, pale blue: East-Roberto zone, blue: Lake zone, yellow: biotite schist-hosted auriferous zone, purple: paragneiss-hosted auriferous zone, white: other auriferous zones) and aluminosilicate-bearing rock (grey). Other lithological units are not represented to simplify the map. Spheres mark drill hole regions where Opinaca Mines' geologists have noted Roberto-type mineralization (orange), East-Roberto type mineralization (yellow), and Mayappo-type mineralization (blue). The "other" auriferous zones (white) are locally constituted of Roberto- and East-Roberto-type mineralization. Green lines represent drill hole traces.

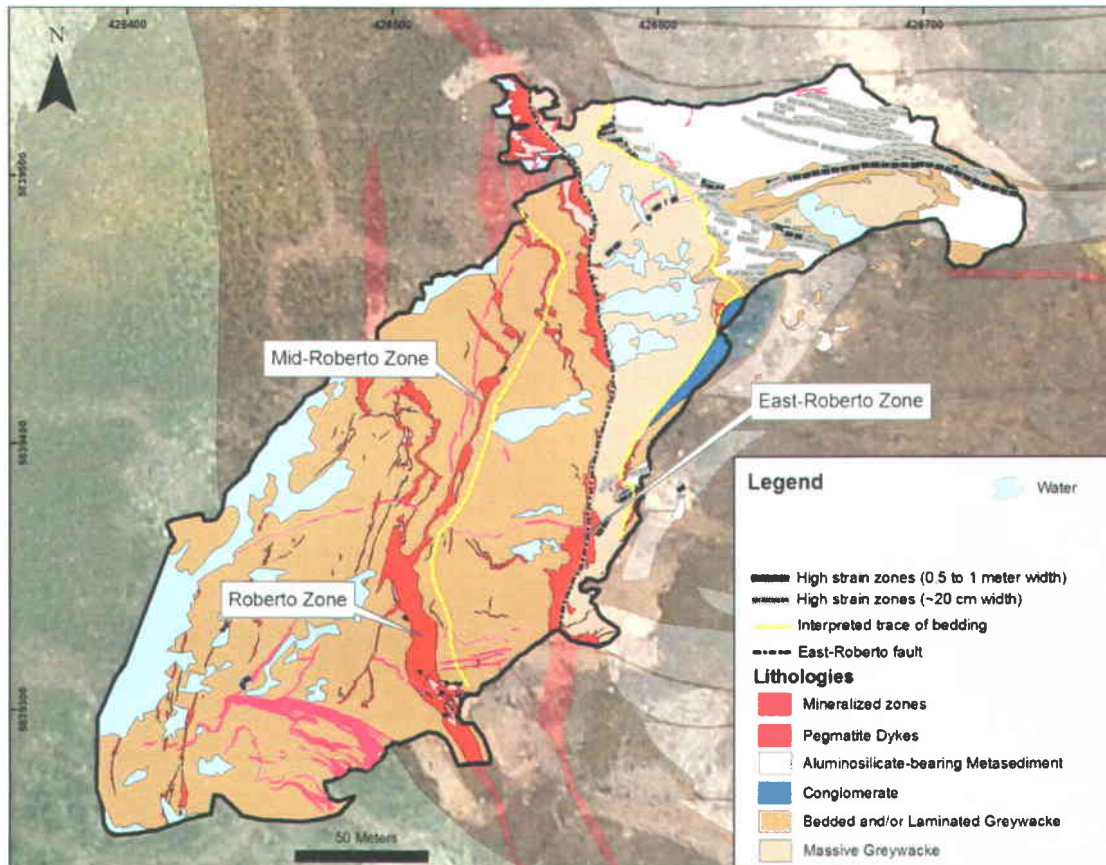


Figure 3.5.2: Geological map showing the location of the two principal (Roberto and East-Roberto) and one subsidiary (Mid-Roberto) auriferous zones present on the large stripped outcrop. Coordinates are in UTM Nad83.

3.5.2 Least Altered Samples

Least altered samples within Élénore's turbidite sequence need to be identified in order to:

1. Calculate an average composition for Élénore's turbidite sequence and investigate if it displays a particular geochemical signature compared to other turbidite sequence of the Superior Province (see section 3.2.1.1 *Turbiditic Greywacke*).
2. Calculate average compositions of specific lithological units within the sequence which can potentially represent least-altered protoliths of mineralized host rocks.

A preliminary group of 106 "unaltered" turbidite samples (all from this study) was first identified through macroscopic inspection of hand samples. Samples within this group do not show evidence of alteration and are completely devoid of veins and weathered surfaces.

Opinaca Mines Ltd.'s channel samples were excluded since they are likely to be contaminated by veinlets and weathering.

The selected samples were inspected through a petrographic microscope in order to better define their mineralogy. Of the 106 "least-altered" samples, 70 contain microcline. In general, the presence of microcline in metasedimentary rocks can be attributed to the nature of the source (i.e. rock initially contained alkali feldspar), potassic alteration, metamorphism, or a combination of these factors. Of the 70 microcline-bearing samples, 34 contain an extremely high proportion of microcline (>50%) which probably indicates that they have been subjected to potassic hydrothermal alteration. On the other hand, 14 contain microcline as poikiloblasts only, which can alternatively result from prograde metamorphic reactions.

The quantitative method developed by Fedo et al. (1995) to estimate the proportion of potassium added to a suite of metasomatized sedimentary rocks was used to complement the petrographic work and identify the samples that have been the least affected by hydrothermal alteration, specifically potassic alteration.

The method consists in plotting the samples in A-CN-K space where A, CN, and K represent molar proportions of Al_2O_3 , $CaO^* + Na_2O$, and K_2O respectively (CaO^* represents Ca in silicate-bearing minerals only) (Figure 3.5.3). On such a diagram, an unaltered suite of sedimentary rocks should plot along a straight line parallel to the A-CN join (Fedo, Nesbitt and Young, 1995). The spread of data along such a line is commonly caused by weathering of plagioclase and K-feldspar to clay minerals (Nesbitt and Young, 1984). This weathering effect can also be estimated by the chemical index of alteration (CIA) which consists in calculating the ratio $[Al_2O_3 / (Al_2O_3 + CaO^* + Na_2O + K_2O)] \times 100$ (where CaO^* represents Ca in silicate-bearing minerals only) (Nesbitt and Young, 1982). The intersection of an extended line passing through the data points with the feldspar join provides an estimate of the rock's initial plagioclase/K-feldspar ratio (Figure 3.5.3) (Fedo, Nesbitt and Young, 1995). Potassic metasomatism, through the conversion of plagioclase to K-feldspar for example, will offset the weathering trend towards the "K" apex (Fedo, Nesbitt and Young, 1995).

In order to test the method, a suite of unaltered samples from the Quetico Subprovince (data from Doyon, 2004) was plotted in A-CN-K space (Figure 3.5.3). This suite was chosen because it was analyzed for CO_2 , which is required to calculate the CaO^* concentration mentioned above. The results show that the distribution trend has a shallower slope than the theoretical weathering trend, which suggests that this suite of samples has been affected to

some degree by potassic metasomatism. Since the suite has presumably not been subjected to hydrothermal alteration, potassium enrichment is most likely associated to common K-adding weathering processes such as K-metasomatism associated with meteoric waters (e.g. Rainbird, Nesbitt and Donaldson, 1990).

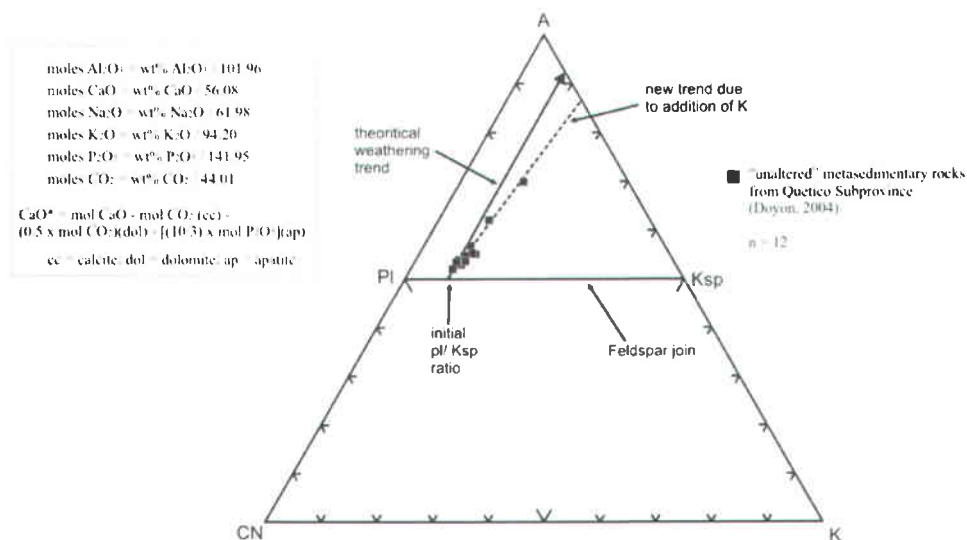


Figure 3.5.3: A-CN-K ternary plot of "unaltered" metasedimentary rocks from the Quetico Subprovince. Although identified as unaltered, the diagram suggests that this suite of samples has been affected by potassic metasomatism. The intersection of the line passing through the data with the feldspar join provides an estimate of the initial plagioclase/K-feldspar ratio.

The 106 turbidites samples interpreted to be least-altered after inspection of hand specimen were grouped by lithology (greywacke, aluminous sequence, massive greywacke, and paragneiss) and plotted in A-CN-K space in order to identify samples that have not undergone significant hydrothermal potassic alteration and that can be used to calculate average compositions. Samples in which abundant microcline was petrographically identified, and samples in which microcline is present as poikiloblasts only, are labelled differently on the diagrams. Figures 3.5.4a and 3.5.4b shows the A-CN-K diagram for 71 greywacke samples that appeared unaltered after hand sample inspection. The slope of the trend line through the data is similar to the theoretical line, which suggests that samples plotting near the line were not significantly altered. On the other hand, a large proportion of samples clearly deviate from the trend line, suggesting that they have been subjected to significant potassic alteration. Accordingly, petrographic work indicates that most of the samples that plot far from the trend line contain abundant microcline (Figures 3.5.4c and 3.5.4d). One can therefore speculate that the presence of abundant microcline results from hydrothermal alteration rather than from a high

proportion of authigenic K-feldspar or from K-adding weathering processes. Interestingly, samples in which microcline is strictly present as poikiloblasts plot near the trend line, which could suggest that the presence of poikiloblastic microcline in these samples results from isochemical metamorphic reactions rather than hydrothermal alteration. Samples plotting below the feldspar join might originate from a more mafic source, as their compositions plot near the composition of gabbro (Figures 3.5.4c and 3.5.4d). Samples considered “least altered” are those that do not contain abundant microcline and that plot outside the “altered” region (shaded triangle) of the A-CN-K diagram.

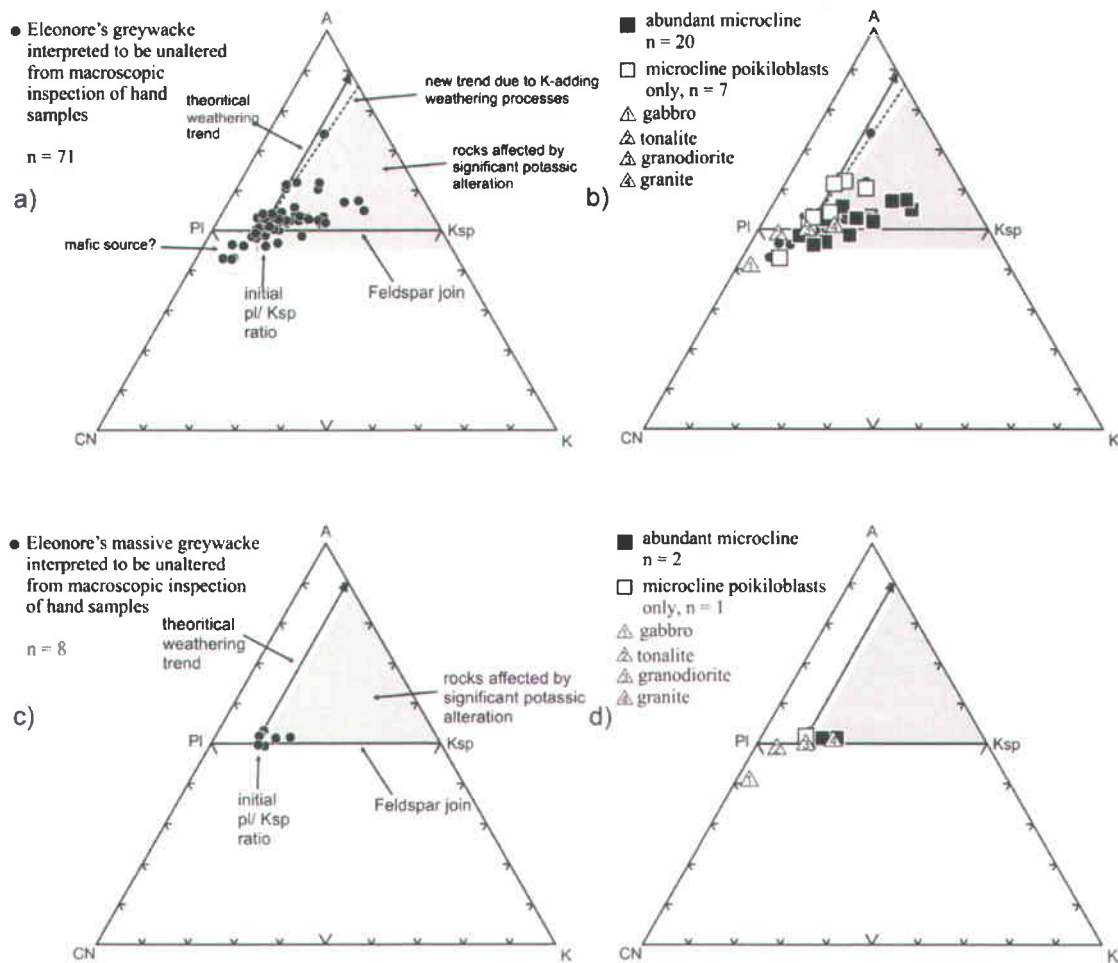


Figure 3.5.4: A-CN-K ternary plots of selected lithological units within Éléonore's turbidite sequence. All samples were initially interpreted to be unaltered after macroscopic inspection. Right-side diagrams show same data as left-side diagrams but with symbols indicating presence of abundant microcline or microcline poikiloblasts (based on petrographic work). Numbered triangles indicate fresh composition of selected lithological units (from Fedo et al., 1995 and references therein). Shaded area indicates regions susceptible to have been subjected to significant potassic alteration. a) and b): greywacke. c) and d): massive greywacke. e) and f): aluminosilicate-bearing sequence. g) paragneiss.

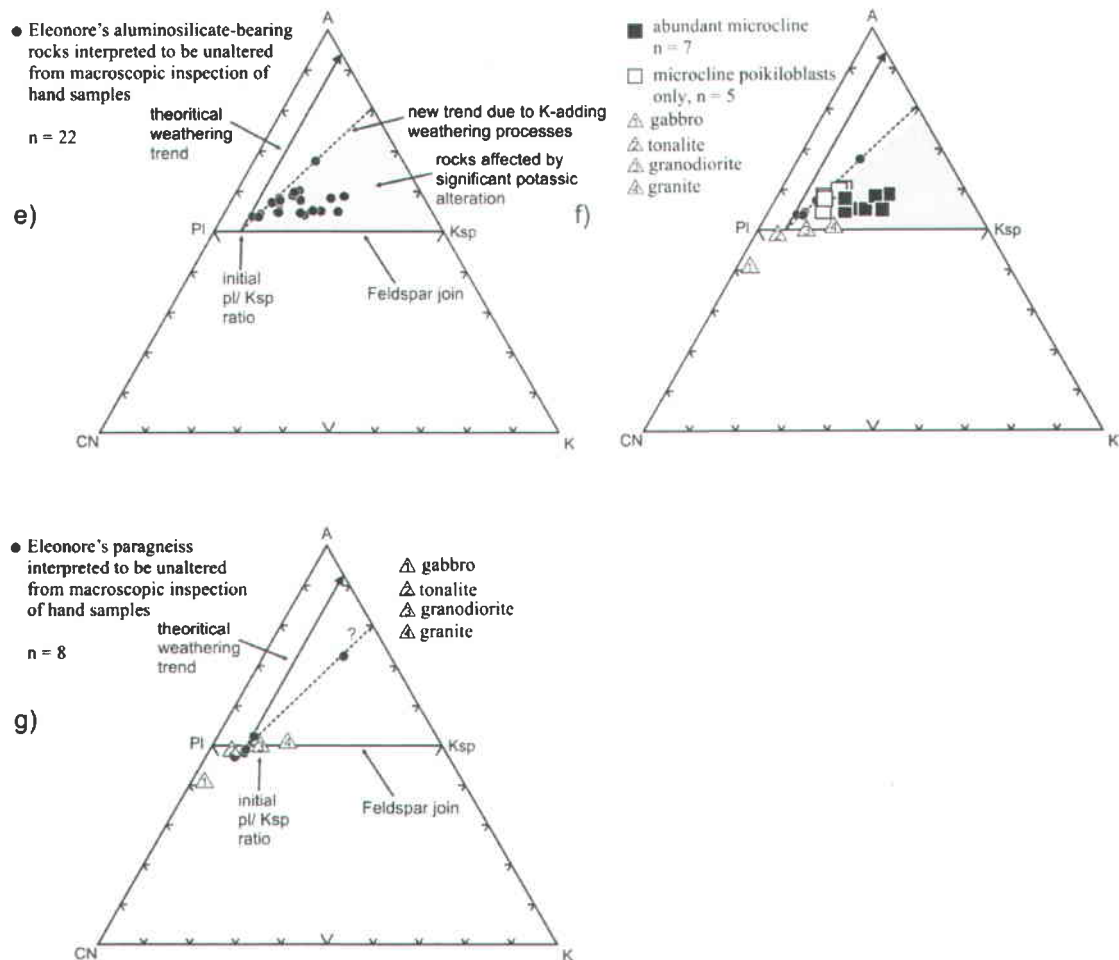


Figure 3.5.4: (continued).

The same exercise was conducted for the massive greywacke, the aluminosilicate-bearing sequence, and the paragneiss units (Figures 3.5.4e to 3.5.4g). The number of samples for the massive greywacke is limited (n=8) which makes it difficult to trace a trend line. However, similarly to what is found for the greywacke samples, massive greywacke samples containing abundant microcline clearly plot to the right of the other samples.

For the aluminosilicate-bearing sequence, the line passing through the samples that do not contain abundant microcline has a shallower slope than the theoretical trend, which may suggest that even those samples were affected by potassic metasomatism. Whether that episode of potassium enrichment is related to an early weathering event or an episode of hydrothermal alteration is difficult to assess. However, since samples containing abundant

microcline clearly deviate from that trend, we can speculate that the microcline-free samples are “fresher” than the microcline-bearing samples. Similarly to what is observed for the greywacke and massive greywacke units, samples only containing microcline-poikiloblasts have fresher compositions than the samples containing abundant microcline.

The distribution of paragneiss samples in A-CN-K space is difficult to interpret since the suite only contains 8 samples and none of the samples contain microcline. Only the sample that plots far from the group is interpreted to be altered. Note the higher initial plagioclase/K-feldspar ratio of the aluminosilicate and paragneiss sequence compared to the greywacke and massive greywacke units. All ratios indicate that these suites of rocks initially contained a certain proportion of alkali feldspars. Samples considered unaltered after both petrographic inspection and A-CN-K investigation were grouped together to calculate the average composition of Éléonore’s turbidite sequence (Tables 2.5.1 and 2.5.2). Unaltered samples located within a 1 km radius of the Roberto deposit were used to calculate average compositions of selected lithological units (Tables 3.2.1 and 3.2.2).

3.5.3 Aluminous Assemblages

Like previously mentioned in section 3.2.1.3 *Aluminosilicate-Bearing Units*, it is uncertain whether the presence of aluminosilicate porphyroblasts is related to acid-leached sedimentary rocks that generated aluminosilicate porphyroblasts during metamorphism, or simply reflects the metamorphosed primary pelitic character of the rocks. The fact that their distribution near the Roberto deposit locally follows the distribution of other lithological units (e.g. conglomerate and/or arenite, Figures 3.2.1, 3.2.7), however, strongly suggests that they represent lithological units that were prone to develop aluminosilicate porphyroblasts upon metamorphism, regardless of how they acquired their aluminous character. Also, the fact that aluminosilicate-bearing rocks are common in the region (Bandyayera and Fliszár, 2007) suggests that they are not confined to the deposit area and that their formation might relate to regional metamorphism.

The possibility that aluminosilicate-bearing rocks result from acid-leached sedimentary rocks can be investigated through the use of isocon diagrams. The use of isocon diagrams was first elaborated by Grant (1986) to provide a simple graphical solution to Gresens (1967) equation for metasomatic alteration. The method consists in plotting the element and/or oxide concentrations of an altered rock against the concentrations of a least-altered equivalent. On such a graph, immobile components (typically TiO_2 , Al_2O_3 , Zr, and Y) that define a straight line

through the origin represent the isocon. Gains and losses of mobile components are given by their displacements relative to the reference isocon. The slope of the isocon should approximate "1" if no significant volume change occurred upon alteration, and that a steeper or gentler slope indicate that the altered rock has suffered volume decrease or increase, respectively. Following that method, it is possible to test if aluminosilicate-bearing rocks represent altered equivalent of greywacke by plotting their element and oxide concentrations to check if they define an isocon. In the affirmative, one could conclude that it is possible (but not necessary) that aluminosilicate-bearing rocks represent altered equivalents of greywacke. In that scenario, the aluminous character of the rocks would result from an acid hydrothermal alteration that leached mobile elements and consequently enriched the relative proportion of immobile elements (including Al_2O_3). On the other hand, if the distribution of elements does not define an isocon, one could conclude that either the interpreted protolith is wrong or that the aluminous character of aluminosilicate-bearing rocks is primary and does not result from alteration (i.e. they are metapelites). In this exercise, the "old greywacke" of section 3.2.1.1 (tables 3.2.1 and 3.2.2) was hypothesized to represent the "unaltered" protolith of aluminosilicate-bearing rocks since like aluminosilicate-bearing rocks, it belongs to the older sedimentary sequence inferred in section 3.2.1.1 *Turbiditic Greywacke*. In order to include a broader compositional spectrum of hypothetical protoliths, the exercise was also conducted using the average composition of massive greywacke which also belongs to the older sequence. The resulting graphs are shown on Figure 3.5.5.

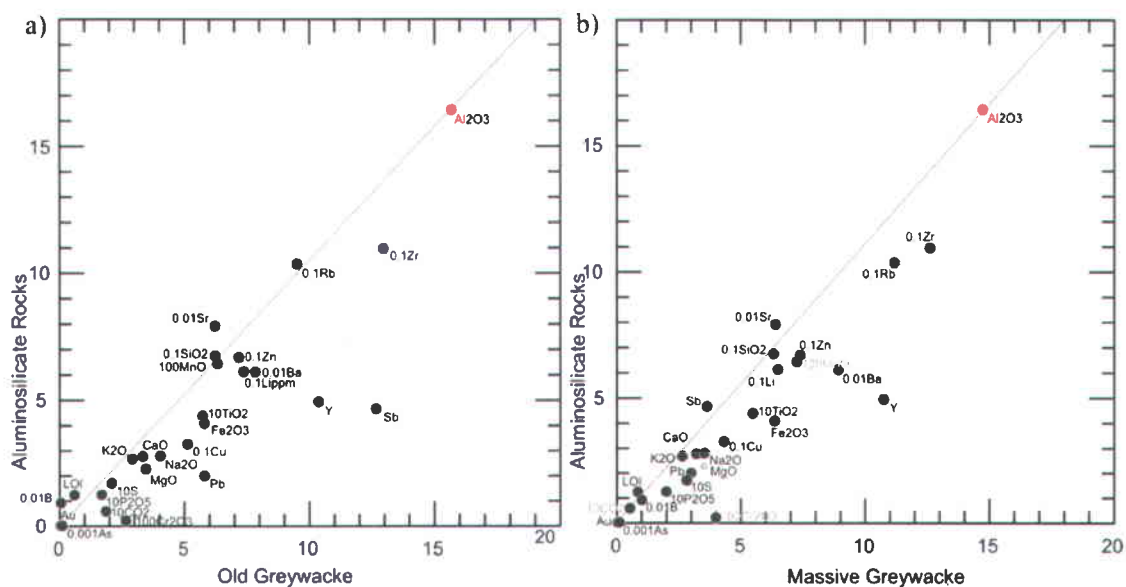


Figure 3.5.5: Diagrams comparing the element and oxide concentrations in aluminosilicate-bearing rocks with concentrations in “old greywacke” (a) and in “massive greywacke” (b). All concentrations represent average compositions of least-altered samples (listed in tables 3.2.1, 3.2.2, 3.5.1, and 3.5.2). Oxide concentrations are in weight percent and element concentrations are in ppm (except for Au which is in ppb). Following the method of Grant (1986), some concentrations are scaled so that they have the same order of magnitude and plot relatively close to each other. For both (a) and (b), the hypothetical isocon line drawn assuming constant aluminum do not pass through any other immobile elements (TiO₂, Zr, or Y), which suggests that neither of the two least-altered candidates represent the protolith of aluminosilicate-bearing rocks.

The results indicate that for both protoliths, isocon lines interpreted based on constant aluminum (constant aluminum is assumed based on the working hypothesis that aluminosilicate-bearing rocks were generated through acid leaching) do not pass through any other immobile elements (TiO₂, Zr, or Y), and no isocon passing through more than one immobile element can be constructed. This suggests that neither of the two least-altered candidates represent the protolith of aluminosilicate-bearing rocks. One can therefore conclude that either the aluminous character of aluminosilicate-bearing rocks is primary, or that their aluminous character results from alteration of an unidentified protolith whose geochemistry differs from the two least-altered candidates used in this model.

3.5.4 Ca-bearing Alteration

Ca-bearing alteration represents the most evident alteration around the Roberto deposit. Ca-bearing alteration principally occurred within the intrados of the deposit-scale fold (Figures 3.5.6 and 3.5.7), but also affected rocks located several km from the deposit (see section 2.5.5). Ca-bearing alteration is locally contained within all lithological units but the pegmatite dykes, and

represents an important component of the principal auriferous zones. Outside auriferous zones, rocks affected by Ca-bearing alteration commonly carry anomalous gold values (<100 and >500 ppb Au) and are locally significantly auriferous (> 1g/t Au).

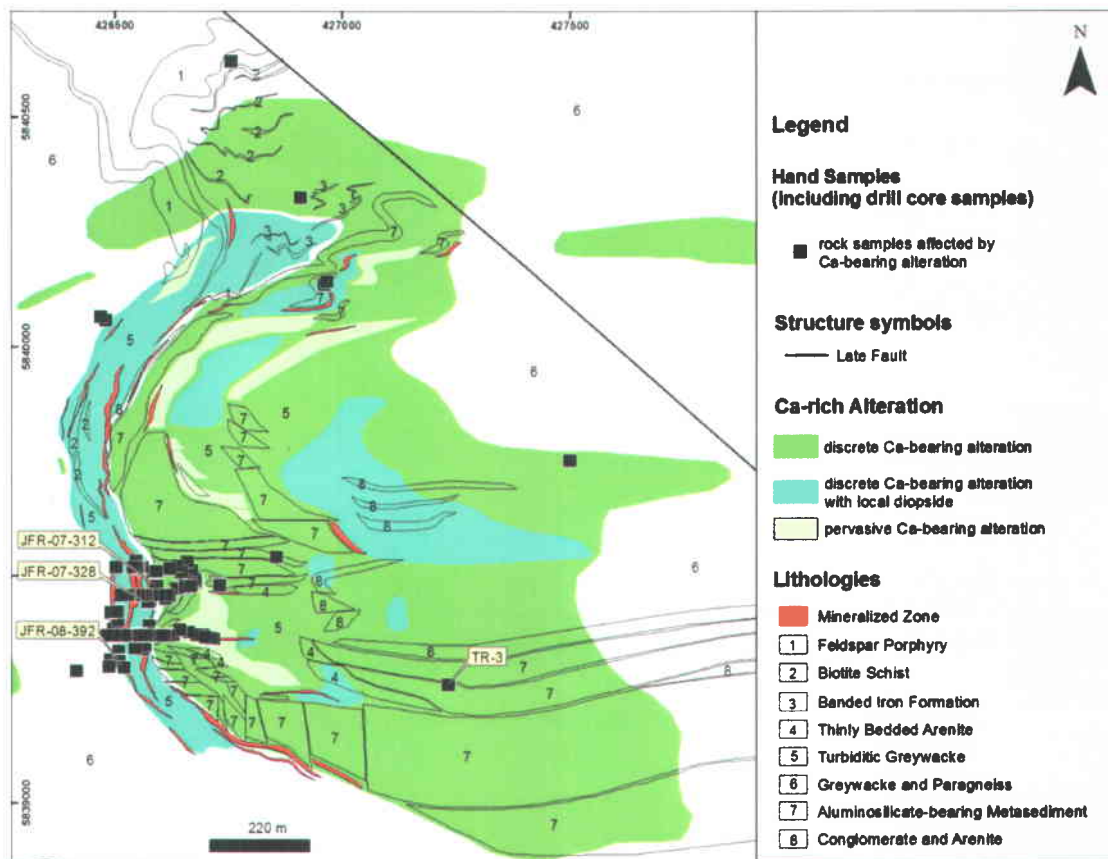


Figure 3.5.6: Geological map of the Roberto deposit area showing regions and hand samples affected by Ca-bearing alteration. Ca-bearing alteration is principally distributed in the intrados of the deposit-scale fold outlined by the principal auriferous zones. The map was constructed from projection of the 3D Gocad model of Figure 3.5.7. Pegmatite dyke swarms and diabase dykes are not displayed to simplify visualization. Labeled samples refer to specific samples used for petrographic or geochemical analysis. Coordinates are in UTM Nad83.

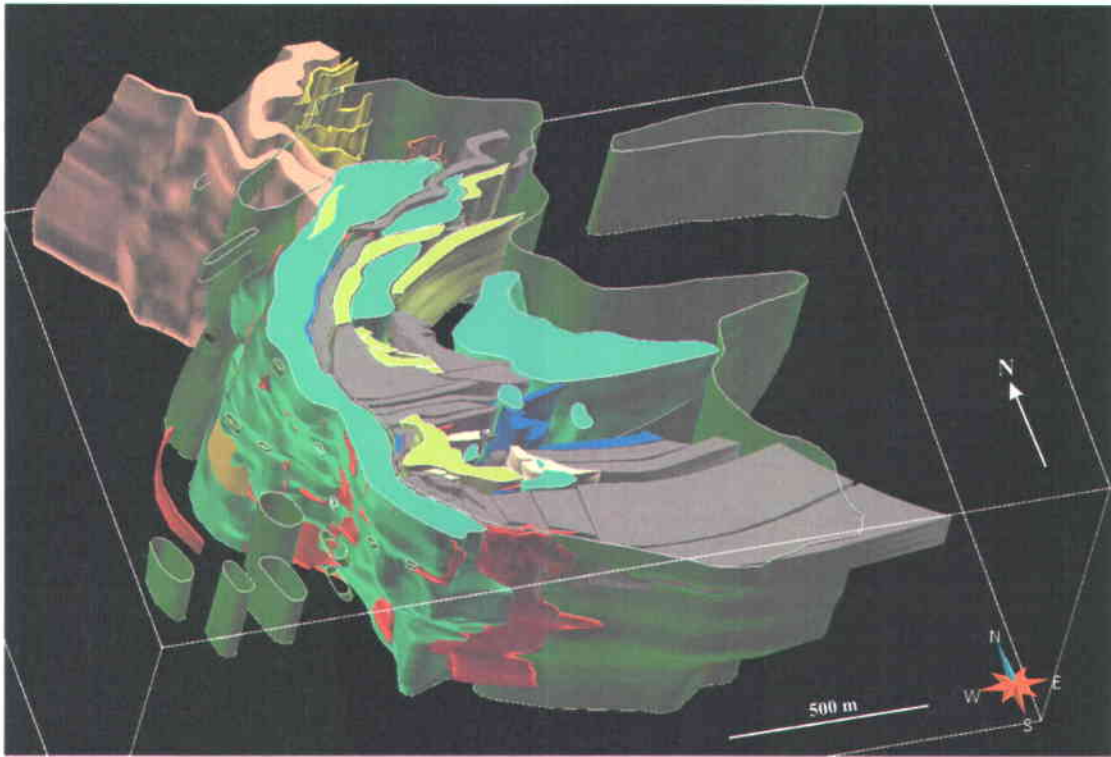


Figure 3.5.7: Gocad snapshot showing the distribution of Ca-bearing alteration from which the map of Figure 3.5.6 was constructed. The green surfaces represent envelopes that limit the general distribution of Ca-bearing alteration (forest green: discrete Ca-bearing alteration, bright green: discrete Ca-bearing alteration with local diopside, yellowish green: pervasive Ca-bearing alteration). LITHOLOGICAL UNITS are color-coded according to previous Gocad snapshots (red: auriferous zones, grey: aluminosilicate-bearing metasedimentary rocks, blue: conglomerate and arenite, yellow: biotite schist, orange: banded iron formation, pale yellow: thinly bedded arenite, pink: feldspar porphyry). Turbiditic greywacke and paragneiss are the dominant rock types present in empty regions of the 3D space. Pegmatite dyke swarms and diabase dykes are not displayed to simplify visualization. The methodology used to construct such representations is described in *Annex 1*.

The textural and geochemical/mineralogical characteristics (see upcoming sections) of Ca-bearing alteration change in function of the host rock. In aluminosilicate-bearing rocks, Ca-bearing alteration formed replacement bands that are concordant (e.g. Figure 3.5.8a) and discordant (e.g. Figure 3.5.8b) to bedding planes. In bedded and massive greywacke, the distribution of Ca-bearing alteration is fracture-controlled and forms 1-5 cm wide replacement bands and selvages, some associated with discrete quartz-feldspar veins (Figure 3.5.8c). In massive greywacke Ca-bearing alteration also locally occurred as pervasive metasomatic replacement zones (Figure 3.5.8d) and fracture-controlled stockworks (Figure 3.5.8e). In auriferous zones and in the vicinity of auriferous zones, Ca-bearing alteration is typically present as calc-silicate-bearing quartz veins and/or Ca-bearing replacement (e.g. Figure 3.5.8f) (see sections below).

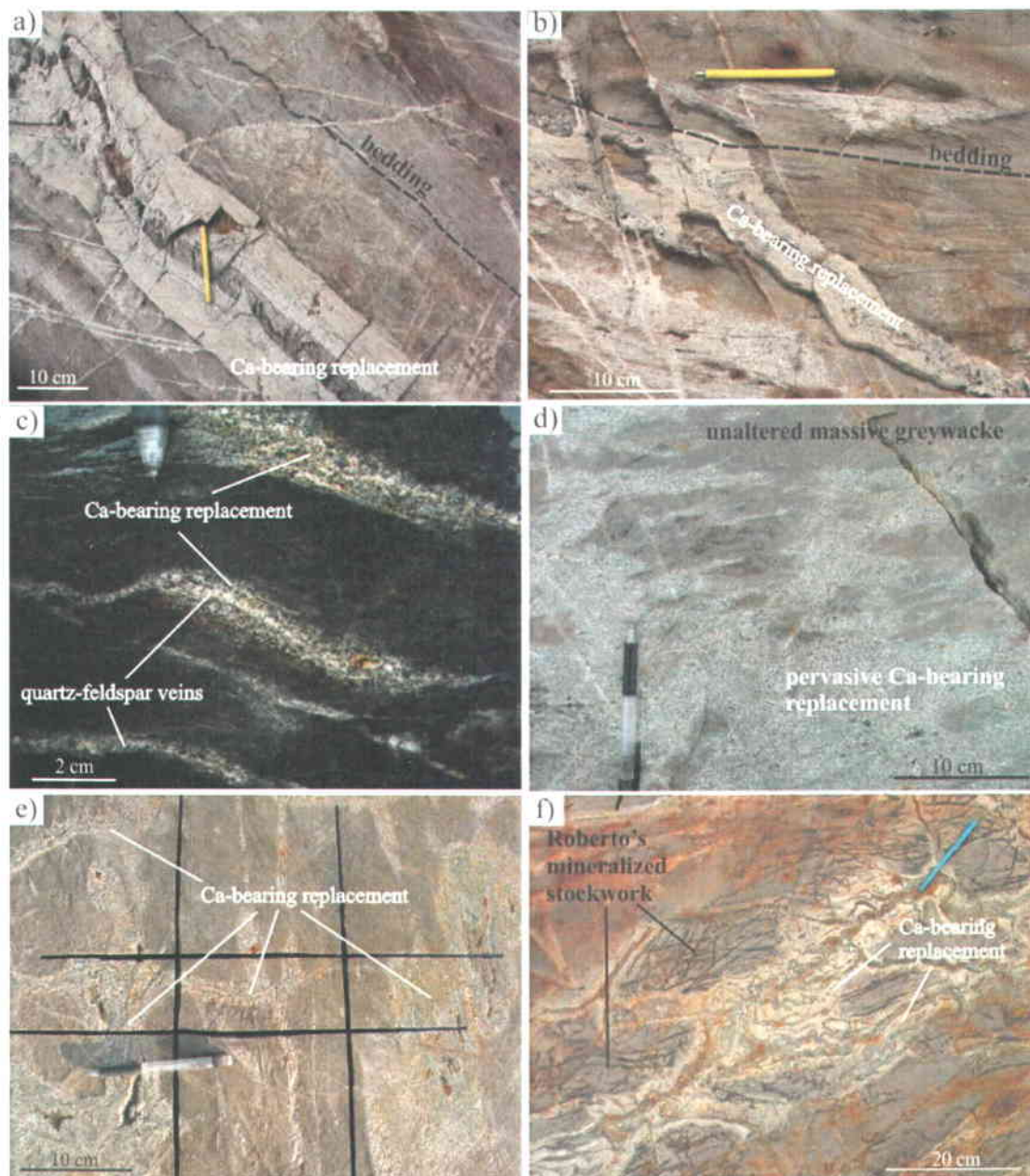


Figure 3.5.8: Photographs showing: a) Ca-bearing replacement concordant to bedding in aluminosilicate-bearing rocks. b) Ca-bearing replacement discordant to bedding in aluminosilicate-bearing rocks. c) Ca-bearing replacement in massive greywacke. Note the local presence of quartz-feldspar veins. d) pervasive Ca-bearing replacement in massive greywacke. e) fracture-controlled Ca-bearing stockwork in greywacke. f) Ca-bearing replacement in auriferous stockwork of Roberto. Photographs (a) and (b) courtesy of Benoit Dubé. Photographs (c) and (d) modified from Ravenelle et al. 2010.

On the large stripped outcrop, Ca-bearing veins and replacement structures are widely distributed over the entire outcrop, but are thicker (up to 50 cm) and more numerous in between Roberto and East-Roberto auriferous zones (Figure 3.5.9). In the eastern part of the outcrop,

Ca-bearing replacement is present in aluminosilicate-bearing units, and pervasive replacement is present in massive greywacke (Figure 3.5.9). At deposit-scale, such pervasive zones are mainly located in the structural hanging wall of the western aluminosilicate-porphyroblasts-bearing unit (Figures 3.5.6 and 3.5.7).

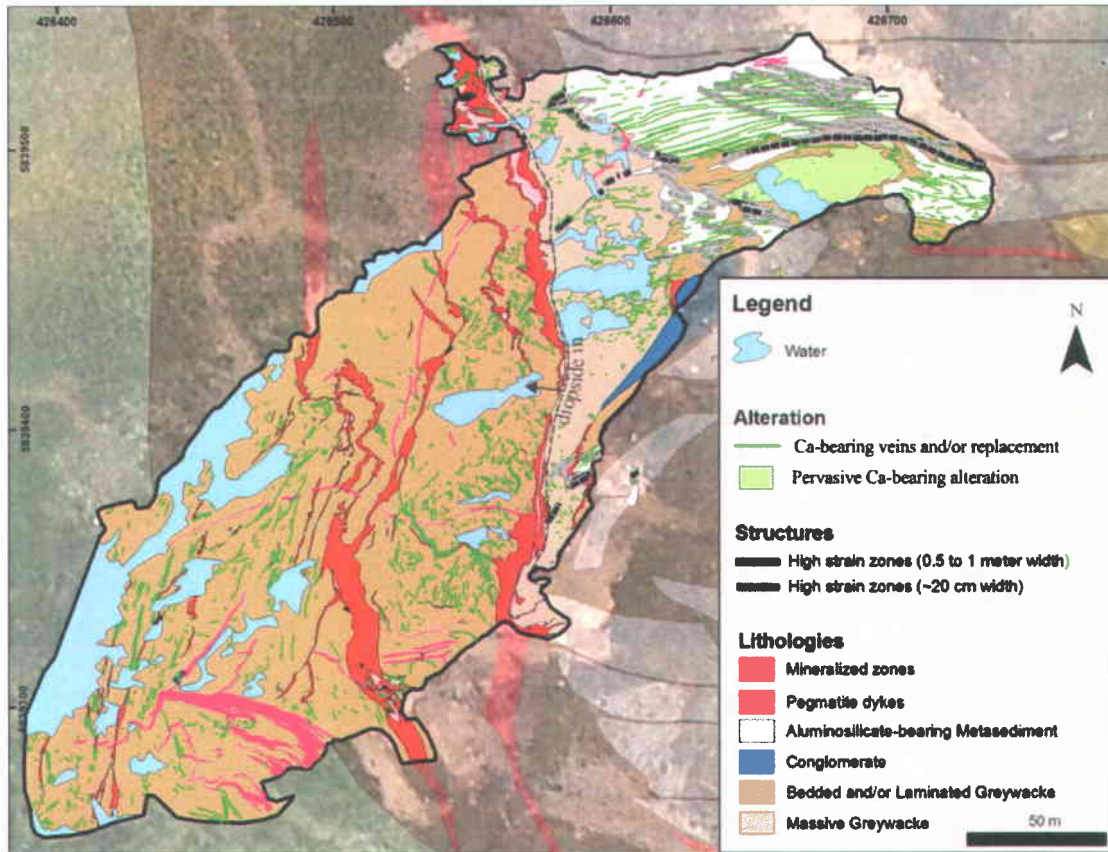


Figure 3.5.9: Geological map of the large stripped outcrop showing the distribution of Ca-bearing alteration. Although not represented on the map, Ca-bearing veins and replacement are also present in auriferous zones. The grey dashed line marks the location at which calc-silicate-bearing veins start to bear significant proportions of diopside. Coordinates are in UTM Nad83.

3.5.4.1 Mineralogical and Petrographic Characteristics of Ca-bearing Assemblages

This section presents the mineralogical and petrographic characteristics of Ca-bearing replacement and calc-silicate-bearing veins. As previously mentioned, the nature of the host rock affects the mineralogy and textural characteristics of Ca-bearing alteration. In aluminosilicate-bearing rocks, Ca-bearing replacement bands can be subdivided into an outer,

intermediate, and central part, all of which having different textures and/or mineral assemblages (Figures 3.5.10 and 3.5.11, and Table 3.5.1).

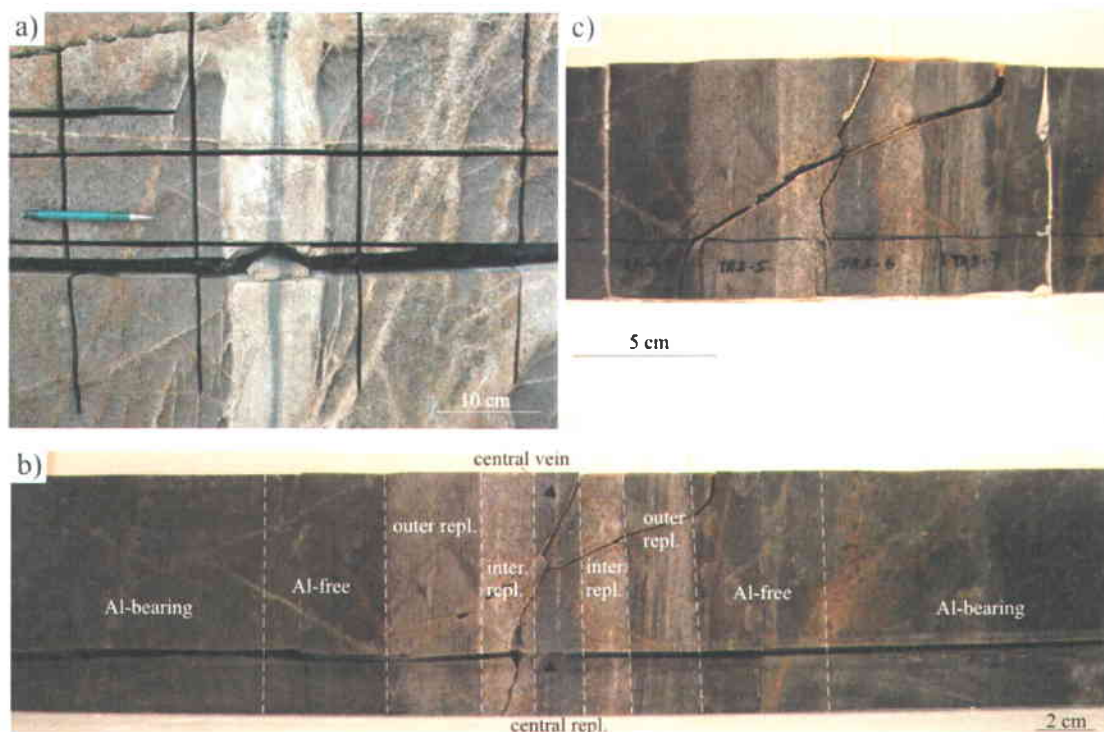


Figure 3.5.10: Photographs showing: a) Ca-bearing replacement in aluminosilicate-bearing rocks on outcrop. b) details of Ca-bearing replacement on sawed section of sample shown in (a). c) close-up of section shown in (b).

Table 3.5.1: Mineralogy and average gold content of Ca-bearing replacement and of host rocks within aluminosilicate-bearing sequence. Forward slash (/) means "replaced by" (e.g. Bo/Chl/Preh means biotite replaced by chlorite and prehnite). Codes of symbols are given in Table 3.5.2.

Location within sample	Mineralogy	aver. Au (ppb)	σ	
Al-bearing part	Qtz-Bo-Sil/Mus/Sr-Plag-Mus-Ml-Tl-Po-Py \pm Asp	18	22	n=9
host rock in ctc with repl. (Al-free)	Qtz-Bo-Plag-Tl-Po-Py \pm Asp	<5	NA	n=6
outer part of repl.	Qtz-Bo/Mus/Preh/Chl-Mus-Prh-Sr-Ss-Cz-Tl-Po \pm Asp	7	10	n=13
intermediate part of repl.	Qtz-Bo/Chl/Mus/Preh-Mus-Prh-Sr-Ss-Cz-Tl-Po \pm Gr \pm Asp			
central part of repl.	Qtz-Bo/Chl/Mus/Preh-Ss-Sr-Cz-Mus-Prh-Po \pm Gr \pm Asp			
central vein (when present)	Qtz-Mus-Preh-Cz-Po			

Table 3.5.2: Symbols of minerals used in this study.

And	andalusite	Chl	chlorite	Mus	muscovite	Qtz	quartz	Tl	tourmaline
Amp	amphibole	Cz	clinozoisite	Plag	plagioclase	Sil	sillimanite	Au	visible gold
Asp	arsenopyrite	Di	diopside	Po	pyrrhotite	Sr	sericite		
Bo	biotite	Gr	garnet	Preh	prehnite	Ss	saussurite		
Carb	carbonate	Ml	microcline	Py	pyrite	Ti	titanite		

The outer part generally consists of sericitized and saussuritized plagioclase, biotite porphyroblasts locally replaced by muscovite/chlorite and/or prehnite, and minor clinozoisite, prehnite, tourmaline, pyrrhotite, and arsenopyrite (Figures 3.5.11c and 3.5.11d). The intermediate part is coarser-grained than the outer part, but except for the addition of Ca-bearing garnet, has the same mineralogy. The central part is also coarser-grained and is characterized by higher percentages of clinozoisite, absence of tourmaline, and by the fact that biotite is completely replaced by muscovite and/or chlorite and/or prehnite (Figures 3.5.11e and 3.5.11f). A central vein composed of quartz, muscovite, prehnite, clinozoisite, and pyrrhotite is locally present. Ca-bearing replacement in aluminosilicate-bearing sequences is typically not auriferous (Table 3.5.1).

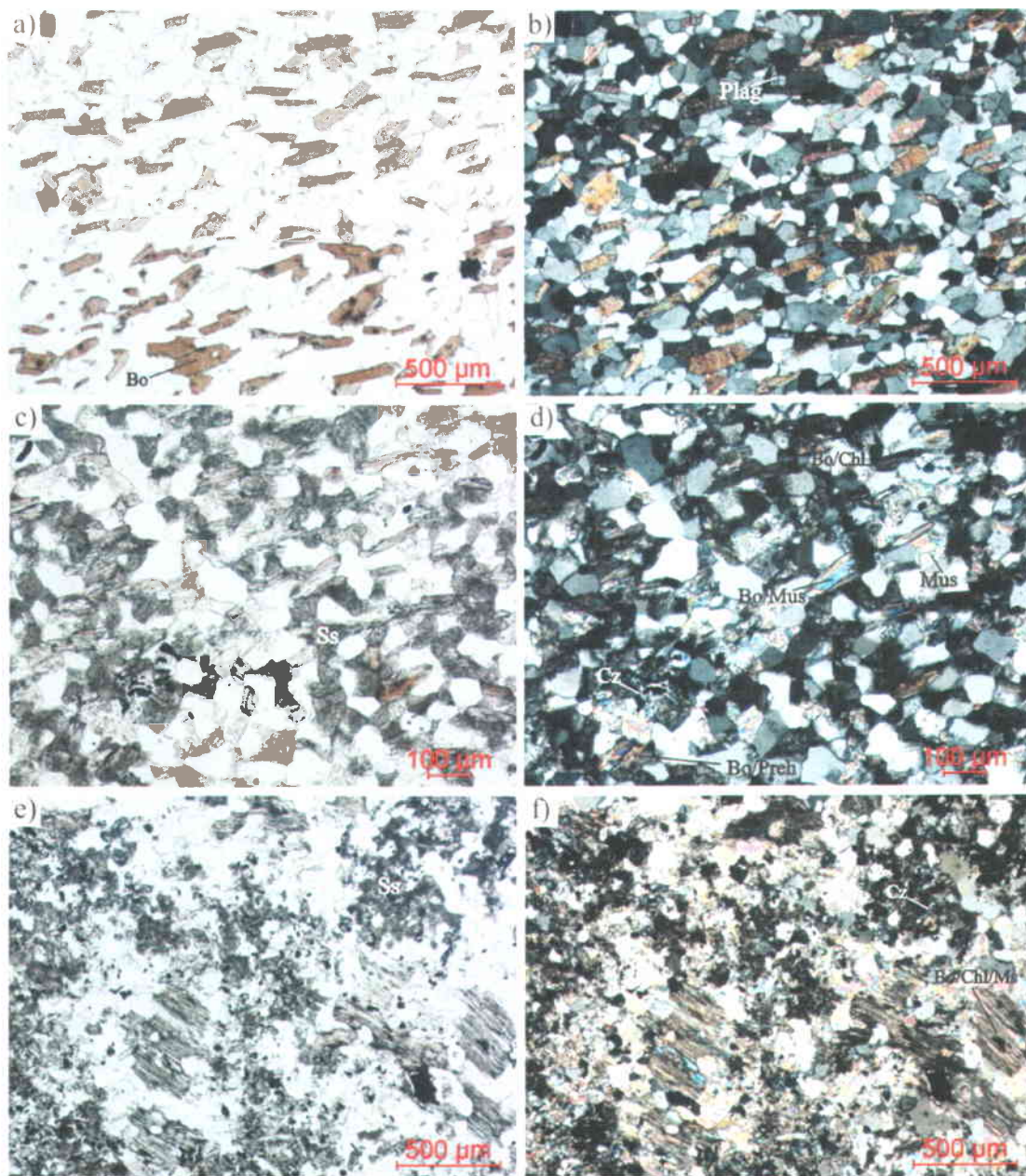


Figure 3.5.11: Natural light (left) and cross-polarized (right) photomicrographs of Ca-bearing replacement and host rocks in aluminosilicate-bearing sequence. a) and b) aluminosilicate-free host rock in contact with Ca-replacement. c) and d) outer part of Ca-bearing replacement. Note the saussuritized plagioclase and the muscovite and/or chlorite and/or prehnite replacing biotite. e) and f) central part of Ca-replacement. Note the presence of coarse (~500 μm) biotite porphyroblasts replaced by chlorite and/or muscovite and/or prehnite. Note also the abundance of clinozoisite and saussuritized plagioclase. Opaque minerals of all photographs are sulphide minerals. Codes of symbols are given in Table 3.5.2.

In other lithological units, such as massive greywacke, host rocks located near Ca-bearing replacement zones are composed of quartz, biotite, plagioclase, microcline, amphibole, and minor tourmaline, pyrrhotite, pyrite, and arsenopyrite (Figures 3.5.12, 3.5.13c and 3.5.13d, and Table 3.5.3). The host rocks in contact with Ca-bearing replacement are coarser-grained and are characterized by more abundant microcline and amphibole, and by the fact that biotite is locally replaced by chlorite (Figures 3.5.13e and 3.5.13f). The Ca-bearing replacement is itself coarser-grained and contains quartz, actinolite, plagioclase, sericitized and saussuritized plagioclase, carbonate, titanite, clinozoisite, prehnite, and accessory tourmaline, pyrrhotite, arsenopyrite, and pyrite (Figures 3.5.13g and 3.5.13h). Where present, central veins are composed of quartz, amphibole, plagioclase, carbonate, diopside, and minor amounts of titanite, prehnite, clinozoisite, saussuritized and sericitized plagioclase, pyrrhotite, pyrite, and arsenopyrite (Figures 3.5.13i and 3.5.13j). Non-pervasive Ca-bearing alteration in massive greywacke is generally not auriferous (Table 3.5.3)

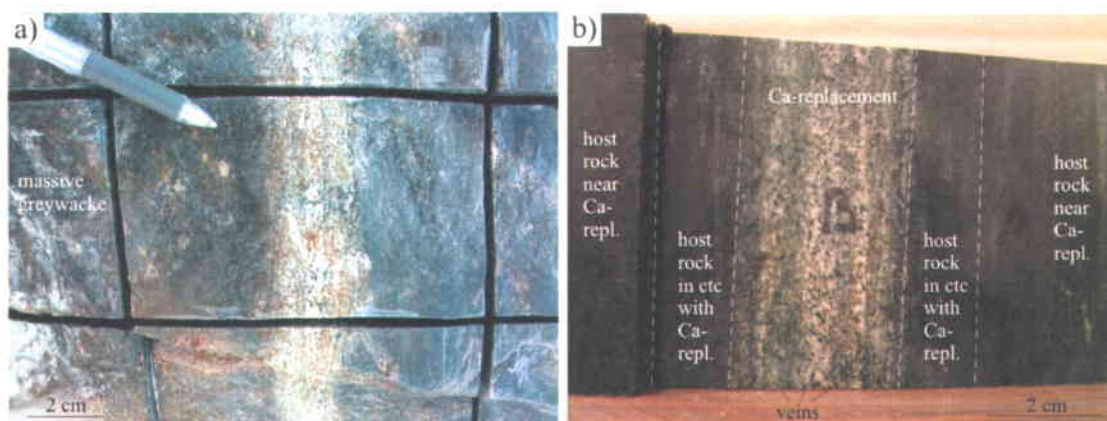


Figure 3.5.12: Photographs showing: a) Ca-bearing replacement within massive greywacke on outcrops. b) details of Ca-bearing replacement on sawed section of sample shown in (a). Note the presence of 3 veins within Ca-bearing replacement.

Table 3.5.3: Mineralogy and average gold content of Ca-bearing replacement in massive greywacke and of massive greywacke host rocks. Forward slash (/) means "replaced by" (e.g. Bo/Chl means biotite replaced by chlorite). Codes of symbols are given in Table 3.5.2.

Location within sample	Mineralogy	aver. Au (ppb)	σ	
massive gw host rock far from Ca-	Qtz-Bo-Plag \pm Amp \pm Tl \pm Ml \pm Py \pm Po	25	15	n=5
host rock near Ca-repl.	Qtz-Bo-Ml-Plag-Amp-Tl-Po \pm Py \pm Asp	11	7	n=9
host rock in ctc with repl.	Qtz-Bo/Chl-Amp-Ml \pm Plag \pm Tl-Po \pm Py \pm Asp	32	40	n=7
Ca-replacement	Qtz-Amp-Plag-Carb-Ti-Prh-Cz-Ss-Sr \pm Tl-Po \pm Py \pm Asp	74	76	n=12
central vein(when present)	Qtz-Amp \pm Di-Plag-Carb-Ti \pm Prh \pm Cz \pm Ss \pm Sr \pm Po \pm Py \pm Asp			

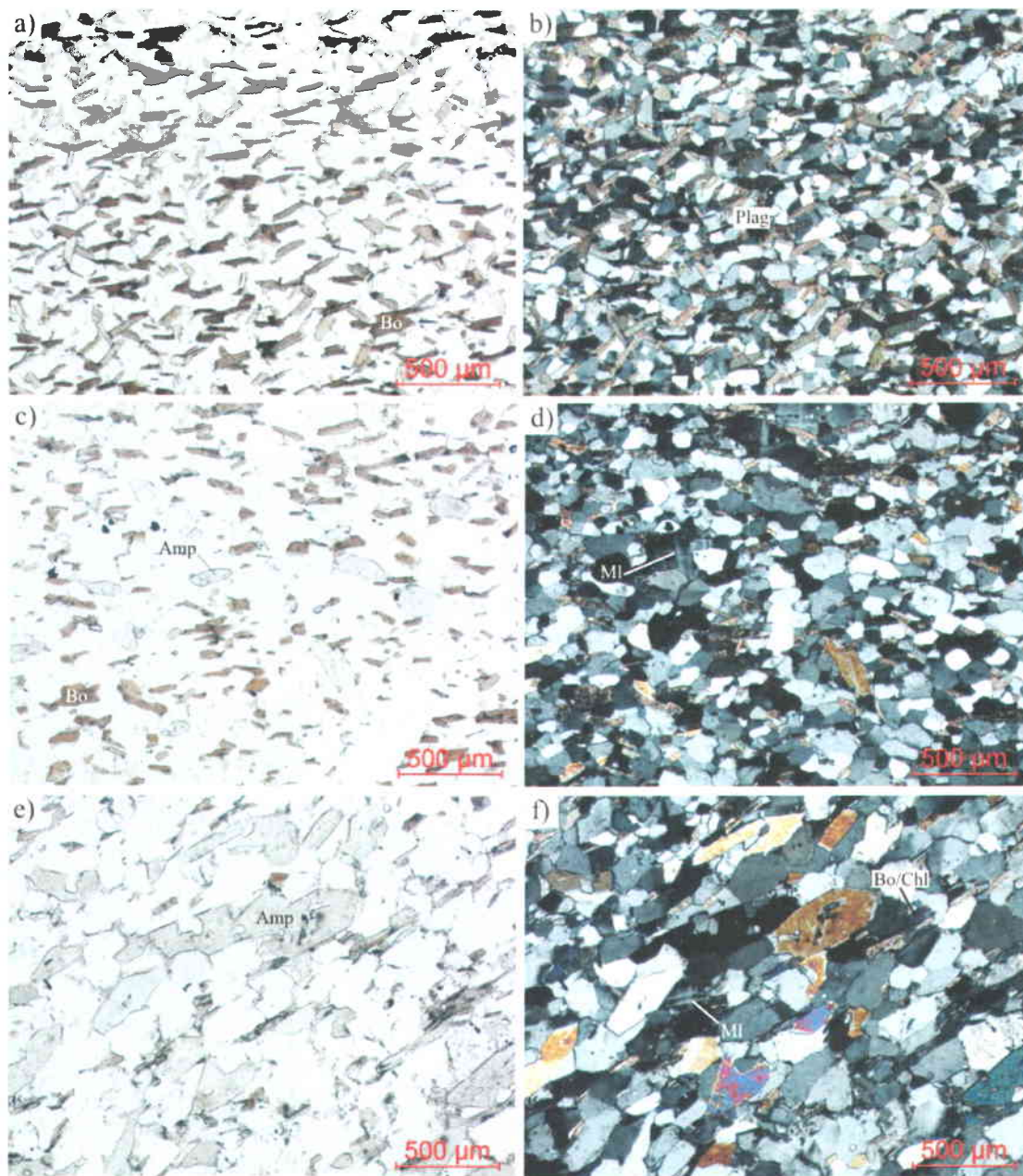


Figure 3.5.13: Natural light (left) and cross-polarized (right) photomicrographs of Ca-bearing replacement in massive greywacke and of massive greywacke host rocks. a) and b) least-altered massive greywacke located far from any significant Ca-bearing alteration. c) and d) massive greywacke host near Ca-bearing replacement. Note the presence of microcline and amphibole crystals. e) and f) massive greywacke host in contact with Ca-bearing replacement. Note the increase in grain size and the replacement of biotite by chlorite. Opaque minerals of all photographs are sulphide minerals. Codes of symbols are given in Table 3.5.2.

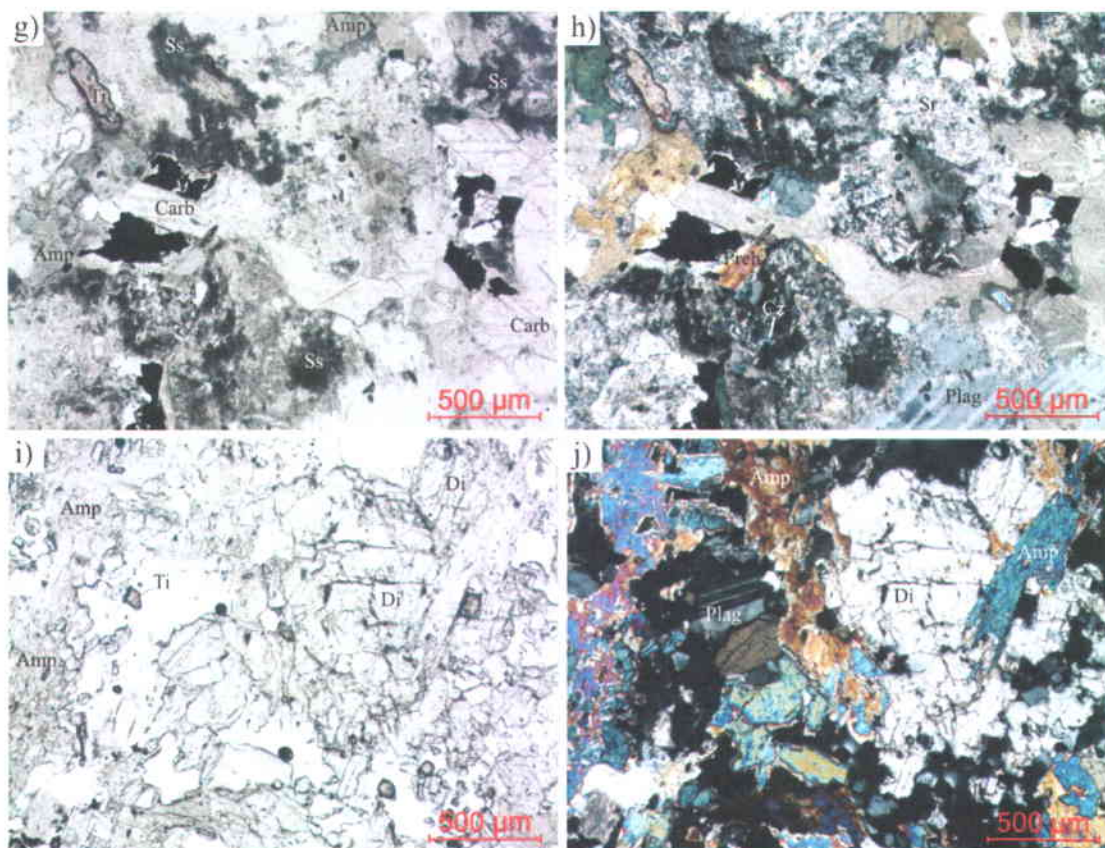


Figure 3.5.13: (continued). g) and h) Ca-bearing replacement in massive greywacke. Note the presence of plagioclase, carbonates, saussurite, titanite, prehnite, and clinozoisite. i) and j) central vein of Ca-bearing alteration in massive greywacke. Note the presence of coarse diopside. Opaque minerals of all photographs are sulphide minerals. Codes of symbols are given in Table 3.5.2.

The mineralogy of fracture-controlled stockworks and pervasive metasomatic replacement zones are dominated by Ca-rich amphibole (actinolite), saussuritized and sericitized plagioclase, local microcline, and accessory pyrrhotite titanite and carbonate. Anomalous gold values (< 1 g/t Au) are locally associated with these pervasive replacement zones.

In greywacke host rocks, Ca-bearing alteration is principally present as calc-silicate-bearing veins (e.g. Figure 3.5.14). Greywacke host rocks located near calc-silicate-bearing veins are characterized by quartz, biotite (locally replaced by chlorite), amphibole, plagioclase, and minor amounts of microcline, tourmaline, pyrrhotite, and arsenopyrite (Figures 3.5.15c and Figure 3.5.15d). Greywacke host rocks in contact with calc-silicate-bearing veins have similar mineralogy but have lower percentages of biotite, higher percentages of amphiboles, arsenopyrite, and tourmaline, and contain saussuritized and sericitized plagioclase (Figures

3.5.15e and 3.5.15f). Calc-silicate-bearing veins in greywacke are composed of quartz, diopside, amphibole, titanite, saussuritized and sericitized plagioclase, and minor pyrrhotite, arsenopyrite, and visible gold (Figures 3.5.15g and 3.5.15h). Tourmaline is absent or in traces only. Calc-silicate-bearing veins and nearby altered greywacke host rocks contain significant gold concentrations (Table 3.5.4). Note, however, that most of those veins were sampled between East-Roberto and Roberto auriferous zones.

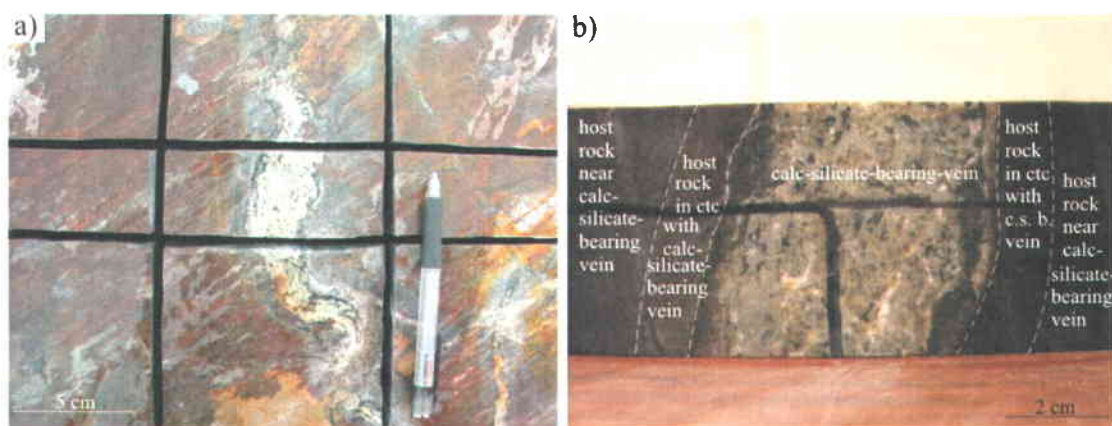


Figure 3.5.14: Photographs showing: a) calc-silicate-bearing vein in greywacke on outcrops. b) details of calc-silicate-bearing vein on sawed section of sample shown in (a).

Table 3.5.4: Mineralogy and average gold content of calc-silicate-bearing veins in greywacke and of greywacke host rocks. Forward slash (/) means "replaced by" (e.g. Bo/Chl means biotite replaced by chlorite). Codes of symbols are given in Table 3.5.2.

Location within sample	Mineralogy	aver. Au (ppb)	σ	
least-altered greywacke	Qtz-Bo-Plag \pm Ml-Po \pm Py	99	149	n=24
host rock near Ca-vein	Qtz-Bo-Bo/Chl-Amp-Plag \pm Ml \pm Tl-Asp-Po	3931	13038	n=22
host rock in ctc with vein	Qtz-Amp-Tl-Bo-Bo/Chl-Ss-Sr-Plag \pm Ml-Asp-Po \pm Au	5095	5148	n=11
calc-silicate-bearing vein	Qtz-Di-Amp-Ss-Sr \pm Ti \pm Po \pm Asp \pm Au	3197	5694	n=36

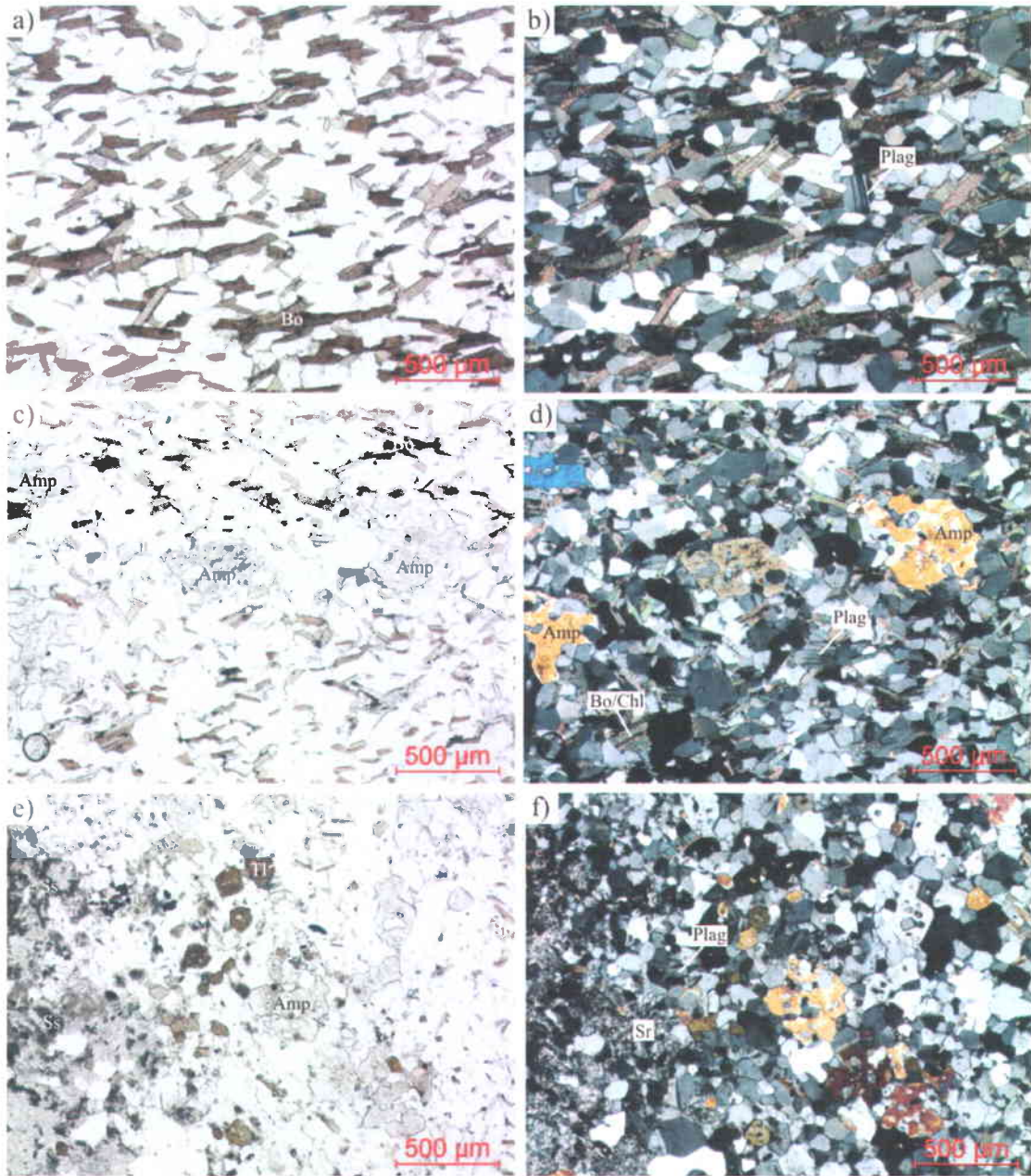


Figure 3.5.15: Natural light (left) and cross-polarized (right) photomicrographs of calc-silicate-bearing vein in greywacke and of greywacke host rocks. a) and b) least-altered greywacke located far from any significant Ca-bearing alteration. c) and d) greywacke host near calc-silicate-bearing vein. Note the presence of amphibole crystals. e) and f) greywacke host in contact with calc-silicate-bearing vein. Note the presence of tourmaline crystals and saussuritized plagioclase. Opaque minerals of all photographs are sulphide minerals. Codes of symbols are given in Table 3.5.2.

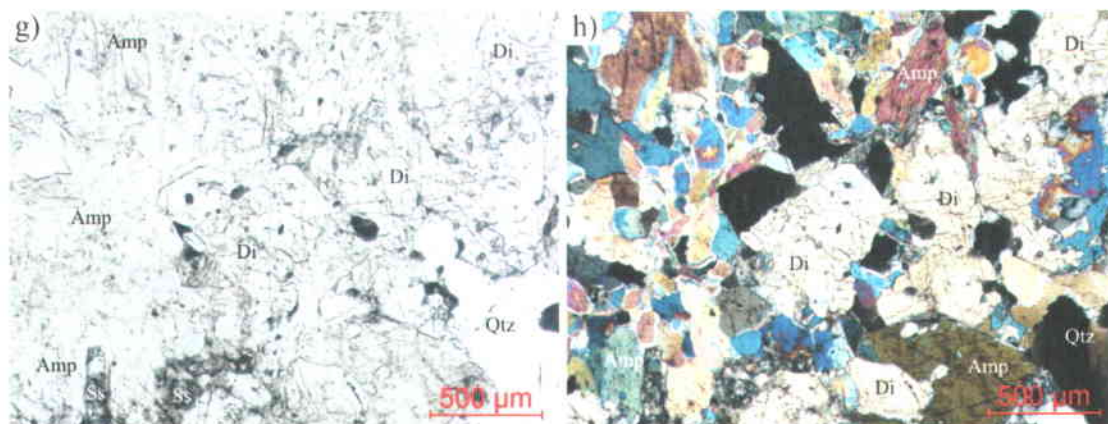


Figure 3.5.15: (continued). g) and h) calc-silicate-bearing vein in greywacke. Note the presence of coarse diopside and amphibole crystals. Opaque minerals are sulphide minerals. Codes of symbols are given in Table 3.5.2.

Calc-silicate-bearing veins are also present in the East-Roberto zone (Figure 3.5.16). There, host rocks located near calc-silicate-bearing veins are composed of quartz, amphibole, tourmaline, microcline, and minor biotite (locally replaced by chlorite and/or prehnite), saussuritized and sericitized plagioclase, clinozoisite, prehnite, titanite, pyrrhotite, arsenopyrite, and pyrite (Figures 3.5.17a and 3.5.17b). The host rocks in contact with calc-silicate-bearing veins have a similar mineralogy, although saussurization of plagioclase is more intense and biotite is absent (Table 3.5.5 and Figures 3.5.17c and 3.5.17d). Calc-silicate-bearing veins in East-Roberto zone are composed of quartz, diopside, amphibole, tourmaline, and minor microcline, plagioclase, clinozoisite, pyrrhotite and arsenopyrite (Figures 3.5.17e and 3.5.17f). Such calc-silicate-bearing veins only bear anomalous gold values in the East-Roberto zone (Table 3.5.5). The greatest gold concentrations within the East-Roberto zone are principally carried by zones of quartz-flooding (see section 3.5.6 *East-Roberto Auriferous Zone*).

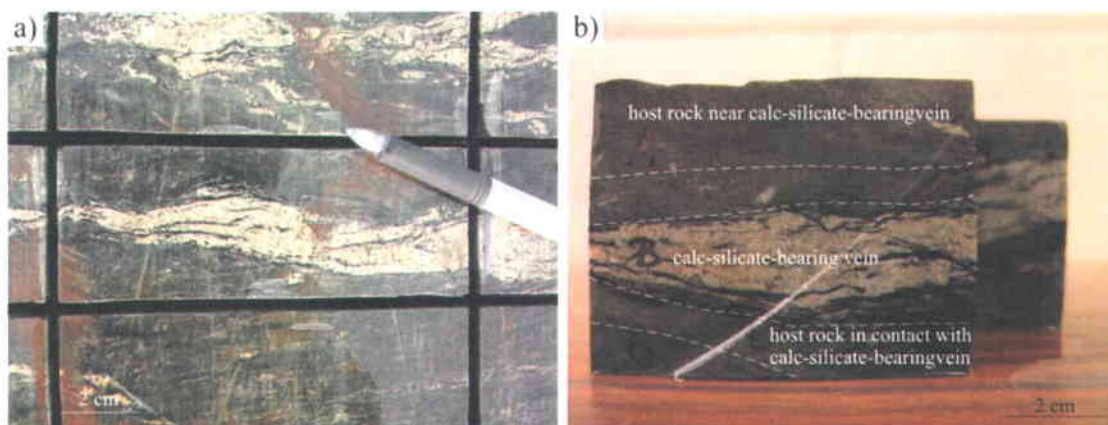


Figure 3.5.16: Photographs showing: a) calc-silicate-bearing vein in East-Roberto zone on outcrops. b) details of calc-silicate-bearing vein on sawed section of sample shown in (a).

Table 3.5.5: Mineralogy and average gold content of calc-silicate-bearing veins and host rocks in East-Roberto zone. Forward slash (/) means “replaced by” (e.g. Bo/Chl/Preh means biotite replaced by chlorite and prehnite). Codes of symbols are given in Table 3.5.2.

Location within sample	Mineralogy	aver. Au (ppb)	σ	
host rock near Ca-vein	Qtz-Amp-Ml-Tl-Ss±Bo/Chl/Preh±Sr±Cz±Preh±Ti-Po-Asp±Py	130	NA	n=1
host rock in ctc with vein	Qtz-Tl-Ss±Amp±Sr±Cz±Preh±Ml±Ti-Po-Asp	NA	NA	
calc-silicate-bearing vein	Qtz-Di-Amp-Tl±Ml±Plag±Cz-Po-Asp±Au	350	277	n=5

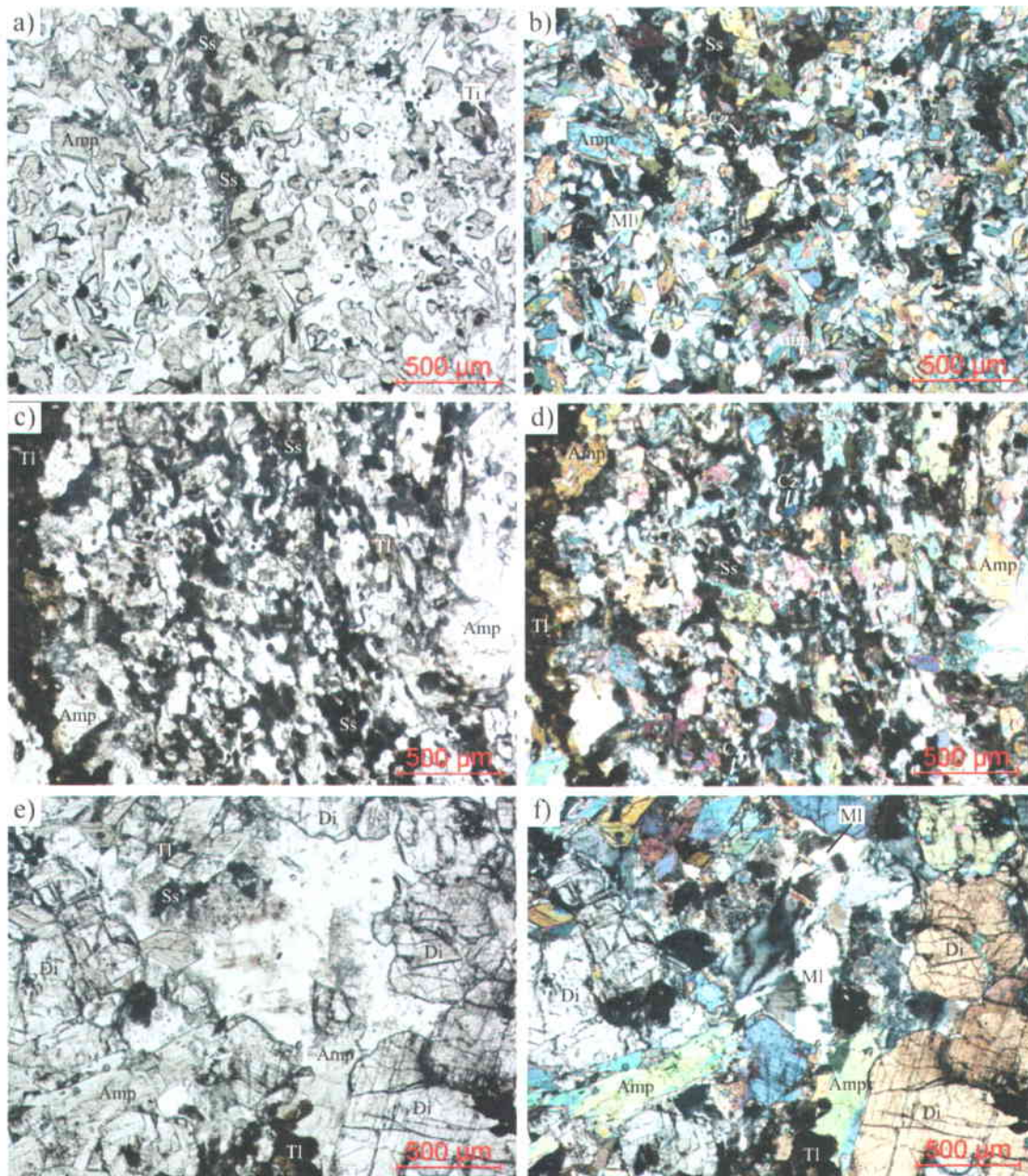


Figure 3.5.17: Natural light (left) and cross-polarized (right) photomicrographs of calc-silicate-bearing vein in East-Roberto zone and of East-Roberto host rocks. a) and b) East-Roberto host near calc-silicate-bearing vein. c) and d) East-Roberto host in contact with calc-silicate-bearing vein. Note the presence of tourmaline crystals and intense saussuritization of plagioclase. e) and f) calc-silicate-bearing vein in East-Roberto zone. Note the presence of diopside, Ca-rich amphibole, microcline, and tourmaline crystals. Opaque minerals of all photographs are sulphide minerals. Codes of symbols are given in Table 3.5.2.

In the Roberto zone, Ca-bearing alteration is present as calc-silicate-bearing veins that locally caused Ca-bearing replacement of the host rocks (e.g. Figure 3.5.18), and as Ca-bearing replacement located near calc-silicate-free veins (e.g. Figure 3.5.20). Ca-bearing replacement associated with calc-silicate-bearing veins is typically characterized by quartz, amphibole, saussuritized plagioclase, biotite replaced by chlorite and/or prehnite and/or muscovite, and minor microcline, tourmaline, sericitized plagioclase, clinozoisite, prehnite, titanite, pyrrhotite, and arsenopyrite (Figures 3.5.19a and 3.5.19b). Calc-silicate-bearing veins within the Roberto zone are composed of diopside, amphibole, quartz, and minor titanite, carbonate, pyrrhotite, arsenopyrite, and visible gold (Figures 3.5.19c and 3.5.19d). Such veins and associated Ca-bearing replacement are associated with high gold values in the Roberto zone (Table 3.5.6).

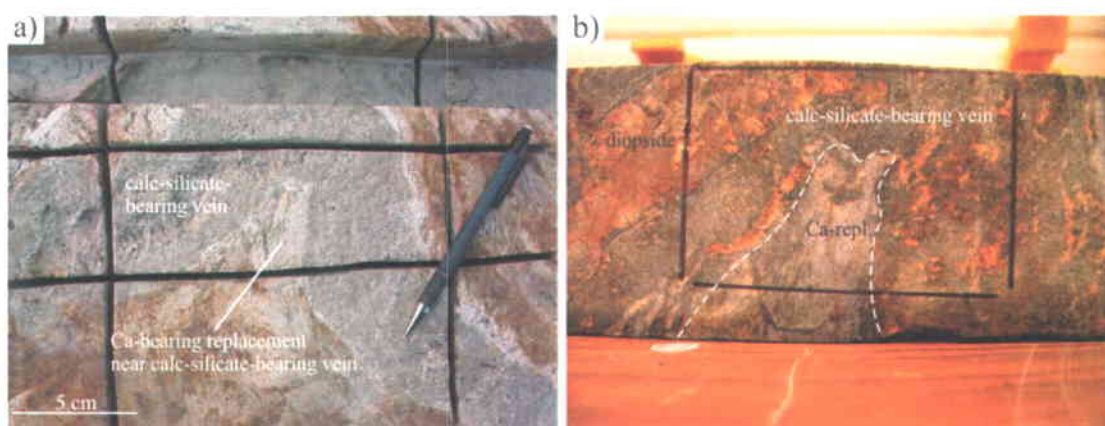


Figure 3.5.18: Photographs showing: a) calc-silicate-bearing vein and Ca-bearing replacement in Roberto zone on outcrops. b) details of calc-silicate-bearing vein and Ca-bearing replacement on sawed section of sample shown in (a).

Table 3.5.6: Mineralogy and average gold content of calc-silicate-bearing veins and host rocks in Roberto zone. Forward slash (/) means “replaced by” (e.g. Bo/Chl/Preh means biotite replaced by chlorite and prehnite). Codes of symbols are given in Table 3.5.2.

Location within sample	Mineralogy	aver. Au (ppb)	σ	
Ca-repl. near calc-silicate-bearing vein	Qtz-Amp-Ss±Bo/Chl/Preh/Ms±Ml±Tl±Sr±Cz±Preh±Ti-Po-Asp	17800	5657	n=2
calc-silicate-bearing vein	Di-Amp-Qtz±Ti±Carb-Po-Asp±Au	38593	57167	n=8

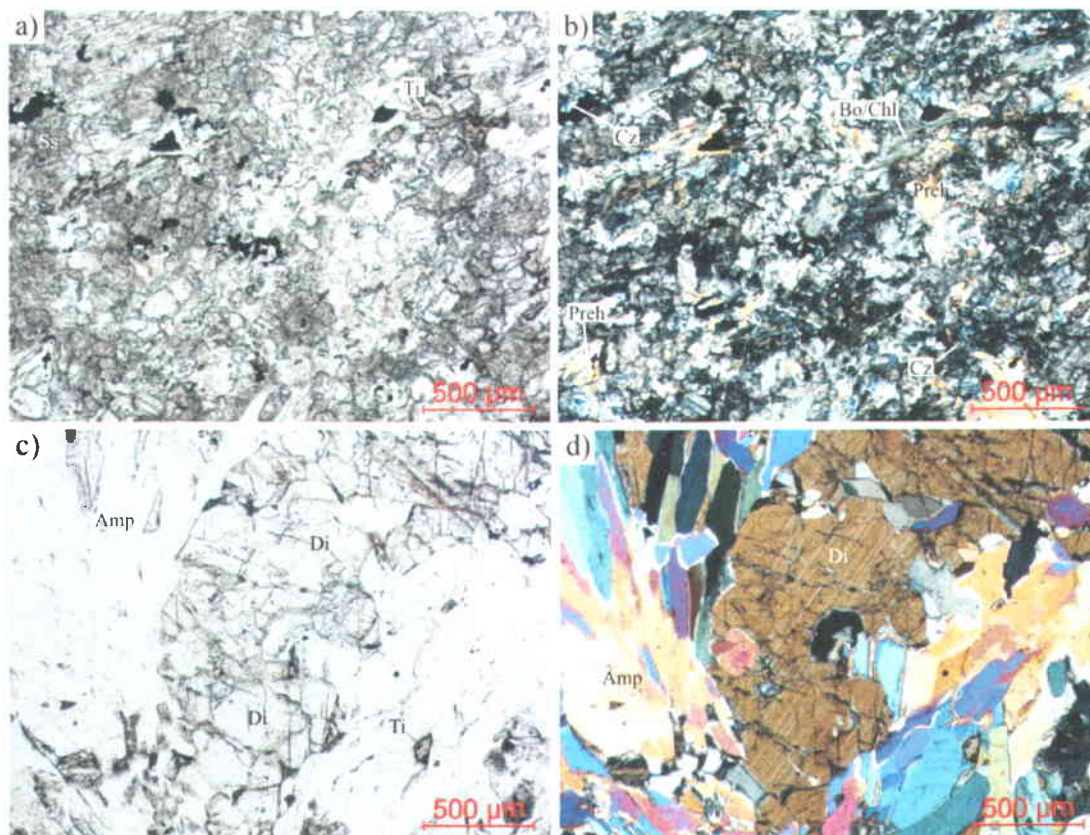


Figure 3.5.19: Natural light (left) and cross-polarized (right) photomicrographs of calc-silicate-bearing vein and Ca-bearing replacement in Roberto zone. a) and b) Ca-bearing replacement near calc-silicate-bearing vein. c) and d) calc-silicate-bearing vein in Roberto. Note the presence of diopside and Ca-amphibole crystals. Opaque minerals of all photographs are sulphide minerals. Codes of symbols are given in Table 3.5.2.

In the Roberto zone, host rocks located near Ca-bearing replacement that is itself located near calc-silicate-free veins (e.g. Figure 3.5.20) are composed of quartz, biotite, microcline, tourmaline, pyrrhotite and arsenopyrite. Host rocks in contact with the Ca-bearing replacement have the same mineralogy except that biotite is absent (Table 3.5.7 and Figures 3.5.21a and 3.5.21b). The Ca-bearing replacement also has a similar mineralogy except that microcline is absent and that saussuritized/sericitized plagioclase and minor titanite are present (Table 3.5.7 and Figures 3.5.21c and 3.5.21d). Calc-silicate-free veins located near Ca-bearing replacement are composed of quartz, biotite replaced by chlorite, prehnite, pyrrhotite, arsenopyrite and minor titanite (Figures 3.5.21e and 3.5.21f). Such veins are highly auriferous (Table 3.5.7).

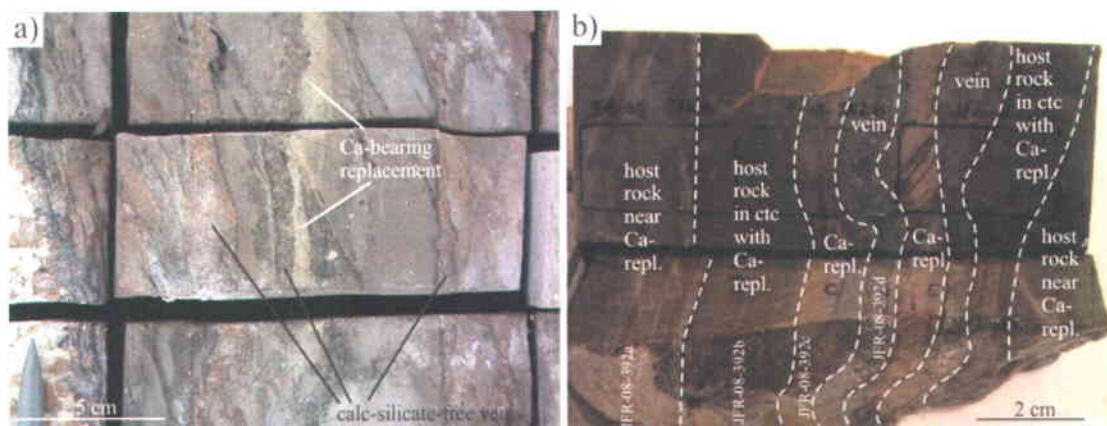


Figure 3.5.20: Photographs showing: a) Ca-bearing replacement in Roberto zone on outcrops. b) details of sample shown in (a). The central vein is calc-silicate-free.

Table 3.5.7: Mineralogy and average gold content of Ca-bearing replacement and host rocks in Roberto zone. Forward slash (/) means “replaced by” (e.g. Bo/Chl means biotite replaced by chlorite). Codes of symbols are given in Table 3.5.2.

Location within sample	Mineralogy	aver. Au (ppb)	σ	
host rock near Ca-replacement	Qtz-Bo-MI-Tl-Po-Asp	15027	21794	n=6
host rock in ctc with Ca-replacement	Qtz-MI-Tl-Po-Asp	1100	NA	n=1
Ca-repl. near calc-silicate-free vein	Qtz-Tl-Ss±Sr±Ti-Po-Asp	3698	3935	n=4
central vein without calc-silicate	Qtz-Bo-Bo/Chl-Preh±Tl-Po-Asp	19403	24953	n=5

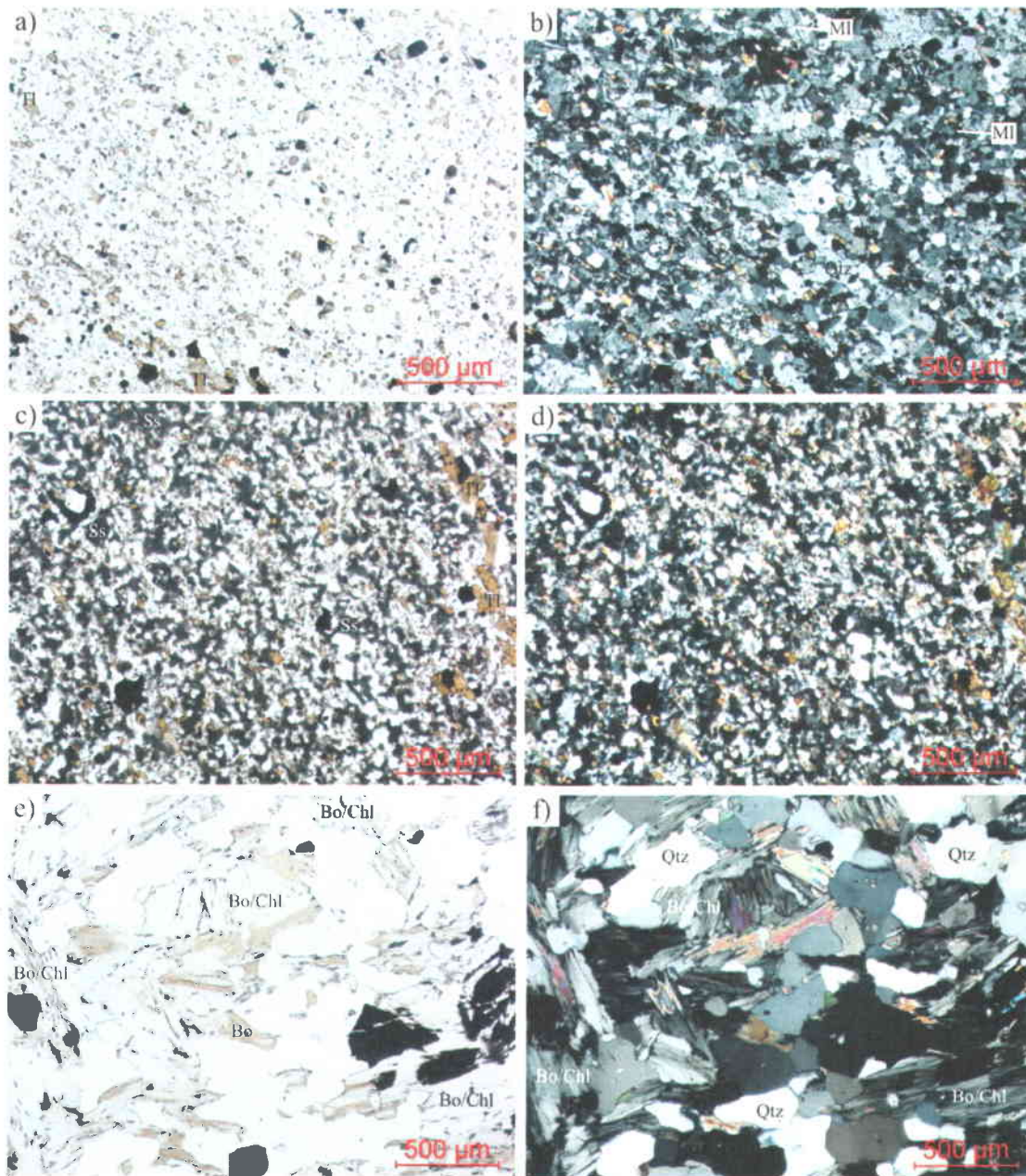


Figure 3.5.21: Natural light (left) and cross-polarized (right) photomicrographs of Ca-bearing replacement (near calc-silicate-free vein) and host rocks in Roberto zone. a) and b) host rock in contact with Ca-bearing replacement. c) and d) Ca-bearing replacement near calc-silicate-free vein in Roberto. Note the intense saussuritization of plagioclase. e) and f) calc-silicate-free vein in Roberto zone. Note the presence of large biotite crystals replaced by chlorite. Opaque minerals of all photographs are sulphide minerals. Codes of symbols are given in Table 3.5.2.

The mineralogy of Ca-bearing alteration changes with its proximity with auriferous zones. This is especially true for the presence of diopside in calc-silicate veins (Figures 3.5.6 and 3.5.7). On the large stripped outcrop, diopside-bearing veins are primarily located in and in between the East-Roberto and Roberto zone (Figure 3.5.9), where such veins are thicker (e.g. Figure 3.5.22a), and are locally spatially associated with significant potassic alteration (microcline) and tourmalinization of the host greywacke (e.g. Figure 3.5.22b).

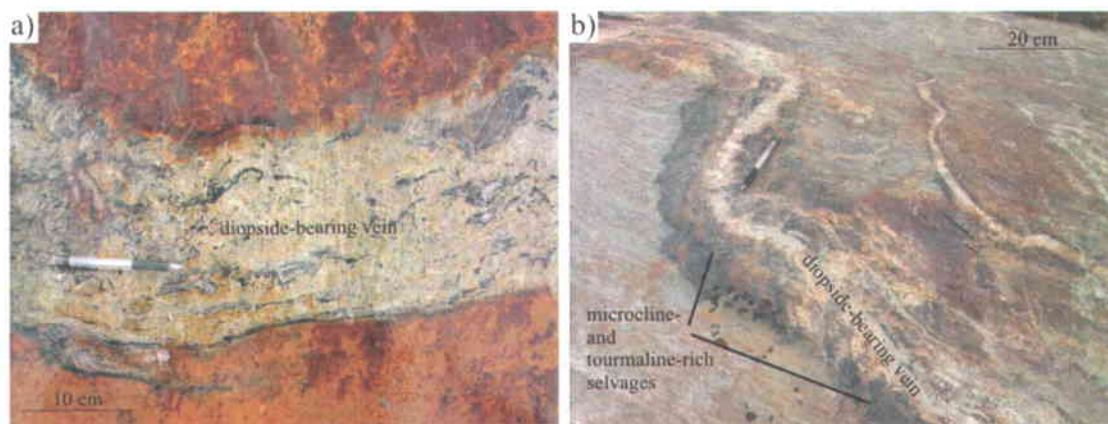


Figure 3.5.22: Photographs showing: a) thick diopside-bearing vein located in between East-Roberto and Roberto auriferous zones. b) microcline- and tourmaline-rich selvages associated with a diopside-bearing vein.

3.5.4.2 *Geochemistry of Ca-bearing Alteration*

This section uses isocon and box diagrams to present the geochemical attributes of Ca-bearing replacement and calc-silicate-bearing veins and complement the mineralogical attributes described in the previous section. Isocon diagrams were constructed for the principal host rocks of Ca-bearing replacement and/or calc-silicate-bearing veins. For the aluminosilicate-bearing sequence, isocon diagrams were constructed based on the geochemistry of one particular sample ("TR-3", see Figure 3.5.6 for its location). Details of the Ca-bearing replacement zones within that sample are shown on Figure 3.5.23. Isocon diagrams were constructed for each individual zone assuming that the aluminosilicate-bearing part represents the least-altered protolith (Figure 3.5.24). Box diagrams were also constructed in order to present a broader compositional spectrum for Ca-bearing replacement hosted within aluminosilicate-bearing sequence (Figure 3.5.25).

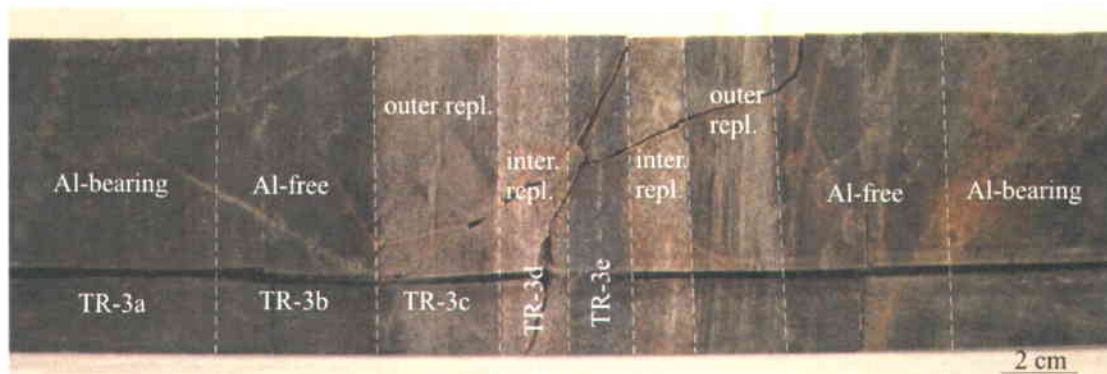


Figure 3.5.23: Photograph showing sample (TR-3) used to create isocons for Ca-replacement in aluminosilicate-bearing sequence. An outcrop photograph of the sample is given in Figure 3.5.10a. The least-altered protolith is interpreted to correspond to the Al-bearing part (TR-3a).

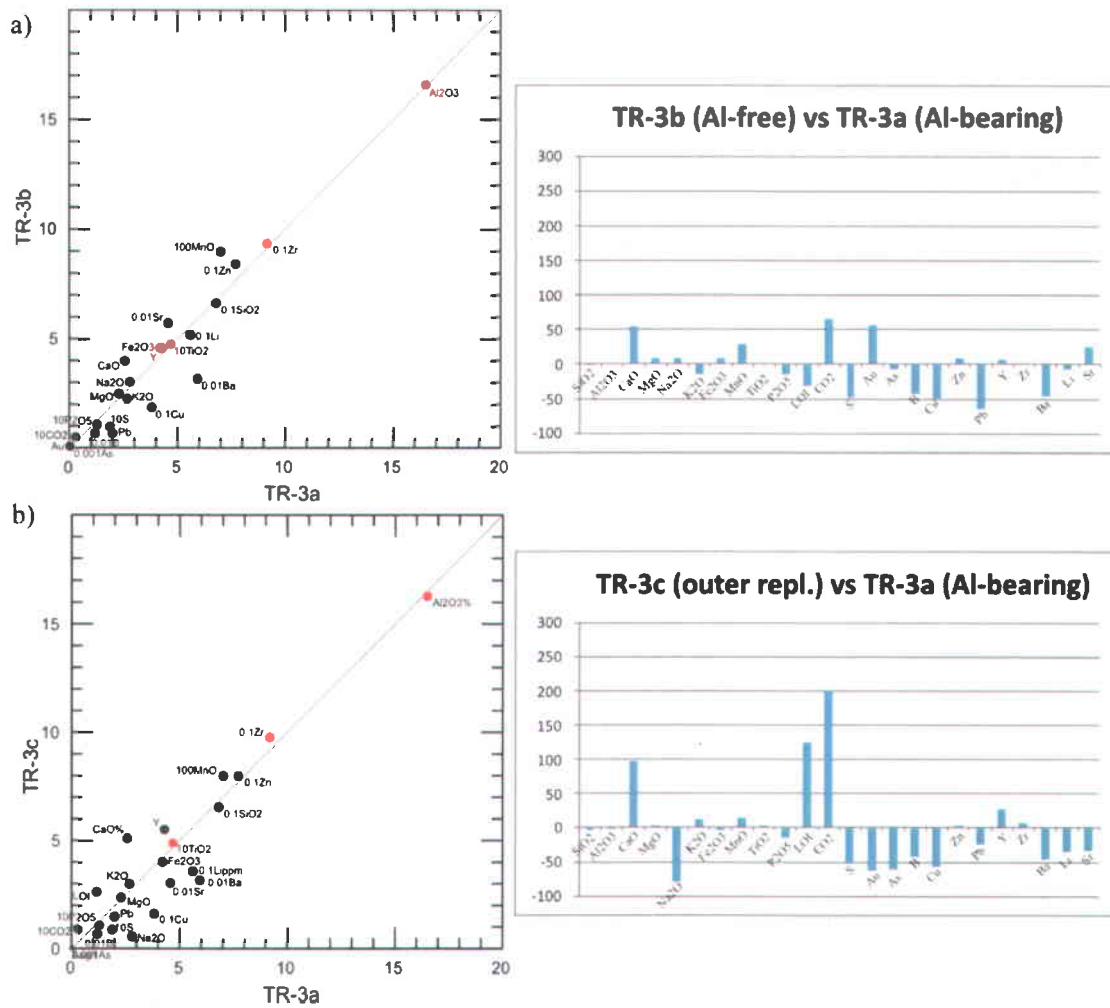


Figure 3.5.24: Isocon diagrams and corresponding mass balance histograms for Ca-bearing replacement in aluminosilicate-bearing sequence. Locations of individual samples are shown on Figure 3.5.23. The least-altered protolith is interpreted to correspond to the Al-bearing part (TR-3a). Oxide concentrations are in weight percent and element concentrations are in ppm (except for Au which is in ppb). Following the method of Grant (1986), some concentrations are scaled so that they have the same order of magnitude and plot relatively close to each other. Red circles indicate immobile elements used to create the isocon. a) isocon diagram and mass balance histogram for the aluminosilicate-free part (TR-3b). b) isocon diagram and mass balance histogram for the outer part of the Ca-bearing replacement (TR-3c).

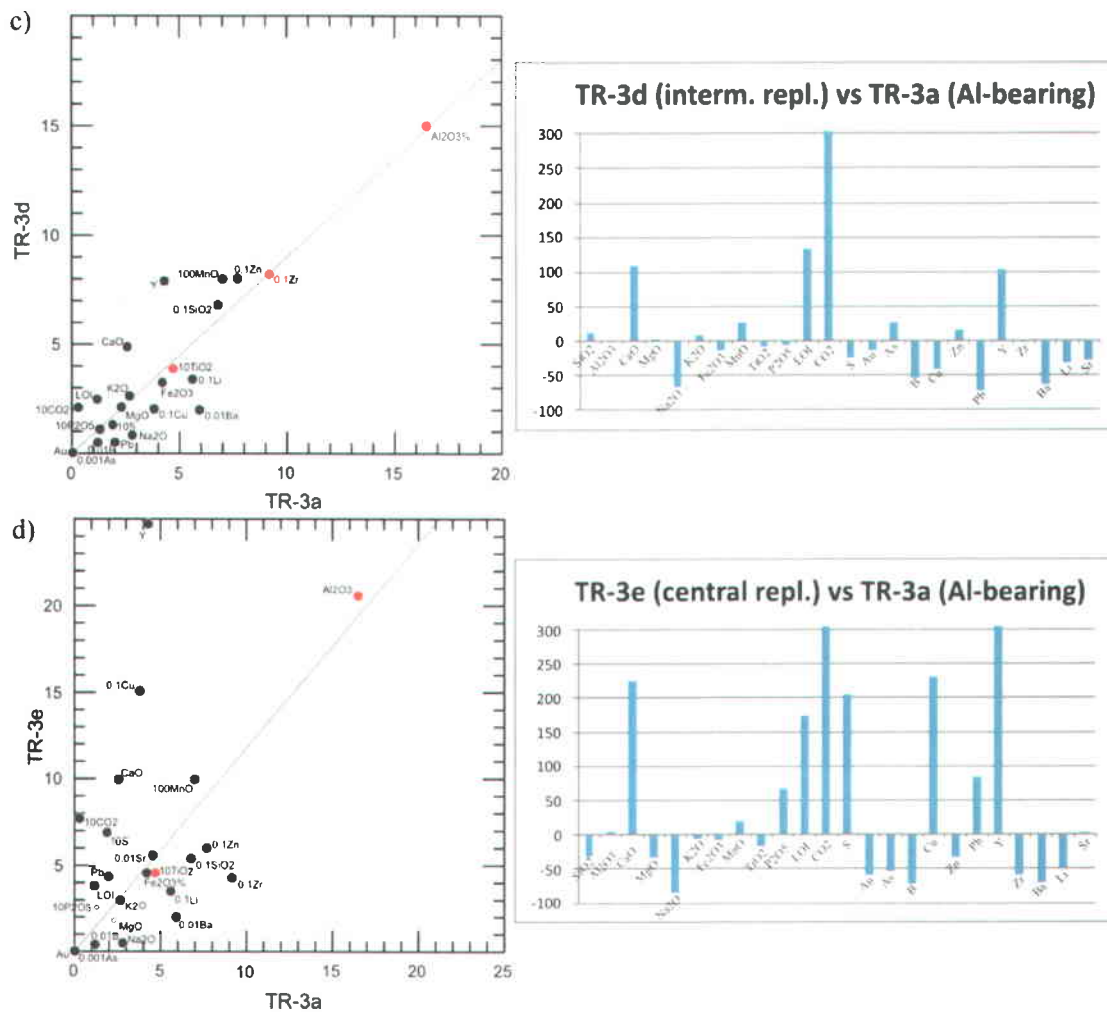


Figure 3.5.24: (continued). c) isocon diagram and mass balance histogram for the intermediate part of the Ca-bearing replacement (TR-3d). b) isocon diagram and mass balance histogram for the central part of the Ca-bearing replacement (TR-3e).

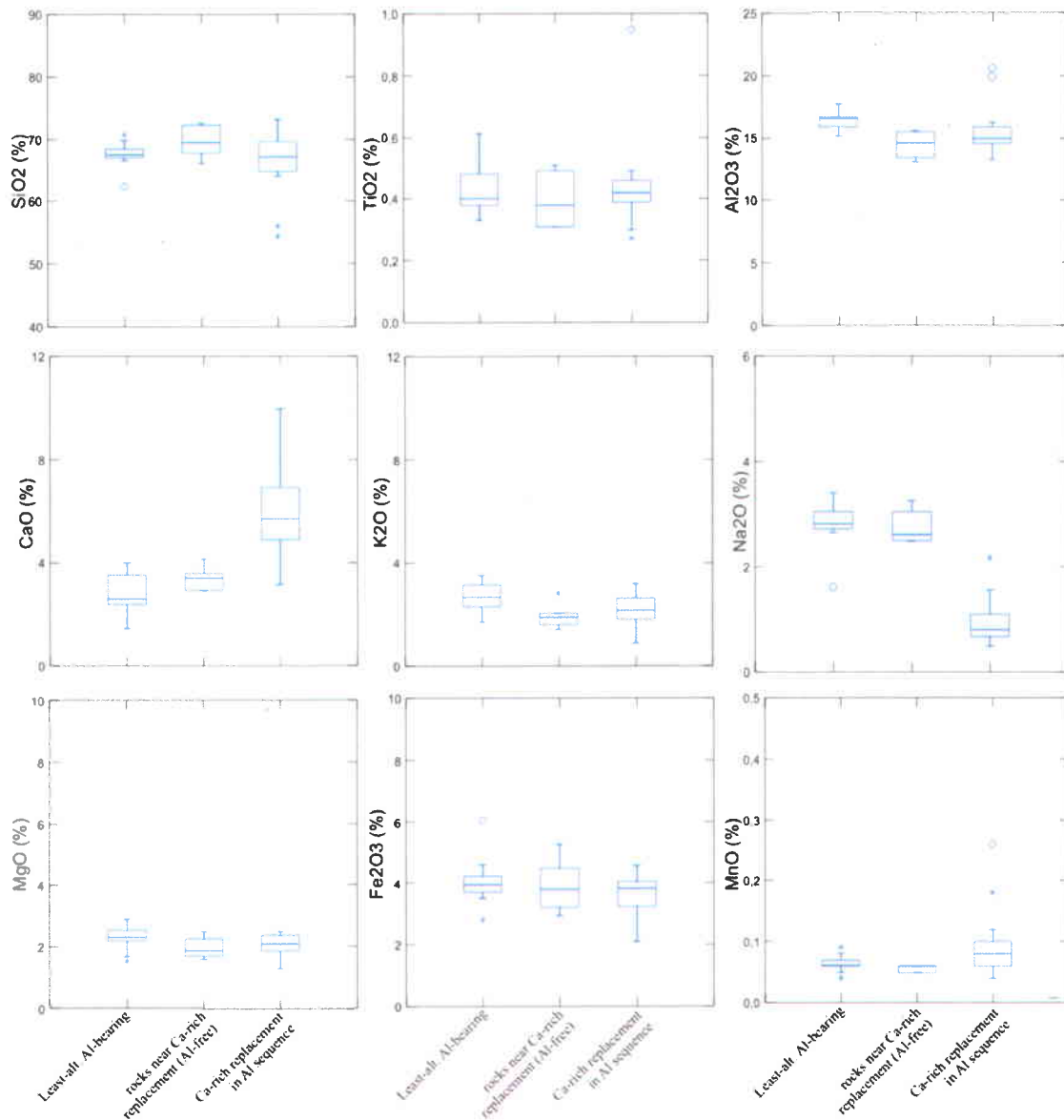


Figure 3.5.25: Box diagrams showing the range of oxide concentrations of Ca-bearing alteration and host rocks within aluminosilicate-bearing sequence. The center horizontal line marks the median of a given suite. The length of each box shows the range within which the central 50% of the values fall, with the box edges at the first and third quartiles. The whiskers show the range of observed values that fall within the inner fences, defined as 1.5 and -1.5 times the absolute value of the box. Values between inner and outer fences (3 and -3 times the absolute value of the box) are plotted with asterisks. Values beyond the outer fences are plotted with empty circles. All samples are from this study. Number of samples: Least-alt. Al-bearing = 9; rocks near Ca-bearing replacement (Al-free) = 6; Ca-bearing replacement in Al sequence = 13. The outer, intermediate, and central parts of the replacement are grouped together within the "Ca-bearing replacement in Al sequence" group.

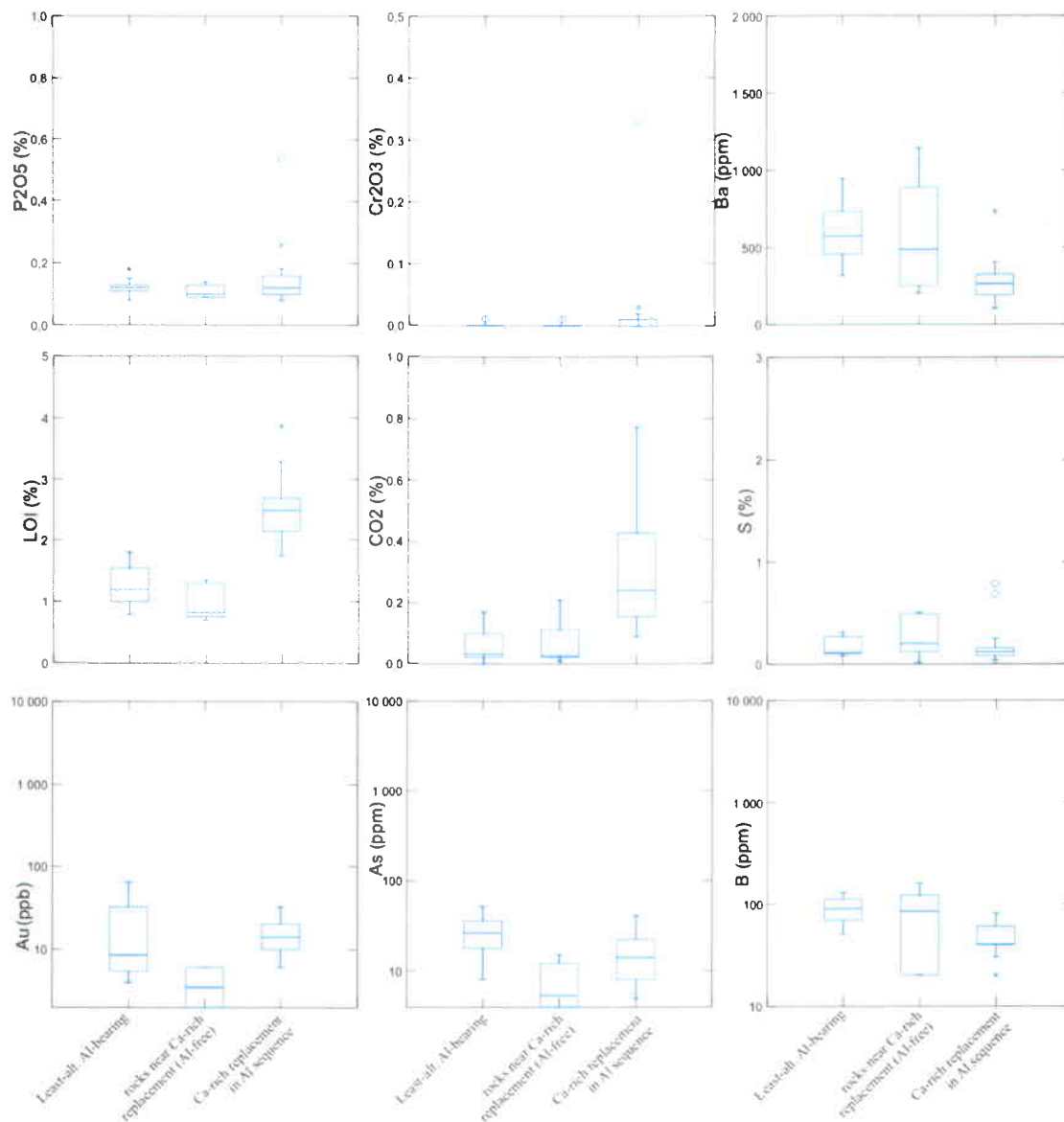


Figure 3.5.25: (continued). Box diagrams showing the range of element concentrations of Ca-bearing alteration and host rocks within aluminosilicate-bearing sequence.

The isocons show that, in terms of major elements, the Al-free part near the Ca-bearing replacement has a similar chemistry than the Al-bearing part, except for CaO which is slightly enriched in the Al-free part (Figure 3.5.24a). The box diagrams, however, indicate that the global range of CaO concentrations does not vary much between the Al-bearing and Al-free parts (Figure 3.5.25). The box diagrams also show that the range of SiO₂ concentrations is slightly higher, and that Al₂O₃ and K₂O are slightly lower in the Al-free parts compared to the Al-bearing parts (Figure 3.5.25). The isocons constructed for Ca-bearing replacement all show significant

gains in CaO and significant losses in Na₂O, Ba, and Sr (Figures 3.5.24b to 3.5.24d). Other gains and losses are observed (e.g. Au, As, B) but that the concentrations remained fairly low. Note also that the shallower slope of the “intermediate replacement” isocon and the steeper slope of the “central replacement” isocon suggest that mass (or volume) has been added and removed, respectively. The box diagrams show that the global ranges of CaO and CO₂ concentrations are significantly higher and the ranges of Na₂O and Ba concentrations lower in Ca-bearing replacement zones (Figure 3.5.25), which corroborates with the relative gains and losses of the isocon diagrams.

For the greywacke sequence, the geochemical effect of calc-silicate-bearing veins on host rocks has been investigated through the construction of isocon diagrams for sample “JFR-07-328” (Figure 3.5.26). This particular sample is more auriferous (> 10 g/t) than most calc-silicate-bearing veins hosted within greywacke (< 5 g/t). Isocon diagrams were constructed for the part near the calc-silicate-bearing vein and the part in contact with the vein, assuming that the “young greywacke” of Tables 3.2.1 and 3.2.2 represents the least-altered protolith (Figure 3.5.27). Box diagrams were also constructed in order to present a broader spectrum of calc-silicate-bearing veins and host greywacke compositions (Figure 3.5.28).

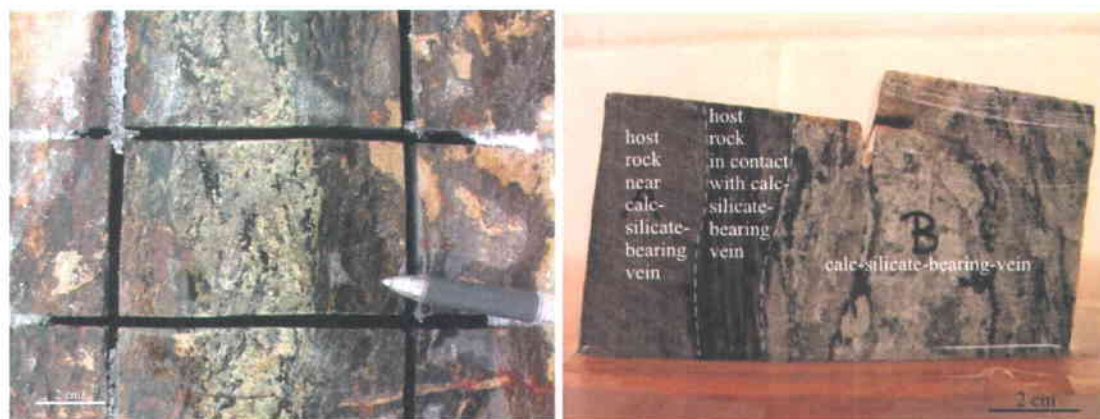


Figure 3.5.26: Photograph showing sample (JFR-07-328) used to create isocons for Ca-replacement in greywacke host rocks. The least-altered protolith is interpreted to correspond to the average composition of the “young greywacke” of Tables 3.2.1 and 3.2.2. See Figure 3.5.6 to see where the sample is located.

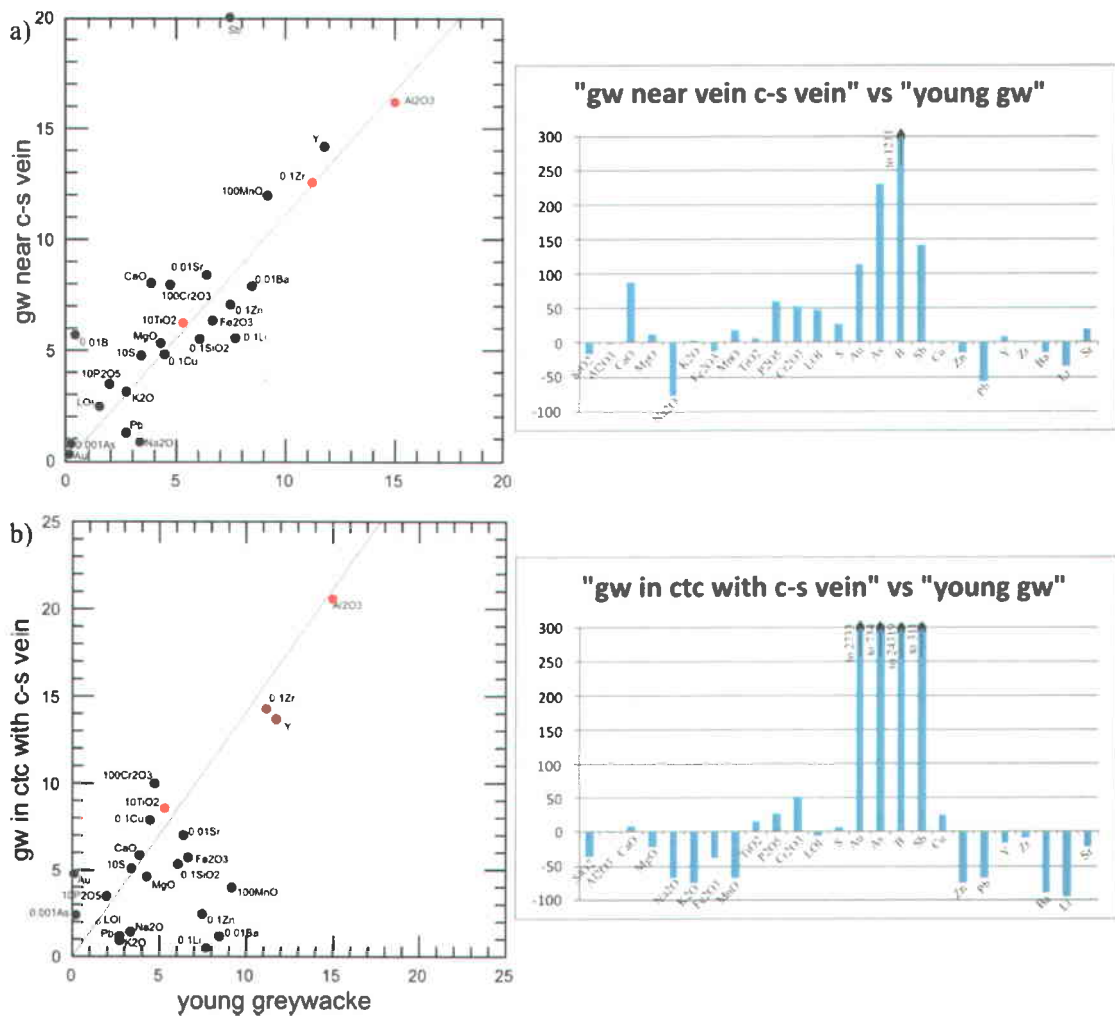


Figure 3.5.27: Isocon diagrams and corresponding mass balance histograms for a greywacke hosting a calc-silicate-bearing vein (JFR-07-328, Figure 3.5.26). The least-altered protolith is interpreted to correspond to the “young greywacke” of Tables 3.2.1 and 3.2.2. Oxide concentrations are in weight percent and element concentrations are in ppm (except for Au which is in ppb). Following the method of Grant (1986), some concentrations are scaled so that they have the same order of magnitude and plot relatively close to each other. Red circles indicate immobile elements used to create the isocon. a) isocon diagram and mass balance histogram for the greywacke host located near the calc-silicate-bearing vein. b) isocon diagram and mass balance histogram for the greywacke in contact with the calc-silicate-bearing vein (see Figure 3.5.26).

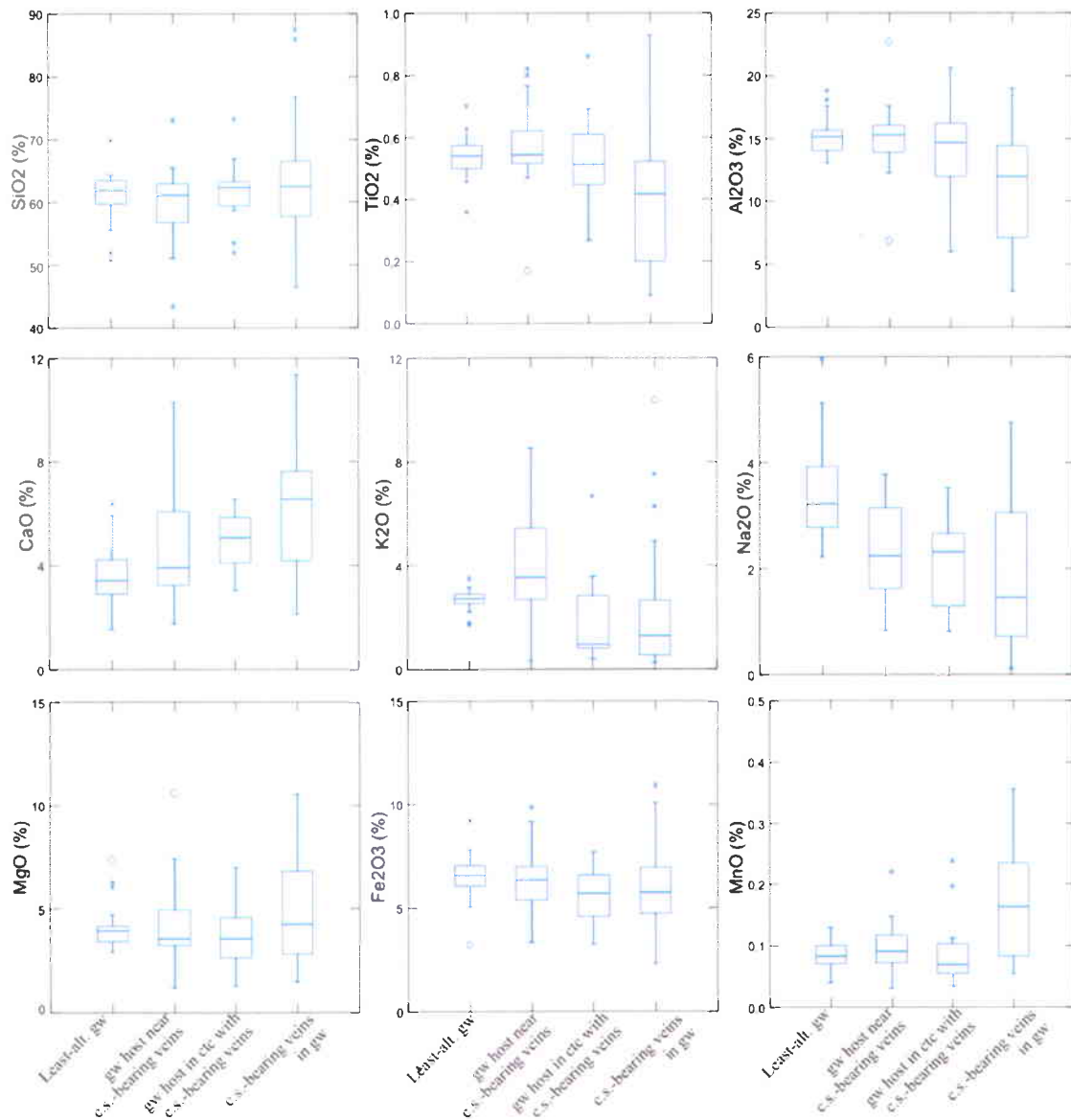


Figure 3.5.28: Box diagrams showing the range of oxide concentrations of calc-silicate-bearing veins and greywacke host rocks. The center horizontal line marks the median of a given suite. The length of each box shows the range within which the central 50% of the values fall, with the box edges at the first and third quartiles. The whiskers show the range of observed values that fall within the inner fences, defined as 1.5 and -1.5 times the absolute value of the box. Values between inner and outer fences (3 and -3 times the absolute value of the box) are plotted with asterisks. Values beyond the outer fences are plotted with empty circles. All samples are from this study. Number of samples: Least-alt. gw = 24; gw host near calc-silicate-bearing veins = 22; gw host in contact with calc-silicate-bearing veins = 11; calc-silicate-bearing veins in gw = 36.

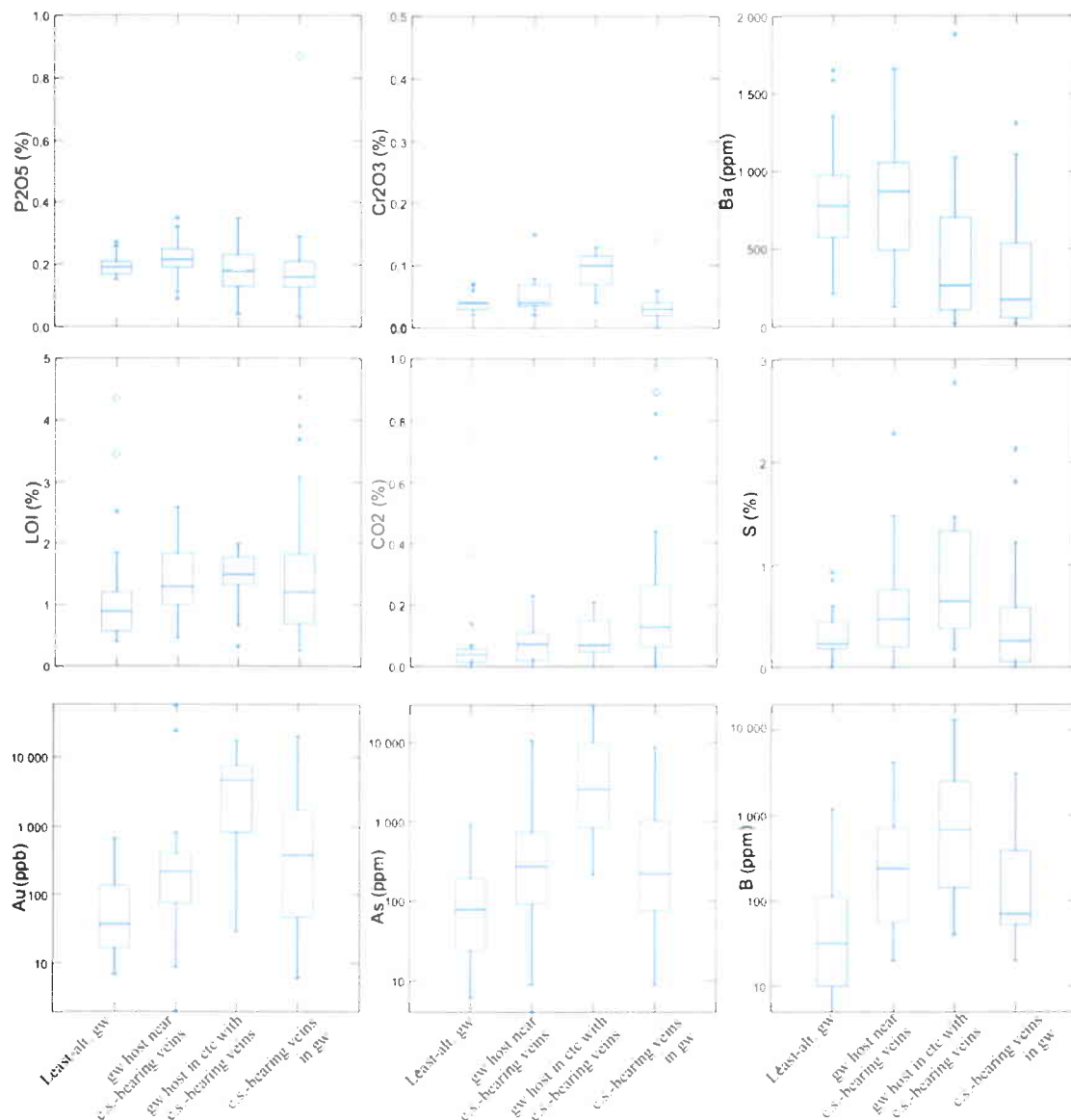


Figure 3.5.28: (continued). Box diagrams showing the range of element concentrations of calc-silicate-bearing veins and greywacke host rocks.

The results show that the isocons constructed for the greywacke host located near the calc-silicate-bearing vein of sample "JFR-07-328" shows significant gains in CaO, Cr₂O₃, S, Au, As, B, and Sb; and significant losses in Na₂O and SiO₂ (Figure 3.5.27a). Other gains and losses are observed (e.g. Pb and Li) but that the concentrations are fairly low and therefore not totally significant. Note also that the steeper slope of the isocon suggests that mass (or volume) has been removed. The box diagrams corroborate with the gains and losses observed on the isocon diagram, although they also show that the ranges of K₂O concentrations in host rocks near calc-

silicate-bearing veins are generally higher than in least-altered greywacke samples (Figure 3.5.28).

The isocon diagram of the host greywacke in contact with the calc-silicate-bearing vein of sample “JFR-07-328” shows that the latter has significant gains in Cr_2O_3 , Au, As, B, and Sb; and significant losses in SiO_2 , Na_2O , K_2O , Fe_2O_3 , MnO , and Ba when compared to the average composition of least-altered young greywacke (Figure 3.5.27b). Such compositional changes are attributed to contamination of the greywacke in contact with the calc-silicate-bearing vein by tourmaline-rich veinlets (Figure 3.5.26). The gains and losses agree with the broader compositional ranges displayed on box diagrams (Figure 3.5.28), except for apparent gains in CaO and S on the box diagrams which are not observed on the isocon diagram of sample “JFR-07-328”.

In Roberto, isocon diagrams were constructed to investigate the alteration associated with the Ca-bearing replacement located near calc-silicate-free quartz-biotite veins. The sample used to create such isocon diagrams is sample “JFR-08-392” (Figure 3.5.29). Isocon diagrams were constructed for the “host rock near Ca-bearing replacement” part, the “host rock in contact with Ca-bearing replacement” part, and the “Ca-bearing replacement” part, assuming that the least-altered protolith is the average composition of “young greywacke” samples of Tables 3.2.1 and 3.2.2 (Figure 3.5.30).

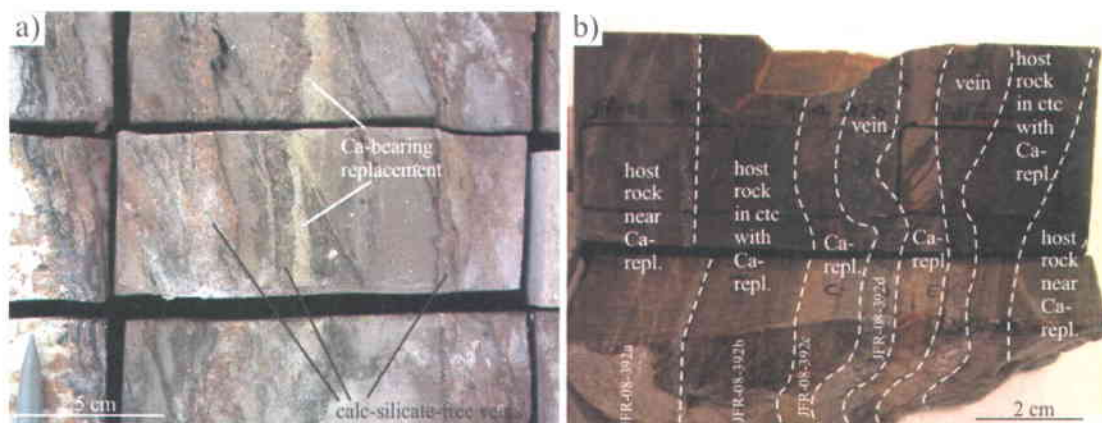


Figure 3.5.29: Photograph showing sample (JFR-08-392) used to create isocons for Ca-bearing replacement near calc-silicate-free quartz-biotite veins in Roberto. The protolith is interpreted to correspond to the average composition of the “young greywacke” of Tables 3.2.1 and 3.2.2. See Figure 3.5.6 to see where the sample is located.

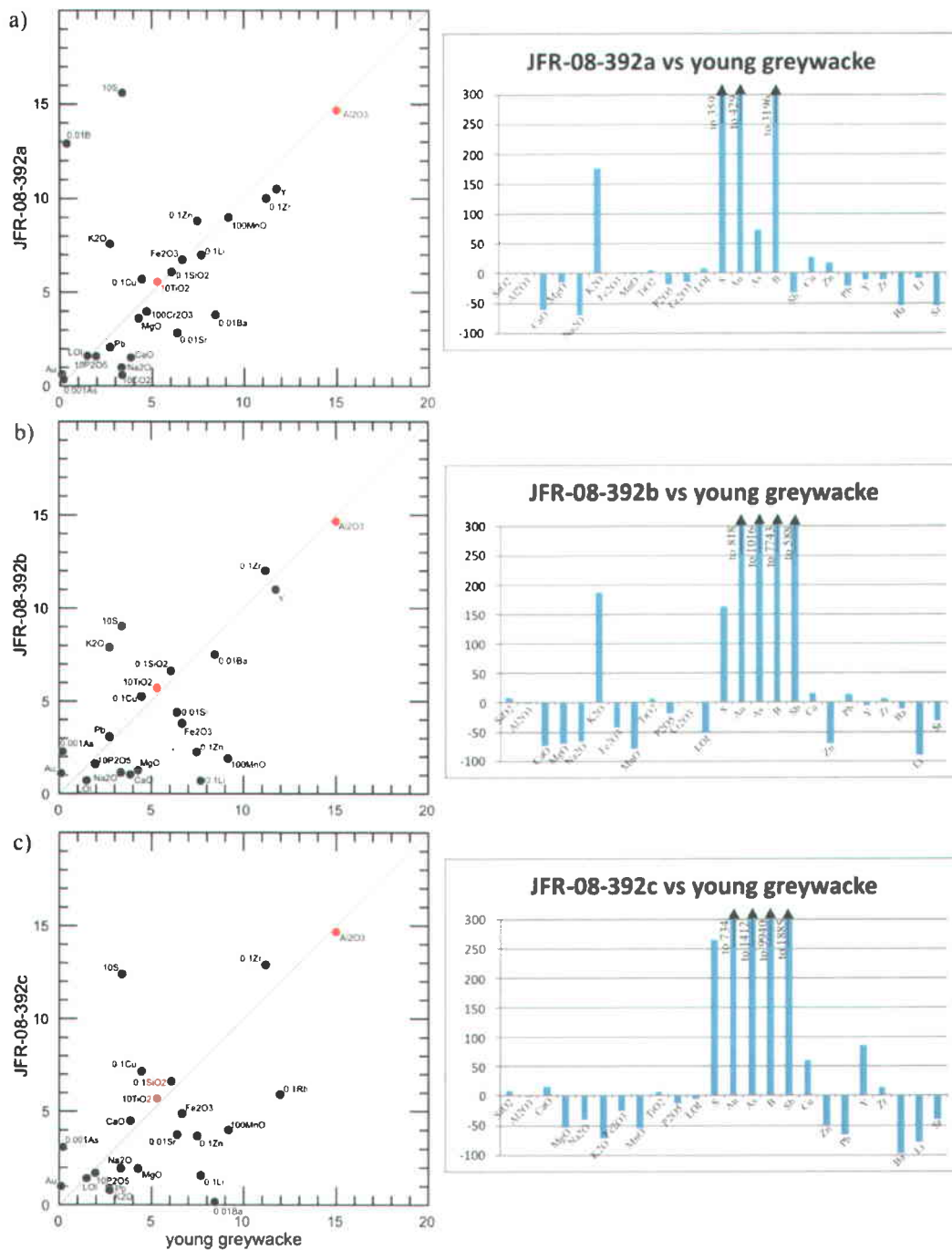


Figure 3.5.30: Isocon diagrams and corresponding mass balance histograms for Ca-bearing replacement (near calc-silicate-free quartz-biotite vein) and Roberto host rocks (from sample JFR-08-392). The least-altered protolith is interpreted to correspond to the “young greywacke” of Tables 3.2.1 and 3.2.2. Oxide concentrations are in weight percent and element concentrations are in ppm (except for Au which is in ppb). Following the method of Grant (1986), some concentrations are scaled so that they have the same order of magnitude and plot relatively close to each other. Red circles indicate immobile elements used to create the isocon. a) Roberto host located near Ca-bearing replacement. b) Roberto host rock in contact with Ca-bearing replacement. c) Ca-bearing replacement near calc-silicate-free quartz-biotite vein in Roberto.

The results show that all parts had significant gains in S, Au, As, and B, and significant losses in Na₂O and MgO (Figure 3.5.30). The “host rock near Ca-bearing replacement” and “host rock in contact with Ca-bearing replacement” parts also show striking gains in K₂O and losses in CaO (Figures 3.5.30a and 3.5.30b), which agrees with their mineralogy (Table 3.5.7) and suggests that their chemistry was not greatly affected by their proximity with the “Ca-bearing replacement” part. Their large gains in K₂O might be spatially related to the calc-silicate-free vein which accordingly bears potassium-rich minerals (Table 3.5.7). Details relating to potassic alteration are further discussed in section 3.5.5 *Potassic Alteration*.

An important observation is that the “Ca-bearing replacement” part only shows little gains in CaO compared with the least altered “young greywacke” (Figure 3.5.30c). However, the “Ca-bearing replacement” part shows significant gains in CaO if another isocon is constructed assuming that the protolith is the K-rich/Ca-poor “host rock in contact with Ca-bearing replacement” part (Figure 3.5.31). Since textural evidence at both microscopic (e.g. Figures 3.5.21c and 3.5.21d) and macroscopic (e.g. Figure 3.5.32) levels suggests that Ca-bearing replacement is superimposed on pre-existing minerals, it is possible that the Ca-bearing replacement postdates the inferred potassic alteration associated with the calc-silicate-free vein. Such a scenario is further discussed in section 3.5.4.3 *Deformational and Metamorphic Characteristics of Ca-bearing Alteration* and other upcoming sections.

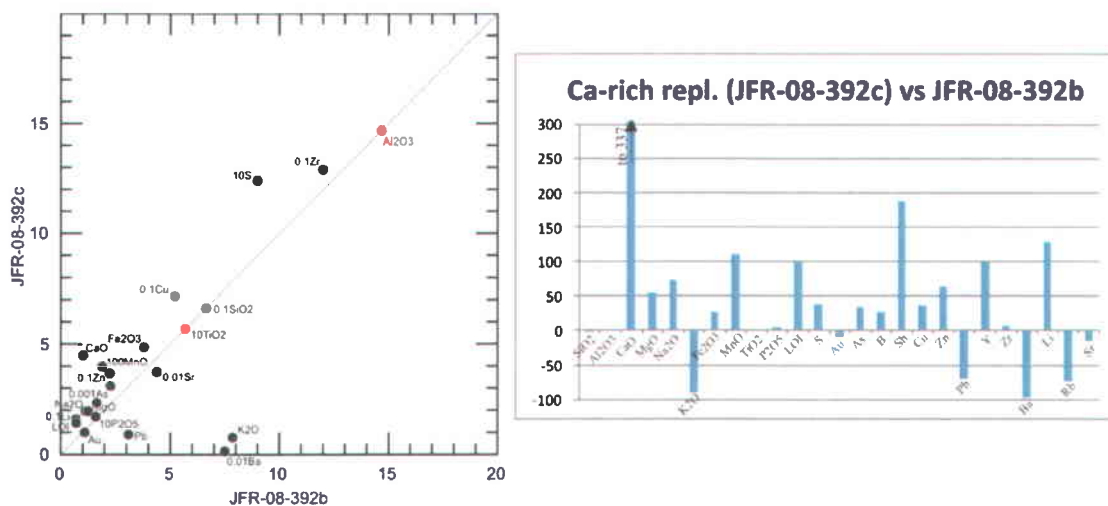


Figure 3.5.31: Isocon diagram and corresponding mass balance histogram for Ca-bearing replacement (near calc-silicate-free vein) assuming that the protolith is the “host rock in contact with Ca-bearing replacement” part of sample JFR-08-392 (Figure 3.5.29). Oxide concentrations are in weight percent and element concentrations are in ppm (except for Au which is in ppb). Following the method of Grant (1986), some concentrations are scaled so that they have the same order of magnitude and plot relatively close to each other. Red circles indicate immobile elements used to create the isocon.

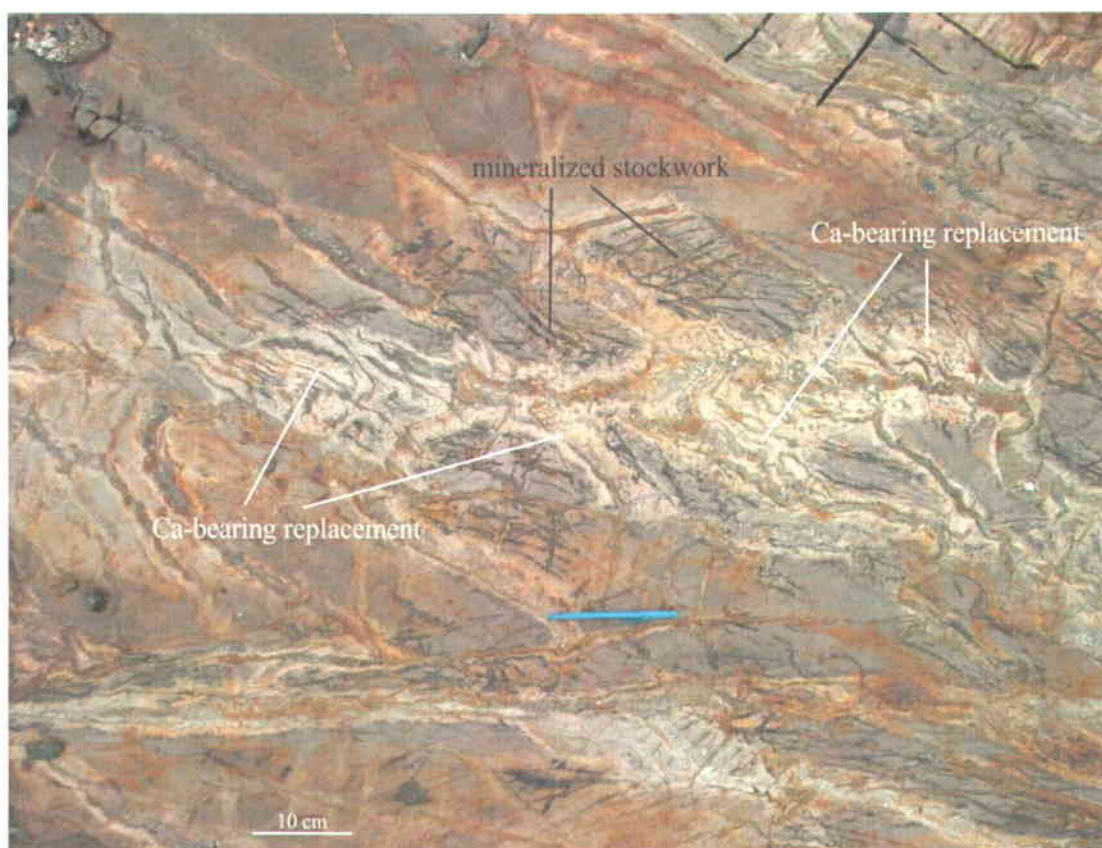


Figure 3.5.32: Photograph showing how Ca-bearing replacement locally appears to be superimposed on pre-existing minerals of Roberto's auriferous stockwork. This explanation is supported by petrographic evidence (e.g. Figures 3.5.21c and 3.5.21d).

In order to present a broader compositional spectrum of Ca-bearing alteration, box diagrams were constructed for all calc-silicate-bearing veins and Ca-bearing replacement within the deposit area, including samples that are considered "distal" to the deposit. In order to investigate how the geochemistry of the Ca-bearing hydrothermal system varies in function of its proximity with the ore zones, the samples were grouped according to their location with respect to the principal auriferous zones (Figure 3.5.33). The definitions of the groups are as follow: "distal" = samples located more than 1.5 km from the principal auriferous zones; "hanging wall" = samples located east of the East-Roberto zone (including samples in massive greywacke and aluminosilicate-bearing rocks); "central" = samples located between East-Roberto and Roberto zones; "footwall" = samples located west of the Roberto zone; "East-Roberto" = samples located within the East-Roberto zone; "Roberto" = samples located within the Roberto zone; "other mz" = samples located within random auriferous zones. The ranges of least-altered greywacke compositions of the deposit area are also represented on the diagrams for comparison.

The results indicate that when compared with Ca-bearing replacement and calc-silicate-bearing veins of the distal and hanging wall regions, Ca-bearing replacement and calc-silicate-bearing veins of the central region globally have greater values of SiO₂, MgO, Au, As, and B, and lower values of Al₂O₃ and Na₂O (Figure 3.5.33). In terms of Au, As, and B, Ca-bearing replacement and calc-silicate-bearing veins of the footwall region have contents that are intermediate between the distal/hanging wall parts and the central part (Figure 3.5.33). The chemistry of calc-silicate-bearing veins within the East-Roberto zone stands out by globally having the highest proportions of K₂O, Ba, B, CaO/Na₂O, and K₂O/Na₂O (Figure 3.5.33). The high K₂O concentrations agree with the ubiquitous presence of microcline within the East-Roberto assemblage (Table 3.5.5 and Figures 3.5.17e and 3.5.17f). On the other hand, the chemistry of calc-silicate-bearing veins and replacement within the Roberto zone and "other mineralized zones" stands out by globally having the highest S, As, and Au contents. Overall, the most auriferous Ca-bearing replacement and/or calc-silicate-bearing veins also have the greatest concentrations of S, As, and B, and are primarily located in the "central", "Roberto", and "other mz" parts (Figure 3.5.33).

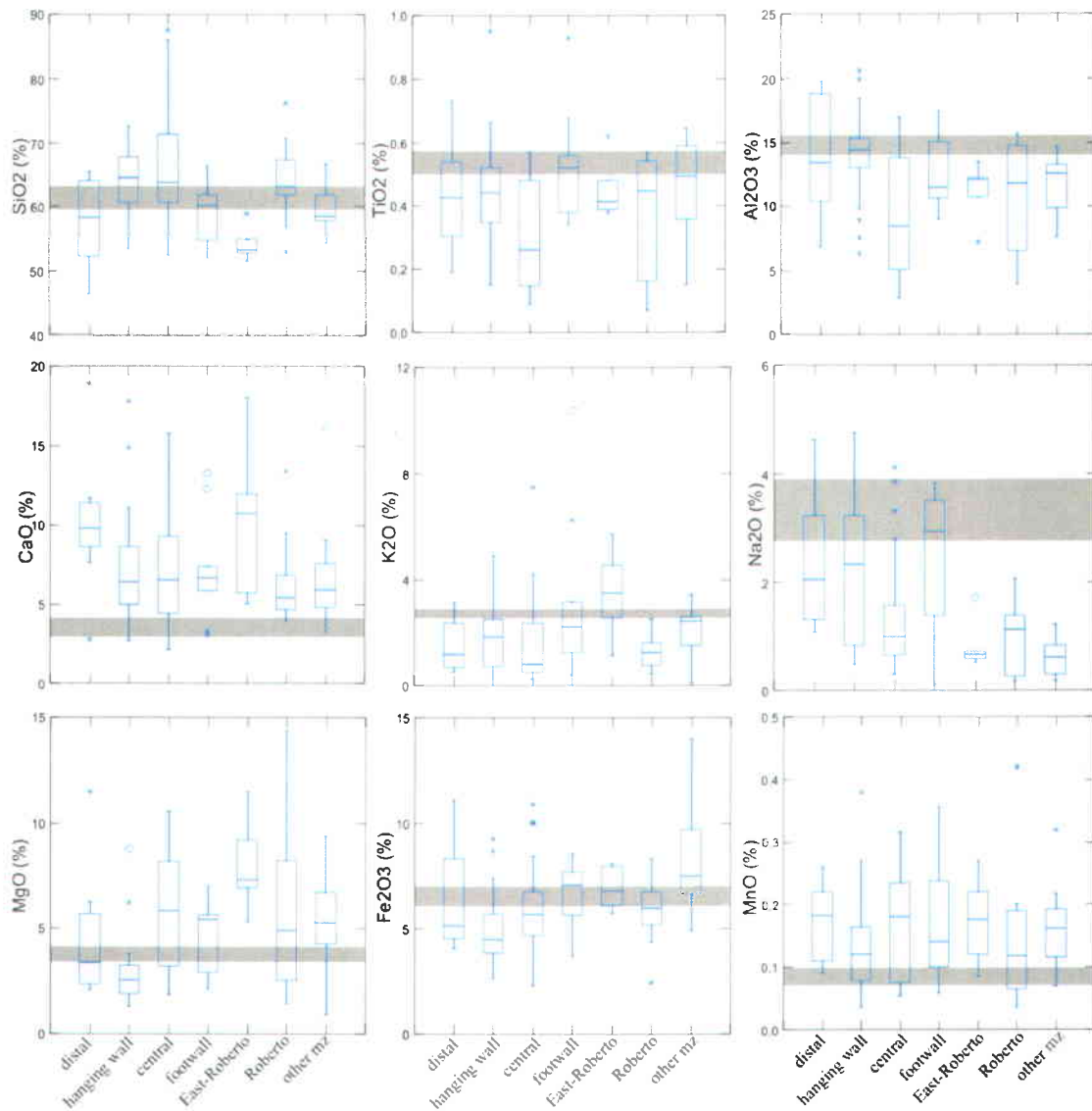


Figure 3.5.33: Box diagrams showing the range of oxide concentrations of calc-silicate-bearing veins and Ca-bearing replacement in function of their location. The center horizontal line marks the median of a given suite. The length of each box shows the range within which the central 50% of the values fall, with the box edges at the first and third quartiles. The whiskers show the range of observed values that fall within the inner fences, defined as 1.5 and -1.5 times the absolute value of the box. Values between inner and outer fences (3 and -3 times the absolute value of the box) are plotted with asterisks. Values beyond the outer fences are plotted with empty circles. Grey regions represent ranges of least-altered greywacke (including “young” and “old” greywacke samples). All samples are from this study. Number of samples: distal = 8; hanging wall = 32; central = 23; footwall = 9; East-Roberto = 5; Roberto = 11; other mz = 7.

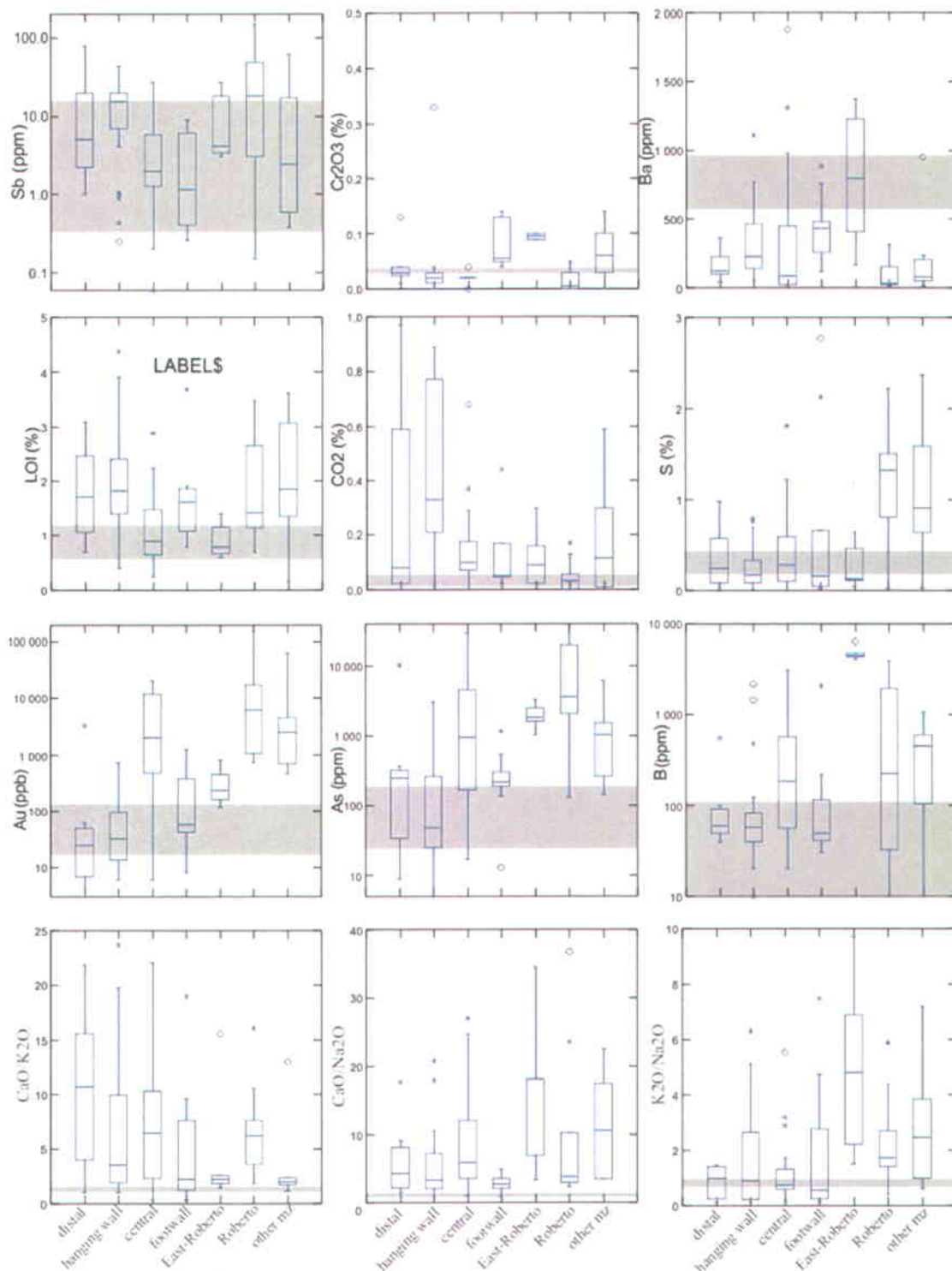


Figure 3.5.33: (continued). Box diagrams showing the range of element concentrations and alkalis ratios of calc-silicate-bearing veins and Ca-bearing replacement in function of their location.

3.5.4.3 *Deformational and Metamorphic Characteristics of Ca-bearing Alteration*

This section presents timing relationships between calc-silicate-bearing veins/Ca-bearing replacement and deformational/metamorphic events that can be established from field observations and petrography. From a macroscopic point of view, it is clear that all calc-silicate-bearing veins and Ca-bearing replacement bands have been affected by D_2 , as they are folded by F_2 folds (Figure 3.5.34), transposed (Figure 3.5.35), and boudinaged into S_2 (Figure 3.5.36). No calc-silicate-bearing veins or Ca-bearing replacement bands postdating D_2 have been documented. The strain in calc-silicate-bearing veins is particularly high in the East-Roberto zone (Figures 3.5.34.c and 3.5.35e).

Microscopic evidence for deformation in calc-silicate-bearing veins include: the omnipresence of undulose extinction in quartz grains, subgrain boundaries within quartz (Figure 3.5.37a) and plagioclase (Figure 3.5.37c), deformation lamellae within quartz (Figure 3.5.37b) and plagioclase (Figure 3.5.37c), and deformation twins within plagioclase (Figure 3.5.37c) and calcite grains (Figure 3.5.37d). Other porphyroblasts present in calc-silicate-bearing veins or Ca-bearing replacement bands, including biotite and amphibole, are locally oriented into S_2 (e.g. biotite: Figures 3.5.38a, 3.5.38b, 3.5.39a to 3.5.39d; amphibole: Figures 3.5.39a, 3.5.39b, 3.5.39e, and 3.5.39f) and locally randomly oriented (e.g. biotite: Figures 3.5.38c to 3.5.38f; amphibole: 3.5.39c and 3.5.39d). The fact that some of the randomly oriented porphyroblasts are locally euhedral and appear post-tectonic suggests that conditions suitable for their growth outlasted D_2 and D_3 , perhaps due to a late- to post-tectonic episode of static recrystallization (Ravenelle et al., 2010). Although diopside porphyroblasts within calc-silicate-bearing veins are not readily oriented by S_2 , the fact that they coexist with amphibole porphyroblasts which are themselves affected by S_2 (Figures 3.5.39e and 3.5.39f) suggests that the diopside porphyroblasts were also affected by D_2 and likely formed early or during D_2 . Tourmaline crystals located within or in the selvages of calc-silicate-bearing veins are commonly oriented by S_2 , specifically in vertical sections (Figure 3.5.40). This suggests that the tourmaline crystals have been affected by D_2 and that their long axis is subparallel to the sub-vertical L_2 lineation. The tourmaline crystals were therefore generated before or during D_2 .

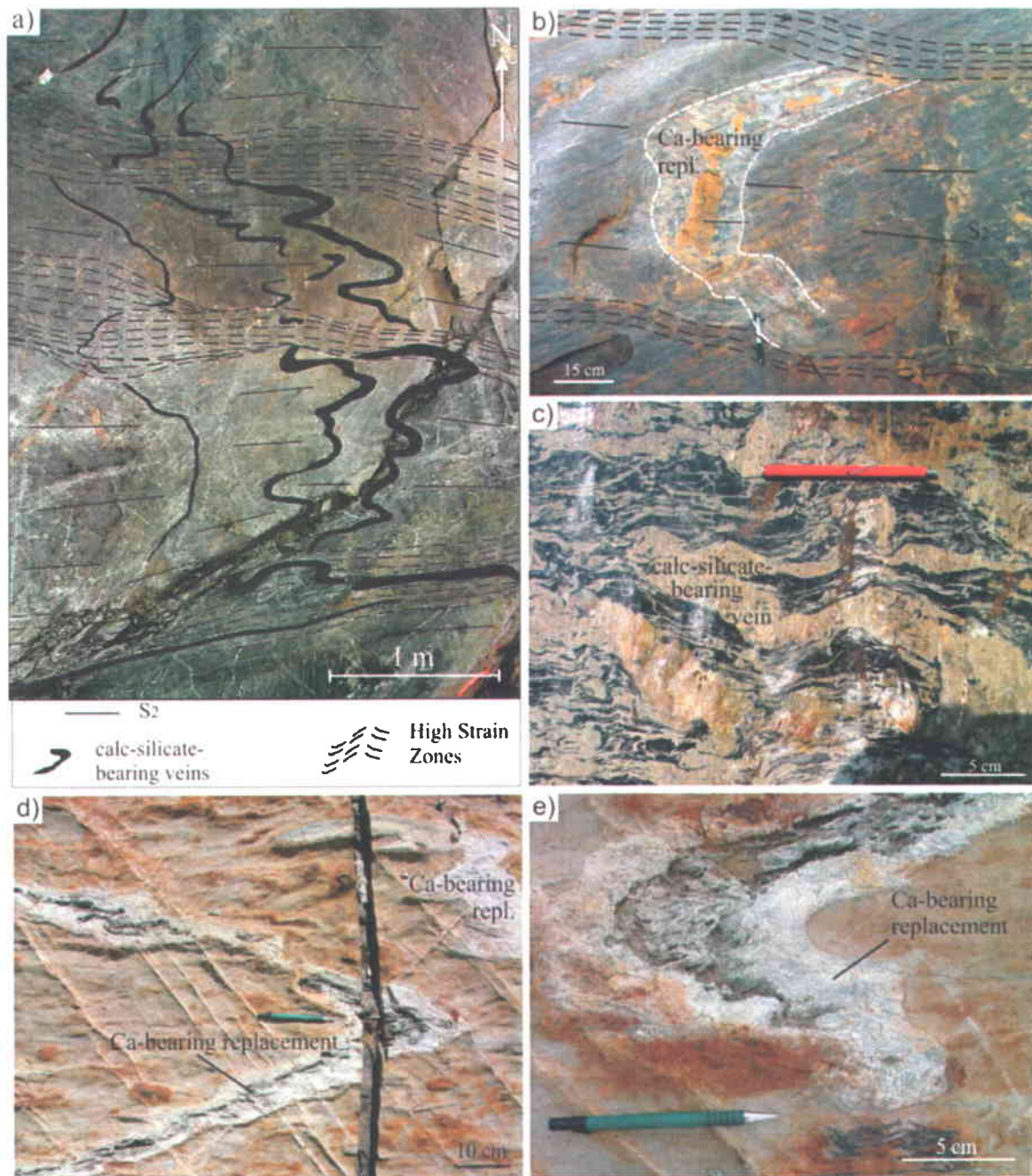


Figure 3.5.34: Photographs showing various calc-silicate-bearing veins or Ca-bearing replacement bands folded by F_2 folds. a) folded calc-silicate-bearing veins transposed by high strain zones. b) F_2 fold in Ca-bearing replacement band with highly transposed limbs. c) isoclinally folded calc-silicate-bearing vein within East-Roberto zone. d) and e) folded Ca-bearing replacement bands in aluminosilicate-bearing sequence. Photograph (a), (b), and (c) are modified from Ravenelle et al. (2010).

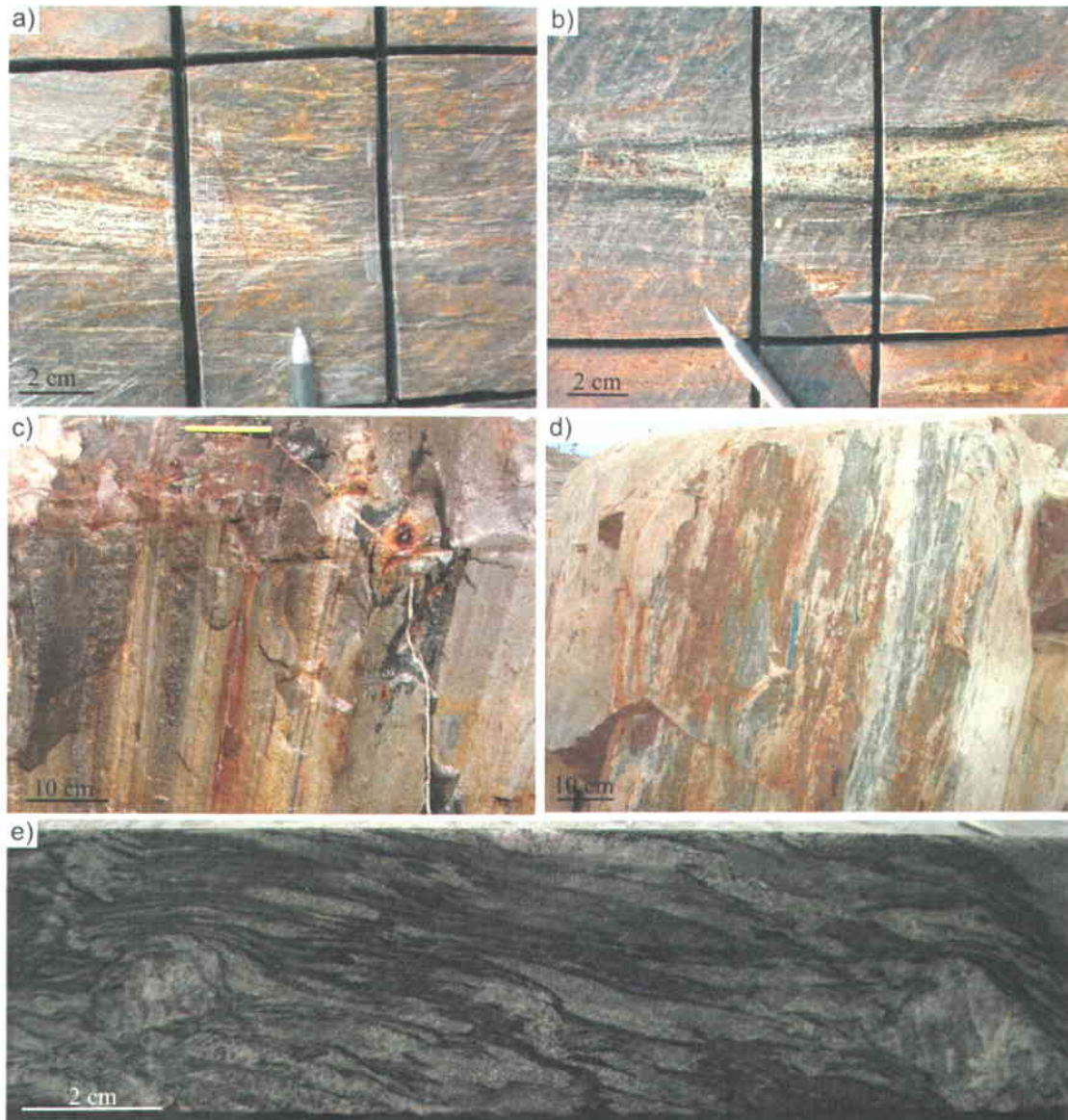


Figure 3.5.35: Photographs of calc-silicate-bearing veins or Ca-bearing replacement bands transposed by S_2 and/or L_2 . a) and b) calc-silicate-bearing veins transposed by high strain zones. c) vertical section showing highly transposed Ca-bearing replacement bands. d) linedated calc-silicate-bearing veins on vertical section of East-Roberto zone. e) highly transposed calc-silicate-bearing veins, quartz veins, and tourmaline-rich host rock in drillcore of East-Roberto zone. Photograph of (c) courtesy of Benoit Dubé.

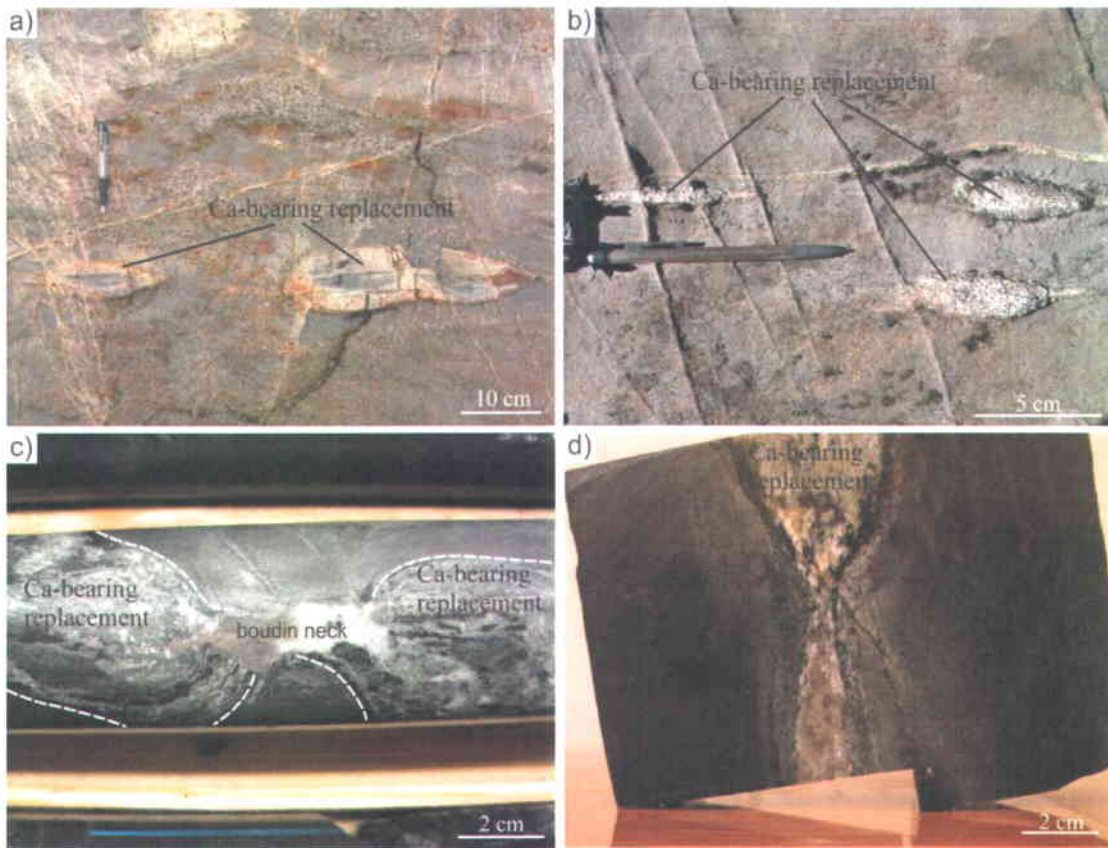


Figure 3.5.36: Photographs showing boudinaged calc-silicate-bearing veins or Ca-bearing replacement bands. a) boudinaged replacement bands within aluminosilicate-bearing rock. b) boudinaged calc-silicate-bearing veins in paragneissic rock. c) boudinaged diopside-bearing vein in drillcore. d) sawed sample face showing boudinaged diopside-bearing vein.

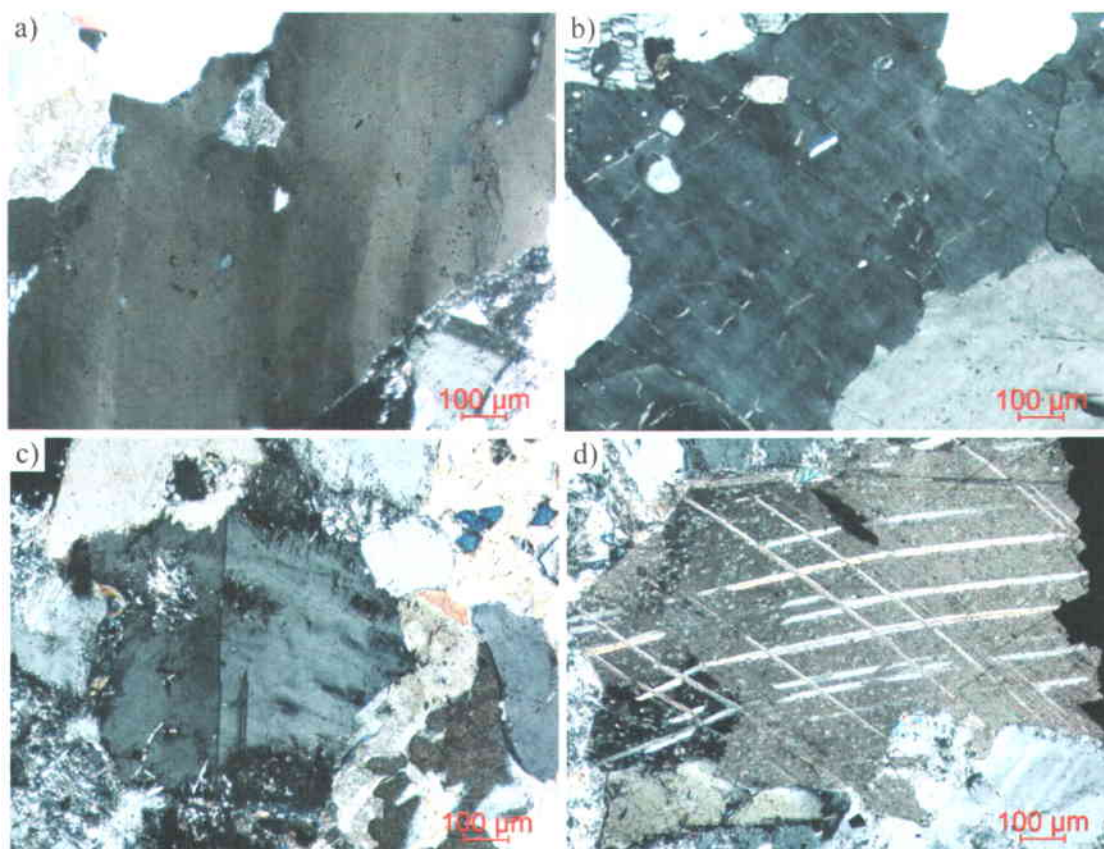


Figure 3.5.37: Photomicrographs in cross-polarized light of deformed crystals within calc-silicate-bearing veins. a) subgrain boundaries (sub-vertical) within quartz grain. b) deformation lamellae (top-left to lower-right) within quartz grain. c) subgrains (right-hand side of crystal) and deformation twins in plagioclase crystals. d) two sets of deformation twins in calcite grain.

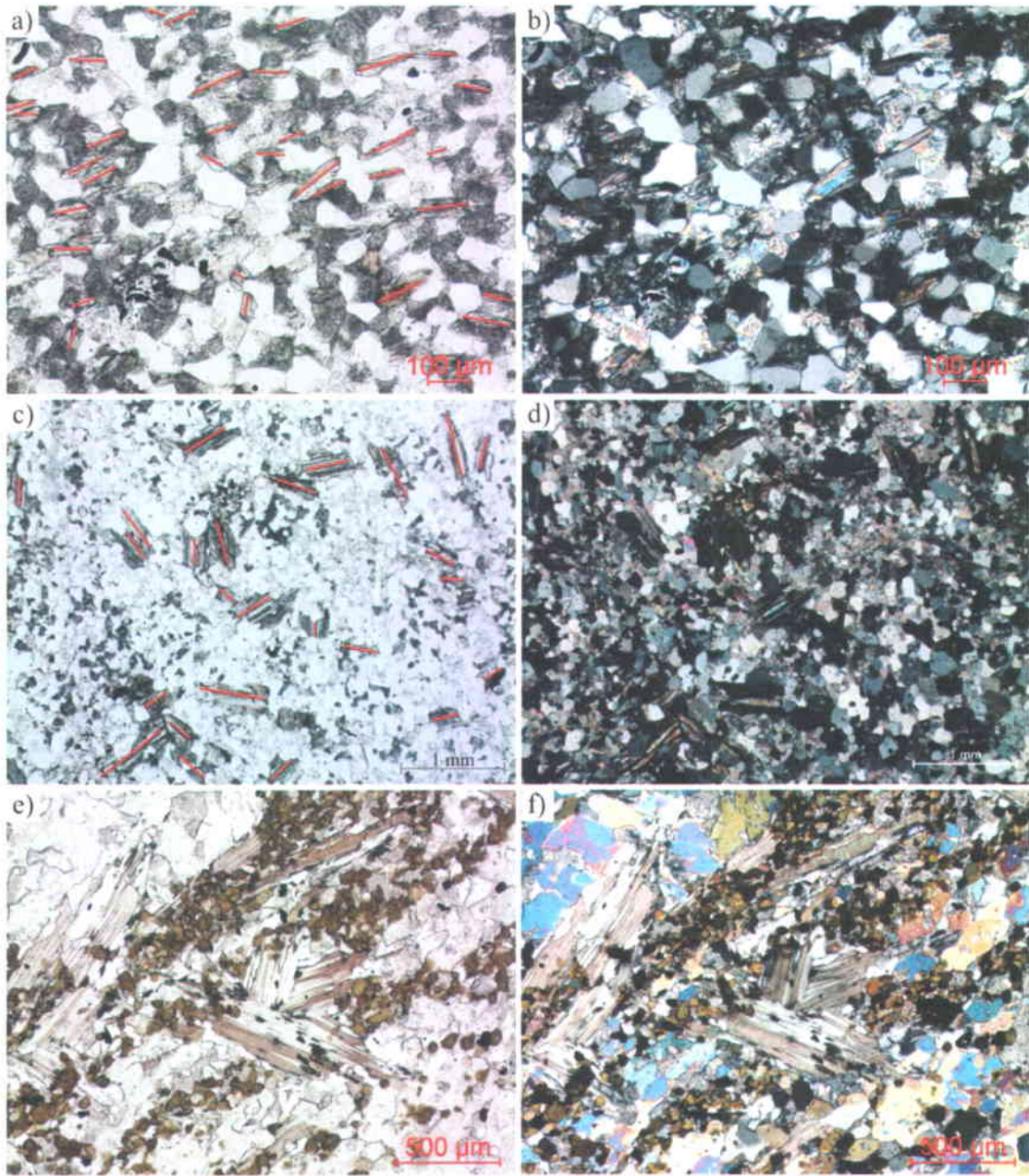


Figure 3.5.38: Natural light (left) and cross-polarized (right) photomicrographs showing preferentially-oriented or randomly-oriented biotite porphyroblasts within calc-silicate-bearing veins or Ca-bearing replacement. a) and b) preferentially oriented biotite with Ca-bearing replacement. c) and d) coarser-grained randomly-oriented biotite porphyroblasts within Ca-bearing replacement. e) and f) coarse-grained randomly-oriented biotite porphyroblasts within calc-silicate-bearing vein.

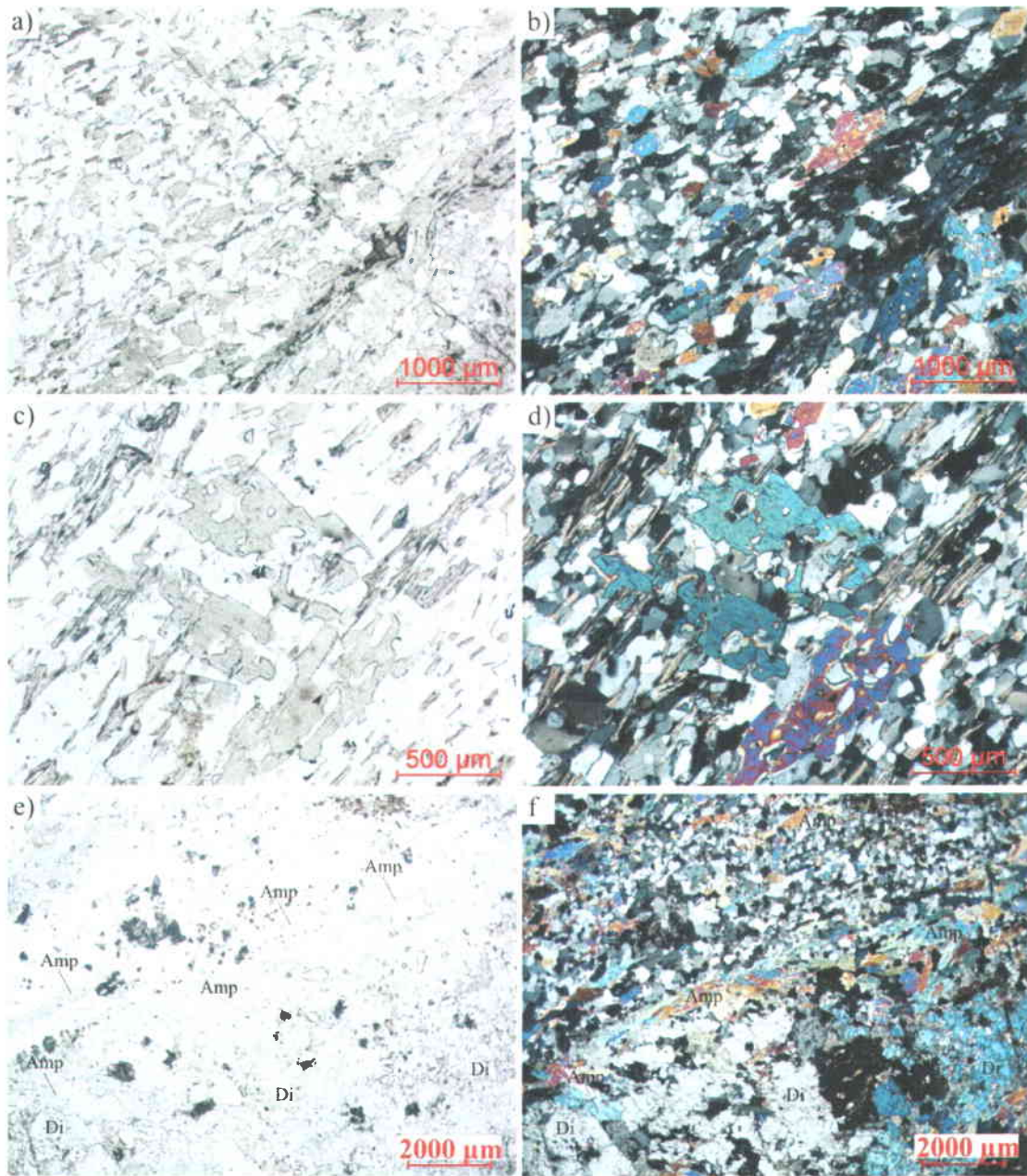


Figure 3.5.39: Natural light (left) and cross-polarized (right) photomicrographs showing preferentially-oriented or randomly-oriented amphibole porphyroblast within calc-silicate-bearing veins or Ca-bearing replacement. a) and b) amphibole porphyroblasts oriented by S_2 in Ca-bearing replacement. c) and d) large amphibole porphyroblasts randomly oriented within Ca-bearing replacement. Note the presence of oriented biotite porphyroblasts. e) and f) diopside porphyroblasts coexisting with deformed amphibole porphyroblasts.

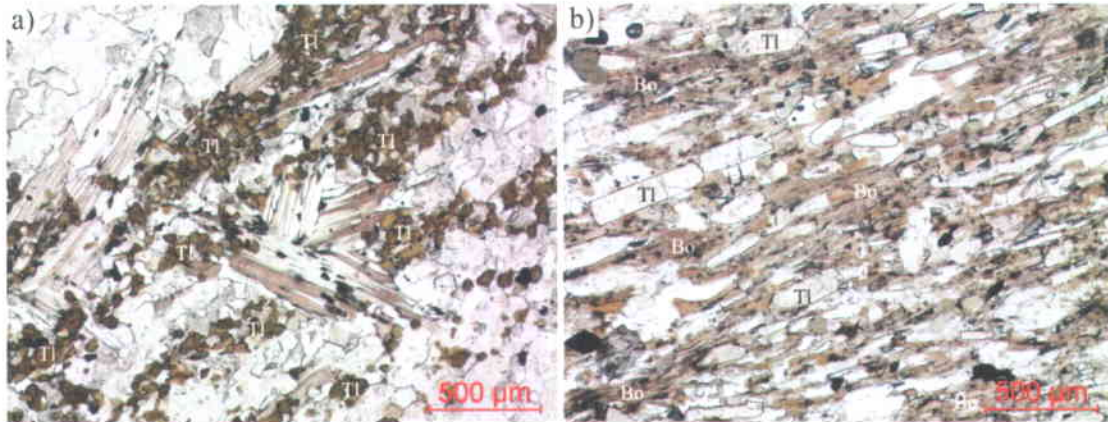


Figure 3.5.40: Natural light photomicrographs of tourmaline crystals within a calc-silicate-bearing vein shown in plan (a) and vertical (b) views. Note the different shape (and pleochroism) of tourmaline crystals between both views. In (b), tourmaline crystals are outlined by dotted lines. Note the long axis of tourmaline crystals which is aligned parallel to the fabric defined by biotite crystals.

In calc-silicate-bearing veins, minerals that are interpreted to belong to an early prograde stage include: biotite, diopside, microcline, plagioclase, and tourmaline. In replacement bands, prograde minerals include biotite, garnet, and plagioclase. Retrograde mineral assemblages are difficult to determine since not all hydrous phases are necessarily retrograde: some may result from hydrothermal alteration (Meinert, 1992). Hydrous minerals within both calc-silicate-bearing veins and Ca-bearing replacement include: clinozoisite/epidote, chlorite, prehnite, muscovite, and saussurite/sericite after plagioclase. The replacement of amphibole and sulphides by clinozoisite and epidote (Figure 3.5.42) occurs in other amphibolite-facies gold deposits where it is attributed to retrograde metamorphism (e.g. Neumayr et al., 1993). In skarn environments, the presence of prehnite and epidote has been attributed to hydrothermal alteration (e.g. Pan, Fleet and Stone, 1991). Although calcite locally replaced plagioclase, which could suggest that it is retrograde, some calcite porphyroblasts may be prograde. Detailed P-T studies are required in order to determine the conditions of formation of hydrous phases replacing prograde minerals and determine whether they result from retrograde metamorphism or late hydrothermal alteration. Table 3.5.8 and Figures 3.5.41 to 3.5.43 summarize the most common minerals that replace prograde minerals within Ca-bearing alteration.

Table 3.5.8: List of minerals replacing prograde minerals within Ca-altered rocks.

Initial prograde mineral	Replacing mineral(s)	Example
biotite	prehnite	Figures 3.6.41c to 3.6.41f
biotite	chlorite	Figures 3.6.41a to 3.6.41d
biotite	muscovite	Figures 3.6.41c and 3.6.41d
amphibole-sulfides	clinozoisite/epidote	Figures 3.6.42a to 3.6.42d
amphibole-sulfides	prehnite	Figures 3.6.42e and 3.6.42f
plagioclase	saussurite/epidote	Figure 3.6.43a
plagioclase	sericite	Figures 3.6.43a and 3.6.43b
plagioclase	carbonate	Figures 3.6.43b

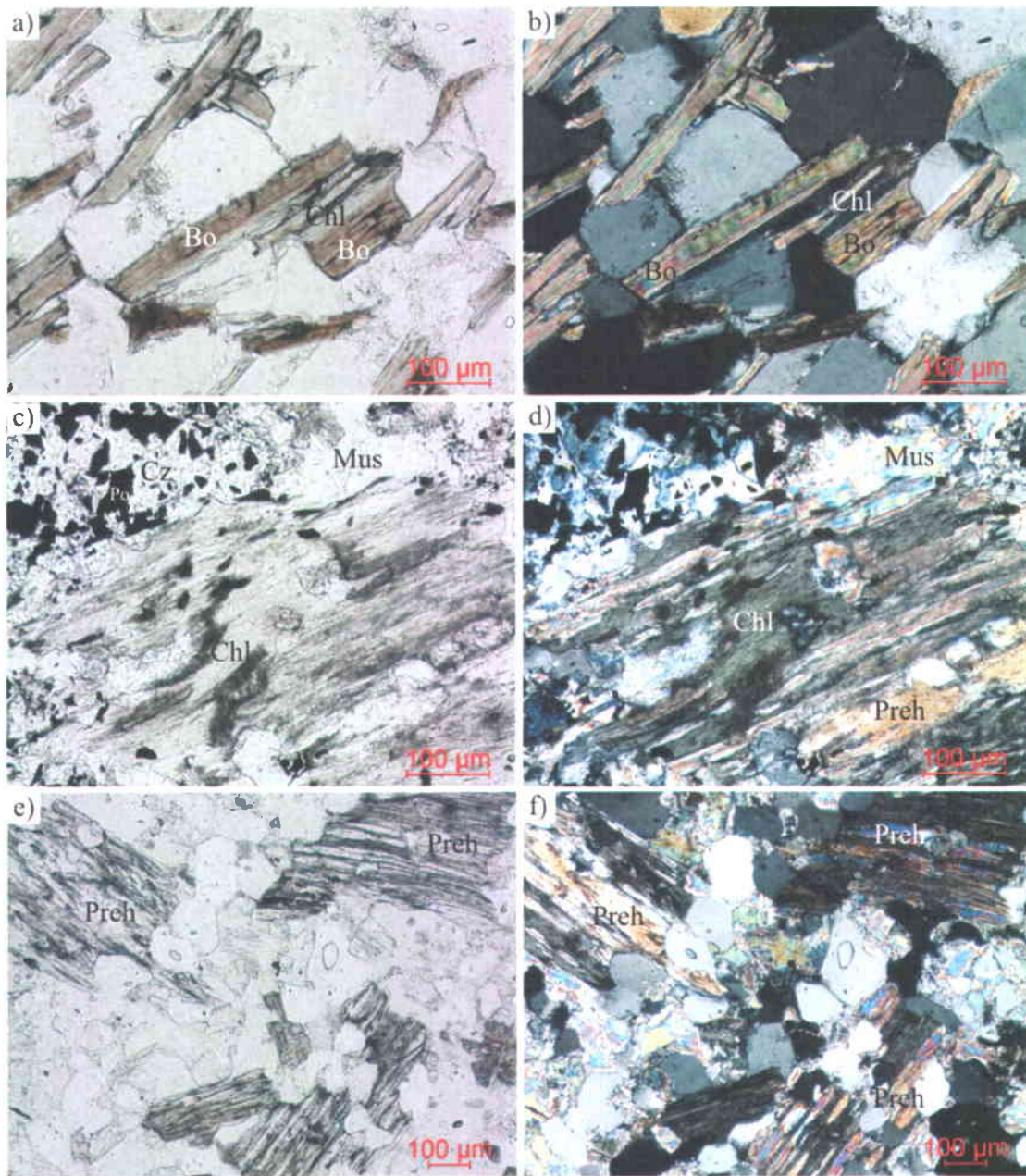


Figure 3.5.41: Natural light (left) and cross-polarized (right) photomicrographs of biotite porphyroblasts retrograded to various minerals within Ca-altered rocks. a) and b) biotite retrograded to chlorite. c) and d) biotite retrograded to chlorite, prehnite, and muscovite. Note the replacement of sulphides by clinozoisite in the upper part of the photograph. e) and f) randomly-oriented biotite porphyroblasts replaced by prehnite.

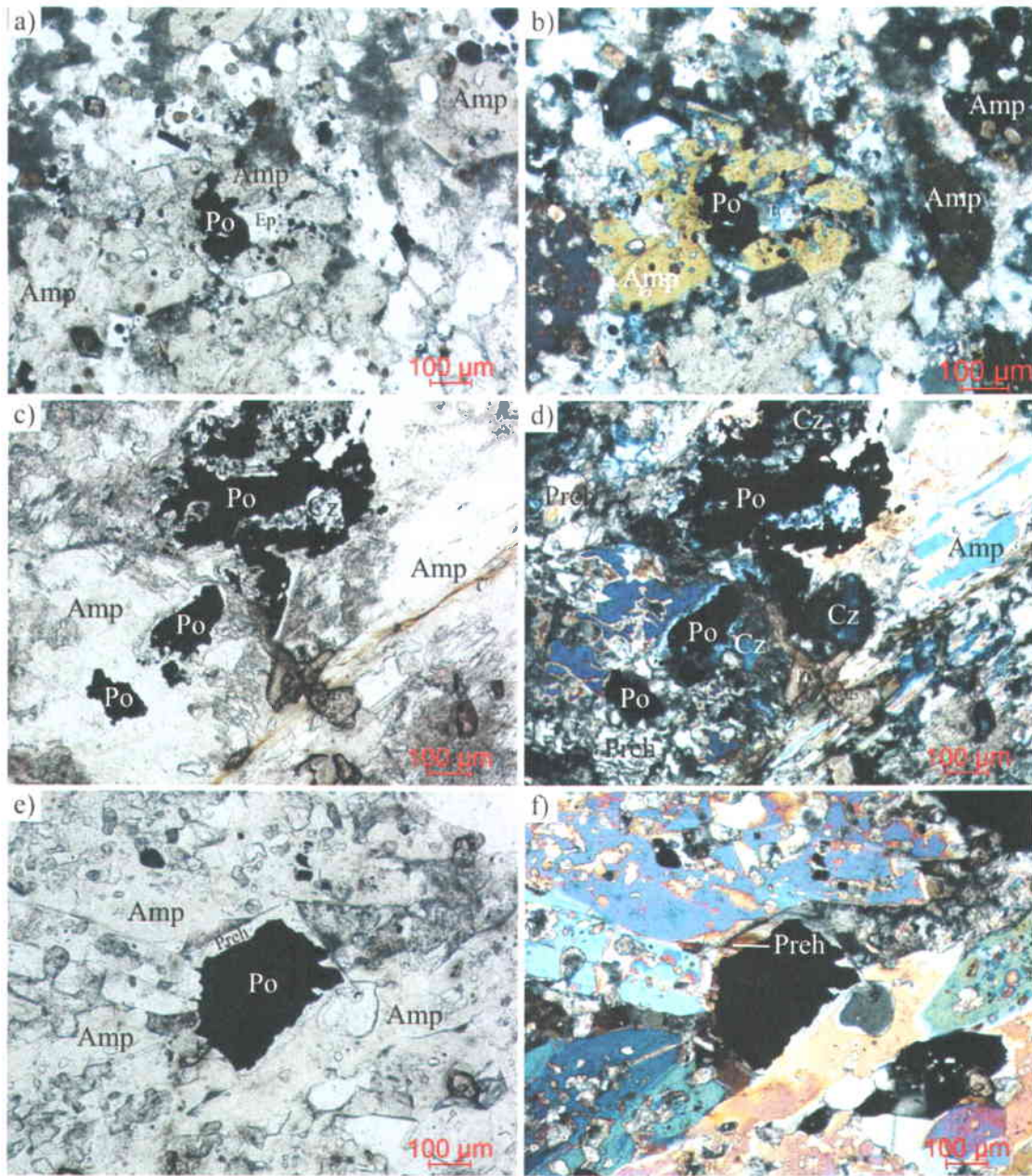


Figure 3.5.42: Natural light (left) and cross-polarized (right) photomicrographs of amphibole porphyroblasts and sulphides retrograded and/or altered to various minerals within Ca-altered rocks. a) and b) pyrrhotite inclusion within amphibole porphyroblast replaced by epidote. c) and d) pyrrhotite replaced by clinozoisite and amphibole replaced by prehnite. e) and f) retrograde prehnite rim between randomly-oriented amphibole porphyroblasts and pyrrhotite.

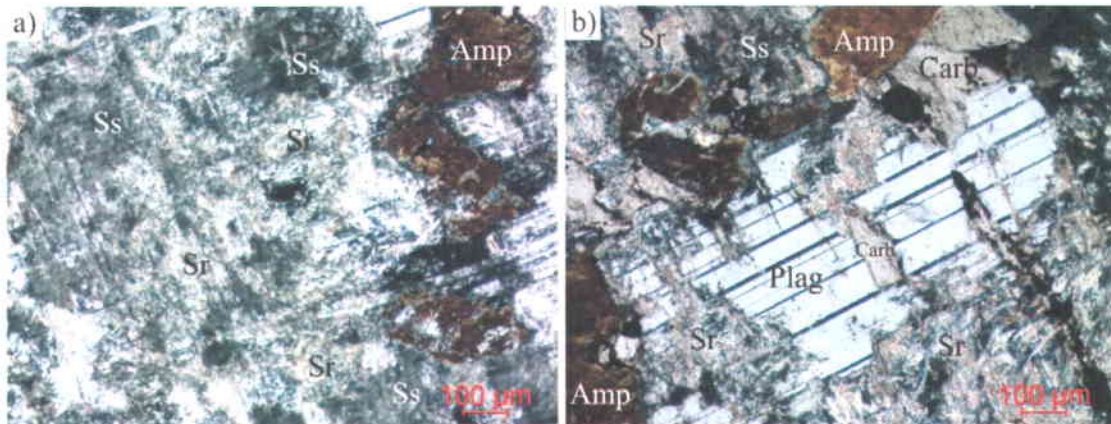
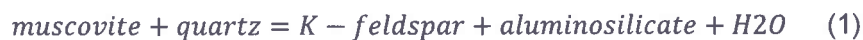


Figure 3.5.43 Cross-polarized photomicrographs of plagioclase altered to various minerals within Ca-altered rocks. a) plagioclase altered to sericite and saussurite. b) plagioclase altered to sericite and carbonate.

Although retrogradation is not confined to Ca-bearing alteration and other mineralized features, retrogradation does appear to be preferentially localized around previously altered rock. The retrogradation might be explained by the occurrence of a late metasomatic fluid which hydrated already mineralized and altered rocks. The timing and origin of the inferred metasomatic fluid is hard to constrain. However, the fact that it does affect late- to post-tectonic amphibole porphyroblasts might indicate that it postdated the episode of static growth.

An important characteristic of metasomatic bands hosted by aluminosilicate-bearing units is that such bands are ubiquitously bounded by ~5 cm-thick halos free of aluminosilicate porphyroblasts (Figure 3.5.44). The fact that aluminosilicate porphyroblasts did not develop around calc-silicate bands of the aluminous zones might indicate that calc-silicate replacement occurred before the formation of porphyroblasts and hence before the peak of metamorphism. This may result from the fact that by increasing the concentration of “CaO” and decreasing the concentration of “K₂O” (Figure 3.5.24a) in the host rock, Ca-bearing alteration precluded the reaction:



from occurring, hence preventing aluminosilicate from forming.

As previously mentioned, deposit-scale variations in the thickness of aluminosilicate-bearing sequences (e.g. Figure 3.5.7) might be explained by variations in the intensity of the Ca-bearing alteration and by the fact that the composition of certain sedimentary sequences are more prone to develop aluminosilicate porphyroblasts upon metamorphism.

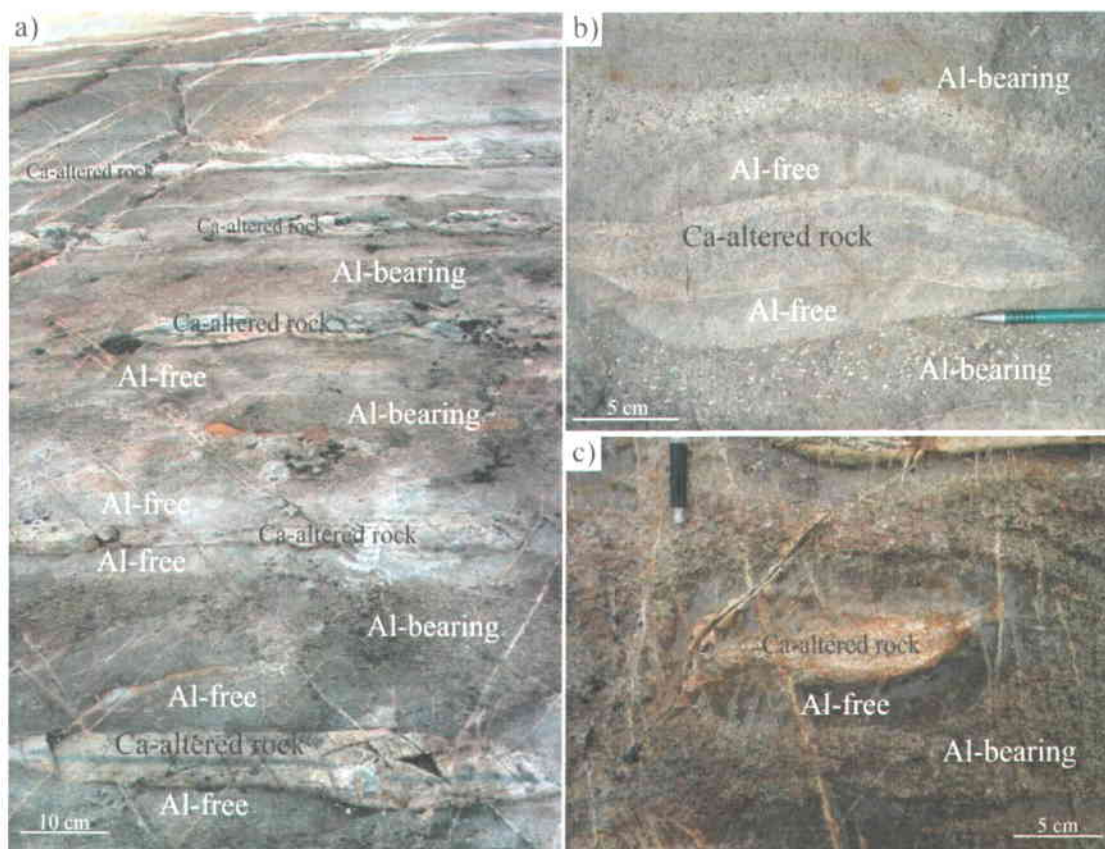


Figure 3.5.44: Photograph showing aluminosilicate-free halos around Ca-bearing bands hosted by the aluminosilicate-bearing sequence.

In summary, the fact that calc-silicate-bearing veins are deformed by D_2 and contain prograde metamorphic minerals (within the veins and in vein selvages) suggests that such veins were emplaced either before or early-in the main tectono-metamorphic event (D_2). The presence of randomly-oriented and sometimes euhedral porphyroblasts within and in vein selvages also indicates that P-T conditions suitable for porphyroblasts growth outlasted the main deformational events. Evidence for a Ca-bearing metasomatic fluid that caused hydration of pre-existing prograde minerals is ubiquitous. The fact that some of the randomly-oriented porphyroblasts are affected by such a fluid suggests that part of the metasomatic replacement occurred after the episode of static growth and hence postdates the main deformational events.

3.5.5 Potassic Alteration

Potassic alteration is principally present as pervasive alteration of the host rock (typically composed of high proportions of microcline and biotite) and as biotite-and microcline-bearing veins and veinlets (e.g. Figures 3.5.21e and 3.5.21f). Like previously described, potassic alteration is difficult to visually recognize in hand specimen, specifically when it is solely present as microcline. Following the method described in section 3.5.2 *Least-Altered Samples*, samples interpreted to have been affected by hydrothermal potassic alteration are displayed on Figure 3.5.45, along with samples considered to be the least-altered. Even though potassic alteration is an important characteristic of auriferous zones (see below), it is not confined to them. However, potassic alteration is not widely distributed over the region and over the Éléonore property (e.g. Figure 2.5.20), which suggests that it is relatively proximal to the deposit area. Within the deposit area, the distribution of potassic alteration at surface is difficult to determine because it relies on a sampling population whose distribution is scarce and sporadic (Figure 3.5.45).

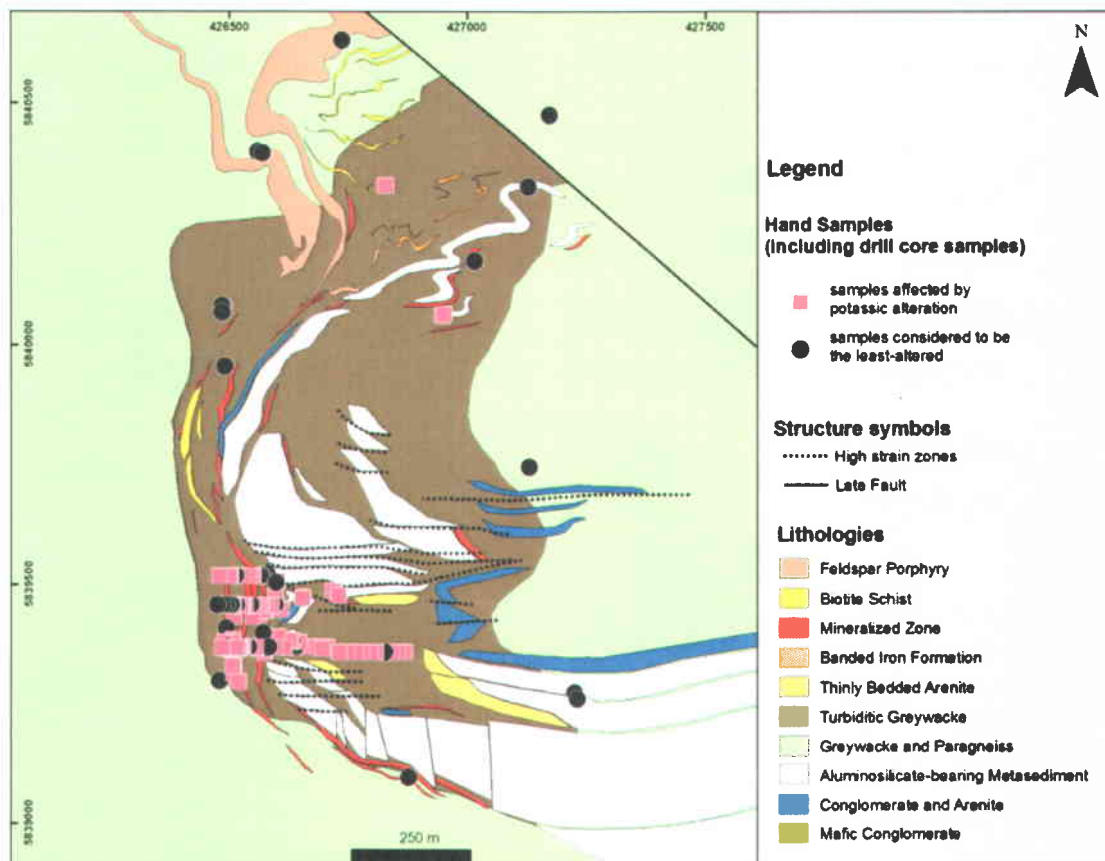


Figure 3.5.45: Geological map of the Roberto deposit showing the distribution of samples affected by potassic alteration and samples considered to be the least altered. Some samples are from drillcore vertically projected on the surface map. Coordinated are in UTM Nad83.

3.5.5.1 Mineralogical and Petrographic Characteristics of K-altered Greywacke

The mineralogy of K-altered samples depends on the nature of the protolith (greywacke, massive greywacke, aluminosilicate-bearing rocks) (Table 3.5.9). K-altered greywacke host rocks are themselves subdivided into two groups: one comprising samples located in auriferous zones, and another comprising samples located outside and/or distant from auriferous bodies. The purpose of the latter subdivision is to investigate whether the mineralogy of K-altered rocks varies with their proximity to ore zones. Mineral assemblages of K-altered greywacke and massive greywacke are similar. The more noticeable differences in the mineralogy of K-altered greywacke outside auriferous zones and K-altered greywacke within auriferous zones are the abundance of tourmaline which formed at the expense of biotite, and higher content of sulphide minerals (typically arsenopyrite and pyrrhotite) in greywacke within auriferous zones (Figure 3.5.46). The mineral assemblage of K-altered aluminosilicate-bearing rocks primarily differs by

the presence of muscovite (Figure 3.5.47). Potassic calc-silicate-free veins and veinlets are typically composed of quartz, microcline, tourmaline, biotite, arsenopyrite, and pyrrhotite (e.g. Figure 3.5.48). Such veins and veinlets are an important component of the Roberto zones' auriferous stockwork (see section 3.5.7 *Roberto Zone*).

Table 3.5.9: Mineralogy of K-altered rocks.

k-altered host rock	mineralogy	example
greywacke outside MZ	Qtz-MI-Bo-Tl-Asp-Po±Plag	Figures 3.6.46a to 3.6.46b
greywacke within MZ	Qtz-MI-Tl-Asp-Po±Bo±Au	Figures 3.6.46c to 3.6.46d
massive greywacke	Qtz-Bo-MI-Asp-Po±Tl	Figures 3.6.47a to 3.6.47b
Al-bearing rocks	Qtz-Bo-Al/Mus/Qtz-Mus-MI-Tl-±Plag±Asp±Po	Figures 3.6.47c to 3.6.47d

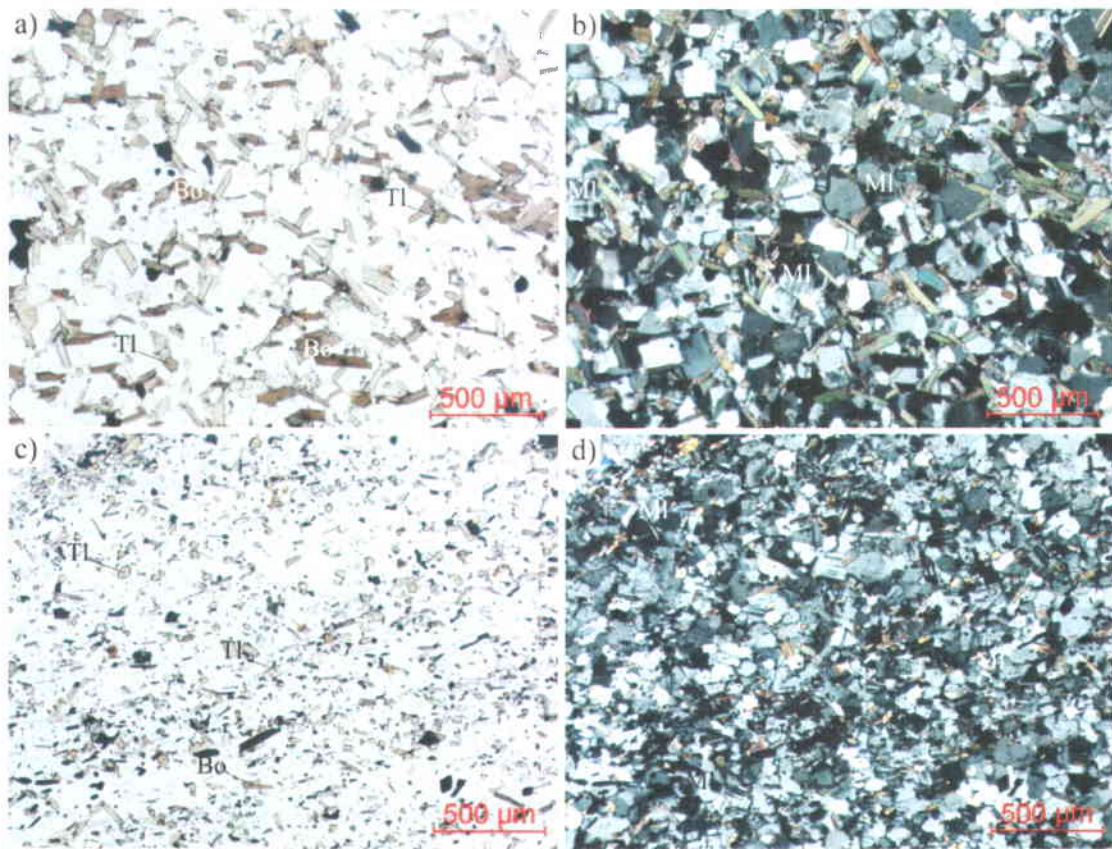


Figure 3.5.46: Natural light (left) and cross-polarized (right) photomicrographs of K-altered greywacke located outside (a, b) and within (c, d) auriferous zones. Note the finer grain size in (c, d) and the predominance of tourmaline crystals over biotite.

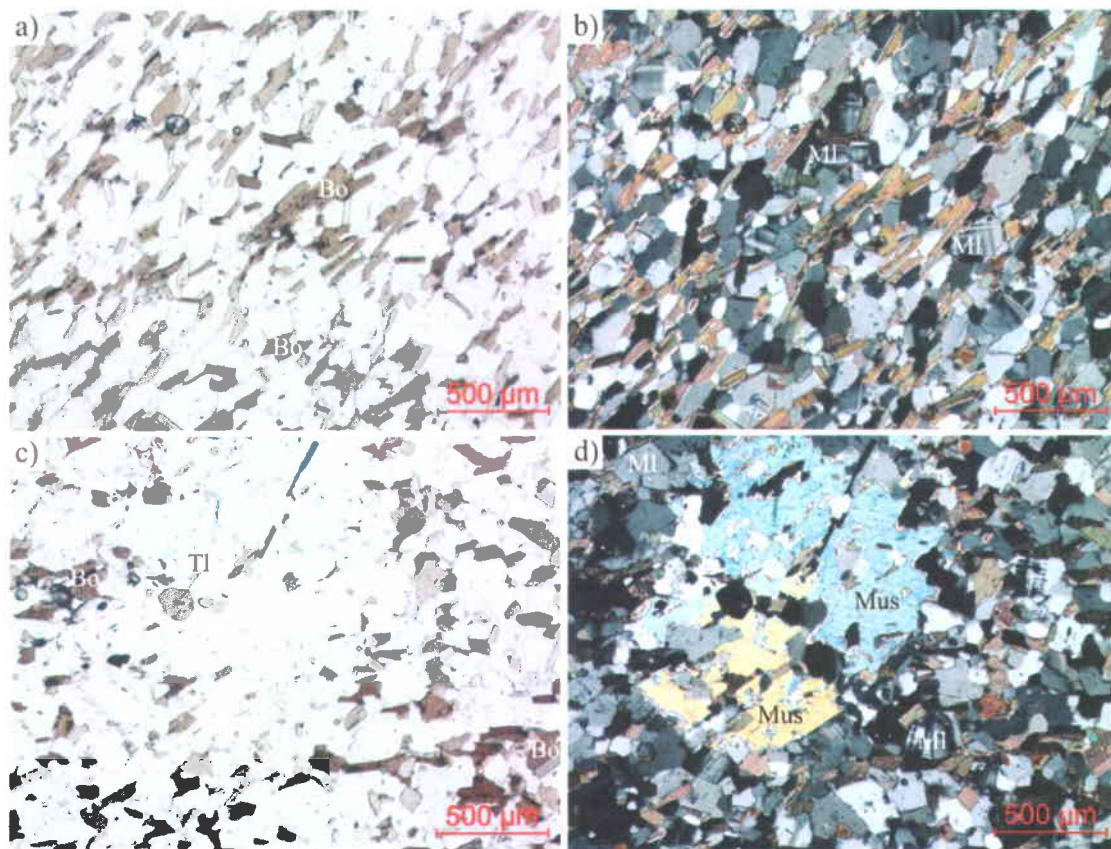


Figure 3.5.47: Natural light (left) and cross-polarized (right) photomicrographs of K-altered greywacke in massive greywacke (a, b) and aluminosilicate-bearing rocks (c, d).

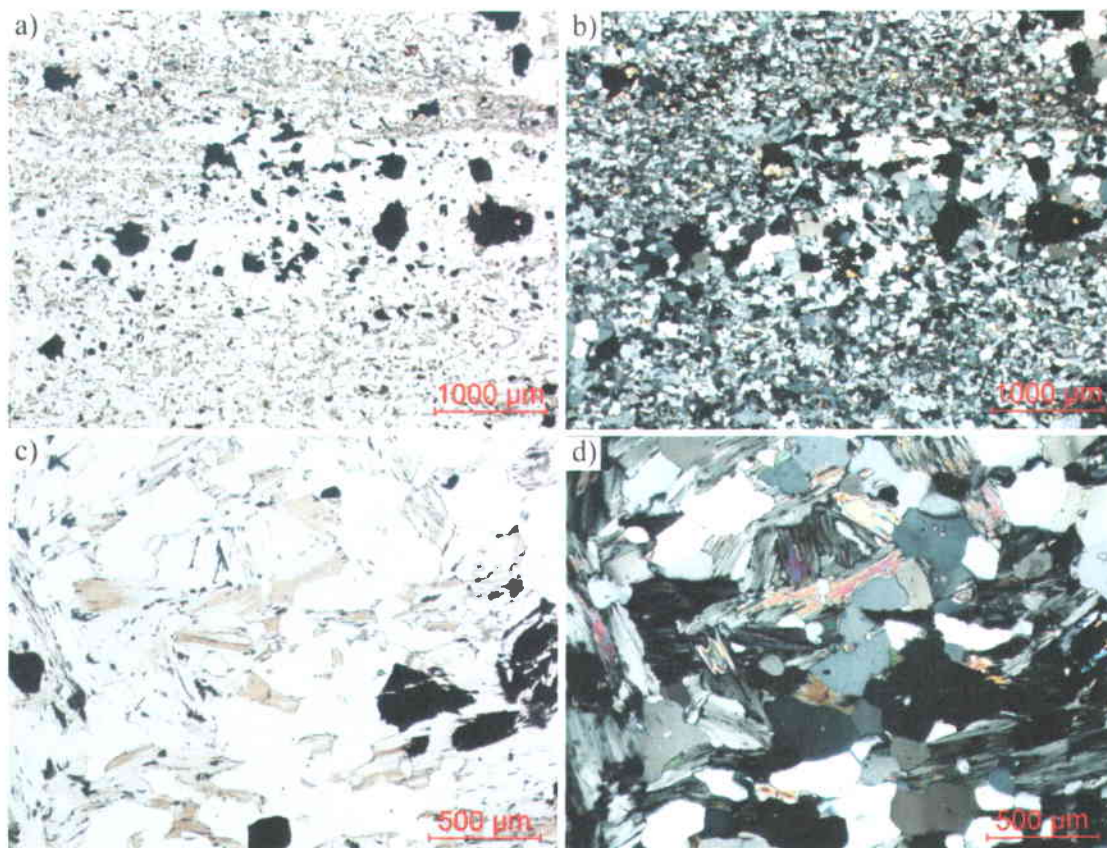


Figure 3.5.48: Natural light (left) and cross-polarized (right) photomicrographs of microcline and/or biotite bearing veins and veinlets within Roberto zone. a) and b) microcline-tourmaline-arsenopyrite-pyrrhotite-bearing quartz veinlets. c) and d) biotite (locally replaced by chlorite)-arsenopyrite-pyrrhotite-bearing quartz vein in Roberto zone.

3.5.5.2 Geochemistry of K-altered Rocks

Potassic alteration is an important component of alteration assemblages associated with gold mineralization at Éléonore. As previously mentioned, although potassic alteration is usually found in principal auriferous zones, it also occurs elsewhere in less-mineralized units of the deposit area (Figure 3.5.45). The study of the distribution of potassic alteration over the deposit area is complicated by the fact that microcline is not easily recognizable in hand specimen. Nonetheless, potassic alteration represents an important part of the auriferous hydrothermal system, and forms, along with Ca-bearing alteration, the hydrothermal footprint of the deposit. This section investigates the geochemical signature associated with potassic alteration by comparing the geochemistry of K-altered rocks with the geochemistry of “least-altered” equivalents. Rock types are subdivided according to the subdivision previously used to study

their petrographic characteristics (greywacke, massive greywacke, and aluminosilicate-bearing rocks). K-altered greywacke samples are themselves subdivided into two groups: one comprising samples located in auriferous zones or near auriferous veins, and another comprising less-mineralized samples located outside and/or far from auriferous bodies. The purpose of the latter subdivision is to investigate whether the geochemical signature associated with potassic alteration in auriferous zones is also present in the less mineralized and more distal parts of the deposit. All samples of massive greywacke and aluminosilicate-bearing rocks are located outside of auriferous zones.

Isocon diagrams were constructed for greywacke, massive greywacke, and aluminosilicate-bearing rocks. K-altered rocks and least-altered equivalents of each rock type were first selected following the method of section 3.5.2 *Least-Altered Samples*. The range of compositions for each group of K-altered and least-altered rocks can be visualized on the box diagrams of Figure 3.5.49. Averages for each group of K-altered and least-altered rocks were then calculated (Tables 3.5.10 and 3.5.11), and isocon diagrams were constructed using the average compositions (Figure 3.5.50). Following the method of Huston (1993), histograms illustrating the various mass changes of each K-altered rock type were constructed based on their respective isocon diagrams (Figure 3.5.50).

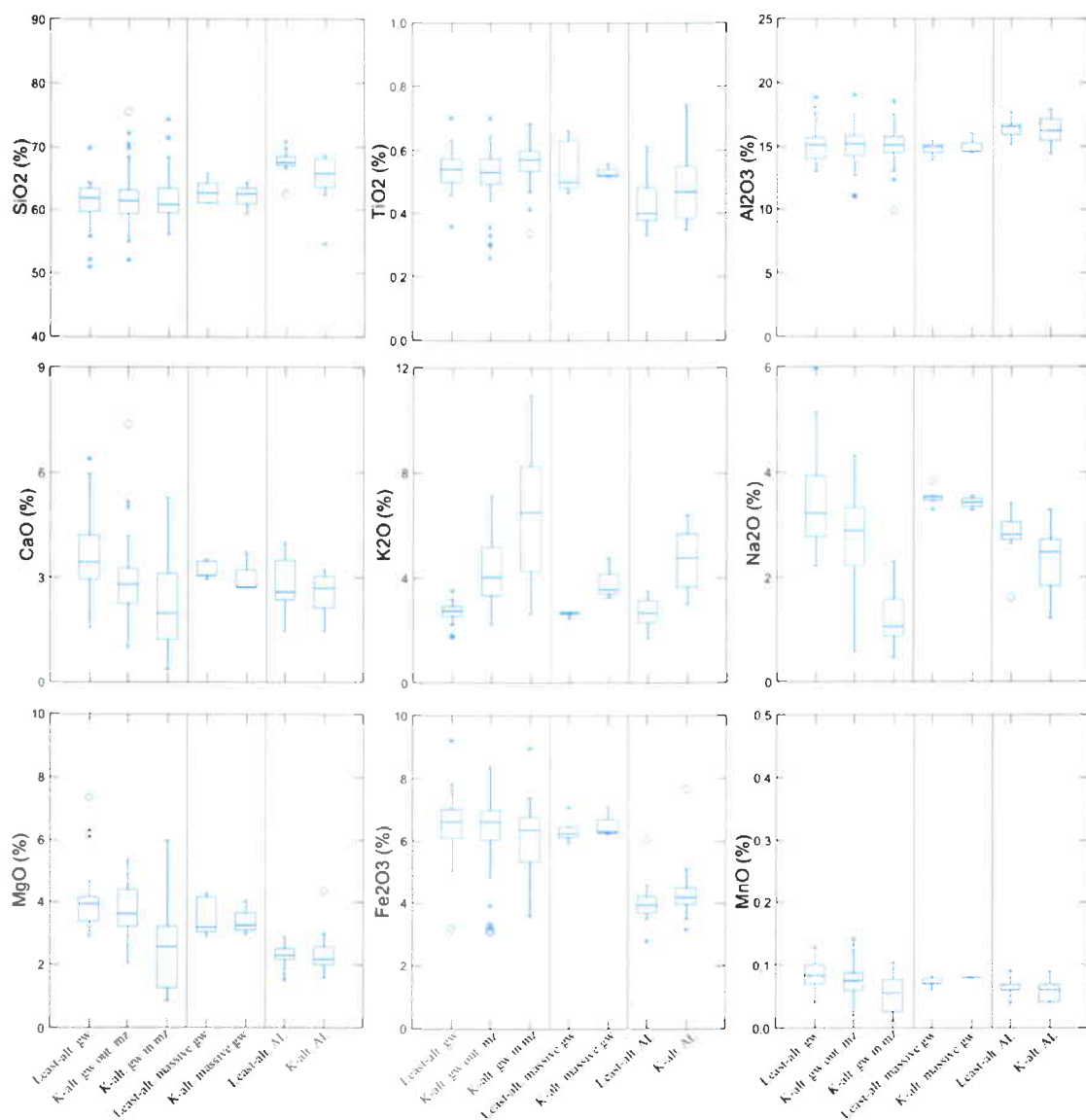


Figure 3.5.49: Box diagrams comparing the range of oxide concentrations of K-altered and least-altered equivalents for greywacke, massive greywacke, and aluminosilicate-bearing rocks. The center horizontal line marks the median of a given suite. The length of each box shows the range within which the central 50% of the values fall, with the box edges at the first and third quartiles. The whiskers show the range of observed values that fall within the inner fences, defined as 1.5 and -1.5 times the absolute value of the box. Values between inner and outer fences (3 and -3 times the absolute value of the box) are plotted with asterisks. Values beyond the outer fences are plotted with empty circles. All samples are from this study. Number of samples: least-altered greywacke (Least-alt. gw) = 24; K-altered greywacke outside mineralized zones (K-alt. gw out. mz) = 40; K-altered greywacke within mineralized zones (K-alt. gw in. mz) = 26; least-altered massive greywacke (Least-alt. massive gw) = 5; K-altered massive greywacke (K-alt. massive gw) = 3; least-altered aluminosilicate-bearing rocks (Least-alt. AL) = 9; K-altered aluminosilicate-bearing rocks (K-alt. AL) = 11.

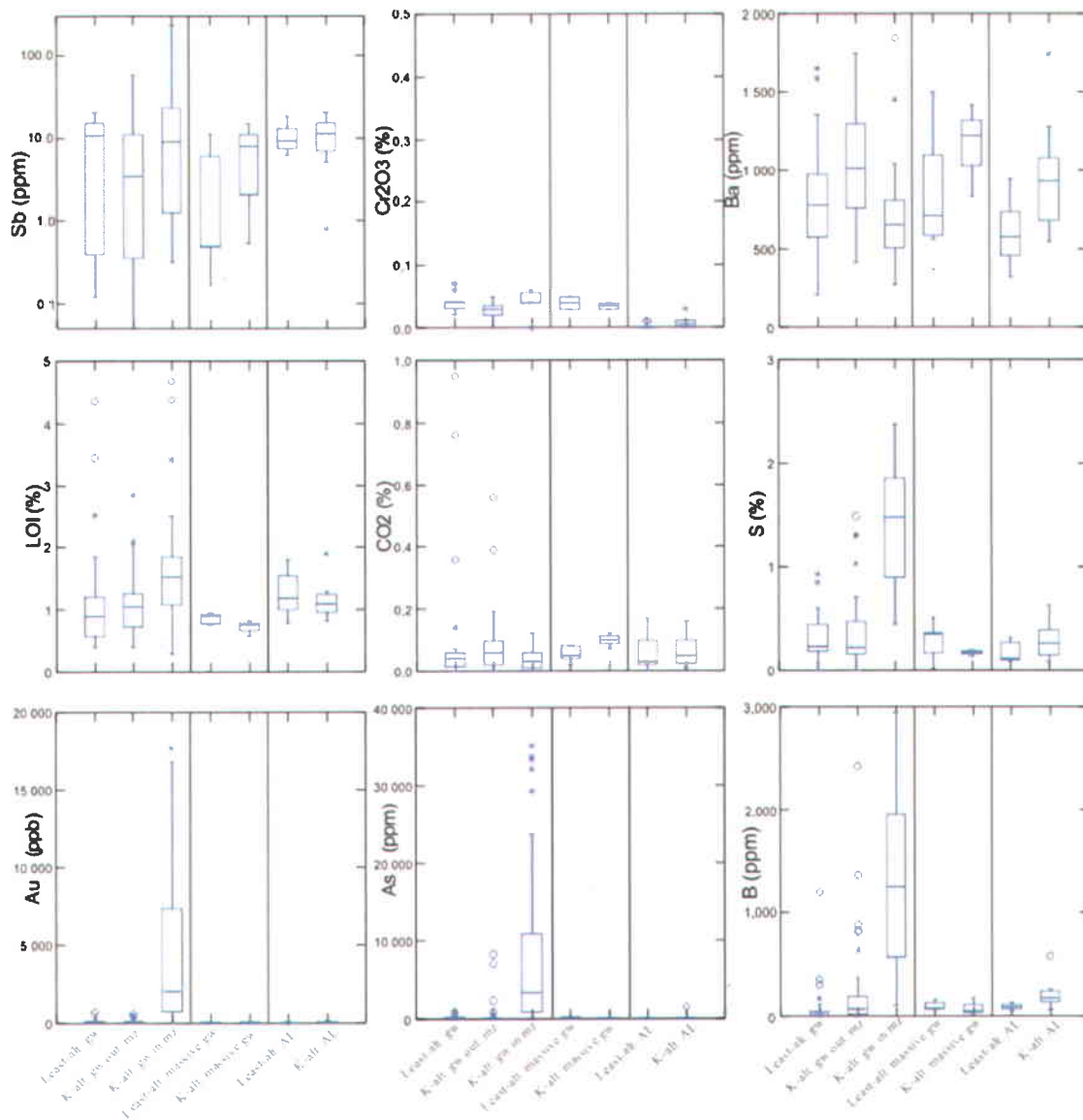


Figure 3.5.49: (continued) Box diagrams comparing the range of element concentrations of K-altered and least-altered equivalents for greywacke, massive greywacke, and aluminosilicate-bearing rocks.

Table 3.5.10: Major element averages of K-altered and least-altered equivalents.

ANALYTE	SiO ₂	Al ₂ O ₃	CaO	MgO	Na ₂ O	K ₂ O	Fe ₂ O ₃	MnO	TiO ₂	P ₂ O ₅	Cr ₂ O ₃	LOI	Sum	CO ₂	S
DETECTION (Highest)	0.01	0.01	0.01	0.03	0.02	0.01	0.01	0.01	0.01	0.01	0.01	0.01	0.01	0.01	0.01
UNITS	%	%	%	%	%	%	%	%	%	%	%	%	%	%	%
Least-Altered Greywacke (n=24) (Standard Deviation)	61.0 3.9	15.2 1.5	3.6 1.2	4.1 1.1	3.4 0.9	2.7 0.4	6.5 1.1	0.1 0.0	0.5 0.1	0.2 0.0	0.0 0.0	1.4 1.3	98.9 0.7	0.3 0.8	0.3 0.2
K-Altered Greywacke Outside Min. Zones (n=40) (Standard Deviation)	62.0 4.4	15.0 1.7	2.9 1.1	3.7 0.9	2.7 0.8	4.3 1.3	6.3 1.4	0.1 0.0	0.5 0.1	0.2 0.0	0.0 0.0	1.1 0.5	98.9 1.0	0.1 0.1	0.4 0.4
K-Altered Greywacke within Min. Zones (n=26) (Standard Deviation)	62.1 4.3	15.1 1.7	2.2 1.2	2.5 0.5	1.2 0.3	6.4 2.3	6.0 1.2	0.1 0.0	0.6 0.1	0.2 0.0	0.0 0.0	1.7 1.4	98.1 1.4	0.0 0.0	1.5 0.6
Least-Altered Massive Greywacke (n=5) (Standard Deviation)	63.0 2.0	14.8 0.6	3.2 0.3	3.5 0.6	3.5 0.2	2.6 0.1	6.4 0.4	0.1 0.0	0.5 0.1	0.2 0.0	0.0 0.0	0.9 0.1	98.7 1.9	0.1 0.0	0.3 0.2
K-Altered Massive Greywacke (n=3) (Standard Deviation)	62.1 2.7	15.0 0.8	3.1 0.6	3.4 0.3	3.4 0.1	3.9 0.8	6.5 0.5	0.1 0.0	0.5 0.0	0.2 0.0	0.0 0.0	0.7 0.1	99.0 1.8	0.1 0.0	0.2 0.0
Least-Altered Aluminosilicate Sequence (n=9) (Standard Deviation)	67.5 2.3	16.5 0.8	2.8 0.9	2.3 0.4	2.8 0.3	2.7 0.6	4.1 0.9	0.1 0.0	0.4 0.1	0.1 0.0	0.0 0.0	1.2 0.4	100.5 0.6	0.1 0.1	0.2 0.1
K-Altered Aluminosilicate Sequence (n=10) (Standard Deviation)	65.0 4.0	16.3 1.1	2.5 0.6	2.4 0.7	2.3 0.2	4.8 1.2	4.5 1.2	0.1 0.0	0.5 0.1	0.1 0.0	0.0 0.0	1.2 0.3	99.7 0.5	0.1 0.1	0.3 0.2

Table 3.5.11: Selected minor element averages of K-altered and least-altered equivalents.

ANALYTE	Au	As	B	Sb	Ag	Cu	Zn	Pb	Y	Zr	Ba	Li	Rb	Sr
DETECTION (Highest)	5	3	10	5	2	0.5	0.5	2	0.5	0.5	3	1	2	2
UNITS	ppb	ppm	ppm	ppm	ppm	ppm	ppm	ppm	ppm	ppm	ppm	ppm	ppm	ppm
Least-Altered Greywacke (n=24) (Standard Deviation)	99 14.9	164 22.7	103 2.51	8 7	<2	44 20	73 10	32 26	12 3	112 17	810 378	75 28	112 31	598 200
K-Altered Greywacke Outside Min. Zones (n=40) (Standard Deviation)	99 14.4	558 170.1	246 46.2	7 10	<2	47 23	73 18	30 22	10 3	120 16	1039 375	68 23	149 50	565 186
K-Altered Greywacke within Min. Zones (n=26) (Standard Deviation)	6873 1072	11331 14100	1635 14.59	31 6.1	<2	58 16	56 23	28 12	12 3	118 17	717 352	37 23	208 53	511 188
Least-Altered Massive Greywacke (n=5) (Standard Deviation)	25 15	110 7.7	101 4.1	4 5	<2	43 2.7	74 7	30 3.2	11 1	126 11	891 403	65 28	112 25	638 61
K-Altered Massive Greywacke (n=3) (Standard Deviation)	22 14	83 72	81 78	8 7	<2	52 7	73 5	23 5	10 2	107 11	1160 297	57 3	144 0	455 87
Least-Altered Aluminosilicate Sequence (n=9) (Standard Deviation)	18 2.2	27 14	92 2.6	5 6	<2	33 14	67 16	20 15	5 1	109 22	612 216	61 25	104 23	791 60.5
K-Altered Aluminosilicate Sequence (n=10) (Standard Deviation)	46 88	179 452	208 13.7	11 6	<2	45 19	74 12	37 22	6 2	108 23	943 350	83 17	173 57	966 571

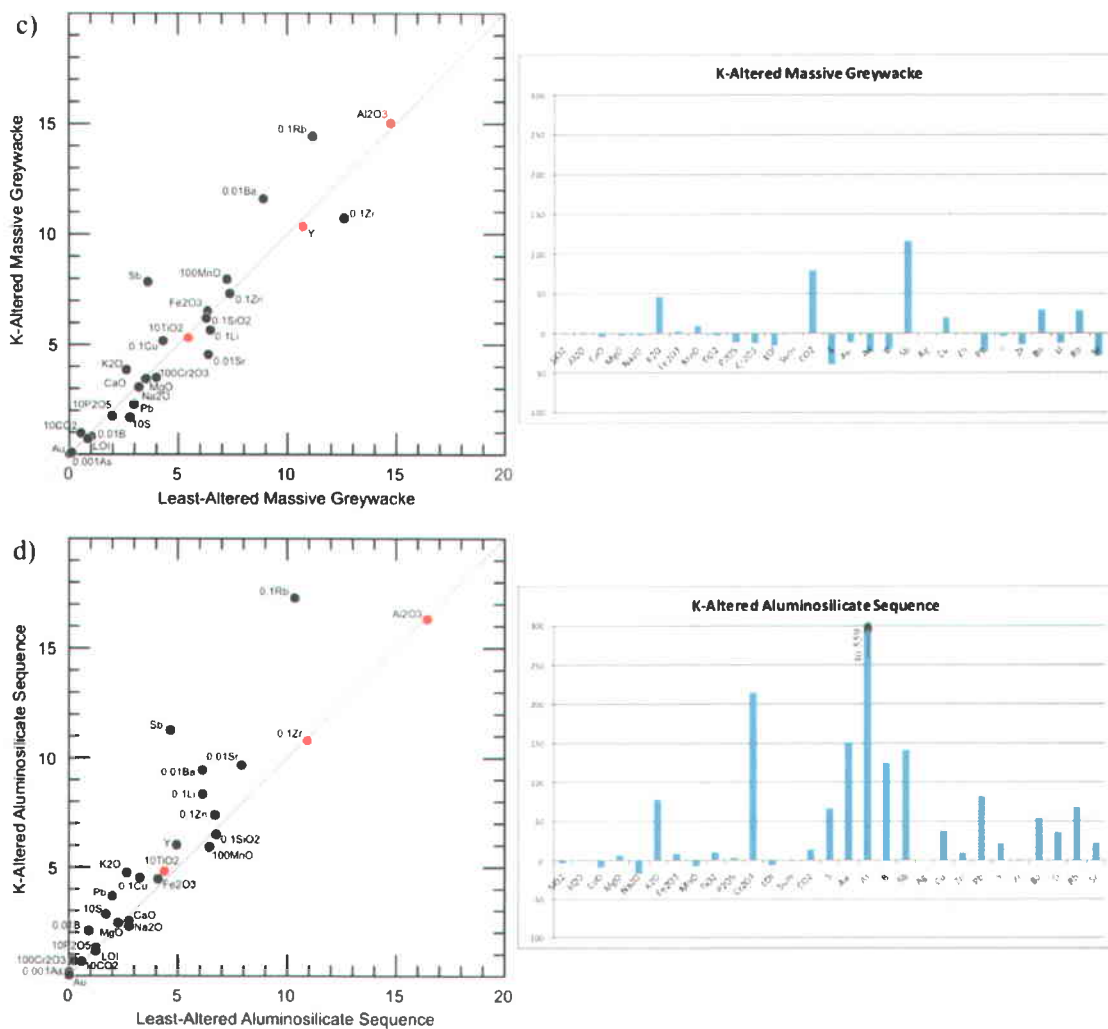


Figure 3.5.50: (continued) c) isocon diagram and mass balance histogram for least-altered and K-altered massive greywacke. d) isocon diagram and mass balance histogram for least-altered and K-altered aluminosilicate-bearing rocks.

The results show that isocons between least-altered and K-altered rocks can be constructed for all rock types based on at least 3 immobile elements (except for the “K-altered greywacke located outside mineralized zones” isocon which is only defined by TiO_2 and Al_2O_3 concentrations) (Figure 3.5.47). The mass balance histogram for “K-altered greywacke located outside mineralized zones” shows that significant gains in S, As, B, Ba, and Rb (among others), and significant losses in CO_2 , MgO, Na_2O , MnO, and Cr_2O_3 (among others), are associated with potassic gains (Figure 3.5.47a). For “K-altered greywacke located within mineralized zones”, the histogram shows that in addition of having gains in S, As, B, and Rb, the gains in K_2O are higher and are coupled with significant gains in Au and Sb (Figure 3.5.47b). Also, like “K-altered greywacke located outside mineralized zones”, “K-altered greywacke located within mineralized

zones" show losses in CO_2 , MgO , Na_2O , and MnO (among others). One discrepancy, however, is that whereas "K-altered greywacke located outside mineralized zones" show gains in Ba, "K-altered greywacke located within mineralized zones" show losses in Ba. The signature of "K-altered massive greywacke" is significantly different from that of K-altered greywacke outside and within mineralized zones. The biggest differences relate to S, Au, As, and B which were partly leached from "K-altered massive greywacke", and to CO_2 which was enriched (Figure 3.5.47c). K-altered aluminosilicate-bearing rocks, on the other hand, share similarities with K-altered greywacke in terms of S, As, and B, although they differ in terms of CO_2 and Cr_2O_3 which were both enriched.

Following the analysis of isocon diagrams and mass balance histograms between K-altered rocks and least-altered equivalents, it can be concluded that the geochemical signature resulting from potassic alteration varies with the host rocks. The comparison between signatures of K-altered greywacke outside mineralized zones and K-altered greywacke within mineralized zones is of significant importance because they presumably share similar protoliths but were affected to different degrees by alteration. Important observations in the signature of the two K-altered greywacke groups include the fact that their As, B, S, CO_2 concentrations and their major elements concentrations behaved similarly, while respective gains and losses of those elements were greater in "K-altered greywacke within mineralized zones" than in "K-altered greywacke outside mineralized zones". These observations strongly suggest that "K-altered greywacke outside mineralized zones" represent hybrids between least-altered rocks and mineralized rocks, and that the geochemical signature associated with potassic alteration and gold mineralization also occurs in more distal parts of the deposit. The distribution of elements on box diagrams also suggests that "K-altered greywacke outside mineralized zones" represent intermediate compositions between least-altered rocks and mineralized rocks (Figure 3.5.49). Spider diagrams constructed for least-altered and K-altered rocks indicate that besides variations in "Er" concentrations, K-altered rocks and least-altered equivalents cannot readily be distinguished in terms of trace elements (Figure 3.5.51).

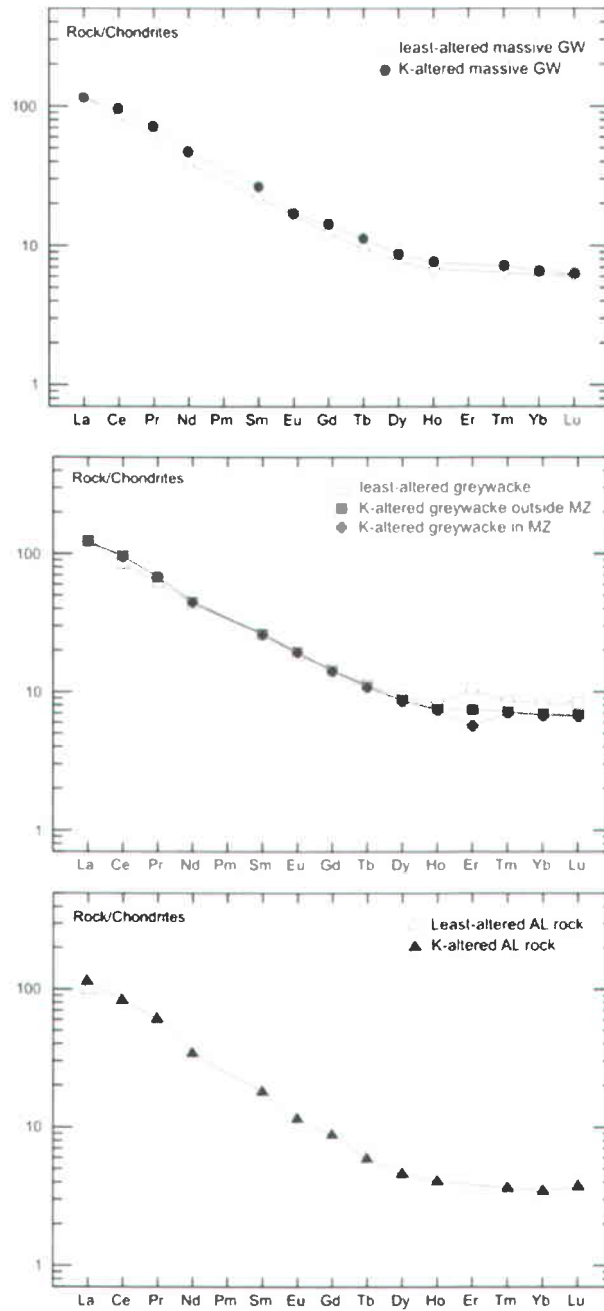


Figure 3.5.51: Chondrite-normalized (Sun and McDonough, 1989) spider diagram comparing trace element signatures of K-altered rocks and least-altered equivalents. Trace element concentrations displayed on the diagram represent averages calculated from the sample populations used to calculate average compositions of Tables 3.5.10 and 3.5.11. No trace element analyses were available for “Least-altered AL rock” besides “La”.

3.5.5.3 *Deformational and Metamorphic Characteristics of Potassic Alteration*

The timing of microcline and/or biotite bearing quartz veins and veinlets relative to the main deformational event (D_2) can be constrained from field observations. The structural characteristics of these veins and veinlets are particularly well defined in auriferous stockworks of the Roberto zone. There, it can be seen that while potassic veinlets have been folded, crenulated and transposed by D_2 (e.g. Figure 3.5.52), some of the veinlets define a cleavage which is axial planar to F_2 folds (Figure 3.5.53). Petrographic inspection indicates that folded veinlets and axial-planar veinlets are in petrogenetic continuity (i.e. mineral grains within them overlap vein boundaries) (e.g. Figures 3.5.53c to 3.5.53f), which suggests synchronous emplacement. Note however that, since the veins are recrystallized (indicated by the presence of polygonal quartz grains), initial cross-cutting relationships between veinlets may have been obliterated. The fact that some of the veinlets have been emplaced through the formation of a cleavage parallel to S_2 (e.g. Figure 3.5.54) suggests that their emplacement was synchronous with D_2 . This interpretation also agrees with the observation that the auriferous stockwork is locally preferentially developed on the short limbs of an F_2 Z-fold (Figure 3.5.55), which strongly suggests that folding mechanisms locally controlled sites of stockwork formation (Ravenelle et al., 2010). Note however, that since the veinlets of the stockwork are also intensely deformed by D_2 , they must have been generated early in D_2 . This interpretation requires that D_2 was a progressive event which occurred over a long period of time and led to complex finite states in deformed rocks. The pronounced stretching observed on vertical sections of the stockwork (e.g. Figure 3.5.52b (vertical) versus Figures 3.5.53a and 3.5.53b (horizontal)) indicates that the X axis of strain ellipsoid is steep within the stockwork, which corroborates with the style of the D_2 deformation observed elsewhere on the property (see section 3.3 *Structural Geology of the Roberto Deposit*).

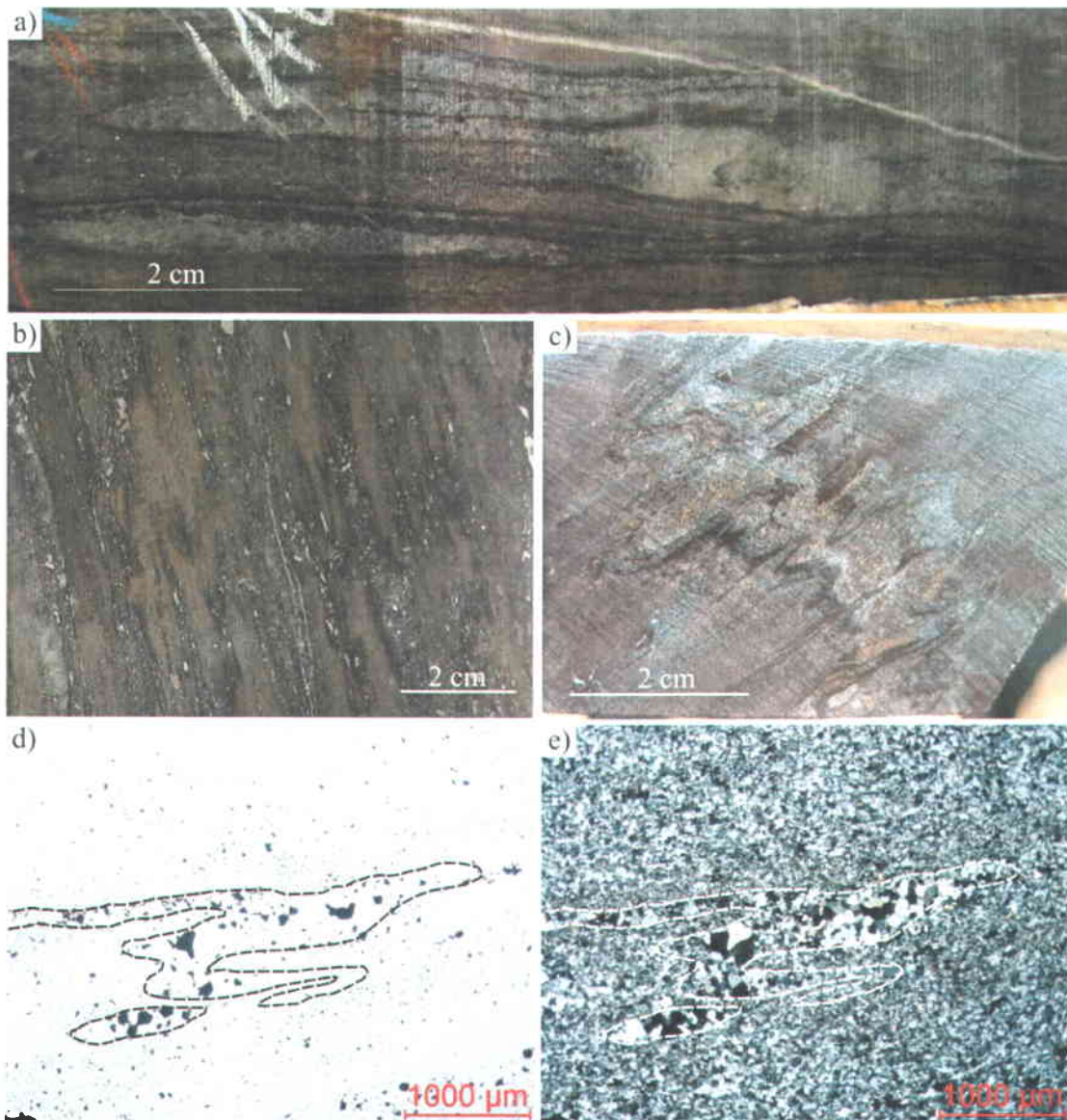


Figure 3.552: Photographs and photomicrographs showing folded and transposed microcline and/or biotite bearing quartz veins and veinlets within the auriferous stockwork of the Roberto zone. a) isoclinally folded quartz vein in "PQ" size drillcore with axial-plane oriented sup-parallel to core axis. b) transposed and tightly folded veinlets on a polished vertical section of a hand sample. c) folded and transposed vein in drillcore. d) and e) natural light (d) and cross-polarized (e) photomicrographs of an isoclinally folded and boudinaged veinlet hosted within a microcline and arsenopyrite rich matrix.

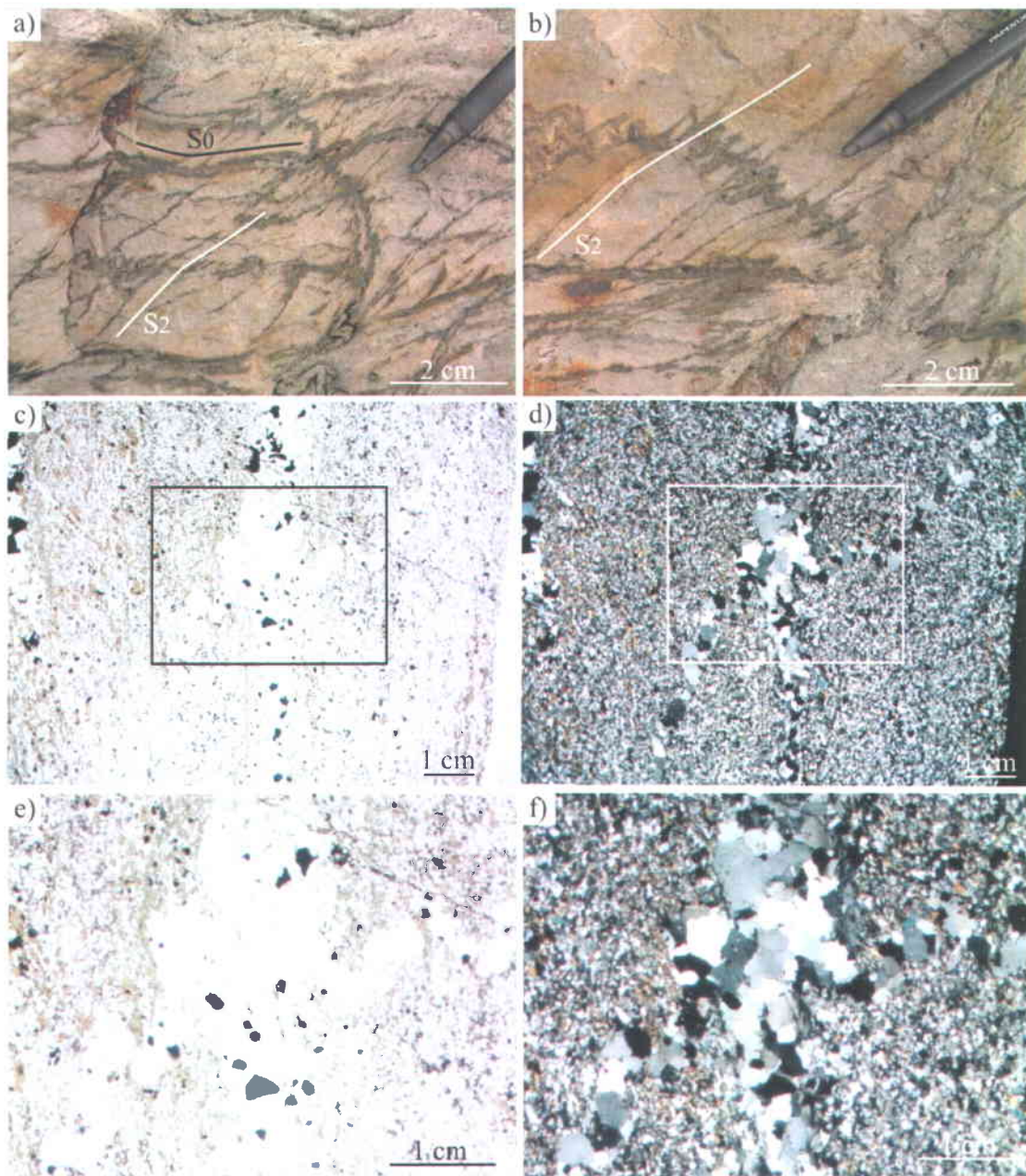


Figure 3.5.53: Photographs and photomicrographs which show textural characteristics of crenulated quartz veinlets and axial-planar quartz veinlets within the auriferous stockwork of the Roberto zone. a) and b) field examples of crenulated veinlets and axial-planar veinlets. c) and d) natural light (c) and cross-polarized (d) photomicrographs showing textures of a crenulated veinlet and an axial-planar veinlet. e) and f) close-up of (c) and (d). No cross-cutting relationship is visible between the two veinlets (i.e. quartz grains overlap the contact between the two veinlets) which suggests petrogenetic continuity.



Figure 3.5.54: Photograph of Roberto's auriferous stockwork showing microcline and/or biotite bearing quartz veinlets emplaced along S_2 planes through the generation of a cleavage oriented at high angle to bedding planes. Microcline and/or biotite bearing quartz veinlets are also emplaced along bedding planes which are folded and crenulated by S_2 . Photograph courtesy of Benoit Dubé.

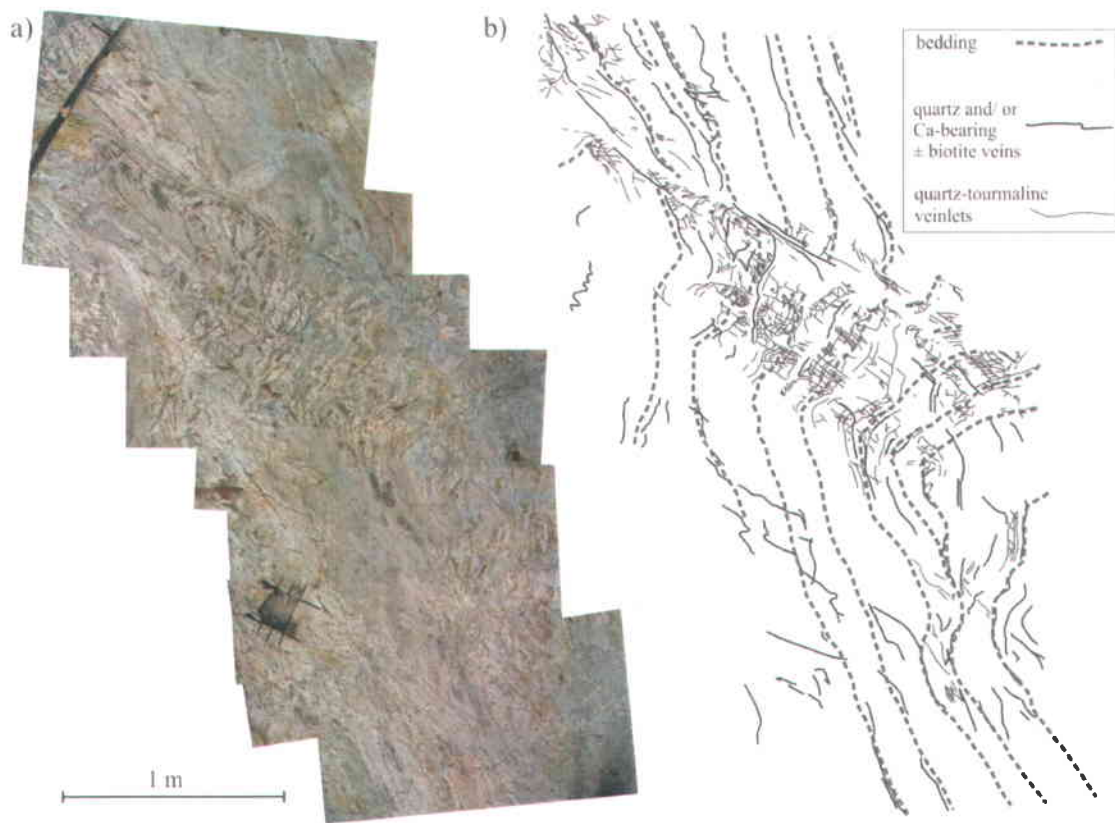


Figure 3.5.55: a) Photograph showing a part of Roberto's auriferous stockwork where the stockwork is preferentially developed on the short limb of a meter-scale F_2 Z-fold. b) interpreted drawing of the photograph in (a) showing the details of the auriferous stockwork. Modified from Ravenelle et al., 2010.

In terms of the relative timing between potassic alteration and peak of metamorphism, mineral assemblages within potassic veins and veinlets and K-altered host rocks (Table 3.5.9) are dominated by minerals which are typically considered prograde (e.g. biotite, microcline). Assuming that metamorphic peak was synchronous with the main deformation (D_2), the inferred prograde origin of minerals within K-altered rocks is consistent with biotite crystals being affected by S_2 (e.g. Figures 3.5.56a and 3.5.56b). The fact that microcline grains are equigranular and polygonal (Figure 3.5.56) indicates that recrystallization occurred during or after the peak of metamorphism. Evidence for retrograde metamorphism within K-altered rocks primarily consists of biotite being replaced by chlorite, which is typically observed in microcline and/or biotite bearing veins and veinlets. As mentioned in *section 3.4 Metamorphism*, the presence of hydrated phases like muscovite in K-altered aluminosilicate-bearing rocks is considered to result from the retrogradation of K-feldspar and aluminosilicate to quartz and muscovite.

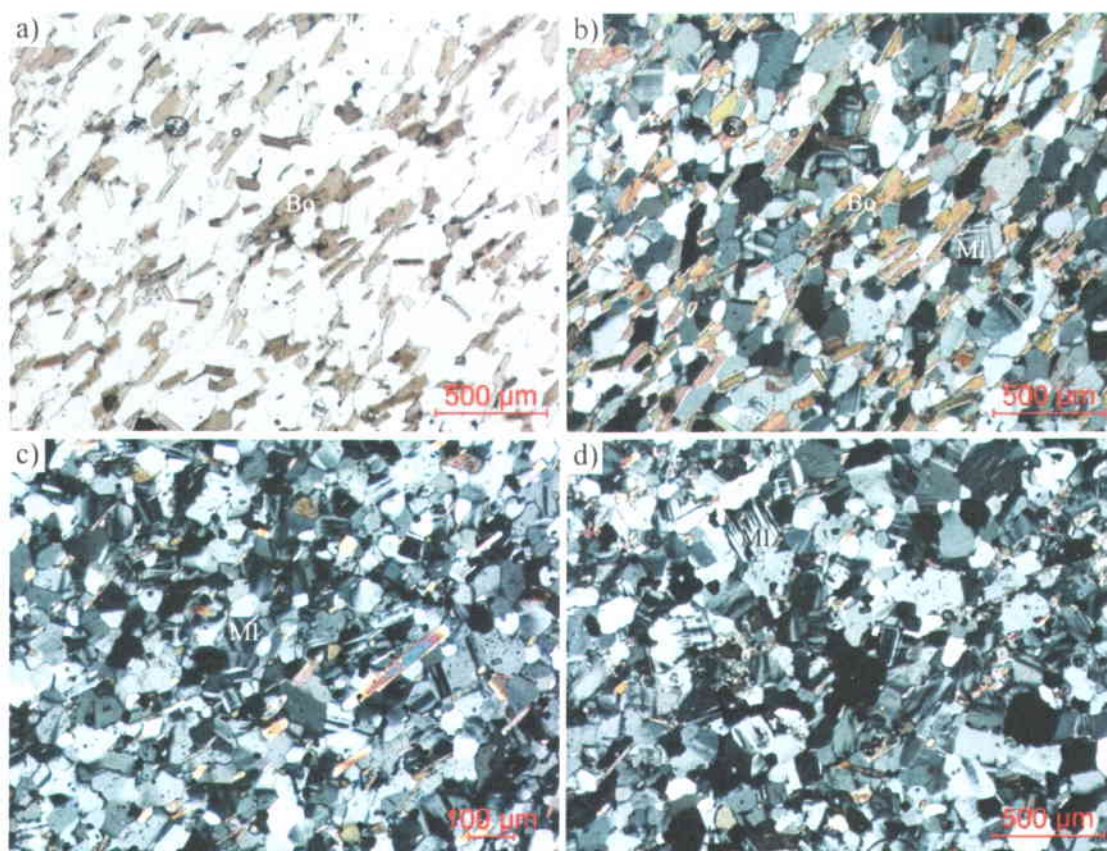


Figure 3.5.56: Photomicrographs showing biotite defining S_2 (a: natural, b: cross-polarized) and recrystallized polygonal microcline and quartz (b to d). In (c), tourmaline crystals are defining S_2 .

3.5.6 East-Roberto Auriferous Zone

At deposit-scale, the East-Roberto auriferous zone (up to 8 g/t Au over 6 m) is located west of the western aluminosilicate-porphroblasts-bearing unit (Figure 3.5.1). On the large stripped outcrop, the East-Roberto zone is separated from the aluminosilicate-bearing sequence by a massive greywacke unit (Figure 3.5.57). Although the overall distribution of the East-Roberto zone is relatively simple on the large stripped outcrop (Figure 3.5.57) and in 3D (Figure 3.5.1), its internal geometry is complex (see section 3.5.6.1 *Structural Characteristics*).

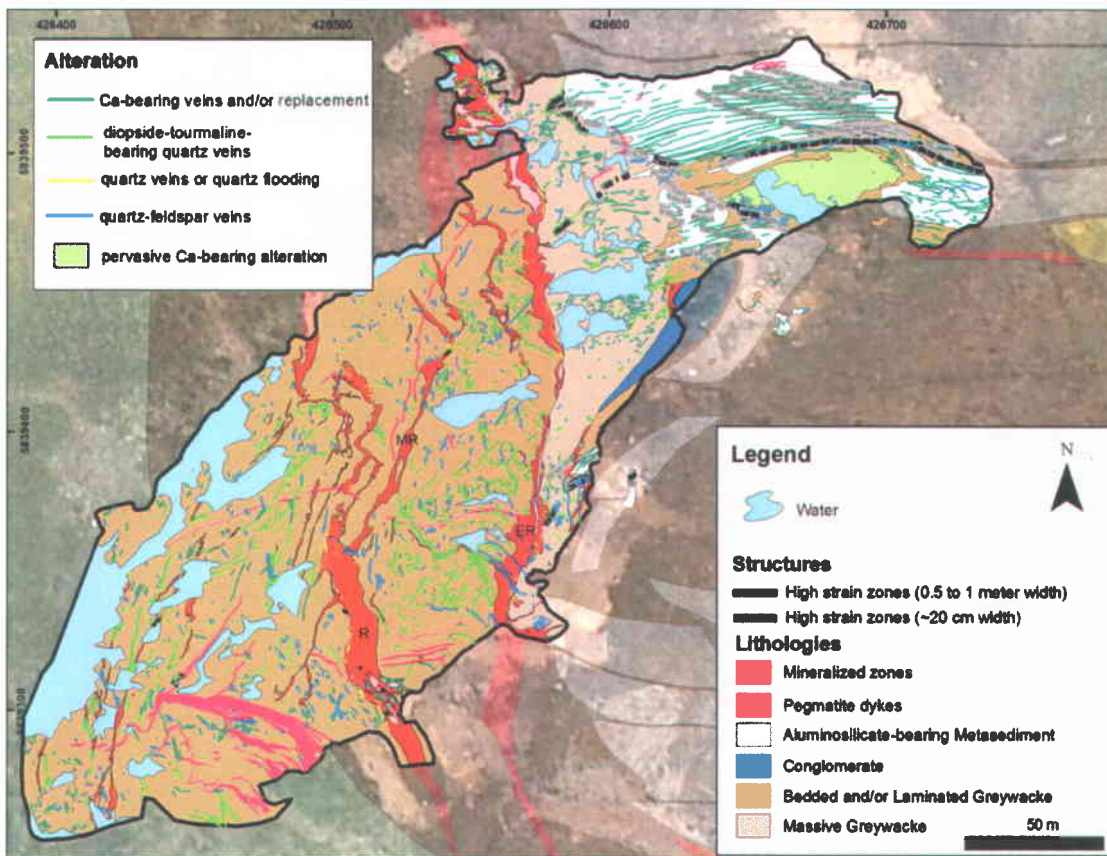


Figure 3.5.57: Geological map of the large stripped outcrop showing the distribution of the principal auriferous zones (R = Roberto, ER = East-Roberto, MR = Mid-Roberto) and different generations of veins.

The East-Roberto zone is composed of several mineralogical assemblages that have different textural characteristics. The western envelope of the East-Roberto zone comprises hydrothermal breccias with angular mm to cm-scale pinkish-brown fragments of metagreywacke composed of various proportions of microcline, biotite, and saussuritized feldspar that are cut and replaced by calc-silicate-bearing quartz veinlets (Figures 3.5.58a and 3.5.58b). These

hydrothermal breccias contain anomalous gold values (<1 g/t Au). Approaching the ore zone, the dominant host assemblage is characterized by a well-defined layering composed of leucocratic calc-silicate-bearing veins injected within black tourmaline-rich altered greywacke (Figures 3.5.58c and 3.5.58d). Such calc-silicate-bearing veins are characterized by the presence of diopside and tourmaline and the local occurrence of microcline (Figure 3.5.17f). The intensity of alteration increases approaching a N-striking post-mineralization brittle fault that bounds the eastern side of the auriferous zone, where the different mineralogical assemblages are gradually replaced by quartz, forming irregular centimeter to meter-wide zones dominated by quartz-rich "silica-flooding" (Figures 3.5.58e and 3.5.58f). These zones of silica replacement are associated with significant gold values (≥ 5 g/t Au) and contain various proportions of quartz, microcline, tourmaline, actinolite, diopside, saussuritized feldspar, clinozoisite and arsenopyrite.

In the northern portion of the stripped outcrop, the East-Roberto auriferous zone contains less diopside and tourmaline, is more silicified and higher grade (~ 12 g/t Au over 7), and is locally highly strained. North of the stripped outcrop, drillcore data shows that the continuation of the East-Roberto zone is also more silicified and higher grade. This more silicified facies of the East-Roberto zone is referred to as the Lake Zone.

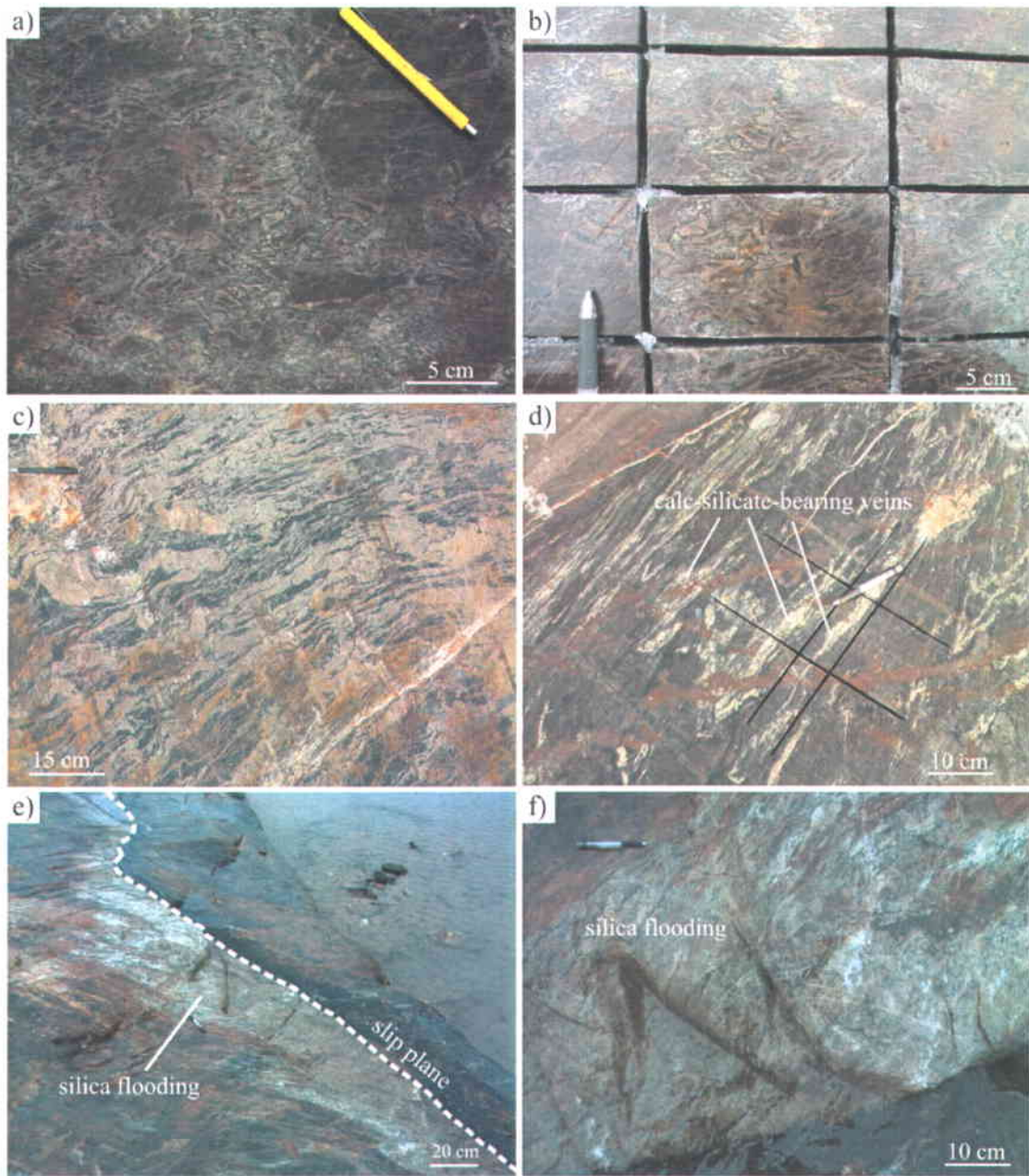


Figure 3.5.58: Photographs of various alteration facies present in the East-Roberto auriferous zone. a) and b) hydrothermal breccia. c) and d) highly strained calc-silicate-bearing veins interlayered with tourmaline-rich rock. e) and f) silica-flooding bounded by East-Roberto slip plane. Photographs (a) and (b) are from Ravenelle et al. (2010).

3.5.6.1 *Structural Characteristics*

This section presents structural and deformational characteristics of the East-Roberto zone and complements the deformational characteristics previously described for the Ca-bearing alteration. The most significant structural aspects of the East-Roberto zone is that although the envelope of the East-Roberto zone has a simple geometry (Figure 3.5.57), the presence of isoclinal folds and intense transposition in auriferous calc-silicate and quartz veins (e.g. Figures 3.5.34c, 3.5.58c, and 3.5.58d) indicates that the zone is internally highly strained. The axial planes of these folds, interpreted as F_2 folds, are dragged (Figure 3.5.58d and 3.5.58e) along the N-striking brittle slip plane that bounds (for the most part) the eastern contact of the East-Roberto zone (Figure 3.3.19, 3.3.17c, and 3.5.58e). The true orientation of the slip along the fault could not be determined. However, the apparent kinematic deduced from dragging of the S_2 fabric suggests a dextral component of movement (Figures 3.3.19 and 3.3.20a to 3.3.20c). The fault and the envelope of the East-Roberto zone are discordant to bedding (Figure 3.3.19) but may potentially mark the contact between the two inferred sedimentary sequences (Figure 3.2.3). As previously described, field relationships suggest that the late slip along the East-Roberto fault can be constrained to have occurred either late D_2 or early D_3 (see section 3.3.4 *Faults and Slip Surfaces*). Whether the fault marks an ancient structure to which the formation of the East-Roberto zone was related remains speculative.

3.5.7 **Roberto Auriferous Zone**

The Roberto auriferous zone (typically averaging 12 g/t Au over 10 meters) represents the core of the auriferous hydrothermal system and the most important auriferous zone of the deposit. The zone is exposed on the large stripped outcrop (Figure 3.5.57) and its 3D distribution is shown on Figure 3.5.1. Although the overall geometry of the zone corresponds to steeply-dipping sheets (Figure 3.5.1), its detailed geometry is locally more complex. For example, the distribution of the Roberto zone is well constrained in the southern part of the large stripped outcrop, where it is bounded by massive greywacke units, but is more complex in the northern part where it is composed of transposed and folded anastomosing zones (Figures 3.5.57).

As previously mentioned, the mineralization style and the alteration assemblages of the Roberto zone also locally occur in other auriferous zones (Figure 3.5.1). Some of the

characteristics of the Roberto zone presented in this section can therefore locally apply to other auriferous zones. The Roberto zone itself, as documented in the southern part of the large stripped outcrop, consists of a stockwork of microcline and/or biotite bearing veins and veinlets (as described in section 3.5.5 *Potassic Alteration*), and calc-silicate-bearing quartz veins (as described in section 3.5.4 *Ca-bearing Alteration*) contained within K-altered sedimentary rocks. The auriferous stockwork is primarily hosted by a thinly-bedded (2-8 cm thick beds) greywacke unit (Figure 3.5.59a) bounded by less-altered massive greywacke. The potassic veinlets are typically composed of quartz, microcline, tourmaline, biotite, arsenopyrite/löllingite, and pyrrhotite (e.g. Figure 3.5.48). The variety of tourmaline present in the Roberto zone, with a characteristics orange color under a petrographic microscope, corresponds to dravite (Mg-rich tourmaline). The distribution of such veins locally controlled the distribution of K-altered regions. For example, Figure 3.5.59b shows that a K-altered region is bounded by potassic veinlets. As previously mentioned, K-altered regions are composed of quartz, microcline, tourmaline (dravite), arsenopyrite/löllingite, and pyrrhotite with minor amount of biotite (e.g. Figures 3.5.46c and 3.5.46d). High grade regions of the auriferous stockwork (> 20 g/t Au) are associated with high proportions of fine-grained microcline and disseminated tourmaline and arsenopyrite/löllingite which typically give a deep pinkish-brown color to the rock (Figure 3.5.59c) and makes high grade regions easily recognizable at surface. In drillcore, the stockwork style of mineralization generally coincides with a well-defined layering characterized by transposed quartz-tourmaline veinlets and microcline-rich bands (Figure 3.5.59d). Reflected light microscopy indicates the presence of gold within arsenopyrite crystals (Figure 3.5.59e) and locally within pyrrhotite crystals, suggesting a genetic link between gold, arsenopyrite, and quartz-tourmaline veinlets that locally host the arsenopyrite and pyrrhotite (Figure 3.5.59f). A more detailed study of sulphides and their genetic relationships with gold mineralization is presented in section 3.5.11 *Occurrence of Sulphide Minerals Relative to Peak of Metamorphism*.

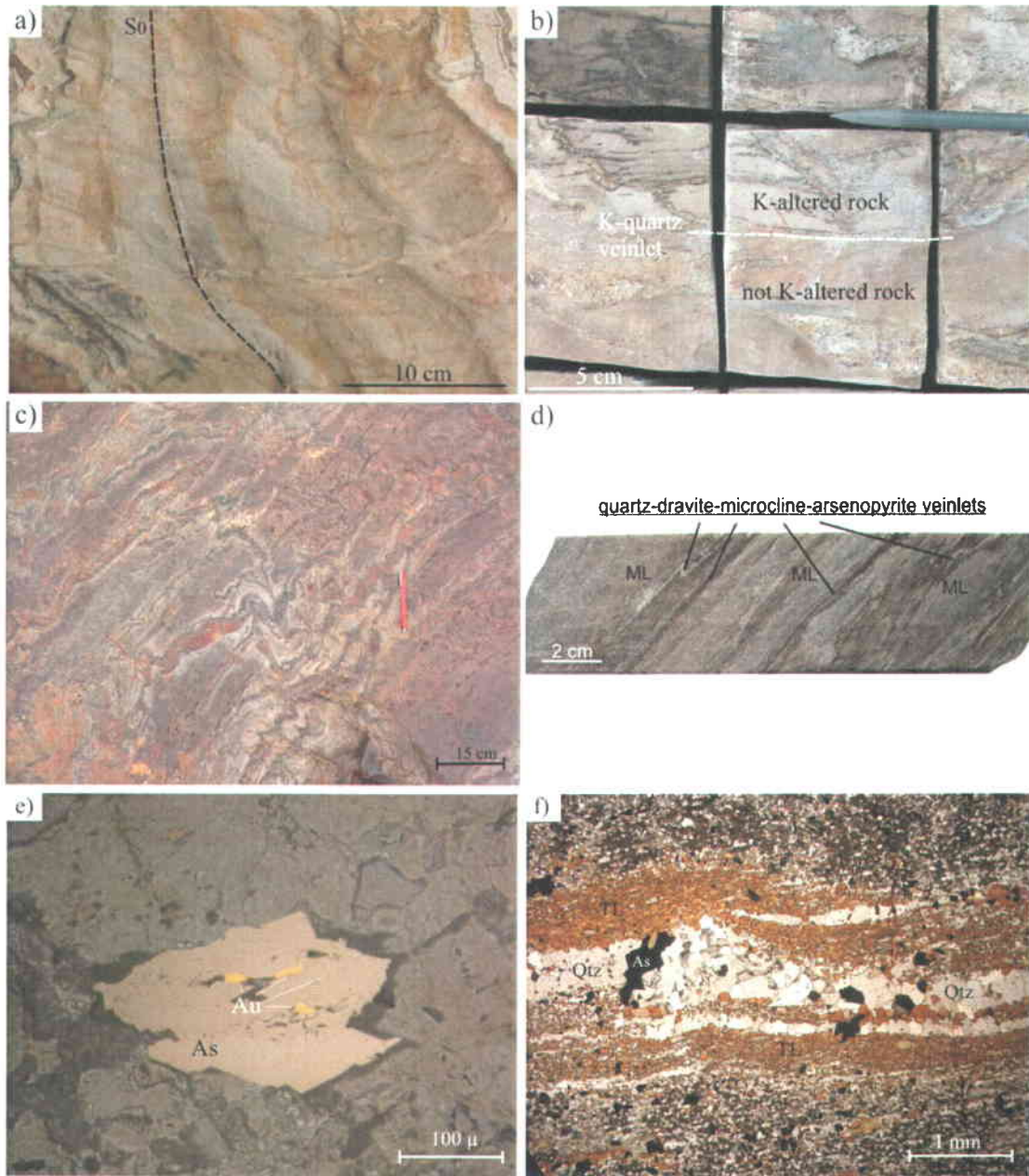


Figure 3.5.59: Photographs and photomicrographs showing different characteristics of the Roberto zone. a) preserved bedding in sedimentary unit that hosts the Roberto zone. b) K-altered rocks associated with microcline and/or biotite bearing veinlets. A veinlet marks the limit of the distribution of the potassic alteration. c) high grade material (> 20 g/t Au). The pinkish-brown color is given by disseminated tourmaline and arsenopyrite/löllingite. d) Roberto stockwork in drillcore. e) microphotograph showing gold hosted by arsenopyrite crystal. f) microphotograph showing arsenopyrite crystals hosted by a quartz veinlet of the auriferous stockwork with abundant tourmaline in the selvages. All photographs from Ravenelle et al., 2010 except (a) and (b).

Bleached-regions that correspond to Ca-bearing metasomatic replacement are locally present in the auriferous stockwork (Figures 3.5.60, 3.4.20, and 3.5.18). The Ca-bearing metasomatic replacement caused saussuritization of plagioclase, partial replacement of sulphides by clinozoisite, and retrogradation of biotite to chlorite and/or prehnite. The metasomatic replacement is hence superimposed on pre-existing minerals and is interpreted to postdate the initial stage of gold mineralization.

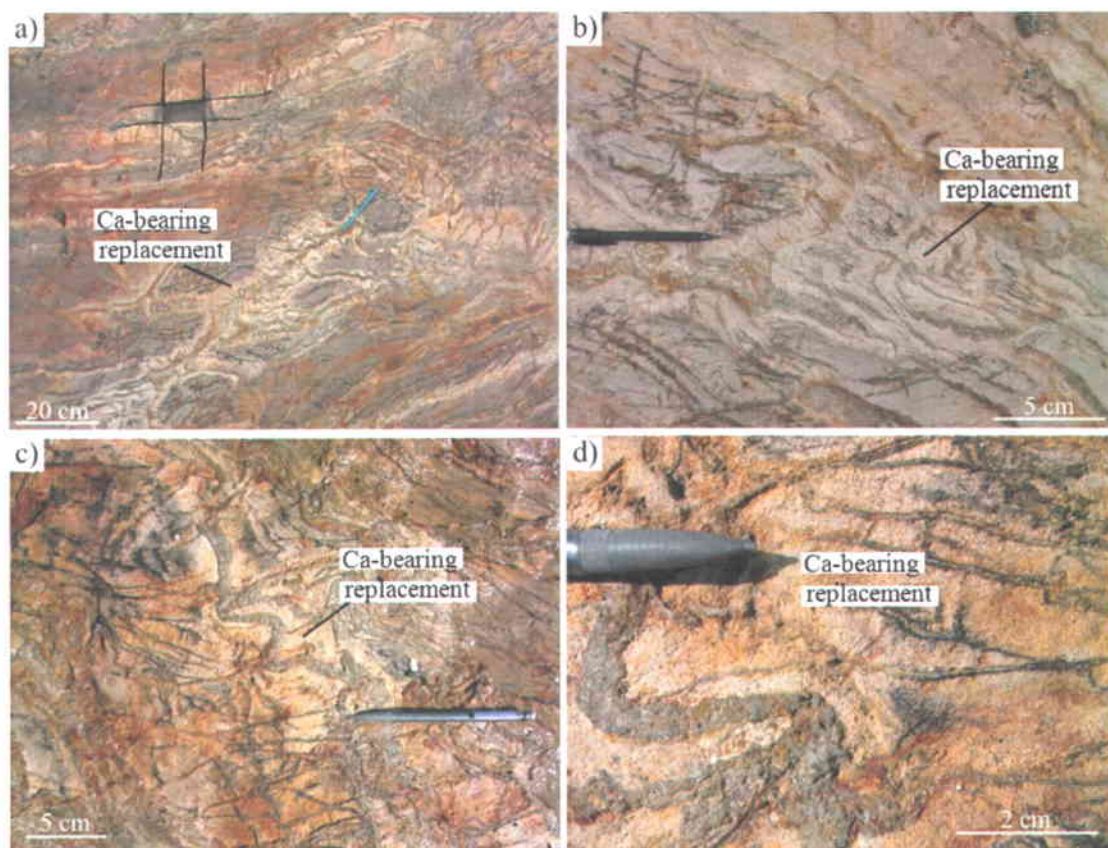


Figure 3.5.60: Photographs of Ca-bearing replacement within Roberto's auriferous stockwork. a) bleached-regions correspond to metasomatic replacement of plagioclase to saussurite and sulphides by clinozoisite. b) Ca-replacement superimposed on quartz-tourmaline veinlets. c) metasomatic replacement of plagioclase to saussurite in the selvages of a vein containing abundant chlorite and prehnite replacing biotite. d) close-up of (c). Note how the alteration in the vein selvages is superimposed on the quartz-tourmaline veinlets.

Calc-silicate-bearing quartz veins of the Roberto zone are generally thick (cm- to dm-scale), and are typically composed of quartz, amphibole, diopside, titanite, carbonate, pyrrhotite, and arsenopyrite/löllingite, and locally visible gold (e.g. Figures 3.5.19c and 3.5.19d). One of the quartz veins which contains actinolite, arsenopyrite, and pyrrhotite is 30 to 50 cm thick (Figure 3.5.61) and bounds the western edge of the Roberto zone over several tens of meters (Figure

3.5.61), from the southern part to the northern part of the Roberto zone. This vein is boudinaged by D_2 and folded by F_2 and F_3 folds. Figure 3.5.61c shows the vein being boudinaged by D_2 and folded by F_3 folds.

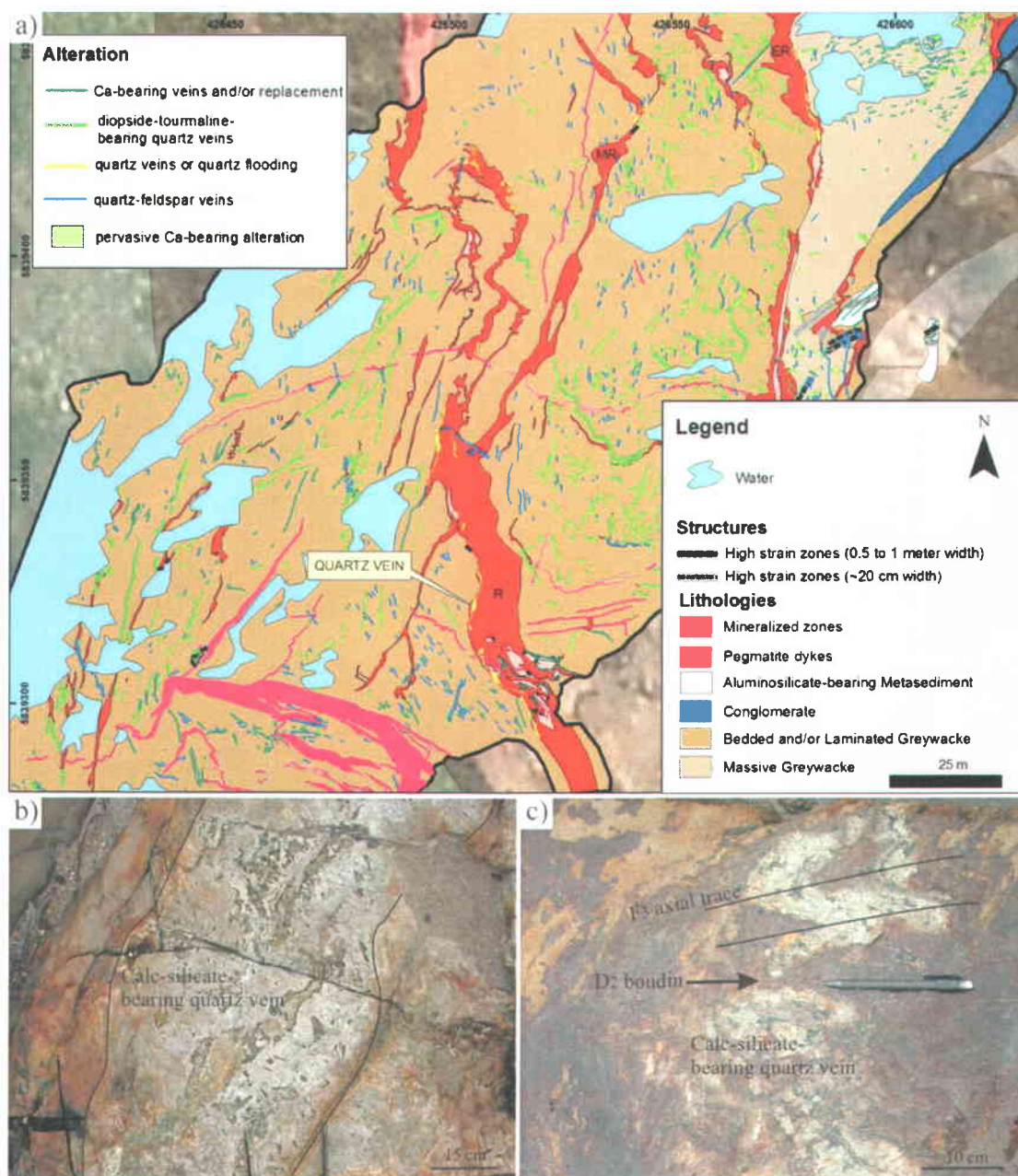


Figure 3.5.61: a) Geological map of a part of the large stripped outcrop showing the distribution of the vein (yellow lines) that bounds the western contact of the Roberto zone. b) photograph showing the mineralogy of the vein shown in (a). The green mineral is Ca-amphibole (actinolite). c) photograph showing F_3 folds and D_2 boudins in the quartz-actinolite-arsenopyrite-pyrrhotite vein shown in (a) and (b).

3.5.7.1 Structural Characteristics

This section presents structural and deformational characteristics of the Roberto zone and complements the deformational characteristics previously described for the Ca-bearing alteration and potassic alteration. An important feature of Roberto's auriferous stockwork is that, although the potassic veins and veinlets locally have multiple attitudes (e.g. Figure 3.5.62a), their orientation and dip are commonly controlled by bedding and S_2 foliation planes (e.g. Figures 3.5.62b, 3.5.53a, 3.5.53b). Where emplaced parallel to S_2 foliation planes, microcline and/or biotite bearing veinlets formed in cleavage planes (e.g. Figure 3.5.54), and where emplaced along bedding planes, tourmaline veinlets are commonly crenulated by S_2 . The calc-silicate-bearing quartz veins, on the other hand, are typically emplaced parallel to bedding planes (e.g. Figures 3.5.62b, 3.5.63), and commonly boudinaged and folded by F_2 folds (Figure 3.5.62 and 3.5.63). Like previously mentioned, the stockwork is locally preferentially developed on the short limb of F_2 folds (e.g. Figures 3.5.55 and 3.5.64) which suggests that folding mechanisms played a role in controlling sites of stockwork fractures filled by veins. Note, however, that the auriferous stockwork is also locally highly deformed by D_2 (Figures 3.5.65). Fault planes cutting through the stockwork are common (Figure Figure 3.5.66), locally bounding the contacts of the stockwork (Figure 3.5.66b). Auriferous stockworks also formed slightly outside the Roberto zone, generally in association with fracture zones (e.g. Figure 3.5.67) or calc-silicate-bearing quartz veins (e.g. Figure 3.5.68).

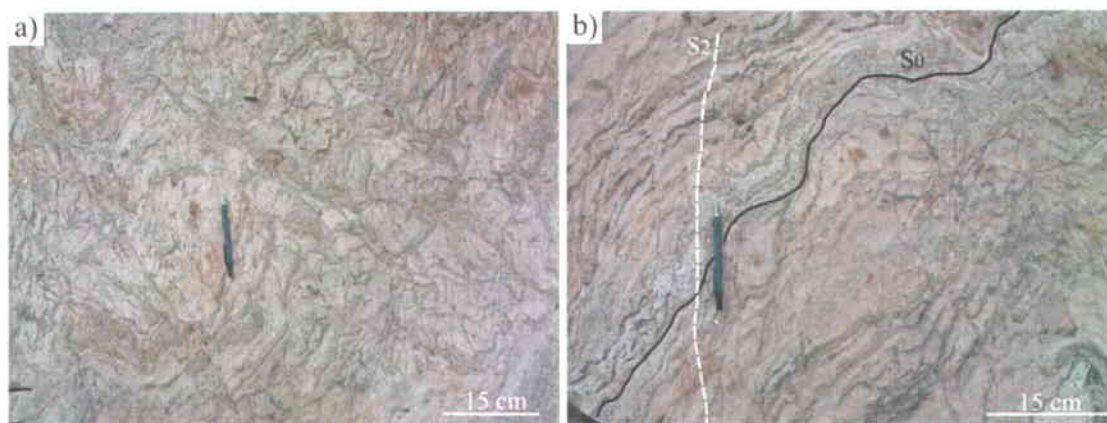


Figure 3.5.62: Photographs showing randomly-oriented veins (a) and veins with attitudes controlled by bedding and foliation planes (b) within Roberto's auriferous stockwork.

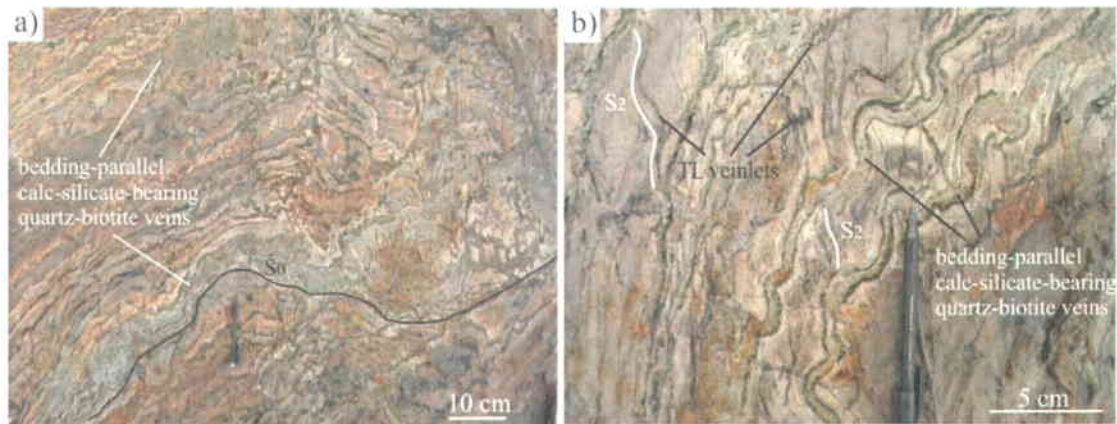


Figure 3.5.63: Photographs showing calc-silicate-bearing quartz-biotite veins emplaced parallel to bedding planes in Roberto's auriferous stockwork.

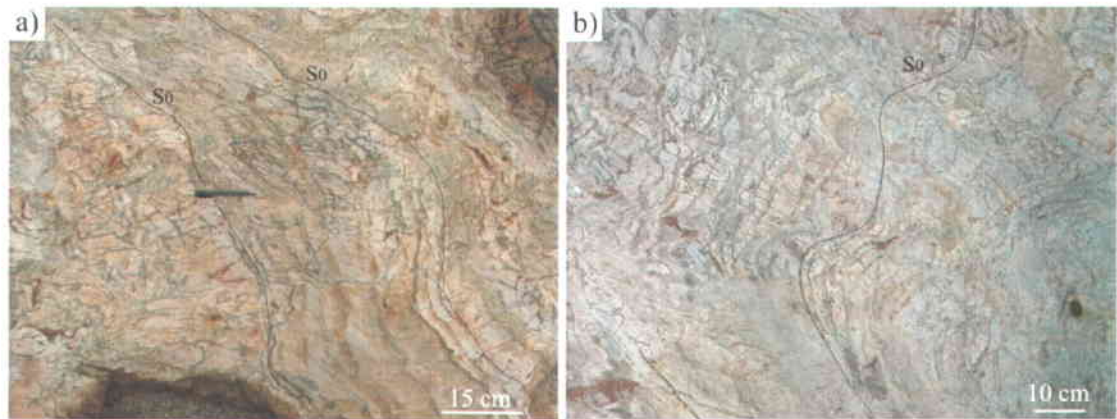


Figure 3.5.64: Photographs showing auriferous stockwork preferentially developed on the short limbs of F_2 folds.

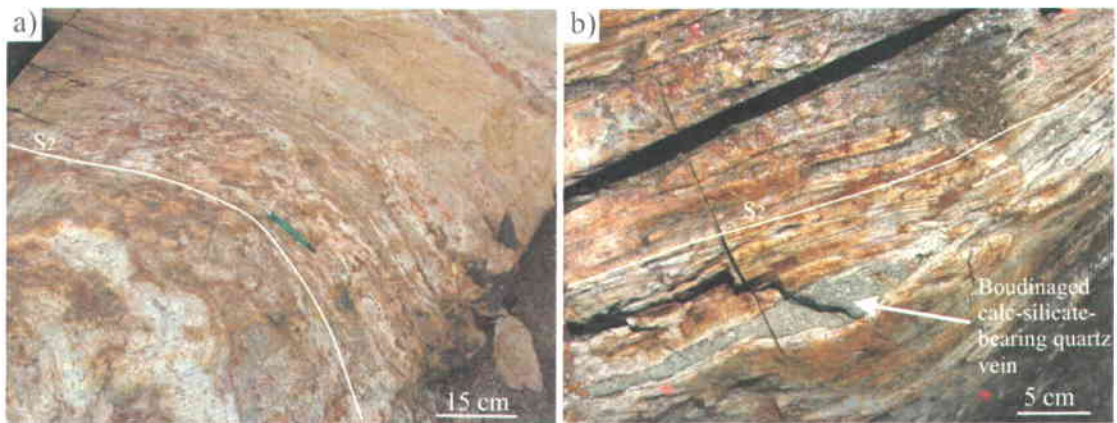


Figure 3.5.65: Photographs showing highly transposed parts of the Roberto zone. a) layering defined by multiple quartz veins transposed along the S_2 foliation. b) Boudinaged calc-silicate-bearing vein oriented parallel to S_2 .

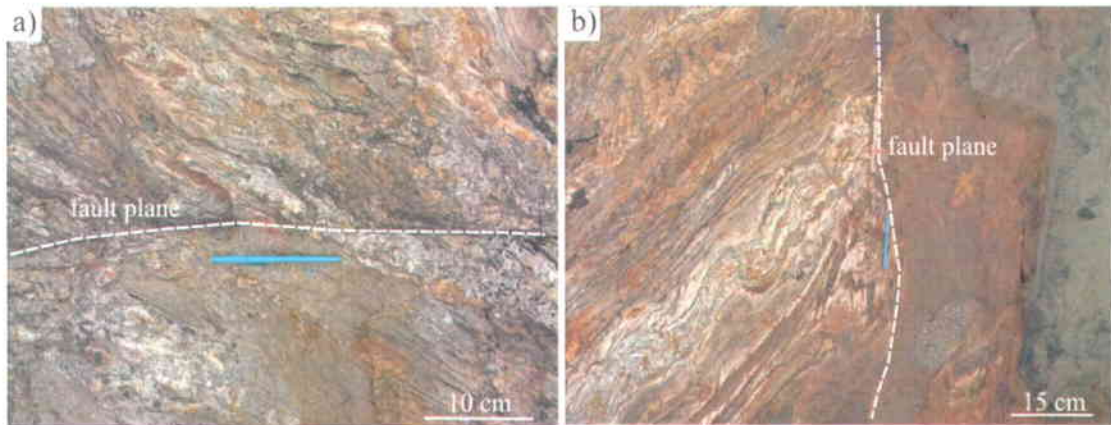


Figure 3.5.66: Photographs showing a) fault planes within Roberto's auriferous stockwork, and (b), a fault bounding the stockwork.

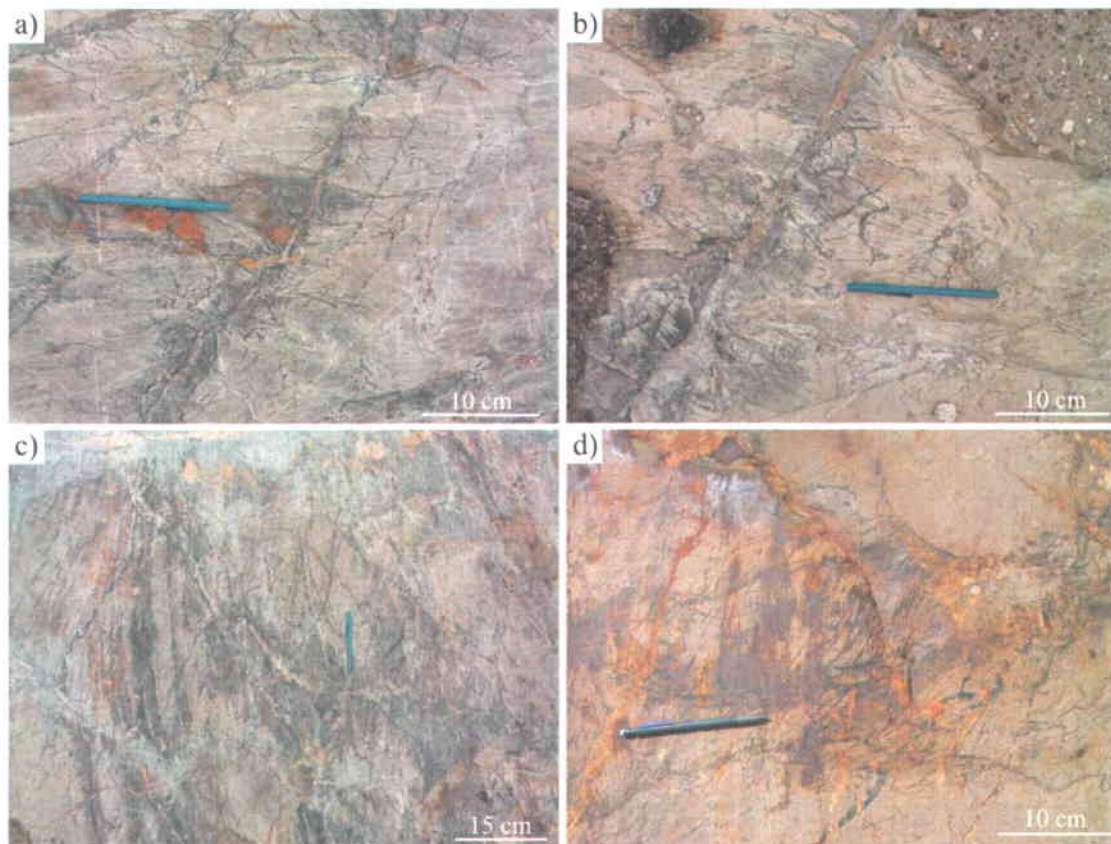


Figure 3.5.67: Photographs showing stockworks locally developing in association with quartz veins and/or veinlets filling fractures outside Roberto's principal stockwork.

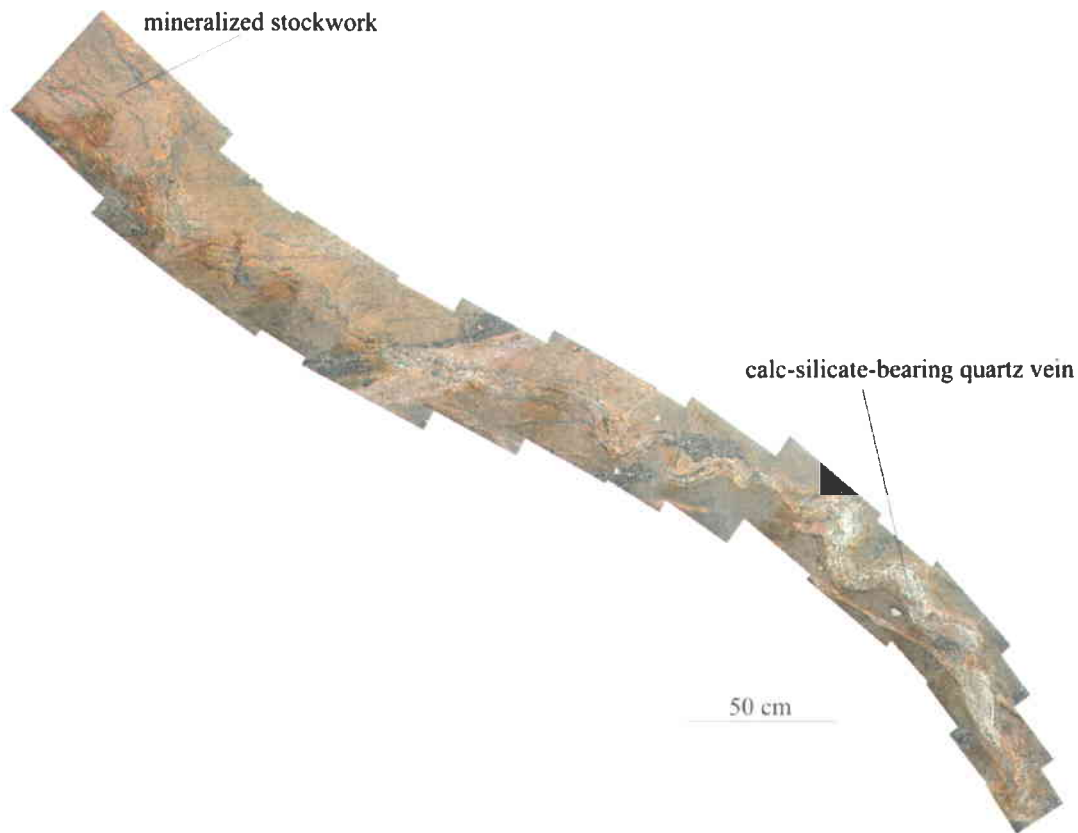


Figure 3.5.68: Mosaic photograph showing an auriferous stockwork developing in association with a calc-silicate-bearing quartz vein located a few meters from Roberto's main stockwork.

3.5.8 Other Auriferous Zones

Auriferous zones and sporadic gold values locally occur between the Roberto and East-Roberto zones and elsewhere in the footwall and hanging wall of the mineralized envelop. In general, these auriferous zones are composed of various proportions of calc-silicate minerals, microcline, tourmaline, arsenopyrite and pyrrhotite, but lack the well-developed auriferous stockwork of the Roberto or intense layering of the East-Roberto zones. On the stripped outcrop, the most significant of such auriferous zones is the Mid-Roberto zone, which branches out from the Roberto zone and almost joins the East-Roberto zone (Figure 3.5.57). Some auriferous zones are hosted in other lithological units including conglomerate, biotite schists and paragneiss which gives them specific characteristics. In the northern limb of the deposit-scale fold, auriferous zones are locally associated with meter-scale quartz-arsenopyrite veins locally containing visible gold. Auriferous zones hosted within paragneiss were intersected through

drilling and appear to have been subjected to a higher grade of metamorphism and hence possess different attributes. For example, gold mineralization in an impressive auriferous zone (60 g/t Au over 30 meters) intersected in the deeper levels of the deposit (~1.2 km depth) is associated with quartz-feldspar-arsenopyrite-pyrrhotite veins that contain visible gold, but where calc-silicate assemblages or microcline are absent (Figures 3.5.69a and 3.5.69b). Importantly, these auriferous quartz-feldspar-arsenopyrite-pyrrhotite veins locally gradually evolve into pegmatitic material (Figure 3.5.69c), which suggests that they are genetically related to an episode of pegmatite magmatism. Other auriferous zones in paragneiss are characterized by highly-deformed quartz-arsenopyrite-pyrrhotite veins hosted within saccharoidal quartz-feldspars-biotite assemblages with pyrrhotite and fine arsenopyrite (Figure 3.5.69d). Local bright green mica (Cr-rich muscovite) also occurs in some zones. Other zones include the Puncho zone (~1-2 g/t Au) which is hosted by banded iron formations and the Mayappo zone (1-2 g/t Au) which is characterized by intense calc-silicate alteration.

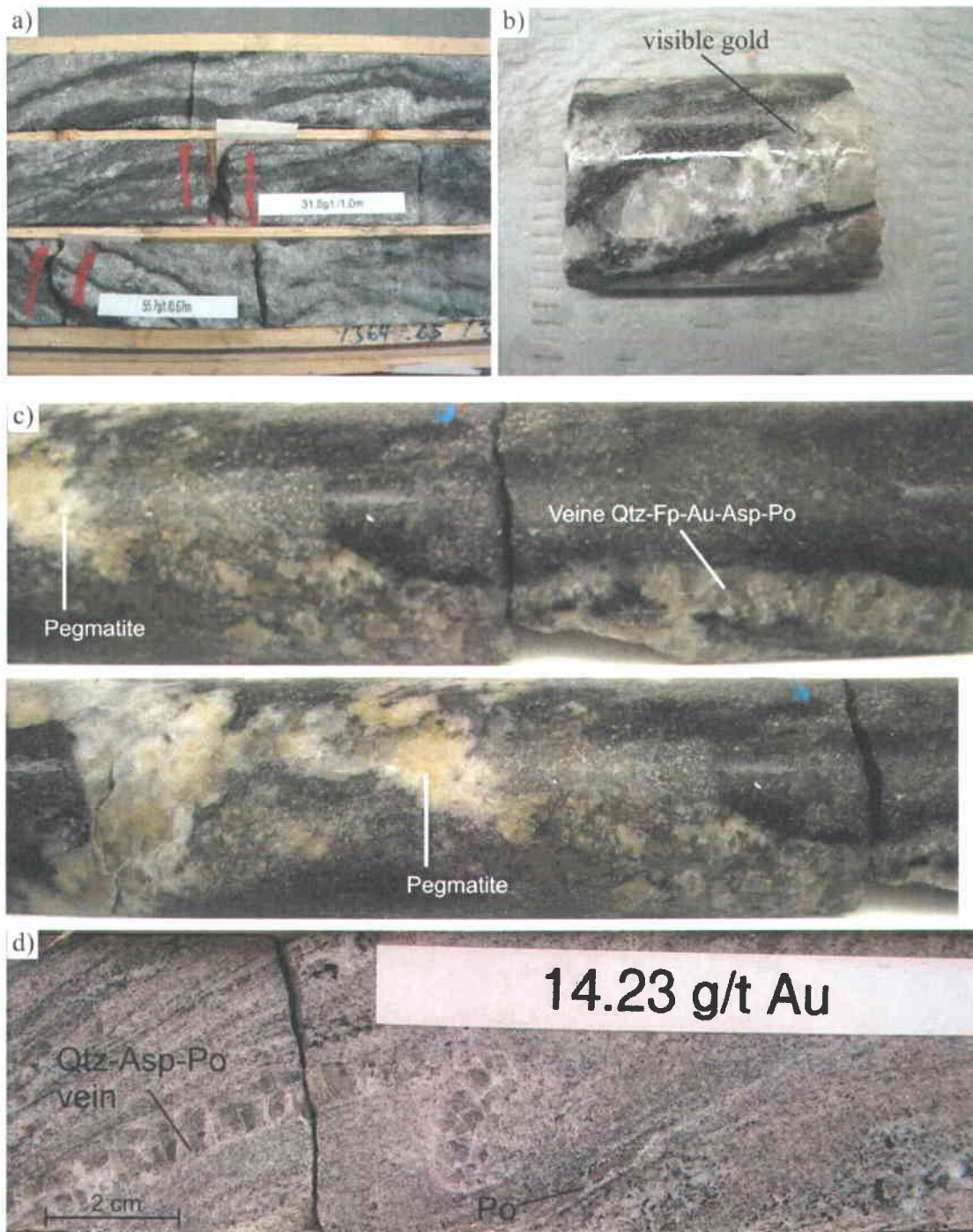


Figure 3.5.69: Photographs of drillcore showing high grade mineralization associated with quartz-feldspar veins (a and b) that locally become pegmatitic (c), and gold mineralization hosted by paragneissic rocks (d). Note the saccharoidal texture in (d) which suggests that the ore has been recrystallized. (d) is from Ravenelle et al. (2010).

3.5.9 Quartz-Feldspar Veins

The stripped outcrop provides the opportunity to document cross-cutting relationships (and hence relative chronology) between different elements of the hydrothermal system. Calc-silicate-bearing quartz veins and auriferous zones are cut by a set of boudinaged extensional dm- to m-scale quartz-feldspar \pm tourmaline \pm arsenopyrite \pm pyrrhotite veins and veinlets (Figures 3.5.57 and 3.5.70) that locally generated tourmaline-rich veinlets or replacement invading the main S_2 fabric, forming irregular black selvages in the wall rock. These veins generally contain anomalous gold values (<1 g/t Au) and locally show pegmatitic textures. The en-echelon or sheeted distribution of the quartz-feldspar veins on the large stripped outcrop suggests that they have been emplaced during the episode of late slip along bedding and fault planes (Figure 3.3.20 and section 3.3.4 *Faults and Slip surfaces*). The quartz-feldspar veins have been locally folded by F_3 folds and have been rotated, which locally led to the formation of flanking folds (following the terminology of (Passchier, 2001)) (Figure 3.5.70c and 3.5.70d). Such flanking folds are best developed where tourmaline was injected along foliation planes in veins margins prior to rotation.

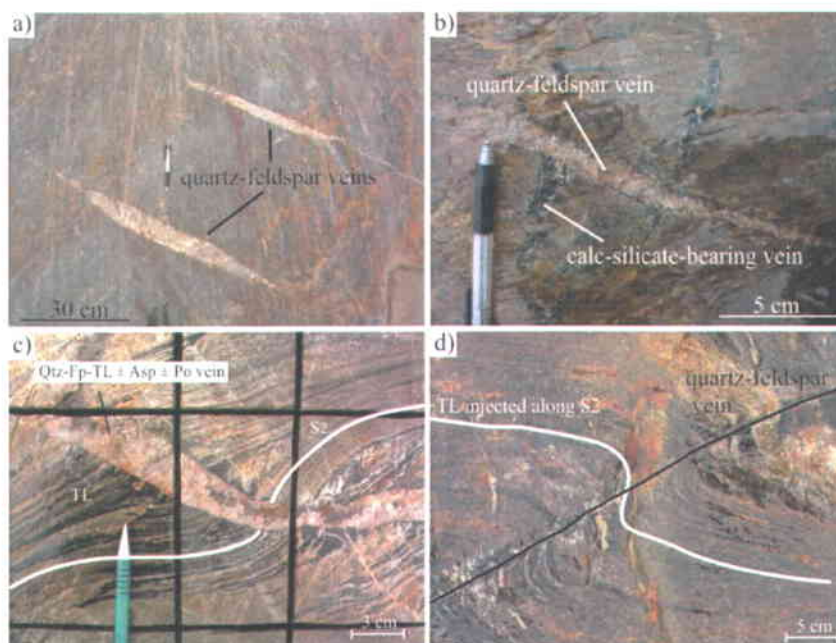


Figure 3.5.70: Photographs of quartz-feldspar veins. Note how such a vein crosscut calc-silicate-bearing veins in (b). In (c) and (d), tourmaline injected along S_2 planes in wall rock of quartz-feldspar veins. Subsequent rotation of the veins has created flanking folds.

3.5.10 Mineralized Pegmatites

Pegmatite dykes ranging from few centimeters to several meters in thickness are widely distributed on the stripped outcrop. Based on relative timing with deformation, there appears to be at least two generations of pegmatite dykes. The first generation is locally boudinaged and/or folded by F_2 folds whereas the second generation is not affected by D_2 structures. An example of a post- D_2 pegmatite dyke is present on the large stripped outcrop where it cross-cuts the N-striking slip plane that transects the East-Roberto zone (Figure 3.3.21a), which as previously described, drags the S_2 fabric and F_2 axial planes. The pegmatite dykes are locally auriferous and contain various proportions of tourmaline, arsenopyrite, pyrrhotite, and tourmaline crystals oriented perpendicular to dyke walls. They also locally generated tourmaline-rich impregnation in the wall rock. Cross-cutting relationships indicate that most dykes postdate the auriferous zones, the calc-silicate-bearing veins, and the quartz-feldspar vein set. However, one potential example of a pre-ore pegmatite dyke was found on trench-08-10 (located ~ 400 meters to the north of the large stripped outcrop). There, a ~40 cm wide quartz vein containing visible gold and arsenopyrite cross-cuts a pegmatite dyke with an aplitic core (Figure 3.5.71). The reverse cross-cutting relationship is exposed a few meters away where a similar dyke cuts across the auriferous quartz vein (Figure 3.5.71), hence suggesting that these pegmatite dykes are contemporaneous with the auriferous quartz veins. Moreover, the petrogenetic continuity of a pegmatite dyke with auriferous quartz-feldspar veins of the high grade zone intersected at depth (Figure 3.5.69c) also suggests that an episode of pegmatite magmatism may have been contemporaneous with a part of the gold mineralization. The two aplite dykes were dated by U/Pb geochronology (see Chapter 4 *Geochronology*). The older and younger aplite dykes are dated at ca. 2615 Ma and 2607 Ma (Dubé, pers. comm., 2010), respectively, which indicates that the auriferous quartz vein was emplaced during that time.

case at Roberto, hence their metamorphic path may provide insights on the timing of gold mineralization relative to peak of metamorphism and associated deformation.

The use of textural relationships between As-free and As-bearing Fe-sulphides is governed by the following reactions:



or, rewritten with formulae: $2\text{FeAsS} = \text{FeAs}_2 + \text{FeS} + 0.5\text{S}_2$

and:



or, rewritten with formulae: $\text{FeAs}_2 + (1/x)\text{FeS}_{(1+x)} = 2\text{FeAsS} + ([1+x]/x)\text{FeS}$.

Reaction (1) corresponds to the prograde metamorphism of arsenopyrite which generates löllingite and pyrrhotite. Note, however, that pyrrhotite is more commonly known to be generated through the desulfidation of pyrite:



which is known as the pyrite-pyrrhotite buffer since the coexistence of both minerals at equilibrium will fix the sulfur fugacity ($f(\text{S}_2)$) at a given temperature (Tomkins, Frost and Pattison, 2006). The $f(\text{S}_2)$ is relevant since it will dictate the temperature at which reactions (1) and (2) will occur (Figure 3.5.72) (Tomkins and Mavrogenes, 2001), and whether or not arsenopyrite melting will occur (Tomkins, Frost and Pattison, 2006). Reaction (2) corresponds to the retrograde reaction between löllingite and pyrrhotite that forms arsenopyrite and pyrrhotite. Textural relationships expected to result from prograde metamorphism of arsenopyrite (reaction (1)) and retrograde metamorphism of löllingite were proposed by Tomkins and Mavrogenes (2001) and are illustrated on Figure 3.5.73. The complete prograde metamorphism of arsenopyrite will result in the equilibrium coexistence of löllingite and pyrrhotite (Figure 3.5.73b). Further retrogradation of löllingite will result in rims of arsenopyrite separating löllingite cores from pyrrhotite (Figure 3.5.73c). Note, however, that löllingite and pyrrhotite may alternatively directly crystallize from an hydrothermal fluid at peak metamorphic conditions (e.g. Neumayr et al., 1993), in which case the two sulphide phases do not need to be adjacent (Neumayr et al., 1993; Tomkins and Mavrogenes, 2001). Subsequent retrograde metamorphism will create arsenopyrite rims on löllingite, but only where löllingite and pyrrhotite are adjacent (Tomkins and Mavrogenes, 2001).

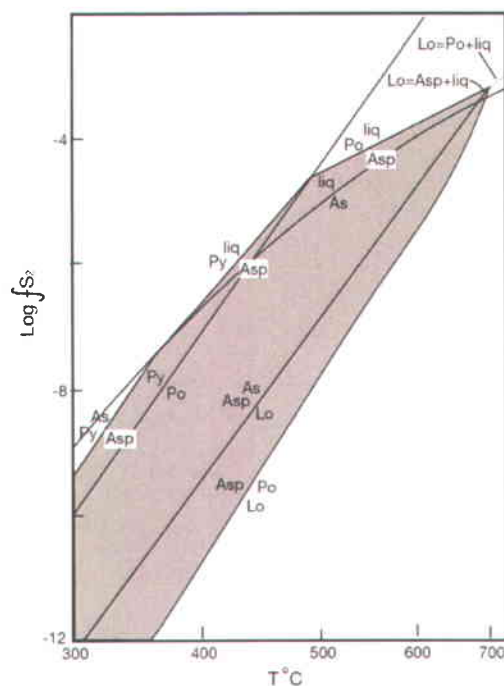


Figure 3.5.72: Sulphidation curves in the system Fe-As-S in the stability range of arsenopyrite (shaded). Modified from Tomkins and Mavrogenes (2001).

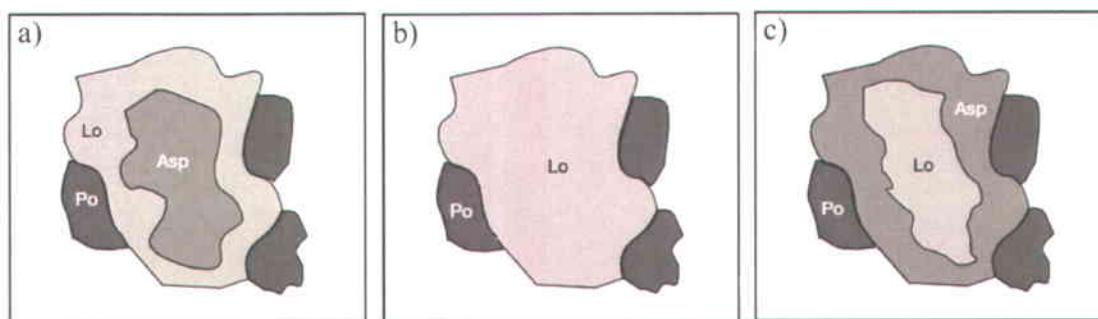


Figure 3.5.73: Sketches from Tomkins and Mavrogenes (2001) showing examples of possible textural relations arising from prograde and retrograde metamorphic reactions discussed in the text. a) Incomplete prograde metamorphism of arsenopyrite to löllingite and pyrrhotite. b) Complete prograde metamorphism of arsenopyrite to löllingite and pyrrhotite. c) Complete prograde metamorphism of arsenopyrite to löllingite and pyrrhotite with subsequent retrograde metamorphism back to arsenopyrite.

Within these sulphide minerals, gold has been known to occur as visible inclusions (detectable by SEM) and as invisible submicroscopic gold (not detectable by SEM) (Genkin et al., 1998; Tomkins and Mavrogenes, 2001). It has also been noted that the solubility of gold within arsenopyrite decreases with increasing temperature (at low and high pressure) prior to its metamorphism to löllingite and pyrrhotite (Tomkins and Mavrogenes, 2001; and references therein). Upon heating, invisible gold will therefore exsolve from the arsenopyrite matrix and form visible gold inclusions. When löllingite is forming through prograde metamorphism, however,

Tomkins and Mavrogenes (2001) have shown that gold partitions as invisible gold into the structure of löllingite. The presence of invisible gold within löllingite does therefore not necessarily indicate that gold directly precipitated with löllingite from a hydrothermal fluid at peak conditions, like initially suggested by Neumayr et al. (1993) (Tomkins and Mavrogenes, 2001). During retrograde metamorphism, invisible gold within löllingite will not partition into arsenopyrite, because the rate of gold diffusion is slower than the rate of arsenopyrite formation (Tomkins and Mavrogenes, 2001). This phenomenon will cause gold to exsolve from the löllingite matrix and form gold inclusions at the löllingite-arsenopyrite interface (Figure 3.5.74) (Tomkins and Mavrogenes, 2001). As retrograde metamorphism continues and löllingite is progressively consumed, gold will further exsolve and form gold inclusions within löllingite, until löllingite is completely consumed (Figure 3.5.74) (Tomkins and Mavrogenes, 2001).

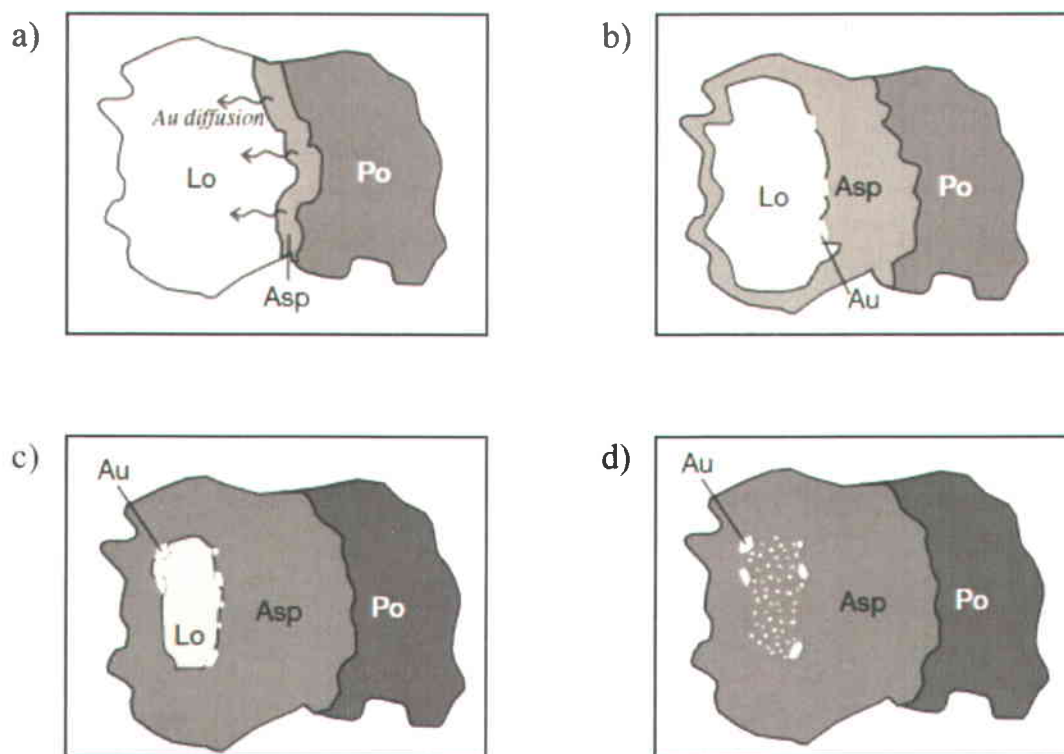


Figure 3.5.74: Theoretical sketches from Tomkins and Mavrogenes (2001) showing progressive stages of destruction of gold-bearing löllingite during stages of retrograde metamorphism (reaction 2). a) Initially, no gold is visible and a thin band of new gold-free arsenopyrite separates pyrrhotite from gold-bearing löllingite. b) With further consumption of löllingite and pyrrhotite, native gold appears at the löllingite-arsenopyrite interface c) As retrograde metamorphism continues, native gold starts to form within the löllingite crystal. d) Eventually, all of the löllingite is consumed and only arsenopyrite and pyrrhotite remain.

3.5.11.1 *Results of Scanning Electron Microscope (SEM) Study*

A scanning electron microscope (SEM) was used to study textural relationships of sulphide minerals which are difficult to document with a petrographic microscope. The study was performed on a total of 10 samples including samples from: the Roberto stockwork (JFR-05-007 and JFR-07-347), the East-Roberto zone (JFR-07-328), an auriferous diopside-bearing quartz vein (JFR-08-398A), auriferous paragneiss (JFR-DC-64 and EDB-2005-03A), a massive sulphide zone within a pegmatite dyke (JFR-08-378B), pegmatite dykes (Geochron-14 and Geochron-16), and an aplite dyke (Geochron-19). The results indicate that all arsenopyrite-bearing samples also contain löllingite, and that the majority of löllingite crystals are separated from pyrrhotite by arsenopyrite (e.g. Figure 3.5.75a). This particular texture (comparable to Figure 3.5.73c) is widespread in all samples and suggests that löllingite has been retrograded into pyrrhotite and arsenopyrite following reaction (2). The blocky undeformed texture of arsenopyrite crystals replacing löllingite in Figure 3.5.75c indicates that retrogradation of löllingite to arsenopyrite occurred late in the tectonic history of the region. The fact that löllingite and arsenopyrite are present within a diopside porphyroblast (Figure 3.5.75b) suggests that the sulphides have been affected by the episode of prograde metamorphism that led to the formation of the host diopside. Those observations suggests that the sequence of events involving reactions (1) and (2) sketched in Figure 3.5.73 took place at Roberto, and that at least some of the arsenopyrite crystals formed prior or close to the peak of metamorphism. This scenario is also supported by the fact that most if not all sulphide grains are composite grains of pyrrhotite, arsenopyrite and löllingite, which suggests that löllingite and pyrrhotite did not precipitate at random like it would be expected if they would have directly precipitated from an hydrothermal fluid at near peak conditions. A pre-peak metamorphic origin for the sulphides may also explain the complex textures locally observed in pyrrhotite grains which may result from a history of prograde and subsequent retrograde reactions involving pyrrhotite (e.g. Figure 3.5.75d).

In some samples, visible gold is present at löllingite-arsenopyrite grain boundaries and/or as visible inclusions in arsenopyrite (Figure 3.5.76). The textural relationships presented in Figure 3.5.76 are analogous to Tomkins and Mavrogenes (2001) sketches where "invisible" gold exsolves from löllingite as the latter is being retrograded into arsenopyrite (Figure 3.5.74d). Those textural relationships indicate that gold was previously enclosed with löllingite crystals and that gold mineralization predates the retrograde phase of metamorphism. It cannot be

determined, however, whether gold mineralization occurred before the peak of metamorphism in association with pre-peak arsenopyrite, or precipitated with löllingite at near peak conditions.

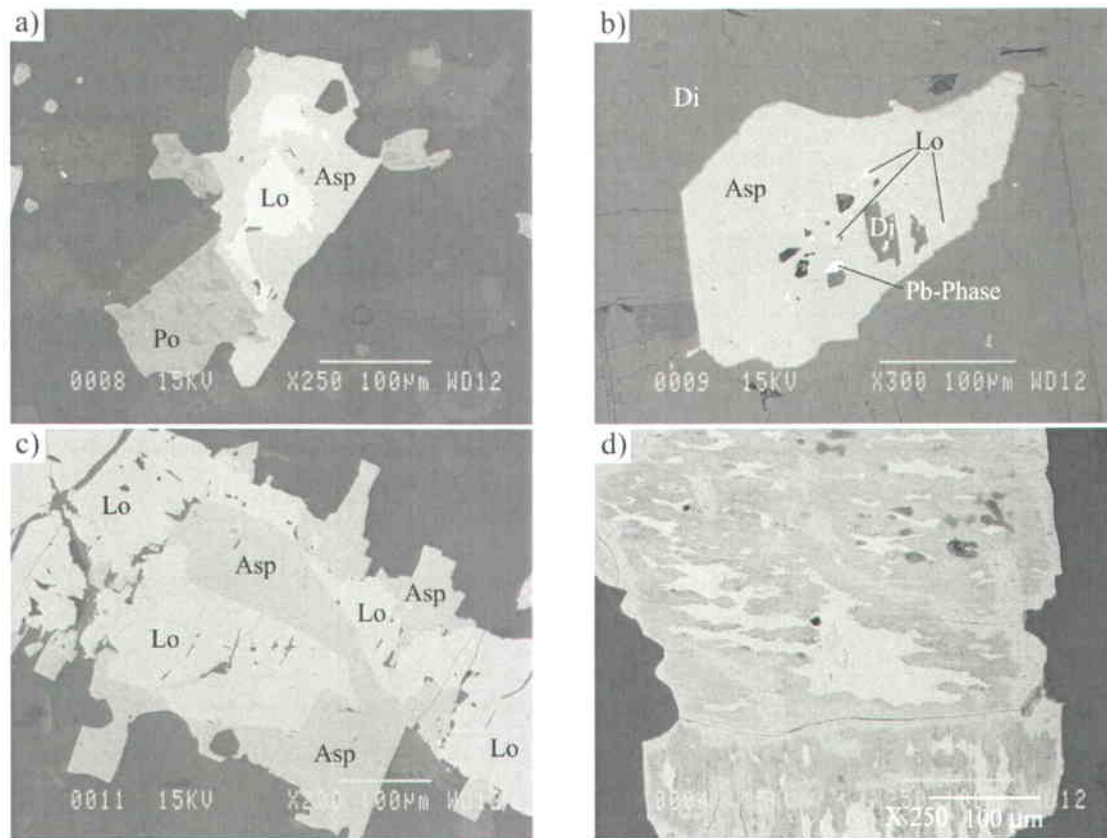


Figure 3.5.75: SEM photomicrographs showing: a) löllingite grain rimmed by arsenopyrite and pyrrhotite. b) arsenopyrite-löllingite composite grain hosted by a diopside porphyroblast. c) blocky arsenopyrite replacing löllingite. d) complex recrystallization texture in pyrrhotite grain (all different colored phases are pyrrhotite). (photograph (a) is from the Roberto stockwork (sample JFR-05-007), photograph (b) is from an auriferous diopside-bearing quartz vein (sample JFR-08-398A), photograph (c) is from an auriferous paragneiss (sample JFR-DC-64), and photograph (d) is from an auriferous paragneiss (sample EDB-2005-03A))

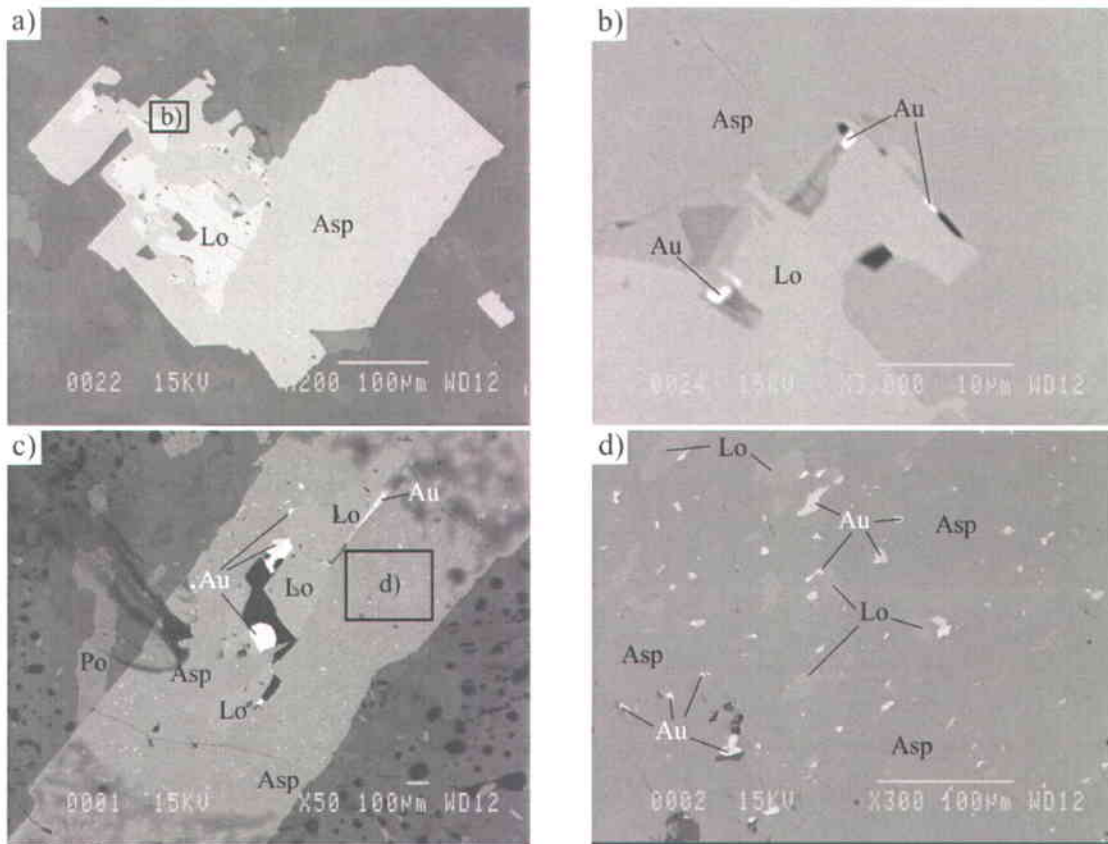


Figure 3.5.76: SEM photomicrographs showing: a) löllingite grain rimmed by arsenopyrite. b) close-up on (a) showing gold grains distributed along löllingite-arsenopyrite boundaries. c) löllingite grain rimmed by arsenopyrite and pyrrhotite showing large gold grains distributed along löllingite-arsenopyrite boundaries and numerous gold inclusions within arsenopyrite. d) close-up on (c) showing numerous gold inclusions within arsenopyrite. (photographs (a) and (b) are from a quartz vein of the Roberto stockwork (sample JFR-07-347) and photographs (c) and (d) are from an auriferous paragneiss (sample EDB-2005-03A))

4 Geochronology

Geochronological work was conducted by Vicki McNicoll at the Geological Survey of Canada (GSC) laboratory in order to define the relative timing between turbiditic greywacke that host the deposit, regional conglomerate sequences, the mineralized phase of the Ell lake diorite, and pegmatitic magmatism hosted within paragneiss units. The results are presented here only as a summary and will be published in a paper by Dubé et al. (in preparation). The maximum ages of sedimentary samples were obtained through U-Pb high precision geochronology performed by high-resolution secondary ion mass spectrometry (SHRIMP) and thermal ionization mass spectrometry (TIMS).

4.1 Samples Location

The location of analyzed geochronological samples is shown on Figure 4.1.1. The characteristics of individual samples are listed in Table 4.1.1. Photographs of geochronological samples in outcrops are shown on Figure 4.1.2.

Table 4.1.1: Characteristics of geochronological samples analyzed on the Eleonore property. Locations of samples dated by Dubé, pers. comm. (2010) and Ravenelle et al., 2010 are shown on Figure 4.1.1. Locations of samples dated by Bandyayera and Fliszár (2007) and David (2005) are shown on Figure 2.1.2.

Sample	Lithology	Age (Ma)	Error	Comments	Method
Geochron-ELE-05-01	Roberto host rock	<2687*	±3	sampled adjacent to mineralized material	SHRIMP/ TIMS
Geochron-ELE-05-02	Al-bearing metasedimentary rock	<2697*	±2	contains Ca-replacement bands	SHRIMP/ TIMS
Geochron-ELE-05-03	conglomerate	<2702**	±3		SHRIMP/ TIMS
Geochron-ELE-05-06	Al-bearing metasedimentary rock	<2704*	±4		SHRIMP/ TIMS
Geochron-ELE-05-07	paragneiss	<2685*	+2-3		SHRIMP/ TIMS
Geochron-ELE-05-08	Roberto host rock	<2675**	±6	sampled in mineralized material	SHRIMP/ TIMS
Geochron-ELE-06-11	paragneiss	2675*	±5		SHRIMP/ TIMS
Geochron-ELE-06-12	feldspar porphyry dyke	<2680*	NA		TIMS
Geochron-ELE-07-15	pegmatite dyke	2603*	NA	crosscuts Roberto	TIMS
Geochron-ELE-07-16	pegmatite dyke	2616*	NA	in footwall of Roberto	TIMS
Geochron-ELE-07-17	pegmatite dyke	2616**	NA	boudinaged by D2	TIMS
Geochron-ELE-08-18	wacke cut by Ell Lake diorite	<2714*	NA		SHRIMP/ TIMS
Geochron-ELE-08-19	aplite	2615*	NA	cut by quartz vein with visible gold and folded by F2 folds	TIMS
Geochron-ELE-08-20	aplite	2607*	±4	crosscuts quartz vein with visible gold	TIMS
Geochron-ELE-09-21	massive greywacke	<2714*	±2		SHRIMP/ TIMS
NA	Ell Lake diorite	2705***	±1.9		TIMS
NA	intermediate tuff	2704****	±1.1		NA
NA	Opinaca pluton	2708.9****	±0.9		NA
NA	Opinaca pluton	2703.5****	±2.8		NA

*Dubé, pers. comm. (2010), **Ravenelle et al. (2010), ***David (2005), ****Bandyayera and Fliszár (2007)

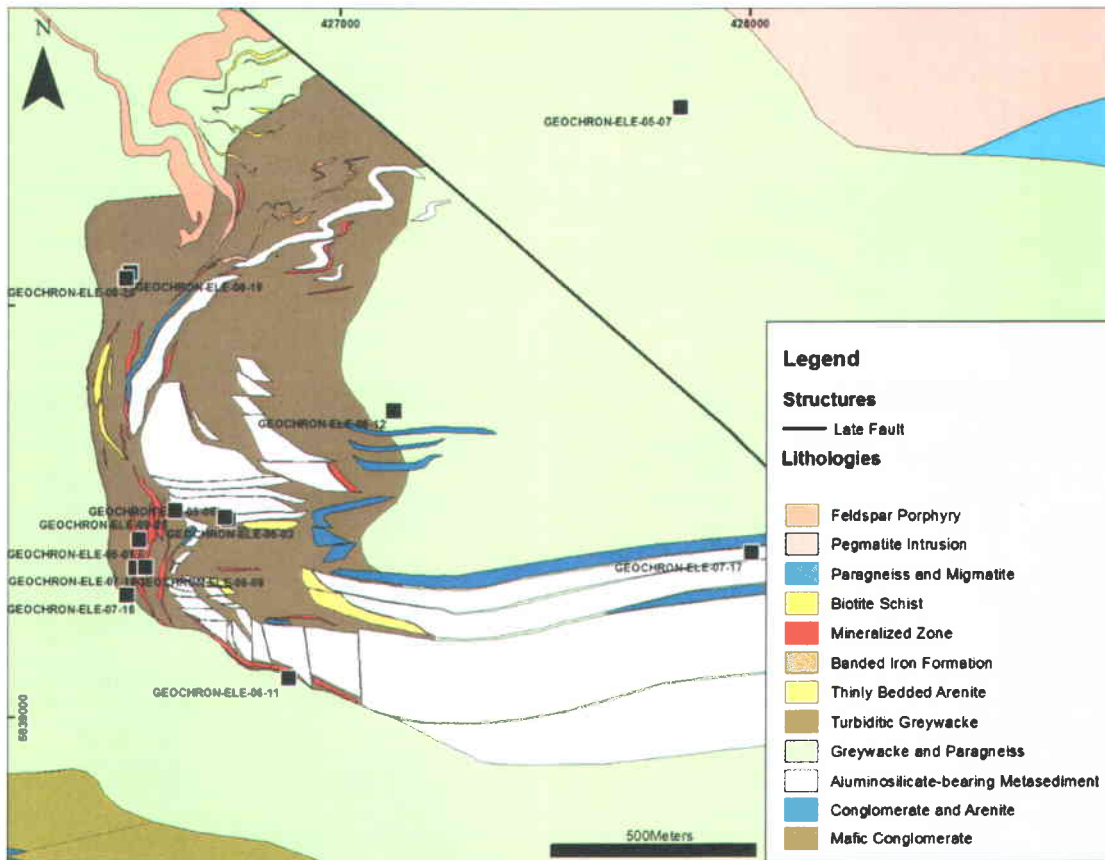


Figure 4.1.1: Map showing the location of analyzed geochronological samples in the vicinity of the Roberto deposit. Coordinates are in UTM Nad83.

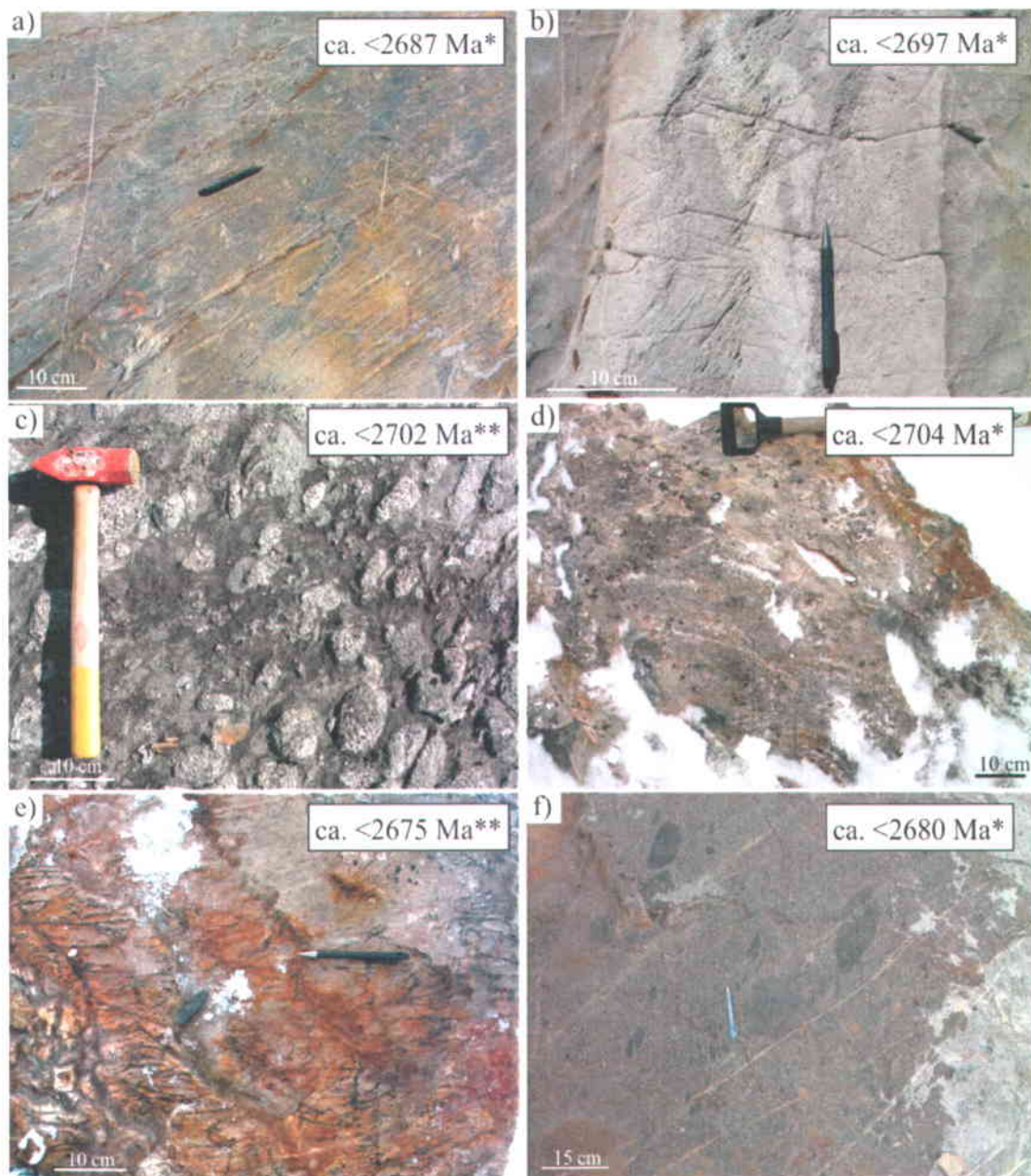


Figure 4.1.2: Photographs of selected geochronological samples in outcrops. a) Geochron-ELE-05-01: Roberto host rock (adjacent to Roberto zone). b) Geochron-ELE-05-02: Al-bearing metasedimentary rock (contains Ca-bearing replacement band). c) Geochron-ELE-05-03: conglomerate. d) Geochron-ELE-05-06: Al-bearing metasedimentary rock. e) Geochron-ELE-05-08: Roberto host rock (in Roberto zone). f) Geochron-ELE-06-12: feldspar-porphyry dyke (contains various rock fragments). *Dubé, pers. comm. (2010), **Ravenelle et al. (2010)

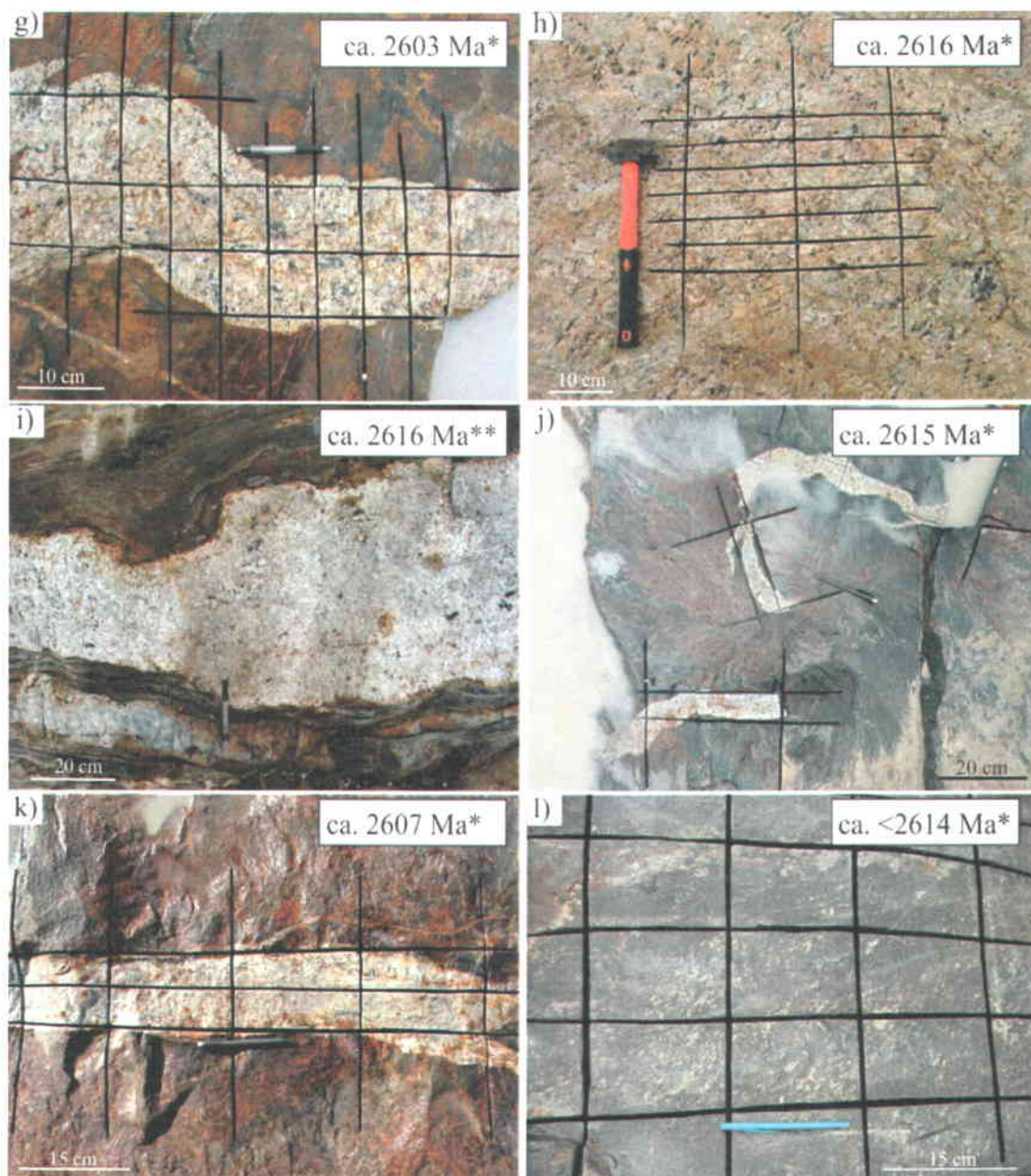


Figure 4.1.2: (continued) Photographs of selected geochronological samples in outcrops. g) Geochron-ELE-07-15: pegmatite dyke (crosscuts Roberto zone). h) Geochron-ELE-07-16: pegmatite dyke (in footwall of Roberto zone). i) Geochron-ELE-07-17: pegmatite dyke (boudinaged by D_2). j) Geochron-ELE-08-19: aplite dyke (cut by an auriferous quartz vein and folded by F_2 folds). k) Geochron-ELE-08-20: aplite dyke (crosscuts auriferous quartz vein). l) Geochron-ELE-08-21: massive greywacke (located east of East-Roberto zone). *Dubé, pers. comm. (2010), **Ravenelle et al. (2010)

4.2 Interpretation of Result

The following statements can be deduced from the geochronological work:

- The greywacke host rock of the Roberto zone, dated at <2675 Ma (Geochron-ELE-05-08), is significantly younger than the phase of the Ell Lake diorite dated at ca. 2705 Ma (David, 2005), which rules out the hypothesis that Roberto is genetically related to the dated phase of the Ell Lake intrusion.
- Crosscutting relationships between two aplite dykes (Geochron-ELE-08-19 and Geochron-ELE-08-20) and an auriferous quartz vein (Figure 3.5.71) indicate that a part of the gold mineralization was introduced between 2615 Ma and 2607 Ma.
- Movement along the East-Roberto brittle fault must have occurred prior to ca. 2603 Ma, the age of a pegmatite dyke that crosscuts the fault (Figure 3.3.21).
- The same pegmatite dyke (Geochron-ELE-07-15) also crosscuts the Roberto zone which indicates that the main stage of auriferous mineralization occurred prior to ca. 2603 Ma.
- The Roberto-East zone or the brittle fault located along its eastern limit potentially marks the contact between two greywacke sequences, as illustrated by the maximum ages of massive greywacke (ca. 2714 Ma, Geochron-ELE-09-21) and aluminosilicate-bearing units (ca. 2697 Ma, Geochron-ELE-05-02) compared to the maximum age of the greywacke that hosts the Roberto zone (ca. 2675 Ma, Geochron-ELE-05-08) (Figure 3.2.3).
- The maximum ages of paragneiss units (ca. 2685 Ma, Geochron-ELE-05-07 and ca. 2675 Ma, Geochron-ELE-06-11) are within limits of the greywacke sequence. Paragneiss and lower-grade metagreywacke sequences therefore cannot be distinguished in terms of their maximum ages.
- The presence of an aplite dyke folded by D_2 (Geochron-ELE-08-19) and a pegmatite dyke boudinaged by D_2 (Geochron-ELE-07-17) dated at ca. 2615 Ma and 2616 Ma respectively, indicates that D_2 was still active at ca. 2615 Ma, and therefore represents a much younger tectonic and metamorphic event compared to other events described in the Superior Province (Dubé et al., 2011).

5 Discussion

The discussion is based on key geological observations presented throughout the previous chapters, and targets acquiring an understanding of the geological processes involved in the formation of the Roberto deposit. The discussion is centered about the tectonic setting of the deposit, the chronology between gold mineralization and deformational/metamorphic events and magmatic phases, and the nature of its hydrothermal system. Geochronological data is also incorporated to help determine the relative timing of key geological features and constrain the absolute age of the gold mineralization. The main characteristics of the Roberto deposit are compared with other amphibolite-facies gold deposits of the Superior Province (Canada) and of the Yilgarn Craton (Australia). A speculative model of formation for the Roberto deposit is then presented.

5.1 Tectonic Setting

The tectonic setting of the Roberto deposit is not well constrained because:

- The nature of the contact between the Opinaca Subprovince and the Eastmain domain of the La Grande Subprovince is not well understood.
- The tectonic process through which the Opinaca basin formed is not well understood.
- The origin of the low-P High-T metamorphism focused around and within the Opinaca basin is not precisely known.

In order to determine the tectonic setting within which the deposit formed, those elements need to be resolved. The true nature of the contact between the Opinaca and La Grande subprovinces is challenging to study because it is obscured by large late- to post-tectonic intrusions. At least two models can be proposed to explain the presence of two adjacent terranes of different metamorphic grade: 1. the current terrane distribution is primary and reflects the original setting of the area; 2. the two terranes were juxtaposed during or after being metamorphosed. The second model requires the presence of a major late- to post-metamorphic deformation zone near the contact between the two subprovinces. Such a deformation zone was not documented in the field but could be interpreted to correspond to the discontinuity in the magnetic grain interpreted by Bandyayera et al., pers. comm. (2008) on a regional-scale airborne magnetic survey.

The geodynamic setting through which the Opinaca sedimentary basin formed is not well understood. However, similarities between the Opinaca Subprovince and the English River Subprovince of Ontario in terms of metamorphic grade and nature of protolith suggest that the Opinaca Subprovince is the eastern extension of the English River Subprovince, which is thought to represent a syn-orogenic flysch basin based on the turbiditic nature of its greywacke and the span of sediment deposition (2705 to 2698 Ma) which occurred after arc activity and close to the time of collisional orogeny (Percival, 2007). A comparative geochemical study also indicates that the geochemistry of Opinaca paragneiss is similar to the geochemistry of paragneiss found in the Quetico Subprovince (Doyon, 2004), which combined with other aspects, might indicate that the two subprovinces had similar source material (Moukhsil et al., 2003). The Quetico Subprovince is thought to represent an accretionary prism (Percival, 1989) associated with a continental arc (Moukhsil et al., 2003).

Tectonic models for the formation of the Opinaca basin need to provide an explanation for the low-P high-T metamorphism and migmatization of the sedimentary rocks. The formation of migmatite and granulite terrains requires high heat flow (Bohlen, 1991), which can be generated in various tectonic settings including convergent plate margins (e.g. Johnson, Hudson and Droop, 2003), continental extensional settings (e.g. Kruckenberg et al., 2008), and back-arc basin settings (e.g. Jones and Brown, 1990). Our current knowledge of the region does not enable to elaborate a detailed tectonic model that favors a specific tectonic process. It can be concluded, however, that the area was affected by an extended period of metamorphism and deformation. The volcanic rocks of the Éléonore property are unconformably overlain by conglomerate sequences dated at $< 2702 \pm 3$ Ma, which may imply that a tectonic uplift occurred ca. 2702 Ma. This inferred event likely marks the onset of D_1 , as it falls within the 2710 to 2697 Ma D_1 age bracket established by Moukhsil et al. (2003). By analogy with the Timiskaming conglomerates in the southern Abitibi, such conglomeratic sequences may mask important deformation zones that may have played a role in the metallogenic history of the region.

In the Opinaca Subprovince, geochronological work performed on migmatites indicates that partial melting attributed to D_2 metamorphism and deformation occurred episodically at ca. 2671 and 2647 Ma (Bandyayera et al., 2010). The fact that the main phase of deformation here attributed to D_2 affected an aplitic pegmatite dyke dated at ca. 2615 Ma (Dubé pers. comm., 2010) indicates that D_2 was still active at that time. Based on the geochronology of rutile and monazite porphyroblasts sampled in and around Roberto's mineralized zones, Dubé et al. (2011) demonstrated that the D_2 event and associated metamorphism was still active between

ca. 2620 and 2605 Ma. Geochronological work therefore indicates that D_2 was a protracted event active over an extended period of time and that prograde metamorphism episodically occurred during that time. This extended period of migmatization and high grade metamorphism is correlative with the metamorphic history of the Ashuanipi described by Guernina and Sawyer (2003) which range between 2682 and 2633 Ma.

5.2 Relative Timing of Gold Mineralization with Deformation, Metamorphism, and Magmatic Phases

The relative timing relationship between gold mineralization and deformational events is key in understanding how the deposit was formed. Field investigation of auriferous structures indicates that all veins of the main auriferous zones have been deformed by D_2 , and that all calc-silicate-bearing veins, quartz-feldspar veins, and pegmatite dykes have been deformed by D_3 . Only in one location, has our structural analysis enabled us to argue in favour of syn- D_2 ore deposition. The argument consists in the presence of a meter-scale F_2 Z-fold where Roberto's auriferous stockwork is preferentially developed in the short limb of the fold and is primarily composed of axial-planar and bedding-parallel auriferous veins and veinlets, suggesting that its formation was controlled by F_2 folding. The axial-planar veinlets define a cleavage and the bedding-parallel veins are crenulated by S_2 indicating that they have been progressively deformed upon being emplaced.

In shear zone-hosted deposits, gold mineralization can be interpreted to occur during shearing as the distribution and geometry of mineralized veins is compatible with the kinematics of the shear zone (e.g. Robert and Brown, 1986). In this instance, early veins are highly deformed while later veins may appear relatively undeformed. On the other hand, gold deposits hosted in fold hinges are commonly interpreted to have formed prior to being deformed, in relation with their primary geological setting (e.g. volcanogenic massive sulphide environment (Galley, Bailes and Kitzler, 1993)). In those cases, folding may mechanically remobilize part of the ore and control the finite geometry of the deposit, but it is not directly responsible for the genesis of the deposit. In some deposits, however, gold mineralization is interpreted to have been emplaced during deformation where folding played an active role in controlling the sites and geometry of mineralized structures. Two of the best known examples of syn-folding mineralization include the gold deposits of the Cambro-Ordovician Meguma Group in Nova-Scotia and of the Ordovician Bendigo gold field in Australia. In these two districts, gold

mineralization occurs in quartz veins distributed within doubly-plunging faulted antiforms that affect greenschist-facies (to amphibolite-facies at Meguma) turbidites, and where geochronological data indicates that the veins were emplaced during folding and faulting (e.g. Kontak et al., 1990; Ryan and Smith, 1998; Schaub and Wilson, 2002). The auriferous quartz veins of such deposits consist of bedding-parallel laminated veins, planar and sigmoidal extensional veins, and saddle reefs. The veins are primarily distributed within fold hinges and their geometry is compatible with the kinematics of folded and faulted structures. Progressive deformation buckles and reorients some of the veins, but the bulk of the veins remains relatively undeformed.

The Roberto deposit shares the following structural elements with the Meguma and Bendigo deposits:

- It is hosted within a km-scale fold hinge in turbiditic sedimentary rocks.
- Auriferous zones are chiefly confined to fold hinges.
- It contains quartz veins (also bearing other minerals) distributed along bedding planes.

There are, however, major structural differences between the Roberto deposit and the Meguma and Bendigo deposits:

- Roberto exhibits several styles of mineralization, and a large proportion of the gold mineralization occurs as replacement ore.
- The vast majority of veins are highly deformed and generally cannot be linked to folding or faulting kinematics.
- Significant shear zones containing structurally controlled veins are not documented.
- Extensional veins are present but postdate the main mineralizing event.
- No chevron folds or saddle reef structures are observed.

Based on the elements listed above, it cannot be concluded that the Roberto deposit directly formed in conjunction with D_2 . That is, the bulk of the field relationships typically suggests that auriferous bodies have been overprinted by D_2 rather than being generated during active F_2 folding. At this stage, however, it can only be concluded that the main auriferous event either occurred before or very early during D_2 . Although no significant shear zones were documented near the auriferous zones, evidence for such shear zones may have been overprinted and obscured by superimposed amphibolite facies metamorphism. The fact that high grade ore shoots are sub-parallel to deposit-scale fold axes does not prove or discard any of the

scenarios, as gold mineralization generated before folding would likely be remobilized and transposed parallel to the fold axis and stretching direction, and gold mineralization generated during folding would also bear geometrical relationships with fold axes (Marshall and Gilligan, 1993).

The mineralogy and the textures of auriferous material suggest that the veins and disseminated ore have been generated before or during peak metamorphism. Mineral assemblages within K-altered and Ca-altered rocks are dominated by minerals which are typically considered prograde. Moreover, the saccharoidal texture of quartz-feldspars-biotite-arsenopyrite-pyrrhotite assemblages in auriferous paragneiss (Figure 3.5.69d) strongly suggests that the recrystallized metamorphic texture is superimposed on pre-existing ore.

The relative timing between gold mineralization and the peak of metamorphism was more precisely determined by the SEM study performed on sulphide minerals. The study suggests that sulphide minerals had a complex metamorphic history involving prograde and retrograde reactions and that the initial arsenopyrite grains formed prior to the peak of metamorphism. The fact that metasomatic bands hosted by aluminosilicate-bearing units are ubiquitously bounded by halos where aluminosilicate porphyroblasts did not develop (Figure 3.5.44) also suggests that part of the hydrothermal system occurred before the formation of peak-metamorphic minerals. Since the metamorphic peak occurred during D_2 , the timing of the arsenopyrite and the metasomatic bands relative to the peak of metamorphism is in agreement with the pre- to early- D_2 timing established from the structural characteristics of the gold mineralization.

There is evidence that some auriferous pegmatite dykes clearly crosscut the auriferous zones and postdate D_2 , suggesting that the presence of gold in some pegmatite bodies is in part related to a contamination process that results from emplacement of dykes through mineralized material. On the other hand, the presence of pegmatite dykes that locally appear to be contemporaneous with mineralized zones and the petrogenetic continuity of pegmatite dykes with auriferous quartz-feldspar veins at depth suggests that an episode of pegmatite (aplite) magmatism dated between 2615 Ma and 2607 Ma was contemporaneous with a part of the gold mineralization. This pegmatite-related auriferous episode may represent either remobilization or a second stage of gold mineralization.

The feldspar porphyry intrusion in the northern part of the deposit and the local feldspar porphyry dykes are affected by the S_2 foliation indicating that they were emplaced before or

early during D_2 . The maximum age of a feldspar porphyry dyke at ca. <2680 Ma (Dubé pers. comm. 2009) suggests that no genetic relationship exists between the dated phases of the Ell Lake intrusion (ca. 2705 Ma) and the dated feldspar porphyry dyke. Because of the uncertainty of the age of the feldspar porphyry phase, its possible role in the genesis of the deposit remains questionable until a more accurate date is defined. A date older than 2675 Ma would indicate that the dykes were emplaced within the older sedimentary sequence. A date younger than 2675 Ma would locate this magmatic phase somewhere between the maximum age of Roberto's host rock (ca. 2675 Ma) and the auriferous pegmatite dykes (ca. 2620 Ma).

A schematic representation of the timing of selected geologic events relative to gold mineralization is presented on Figure 5.2.1. The age bracket of the D_1 deformation is challenging to constrain. The conglomeratic sequences dated at ca. 2702 Ma (Ravenelle et al., 2010) interpreted to result from a tectonic uplift related to D_1 suggest that D_1 was active at that time. The minimum age of D_1 is constrained by the age of the oldest migmatization event in the Opinaca, which is attributed to D_2 and was dated at ca. 2671 Ma by Bandyayera et al. (2010). It could not be determined whether D_1 was still active after 2675 Ma and affected Roberto's host rock, and if D_1 was associated with prograde metamorphism and/or gold mineralizing events. The age bracket of the D_2 deformation is constrained by the oldest migmatization event in the Opinaca and a post- D_2 pegmatite dyke dated at ca. 2603 Ma Dubé pers. comm. (2010). The fact that an aplitic pegmatite dyke folded by F_2 folds is dated at ca. 2615 indicates that D_2 was still active at that time.

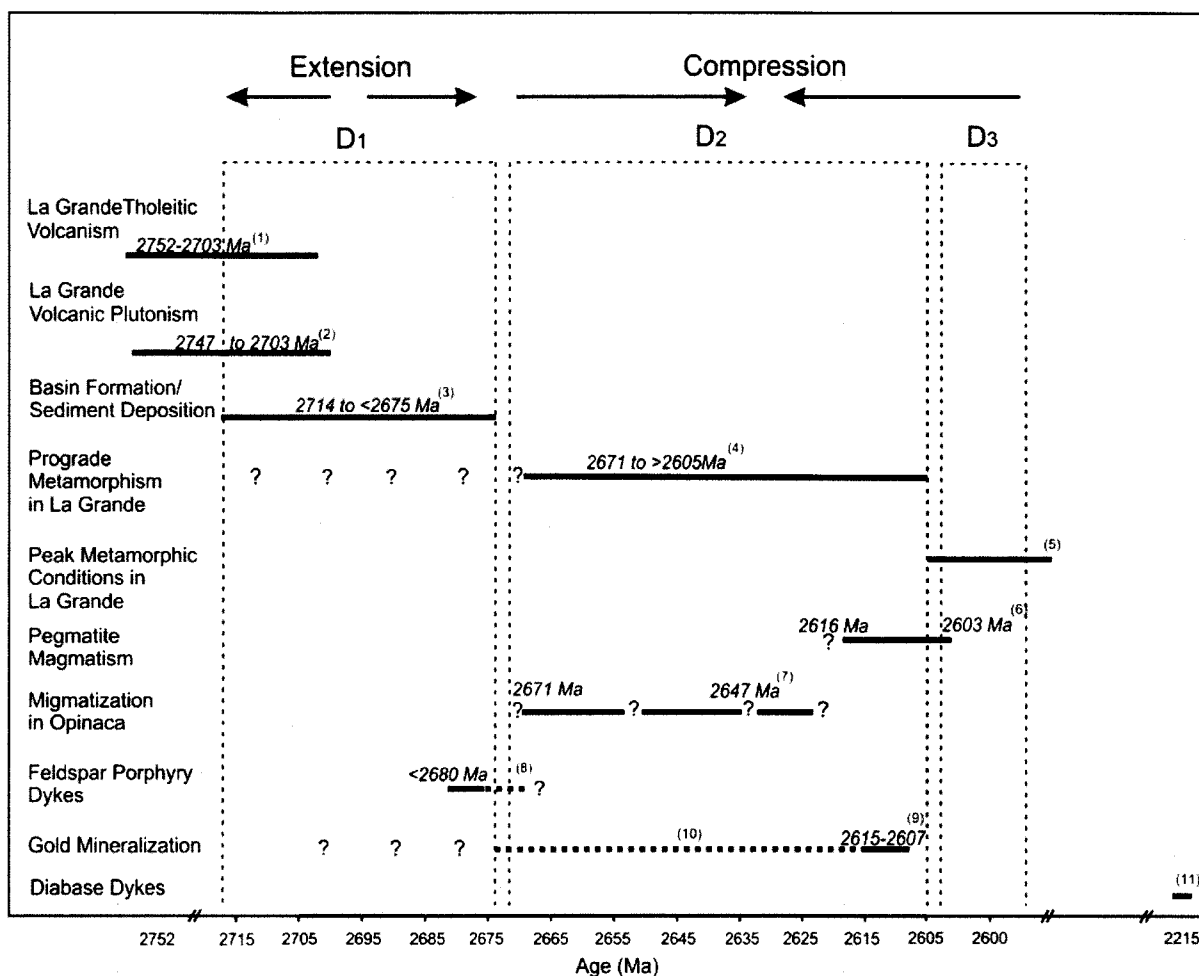


Figure 5.2.1: Schematic representation of the timing of selected geologic events relative to gold mineralization. The age brackets of the various events are constrained by: (1) the geochronology of volcanic rocks summarized by Moukhsil et al. (2003); (2) the geochronology of volcanic rocks summarized by Moukhsil et al. (2003) and the age of the Opinaca pluton (ca. 2703 Ma) from Bandyayera and Fliszár (2007); (3) the oldest and the youngest maximum ages obtained for sedimentary rocks in the vicinity of the Eleonore property (ca. <2714 Ma and <2675 Ma, respectively) from Ravenelle et al. (2010) and Dubé pers. comm. (2010); (4) the age of the onset of the migmatization in the Opinaca (ca. 2671 Ma) from Bandyayera et al. (2010) and the youngest age of D₂ metamorphic minerals obtained by Dubé et al. (2011); (5) the minimum age of D₃ (as the P-T conditions during D₃ are interpreted to be similar to the conditions of peak metamorphism attained during D₂) from a pegmatite dyke folded by F₃ folds dated at ca. 2603 Ma from Dubé pers. comm. (2010). The younger limit of D₃ is not constrained; (6) the oldest and youngest ages obtained for pegmatite dykes in the vicinity of the Roberto deposit (ca. 2616 and 2603 Ma, respectively) from Dubé pers. comm. (2010); (7) the ages of migmatite events defined by Bandyayera et al. (2010) (ca. 2671 and 2647 Ma, respectively); (8) the maximum age of a feldspar porphyry dyke in the vicinity of the Roberto deposit (ca. <2680 Ma) from Dubé pers. comm. (2010); (9) the age of a pegmatite dyke with an aplitic core cut by an auriferous quartz vein (ca. 2615 Ma) and the age of a pegmatite dyke with an aplitic core that crosscuts the same quartz vein (ca. 2607 Ma) from Dubé pers. comm. (2010); (10) the maximum age of Roberto's host rock (ca. <2675 Ma) from Ravenelle et al. (2010) and the age bracket of an auriferous quartz vein emplaced between ca. 2615 and 2507 Ma; (11) the age of diabase dykes (ca. 2216 Ma) defined by Buchan, Mortensen and Card (1993).

5.3 Structural Controls on Gold Mineralization

The Roberto zone has the characteristic of being confined to a thinly-bedded and laminated greywacke unit bounded by more massive greywacke. The presence of numerous auriferous veins emplaced parallel to bedding suggests that bedding planes played an active role in focusing hydrothermal fluids, like suggested in other gold deposits (for example at the Telfer gold deposit Australia (Goellnicht et al., 1989)). Evidence for post-mineralization folding-related slip along bedding planes, as portrayed by dragging of S_2 along bedding planes on outcrops, is ubiquitously found within the Roberto zone, but it could not be demonstrated that bedding-parallel slip occurred at a previous stage and channelized fluids. We can speculate, however, that the thin beds and laminations of the host greywacke acted as mechanically active layers and could have helped focus hydrothermal fluids.

The structural controls of the East-Roberto zone are challenging to determine since its primary structural relationships are obscured by the high level of strain superimposed on it. Nonetheless, the East-Roberto zone has the characteristic of being bounded to the east by a brittle fault, which even though shows clear evidence of post-ore displacement, may initially have served as a pathway to channel hydrothermal fluids prior to being reactivated.

At deposit-scale, the overall distribution of the main auriferous zones indicates that deposit has been folded by F_2 and F_3 folds. Regardless of the fact that the active role of F_2 folds in generating sites of gold deposition is ambiguous, there is evidence that F_2 and F_3 folds control the finite deposit-scale geometry of the main auriferous zones and the attitudes of ore shoots within those zones. The auriferous zones are confined to the F_2/F_3 refolded geometry which suggests that auriferous zones were preserved in fold hinges as opposed to being destroyed and remobilized on highly stretched limbs. The fact that the attitudes of ore shoots are sub-parallel to F_2 and F_3 fold axes also suggests that gold mineralization was transposed parallel to fold axes. As demonstrated by other researchers, folding can play an active role in remobilizing and transposing previously generated mineralization along preferred axes, typically fold axes (Marshall and Gilligan, 1993). Other examples where gold mineralization is spatially associated with F_2 and/or F_3 folds are found elsewhere in the region (e.g. Virginia Mines' Auclair property (Chapdelaine and Huot, 1997) and Eastmain Resources' Clearwater property (Cadieux, 2000; Tremblay, 2006). Targeting regions affected by large-scale folds might therefore prove to be a valuable prospecting criterion.

5.4 Nature of the Hydrothermal System

In terms of mineralogy, the Ca-bearing alteration characterized by the presence of diopside, actinolite, and clinozoisite, in association with microcline, tourmaline, arsenopyrite, and pyrrhotite share analogies with the mineralogical assemblage that characterizes the «gold-skarn» hydrothermal signature of amphibolite-facies gold deposits (e.g. Mueller and Groves, 1991) such as those found in hypozonal orogenic settings.

The early timing of gold mineralization relative to deformation and metamorphism (see section 5.2 *Relative timing of Gold Mineralization with Deformation and Metamorphism, and Magmatic Phases*) does not rule out the potential input of hydrothermal fluids originating from the breakdown of hydrous minerals during prograde metamorphic reactions. Some researchers have indeed demonstrated that different crustal levels of orogenic belts may experience prograde metamorphism at different time (Stüwe, Will and Zhou, 1993). Stüwe (1998) introduced the concept of “deep-later” and “deep-earlier” metamorphic timing relationships to classify different case scenarios where fluids released at some crustal levels may be emplaced in rocks that are on retrograde or prograde paths elsewhere in the metamorphic pile. In the “deep-later” scenario, peak metamorphism at deep levels occurs later than at shallow levels, and prograde devolatilization at depth may well be active while rocks at shallower levels are on the retrograde path (Stüwe, 1998). This scenario is relevant to many orogenic deposits where quartz vein emplacement and gold mineralization postdate the peak of metamorphism of their host rocks, but could still be related to the same metamorphic event (Stüwe, 1998). In the “deep-earlier” scenario, peak metamorphism at shallow levels occurs later than at deep levels, so that metamorphic fluids released during prograde devolatilization at depth may infiltrate shallower levels that are on their prograde path (Stüwe, 1998). The prevalence of one scenario over another is in part related to the heating mechanism. Heating associated with crustal thickening and burial of rocks to deep crustal levels will lead to “deep-later” metamorphic timing, whereas heating related to magmatic underplating from below or by magmatic intrusion in the middle of the crust will lead to “deep-earlier” metamorphic timing (Stüwe, 1998). Although the heating mechanism is not constrained at the Roberto deposit, a “deep-earlier” model could potentially explain the early timing of gold mineralization relative to deformation and metamorphism, and the fact that part of the gold mineralization dated between 2615 Ma and 2607 Ma and affected by prograde metamorphism is significantly younger than the age of the two migmatization episodes of the Opinaca dated at 2671 Ma and 2647 Ma.

The potential input of metamorphic fluids should not be ruled out on the basis that gold mineralization was introduced early relative to tectono-metamorphic events. This could further suggest that Ca-bearing veins and replacement represent metamorphosed equivalents of quartz-carbonate veins and carbonate alteration typical of orogenic deposits, respectively.

The potential input from magmatic fluids should also not be discarded. Even though geochronological data from the Ell Lake diorite and Roberto's host rocks ruled out the hypothesis that Roberto's hydrothermal system is genetically related to the Ell Lake intrusion, and even though most pegmatite dykes clearly postdate the main auriferous zones, the presence of feldspar porphyry intrusions in the vicinity of the deposit, and the presence of pegmatite dykes that locally appear to be contemporaneous with a part of the mineralization indicates that magmatic phases may have been coeval with parts of the gold mineralization. Evidence for the contemporaneity of pegmatite magmatism and gold mineralization resides in the fact that conflicting cross-cutting relationships were observed on Trench 08-10. There, a quartz vein containing visible gold and arsenopyrite cross-cuts a pegmatite dyke with an aplitic core and a similar dyke cuts across the auriferous quartz vein. Those relationships imply that auriferous quartz veins were being generated while pegmatite dykes were being emplaced, but do not necessarily require that the vein and the dykes be genetically related. However, some pegmatite dykes do appear to be cogenetic with a part of the mineralization, as some pegmatite dykes within the high grade zone intersected at depth are in petrogenetic continuity with auriferous quartz-feldspar veins. The contrasts between the various styles of gold mineralization, from early stockwork to late pegmatitic veins, may indicate that Roberto was affected by a long-lasting tectono-metamorphic event during which gold mineralization was generated, deformed, metamorphosed, and remobilized in a "deep-earlier" metamorphic setting.

5.5 Comparison with other Canadian Gold Deposits

There are several types of gold deposits in Canada. Some of the more important ones include: orogenic (greenstone-hosted quartz-carbonate vein) deposits, gold-rich volcanogenic massive sulphide deposits (Au-VMS), intrusion-related deposits, and epithermal deposits (Poulsen, Robert and Dubé, 2000). The various types of deposits are interpreted to have been generated in various parts of the crust and in different geological environments. This section reviews important characteristics of the most important deposit types and compares their attributes with the Roberto deposit.

Important characteristics of the Roberto deposit and other gold deposit types, in terms of age, host rock, alteration assemblages, sulphide minerals, mineralization style, and relative timing of gold mineralization with deformation and metamorphism, are compiled in Table 5.5.1. Since the metamorphic grade of orogenic deposits greatly influences alteration assemblages, greenschist-facies and amphibolite-facies orogenic deposits are listed separately.

Table 5.5.1: General characteristics of various types Canadian gold deposits. ¹(Dubé and Gosselin, 2007), ²(Taylor, 2007), ³(Dubé et al., 2007), ⁴(Hart, 2007), ⁵(Poulsen et al., 2000), ⁶(Ravenelle et al., 2010). GF = greenschist-facies and AF = amphibolite-facies.

Type	Age	Host Rocks	Alteration Assemblages	Sulphide Minerals	Mineralization Style	Relative Timing with Deformation	Relative Timing with Metamorphism
Orogenic (GF) ¹	Precambrian	mafic and ultramafic metavolcanic	Qtz, Fe-Carb, Sr, Cr-Mica	Py	laminated and extensional veins	syn-def.	post-peak
Orogenic (AF) ¹	Precambrian	mafic and ultramafic metavolcanic	Qtz, Bo, Amp, Di, Gr	Po, Asp	laminated and extensional veins	syn-def.	syn-peak
Epithermal ²	mainly Tertiary	volcanic and intrusive	Qtz, Sr, Ad, Al, Ss, Carb, Ba	Py, Cpy, En, Sp, Gn	veins, breccias, and replacement	pre-def.	pre-peak
Au-VMS ³	mainly Archean	felsic volcanic and volcanoclastic	Qtz, Sr, And, Ky, Prp, St	Py, Cpy, Sp, Po, Gn	massive sulphide lenses and s.w.	pre-def.	pre-peak
Intrusion-related ⁴	Cretaceous	intrusive and surrounding sed. rocks	Qtz, Felds, Mica, Sh, Di	Po, Cpy, Asp	sheeted veins	late-def.	post-peak
Non-carbonate ⁵ stockwork-disseminated	Tertiary to Archean	metasedimentary and volcanoclastic	Qtz, Sr, K-spar, Bo, Ab, Carb	Py, Cpy, Asp	stockwork, disseminated, and sheeted veins	pre-def.	pre-peak
Roberto ⁶	< 2675 Ma	metasedimentary	Qtz, Mi, Bo, Ti, Di, Amp, Cz	Asp, Po, Lo	stockwork and disseminated ore	pre- to early-def.	pre- to syn-peak

Table 5.5.2: General characteristics of selected amphibolite-facies gold deposits. ¹(Dubé et al., 2000), ²(Powell, Pattison and Johnston, 1999), ³(Mueller et al., 1996), ⁴(Bucci et al., 2004), ⁵(Neumayr et al., 1993), ⁶(Ravenelle et al., 2010), ⁷(Phillips and Nooy, 1988).

Deposit	Age	Host Rocks	Inner alteration Assemblages		Outer Alteration Assemblages	
Madsen ¹	between 2744 and 2699 Ma	mafic flows and volcanoclastic rocks	Ac, Hb, Mi, Di, Cc, Ti, Cz, Gr	Py, Po, Asp	And, Gr, Bo, St, Amp	Py, Po
Hemlo ²	> 2678 Ma	sedimentary, volcanic, and QFP	Qtz, Mi	Gn, Cpy, Sp, Rg, Or, Ch	Ky, Sil, St, Gr	
Big Bell ³	ca. 2662 Ma	mafic and ultramafic rocks	Mus, Mi, And, Sil	Py	Bo, Pl	
Chalice ⁴	2644 Ma and 2626 Ma	mafic volcanic rocks	Qtz, Ab, Di, Ti, Gr	Po, Py		
Zakanaka ⁵	between 3314 and 2950 Ma	mafic volcanic rocks	Qtz, Di, Cc, Mi, Ac, Bo	Po, Py	Bo	
Roberto ⁶	< 2675 Ma	sedimentary rocks	Qtz, Mi, Bo, Ti, Di, Amp, Cz	Asp, Lo, Po	Qtz, Ac, Ti	Py, Po

Deposit	Mineralization Style	Structural Setting	Relative Timing with Main Deformation	Relative Timing with Metamorphic Peak	Association with intrusions
Madsen ¹	stratabound, replacement and disseminated	fold hinges and high strain zones	pre or early	pre- or syn-peak	none
Hemlo ²	disseminated	shear zone	pre	pre-peak	quartz-feldspar porphyries
Big Bell ³	replacement	in foliated rocks	syn/or late ³	pre/or post ³	none
Chalice ⁴	veins and replacement	fold hinges	syn to late	syn- to post-peak	in part with a late monzogranite dyke
Zakanaka ⁵	veins	margins of locally folded ductile shear zones	syn	syn-peak	none
Roberto ⁶	stockwork and disseminated	fold hinges	pre or early	pre- or syn-peak	in part with late pegmatite dykes

The Roberto deposit shares most analogies with non-carbonate stockwork-disseminated deposits in terms host rocks, alteration assemblages, and mineralization style (Table 5.5.1). World-wide, non-carbonate stockwork-disseminated gold deposits typically form at shallow to mid-crustal depth (Poulsen, Robert and Dubé, 2000), and are not typically affected by amphibolite-facies metamorphism. The Hemlo deposit potentially represents a Canadian example of a non-carbonate stockwork-disseminated gold deposit (Poulsen, Robert and Dubé, 2000) that was subsequently metamorphosed to amphibolite facies grade (Powell, Pattison and Johnston, 1999), although according to some, the Hemlo deposit formed during active deformation (Lin, 2001). The Roberto deposit shares analogies with the Hemlo deposit in terms of host rocks, inner alteration assemblages, mineralization style (Table 5.5.2), and the deformed character of the mineralization. However, the clear spatial relationship between gold mineralization and quartz-feldspar porphyry intrusions at Hemlo (Davis and Lin, 2003), and the presence of realgar and base metal minerals like molybdenite, galena, chalcopyrite, and sphalerite (Harris, 1989) are distinct from Roberto.

Even though the Roberto deposit shares analogies with most of the deposit types listed in Table 5.5.1, it has fundamental differences from them. For example, in terms of alteration assemblages and sulphide mineralogy, Roberto is similar to amphibolite facies orogenic deposits. Laminated and extensional veins characteristic of orogenic deposits are locally present at Roberto, but unlike veins in orogenic deposits, the veins at Roberto are not hosted within a shear zone, and the geometry and distribution of the veins is not ubiquitously controlled by shear kinematics. Overprinting of amphibolite facies metamorphism may have obscured the presence of controlling shear zones near the Roberto deposit. The potassic alteration typical of epithermal deposits is locally present at Roberto, but the sulphide mineralogy, the mineral textures (colloform and crustiform veins, vuggy silica), and the style of mineralization characteristic of epithermal deposits are lacking at Roberto. Roberto also lacks massive sulphide lenses characteristics of Au-VMS deposits, and although its alteration mineralogy has similarities with intrusion-related deposit, Roberto is copper-poor and a clear genetic relationship with intrusive phases has not been demonstrated.

A clan of gold deposits classified as reduced intrusion-related gold systems (IRGS) has been characterized in the Tintina Gold Province, which extends across Yukon and Alaska (Goldfarb et al., 2005; Hart and Goldfarb, 2005; Hart, 2007). Such deposits are low grade deposits hosted within magnetite-free intrusions and surrounding rocks. When hosted in

intrusive rocks, gold mineralization occurs in sheeted and rarely stockwork auriferous quartz veins with Au±Bi±W±Te signatures locally associated with scheelite (Hart and Goldfarb, 2005). The characteristic gold-correlative Bi and Te geochemical signatures of intrusion-related mineralization are also a feature of numerous hydrothermal deposit types and thus are not distinctive (Hart and Goldfarb, 2005). When hosted in sedimentary rocks located at proximity to the causative pluton, gold occurs in association with replacement, disseminated, and fracture controlled mineralization characterized by Au-As±Sb signatures with diopside±chlorite±actinolite skarns (Hart and Goldfarb, 2005; Hart, 2007). In the more distal parts, vein assemblages contain Pb-Zn-Ag.

Roberto shares the following characteristics with IRGS:

- Sedimentary host rock (only locally for IRGS).
- Replacement, disseminated, and fracture controlled style of mineralization.
- Au-As±Sb signature locally associated with diopside, chlorite, and actinolite.

Although Roberto shares those characteristics, it bears fundamental discrepancies with IRGS including:

- IRGS are post-orogenic and occurs ~10 Ma after the peak of metamorphism (Hart and Goldfarb, 2005), whereas gold mineralization at Roberto occurred prior or early during the main deformational event and before or close to the peak of metamorphism.
- IRGS hosted in sedimentary rocks have clear genetic relationships with nearby plutons, whereas the only significant pluton documented close to Roberto, the Ell Lake diorite, has no genetic relationship since it is ~30 Ma older than Roberto's host rock (Ravenelle et al., 2010).
- Thermal gradients surrounding IRGS cooling plutons are steep, which results in concentric metal zones that develop outward for a few kilometers outside the pluton, or just beyond the thermal aureole of the pluton (Hart and Goldfarb, 2005), whereas no metal zoning has been documented in the region around Roberto and on the Eleonore property as a whole.

5.6 Comparison with other Amphibolite-Facies Gold deposits

Amphibolite facies gold deposits share analogies with greenschist facies gold deposits in terms of their structural controls, metal inventories and ore chemistry (Groves, et al., 1992,

Ridley, Groves and Knight, 2000), but their mineral assemblages commonly differ and reflect their higher metamorphic grade. Most Archean amphibolite facies gold deposits have been documented in the Yilgarn craton of Western Australia, although the biggest amphibolite facies deposit is the Kolar deposit of the Indian Shield (Ridley, Groves and Knight, 2000). Numerous amphibolite facies gold deposits have been the focus of debates regarding the source of hydrothermal fluids and the relative timing between gold mineralization, deformation, peak of metamorphism, and association with intrusive bodies (e.g. Hemlo (Ontario): (Pan and Fleet, 1992, Powell, Pattison and Johnston, 1999, Lin, 2001, Muir, 2002); Big Bell (W. Australia): (Phillips and Nooy, 1988, Kerrich and Cassidy, 1994, Mueller, et al., 1996)).

This section reviews and compares important characteristics of amphibolite-facies gold deposits in terms of mineral assemblages, absolute age of gold mineralization, host rocks, ore style, structural setting, and relative timing with deformation, metamorphism, and magmatic phases. The characteristics of five selected deposits are summarized in Table 5.5.2. These deposits include Madsen (Red Lake Ontario), Hemlo (Ontario), Big Bell (Australia), Chalice (Australia), and Zakanaka (Mt. York, Australia).

The amphibolite-facies deposit listed in Table 5.5.2, including Roberto, are all similar in terms of alteration assemblages. There are a few similarities and discrepancies in terms of mineralization style and structural settings (most of the deposits are characterized by veins and/or replacement and/or disseminated style of mineralization hosted within fold hinges or high strain zones), but key differences relate to the timing of the gold mineralization relative to deformation and metamorphism. In the case of the Hemlo deposit, although still highly controversial, it is generally accepted that although it is hosted within a shear zone (or high strain zone), the main phase of gold mineralization has recorded a large part of the strain and occurred prior to the main phase of deformation and metamorphism (Powell, Pattison and Johnston, 1999; Poulsen, Robert and Dubé, 2000; Lin, 2001) or prior to early during the main phase of deformation (Lin, 2001). At the Zakanaka deposit, the relative timing between gold mineralization, deformation, and peak of metamorphism is more tightly constrained, as the presence of deformed and undeformed shear zone-hosted veins indicates that the ore was introduced syn-deformation, and temperature estimates for vein emplacement and peak metamorphic minerals suggest that gold mineralization was synchronous with the peak of metamorphism (Neumayr et al., 1993). At Big Bell, the relative timing of gold mineralization with deformation and metamorphism is controversial. Whereas some authors state that the deposit formed early or during the main phase of deformation and metamorphism, others argue that it

formed late during the main deformational event and after the peak of metamorphism. For example, Phillips and de Nooy (1988) argue that the recrystallized texture of the mineral assemblage associated with gold mineralization at Big Bell is indicative that the gold mineralization is broadly synchronous with the peak of metamorphism, whereas Mueller et al. (1996) argue that the gold mineralization was emplaced ~80 Ma after the peak of metamorphism based on the relative geochronological ages between alteration minerals (almandine) and granodiorite dykes to which peak metamorphic assemblages are spatially related. At the Chalice deposit, detailed geochronological work provides evidence for at least two distinct stages of gold mineralization. The main stage of gold mineralization is associated with foliation-parallel quartz-albite-diopside-titanite-pyrrhotite veins, and the second stage is associated with foliation-discordant quartz-amphibole±pyroxene±molybdenite veins spatially associated with a gold-bearing monzogranite dyke (Bucci et al., 2004). Geochronological work indicates that the first stage of gold mineralization was broadly synchronous with the metamorphic peak, that the second stage of gold mineralization occurred ~20 m.y. after, and that the overall auriferous hydrothermal system lasted for up to 35 m.y. (Bucci et al., 2004). The Madsen mine is similar to the Roberto deposit in all aspects listed in Table 5.5.2 except for the nature of its host rocks and the fact that an auriferous phase associated with late pegmatite dykes is absent. The Madsen and Roberto deposits also share the fact that, although deformed and hosted in fold hinges, they are not hosted within clearly defined shear zones. The Roberto deposit, like Madsen, lacks strong evidence for syn-deformation gold emplacement and is interpreted to have formed before or early during the main deformational event (Dubé et al., 2000).

It can be concluded that although Roberto cannot easily be classified as a known deposit type, Roberto shares several attributes of amphibolite-facies gold deposit, being characterized by a protracted history, potentially two stages of gold mineralization, complex structural features, ambiguous timing of gold mineralization relative to deformational events, and skarn-like alteration assemblages.

5.7 Speculative Genetic Model

A speculative tectonic and genetic model of formation for the Roberto deposit can be elaborated based on the relative timing of relevant geological events and auriferous mineralization. As previously mentioned, the geodynamic setting of the Roberto deposit is not well constrained. The tectonic model presented herein is therefore purely speculative and only

illustrates a scenario that leads to the formation of a large sedimentary basin followed by an extended period of deformation and metamorphism.

The model involves an initial extension phase attributed to D_1 , which leads to the deposition of turbiditic greywacke and conglomerate sequences. Conglomerate units, including the one dated at ca. <2702 Ma (Ravenelle et al., 2010) are interpreted to have been deposited during that extension phase. The Ell Lake intrusion, dated at ca. 2705 Ma by David (2005) is interpreted to have been emplaced during that time. Basins that formed in extensional environments are commonly succeeded by a sag stage during which younger sedimentary rocks are unconformably deposited (Gibbs, 1984). The younger sedimentary sequence dated at ca. <2675 Ma (Ravenelle et al., 2010), which hosts the Roberto zone, could have been deposited during a late subsidence stage. Extensional environments are known to be the locus of hydrothermal activity and mineral deposits (Goodfellow and Lydon, 2007), but further work is required to determine if any auriferous hydrothermal activity did occur during that phase. However, an early stage of low grade auriferous mineralization could explain the relatively high background gold content of Éléonore's least-altered greywacke compared to other Archean sequences (Table 2.5.2). Alternatively, the gold enrichment in Éléonore's greywacke may be related to the presence of gold in diagenetic arsenopyrite, as it has been proposed for certain orogenic and Carlin-type deposits (Large et al., 2007; Large et al., 2009; Large, Bull and Maslennikov, 2011).

The extensional phase was followed by a compressive phase attributed to D_2 during which previously formed normal faults could have been reactivated as thrust faults during basin inversion. Gold mineralization is interpreted to have been introduced during this protracted large scale compressive phase, in an orogenic setting characterized by active deformation and greenschist facies metamorphism. Gold mineralization was deposited along preferable beds in the vicinity of high strain zones and faults that served as pathways for hydrothermal fluids. Minor feldspar porphyry dykes dated at ca. <2680 Ma (Dubé pers. comm., 2010) were emplaced slightly before or at the beginning of that compressive stage. Further work is required to determine the nature and provenance of Roberto's auriferous hydrothermal system and the role of the feldspar porphyry dykes. However, the gold-skarn signature of the Roberto deposit is characteristic of hypozonal orogenic deposits, which permits to speculate that Roberto's hydrothermal system may have been driven by metamorphic reactions and major high strain zones. The distribution of other gold occurrences along the contacts between the Opinaca and La Grande subprovinces (Figure 2.4.1) potentially reflects the importance of metamorphic

gradients and associated major deformation zones in generating gold deposits (Gauthier, Trepanier and Gardoll, 2007).

At deeper crustal levels, migmatites and S-Type granites formed and created high-temperature halos within which rocks were metamorphosed to amphibolite facies. Ongoing D_2 compression deformed previously-generated auriferous zones and generated new ones as pegmatite dykes were emplaced. Ongoing prograde metamorphism affected previously-generated auriferous zones and metamorphosed them to amphibolite facies. In such a scenario, the diopside-bearing quartz veins could represent the metamorphosed product of former quartz-carbonate veins. This scenario is consistent with deep-earlier settings of Stüwe (1998) described above. The Boron and arsenic signature may originate from the composition of the immediate setting, most likely from the sedimentary rocks. Auriferous zones were further cut by swarms of younger pegmatite dykes. Such dykes may represent products of partial melting that originate from the nearby migmatites, as they are distributed along the contact between the two subprovinces (Bandyayera and Fliszár, 2007). This compressive phase is interpreted to have been active between ca. 2671 Ma and 2603 Ma, the age of the oldest migmatite event in the Opinaca (Bandyayera et al., 2010) and a post- D_2 pegmatite dyke dated at ca. 2603 Ma Dubé pers. comm. (2010). During that period, a part of the gold mineralization is constrained to have occurred between ca. 2615 and 2607 Ma, the age of two aplitic pegmatite dykes that have opposite crosscutting relationships with an auriferous quartz vein. However, the typical highly-deformed character of the gold mineralization suggests that the bulk of the gold mineralization probably formed earlier.

A later compressive stage attributed to D_3 occurred at similar metamorphic conditions, and refolded all rock sequences, including the pegmatites and the auriferous zones. Subsequent deformation, by later faults and/or folds, is interpreted to have tilted the initially shallowly-plunging F_2/F_3 folded geometry to its current steep attitude, as illustrated by the drastic change in the plunge of F_3 folds on Figure 2.5.15.

6 Conclusions

- Roberto is an epigenetic gold deposit mainly hosted within an amphibolite-facies turbiditic sequence. The main phase of gold mineralization is associated with stockworks of biotite-microcline-tourmaline-arsenopyrite-pyrrhotite-bearing quartz veins and veinlets, and calc-silicate-arsenopyrite-pyrrhotite-bearing quartz veins contained within microcline-tourmaline-arsenopyrite-pyrrhotite-bearing sedimentary rocks. In terms of mineralogy, the Ca-bearing alteration characterized by the presence of diopside, actinolite, and clinozoisite, in association with microcline, tourmaline, arsenopyrite, and pyrrhotite shares analogies with the mineralogical assemblage that characterizes the gold-skarn hydrothermal signature of amphibolite-facies gold deposits such as those found in hypozonal orogenic settings.
- Roberto is affected by polyphase folding but is not hosted within a shear zone. Field observations indicate that the main part of the gold mineralization has been largely overprinted by D_2 and D_3 . Only in one specific location has our structural analysis enabled us to generate arguments supporting syn- D_2 ore deposition.
- The mineralogy and the textures of auriferous material suggest that the veins and disseminated ore have been generated before or during the peak of metamorphism, and SEM studies on sulphide minerals indicate that the latter had a complex metamorphic history involving prograde and retrograde reactions.
- Since the metamorphic peak occurred during D_2 , the timing of the main auriferous event relative to the peak of metamorphism is in agreement with the pre- to early- D_2 timing established from the structural characteristics of the gold mineralization.
- The tectonic setting of the area represents an important clue in understanding the genesis of the Roberto deposit, and even though the origin of the low-P high-T metamorphism is unknown, a "deep-earlier" type model explains the early timing of gold mineralization relative to deformation and metamorphism. Accordingly, the potential input of metamorphic fluids should not be ruled out on the basis that gold mineralization was introduced early relative to tectono-metamorphic events. This could further suggest that Ca-bearing veins and replacement zones respectively represent metamorphosed equivalents of quartz-carbonate veins and carbonate alteration typical of orogenic deposits formed at greenschist facies.

- Geochronology constrains the absolute age of the main stage of gold mineralization to occur between ca. 2675 Ma and 2603 Ma, the maximum age of Roberto's host rock and the age of a pegmatite dyke that crosscuts the main auriferous zones, respectively.
- Some of the pegmatite dykes that crosscut the mineralized zones are auriferous, which is interpreted to result from a contamination process caused by emplacement of dykes through mineralized material. Other pegmatite dykes are in petrogenetic continuity with auriferous quartz-feldspar veins, and crosscutting relationships between two aplite dykes and an auriferous quartz vein indicate that such dykes were broadly coeval with a part of the gold mineralization which occurred between ca. 2615 Ma and 2607 Ma. Pegmatite magmatism was therefore contemporaneous with at least a part of the gold mineralization and/or represents a second stage of gold mineralization.
- Even though geochronological data from the Ell Lake diorite and Roberto's host rocks rules out the hypothesis that Roberto's hydrothermal system is genetically related to the Ell Lake intrusion, the potential input from magmatic fluids in generating the main part of the gold mineralization should not be discarded, as indicated by the presence of feldspar porphyry intrusions in the vicinity of the deposit.
- The contrasts between the various styles of gold mineralization, from early stockwork to late pegmatitic veins, indicate that Roberto was affected by a long-lasting tectono-metamorphic event during which gold mineralization was generated, deformed, metamorphosed, and remobilized.
- The structural controls and relationships of the Roberto deposit are obscured by intense superimposed strain. Evidence for post-mineralization folding-related slip along bedding planes is ubiquitous in the Roberto zone, but whether or not such slip initially channelized fluids remains speculative. The East-Roberto zone has the characteristic of being distributed along a brittle fault, which even though shows clear evidence of post-ore displacement, may initially have served as a pathway for hydrothermal fluids prior to being reactivated.
- At deposit-scale, there is evidence that F_2 and F_3 folds control the finite deposit-scale geometry of the main auriferous zones and the attitudes of ore shoots within those zones. The auriferous zones are globally confined to the F_2/F_3 refolded geometry which suggests that auriferous zones were preserved in fold hinges as opposed to being destroyed and remobilized on highly stretched limbs. Other examples where gold mineralization is spatially associated with F_2 and/or F_3 folds are found elsewhere in the James Bay area (e.g. Virginia

Mines' Auclair property (Chapdelaine and Huot, 1997) and Eastmain Resources' Clearwater property (Cadieux, 2000; Tremblay, 2006).

- Targeting regions affected by large-scale polyphase folding, especially near the contact between the Opinaca and La Grande Subprovinces, might prove to be a valuable prospecting criterion.

7 References

Aucoin, M. 2008. "Métallogénie de la zone Marco, gîte aurifère Corvet Est, Baie James, Québec, Canada". M.Sc., Québec, Université Laval, 97p.

Bandyayera, D. and Fliszár, A. 2007. "Géologie de la région de la baie Kasipasikatch (33C09) et du lac Janin (33C16)". Ressources Naturelles et Faune Québec, RP 2007-05, 15p.

Bandyayera, D., Rhéaume, P., Maurice, C., Bédard, É., Morfin, S. and Sawyer, E. W. 2010. "Synthèse Géologique du Secteur du Réservoir Opinaca, Baie-James". Ministère des Ressources Naturelles et de la Faune du Québec, RG 2010-02, 44p.

Barber, J. and Yardley, B. 1985. "Conditions of high grade metamorphism in the Dalradian of Connemara, Ireland". Journal of Geological Society, vol. 142, p. 87.

Bécu, V., Ravenelle, J. F., Malo, M., Dubé, B., Gauthier, M. and Simoneau, J. 2007. "Résultats préliminaires de l'étude de la minéralisation Cu-Au-Ag de l'indice du Lac Eil et de ses implications sur la genèse du gisement d'or Roberto, propriété Éléonore, Baie James". Rapport d'étape DIVEX, 40p.

Bohlen, S. 1991. "On the formation of granulites". Journal of Metamorphic Geology, vol. 9, p. 223-229.

Bucci, L. A., McNaughton, N. J., Fletcher, I. R., Groves, D. I., Kositcin, N., Stein, H. J. and Hagemann, S. G. 2004. "Timing and duration of high-temperature gold mineralization and spatially associated granitoid magmatism at Chalice, Yilgarn Craton, Western Australia". Economic Geology, vol. 99, p. 1123-1144.

Buchan, K., Mortensen, J. and Card, K. 1993. "Northeast-trending Early Proterozoic dykes of southern Superior Province: multiple episodes of emplacement recognized from integrated paleomagnetism and U-Pb geochronology". Canadian Journal of Earth Sciences, vol. 30, p. 1286-1296.

Cadieux, A. M. 2000. "Géologie du gîte aurifère Eau Claire, propriété Clearwater, Baie James, Québec". M.Sc. thesis, Quebec City, Quebec, Université Laval, 242p.

Chapdelaine, M. and Huot, F. 1997. "Projet Auclair; rapport des travaux, Été 1997. Mines d'or Virginia". Ministère des Ressources Naturelles du Québec, GM 55428, 113p.

Cobbold, P. and Quinquis, H. 1980. "Development of sheath folds in shear regimes". Journal of Structural Geology, vol. 2, p. 119-126.

Condie, K. 1981. Archean greenstone belts. Amsterdam: 434p.

Cook, N. and Chryssoulis, S. 1990. "Concentrations of invisible gold in the common sulfides". Canadian Mineralogist, vol. 28, p. 1-16.

Couture, J. and Guha, J. 1990. "Relative timing of emplacement of an Archean lode-gold deposit in an amphibolite terrane: The Eastmain River deposit, northern Quebec". Canadian Journal of Earth Sciences, vol. 27, p. 1621-1636.

David, J. and Parent, M. 1997. "Géochronologie U-Pb du Projet Moyen-Nord". Ministère des Ressources Naturelles du Québec, GM 59903, 88p.

Davis, D. W. and Lin, S. 2003. "Unraveling the geologic history of the Hemlo Archean gold deposit, Superior Province, Canada: a U-Pb geochronological study". Economic Geology, vol. 98, p. 51.

Doyon, J. 2004. "Comparaison de la composition des roches métasédimentaires archéennes dans six bassins de la province du Supérieur : une étude géochimique et statistique". M.Sc. thesis, Chicoutimi, Quebec, Université du Québec à Chicoutimi, 214p.

Dube, B., Ravenelle, J. F., McNicoll, V., Malo, M., Creaser, R., Nadeau, L. and Simoneau, J. 2011. "The world-class Roberto gold deposit, Éléonore property, James Bay area, Quebec: insights from geology and geochronology". Geological Association of Canada Annual Meeting Abstract

Dubé, B., Balmer, W., Sanborn-Barrie, M., Skulski, T. and Parker, J. 2000. "A preliminary report on amphibolite-facies, disseminated-replacement-style mineralization at the Madsen gold mine, Red Lake, Ontario". Geological Survey of Canada, Current Research, vol. p. 14.

Dubé, B. and Gosselin, P. 2007. "Greenstone-hosted quartz-carbonate vein deposits". In W. D. Goodfellow, (ed.). Mineral Deposits of Canada: A Synthesis of Major Deposit-Types, District Metallogeny, the Evolution of Geological Provinces, and Exploration Methods. Geological Association of Canada, Mineral Deposits Division, Special Publication, 2007, p. 49-73.

Dubé, B., Gosselin, P., Mercier-Langevin, P., Hannington, M. and Galley, A. 2007. "Gold-rich volcanogenic massive sulphide deposits". In W. D. Goodfellow, (ed.). Mineral Deposits of Canada: A Synthesis of Major Deposit-Types, District Metallogeny, the Evolution of Geological

Provinces, and Exploration Methods. Geological Association of Canada, Mineral Deposits Division, Special Publication, 2007, p. 75-94

Duebendorfer, E. 2003. "The interpretation of stretching lineations in multiply deformed terranes: an example from the Hualapai Mountains, Arizona, USA". Journal of Structural Geology, vol. 25, p. 1393-1400.

Fedo, C. M., Nesbitt, W. H. and Young, G. M. 1995. "Unraveling the effects of potassium metasomatism in sedimentary rocks and paleosols, with implications for paleoweathering conditions and provenance". Geology, vol. 23, p. 921-924.

Franconi, A. 1978. "La bande volcanosedimentaire de la riviere Eastmain inferieure a l'ouest de la longitude 76 (degres) 15 (min)". Ministère des Richesses Naturelles du Québec, DPV 574, 177p.

Franconi, A. 1983. "Région de la Gorge Prosper". Ministère de l'Énergie et des Ressources du Québec, MM 82-02, 52p.

Galley, A. G., Bailes, A. H. and Kitzler, G. 1993. "Geological setting and hydrothermal evolution of the Chisel Lake and North Chisel Zn-Pb-Cu-Ag-Au massive sulfide deposits, Snow Lake, Manitoba". Exploration and Mining Geology, vol. 2, p. 271-295.

Gapais, D., Bale, P., Choukroune, P., Cobbold, P., Mahjoub, Y. and Marquer, D. 1987. "Bulk kinematics from shear zone patterns: some field examples". Journal of Structural Geology, vol. 9, p. 635-646.

Gauthier, M. and Larocque, M. 1998. "Cadre géologique, style et répartition des minéralisations métalliques de la Basse et de la Moyenne Eastmain, Territoire de la Baie James". Ministère des Ressources Naturelles du Québec, MB 98-10, 86p.

Gauthier, M., Trepanier, S. and Gardoll, S. 2007. "Metamorphic Gradient: A Regional-Scale Area Selection Criterion for Gold in the Northeastern Superior Province, Eastern Canadian Shield". SEG Newsletter

Genkin, A., Bortnikov, N., Cabri, L., Wagner, F., Stanley, C., Safonov, Y., McMahon, G., Friedl, J., Kerzin, A. and Gamyranin, G. 1998. "A multidisciplinary study of invisible gold in arsenopyrite from four mesothermal gold deposits in Siberia, Russian Federation". Economic Geology, vol. 93, p. 463.

Gibbs, A. 1984. "Structural evolution of extensional basin margins". Journal of the Geological Society, vol. 141, p. 609-620.

Goellnicht, N., Groves, D., McNaughton, N. and Dimo, G. 1989. "An epigenetic origin for the Telfer gold deposit". Econ. Geol. Monograph, vol. 6, p. 151-167.

Goldack-Airborne-Surveys. 2008. "Levé aéromagnétique sur le territoire de la Baie-James - Opinaca, sud de LG-3 et sud de LG-4 ". DP 2008-01, 50p.

Goldfarb, R., Baker, T., Dube, B., Groves, D. I., Hart, C. J. R. and Gosselin, P. 2005. "Distribution, character and genesis of gold deposits in metamorphic terranes".

Goodfellow, W. and Lydon, J. 2007. "Sedimentary exhalative (SEDEX) deposits". Mineral Deposits of Canada: A Synthesis of Major Deposit Types, District Metallogeny, the Evolution of Geological Provinces, and Exploration Methods: Geological Association of Canada, Mineral Deposits Division, Special Publication, vol. p. 163-183.

Grant, J. 1986. "The isocon diagram; a simple solution to Gresens' equation for metasomatic alteration". Economic Geology, vol. 81, p. 1976.

Gresens, R. 1967. "Composition-volume relationships of metasomatism". Chemical Geology, vol. 2, p. 47-65.

Groves, D., Goldfarb, R., Robert, F. and Hart, C. 2003. "Gold deposits in metamorphic belts: Overview of current understanding, outstanding problems, future research, and exploration significance". Economic Geology, vol. 98, p. 1-29.

Guernina, S. and Sawyer, E. W. 2003. "Large-scale melt-depletion in granulite terranes: an example from the Archean Ashuanipi Subprovince of Quebec". Journal of Metamorphic Geology, vol. 21, p. 181-201.

Harris, D. C. 1989. The mineralogy and geochemistry of the Hemlo gold deposit, Ontario. Geological Survey of Canada, Economic Geology Report 38p.

Hart, C. and Goldfarb, R. 2005. "Distinguishing intrusion-related from orogenic gold systems". 2005 New Zealand Minerals and Mining Conference Proceedings

Hart, C. J. R. 2007. "Reduced intrusion-related gold systems". Mineral Deposits of Canada: A Synthesis of Major Deposit-Types, District Metallogeny, the Evolution of Geological Provinces.

and Exploration Methods: Geological Association of Canada, Mineral Deposits Division, Special Publication, vol. 5, p. 95-112.

Hart, C. J. R. 2007. "Reduced intrusion-related gold systems". In W. D. Goodfellow, (ed.). *Mineral Deposits of Canada: A Synthesis of Major Deposit-Types, District Metallogeny, the Evolution of Geological Provinces, and Exploration Methods*. Geological Association of Canada, Mineral Deposits Division, Special Publication, 2007, p. 95-112.

Huston, D. 1993. "The effect of alteration and metamorphism on wall rocks to the Balcooma and Dry River South volcanic-hosted massive sulfide deposits, Queensland, Australia". Journal of Geochemical Exploration, vol. 48, p. 277-307.

Johnson, T. E., Hudson, N. F. C. and Droop, G. T. R. 2003. "Evidence for a genetic granite-migmatite link in the Dalradian of NE Scotland". Journal of the Geological Society, vol. 160, p. 447-457.

Jones, K. A. and Brown, M. 1990. "High-temperature 'clockwise' P-T paths and melting in the development of regional migmatites: an example from southern Brittany, France". Journal of Metamorphic Geology, vol. 8, p. 551-578.

Kontak, D. J., Smith, P. K., Kerrich, R. and Williams, P. F. 1990. "Integrated model for Meguma Group lode gold deposits, Nova Scotia, Canada". Geology, vol. 18, p. 238-242.

Kruckenberger, S. C., Whitney, D. L., Teyssier, C., Fanning, C. M. and Dunlap, W. J. 2008. "Paleocene-Eocene migmatite crystallization, extension, and exhumation in the hinterland of the northern Cordillera: Okanogan dome, Washington, USA". Geological Society of America Bulletin, vol. 120, p. 912-929.

Large, R. R., Maslennikov, V. V., Robert, F., Danyushevsky, L. V. and Chang, Z. 2007. "Multistage sedimentary and metamorphic origin of pyrite and gold in the giant Sukhoi Log deposit, Lena gold province, Russia". Economic Geology, vol. 102, p. 1233-1267.

Large, R. R., Danyushevsky, L., Hollit, C., Maslennikov, V., Meffre, S., Gilbert, S., Bull, S., Scott, R., Emsbo, P. and Thomas, H. 2009. "Gold and trace element zonation in pyrite using a laser imaging technique: Implications for the timing of gold in orogenic and Carlin-style sediment-hosted deposits". Economic Geology, vol. 104, p. 635-668.

Large, R. R., Bull, S. W. and Maslennikov, V. V. 2011. "A carbonaceous sedimentary source-rock model for Carlin-type and orogenic gold deposits". Economic Geology, vol. 106, p. 331-358.

Lin, S. F. 2001. "Stratigraphic and structural setting of the Hemlo gold deposit, Ontario, Canada". Economic Geology and the Bulletin of the Society of Economic Geologists, vol. 96, p. 477-507.

London, D. 2008. Pegmatites. M. A. o. Canada, Special Publications. Quebec: 347

Marshall, B. and Gilligan, L. B. 1993. "Remobilization, syn-tectonic processes and massive sulphide deposits". Ore Geology Reviews, vol. 8, p. 39-64.

Meinert, L. D. 1992. "Skarns and skarn deposits". Geoscience Canada, vol. 19, p. 145-162.

Mercier-Langevin, P., Daigneault, R., Goutier, J., Dion, C. and Archer, P. 2012. "Geology of the Archean Intrusion-Hosted La-Grande-Sud Au-Cu Prospect, La Grande Subprovince, James Bay Region, Québec". Economic Geology, vol. 107, p. 935-962.

Moukhsil, A. 2000. "Géologie de la région des lacs Pivert (33C/01), Anatacau (33C/02), Kauputauchechun (33C/07) et Wapamisk (33C/08)". Ministère des Ressources Naturelles du Québec, RG 2000-04, 47p.

Moukhsil, A., Legault, M. I., Boily, M., Doyon, J., Sawyer, E. and Davis, D. W. 2003. "Synthèse géologique et métallogénique de la ceinture de roches vertes de la Moyenne et de la Basse-Eastmain (Baie-James)". Géologie Québec, Ressources Naturelles, Faune et Parcs, Et 2002-06, 55p.

Mueller, A. and Groves, D. 1991. "The classification of Western Australian greenstone-hosted gold deposits according to wallrock-alteration mineral assemblages". Ore Geology Reviews, vol. 6, p. 291-331.

Nesbitt, H. and Young, G. 1982. "Early Proterozoic climates and plate motions inferred from major element chemistry of lutites". Nature, vol. 299, p. 715-717.

Nesbitt, H. and Young, G. 1984. "Prediction of some weathering trends of plutonic and volcanic rocks based on thermodynamic and kinetic considerations". Geochimica et Cosmochimica Acta, vol. 48, p. 1523-1534.

Neumayr, P., Cabri, L., Groves, D., Mikucki, E. and Jackman, J. 1993. "The mineralogical distribution of gold and relative timing of gold mineralization in two Archean settings of high metamorphic grade in Australia". Canadian Mineralogist, vol. 31, p. 711-725.

Neumayr, P., Groves, D., Ridley, J. and Koning, C. 1993. "Syn-amphibolite facies archaean lode gold mineralisation in the Mt. York District, Pilbara Block, Western Australia". Mineralium Deposita, vol. 28, p. 457-468.

Pan, Y., Fleet, M. E. and Stone, W. E. 1991. "Skarn mineralization (Cr, Fe, Au) in an Archean greenstone belt, White River Property, Hemlo area, Ontario". Economic Geology, vol. 86, p. 1626-1645.

Passchier, C. 2001. "Flanking structures". Journal of Structural Geology, vol. 23, p. 951-962.

Percival, J. A. 1989. "A Regional Perspective of the Quetico Meta-Sedimentary Belt, Superior Province, Canada". Canadian Journal of Earth Sciences, vol. 26, p. 677-693.

Percival, J. A. 2007. "Geology and metallogeny of the Superior Province, Canada". In W. D. Goodfellow, (ed.). Mineral Deposits of Canada: A Synthesis of Major Deposit-Types, District Metallogeny, the Evolution of Geological Provinces, and Exploration Methods. Geological Association of Canada, Mineral Deposits Division, Special Publication, 2007, p. 903-928

Phillips, G. N. and Nooy, D. 1988. "High-grade metamorphic processes which influence Archaean gold deposits, with particular reference to Big Bell, Australia". Journal of Metamorphic Geology, vol. 6, p. 95-114.

Poulsen, K., Robert, F. and Dubé, B. 2000. Geological classification of Canadian gold deposits. Geological Survey of Canada Bulletin 540. 106

Powell, W., Pattison, D. and Johnston, P. 1999. "Metamorphic history of the Hemlo gold deposit from Al₂SiO₅ mineral assemblages, with implications for the timing of mineralization". Canadian Journal of Earth Sciences, vol. 36, p. 33-46.

Rainbird, R., Nesbitt, H. and Donaldson, J. 1990. "Formation and diagenesis of a sub-Huronian saprolith: comparison with a modern weathering profile". The Journal of Geology, vol. 98, p. 801-822.

Ramsay, J. and Huber, M. 1987. The techniques of modern structural geology: Folds and fractures. 391

Ramsay, J. G. 1980. "Shear zone geometry: A review". Journal of Structural Geology, vol. 2, p. 83-99.

Ravenelle, J. F., Dube, B., Malo, M., McNicoll, V., Nadeau, L. and Simoneau, J. 2010. "Insights on the geology of the world-class Roberto gold deposit, Éléonore property, James Bay area, Quebec". Geological Survey of Canada, Current Research, vol. 2010-1, p. 26.

Remick, J. H. 1977. "Wemindji area (Municipality of James Bay) - Preliminary report.". Ministère des Richesses naturelles du Québec, DPV-446, 51p.

Robert, F. and Brown, A. C. 1986. "Archean gold-bearing quartz veins at the Sigma Mine, Abitibi greenstone belt, Quebec; Part II, Vein paragenesis and hydrothermal alteration". Economic Geology, vol. 81, p. 593-616.

Robert, F., Poulsen, K. H., Cassidy, K. F. and Hodgson, C. J. 2005. "Gold metallogeny of the Superior and Yilgarn". In J. W. Hedenquist, J. F. H. Thompson, R. J. Goldfarb and J. P. Richards, (ed.). Economic Geology 100th Anniversary Volume. Society of Economic Geologists, 2005, p. 1001-1033

Ryan, R. J. and Smith, P. K. 1998. "A review of the mesothermal gold deposits of the Meguma Group, Nova Scotia, Canada". Ore Geology Reviews, vol. 13, p. 153-183.

Savard, M. and Ouelette, J. F. 2005. "Technical Report and Recommendations, May 2005 Drilling Program, Eleonore Property, Québec". Mines d'Or Virginia Inc., 114p.

Schaubs, P. M. and Wilson, C. J. L. 2002. "The relative roles of folding and faulting in controlling gold mineralization along the Deborah Anticline, Bendigo, Victoria, Australia". Economic Geology, vol. 97, p. 351.

Shaw, D. 1956. "Geochemistry of pelitic rocks. Part III: Major elements and general geochemistry". Geological Society of America Bulletin, vol. 67, p. 919-934.

Simard, M. and Gosselin, C. 1999. "Géologie de la région du lac Lichteneger : (33B)". Ministère des Ressources Naturelles du Québec, RG 98-15, 25p.

Skjerna, L. 1980. "Rotation and deformation of randomly oriented planar and linear structures in progressive simple shear". Journal of Structural Geology, vol. 2, p. 101-109.

Stüwe, K., Will, T. M. and Zhou, S. 1993. "On the timing relationship between fluid production and metamorphism in metamorphic piles: some implications for the origin of post-metamorphic gold mineralisation". Earth and planetary science letters, vol. 114, p. 417-430.

Stüwe, K. 1998. "Tectonic constraints on the timing relationships of metamorphism, fluid production and gold-bearing quartz vein emplacement". Ore Geology Reviews, vol. 13, p. 219-228.

Sun, S. and McDonough, W. 1989. "Chemical and isotopic systematics of oceanic basalts: implications for mantle composition and processes". Geological Society London Special Publications, vol. 42, p. 313.

Taylor, B. E. 2007. "Epithermal gold deposits". In W. D. Goodfellow, (ed.). Mineral Deposits of Canada: A Synthesis of Major Deposit-Types, District Metallogeny, the Evolution of Geological Provinces, and Exploration Methods. Geological Association of Canada, Mineral Deposits Division, Special Publication, 2007, p. 113-139

Tomkins, A. and Mavrogenes, J. 2001. "Redistribution of gold within arsenopyrite and lollingite during pro- and retrograde metamorphism: Application to timing of mineralization". Economic Geology, vol. 96, p. 525-534.

Tomkins, A., Frost, B. and Pattison, D. 2006. "Arsenopyrite melting during metamorphism of sulfide ore deposits". Canadian Mineralogist, vol. 44, p. 1045-1062.

Tremblay, M. 2006. "Minéralisation et déformation du gîte aurifère de la zone Eau Claire, propriété Clearwater, Baie James". M.Sc. thesis, Chicoutimi, Quebec, Université du Québec à Chicoutimi, 181p.

Van Den Driessche, J. and Brun, J. P. 1987. "Rolling structures at large shear strain". Journal of Structural Geology, vol. 9, p. 691-704, IN9-IN10.

Williams, G. 1978. "Rotation of contemporary folds into the X direction during overthrust processes in Laksefjord, Finnmark". Tectonophysics, vol. 48, p. 29-40.

Wodicka, N., Lamothe, D. and Leclair, A. 2009. "Géochronologie U-Pb du Projet Ashuanipi". Ministère des Ressources Naturelles et de la Faune du Québec, GM 63858, 21p.

Yardley, B. 1989. An introduction to metamorphic petrology. 248

8 Annex 1: Mapping Techniques and Use of Three-Dimensional software

8.1 Detailed Mapping of the Large Stripped Outcrop

This study benefits from a very large stripped outcrop (100m x 400m) excavated by Opinaca Mines Ltd., which exhibits the core of the ore body (Figures 8.1.1 and 8.1.2). Using heavy machinery, the massive operation required the removal of approximately 75,000 m³ of material. Subsequent cleaning with high-pressure pumps and shovels was performed by a crew of 4 to 7 men over a period of 3 months.



Figure 8.1.1: Map showing available outcrop exposures and localization of Roberto's auriferous zones. Aerial photograph in background courtesy of Opinaca Mines Ltd. Coordinates are in UTM Nad83.

Fast, detailed, and accurate mapping of the large area was made possible by the use of highly precise Real Time Kinematic (RTK) Global Positioning System (GPS). Whereas "normal"

navigation systems have accuracy in the order of 3 meters, RTK navigation systems have sub-centimeter accuracy (http://en.wikipedia.org/wiki/Real_Time_Kinematic). The RTK GPS used in this study was the Trimble TSC1 GPS. The Trimble GPS system is composed of a fixed base station of precisely known location, and a mobile unit composed of a receiver, a controller, and a radio modem. The mobile unit communicates with the base station through the radio modem and compares its measurements with the ones received from the base station.

The use of RTK GPS was combined with ESRI ArcGIS software to adopt a modern method for mapping and cataloging geological information. The method is fast and practical and does not require the use of a grid nor digitizing tablet. A given geological feature is mapped by recording a number of points (generally at every meter or so, depending on the amount of details required) to which a specific name is given and entered in the GPS controller after each reading. For example, a point recorded along a pegmatite dyke contact could be named "Peg-A-1". Subsequent points along the same contact would then be named "Peg-A-2, Peg-A-3, etc.". Points along a different pegmatite contact would be named "Peg-B-1, Peg-B-2, Peg-B-3, etc.". Although trivial, the use of appropriate nomenclature to name points is crucial as it represents the only way of recognizing the mapped features once data points are imported in ArcGIS. On the outcrop surface, check marks are drawn where each point was taken in order to avoid re-mapping the same feature twice.



Figure 8.1.2: Bird's eye view of the large stripped outcrop that exhibits the core of Roberto's auriferous system. Photo courtesy of Peter Lauder (Opinaca Mines Ltd.).

Once imported in ArcGIS, features are digitized by connecting individual points using the alpha-numeric sequencing. Features with width less than 15 cm are drawn in "lines" shapefiles², whereas features with width greater than 15 cm are drawn in "polygon" shapefiles. Mappable features include lithological contacts, mineralized zones outline, alteration zones outline, centimeter to meter-scale veins and dykes, and structural features (e.g. brittle faults, high strain zones, etc.). Location of structural measurements and sample locations can also be recorded and are imported in "point" shapefiles. Individual shapefiles are classified as lithological units, veins/dykes, structures, samples, etc.

² In ArcGIS, a shapefile stores non-topological geometry and attribute information for the spatial features in a data set. The geometry for a feature is stored as a shape comprising a set of vector coordinates. Shapefiles can support point, line, and area (polygon) features.

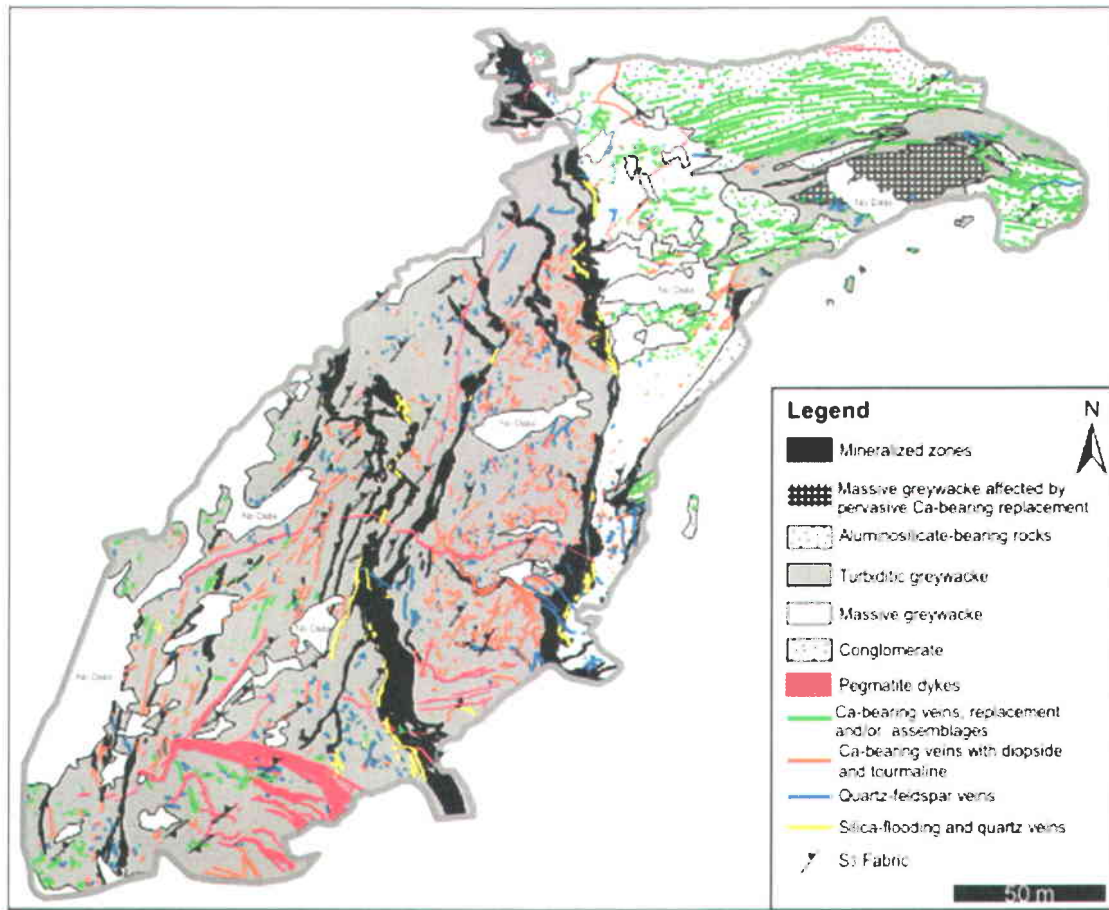


Figure 8.1.3: Detailed map of the large stripped outcrop created using RTK GPS and ArcGIS. Features are catalogued according to specific criteria, which can be utilized to create user-defined symbologies, queries, and legends.

Once digitized in shapefiles, every mapped feature is catalogued using user-defined pick-lists. The use of pick-lists ensures that a given feature is consistently catalogued with the same nomenclature. Example of information catalogued include: feature type (e.g. vein, dyke), lithology type (e.g. pegmatite, diabase), width, mineralogy (e.g. diopside-bearing), orientation (e.g. strike, dip), etc. The features can then be displayed on the map according to user-defined symbology constructed from up to three catalogued criteria. The resulting maps are detailed, accurate, and interactive since their content can easily be modified according to symbology and/or query options (Figure 8.1.3). Using query functions, different subsets of data can be displayed and/or imported into other software for analysis (e.g. Excel, stereonet software, etc.) (see *Annex 1*). The geology of the stripped outcrop will be presented in upcoming sections of this chapter.

8.2 Construction of 3D Representations

State of the art software can nowadays be utilized to maximize the use of drillcore data and construct interpretative representations of subsurface geology. Such representations are particularly useful to study the geology of ore deposits located in poorly exposed regions where a large proportion of available data is provided by diamond drilling. Using Gocad®, surfaces representing the base and top of selected lithological units and alteration facies were constructed. These surfaces were combined with 3D representations of the principal auriferous zones, constructed by Opinaca Mines Ltd., in order to provide an interpretative representation of the deposit's subsurface geology. Subsurface measurements of structural fabrics, enabled by the use of a core orienting device (Reflex ACT®), can furthermore be displayed in Gocad's 3D environment, allowing a protracted visualization of structural fabrics. This section presents the methodology used in the construction of the 3D representations. The results will subsequently be incrementally presented within various sections that treat the geology of the Roberto deposit.

8.2.1.1 *Methodology for Building Surfaces*

Gocad enables geologists to perform structural analysis and interpret the distribution of lithological units in 3D, in a similar way to what is traditionally done when tracing contacts on a 2D map. Instead of relying on interpreted parallel 2D-section views to build surfaces, this study uses a non-traditional methodology that permits construction of surfaces from direct 3D visualization of drillcore data. This method offers the advantage of exhibiting geometrical details that could not otherwise be easily noticeable on 2D-section views, specifically because of the polydeformed nature of the area. Data from 763 drill holes were used in the construction of the 3D representations. Data from holes drilled after December 2008 was not included in this study.

Before building surfaces representing the base and top of selected lithological units, some rules/assumptions were made in order to limit the degree of freedom of the interpretation and create representations that are geologically valid³. These rules/assumptions include: 1) single surfaces must not show sharp dip changes (e.g. Figure 8.1.4). 2) surfaces must not contain significant "bulls eye" regions (i.e. bulges or depressions) (e.g. Figure 8.1.4). 3) folds are only

³ To be geologically valid, a representation composed of a group of surfaces must have a geometry compatible with known geological structures (e.g. sets of planar strata, folded strata, faulted strata, etc.).

interpreted were sufficient data render their presence obvious. Surfaces that did not obey the first 2 rules were segmented into 2 or more surfaces until the rules were obeyed.

Lithological units are color-coded and painted on drill hole traces (Figure 8.1.5a). Surfaces are built in regions that respect the rules mentioned above by adding well markers on appropriate drill hole traces (Figure 8.1.5a). Well markers of a given surface are tagged with an alpha-numerical name composed of the lithology name and a given number (e.g. "AL_37" for the 37th group of well markers from which a surface will be created for an aluminosilicate-bearing unit). Surfaces can subsequently be created by using the "New Surface from Well Markers" Gocad function (Figure 8.1.5b). Surfaces created in this fashion share the same name as the group of well markers from which it was created (e.g. "AL_37_Surf"). This method allows to rapidly and easily modify the geometry of a surface if subsequently needed, by adding or removing a well marker and recreating the surface.

The resulting representation is composed of a large number of surfaces of various sizes (Figure 8.1.6a). In order to improve the cosmetic aspect of the representations, new surfaces are created from sets of parallel curves⁴ digitized on the initial surfaces (Figure 8.1.6b). This step allows filling gaps between surfaces and adding structural style to the representations (Figure 8.1.6c). The spacing between curves of a given set is generally in the order of 30 meters. This relatively short spacing better constrains the interpolation and allows generating detailed surfaces. Final surfaces are capped for cosmetic aspects (Figure 8.1.7) and generation of voxel models⁵ if subsequently needed.

⁴ Curve is the Gocad term for line.

⁵ A voxel model is composed of a multitude of cubes of a given size to which selected properties (e.g. gold content, geochemical or geophysical attributes, lithology) can be added. The distribution of these properties can subsequently be modelled through various contouring methods. Groups of surfaces must delimit « closed » volume spaces in order to allow generation of voxel models.

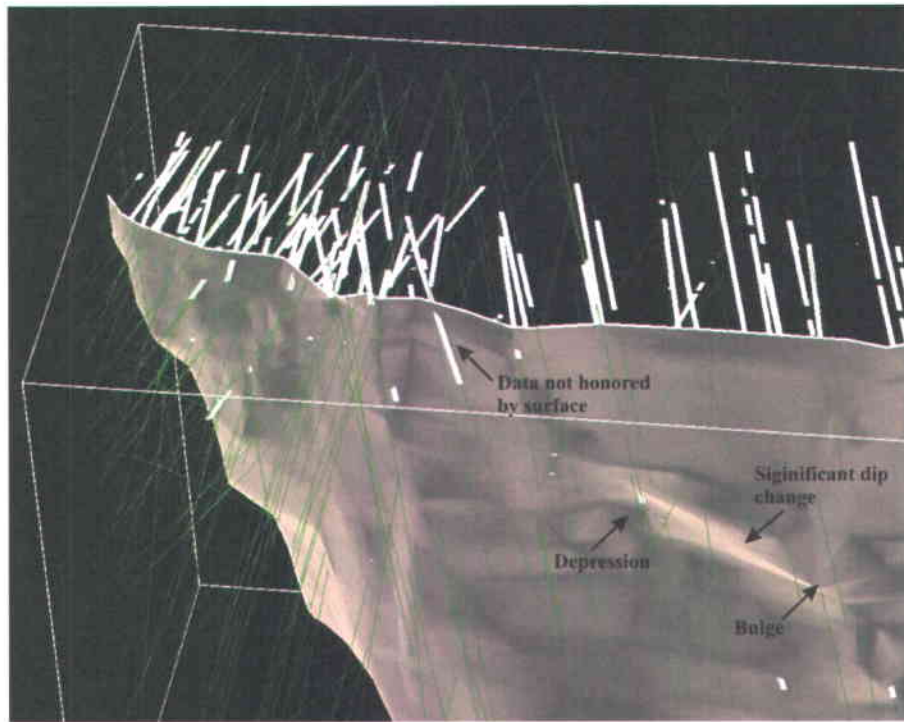


Figure 8.2.1: Gocad snapshot showing a surface with sharp dip changes and “bulls eye” regions. In these regions, the surface is not considered to be geologically valid. Surfaces created through interpolation of 2D sections views are more susceptible to have regions that do not honor the data. Width of snapshot is 500 meters.

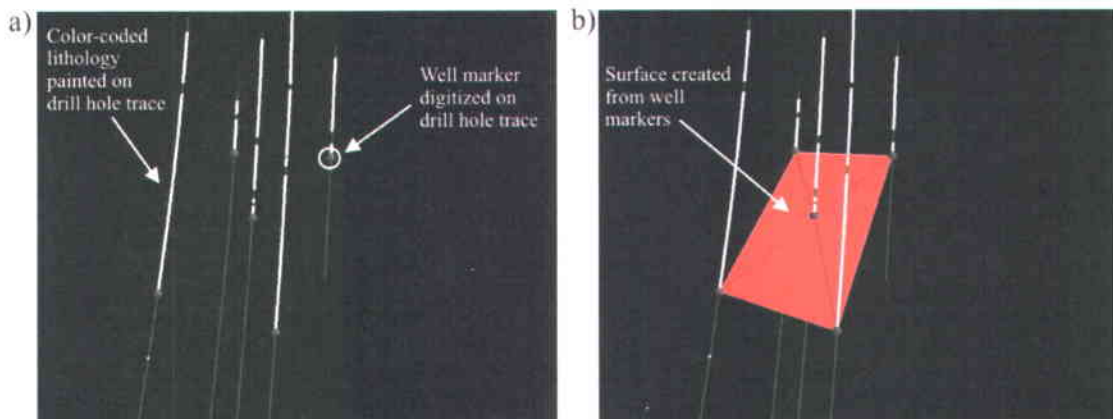


Figure 8.2.2: Gocad snapshots showing how surfaces are constructed. a) Well markers added on selected drill hole traces. b) Surface created from well markers displayed in (a). This process is done within the 3D environment and does not require the use of section or plan views.

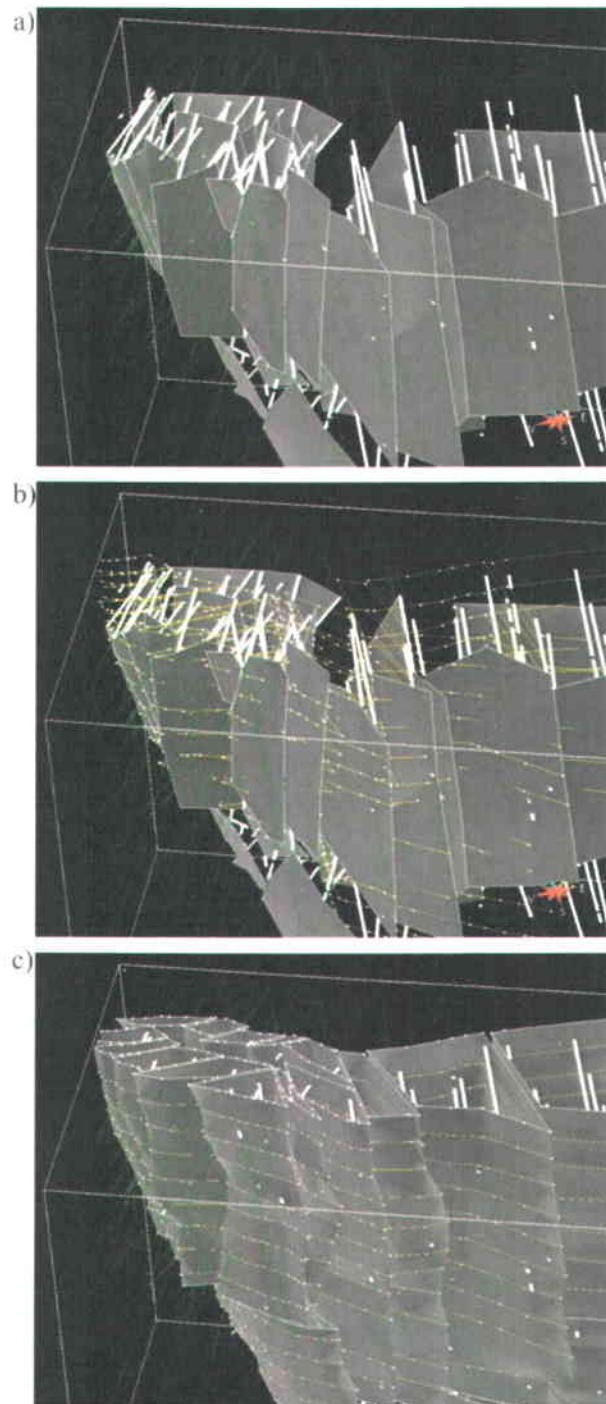


Figure 8.2.3: Gocad snapshots showing various steps of method used to generate surfaces. a) Surfaces respecting initial rules/assumptions, created from well markers. b) Sets of digitized parallel curves filling gaps between surfaces shown in (a). c) Surfaces created through interpolation of curves shown in (b). The structural style, with many faults/discontinuities, partly results from the assumptions from which the model was constructed. Geological interpretations of the discontinuities are presented in section 3.3.2 *Folds and Fold Interference at Surface*). Width of snapshots is 500 meters.

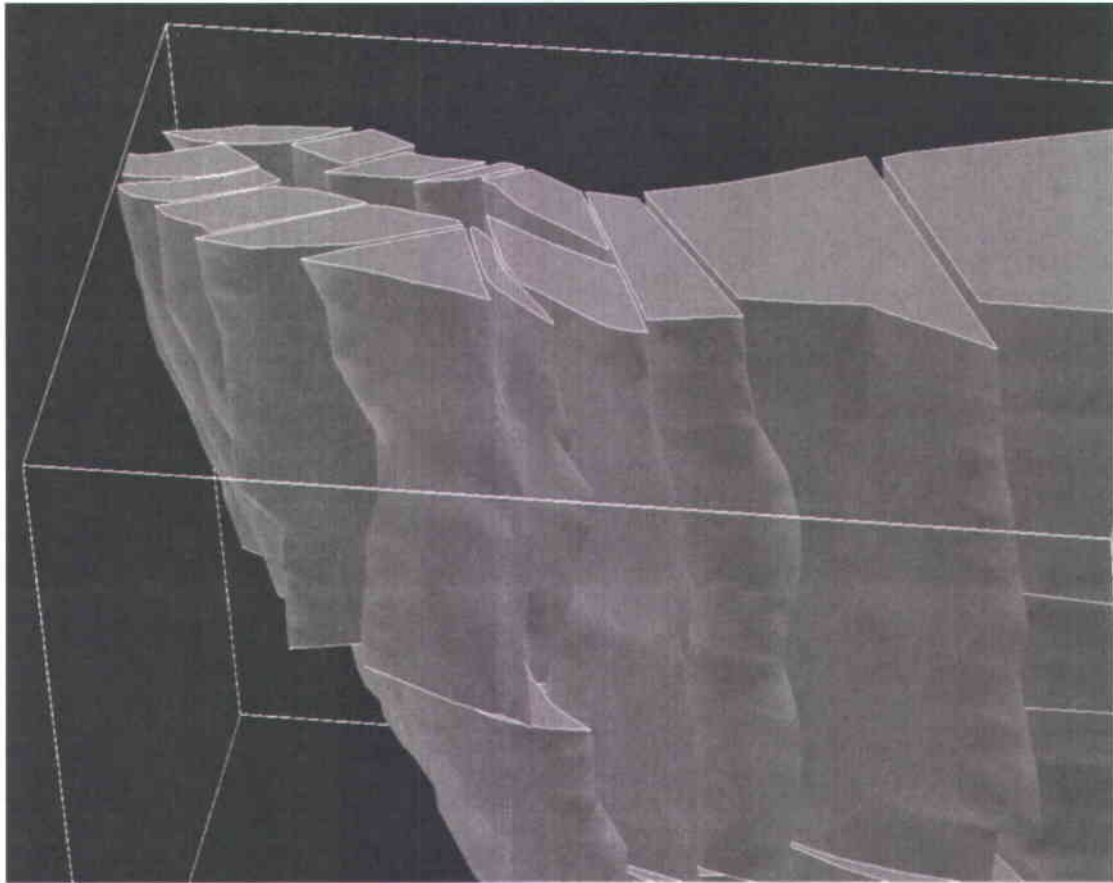


Figure 8.2.4: Final aspect of lithological surfaces created through the method elaborated in this study. Spacing between each “block” is exaggerated to prevent surfaces from crossing each other. Width of snapshot is 500 meters.

Surfaces representing the global distribution of alteration facies and dyke swarms were also created. Since the distribution of these elements is generally complex and not continuous, the surfaces represent general envelopes within which a given element is present in significant proportions (e.g. Figure 8.1.8). Such surfaces are created through interpolation of horizontal parallel curves (Figure 8.1.8). The spacing between curves of a given set is generally between 50 and 100 meters.

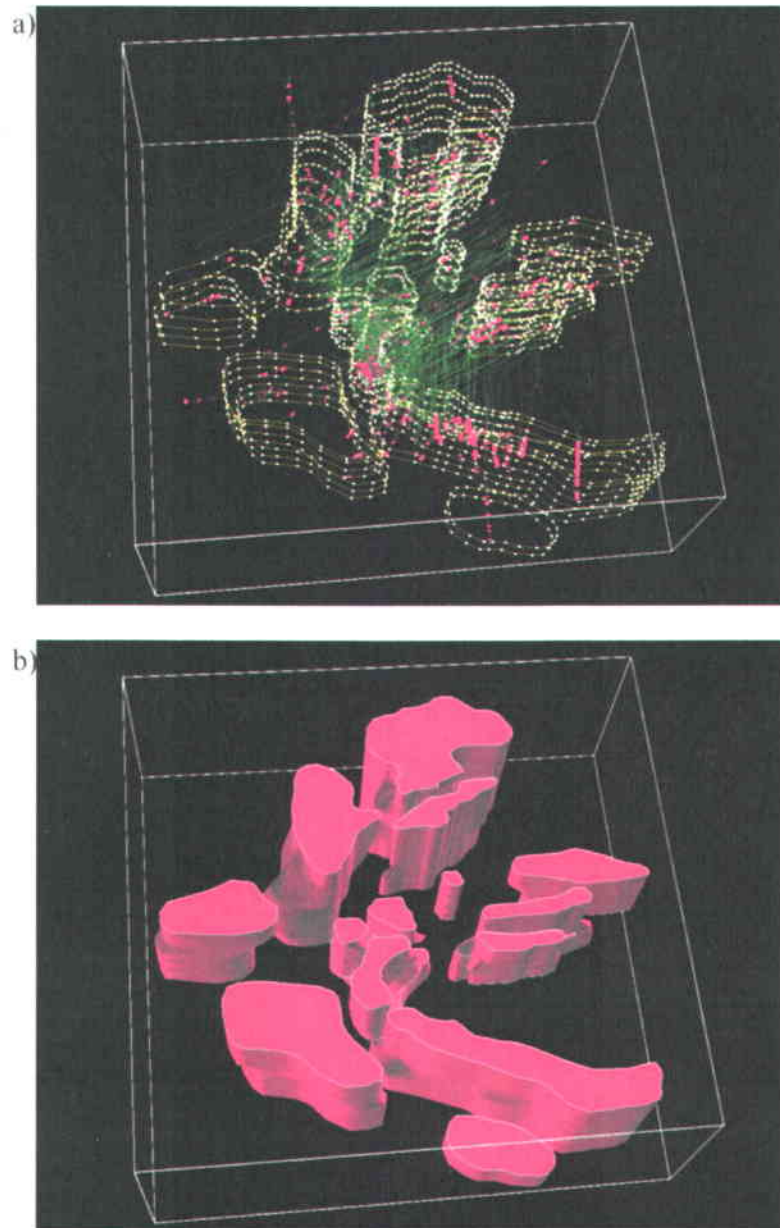


Figure 8.2.5: Gocad snapshots showing: a) Sets of horizontal parallel curves delimitating the distribution of dyke swarms (in this case pegmatite dykes). b) Surfaces created by interpolating through sets of parallel curves shown in (a). Width of snapshot is 2.5 km.

8.2.2 Visualization of Structural Data Measured on Oriented Core

To the request of Opinaca Mines Ltd., the Reflex ACT© core orientating device (Figure 8.1.9a) was used during numerous diamond drilling runs. The device uses three accelerometers to analyze the Earth's gravitational field and measure the "low side" of the core tube (side of the

core tube closest to the ground) during every minute of drilling (<http://reflexinstruments.com>). The number of minutes of a given run is recorded by the driller and is input in the device once the tool is returned to the surface. The tool performs calculations and informs the driller of the core's low side position (Figure 8.1.9b). The driller then marks the core at the appropriate location and empties out the core tube. Once out of the core tube, the core can be reassembled by fitting pieces together. Starting from the driller's mark on the core's low side, a line is drawn over the length of the fitted core which indicates the low side of the core. Knowing the position of the core's low side, geologists can measure any structural fabrics (foliation, bedding, layering, fractures, veins, dykes, etc.) by measuring " α " (angle between the plane to be measured and the core axis) and " β " (angle between the lowest (down-dip) position of the plane to be measured and the core's low side (i.e. the line previously drawn on the core) angles. These angles can subsequently be entered into software which calculates the orientation (typically in dip-direction and dip nomenclature) of the measurements.

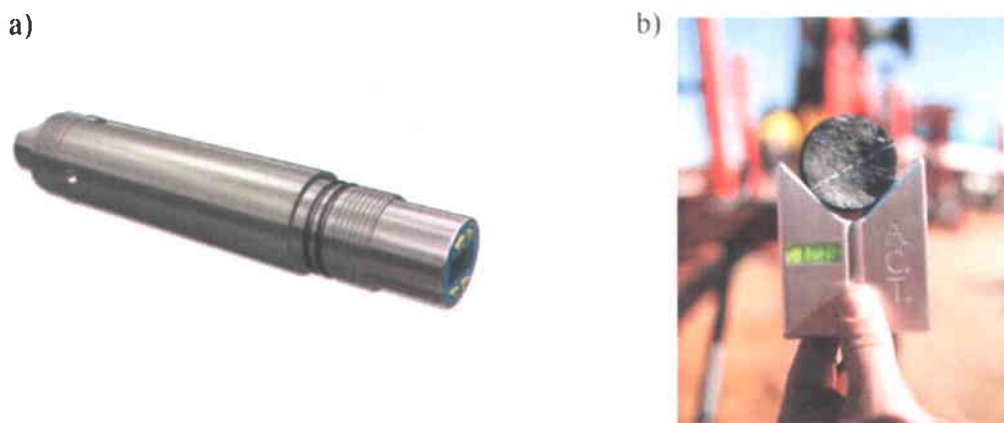


Figure 8.2.6: Photographs of : a) Reflex ACT© core orientating device. b) Oriented core onto which core's low side can be marked. (Photographs from <http://reflexinstruments.com>)

Measurements of structural fabrics on drillcore, enabled by the Reflex ACT© device, are particularly useful in regions where the deposit does not outcrop at surface. The measurements can be visualized in Gocad©, and are particularly well illustrated when using the Sparse© plug-in (e.g. Figure 8.1.10). The overall method for orientating core and measuring data on drillcore is validated by the fact that, where available, structural features measured at surface are consistent with drillcore measurements located underneath (Figure 8.1.11).

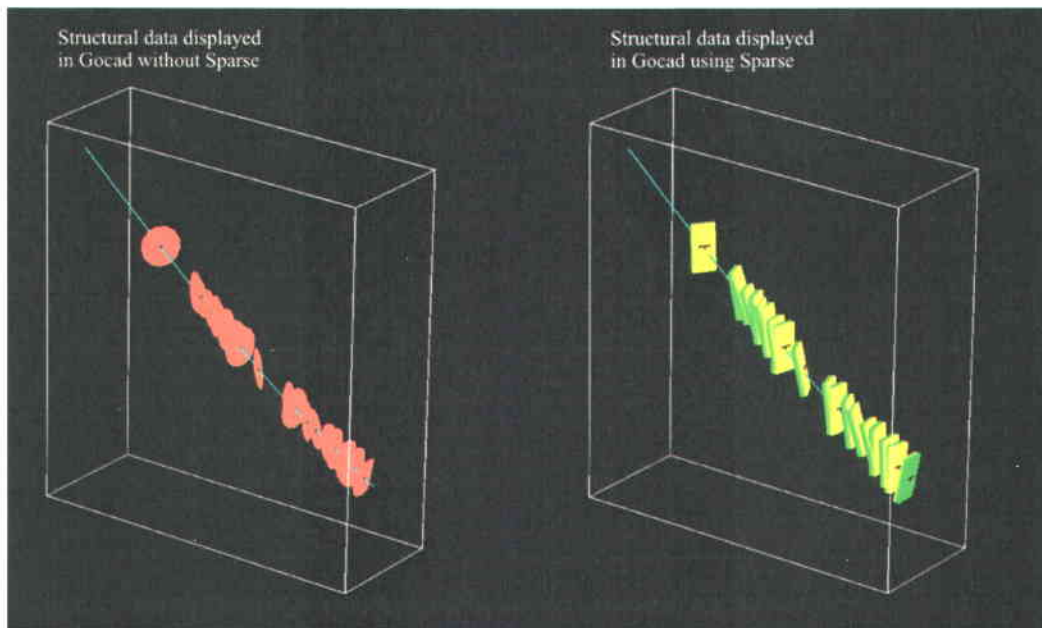


Figure 8.2.7: Gocad Snapshot showing visual aspects of structural data (e.g. foliation measurements) displayed on a drill hole trace (blue line). Measurements on the right hand side are displayed using the Sparse plug-in, which greatly enhances the visual quality of the representation. Drill hole trace is 500 meters long.

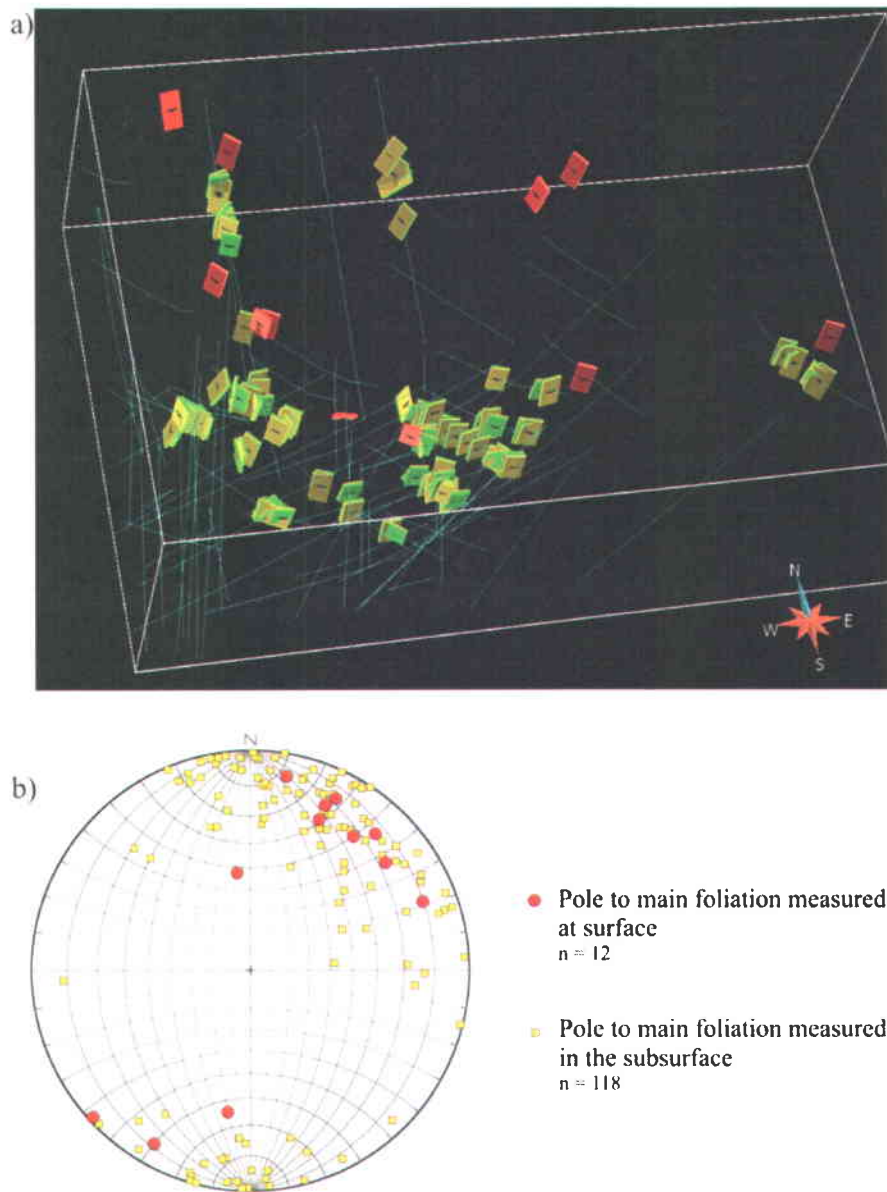


Figure 8.2.8: Figure comparing surface and subsurface structural measurements of main foliation over a selected area of the Roberto deposit. Subsurface measurements were measured on drillcore oriented with the Reflex ACT device. a) Gocad snapshot showing 3D structural tablets of foliation measurements measured at surface (red/orange) and foliation measurements measured on oriented drillcore (yellow/green). Width of snapshot is 1 km. Drillcore data shown for the first 300 meters below surface. Blue lines represent drill hole traces. b) Equal area net (lower hemisphere) showing the attitude of poles to foliation displayed in (a). The similarity between the two sets of data suggests that the overall method for orientating core and measuring subsurface data is valid.

8.3 Integration of Data to Perform Analysis and Queries

This section presents how 2D and 3D geological software can be used to maximize data analysis on multi-sourced data.

8.3.1 2D- ArcGIS

Like most GIS software, ArcGIS allows to import multi-sourced data into a common environment. Air photographs, airborne magnetic survey, topographic maps, lithological maps, and geochemical and structural data can easily be displayed and superposed on each other to visualize, interpret, and trace geological contacts.

ArcGIS also allows linking data tables to shapefiles and performing powerful queries. For example, it is possible to link an Excel spreadsheet containing geochemical results, and another spreadsheet containing petrographic characteristics, to a hand sample shapefile. Values and fields of individual tables can be modified without affecting the content of other tables, and without affecting the link that joins them. Any combinations of search criteria within any tables can be performed. In this study, up to 200 searchable fields are available to query a database of approximately 400 hand samples (including surface and drillcore samples). These fields include general characteristics of the samples (surface versus drillcore sample, lithology, alteration type, type of analyses perform on the sample, etc.), geochemical results (gold assays, major and minor elements), and petrographic characteristics (mineralogy, alteration, types of structural fabrics, etc.).

The versatility of the query engine is illustrated in Figure 8.1.12a, which shows query results for surface hand samples that are sedimentary rocks with less than 1000 ppb of gold in which microcline has been petrographically observed. Such query results can be exported into an Excel spreadsheet, which on top of containing the fields used in the definition query, contains all other fields linked to the selected samples. This means that all elemental geochemical results and all noted petrographic characteristics are included

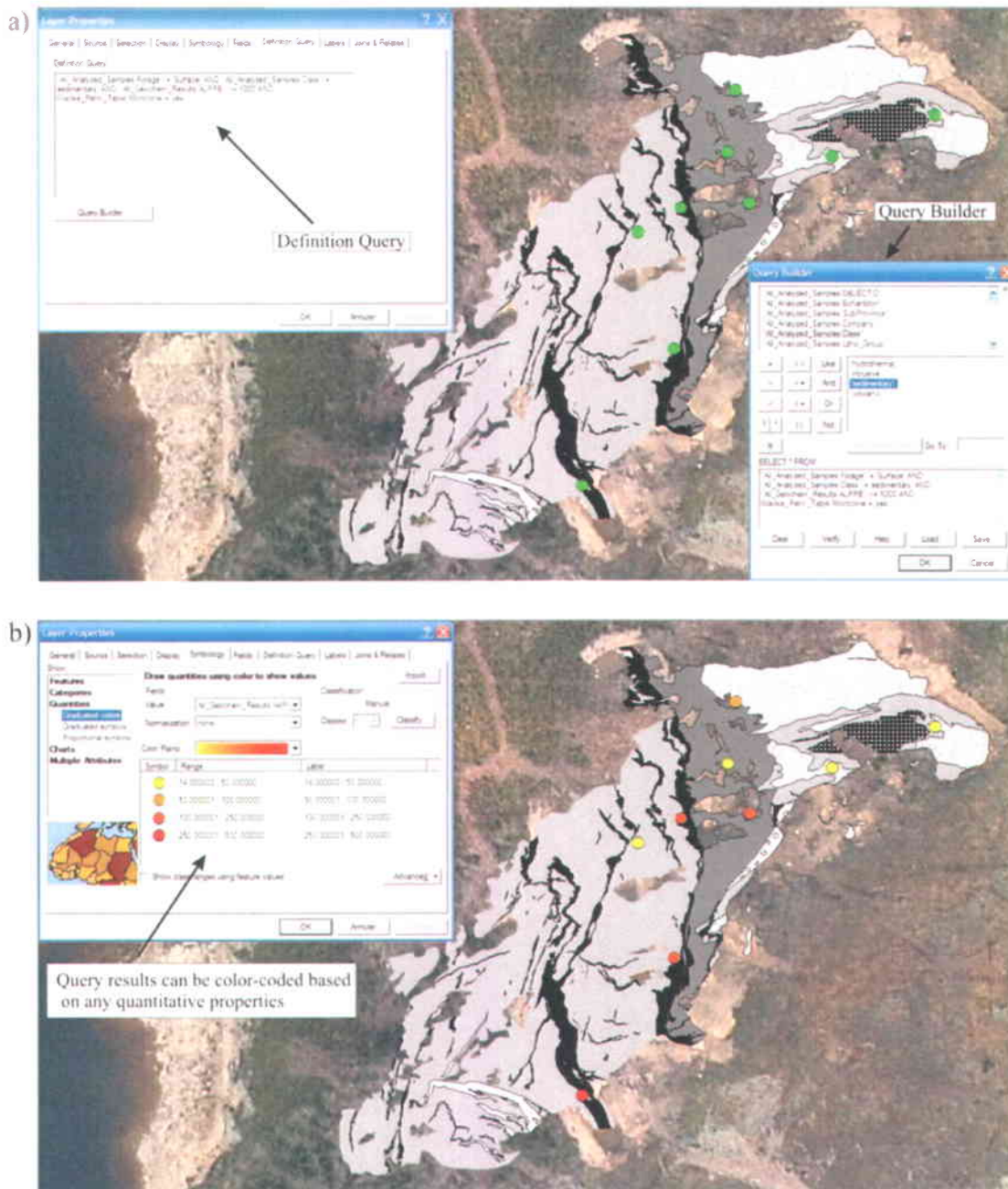


Figure 8.3.1: Views of stripped outcrop in ArcGIS showing: a) Query results (green circle) for surface hand samples that are sedimentary rocks with less than 1000 ppb of gold in which microcline has been petrographically observed. Such queries can easily be constructed using the query builder (lower right insert window) which lists unique values for all available fields. b) Query results of (a) color-coded according to their arsenic content.

in the export file. It is then possible to create graphs of any elements (for example CaO versus K₂O), for the new sample population. Moreover, it is possible to consult any other catalogued characteristics, like whether or not samples are located close to a calc-silicate vein, had microprobe work perform on them, have a thin section showing the vertical plane, etc. The same query method can be applied to structural data in order to create and display specific datasets, which can then be imported into stereonet software to perform geometrical analysis. Alternatively, data points can be graphically selected to create exportable datasets.

ArcGIS also offers the possibility to color-code shapefile objects according to quantitative properties. For example, Figure 8.1.12b displays the query results of Figure 8.1.12a color-coded according to their arsenic content. This application is particularly useful to display geochemical analyses of channel samples (e.g. Figure 8.1.13). Using the “Geostatistical Analyst” package in ArcGIS, quantitative data can also be contoured.

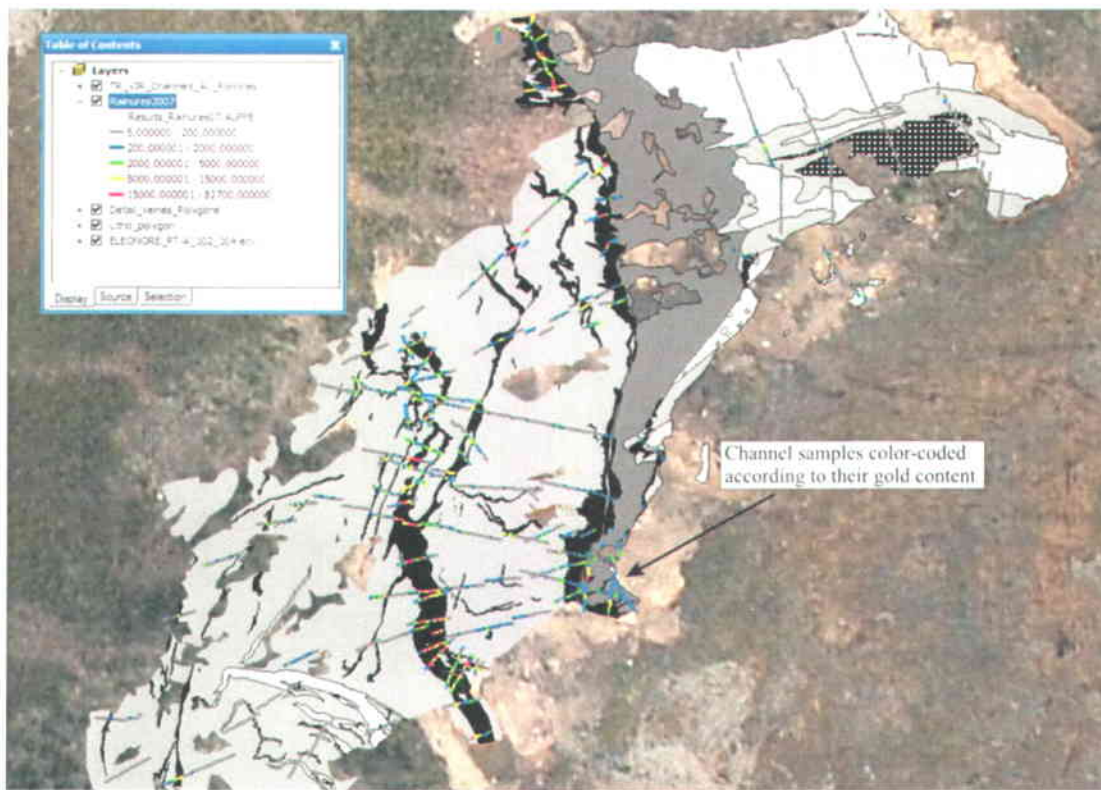


Figure 8.3.2: View of stripped outcrop in ArcGIS showing channel samples color-coded according to their gold content.

8.3.2 3D-Gocad

As previously described in section 8.2, Gocad maximizes the use of subsurface data by allowing the display of various types of drillcore information (e.g. lithological units, geochemical analyses, structural data, etc.), which greatly enhances analysis and interpretation. Surface data can also be imported and integrated to complement subsurface data. This applies to structural measurements, hand samples, 2D geological maps, magnetic surveys, etc. (e.g. Figure 8.1.14). ArcGIS and Gocad are compatible, which allows to easily export/import interpretations from one to the other.

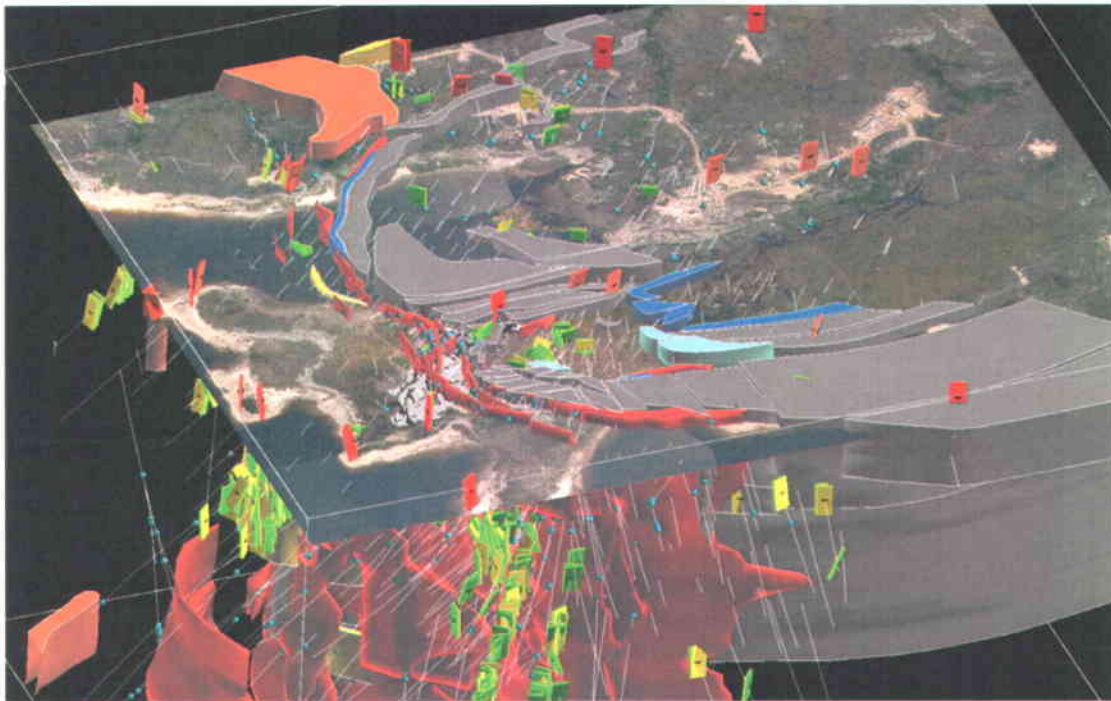


Figure 8.3.3: Gocad snapshot of the Roberto deposit showing multi-sourced data imported into Gocad's 3D environment. Colored volumes represent auriferous zones (red) and lithological units (grey, blue, pale blue, orange, yellow). Surface airphoto and geological map of stripped outcrop (pale grey/black) were moved down 30 meters to enhance the visual aspect of the snapshot. Yellow/green and red/orange tablets represent drillcore bedding measurements and surface foliation measurements, respectively. Pale blue spheres show location of gold assays greater or equal to 5 g/t gold. White lines represent drill hole traces. Width of snapshot is approximately 2 km.

Like ArcGIS, Gocad also enables to color-code objects according to quantitative properties. For example, gold assays of drillcore samples can be color-coded according to their gold content. Simple queries on objects properties can also be performed, but their usefulness is limited unless the GIS3D package is added. Although not used in this study, GIS3D allows

performing powerful queries, and has been successfully utilized to generate drilling targets in other ore deposits.

Gocad contains many useful functions to analyze data, like the possibility to display structural data on stereonets, to create plan and section views at any depth and location, to display geochemical analyzes on drill hole traces, and to create logs showing various properties of individual drill holes (e.g. Figure 8.1.15). Using voxel models, Gocad also enables modeling of selected properties, like contouring gold assays in 3D, and performing geophysical inversions. In this study, Gocad was primarily used to investigate the structural geology of the deposit.

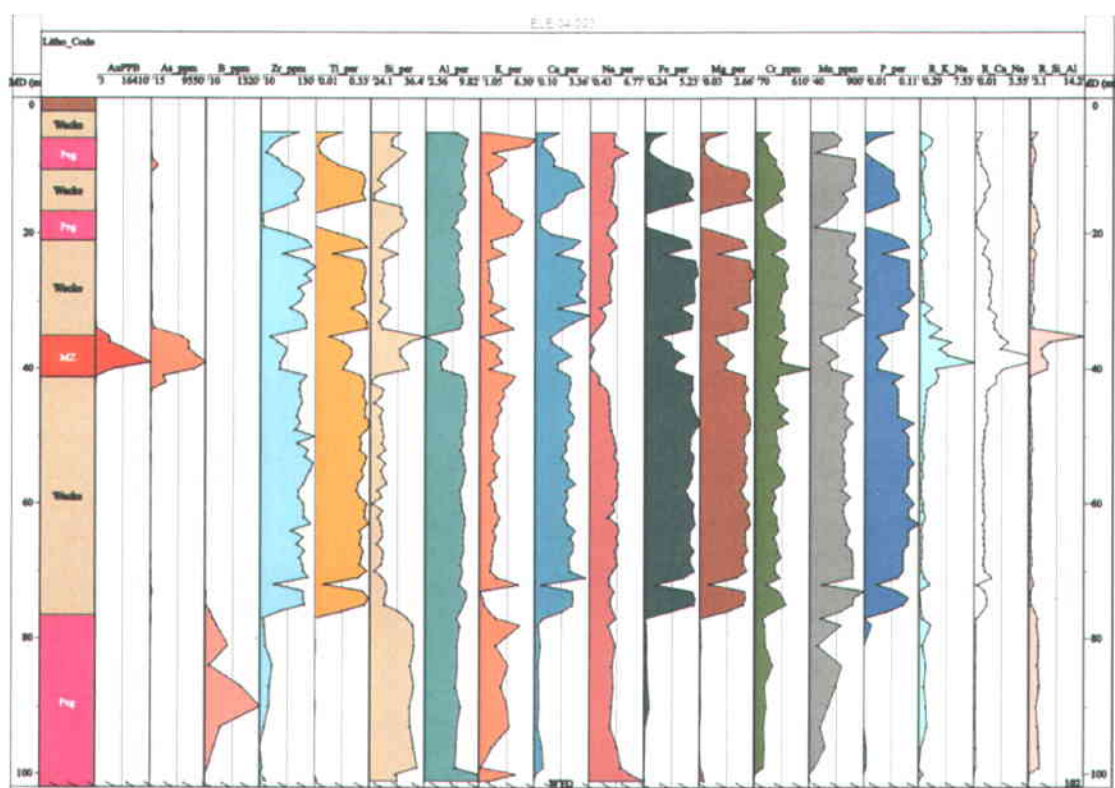


Figure 8.3.4: Example of a drill hole log created in Gocad showing variations of selected major elements with depth.

9 Annex 2: Detailed Map of the Large Stripped Outcrop

Figure 9.1.1: Detailed map of the large stripped outcrop showing distribution of lithological units, veins, and structural features. Coordinates are in UTM Nad83.

